University of Oxford

Department of Chemistry



Synthesis and characterisation of mineral-derived and hybrid layered double hydroxides

Wing Lam Joyce Kwok

Balliol College

Trinity Term 2020

This thesis is submitted in partial fulfilment of the requirement for the degree of Doctor of Philosophy at the University of Oxford

Preface

The work described in this thesis was carried out in the Chemistry Research Laboratory at the University of Oxford between October 2016 and March 2020 under the supervision of Professor Dermot O'Hare. All the work was performed by the author unless otherwise stated and no part has been previously submitted for any other degree.

Part of the work contained in this thesis has been published in the following journal papers:

W.L.J. Kwok, D.-G. Crivoi, C. Chen, J.-C. Buffet and D. O'Hare. *Dalton Trans.* 2018, 47, 143–149.

W.L.J. Kwok, H. Suo, C. Chen, J.-C. Buffet and D. O'Hare. *Manuscript submitted*.

Abstract

Synthesis and characterisation of mineral-derived and hybrid layered double hydroxides

Wing Lam Joyce Kwok **DPhil Thesis**

Balliol College **Trinity Term 2020**

This thesis discusses the development of atom efficient and scalable synthesis methods for the synthesis of industrially relevant layered double hydroxides (LDHs) using a green source of magnesium derived from a waste mineral. LDHs are introduced in Chapter 1 as compositionally flexible and versatile anionic clays. The structure of LDHs confers unique and interesting properties to these inorganic compounds and as such, LDHs have found application in a wide range of applications including environmental remediation and drug delivery. Naturally occurring LDHs are low in abundance but synthetic LDHs are facile to prepare and a variety of methods are available. The growing global demand for energy and resources calls for changes in the supply chain, so there is increasing interest in technologies and methods that are more environmentally friendly.

The analytical techniques and synthetic methods used are detailed in Chapter 2 ahead of the results and discussions in subsequent chapters. In Chapter 3, the mineral struvite, $MgNH_4PO_4.6H_2O$, is investigated as an alternative starting material for magnesium based LDHs. Struvite was acquired from wastewater treatment plants (WWTPs) and compared with a synthetic struvite. To transform this underutilised resource into commercially relevant LDHs, the effect of temperature, pH and time were investigated. The properties and morphologies of the LDHs synthesised from struvite have been characterised in detail by a number of techniques including surface area analyses and electron microscopies.

Silica@LDH hybrid materials are investigated in Chapter 4. The effects of stirring speed and metal solution addition rate were systematically investigated and optimised. Strategies for core-shell synthesis using commercial silicas have also been developed to prepare high surface area silica@LDH hybrid materials that have been used as catalyst supports for ethylene polymerisation.

In Chapter 5, the thermal properties of the mineral-derived and hybrid LDH materials are studied to probe their suitability for carbon dioxide (CO_2) capture. The LDHs were calcined to obtain the mixed oxide form of LDHs, layered double oxides (LDOs), and the properties of these calcined materials at different temperatures were studied. Selected LDOs were tested in CO_2 adsorption experiments and their performance has been compared to that of LDOs from commercial and conventional LDHs.

Lastly, the findings of the works in this thesis are summarised in Chapter 6 and avenues for future investigations are also proposed. Supplementary information and data mentioned in the main thesis are included in the Appendices.

Acknowledgements

Almost a decade has passed since I first step foot in Balliol to meet Dermot, Rachel and William, and if you had told me then where I would be in 2020, I would have laughed and brushed it off as some wild aspiration that only a fictional version of me would achieve. And yet, here I sit, concluding my time in Oxford by reflecting on the journeys I have been on in the last nine or so years, and the people who have been integral in those times, that have transformed me from a sickly teenager to a more robust human.

To Dermot: thank you for being an incredibly supportive and inspiring tutor and supervisor. It was a privilege to join your group and I am very grateful to have had the opportunity to work for you. I would also like to thank SCG Chemicals Ltd. for funding this DPhil and providing me with a valuable insight into the chemical industry.

This thesis would not have been possible without the generosity of JC, who has probably read enough about struvite and core-shell to last several lifetimes. I am immensely grateful for your support. My thanks go to Dana who supervised me for some of my DPhil. Your tutelage was excellent and it was a pleasure to work alongside you. Thank you Chunping, the fountain of LDH knowledge, for helping me decipher many graphs and overseeing my work – your guidance is priceless. Thank you to Katarina and Tom who have been awesome tute partners and then lab colleagues. It has been great to explore LDHs with you Katarina, and I am excited to follow your career in baking! The O'Hare group has been such a great place to work and I would like to thank all group members, past and present, for making it so. In particular, I would like to thank (chirpy) Phil and Justin for bringing to life my alter ego Pints of Wine.

My acknowledgements would not be complete without thanking my friends and teammates. Ultimate has been a turning point for my mental and physical health, so I will always be grateful that my sister Karen introduced me to the sport, and that the university ultimate team took me in and became my friendship group. I would like to thank the following lovely humans in particular: SJ, Christine, Noémi, and Cathryn. I hold dear countless memories of our Oxford days together and I am so grateful to have gotten to know you all off the pitch. I am humbled by how generous you all are: even when I did not voice my troubles you were able to support me unconditionally, and that is an unmeasurable degree of kinship.

Finally, to Matthew and my loving family, thank you for your endless love, support and encouragement. Without you, these acknowledgements would never have taken place. I treasure each of you dearly and it goes beyond words how grateful I am for you all. It is with sadness that my incredible granny was not able to see me complete this degree, but it is with the strength that she taught me that I am able to conclude my time at Oxford with additional letters to my name.

Nomenclature

Below is a summary of commonly used terms and abbreviations in this thesis.

ºC	Degrees Celsius
Å	Angstrom (10^{-10} m)
AIM-LDH	Aqueous immiscible organic layered double hydroxide
AMO-LDH	Aqueous miscible organic layered double hydroxide
AMO-SLDH	Aqueous miscible organic struvite layered double hydroxide
AMOST	Aqueous miscible organic solvent treatment
BDL	Below detection limit
BET	Brunauer-Emmett-Teller
BJH	Barrett-Joyner-Halenda
CDL	Crystallite domain length
c-LDH	Conventional (water-washed) layered double hydroxide
CO_2	Carbon dioxide
D.I. water	Deionised water
DFS-echo	Double-frequency sweeps before Hahn echo
DPMAS	Direct polarisation magic angle spinning
dTGA	First derivative of thermal gravimetric analysis curve
EtOH	Ethanol
FTIR	Fourier Transform infra-red
FWHM	Full width at half maximum

g	Gram
GHG	Greenhouse gas
h	Hour/hours
HPDEC	High power decoupling
HR-SEM	High resolution scanning electron microscopy
ICP-MS	Inductively coupled plasma mass spectrometry
LDH	Layered double hydroxide
LDO	Layered double oxide
MMO	Mixed metal oxide
mmol	Millimol (10^{-3} mol)
NaOH	Sodium hydroxide
ppm	Parts per million
rpm	Revolutions per minute
SEM	Scanning electron microscopy
SEM-EDX	Scanning electron microscopy energy-dispersive X-ray spectroscopy
SLDH	Struvite layered double hydroxide
SLDO	Struvite layered double oxide
ssNMR	Solid state nuclear magnetic resonance
TEM	Transmission electron microscopy
TGA	Thermogravimetric analysis
WWTP	Wastewater treatment plant
XRD	X-ray diffraction

Table of contents

Chapter 1: Introduction 1

1.1 Layered double hydroxides (LDHs) 1

1.2 Applications of LDHs 7

1.2.1 Anion exchange 7

1.2.2 Adsorption 9

1.2.3 Catalysis 11

1.3 Synthesis of LDHs 13

1.3.1 Co-precipitation 14

1.3.2 Urea hydrolysis 16

1.3.3 Reconstruction 17

1.3.4 Reverse micelle 17

1.4 Post-synthesis modifications of LDHs 19

1.4.1 Delamination of LDHs 19

1.4.2 Aqueous miscible organic solvent treatment (AMOST) 20

1.5 Green alternatives to traditional LDH synthesis methods 22

1.5.1 Green chemistry 22

1.5.2 Mechanochemical 23

1.5.3 Microwaves 25

1.6 Green reagents for LDH syntheses 26

1.6.1 Bases 26

1.6.2 Metals 27

1.6.3 Circular economy 29

1.6.4 Circular economy – an example from biofuels....30

1.7 Thesis overview....34

1.8 References....35

Chapter 2: Experimental details....42

2.1 Analytical techniques for characterisation....42

2.2 Experimental details for Chapter 3....46

2.2.1 Materials....46

2.2.2 Synthesis of struvite LDH (SLDH): Method 1 (M1)....46

2.2.3 Synthesis of SLDH: Method 2 (M2)....48

2.2.4 Decomposition of struvite in alkali....50

2.2.5 Synthesis of zinc SLDH....51

2.2.6 Synthesis of aqueous miscible organic SLDH (AMO-SLDH)....52

2.2.7 Synthesis of conventional LDH (c-LDH)....53

2.3 Experimental details for Chapter 4....54

2.3.1 Materials....54

2.3.2 Synthesis of silica (modified Stöber method)....54

2.3.3 General synthesis procedure for core-shell SiO_2@Mg_2Al-CO_3-AMO-LDHs (*in situ* co-precipitation)....54

2.3.4 Synthesis of SiO_2@Mg_2Al-CO_3-AMO-LDHs using commercial SiO_2 55

2.4 Experimental details for Chapter 5....58

2.4.1 Materials....58

2.4.2 Thermal treatment of SLDHs and SiO_2@LDHs....58

2.4.3 Synthesis of reference LDHs....58

2.4.4 Carbon dioxide adsorption....60

Chapter 3: Development of mineral sources for LDH syntheses 61

3.1 Introduction 61

3.1.1 Struvite – magnesium ammonium phosphate ($MgNH_4PO_4.6H_2O$) 61

3.1.2 Properties of struvite 63

3.2 Atom efficient syntheses of LDHs from struvite 65

3.2.1 Method 1 (M1) 65

3.2.2 Method 2 (M2) 75

3.3 Study of the transformation of struvite to LDH 85

3.4 Synthesis of SLDHs containing zinc 96

3.4.1 Introduction 96

3.4.2 Preparation of Zn_2MgAl-SLDH 97

3.5 Aqueous miscible organic solvent treatment (AMOST) of SLDHs 103

3.6 Study of struvite from wastewater treatment plants (WWTPs) 108

3.7 Preparation of SLDH from WWTP struvite 119

3.8 Conclusion 128

3.9 References 129

Chapter 4: Core-shell silica@layered double hydroxide hybrid materials 132

4.1 Introduction 132

4.2 Variation of stirring speed 135

4.3 Variation of metal addition rate 147

4.4 Synthesis of SiO_2@AMO-LDHs using commercial silica 152

4.4.1 Commercial SiO_2 152

4.4.2 Commercial SiO_2@LDH preparation 155

4.5 Preliminary synthesis of core-shell SiO_2@SLDH from struvite 179

4.6 Conclusion 186

4.7 References 187

Chapter 5: Calcined materials and applications 188

5.1 Introduction 188

5.1.1 Climate change 188

5.1.2 Carbon capture 188

5.1.3 Capturing CO_2 with inorganic materials 190

5.2 Calcination of LDH-based materials 192

5.2.1 Calcination of core-shell SiO_2@Mg_2Al-CO_3-AMO-LDHs 192

5.2.2 Calcination of SLDHs 198

5.3 CO_2 adsorption – TGA measurement 204

5.4 CO_2 adsorption – static measurement 210

5.5 Conclusion 214

5.6 References 215

Chapter 6: Conclusion and outlook 217

Appendix A: Appendix for Chapter 3 ..... A.1

A.1 M1-SLDHs A.1

A.2 M2-SLDHs A.7

A.3 Study of the transformation of struvite to LDH A.9

A.4 Synthesis of SLDHs containing zinc A.12

A.5 Aqueous miscible organic solvent treatment (AMOST) of SLDHs.. A.14

A.6 Preparation of SLDH from WWTP struvite A.16

A.7 Reference c-LDH (Ref-LDH) A.19

A.8 Attempted synthesis of SLDH in acidic conditions A.21

Appendix B: Appendix for Chapter 4 ..... B.1

B.1 Chemical composition of core-shell SiO_2@Mg_2Al-CO_3-AMO-LDHs B.1

B.2 Characterisation of Stöber silica B.2

B.3 Variation of stirring speed B.3

B.4 Variation of metal addition rate B.19

B.5 Variation of ageing time B.30

B.6 Characterisation of commercial SiO_2 ..... B.32

B.7 Commercial SiO_2@Mg_2Al-CO_3-AMO-LDHs B.36

B.7.1 Grace Davison LC60A 35-70 silica B.36

B.7.2 Grace Davison LC150A 35-70 silica B.45

B.7.3 Fuji 1 silica B.50

B.7.4 Fuji 2 silica B.55

B.7.5 PQ ES70X silica B.58

B.7.6 PQ ES70Y silica B.61

B.8 Alternative procedure – urea hydrothermal B.64

B.9 Reference AMO-LDHs B.66

B.10 Preliminary syntheses of SiO_2@SLDH B.68

Appendix C: Appendix for Chapter 5 ..... C.1

C.1 Calcination of SiO_2@Mg_2Al-CO_3-AMO-LDHs C.1

C.2 Calcination of SLDHs C.3

C.3 Reference LDH C.4

C.4 CO_2 adsorption – TGA measurement C.5

Chapter 1: Introduction

1.1 Layered double hydroxides (LDHs)

LDHs are a class of inorganic compounds with the general formula $[M_{1-x}M_x'(OH)_2]^{y+}[A^{n-}]_{y/n}.zH_2O$, where M and M′ are typically metal di- and trications, respectively, $0 < x < 1$, and A an n-valent interlayer anion.[1] Pure LDH phases are usually found for stoichiometries in the range $0.22 \leq x \leq 0.33$,[2] but values of x as low as 0.07[3] and as high as 0.48[4] have been reported. The parent of this class is the naturally occurring mineral hydrotalcite, $Mg_6Al_2(OH)_{16}CO_3.4H_2O$. Whilst magnesium and aluminium is a common combination, LDHs have been successfully prepared using a wide variety of metals including transition metals and lanthanides.[5, 6] In a few special cases, LDHs have been synthesised with monovalent lithium cations and tetravalent cations such as Zr^{IV}, Ti^{IV} and Sn^{IV}.[7-9] Ternary and quaternary combinations are also possible.

The structure of these anionic clays is similar to that of the mineral brucite, $Mg(OH)_2$, which has the CdI_2 structure typical of MX_2 compounds with small polarising cations and polarisable anions. In LDHs, two dimensional arrays of edge-sharing M^{2+} and M^{3+} hydroxide octahedra stack to form the overall 3D structure and charge-compensating anions occupy the interlayer region in order to maintain charge neutrality.[10] The hydroxide layers may stack in different ways to give rise to polytype structures of hexagonal or rhombohedral symmetry (Figure 1.1).[11] There are three possible two-layer polytypes, which all have hexagonal symmetry, and nine possible three-layers polytypes, two of which have rhombohedral symmetry and the remaining seven have hexagonal symmetry.[1] In all polytypes, the cations are distributed homogeneously.

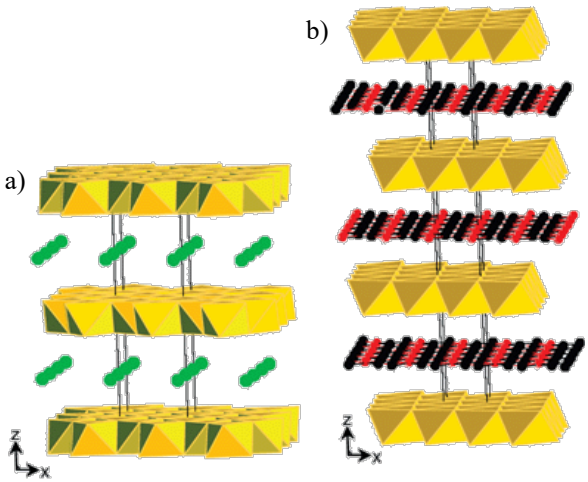


Figure 1.1 Cartoon representation of a) hexagonal and b) rhombohedral stacking in LDHs.[11]

The polytype of an LDH may be determined by examining its powder X-ray diffraction (XRD) pattern (Figure 1.2). An LDH has a characteristic XRD diffractogram containing strong basal (00*l*) reflections at low angles, 01*l* and/or 10*l* reflections at intermediate angles, and a 110 reflection at high angle. The basal reflections allow direct determination of the basal spacing normal to the 00*l* plane (c_0), which equals the thickness of one hydroxide layer plus one interlayer. For an *n*-layer polytype, the unit cell parameter $c = nc_0$ and the lowest angle reflection is labelled 00*n*.[12] The lattice parameter a_0 is calculated from the 110 reflection: $a_0 = 2d_{110}$. This parameter corresponds to the distance between two metal cations and its value therefore reflects the radii of the cations.[2]

Systematic absences in the spectra distinguish the polytypes. For rhombohedral structures, reflections are systematically absent unless $-h + k + l = 3n$ where n is an integer. If reflections are present when $-h + k + l \neq 3n$, the LDH has hexagonal symmetry.[1, 12] It is possible to distinguish between $3R_1$ and $3R_2$ polytypes of carbonate- and sulphate-LDHs using the following simplified criteria: the $3R_1$ polytype gives rise to strong Bragg reflections with $l = 3n - 1$ (*e.g.* 012, 015 and 018), and the XRD diffractograms of the $3R_2$ polytype will have strong Bragg reflections with $l = 3n + 1$ (*e.g.* 101, 104, 107, and 10.10).[12] It is also possible to distinguish the hexagonal polytypes

but this depends, additionally, on the nature of the interlayer anion. For example, in the case of carbonate-LDHs, the $3H_1$ polytype has the strongest 10*l* reflections with $l = 3n$, whilst the $3H_2$ polytype has the strongest reflections with $l = 3n + 1$ ($n = 1, 2, 3$). For sulphate-LDHs, the polytype is $3H_1$ if all the 10*l* reflections show intensities of the same order, and it is classified as $3H_2$ if the 10*l* reflections with $l = 3$ are much weaker than the others.[12, 13]

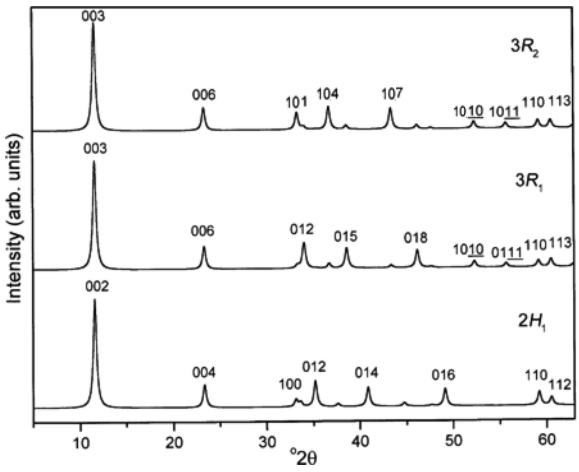


Figure 1.2 Simulated powder XRD diffractograms of $2H_1$, $3R_1$, and $3R_2$ polytypes of LDHs.[14, 15]

The interlayer gallery may expand and contract to accommodate a wide range of anions because there is no crosslinking between the cation layers. Intercalated species range from small monatomic halides and oxyanions, to large surfactants and proteins.[11] The interlayer distance is a function of the size of the intercalated anion and generally increases with increasing anion size (*e.g.* the ionic radii of halides and the number of carbons in an organic anion). The basal spacing recorded for carbonate LDHs (d_{003} = 7.65 Å) indicates that the carbonate anion (CO_3^{2-}) intercalates with its molecular axis parallel to the hydroxide layers.[16] This allows for strong hydrogen bonding between the carbonate anion, hydroxide layers and interlayer water molecules. Consequently, carbonate has a particularly high affinity for LDHs and it is often difficult to synthesise carbonate-free LDHs directly.[2]

The intercalated species is also known to mediate the stacking of the cation layers as favourable interactions can stabilise the structure. Thus, anions are typically selective for the polytype whose interlayer site symmetry best matches their own symmetry. For example, the rhombohedral polytype $3R_1$ is believed to be observed for most carbonate-LDHs because the prismatic arrangement of hydroxyl groups allows those in both the upper and lower layers to form hydrogen bonds with the oxygen atoms of the carbonate anions, which have D_{3h} symmetry.[1, 17]

Similarly, laboratory synthesised sulphate-LDHs crystallise in the $3R_1$ polytype and studies show that the sulphate anion (SO_4^{2-}) intercalates with one of its S–O bonds parallel to the crystallographic *c*-axis.[18] The sulphate anion is able to coordinate to the trigonal prismatic interlayer sites because it has C_{3v} symmetry, which is a subset of D_{3h}. The existence of naturally occurring sulphate-LDHs with the 1H polytype may also be rationalised by symmetry considerations: the interlayer sites have octahedral symmetry (O_h) and C_{3v} is also a subset of O_h.[19]

The stacking of the hydroxide layers is also influenced by long-range interactions between cations. Hexagonal stacking to give the $2H_1$ polytype with eclipsed cations requires higher energy than rhombohedral stacking to give $3R_1$ where cations are staggered.[12, 20] Consequently, among the large number of synthetic carbonate-LDHs, no examples of $2H_1$ polytype have been directly prepared.

Materials with layered structures are susceptible to stacking disorders because of their very nature of being layered – *i.e.* weak interlayer interactions and high symmetry within the layers. Stacking disorders manifest as anisotropic broadening of Bragg reflections in powder XRD diffractograms and can have contributions from stacking faults, turbostraticity, interstratification, cation vacancies, and disorder in the interlayer.[15]

Stacking faults are interruptions in an idealised stacking sequence – *e.g.* a $3R_1$ crystal containing layers that have the local symmetry of a $2H_1$ polytype (Figure 1.3)[21] – and contribute to thermodynamic stability by increasing entropy.[14] When stacking faults occur, the positions of the cations in adjacent layers will not be correlated in the *c*-direction and this leads to broadening of the *h*0*l* and 0*kl* Bragg reflections.[17, 21, 22]

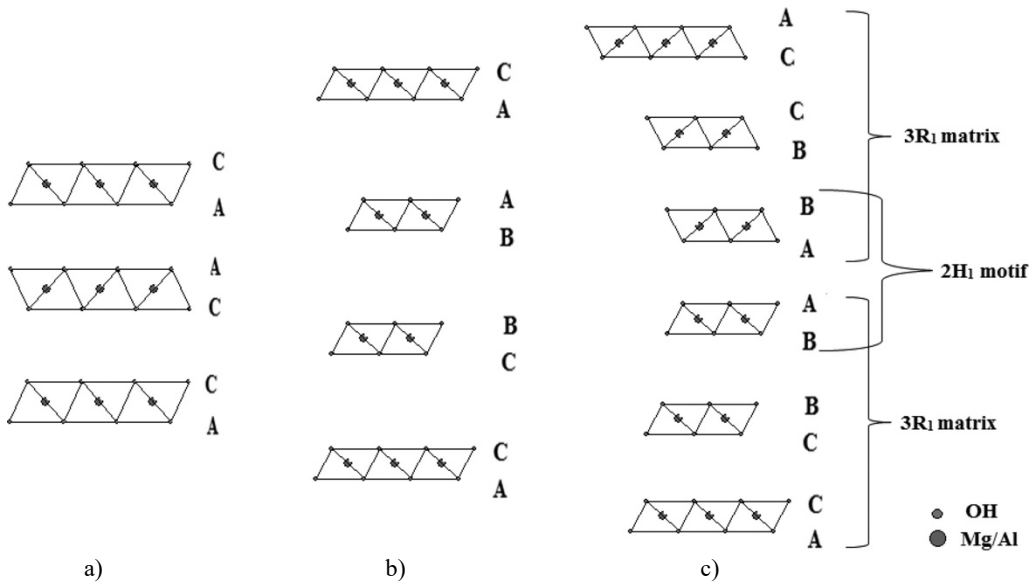


Figure 1.3 Schematic representation of a) a $2H_1$ polytype, b) a $3R_1$ polytype, and c) a $3R_1$ polytype with $2H_1$ faults. Interlayer species omitted for clarity.[21]

If the number of faults is so large that the cations are completely uncorrelated along the *c*-direction (*i.e.* the layers are randomly oriented), the structure is said to be turbostratically disordered. The *h*0*l* and 0*kl* Bragg reflections of such LDHs exhibit "shark's fin" peak shapes.

Interstratification, also known as mixed layering, is the coexistence of interlayers having different anion and/or water content and accordingly, different interlayer distances.[12] The Bragg reflections broadened by interstratification are all non-*hk*0 reflections.[15]

Water molecules also occupy the interlamellar space in LDHs and the extent of hydration is another factor influencing polytype selectivity. Interlayer water is distributed between

the hydration spheres of the interlayer anions and the metal hydroxide layers. If each *n*-valent anion occupies N number of sites, then for an LDH with the formula $M^{II}_{1-x}M^{III}_{x}(OH)_2(A^{n-})_{x/n}{\cdot}zH_2O$, the maximum amount of water that can be accommodated in the interlayer galleries is $1 - Nx/n$.[2, 23] For example, the three oxygen atoms in carbonate occupy three sites and the remainder are occupied by water or left vacant. The general formula for a carbonate LDH is therefore $M^{II}_{1-x}M^{III}_{x}(OH)_2(CO_3)_{x/2}.(H_2O)_{1-3x/2-\Delta}$ where Δ represents the number of vacant interlayer sites. The experimentally determined amount of water can exceed $1 - Nx/n$, in which case it is assumed that there is water adsorbed on external surfaces in addition to interlayer water.

Pesic *et al*.[24] determined in MgAl-CO_3-LDHs that interlayer water is more strongly bound than surface adsorbed water by *ca.* 12 kJ mol^{-1}. In the interlayer region, the water molecules exhibit translational diffusion as well as reorientation motions, so hydrogen bonds are rapidly breaking and reforming as the water molecules move between sites. Thermodynamic measurements also suggest that the entropy of interlamellar water is lower than that of bulk water. Wang *et al*.[25] calculate there to be on average 3.8 hydrogen bonds per interlayer water molecule in LDHs, which is greater than that in bulk water (3.2) and close to that of ice (4).

Some interlayer anions can grow their hydration sphere depending on the temperature and pH of precipitation, washing and drying processes, and relative humidity.[26, 27] For example, sulphate-LDHs are known to crystallise with different levels of hydration and can reversibly exchange their intercalated water with the vapour phase.[18] Studies on ZrCr-SO_4-LDHs by *in situ* XRD show that the changes in basal spacing are accompanied by discrete structural transformations.[28, 29] The LDHs had rhombohedral symmetry (3R)

with an 8.2–8.5 Å basal spacing, and hexagonal symmetry (2H) with a 10.6–10.7 Å basal spacing.

1.2 Applications of LDHs

Compositional flexibility is one of the advantages of LDHs among inorganic layered materials. A great number of possible combinations of metals, metal ratios, and anions are possible, giving rise to a variety of chemical and physical properties such as photosensitivity, biocompatibility and anion exchange. LDHs have thus garnered attention in a wide range of fields for both fundamental research and practical applications.

1.2.1 Anion exchange

Owing to their ability to reversibly intercalate anions, LDHs have been utilised in environmental remediation as ion exchangers and adsorbents.[30-34] The selectivity and affinity of anions for the interlayer region is known to depend on the charge density of the anion and their ability to form stabilising interactions, such as hydrogen bonds, with the metal hydroxide layers.[35] For example, the ion-exchange equilibrium constants for common anions in MgAl-LDHs are $CO_3^{2-} > SO_4^{2-} > OH^- > F > Cl^- > Br^- > NO_3^- > I^-$.[16]

Contaminants in wastewater such as heavy metals, organic dyes, pesticides and pharmaceuticals are an environmental concern and originate from a number of industries including plastics and battery manufacturing.[36] Huang *et al.*[33] have shown that fluoride (F^-) and arsenic (As^V) ions can be removed from aqueous solution by anion exchange with MgAl-LDHs intercalated with chloride (Cl^-) and carbonate. Functionalised LDHs have also been deployed. For example, Ma *et al.*[37, 38] reported the removal of heavy metals ($M^{II} = Co^{2+}$, Ni^{2+}, Cu^{2+}, Zn^{2+}, Ag^+, Pb^{2+}, Cd^{2+}, and Hg^{2+}) using MgAl-LDHs intercalated with molybdenum sulfide (MoS_4-LDH). The studies show that the ion exchange products

depend on the concentration of the ions (Figure 1.4). When a stoichiometric amount of M^{II} is added to the MoS_4-LDH, the metal cations are captured by MoS_4^{2-} to form $[M^{II}(MoS_4)_2]^{2-}$ that remain in the interlayer. When there is an excess of M^{II}, the MoS_4^{2-} units become coordinatively saturated with M^{II}, resulting in the formation of $M^{II}MoS_4$. These neutral units are deintercalated and replaced by the counter anions of the M^{II} salt.

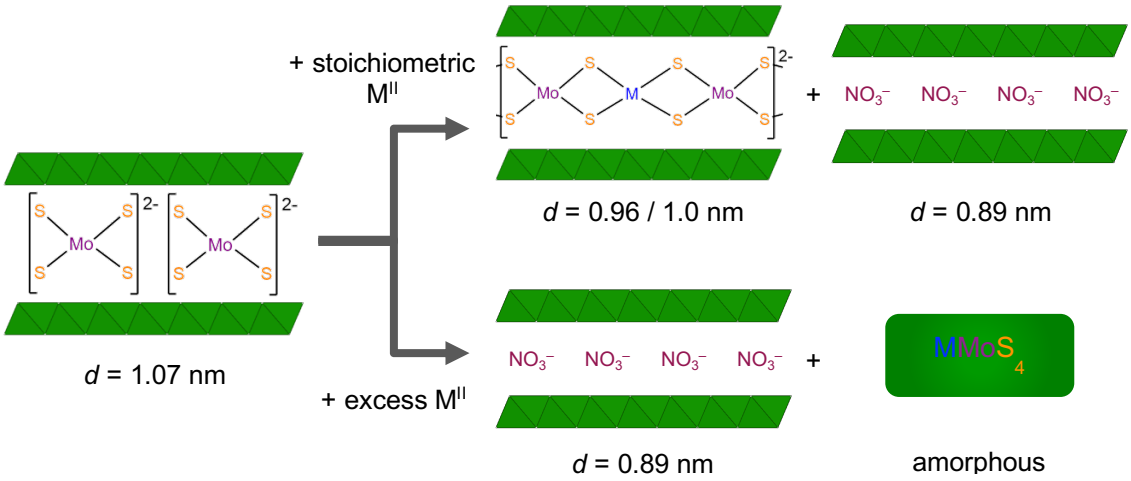


Figure 1.4 Ion exchange reactions in MoS_4-LDH at different M^{II} concentrations.[37]

Drug delivery is another application in which the ability to intercalate and release molecules is essential. LDHs have been studied as hosts for a range of biologically active anions such as amino acids,[39] DNA,[40] and vitamins,[41] in addition to drugs.[42-45] The intercalation of such anions can enhance the stability of the molecules (*e.g.* to heat or light) and modify the rate at which they are released.[42, 43] Improvements in drug efficacies have also been reported. For example, Choy *et al.*[46] intercalated methotruxate (MTX), an anti-cancer drug, into Mg_2Al-LDHs by ion-exchange and found that the MTX-LDH hybrid was more effective at suppressing tumour proliferation than the pristine MTX. MTX has a short plasma half-life so its concentration decreases rapidly after administration, but in the MTX-LDH hybrid the drug is stabilised and protected so it can reach the tumour cell membrane without any decomposition.

1.2.2 Adsorption

Surface adsorption is another mechanism by which LDHs remove contaminants and can occur simultaneously alongside anion exchange. LDHs have relatively high surface areas (30–150 m^2 g^{-1}) and high charge density, so sorption takes place through electrostatic interactions with the exposed cationic surfaces of the hydroxide layers.[47] The abundance of surface hydroxyl groups also allows the possibility of hydrogen bonding and acid-base interactions.

Furthermore, by means of thermal treatment, LDHs are also precursors to mixed metal oxides (MMOs) which are commonly referred to as layered double oxides (LDOs). LDOs often exhibit higher sorption capacities than the parent LDH as they have higher surface areas and porosities, and different acid/base properties. The structure of an LDO is unique: it is directly related to the arrangement of the metals in the parent LDH and cannot be mechanically achieved.[48] The thermal decomposition of LDHs takes place stepwise, so the composition of an LDO depends on the conditions applied (*e.g.* temperature, temperature ramp rate, and gas flow). Consequently, an LDO may contain amorphous as well as crystalline phases and have different surface acid/base properties.[49, 50]

It is known that the metals, metal ratio and interlayer species affect the decomposition process.[51, 52] For simplicity, the following analysis concerns the thermal decomposition of a MgAl-CO_3-LDH (Figure 1.5). The primary phase of thermal decomposition is typically dehydration (*ca.* 70–190 ºC).[53] Surface water molecules that are weakly bound by physisorption (physical adsorption) are the first to be liberated, followed by interlayer water molecules. The loss of interlayer water results in a decrease in the LDH basal spacing by ~0.9 Å.[53, 54]

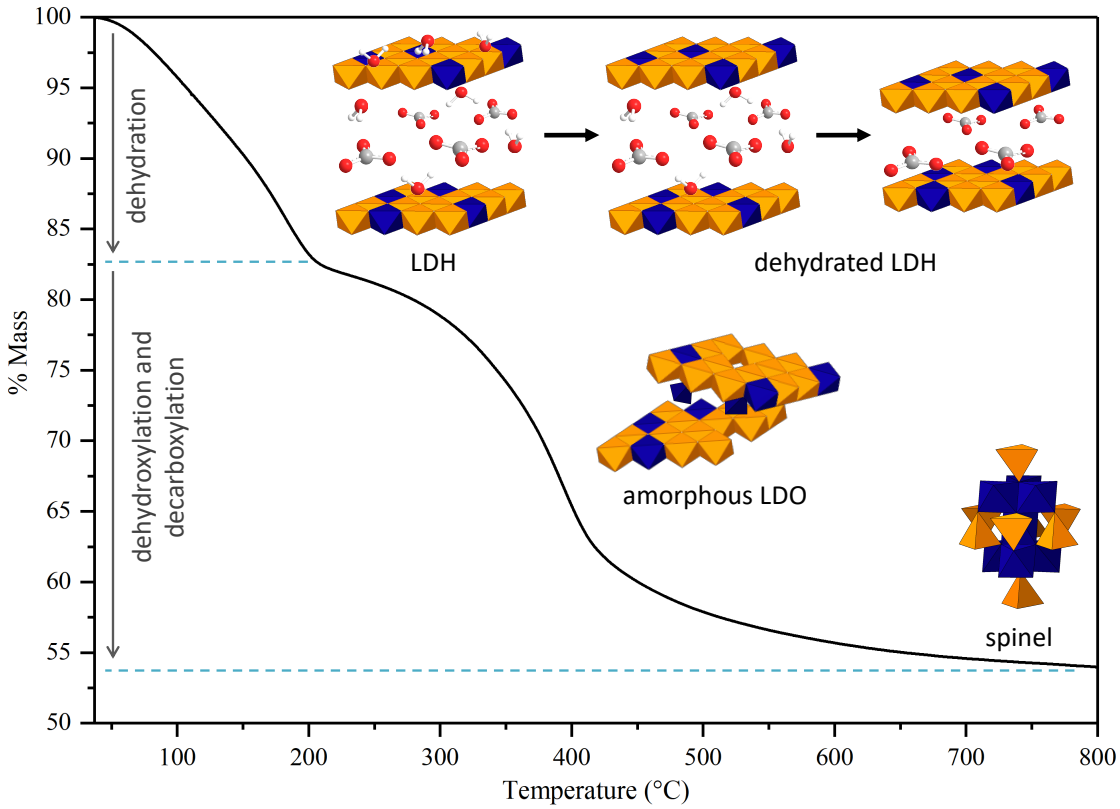


Figure 1.5 Thermal gravimetric analysis (TGA) of an Mg_3Al-CO_3-LDH illustrated with schematic representations of the thermal decomposition products. Not drawn to scale.

The second endothermic event (*ca.* 200–500 ºC) concerns the decomposition of the layers (dehydroxylation) and interlayer species. For carbonate-LDHs, this means decarboxylation to liberate carbon dioxide gas (CO_2). High temperature XRD (HTXRD), solid state nuclear magnetic resonance spectroscopy (ssNMR) and diffuse reflectance infrared Fourier transform spectroscopy (DRIFTS) have been used to study this stage of decomposition *in situ*.[53, 55] The results indicate that in MgAl-CO_3-LDHs, the removal of OH groups associated with Al^{3+} occurs first (onset temperature at *ca.* 200 ºC), whilst those bonded to Mg^{2+} remain intact up to *ca.* 280 ºC.[53] Dehydroxylation of Al^{3+} results in the diffusion of some Al^{3+} out of the brucite-like layers into the interlayer space. These Al^{3+} are tetrahedrally coordinated (T_d) by three oxygens in the layer and one apical oxygen in the interlayer.[54, 55] This results in vacancies in the layers (Schottky defects) and leaves the Mg^{2+} ions coordinated by more oxygen, O^{2-}. Quantum calculations and FTIR

studies suggest that sites having relatively more O^{2-} anions coordinated to Mg^{2+} show enhanced basicity.[56, 57]

In situ DRIFTS results indicate that interlayer carbonate interacts more strongly with the LDH layers after interlayer water is removed.[53] Thus, decarboxylation of the interlayer space occurs alongside dehydroxylation, but is most appreciable above 400 ºC. The loss of carbonate triggers the collapse of the layered structure, resulting in the formation of a porous and amorphous mixed oxide.[58, 59]

The loss of CO_2 is complete at *ca.* 580 ºC and further heating increases the crystallinity of the LDO, eventually leading to the formation of an ordered spinel ($MgAl_2O_4$) phase.[55] The surface basicity of the spinel is lower than that of the mixed oxides as a result of Al^{3+} migration to the surface.[60] Thus, in addition to the identity of the cations, the acidity and basicity of LDOs is dependent on the calcination temperature.

It is found that LDHs calcined at intermediate temperatures (*ca.* 300–600 ºC) can be reconstructed into their original layered structure by rehydration, adsorption of anions, or simply exposure to air.[10, 48, 61] As such, LDOs have been shown to be effective adsorbents of environmental pollutants in both solution and gas phases.[31, 62, 63] This "memory effect" is a valuable property of LDHs as it can be used to intercalate functional inorganic and organic anions into LDHs galleries, and can also grant access to materials that are otherwise difficult to synthesise (Section 1.3.3).[64-66]

1.2.3 Catalysis

LDHs have been widely investigated in heterogeneous catalysis as finished catalysts, catalyst supports, and catalyst precursors for a variety of applications including photochemistry,[67-69] electrochemistry[70-72] and organic transformations.[73-75] An important characteristic of LDHs is the uniform distribution of M^{II} and M^{III} cations in the hydroxide

layers.[76] This can be utilised to synthesise catalyst precursors containing homogeneous distributions of metal cations, which can be subsequently reduced to obtain stable and well dispersed metal nanoparticles on the surface of the support.[63]

Wen *et al.*[77] demonstrated that CuCeMgAlO mixed oxides derived from CuCeMgAl-LDHs were highly active for the reduction of nitrogen oxides (NO_x) and oxidation of carbon monoxide (CO). Calcination of the LDH at 750 ºC generated oxygen vacancies in the lattice, which are active sites for NO adsorption, and also resulted in the replacement of some Ce^{4+} ions by Cu^{+}, which are active sites for CO adsorption. The high activity of this catalyst is attributed to the synergistic effect of the copper and cerium that is absent in the poorer-performing CuMgAlO and CeMgAlO catalysts. The catalyst also showed good resistance to H_2O and SO_2 poisoning because the water-gas shift reaction (WGSR)[78] and reaction of SO_2 with CO on Cu^{+} sites removed these pollutants as H_2 and S, respectively.

Electrostatic interactions can also be harnessed to achieve a uniform distribution of anions, including noble metal and transition metal clusters, on the surface.[79] This templating effect prevents aggregation and sintering of the nanoparticles, which is a problem often observed with supported catalysts prepared by conventional impregnation methods.[76] Li *et al.*[80] utilised these electrostatic interactions to prepare ultrafine gold nanoclusters (AuNCs, *ca.* 1.5 ± 0.6 nm) on LDHs (Figure 1.6). The AuNCs/LDHs exhibited higher catalytic activity for the oxidation of 1-phenylethanol in toluene than Au/LDHs prepared by a conventional deposition precipitation method. The higher alcohol oxidation activity is attributed to the small AuNC nanoparticle size and strong interactions between the AuNCs and cations in the LDH, which are both closely linked to the synthesis method.

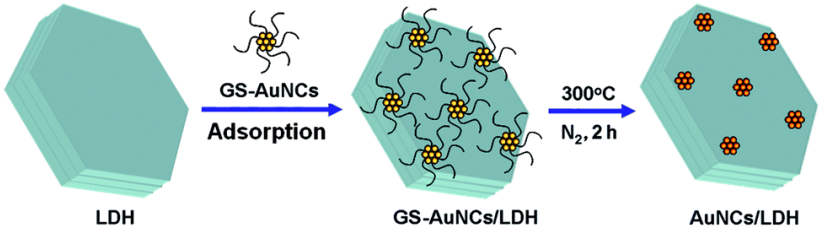


Figure 1.6 Utilisation of electrostatic interactions between the LDH surface and anionic glutathione-capped gold nanoclusters (GS-AuNCs) to prepare well-dispersed and stable catalysts for the aerobic oxidation of alcohols.[80]

The uniform dispersion of metal cations and their redox activity makes LDHs promising electrode materials for energy conversion and storage devices.[81-83] These applications typically use LDH nanosheets (Section 1.4) as the atomic thickness of delaminated LDH layers increases the efficiency of the electrode by reducing the diffusion distance for the ions in the electrolyte to the surface of the active material.[84]

1.3 Synthesis of LDHs

There are a number of routes to synthesise LDHs and the method chosen for a given application will depend on the properties desired of the final material.[85] Factors that must be considered include temperature, pH, ageing time, stirring speed, and supersaturation. For example, it is widely accepted that an alkaline pH is required for LDH synthesis, but the optimal pH will depend on the nature of the cations used and where their hydroxide precipitation curves intersect.[86] The size and crystallinity of LDHs will generally increase with increasing ageing time, but the stirring speed during the ageing process will also affect the morphology and porosity. The shear forces exerted on the particles at high stirring speeds prevent aggregation of nuclei and platelets, resulting in porous, cross-linked networks of nanoflakes (Figure 1.7a). Without stirring the nanoflakes are more likely to be deposited randomly and form a more compact material to minimise surface energy and excluded volume (Figure 1.7b).[87]

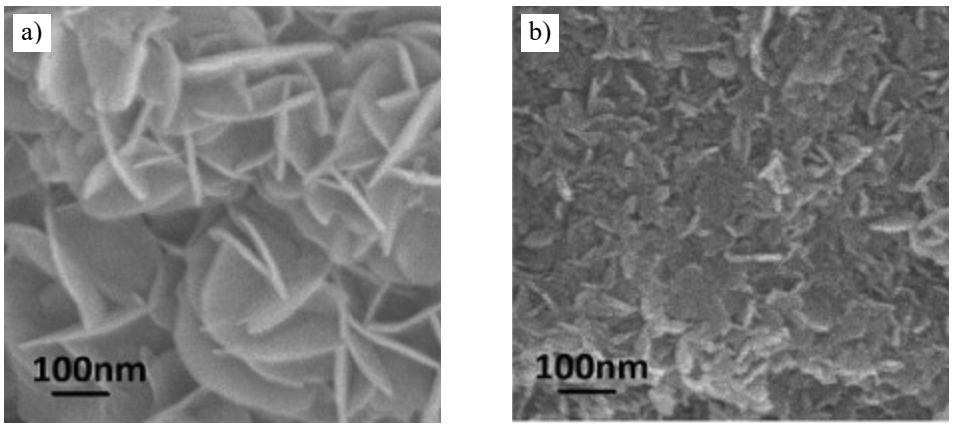


Figure 1.7 Scanning electron microscopy (SEM) images of Mg_3Al-CO_3-LDH prepared a) with and b) without stirring.[87]

1.3.1 Co-precipitation

Co-precipitation is the most common technique used to synthesise LDHs.[1, 49] In this method, two or more cations are precipitated simultaneously in an alkaline solution containing the desired interlayer anion under conditions of either high or low supersaturation. In the variable pH co-precipitation method, the metal salts and anions are added to a base until the pH reaches a specified value, after which the pH is maintained until the precipitation is complete by adding further base. More commonly, the precipitation is performed at constant pH, where the metal salts and a base are simultaneously added at such a rate that the pH remains constant. In both cases, the resulting suspension is aged to allow growth of the nuclei, a process that involves Ostwald ripening.[88] Ostwald ripening is the growth of larger particles at the expense (*i.e.* dissolution) of smaller particles, which is driven by the difference in solubility between small and large particles. Low supersaturation conditions usually give rise to precipitates of higher crystallinity than high supersaturation conditions because the rate of crystal growth exceeds that of nucleation.[2, 89]

Co-precipitation often yields products with a broad crystallite size distribution because nucleation and crystal growth take place simultaneously. Zhao *et al.*[90] have reported a

modification that can be employed when a narrower size distribution is preferred. As the name suggests, in the separate nucleation and ageing steps (SNAS) method, these two processes are distinct. By rapidly mixing the parent solutions in a colloid mill (*e.g.* 3000 rpm, 2 minutes) before ageing in a second discrete step (*e.g.* 100 ºC, 13 h), agglomeration of nuclei is restricted, and subsequent ageing allows them to grow at approximately the same rate. This results in LDH particles with a narrow size distribution (Figure 1.8).

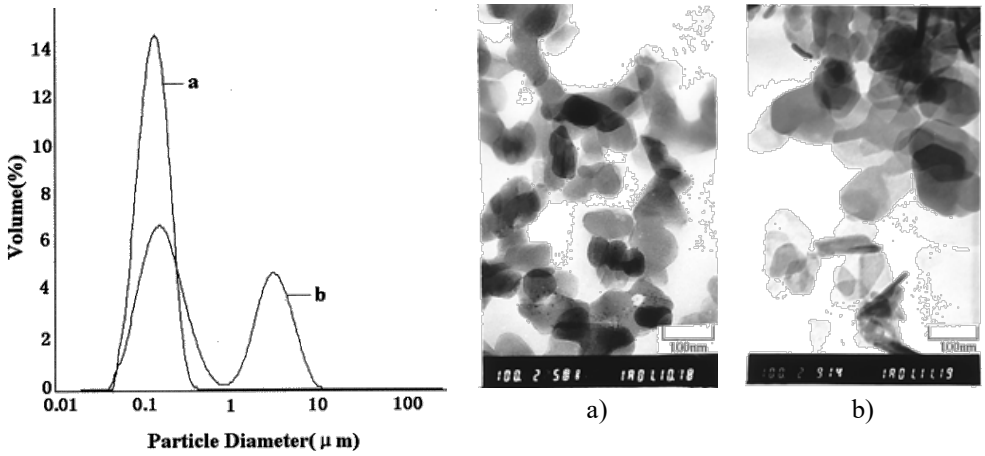


Figure 1.8 Particle size distribution and transmission electron microscopy (TEM) micrographs of Mg_2Al-CO_3-LDH prepared by a) SNAS and b) conventional co-precipitation methods.[90]

Hydrothermal treatment can be used in tandem with co-precipitation to improve LDH crystallinity and control particle size. Typically, the precipitated LDH and mother liquors are heated in a sealed vessel at temperatures between 100–200 ºC under autogenous pressure. Crystallinity is found to increase with increasing temperature, pressure and time.[86, 91, 92] The hydrothermal method is also a valuable tool for the synthesis of LDHs from powder starting materials.[93, 94] Newman *et al.*[95] were able to prepare a hitherto theoretical $3R_2$ polytype of LDH by hydrothermal treatment of magnesium oxide (MgO) and alumina (Al_2O_3).

1.3.2 Urea hydrolysis

Highly crystalline LDHs with narrow particle size distributions are reliably obtained by the urea hydrolysis method. Urea, $CO(NH_2)_2$, is a weak Brønsted base (pK_b 13.8) that is highly soluble in water. When its solution is heated, it undergoes a two-step hydrolysis reaction (Equations 1.1 and 1.2) to yield solutions that are pH 7–9, depending on the temperature, making it a suitable agent for precipitating many LDHs.[92, 96, 97]

$$CO(NH_2)_2 \rightarrow NH_4CNO \qquad \text{Equation 1.1}$$

$$NH_4CNO + 2H_2O \rightarrow 2NH_4^+ + CO_3^{2-} \qquad \text{Equation 1.2}$$

Good control over the solution pH is possible because the rate of urea hydrolysis is slow and depends on the temperature and duration of heating. The rate constant increases *ca.* 200 times when the temperature is increased from 60 to 100 ºC.[97] Any increase in pH can be countered by simply cooling the solution. The evolution of ammonia (NH_3) above pH 7 also prevents the solution from becoming highly basic.[98]

The slow rate of urea decomposition leads to homogeneous solutions with a low degree of supersaturation during precipitation.[99] This results in a slow nucleation rate and consequently, LDHs obtained by this method are usually highly crystalline, uniform, and large (Figure 1.9).

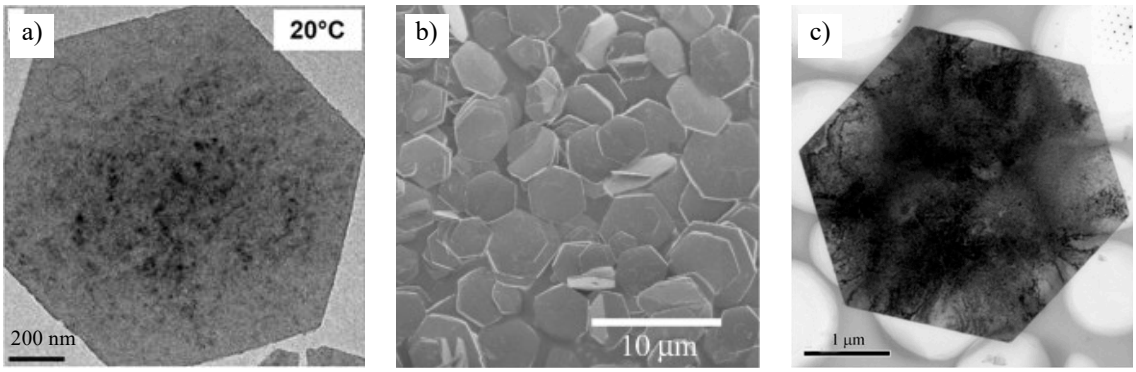


Figure 1.9 SEM images of a) NiFe-,[100] b) MgAl-,[101] and c) $Co^{II}Co^{III}$-LDHs[102] prepared by urea hydrolysis.

As with hydrothermal treatment, crystallite size increases with increasing ageing time. When the total metal concentration is increased however, crystallite size is found to decrease.[92] For a nucleus to participate in crystal growth it must have a critical nucleus radius, r_c. The value of r_c decreases in a highly supersaturated solution, whilst an increase in concentration also increases the number of nuclei that exceed r_c. Thus, a larger number of nucleation sites are formed, and this results in an overall reduction in crystal size.

1.3.3 Reconstruction

As previously mentioned in Section 1.2.2, LDHs may be reversibly transformed into LDOs by thermal treatment at intermediate temperatures and this can be harnessed to synthesise other LDHs indirectly. Key examples of this are carbonate-free LDHs, which are difficult to prepare directly because of the high affinity of carbonate for the interlayer space (Section 1.1). Removal of interlayer carbonate is facile with thermal treatment (Section 1.2.2) and the resulting LDO may be immersed in solutions containing the desired anion to prepare carbonate-free LDHs. This strategy has been used to intercalate nitrate and phosphate into LDHs, as well as more complex anions such as dyes and transition metal catalysts.[61, 64-66, 103, 104]

1.3.4 Reverse micelle

A novel approach to controlling LDH particle size is the use of water-in-oil microemulsions, otherwise known as reverse micelle systems. Reverse micelles are spherical aggregates of surfactant that form when a surfactant is added to an organic solvent, and may form in the presence and absence of water.[105] The polar head groups and water molecules form nanosized "water pools" in the core of surfactant aggregates and these are characterised by the water-surfactant molar ratio, $w = [H_2O]/[S]$.[106] The thermodynamic driving forces for the formation of these structures are: i) favourable

enthalpic interactions that arise between species of similar polarity and ii) maximisation of the overall entropy of the system by liberation of solvation spheres.[107]

LDH nanoplatelets have been prepared in reverse microemulsions of sodium dodecyl sulfate in water and isooctane, with 1-butanol as a cosurfactant ($w = 24$).[84, 106, 108, 109] An aqueous solution of metal salts can be dispersed in the organic solution and LDH precipitates within the aqueous environment of the micelles when an alkaline solution is added (Figure 1.10). Brownian motion causes spontaneous and short-lived coalescence of the reverse micellar aggregates. During such encounters, water and solute are exchanged between pools. Nanoplatelet growth, in both the *ab*-plane and along the *c*-axis, is restricted by the size of the water pools, which in turn depends on *w*. Hu *et al.*[106] were able to obtain Mg_2Al-LDH nanoplatelets with a narrow size distribution (40–50 nm diameter and 10 nm thickness). Ni_2Al-LDHs prepared by this technique were also reported to be larger and more ordered than the equivalent LDHs synthesised by conventional co-precipitation.[110]

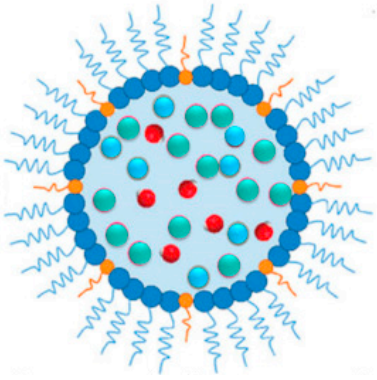


Figure 1.10 Cartoon representation of a reverse micelle for LDH synthesis.[84]

A shortcoming of the reverse micelle method is the use of surfactants, which results in costly and time-consuming separation of the ultrathin LDH nanoplatelets from the liquid medium. To overcome this, Xu *et al.*[111] developed a surfactant-free microemulsion

method that uses toluene, isopropanol, and water. The authors were able to synthesise single layer Mg_2Al-Cl-LDH nanosheets that were free of organic species.

1.4 Post-synthesis modifications of LDHs

LDHs prepared by traditional co-precipitation methods are typically dense, low surface area materials that have low dispersibility in non-polar solvents.[112, 113] These properties originate from the intrinsic high surface charge and hydrophilicity of the hydroxide sheets. The synthesis of well-dispersed LDH nanosheets is desirable but difficult due to *ab*-face stacking of the layers caused by electrostatic attractions and hydrogen bonding between the highly charged layers, abundant guest anions and interlayer water molecules.

1.4.1 Delamination of LDHs

Delamination is the "top-down" method for separating the tightly packed layers of layered materials into sheets that are typically a few atomic layers thick. The resulting platelets have much greater specific surface areas than their parent materials and are useful building blocks for nanomaterials.

LDHs are more difficult to delaminate than cationic clays such as laponite, due to strong electrostatic interactions between the sheets and interlayer anions, as well as substantial hydrogen bonding, so modification of the interlayer environment is necessary to firstly weaken the forces between the layers.[114, 115] This can be achieved by anion exchange using large organic surfactants. The intercalation of long chain surfactants increases the basal spacing of the LDH as they preferentially align with their alkyl chains perpendicular to the hydroxide layers. Delamination is accomplished by dispersing the organo-LDH in an appropriate solvent such as toluene,[116] formamide,[117-120] or butanol.[121, 122] Solvation of the hydrophobic tails weakens the attractive dispersive forces between the aliphatic

chains tethered onto adjacent layers, thereby facilitating separation of the layers (Figure 1.11).[123]

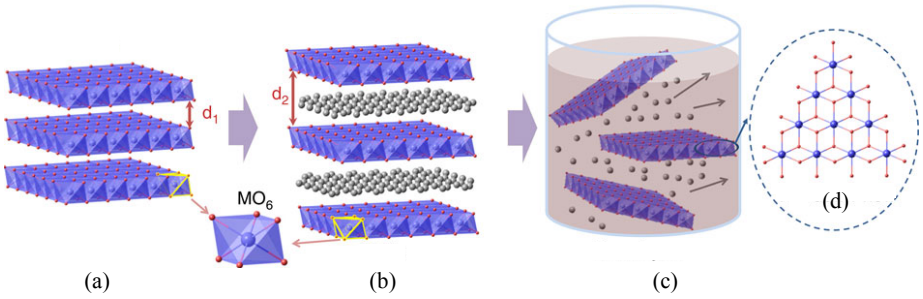


Figure 1.11 Schematic representation of anion exchange and delamination of an LDH: a) LDH with interlayer distance d_1, b) intercalated LDH with interlayer spacing d_2 where $d_2 > d_1$, c) exfoliated LDH monolayers and liberated anions dispersed in a colloidal solution, d) top-down view of an LDH layer.[120]

1.4.2 Aqueous miscible organic solvent treatment (AMOST)

From environmental and economical perspectives, alternatives are preferred to delamination techniques that involve organic intercalates and solvents.[114] To this end, Wang *et al*.[112] have developed a post-synthesis method to exfoliate LDHs without the use of surfactants (Figure 1.12). In the aqueous miscible organic solvent treatment (AMOST) method, LDHs are synthesised by conventional procedures, *e.g.* co-precipitation, but before the washed solid is dried it is re-dispersed in an organic solvent that is 100% miscible with water such as acetone or ethanol. The resulting AMO-LDHs are less aggregated (Figure 1.13), highly porous and have specific surface areas in excess of 300 $m^2\ g^{-1}$, compared to 13 $m^2\ g^{-1}$ of the equivalent water-washed LDH (c-LDH).[124] Additionally, the replacement of surface and interlayer water molecules by AMO solvent molecules makes them more capable of solvation by non-polar solvents, so AMO-LDHs are highly dispersible in non-polar hydrocarbon solvents.[125, 126]

Characterisation of AMO-LDHs by XRD shows that the basic LDH structure is unchanged by AMOST, but broadening and decreases in intensities of the Bragg diffraction peaks, especially the 00*l*, indicates that there is a significant reduction in the stacking length of the LDH nanoplates.[108, 113]

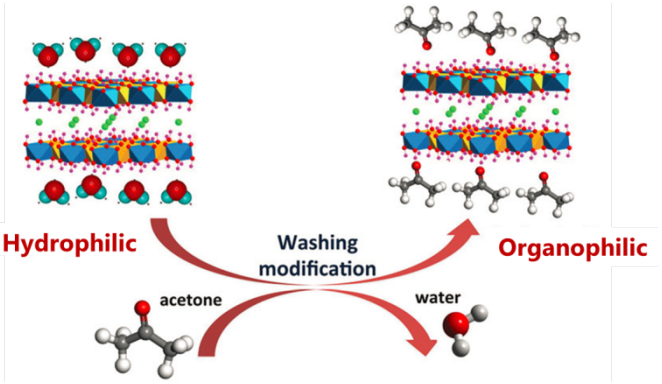


Figure 1.12 Schematic illustration of the AMOST process.[126]

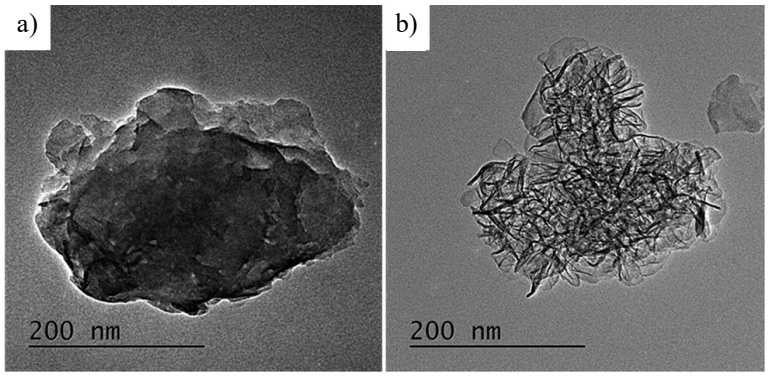


Figure 1.13 TEM images of a) c- and b) ethanol AMO-LDH.[125]

Recently, Erastova *et al.*[127] used molecular dynamics (MD) to show that AMO solvents disrupt the hydrogen bonding interactions between the layers in a concentration-dependent fashion, leading to delamination. Ruengkajorn *et al.*[128, 129] have also expanded the library of solvents for which this treatment method works to include aqueous immiscible organic solvents (AIM) such as diethyl ether and ethyl acetate. MD simulations suggest that, unlike AMO, AIM solvents do not enter the first hydration shell but are capable of distorting the H-bond network at the second hydration shell. This

interaction allows some of the residual water molecules to be displaced and results in free-flowing, high surface area LDH powder.

1.5 Green alternatives to traditional LDH synthesis methods

1.5.1 Green chemistry

The term "green chemistry" concerns sustainability and risk mitigation at all stages of a chemical lifecycle (*e.g.* from feedstock, through processing and reactions, to utilisation and waste). The guiding framework for green chemistry is a set of twelve principles proposed by Anastas and Warner in 1998 (Table 1.1).[130]

Table 1.1 The twelve principles of green chemistry

1	*Prevention* It is better to prevent waste than to treat or clean up waste after it has been created.
2	*Atom economy* Synthetic methods should be designed to maximize incorporation of all materials used in the process into the final product.
3	*Less hazardous chemical syntheses* Wherever practicable, synthetic methods should be designed to use and generate substances that possess little or no toxicity to human health and the environment.
4	*Designing safer chemicals* Chemical products should be designed to preserve efficacy of function while reducing toxicity.
5	*Safer solvents and auxiliaries* The use of auxiliary substances (*e.g.* solvents and separation agents) should be made unnecessary wherever possible and, innocuous when used.
6	*Design for energy efficiency* Energy requirements should be recognized for their environmental and economic impacts and should be minimized. Synthetic methods should be conducted at ambient temperature and pressure.
7	*Use of renewable feedstocks* A raw material or feedstock should be renewable rather than depleting whenever technically and economically practicable.
8	*Reduce derivatives* Unnecessary derivatization (use of blocking groups, protection/deprotection, temporary modification of physical/chemical processes) should be minimized or avoided if possible, because such steps require additional reagents and can generate waste.
9	*Catalysis* Catalytic reagents (as selective as possible) are superior to stoichiometric reagents.
10	*Design for degradation* Chemical products should be designed so that at the end of their function they break down into innocuous degradation products and do not persist in the environment.
11	*Real-time analysis for pollution prevention* Analytical methodologies need to be further developed to allow for real-time, in-process monitoring and control prior to the formation of hazardous substances.
12	*Inherently safer chemistry for accident prevention* Substances and the form of a substance used in a chemical process should be chosen to minimize the potential for chemical accidents, including releases, explosions, and fires.

A material that is generated by a process but does not have any realised value can be considered waste. Similarly, the loss of underutilised energy is also waste. Two useful measures of the potential environmental acceptability of chemical processes are the E factor (the environmental impact factor, Equation 1.3)[131] and the percentage atom economy (Equation 1.4). The E factor quantifies the amount of waste generated per kilogram of product, whilst atom economy is a theoretical number that expresses how much of a reaction mixture is incorporated into the desired product (assuming a 100% yield and exact stoichiometric amounts). An ideal reaction (*i.e.* 100% atom economy) would incorporate all of the atoms of the reactants in the final product.

$$\text{E factor} = \frac{\text{mass of waste}}{\text{mass of desired product}} \qquad \text{Equation 1.3}$$

$$\text{Atom economy} = \frac{\text{relative molecular mass of desired product}}{\text{relative molecular mass of all reagents}} \times 100\% \qquad \text{Equation 1.4}$$

Large-scale production of LDHs by traditional methods such as co-precipitation, ion-exchange and sol-gel, is energy intensive and poses an environmental concern because large volumes of highly basic and salt-rich wastewater are produced – often up to hundreds of times the mass of the product.[132, 133] The metal salts used as reagents for these syntheses can be expensive, as are the treatment procedures required for the safe disposal of the waste they generate.[134]

1.5.2 Mechanochemical

Mechanochemical approaches have been reported in recent years as a promising alternative to conventional aqueous methods.[133] Direct mechanochemical syntheses can be solvent free (*e.g.* dry one- or two-step grinding) and have significantly shorter preparation times.[135, 136] Qu *et al.*[137] prepared lithium aluminium LDHs (LiAl-LDHs) by firstly dry milling the metal hydroxides (LiOH and $Al(OH)_3$) and then wet milling the

powder with the minimum amount of water required for crystallisation. The water added was completely consumed by forming the LDH so no further drying or washing was necessary.

The syntheses of some LDHs have also been simplified by mechanochemical routes. For example, Iwasaki *et al.*[138] prepared cobalt iron LDHs ($Co^{2+}_{0.52}Fe^{2+}_{0.16}Fe^{3+}_{0.32}$-Cl-LDH) using just cobalt chloride ($CoCl_2$) solution in a carbon steel ball mill. Corrosion of the carbon steel balls by the $CoCl_2$ solution (pH 5) was responsible for the iron component of the LDHs, and electron transfer during the elution of Fe^{2+} and Fe^{3+} caused electrolysis of water to generate hydroxide ions, which led to the formation of the LDH. Conventional methods for CoFe-LDH synthesis are typically complicated and yield poorly crystalline products, but this mechanochemical method produced CoFe-LDHs of high purity and crystallinity. This work has been extended to nickel iron LDHs (NiFe-LDHs) but further studies are required to understand the mechanism and increase the yields.[139]

Solvent-free mechanochemical routes are also suitable for the preparation of carbonate-free LDHs. Meixnerite-type LDHs (MgAl-OH-LDHs) and nitrate LDHs are typically difficult to obtain with high purity by co-precipitation due to the preferential incorporation of carbonate present in aqueous solutions. By grinding the hydroxides, Tongamp *et al.*[140, 141] prepared MgAl-OH- and MgAl-NO_3-LDHs, without significant effort to avoid carbonation.

Mechanochemical methods are often coupled with hydrothermal ageing: highly crystalline LDHs can be synthesised at lower temperatures, or in shorter reaction times, compared to direct hydrothermal syntheses.[133, 142] Du *et al.*[143] prepared a nickel magnesium aluminium LDH ($Ni_{3.6}Mg_{2.4}Al_2$-CO_3-LDH) by grinding the nitrate salts in a pestle and mortar with sodium carbonate (Na_2CO_3) and sodium hydroxide (NaOH), and

treating the resulting powder hydrothermally for 24 hours (Figure 1.14). They found that the LDH had higher crystallinity, higher surface area and stronger basicity than the equivalent LDH prepared by co-precipitation. Intimate contact between the reactants and plastic deformations during milling are thought to produce LDHs with higher surface areas and higher densities of lattice defects, which may enhance their catalytic reactivity.[144, 145]

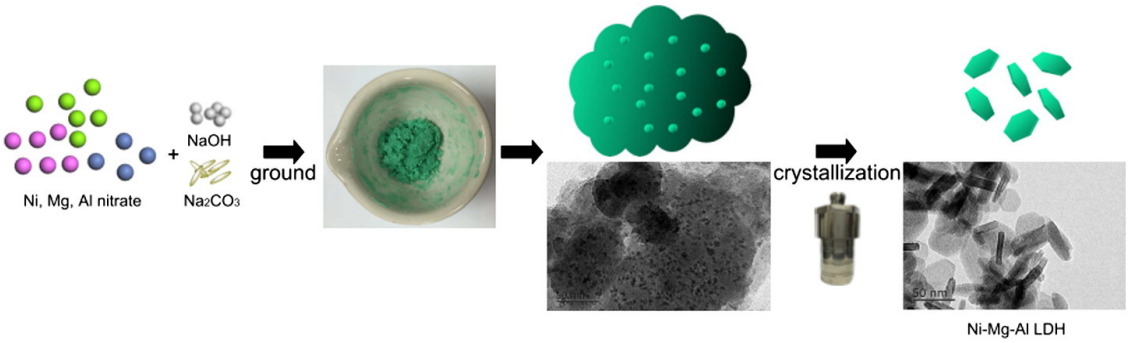


Figure 1.14 Solvent-free synthesis of NiMgAl-LDH.[143]

1.5.3 Microwaves

Microwave-assisted hydrothermal syntheses have also attracted attention in recent years. Traditional heating methods rely on conduction and convection, making them slow and inefficient because various materials with different thermal conductivities must be penetrated, and the reaction vessel often ends up at a higher temperature than the reaction mixture. In contrast, microwave irradiation produces efficient internal heating through dipolar polarisation and ionic conduction, leading to shorter reaction times and enhanced product yields.[146] The energy of a microwave photon (*ca.* 1 J mol^{-1} for a wave of frequency 2.45 GHz) is too low to cleave chemical bonds. Instead, when a material is irradiated with microwaves, the dipoles or ions in the material align themselves with the electric field.[147] Since electromagnetic radiation produces an oscillating field, these dipoles will be continuously realigning. Heating occurs when the rotations of the polar species lags behind the electric field oscillations, as this causes electrical resistance. If

the frequency of the field is much higher than the response time of the dipoles, or if the dipoles align easily with the field, no heating occurs. In the ionic conduction mechanism, heat is generated by the collision of oscillating ions. Most devices use a microwave frequency of 2.45 GHz, which is also the most common in domestic microwaves.[146]

In addition to being energy-saving, microwave-assisted hydrothermal syntheses produce LDHs with enhanced crystallinity, higher surface area and uniform particle size.[148] Samples formed under microwave irradiation exhibit more surface defects and as a result, greater amounts of acidic and basic sites.[149] Further, Kannan *et al.*[150] reported that microwave treatment afforded a more ordered arrangement of water molecules in the interlayer space, which led to the accommodation of more water molecules in the structure.

1.6 Green reagents for LDH syntheses

1.6.1 Bases

Making LDH syntheses more environmentally friendly involves making changes to reagent sourcing as well as the reaction procedures. Traditionally, strong bases such as sodium hydroxide (NaOH) are used and this generates a large volume of alkaline wastewater that is expensive to treat, which means it is sometimes discharged into the environment without treatment. Recognising the need for environmentally friendly alternatives, Xu *et al.*[132] developed an atom-economic method that uses urea as the base. By heating urea and the metal hydroxides hydrothermally, both in a conventional oven and by microwave irradiation, the washing and filtering steps were circumvented because there were no by-products. The ammonia produced in the reaction was also recycled – to prepare fresh urea.

Similarly, Zhang *et al.*[151] used ammonia hydrate ($NH_3.H_2O$) to precipitate a calcium-doped magnesium aluminium LDH (Ca/Mg_3Al-LDH). The use of aluminium trichloride ($AlCl_3.6H_2O$) allowed the ammonium to be captured as NH_4Cl by distillation of the mother liquor, and the distilled water was used to wash the LDH.

1.6.2 Metals

LDHs are commonly manufactured at scale using soluble metal salts, such as nitrates and chlorides, or oxides – sometimes obtained by calcining the salts. The global demand for LDHs means that there is scope for reducing the carbon footprint of these materials if a greener alternative source of cations could be found. At an LDH plant in Dalian (Liaoning province, China) magnesium chloride ($MgCl_2$) from seawater is used to prepare magnesium aluminium LDHs (MgAl-LDHs).[49] Prior to establishment of the LDH plant, there was no demand for the $MgCl_2$ that was produced during crystallisation of sodium and potassium chlorides from seawater. It was often returned to the sea and had adverse effects on the marine ecosystem. Nowadays, the LDH manufacturing process generates sodium chloride as a by-product and this is used in a neighbouring plant to regenerate sodium hydroxide for the LDH plant.

The first direct synthesis of a $3R_2$ polytype LDH was achieved by hydrothermal treatment of magnesium oxide (MgO) and alumina (Al_2O_3).[95] Xu and Lu[94] have studied the formation mechanism in detail and postulated a dissociation-deposition-diffusion mechanism for LDH formation from the oxides (Equations 1.5–1.7). Notably, they also reported that all reactions involve the hydroxide ion (OH^-) and so confirm that pH plays a very important role in LDH synthesis.

$$MgO + H_2O \leftrightarrow Mg(OH)_2 \leftrightarrow Mg^{2+} + 2OH^- \qquad \text{Equation 1.5}$$

$$Al_2O_3 + 3H_2O \leftrightarrow 2Al(OH)_3 \leftrightarrow 2Al(OH)_2^+ + 2OH^- \leftrightarrow 2Al(OH)^{2+} + 4OH^- \leftrightarrow 2Al^{3+} + 6OH^- \qquad \text{Equation 1.6}$$

$$Al(OH)_3 + OH^- \leftrightarrow Al(OH)_4^- \quad \text{Equation 1.7}$$

MgO is commonly produced by calcination of natural minerals such as brucite ($Mg(OH)_2$), hydromagnesite ($Mg_2CO_3(OH)_2$) and magnesite ($MgCO_3$). However, these resources are mainly found in China, Russia and North Korea however, so MgO is costly. Furthermore, there are environmental concerns, including soil degradation and soil alkalisation, associated with magnesite mining in China.[152] An alternative source of MgO is dolomite ($CaMg(CO_3)_2$), which is more widely distributed worldwide and less expensive. MgAl- and MgFe-LDHs have been prepared using calcined dolomite as a source of magnesium have been reported.[153-156] However, dolomite must be calcined at 900–1000 ºC in order to generate MgO, which is energy intensive, and carbon dioxide, a greenhouse gas (GHG), is also released during the process. More recently, Mao *et al.*[157] developed an alternate approach to using dolomite for LDH syntheses. The researchers dissolved dolomite in an aqueous solution of aluminium chloride ($AlCl_3.6H_2O$) with the aid of hydrothermal treatment to obtain a slurry containing Ca^{2+}, Mg^{2+} and Al^{3+} (initial pH 0.14, pH of the slurry pH 3.65). This solution was then combined with NaOH to precipitate CaMgAl-LDH.

Perera-Solis *et al.*[158] have very recently demonstrated that MgFe-LDHs may be produced from an unwanted waste material called ochre, which is a mixture of ferric hydroxides. The acid-soluble material was used as a source of Fe^{3+} cations and they obtained LDHs with the formula $Mg_{0.68}Fe_{0.32}(CO_3)_{0.16}{\cdot}mH_2O$, by constant pH co-precipitation with magnesium nitrate hexahydrate ($Mg(NO_3)_2.6H_2O$) and sodium carbonate (Na_2CO_3) at 65 ºC and pH 10. This transformation is a profound example of circular economy as the obtained LDH was then used in a catalytic ketonic decarboxylation reaction that can be used in biomass conversion.

1.6.3 Circular economy

The circular economy concept emerged in Boulding's landmark essay on sustainability in 1966.[159] In contrast to a traditional linear economy (make, use, dispose), circular economy is an economic system where products and materials are kept in use, and waste and pollution are minimised by design.

Reusing and recycling products at the end of their useful life are choices that manufacturers and consumers are making in order to combat the increasing amounts of waste generated by the increasing world population. Furthermore, the transformation of waste materials into added-value products is an increasingly important practice as we seek to make our economies more sustainable and environmentally friendly.

Unfortunately, there are numerous legal and practical barriers to utilising waste as feedstocks. In the European Union, waste is defined as "any substance or object which the holder discards or intends or is required to discard".[160] A substance is considered a non-waste by-product if the following conditions are met: a) further use of the substance or object is certain; b) the substance or object can be used directly without any further processing other than normal industrial practice; c) the substance or object is produced as an integral part of a production process; and d) further use is lawful, *i.e.* the substance or object fulfils all relevant product, environmental and health protection requirements for the specific use and will not lead to overall adverse environmental or human health impacts.[160]

In order for waste to become a new or secondary raw material, it must obtain end-of-waste (EoW) status.[160] The basic requirements for a recovered waste to achieve EoW are: a) the substance or object is to be used for specific purposes; b) a market or demand exists for such a substance or object; c) the substance or object fulfils the technical requirements

for the specific purposes and meets the existing legislation and standards applicable to products; and d) the use of the substance or object will not lead to overall adverse environmental or human health impacts. To protect the environment and human health there are further criteria to be fulfilled, which include permissible waste input material, allowed treatment processes and quality criteria (*i.e.* composition quality control and limiting values for pollutants). For waste producers and waste holders, obtaining EoW status can take many years and be an expensive process, reducing the incentive to do so.

1.6.4 Circular economy – an example from biofuels

The development of biofuels is one of the most well-known examples of renewable technologies where economic and environmental demands directed the foci of research. First-generation biofuels, also known as "conventional biofuels", include ethanol and biodiesel. They are made from food crops grown on arable land such as sugarcane, corn and vegetable oil.[161] It has been calculated that corn ethanol provides a considerably smaller reduction in GHG emissions (18%) than sugarcane ethanol (91%) when replacing gasoline.[162] This is due to the high fertilizer input in corn farming and energy required to power the process.[163]

Biodiesel is an alternative diesel made from renewable, biological sources such as vegetable oils or animal fats. The feedstocks cannot be used directly as fuel because they contain water and other impurities, so are converted to fatty acid methyl esters (FAME) by transesterification.[164] Biodiesel yields 93% more energy than that invested in its production (whilst ethanol yields just 25% more) and GHG emissions are reduced 41% relative to fossil fuels.[165]

However, although renewable, crops require land and critics argue that diverting farmland and crops to biofuel production would create a "food versus fuel" dilemma.[166]

The depletion of crude oil, political instability, and international conflict have all contributed to the rising crude oil prices since the beginning of the millennium, which in turn have raised food prices.[167] Public protests erupted in Mexico in 2007 over the soaring price of corn, the key ingredient of the country's staple tortilla that many of the poorest survive on.[168] In the US, it was also argued that corn is better used to provide nutrition to the hungry, both in the US and internationally as food aid.[167]

The change in land use can also result in deforestation, soil erosion, loss of biodiversity and rises in GHG emissions.[165, 169, 170] A primary example of this is the Amazon rainforest in Brazil. In 2015, a study found that the amount of carbon absorbed and stored by the Amazon rainforest had fallen by one third over the previous decade.[171] In addition, the nitrogen-based fertiliser used in growing sugarcane for bioethanol leads to significant emissions of nitrous oxide (N_2O), a powerful GHG.

Socioeconomical and environmental concerns over food crop-based biofuels prompted the development of non-edible renewable feedstocks. Lignocellulosic biomass, from agricultural residues, forestry wastes, and wastepaper, is a promising second-generation biofuel source. The term "biomass" essentially covers any material of recent biological origin, so includes animal manure and municipal biosolids (sewage) as well as trees and grasses.[162] Carbohydrates are the most abundant component of biomass and can be categorised into two groups: mono- and polysaccharides.

Lignocellulose, the fibrous material that forms the cell walls of plants, is the most common form in which polysaccharides occur in nature. Its composition depends on the plant species but is typically 28–55 wt.% cellulose, 17–35 wt.% hemicellulose, and 17–35 wt.% lignin.[172] Lignin is an irregular polymer of phenylpropane units that confers structural rigidity to plants. Softwood lignins are formed from coniferyl alcohol,

hardwood lignins are formed from coniferyl and sinapyl alcohol, and grasses are formed from coniferyl, sinapyl and *p*-coumaryl alcohol (Figure 1.15). Its empirical formula is $C_9H_{10}O_2(OCH_3)_n$, where *n* varies from 0.94 for softwood to 1.40 for hardwood, and 1.18 for grasses.[173] The structure of lignin is complex because the biosynthesis of lignin involves enzyme-initiated, free-radical polymerisation of these alcohol precursors.[174]

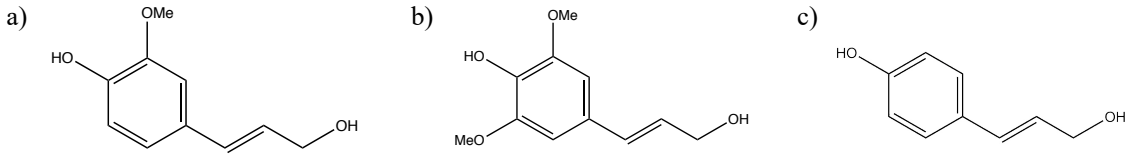


Figure 1.15 Lignin monomers. a) coniferyl alcohol, b) sinapyl alcohol, and c) *p*-coumaryl alcohol.

Lignin is a by-product of little commercial importance in the pulp and paper industry. Two commonly used routes to transform these complex polymers into higher value chemicals are: biomass to liquid (BTL), which involves gasification to syngas (CO and H_2) followed by the Fischer-Tropsch synthesis; and pyrolysis or liquefaction of biomass to bio-oil followed by catalytic upgrading.[175, 176]

Lignin pyrolysis oil shows potential as a second-generation energy carrier but a number of undesirable properties, such as low thermal stability, high viscosity and poor energy density, preclude its direct application as a fuel in existing infrastructures.[177-179] These properties originate from the highly diverse and oxofunctionalised chemical composition of bio-oils, which contrasts heavily with fossil fuels that are essentially molecular hydrocarbons.[180-182] The oxygen content of bio-oils can be 10–40 wt.% and more than 300 oxygenated components have been identified in bio-oils including organic acids, phenolics, aldehydes, and ketones.[180, 183-187] Bio-oils also contain 15–30 wt.% water as a result of moisture in the feedstock and dehydration during pyrolysis.[188]

Hydroprocessing reactions are therefore commonly employed to upgrade bio-oils to fuels. The main reaction performed in biomass hydrotreatment is hydrodeoxygenation

(HDO), which is achieved commercially using sulfided molybdenum catalysts supported on gamma alumina (γ-Al_2O_3).[189] More recently, researchers have combined the high hydrogenation ability of metal nanoparticles with acidic supports to create bifunctional catalysts, *e.g.* Pd-Mo on silica,[190] that show enhanced deoxygenation performance compared with the metal catalysts on inert supports. The performance of calcined Pd-impregnated MgAl-LDHs in the HDO of phenol has also been investigated but were found to be more selective for the partially hydrogenated product, cyclohexanone.[191]

The water footprint and land use for the cultivation of energy crops have raised questions about the feasibility of biofuels and so attention has recently been drawn towards microalgae as a third-generation biofuel source.[192] Unlike other oil crops, such as soybean and palm, microalgae grow extremely quickly (commonly doubling their biomass in 24 hours) and many are rich in lipids. The oil content in microalgae can exceed 80% by weight of dry biomass, though is usually between 20–50%.[193] It has been calculated that microalgae would require 20 times less land than oil palm to produce the same volume of biodiesel.[194] Moreover, microalgae can produce fatty acids with unusual chain lengths and a high degree of unsaturation (*e.g.* eicosapentaenoic acid, EPA) , which are not commonly found elsewhere in nature.[195]

The principles of green chemistry and circular economy are well illustrated by the biofuel case. Environmental sustainability first drove research into crop-based biofuels and socioeconomical sustainability then directed studies towards the use of waste materials. This shift highlights the importance of changing attitudes and practices to minimise environmental damage and to preserve quality of life.

1.7 Thesis overview

The aims of this thesis are to develop atom-efficient and scalable syntheses of commercially relevant MgAl-LDHs. The analytical techniques and synthetic methods are detailed in Chapter 2 in advance of the discussions. In Chapter 3, the use of an alternative starting material, the mineral struvite ($MgNH_4PO_4.6H_2O$), for MgAl-LDH synthesis is investigated. The studies were firstly conducted on synthetic struvite and then applied to struvites obtained from industrial (wastewater) sources. Chapter 4 presents the optimisation of LDH crystallisation on silica cores for the preparation of hybrid LDH materials for catalysis. The effects of stirring speed and solution addition rate were systematically investigated to achieve well-defined core-shell materials with high surface areas and porosities. Finally, in Chapter 5, the thermal properties of the mineral-derived and hybrid LDH materials are discussed. The performance of the thermally activated compounds in carbon dioxide adsorption is also reported.

1.8 References

1. X. Duan and D. G. Evans, *Layered Double Hydroxides*, Struct. Bond., Springer-Verlag Berlin Heidelberg, 2005.
2. F. Cavani, F. Trifirò and A. Vaccari, *Catal. Today*, 1991, **11**, 173-301.
3. E. López-Salinas, M. García-Sánchez, J. A. Montoya, D. R. Acosta, J. A. Abasolo and I. Schifter, *Langmuir*, 1997, **13**, 4748-4753.
4. F. M. Labajos, M. J. Sánchez-Montero, M. J. Holgado and V. Rives, *Thermochim. Acta*, 2001, **370**, 99-104.
5. J. M. Fernández, C. Barriga, M. A. Ulibarri, F. M. Labajos and V. Rives, *Chem. Mater.*, 1997, **9**, 312-318.
6. P. Vicente, M. E. Pérez-Bernal, R. J. Ruano-Casero, D. Ananias, F. A. Almeida Paz, J. Rocha and V. Rives, *Micropor. Mesopor. Mat.*, 2016, **226**, 209-220.
7. S. Velu, V. Ramaswamy and S. Sivasanker, *Chem. Commun.*, 1997, 2107-2108.
8. S. Velu, K. Suzuki, M. Okazaki, T. Osaki, S. Tomura and F. Ohashi, *Chem. Mater.*, 1999, **11**, 2163-2172.
9. X. Shu, W. Zhang, J. He, F. Gao and Y. Zhu, *Solid State Sci.*, 2006, **8**, 634-639.
10. S. Miyata, *Clays Clay Miner.*, 1975, **23**, 369-375.
11. A. I. Khan and D. O'Hare, *J. Mater. Chem.*, 2002, **12**, 3191-3198.
12. V. Rives, *Layered Double Hydroxides: Present and Future*, Nova Science Publishers, 2001.
13. A. Bookin and V. Drits, *Clays Clay Miner.*, 1993, **41**, 551-557.
14. A. Radha, C. Shivakumara and P. V. Kamath, *Clays Clay Miner.*, 2005, **53**, 520-527.
15. G. S. Thomas, M. Rajamathi and P. V. Kamath, *Clays Clay Miner.*, 2004, **52**, 693-699.
16. S. Miyata, *Clays Clay Miner.*, 1983, **31**, 305-311.
17. G. S. Thomas and P. V. Kamath, *J. Chem. Sci.*, 2006, **118**, 127-133.
18. S. Radha and P. V. Kamath, *Cryst. Growth Des.*, 2009, **9**, 3197-3203.
19. T. Witzke and G. Raade, *Neu. Jb. Mineral., Mh*, 2000, **10**, 455-465.
20. W. Hofmeister and H. V. Platen, *Crystallogr. Rev.*, 1992, **3**, 3-26.
21. R. Shivaramaiah and A. Navrotsky, *Inorg. Chem.*, 2015, **54**, 3253-3259.
22. W. A. Sławiński, A. O. Sjåstad and H. Fjellvåg, *Inorg. Chem.*, 2016, **55**, 12881-12889.
23. T. Hibino and A. Tsunashima, *Chem. Mater.*, 1997, **9**, 2082-2089.
24. L. Pesic, S. Salipurovic, V. Markovic, D. Vucelic, W. Kagunya and W. Jones, *J. Mater. Chem.*, 1992, **2**, 1069-1073.
25. J. Wang, A. G. Kalinichev, J. E. Amonette and R. J. Kirkpatrick, *Am. Mineral.*, 2003, **88**, 398-409.
26. X. Hou, D. Bish, S.-L. Wang, C. Johnston and R. Kirkpatrick, *Am. Mineral.*, 2003, **88**, 167-179.
27. S. Radha, Churchil A. Antonyraj, P. Vishnu Kamath and S. Kannan, *Z. Anorg. Allg. Chem.*, 2010, **636**, 2658-2664.
28. R. Mostarih and A. de Roy, *J. Phys. Chem. Solids*, 2006, **67**, 1058-1062.
29. M. Khaldi, A. De Roy, M. Chaouch and J. P. Besse, *J. Solid State Chem.*, 1997, **130**, 66-73.
30. J. Das, B. S. Patra, N. Baliarsingh and K. M. Parida, *Appl. Clay Sci.*, 2006, **32**, 252-260.
31. K.-H. Goh, T.-T. Lim and Z. Dong, *Water Res.*, 2008, **42**, 1343-1368.
32. C. Chen, P. Gunawan and R. Xu, *J. Mater. Chem.*, 2011, **21**, 1218-1225.

33. P.-P. Huang, C.-Y. Cao, F. Wei, Y.-B. Sun and W.-G. Song, *RSC Adv.*, 2015, **5**, 10412-10417.
34. R. Marangoni, M. Bouhent, C. Taviot-Guého, F. Wypych and F. Leroux, *J. Colloid Interface Sci.*, 2009, **333**, 120-127.
35. S. V. Prasanna and P. V. Kamath, *Ind. Eng. Chem. Res.*, 2009, **48**, 6315-6320.
36. M. Zubair, M. Daud, G. McKay, F. Shehzad and M. A. Al-Harthi, *Appl. Clay Sci.*, 2017, **143**, 279-292.
37. L. Ma, Q. Wang, S. M. Islam, Y. Liu, S. Ma and M. G. Kanatzidis, *J. Am. Chem. Soc.*, 2016, **138**, 2858-2866.
38. L. Ma, S. M. Islam, C. Xiao, J. Zhao, H. Liu, M. Yuan, G. Sun, H. Li, S. Ma and M. G. Kanatzidis, *J. Am. Chem. Soc.*, 2017, **139**, 12745-12757.
39. S. Aisawa, S. Takahashi, W. Ogasawara, Y. Umetsu and E. Narita, *J. Solid State Chem.*, 2001, **162**, 52-62.
40. J.-H. Choy, S.-Y. Kwak, J.-S. Park, Y.-J. Jeong and J. Portier, *J. Am. Chem. Soc.*, 1999, **121**, 1399-1400.
41. X. Gao, L. Lei, D. O'Hare, J. Xie, P. Gao and T. Chang, *J. Solid State Chem.*, 2013, **203**, 174-180.
42. A. I. Khan, L. Lei, A. J. Norquist and D. O'Hare, *Chem. Commun.*, 2001, 2342-2343.
43. A. I. Khan, A. Ragavan, B. Fong, C. Markland, M. O'Brien, T. G. Dunbar, G. R. Williams and D. O'Hare, *Ind. Eng. Chem. Res.*, 2009, **48**, 10196-10205.
44. B. Li, J. He, D. G. Evans and X. Duan, *Appl. Clay Sci.*, 2004, **27**, 199-207.
45. S. Guan, R. Liang, C. Li, D. Yan, M. Wei, D. G. Evans and X. Duan, *J. Mater. Chem. B*, 2016, **4**, 1331-1336.
46. J.-H. Choy, J.-S. Jung, J.-M. Oh, M. Park, J. Jeong, Y.-K. Kang and O.-J. Han, *Biomaterials*, 2004, **25**, 3059-3064.
47. F. Li, Y. Wang, Q. Yang, D. G. Evans, C. Forano and X. Duan, *J. Hazard. Mater.*, 2005, **125**, 89-95.
48. K. L. Erickson, T. E. Bostrom and R. L. Frost, *Mater. Lett.*, 2005, **59**, 226-229.
49. D. G. Evans and X. Duan, *Chem. Commun.*, 2006, 485-496.
50. X. Zhao, F. Zhang, S. Xu, D. G. Evans and X. Duan, *Chem. Mater.*, 2010, **22**, 3933-3942.
51. G. M. Lombardo, G. C. Pappalardo, F. Costantino, U. Costantino and M. Sisani, *Chem. Mater.*, 2008, **20**, 5585-5592.
52. G. Yu, Y. Zhou, R. Yang, M. Wang, L. Shen, Y. Li, N. Xue, X. Guo, W. Ding and L. Peng, *J. Phys. Chem. C*, 2015, **119**, 12325-12334.
53. W. Yang, Y. Kim, P. K. T. Liu, M. Sahimi and T. T. Tsotsis, *Chem. Eng. Sci.*, 2002, **57**, 2945-2953.
54. M. Bellotto, B. Rebours, O. Clause, J. Lynch, D. Bazin and E. Elkaïm, *J. Phys. Chem.*, 1996, **100**, 8535-8542.
55. K. J. D. MacKenzie, R. H. Meinhold, B. L. Sherriff and Z. Xu, *J. Mater. Chem.*, 1993, **3**, 1263-1269.
56. H. Kawakami and S. Yoshida, *J. Chem. Soc., Faraday Trans. 2*, 1984, **80**, 921-932.
57. J. Shen, M. Tu and C. Hu, *J. Solid State Chem.*, 1998, **137**, 295-301.
58. F. Rey, V. Fornes and J. M. Rojo, *J. Chem. Soc., Faraday Trans.*, 1992, **88**, 2233-2238.
59. W. T. Reichle, S. Y. Kang and D. S. Everhardt, *J. Catal.*, 1986, **101**, 352-359.
60. J. I. Di Cosimo, V. K. Díez, M. Xu, E. Iglesia and C. R. Apesteguía, *J. Catal.*, 1998, **178**, 499-510.
61. L. M. Parker, N. B. Milestone and R. H. Newman, *Ind. Eng. Chem. Res.*, 1995, **34**, 1196-1202.

62. M. A. Ulibarri, I. Pavlovic, C. Barriga, M. C. Hermosín and J. Cornejo, *Appl. Clay Sci.*, 2001, **18**, 17-27.
63. C. Li, M. Wei, D. G. Evans and X. Duan, *Small*, 2014, **10**, 4469-4486.
64. U. Costantino, N. Coletti, M. Nocchetti, G. G. Aloisi and F. Elisei, *Langmuir*, 1999, **15**, 4454-4460.
65. E. P. Giannelis, D. G. Nocera and T. J. Pinnavaia, *Inorg. Chem.*, 1987, **26**, 203-205.
66. H. Tagaya, A. Ogata, T. Kuwahara, S. Ogata, M. Karasu, J.-i. Kadokawa and K. Chiba, *Microporous Mater.*, 1996, **7**, 151-158.
67. J. L. Gunjakar, I. Y. Kim, J. M. Lee, N.-S. Lee and S.-J. Hwang, *Energy Environ. Sci.*, 2013, **6**, 1008-1017.
68. L. Mohapatra and K. Parida, *J. Mater. Chem. A*, 2016, **4**, 10744-10766.
69. Y. F. Zhao, B. Li, Q. Wang, W. Gao, C. L. J. Wang, M. Wei, D. G. Evans, X. Duan and D. O'Hare, *Chem. Sci.*, 2014, **5**, 951-958.
70. G. Fan, F. Li, D. G. Evans and X. Duan, *Chem. Soc. Rev.*, 2014, **43**, 7040-7066.
71. M. F. P. Duarte, I. M. Rocha, J. L. Figueiredo, C. Freire and M. F. R. Pereira, *Catal. Today*, 2017.
72. R. Li, Y. Wang, W. Li, S. Zhou, P. Tian, H. Gao, X. Liu and J. Zang, *Chem. Commun.*, 2019, **55**, 13370-13373.
73. K. K. Rao, M. Gravelle, J. S. Valente and F. Figueras, *J. Catal.*, 1998, **173**, 115-121.
74. J. C. A. A. Roelofs, D. J. Lensveld, A. J. van Dillen and K. P. de Jong, *J. Catal.*, 2001, **203**, 184-191.
75. D. G. Cantrell, L. J. Gillie, A. F. Lee and K. Wilson, *Appl. Catal., A*, 2005, **287**, 183-190.
76. S. He, Z. An, M. Wei, D. G. Evans and X. Duan, *Chem. Commun.*, 2013, **49**, 5912-5920.
77. B. Wen, M. He and C. Costello, *Energy Fuels*, 2002, **16**, 1048-1053.
78. D. S. Newsome, *Cat. Rev.*, 1980, **21**, 275-318.
79. Y. He, L. Liang, Y. Liu, J. Feng, C. Ma and D. Li, *J. Catal.*, 2014, **309**, 166-173.
80. L. Li, L. Dou and H. Zhang, *Nanoscale*, 2014, **6**, 3753-3763.
81. Z.-A. Hu, Y.-L. Xie, Y.-X. Wang, H.-Y. Wu, Y.-Y. Yang and Z.-Y. Zhang, *Electrochim. Acta*, 2009, **54**, 2737-2741.
82. J. Han, Y. Dou, J. Zhao, M. Wei, D. G. Evans and X. Duan, *Small*, 2013, **9**, 98-106.
83. M. Shao, R. Zhang, Z. Li, M. Wei, D. G. Evans and X. Duan, *Chem. Commun.*, 2015, **51**, 15880-15893.
84. X. Long, Z. Wang, S. Xiao, Y. An and S. Yang, *Mater. Today*, 2016, **19**, 213-226.
85. M. R. Othman, Z. Helwani, Martunus and W. J. N. Fernando, *Appl. Organomet. Chem.*, 2009, **23**, 335-346.
86. J. T. Kloprogge, L. Hickey and R. L. Frost, *J. Solid State Chem.*, 2004, **177**, 4047-4057.
87. S. Zeng, X. Xu, S. Wang, Q. Gong, R. Liu and Y. Yu, *Mater. Chem. Phys.*, 2013, **140**, 159-167.
88. L. Ratke and P. W. Voorhees, *Growth and coarsening: Ostwald ripening in material processing*, Springer Science & Business Media, 2013.
89. K. Li, G. Wang, D. Li, Y. Lin and X. Duan, *Chin. J. Chem. Eng.*, 2013, **21**, 453-462.
90. Y. Zhao, F. Li, R. Zhang, D. G. Evans and X. Duan, *Chem. Mater.*, 2002, **14**, 4286-4291.
91. L. Hickey, J. T. Kloprogge and R. L. Frost, *J. Mater. Sci.*, 2000, **35**, 4347-4355.
92. J.-M. Oh, S.-H. Hwang and J.-H. Choy, *Solid State Ion.*, 2002, **151**, 285-291.
93. L. Liao, N. Zhao and Z. Xia, *Mater. Res. Bull.*, 2012, **47**, 3897-3901.
94. Z. P. Xu and G. Q. Lu, *Chem. Mater.*, 2005, **17**, 1055-1062.

95. S. P. Newman, W. Jones, P. O'Connor and D. N. Stamires, *J. Mater. Chem.*, 2002, **12**, 153-155.
96. W. H. R. Shaw and J. J. Bordeaux, *J. Am. Chem. Soc.*, 1955, **77**, 4729-4733.
97. U. Costantino, F. Marmottini, M. Nocchetti and R. Vivani, *Eur. J. Inorg. Chem.*, 1998, **1998**, 1439-1446.
98. H. H. Willard and N. K. Tang, *J. Am. Chem. Soc.*, 1937, **59**, 1190-1196.
99. J. Liu, J. Song, H. Xiao, L. Zhang, Y. Qin, D. Liu, W. Hou and N. Du, *Powder Technol.*, 2014, **253**, 41-45.
100. C. Hobbs, S. Jaskaniec, E. K. McCarthy, C. Downing, K. Opelt, K. Güth, A. Shmeliov, M. C. D. Mourad, K. Mandel and V. Nicolosi, *NPJ 2D Mater. Appl.*, 2018, **2**, 4.
101. T. Hibino and H. Ohya, *Appl. Clay Sci.*, 2009, **45**, 123-132.
102. H. Lin, Y. Zhang, G. Wang and J.-B. Li, *Front. Mater. Sci.*, 2012, **6**, 142-148.
103. R. L. Frost, A. W. Musumeci, M. O. Adebajo and W. Martens, *J. Therm. Anal. Calorim.*, 2007, **89**, 95-99.
104. T. Sato, T. Wakabayashi and M. Shimada, *Ind. Eng. Chem. Prod. Res. Dev.*, 1986, **25**, 89-92.
105. M. P. Pileni, *J. Phys. Chem.*, 1993, **97**, 6961-6973.
106. G. Hu and D. O'Hare, *J. Am. Chem. Soc.*, 2005, **127**, 17808-17813.
107. J. N. Israelachvili, *Intermolecular and Surface Forces*, Elsevier Science & Technology, Saint Louis, United States, 2010.
108. G. Hu, N. Wang, D. O'Hare and J. Davis, *J. Mater. Chem.*, 2007, **17**, 2257-2266.
109. C. J. Wang, Y. A. Wu, R. M. J. Jacobs, J. H. Warner, G. R. Williams and D. O'Hare, *Chem. Mater.*, 2011, **23**, 171-180.
110. M. E. Pérez-Bernal, R. J. Ruano-Casero, F. Benito and V. Rives, *J. Solid State Chem.*, 2009, **182**, 1593-1601.
111. J. Xu, L. Zhang, D. Li, J. Zhao and W. Hou, *Colloid. Polym. Sci.*, 2013, **291**, 2515-2521.
112. Q. Wang, X. Zhang, J. Zhu, Z. Guo and D. O'Hare, *Chem. Commun.*, 2012, **48**, 7450-7452.
113. Q. Wang and D. O'Hare, *Chem. Commun.*, 2013, **49**, 6301-6303.
114. Q. Wang and D. O'Hare, *Chem. Rev.*, 2012, **112**, 4124-4155.
115. T. Hibino and M. Kobayashi, *J. Mater. Chem.*, 2005, **15**, 653-656.
116. M. a. Jobbágy and A. E. Regazzoni, *J. Colloid Interface Sci.*, 2004, **275**, 345-348.
117. Q. Wu, A. Olafsen, O. B. Vistad, J. Roots and P. Norby, *J. Mater. Chem.*, 2005, **15**, 4695-4700.
118. R. Ma, Z. Liu, L. Li, N. Iyi and T. Sasaki, *J. Mater. Chem.*, 2006, **16**, 3809-3813.
119. Z. Liu, R. Ma, M. Osada, N. Iyi, Y. Ebina, K. Takada and T. Sasaki, *J. Am. Chem. Soc.*, 2006, **128**, 4872-4880.
120. F. Song and X. Hu, *Nat. Commun.*, 2014, **5**.
121. M. Adachi-Pagano, C. Forano and J.-P. Besse, *Chem. Commun.*, 2000, 91-92.
122. B. R. Venugopal, C. Shivakumara and M. Rajamathi, *J. Colloid Interface Sci.*, 2006, **294**, 234-239.
123. R. Chalasani, A. Gupta and S. Vasudevan, *Sci. Rep.*, 2013, **3**, 3498.
124. C. Chen, M. Yang, Q. Wang, J.-C. Buffet and D. O'Hare, *J. Mater. Chem. A*, 2014, **2**, 15102-15110.
125. M. S. Yang, O. McDermott, J.-C. Buffet and D. O'Hare, *RSC Adv.*, 2014, **4**, 51676-51682.
126. C. P. Chen, A. Wangriya, J.-C. Buffet and D. O'Hare, *Dalton Trans.*, 2015, **44**, 16392-16398.

127. V. Erastova, M. T. Degiacomi, D. O'Hare and H. C. Greenwell, *RSC Adv.*, 2017, **7**, 5076-5083.
128. K. Ruengkajorn, V. Erastova, J.-C. Buffet, H. C. Greenwell and D. O'Hare, *Chem. Commun.*, 2018, **54**, 4394-4397.
129. K. Ruengkajorn, C. M. R. Wright, N. H. Rees, J.-C. Buffet and D. O'Hare, *Mater. Chem. Front.*, 2018, **2**, 2277-2285.
130. P. T. Anastas and J. C. Warner, *Green Chemistry: Theory and Practice*, Oxford University Press, 1998.
131. R. A. Sheldon, *Green Chem.*, 2007, **9**, 1273-1283.
132. X. Xu, D. Li, J. Song, Y. Lin, Z. Lv, M. Wei and X. Duan, *Particuology*, 2010, **8**, 198-201.
133. J. Qu, Q. Zhang, X. Li, X. He and S. Song, *Appl. Clay Sci.*, 2016, **119**, 185-192.
134. F. J. W. J. Labuschagné, A. Wiid, H. P. Venter, B. R. Gevers and A. Leuteritz, *Green Chem. Lett. Rev.*, 2018, **11**, 18-28.
135. N. Thomas, *Mater. Res. Bull.*, 2012, **47**, 3568-3572.
136. C. Ramesh, T. Satoko, S. Akinari, S. Kohji, O. Kenta and H. Takahiro, *Chem. Lett.*, 2007, **36**, 446-447.
137. J. Qu, X. He, B. Wang, L. Zhong, L. Wan, X. Li, S. Song and Q. Zhang, *Appl. Clay Sci.*, 2016, **120**, 24-27.
138. T. Iwasaki, K. Shimizu, H. Nakamura and S. Watano, *Mater. Lett.*, 2012, **68**, 406-408.
139. T. Iwasaki, H. Yoshii, H. Nakamura and S. Watano, *Appl. Clay Sci.*, 2012, **58**, 120-124.
140. W. Tongamp, Q. Zhang and F. Saito, *J. Mater. Sci.*, 2007, **42**, 9210-9215.
141. W. Tongamp, Q. Zhang and F. Saito, *Powder Technol.*, 2008, **185**, 43-48.
142. F. Zhang, N. Du, S. Song, J. Liu and W. Hou, *J. Solid State Chem.*, 2013, **206**, 45-50.
143. W. Du, L. Zheng, X. Li, J. Fu, X. Lu and Z. Hou, *Appl. Clay Sci.*, 2016, **123**, 166-172.
144. J. Salmones, B. Zeifert, M. H. Garduño, J. Contreras-Larios, D. R. Acosta, A. R. Serrano and L. A. Garcia, *Catal. Today*, 2008, **133-135**, 886-890.
145. J. Qu, L. Sha, C. Wu and Q. Zhang, *Nanomaterials*, 2019, **9**, 80.
146. M. Nüchter, B. Ondruschka, W. Bonrath and A. Gum, *Green Chem.*, 2004, **6**, 128-141.
147. I. Bilecka and M. Niederberger, *Nanoscale*, 2010, **2**, 1358-1374.
148. P. Benito, F. M. Labajos and V. Rives, 2009, **81**, 1459.
149. M. J. Climent, A. Corma, S. Iborra, K. Epping and A. Velty, *J. Catal.*, 2004, **225**, 316-326.
150. S. Kannan and R. Vir Jasra, *J. Mater. Chem.*, 2000, **10**, 2311-2314.
151. Y. Zhang, J. Wang, X. Liu, P. Gao, C. Gong and L. Lei, *Environ. Prog. Sustain. Energy*, 2015, **34**, 234-239.
152. S.-S. Fu, P.-J. Li, Q. Feng, X.-J. Li, P. Li, Y.-B. Sun and Y. Chen, *Pedosphere*, 2011, **21**, 98-106.
153. K. Hosni and E. Srasra, *Appl. Clay Sci.*, 2009, **43**, 415-419.
154. X. Qiu, K. Sasaki, T. Hirajima, K. Ideta and J. Miyawaki, *Chem. Eng. J.*, 2013, **225**, 664-672.
155. X. Qiu, M. Yoshida, T. Hirajima and K. Sasaki, *Mater. Trans.*, 2015, **56**, 224-228.
156. M. Yoshida, P. Koilraj, X. Qiu, T. Hirajima and K. Sasaki, *J. Environ. Chem. Eng.*, 2015, **3**, 1614-1621.

157. N. Mao, C. H. Zhou, J. Keeling, S. Fiore, H. Zhang, L. Chen, G. C. Jin, T. T. Zhu, D. S. Tong and W. H. Yu, *Appl. Clay Sci.*, 2018, **159**, 25-36.
158. D. D. Perera-Solis, M. Pimlott, E. Fidment, A. Whiting and H. C. Greenwell, *Minerals*, 2019, **9**, 681.
159. K. E. Boulding, H. Jarrett, *The economics of the coming spaceship Earth*, Environmental Quality in a Growing Economy, Johns Hopkins University Press, Baltimore, MD, 1966.
160. Directive 2008/98/EC of The European Parliament and of The Council of 19 November 2008 on waste and repealing certain Directives, 2008
161. R. A. Lee and J.-M. Lavoie, *Anim. Front.*, 2013, **3**, 6-11.
162. J. Goldemberg, *Biotechnol. Biofuels*, 2008, **1**, 6.
163. M. Wang, Updated energy and greenhouse gas emission results of fuel ethanol, The 15th International Symposium on Alcohol Fuels, San Diego, 2005.
164. L. C. Meher, D. Vidya Sagar and S. N. Naik, *Renew. Sustain. Energy Rev*, 2006, **10**, 248-268.
165. J. Hill, E. Nelson, D. Tilman, S. Polasky and D. Tiffany, *Proc. Natl. Acad. Sci.*, 2006, **103**, 11206-11210.
166. D. O. Hall, *Energy Policy*, 1991, **19**, 711-737.
167. M. Muller, T. Yelden and H. Schoonover, *Food versus Fuel in the United States*, Institute for Agriculture and Trade Policy, Minneapolis, Minnesota, 2007.
168. J. C. McKinley, *The New York Times*, 19th January 2007, A12
169. T. Searchinger, R. Heimlich, R. A. Houghton, F. Dong, A. Elobeid, J. Fabiosa, S. Tokgoz, D. Hayes and T.-H. Yu, *Science*, 2008, **319**, 1238-1240.
170. A. Mohr and S. Raman, *Energy Policy*, 2013, **63**, 114-122.
171. R. J. W. Brienen, O. L. Phillips, T. R. Feldpausch, E. Gloor, T. R. Baker, J. Lloyd, G. Lopez-Gonzalez, A. Monteagudo-Mendoza, Y. Malhi, S. L. Lewis*, et al.*, *Nature*, 2015, **519**, 344-348.
172. H. Wang, J. Male and Y. Wang, *ACS Catal.*, 2013, **3**, 1047-1070.
173. J. A. Melero, J. Iglesias and A. Garcia, *Energy Environ. Sci.*, 2012, **5**, 7393-7420.
174. R. J. Evans, T. A. Milne and M. N. Soltys, *J. Anal. Appl. Pyrolysis*, 1986, **9**, 207-236.
175. J. C. Serrano-Ruiz and J. A. Dumesic, *Energy Environ. Sci.*, 2011, **4**, 83-99.
176. R. P. Anex, A. Aden, F. K. Kazi, J. Fortman, R. M. Swanson, M. M. Wright, J. A. Satrio, R. C. Brown, D. E. Daugaard, A. Platon*, et al.*, *Fuel*, 2010, **89**, Supplement 1, S29-S35.
177. S. K. Singh and J. D. Ekhe, *RSC Adv.*, 2014, **4**, 27971-27978.
178. D. C. Elliott, *Energy Fuels*, 2007, **21**, 1792-1815.
179. A. Oasmaa and S. Czernik, *Energy Fuels*, 1999, **13**, 914-921.
180. S. Czernik and A. V. Bridgwater, *Energy Fuels*, 2004, **18**, 590-598.
181. P. M. Mortensen, J. D. Grunwaldt, P. A. Jensen, K. G. Knudsen and A. D. Jensen, *Appl. Catal., A*, 2011, **407**, 1-19.
182. C. Zhao and J. A. Lercher, *Angew. Chem. Int. Ed.*, 2012, **51**, 5935-5940.
183. J. Barbier, N. Charon, N. Dupassieux, A. Loppinet-Serani, L. Mahé, J. Ponthus, M. Courtiade, A. Ducrozet, A.-A. Quoineaud and F. Cansell, *Biomass Bioenerg.*, 2012, **46**, 479-491.
184. D. C. Elliott, P. Biller, A. B. Ross, A. J. Schmidt and S. B. Jones, *Bioresour. Technol.*, 2015, **178**, 147-156.
185. G. Jiang, D. J. Nowakowski and A. V. Bridgwater, *Energy Fuels*, 2010, **24**, 4470-4475.
186. A. Oasmaa, D. C. Elliott and J. Korhonen, *Energy Fuels*, 2010, **24**, 6548-6554.

187. H. Aubin and C. Roy, *Fuel Sci. Technol. Int.*, 1990, **8**, 77-86.
188. D. C. Elliott, *Biomass Bioenerg.*, 1994, **7**, 179-185.
189. E. Furimsky, *Appl. Catal., A*, 2000, **199**, 147-190.
190. H. Duan, J. Dong, X. Gu, Y.-K. Peng, W. Chen, T. Issariyakul, W. K. Myers, M.-J. Li, N. Yi, A. F. R. Kilpatrick*, et al.*, *Nat. Commun.*, 2017, **8**, 591.
191. W. L. J. Kwok, MChem Part II, University of Oxford, 2016.
192. A. Singh, P. S. Nigam and J. D. Murphy, *Bioresour. Technol.*, 2011, **102**, 10-16.
193. Y. Chisti, *Biotechnol. Adv.*, 2007, **25**, 294-306.
194. Y. Chisti, *Trends Biotechnol.*, 2008, **26**, 126-131.
195. S. K. Hess, B. Lepetit, P. G. Kroth and S. Mecking, *Eur. J. Lipid Sci. Technol.*, 2018, **120**, 1700152.

Chapter 2: Experimental details

2.1 Analytical techniques for characterisation

The specific surface area of the samples was determined by the Brunauer-Emmett-Teller (BET) method using the N_2 adsorption and desorption isotherms collected at 77 K on a Micromeritics TriStar II 3030 instrument. Struvite samples were degassed at 30 ºC overnight before analysis. LDH samples were degassed at 110 ºC overnight before analysis.

Fourier transform infra-red (FTIR) spectra in Chapters 3 and 5 were collected on a Bruker VERTEX 80 spectrometer fitted with a DuraSamplIR II diamond ATR (attenuated total reflection) accessory. For each spectrum, the instrument was set to record 50 scans between 4000–500 cm^{-1} at 4 cm^{-1} resolution. The diamond gave rise to absorption bands between 2300–1800 cm^{-1}. These did not interfere with the analysis.

FTIR spectra in Chapter 4 were collected on a ThermoScientific Nicolet iS5 spectrometer fitted with an iD3 ATR accessory. The instrument was set to record 40 scans between 4000–700 cm^{-1} at 4 cm^{-1} resolution.

Elemental analysis by inductively coupled plasma mass spectrometry (ICP-MS) was performed by Dr Alaa Abdul-Sada (University of Sussex). Analyses were conducted on 20–30 mg samples digested in concentrated nitric acid (c. HNO_3) and diluted. Each solution was analysed three times. Silica-based samples were not completely digested by the acid, so the results refer to the acid-soluble fraction of these samples.

Powder X-ray diffraction (XRD) spectra were collected on a PANAnalytical X'Pert Pro Diffractometer in scanning mode using Cu Kα radiation (α1 = 1.540598 Å, α2 = 1.54426 Å, weighted average = 1.541847 Å). Scans were recorded between 2θ = 5.0100–

72.9760º, with step size 0.0170º and scan step time 55.8800 s. The samples were mounted on stainless steel holders that gave rise to peaks at 43.36, 44.29, and 50.51º. These did not interfere with the analysis.

Scanning electron microscopy (SEM) images in Chapter 3 were collected at the David Cockayne Centre for Electron Microscopy (Department of Materials, University of Oxford) on a Zeiss EVO MA10 microscope with an acceleration voltage of 3 kV. Samples were mounted onto 12 mm pin stubs using silver dag at least 24 hours prior to imaging to allow the dag to dry and out gas.

SEM for Chapter 4 was performed at the Harwell Research Complex on a JSM-6610LV microscope with an accelerating voltage of 200 kV. Samples were prepared by dispersion in ethanol using sonication, cast onto carbon tabs and sputter coated with 10 nm Au using a Quorum Q150T ES.

High resolution scanning electron microscopy (HR-SEM) with energy-dispersive X-ray spectroscopy (EDX) was performed by Miss Meng Lyu (University of Oxford) at the David Cockayne Centre for Electron Microscopy (Department of Materials, University of Oxford) on a Zeiss Merlin-EBSD microscope with an operating voltage of 5 kV. Samples were mounted onto 12 mm pin stubs using silver dag at least 24 hours prior to imaging to allow the dag to dry and out gas.

Transmission electron microscopy (TEM) images for Chapter 3 were acquired by Dr Dana-Georgiana Crivoi (University of Oxford) and Dr Chunping Chen (University of Oxford) at the David Cockayne Centre for Electron Microscopy (Department of Materials, University of Oxford) on a JEOL JEM-2100 microscope with an accelerating voltage of 200 kV. Samples were prepared by dispersion in ethanol using sonication and cast onto copper grids coated with carbon mesh.

TEM images for Chapter 4 were acquired at the Harwell Research Complex on a JEOL 2100 microscope with an accelerating voltage of 200 kV. Samples were prepared by dispersion in ethanol using sonication and cast onto copper grids coated with carbon mesh.

Tap density was calculated by a standard testing method (ASTM D7481-09). The powder was filled into a volumetric cylinder and a precise weight of sample (m) was measured. The volume was measured before (V_0) and after 1000 taps (V_t), with the volume recorded after every 100 taps. The loose bulk and tap densities are defined as:

$$\text{Loose bulk density} = m/V_0$$

$$\text{Tap density} = m/V_t$$

Thermogravimetric analysis (TGA) was carried out on a Mettler Toledo TGA/DSC 1 instrument. Samples (~10 mg) were heated in an alumina crucible from 25 to 800 ºC at a rate of 5 ºC min^{-1} under N_2 (~100 cm^3 min^{-1}).

Temperature programmed desorption with ammonia (TPD-NH_3) traces were recorded on a Micromeritics AutoChem II 2920 Chemisorption Analyser equipped with a thermal conductivity detector (TCD). The sample (~100 mg) was loaded in a quartz U-tube and first purged in a flow of N_2 (20 cm^3 min^{-1}) at room temperature for 10 minutes to remove impurities. The temperature was then raised to 150 ºC at a rate of 10 ºC min^{-1} and held at this temperature for 30 minutes to remove water. The temperature was then reduced to 100 ºC, the gas changed to 10% ammonia in helium (10 cm^3 min^{-1}), and the sample purged for 30 minutes. Physically adsorbed ammonia was then removed by changing the gas flow to helium (He, 50 cm^3 min^{-1}) for 1 hour. For the desorption step, the sample was heated from 100 to 600 ºC under He flow (50 cm^3 min^{-1}).

Solid state nuclear magnetic resonance (ssNMR) spectra were collected by Dr Nicholas Rees (University of Oxford) on a Bruker Avance III HD spectrometer equipped with a 9.4 T magnet using 4.0 mm O.D zirconia rotors. ^{27}Al DPMAS (direct polarisation magic angle spinning) ssNMR spectra were acquired at 104.2 MHz with a MAS rate of 10 or 15 kHz (for struvite LDHs and silica@LDHs, respectively). A single pulse excitation was applied using a short pulse width (0.23 μs) to get the quantitative MAS spectra. The ^{27}Al chemical shifts are referenced to an aqueous solution of $Al(NO_3)_3$. ^{29}Si DPMAS ssNMR spectra were recorded at 79.4 MHz with a MAS rate of 10 kHz. A one-pulse sequence and SPINAL-64 proton decoupling was applied to get the quantitative MAS spectra. The ^{29}Si chemical shifts are referenced to kaolinite (with δ = –91.7 ppm on a scale where δ_{TMS} = 0) as a secondary reference. ^{23}Na DPMAS ssNMR were recorded at 105.8 MHz with a MAS rate of 10 kHz. The ^{23}Na chemical shifts are referenced to 1M NaCl in water.

Zeta potential measurements were carried out at the Begbroke Science Park (Department of Materials, University of Oxford) using a Malvern Zetasizer Nano ZS. Samples were dispersed and sonicated in ethanol at 0.1 wt.% for 15 minutes before measurement.

2.2 Experimental details for Chapter 3

2.2.1 Materials

Synthetic struvite ($MgNH_4PO_4.6H_2O$) was purchased from Alfa Aesar and used without further purification. Six struvites were procured from wastewater treatment plants (WWTPs) across the world. Struvites from Niersverband and ASG were washed with deionsed (D.I.) water and dried in a vacuum oven at 30 ºC overnight prior to use. Struvite from Aa en Maas was dried in a vacuum oven at 30 ºC overnight prior to use. All other WWTP struvites were used without treatment.

Hydrochloric acid (HCl, 37%), nitric acid (HNO_3, 70%), sodium carbonate (Na_2CO_3), sodium hydroxide (NaOH), aluminium nitrate nonahydrate ($Al(NO_3)_3.9H_2O$), magnesium nitrate hexahydrate ($Mg(NO_3)_2.6H_2O$), zinc nitrate hexahydrate ($Zn(NO_3)_2.6H_2O$) and ethanol (EtOH, ≥99.8%) were purchased from Sigma Aldrich and used without further purification.

2.2.2 Synthesis of struvite LDH (SLDH): Method 1 (M1)

Mg_3Al-CO_3-SLDH – 35 ºC struvite dissolution; 35 ºC ageing

$MgNH_4PO_4.6H_2O$ (22.4 mmol) was dispersed in 200 cm^3 D.I. water in a three-neck round bottom flask heated in a 35 ºC oil bath. The mixture was stirred (1000 rpm) for 1 hour. Na_2CO_3 (28.9 mmol) was added to the mixture and stirred for a further 30 minutes. A solution of $Al(NO_3)_3.9H_2O$ (7.2 mmol) in 200 cm^3 D.I. water was then added dropwise (2 cm^3 min^{-1}), keeping the temperature at 35 ºC and maintaining pH 11.5 by addition of 1 M NaOH. The mixture was stirred at 35 ºC for 5 days. The slurry was filtered and washed with D.I. water until the supernatant was pH 7. The solid was dried in a vacuum oven at 30 ºC overnight.

Mg_3Al-PO_4-SLDH – 35 ºC struvite dissolution; 35 ºC ageing

$MgNH_4PO_4.6H_2O$ (22.4 mmol) was dispersed in 200 cm^3 D.I. water in a three-neck round bottom flask under a nitrogen (N_2) atmosphere. 1 M NaOH was added to adjust the pH to 11.5 and the mixture was stirred (1000 rpm) at 35 ºC for 30 minutes. A solution of $Al(NO_3)_3.9H_2O$ (7.2 mmol) in 200 cm^3 degassed D.I. water was then added dropwise (2 cm^3 min^{-1}), keeping the temperature at 35 ºC and maintaining pH 11.5 by addition of 1 M NaOH. The mixture was stirred at 35 ºC for 5 days. The slurry was filtered and washed with degassed D.I. water until the supernatant was pH 7. The solid was dried in a vacuum oven at 30 ºC overnight.

Mg_3Al-CO_3-SLDH – 55 ºC struvite dissolution; 55 ºC ageing

$MgNH_4PO_4.6H_2O$ (11.25 mmol) was dispersed in 20 cm^3 D.I. water in a three-neck round bottom flask. The mixture was stirred (1000 rpm) at 55 ºC for 30 minutes. Na_2CO_3 (15.0 mmol) was then added and the mixture stirred for a further 30 minutes. A solution of $Al(NO_3)_3.9H_2O$ (3.75 mmol) in 20 cm^3 D.I. water was added to the basic struvite mixture dropwise (2 cm^3 min^{-1}), keeping the temperature at 55 ºC and maintaining pH 11.5 by addition of 1 M NaOH. Once addition was complete, the mixture was stirred at 55 ºC for 2, 4, 8, or 24 hours. After the ageing period, the slurry was filtered and washed with D.I. water until the supernatant was pH 7. The solid was then dried in a vacuum oven at 30 ºC overnight.

Mg_3Al-CO_3-SLDH – 75 ºC struvite dissolution; 75 ºC ageing

$MgNH_4PO_4.6H_2O$ (11.25 mmol) was dispersed in 20 cm^3 D.I. water in a three-neck round bottom flask. The mixture was stirred (1000 rpm) at 75 ºC for 30 minutes. Na_2CO_3 (15.0 mmol) was then added and the mixture stirred for a further 30 minutes. A solution of $Al(NO_3)_3.9H_2O$ (3.75 mmol) in 20 cm^3 D.I. water was added to the basic struvite mixture dropwise (2 cm^3 min^{-1}), keeping the temperature at 75 ºC and maintaining

pH 11.5 by addition of 1 M NaOH. Once addition was complete, the mixture was stirred at 75 ºC for 2, 4, or 8 hours. After the ageing period, the slurry was filtered and washed with D.I. water until the supernatant was pH 7. The solid was then dried in a vacuum oven at 30 ºC overnight.

2.2.3 Synthesis of SLDH: Method 2 (M2)

Mg_3Al-CO_3-SLDH – 65 ºC struvite decomposition; 35 ºC ageing

$MgNH_4PO_4.6H_2O$ (22.4 mmol) was dispersed in 20 cm^3 1 M NaOH in a three-neck round bottom flask. The mixture was stirred (1000 rpm) at 65 ºC for 2 hours under a flow of N_2. The ammonia off-gases were collected via a trap containing 1M HCl. Na_2CO_3 (28.9 mmol) was added to the mixture and stirred for a further 5 minutes. A solution of $Al(NO_3)_3.9H_2O$ (7.2 mmol) in 200 cm^3 D.I. water was then added dropwise (2 cm^3 min^{-1}), keeping the temperature at 65 ºC and maintaining pH 11.5 by addition of 1 M NaOH. The mixture was then stirred at 35 ºC for 2 days. The slurry was filtered and washed with D.I. water until the supernatant was pH 7. The solid was then dried in a vacuum oven at 30 ºC overnight.

Mg_3Al-CO_3-SLDH – 85 ºC struvite decomposition; 35 ºC ageing

$MgNH_4PO_4.6H_2O$ (22.4 mmol) was dispersed in 20 cm^3 1 M NaOH in a three-neck round bottom flask. The mixture was stirred (1000 rpm) at 85 ºC for 2 hours under a flow of N_2. The ammonia off-gases were collected via a trap containing 1M HCl. Na_2CO_3 (28.9 mmol) was added to the mixture and stirred for a further 5 minutes. A solution of $Al(NO_3)_3.9H_2O$ (7.2 mmol) in 200 cm^3 D.I. water was then added dropwise (2 cm^3 min^{-1}), keeping the temperature at 85 ºC and maintaining pH 11.5 by addition of 1 M NaOH. The mixture was then stirred at 35 ºC for 2 days. The slurry was filtered and washed with D.I. water until the supernatant was pH 7. The solid was then dried in a vacuum oven at 30 ºC overnight.

Mg_3Al-CO_3-SLDH – 65 ºC struvite decomposition; 65 ºC ageing

$MgNH_4PO_4.6H_2O$ (11.25 mmol) was dispersed in 10 cm^3 1 M NaOH in a three-neck round bottom flask. The mixture was stirred (1000 rpm) at 65 ºC for 1 hour under a flow of N_2. The ammonia off-gases were collected via a trap containing 1 M HCl. Na_2CO_3 (15.0 mmol) was added to the mixture and stirred for a further 5 minutes. A solution of $Al(NO_3)_3.9H_2O$ (3.75 mmol) in 20 cm^3 D.I. water was added to the basic struvite mixture dropwise (2 cm^3 min^{-1}), keeping the temperature at 65 ºC and maintaining pH 11.5 by addition of 1 M NaOH. Once addition was complete, the mixture was stirred at 65 ºC for 2 hours. After the ageing period, the slurry was filtered and washed with D.I. water until the supernatant was pH 7. The solid was then dried in a vacuum oven at 30 ºC overnight.

Mg_3Al-CO_3-SLDH – 85 ºC struvite decomposition; 85 ºC ageing

$MgNH_4PO_4.6H_2O$ (37.5 mmol) was dispersed in 33 cm^3 1 M NaOH in a three-neck round bottom flask. The mixture was stirred (1000 rpm) at 85 ºC for 1 hour under a flow of N_2. The ammonia off-gases were collected via a trap containing 1 M HCl. Na_2CO_3 (50.0 mmol) was added to the mixture and stirred for a further 5 minutes. A solution of $Al(NO_3)_3.9H_2O$ (12.5 mmol) in 33 cm^3 D.I. water was added to the basic struvite mixture dropwise (2 cm^3 min^{-1}), keeping the temperature at 85 ºC and maintaining pH 11.5 by addition of 1 M NaOH. Once addition was complete, the mixture was stirred at 85 ºC for 2 hours. After the ageing period, the slurry was filtered and washed with D.I. water until the supernatant was pH 7. The solid was then dried in a vacuum oven at 30 ºC overnight.

Mg_3Al-PO_4-SLDH – 85 ºC struvite decomposition; 85 ºC ageing

$MgNH_4PO_4.6H_2O$ (37.5 mmol) was dispersed in 33 cm^3 degassed 1 M NaOH in a three-neck round bottom flask. The mixture was stirred (1000 rpm) at 85 ºC for 1 hour under a flow of N_2. The ammonia off-gases were collected via a trap containing 1 M HCl. A solution of $Al(NO_3)_3.9H_2O$ (12.5 mmol) in 33 cm^3 degassed D.I. water was added to the

basic struvite mixture (2 cm^3 min^{-1}), keeping the system under N_2, the temperature at 85 ºC and maintaining pH 11.5 by addition of degassed 1 M NaOH. Once addition was complete, the mixture was stirred at 85 ºC for 2 hours. After the ageing period, the slurry was filtered and washed with degassed D.I. water until the supernatant was pH 7. The solid was then dried in a vacuum oven at 30 ºC overnight.

Table 2.1 Properties of Mg_3Al-CO_3-SLDHs prepared using M2 (85 ºC).

Struvite source	Yield (%)	Colour	N_2 BET specific surface area (m^2 g^{-1})	Tap density (g cm^{-3})	XRD (º, *hkl*)	FTIR (cm^{-1})
Alfa Aesar	95	White	150–184	0.56–0.64	11.35 (003), 60.61 (110)	3446 (broad), 1648 (medium), 1363 (strong), 1032 (m), 583 (s)
NuReSys	80	Light tan	152–174	0.40	11.37 (003), 60.72 (110)	
Aa en Maas	90	Tan	54–136	0.60–0.68	11.46 (003), 60.63 (110)	

2.2.4 Decomposition of struvite in alkali

$MgNH_4PO_4.6H_2O$ (37.5 mmol) was dispersed in 33 cm^3 1 M NaOH in a three-neck round bottom flask. The mixture was stirred (1000 rpm) at 85 ºC for 1 or 3 hours under a flow of N_2. The ammonia off-gases were collected via a trap containing 1 M HCl. After the ageing period, the flask was cooled rapidly, and the slurry was filtered and washed with D.I. water until the supernatant was pH 7. The solid was dried in a vacuum oven at 30 ºC overnight.

2.2.5 Synthesis of zinc SLDH

Zn_2MgAl-CO_3-SLDH – M2 (unmodified)

$MgNH_4PO_4.6H_2O$ (12.5 mmol) was dispersed in 33 cm^3 1 M NaOH in a three-neck round bottom flask. The mixture was stirred (1000 rpm) at 85 ºC for 1 hour under a flow of N_2. The ammonia off-gases were collected via a trap containing 1 M HCl. Na_2CO_3 (50.0 mmol) was added to the mixture and stirred for a further 5 minutes. A solution of $Al(NO_3)_3.9H_2O$ (12.5 mmol) and $Zn(NO_3)_2.6H_2O$ (25.0 mmol) in 33 cm^3 D.I. water was added to the basic struvite mixture dropwise (2 cm^3 min^{-1}), keeping the temperature at 85 ºC and maintaining pH 11.5 by addition of 1 M NaOH. Once addition was complete, the mixture was stirred at 85 ºC for 2 hours. After the ageing period, the slurry was filtered and washed with D.I. water until the supernatant was pH 7. The solid was then dried in a vacuum oven at 30 ºC overnight.

Zn_2MgAl-CO_3-SLDH – M2 (pH 9)

$MgNH_4PO_4.6H_2O$ (12.5 mmol) was dispersed in 33 cm^3 1 M NaOH in a three-neck round bottom flask. The mixture was stirred (1000 rpm) at 85 ºC for 1 hour under a flow of N_2. The ammonia off-gases were collected via a trap containing 1 M HCl. Na_2CO_3 (50.0 mmol) was added to the mixture and stirred for a further 5 minutes. A solution of $Al(NO_3)_3.9H_2O$ (12.5 mmol) and $Zn(NO_3)_2.6H_2O$ (25.0 mmol) in 33 cm^3 D.I. water was added to the basic struvite mixture dropwise (2 cm^3 min^{-1}), keeping the temperature at 85 ºC and maintaining pH 9 by addition of 1 M NaOH. Once addition was complete, the mixture was stirred at 85 ºC for 2 hours. After the ageing period, the slurry was filtered and washed with D.I. water until the supernatant was pH 7. The solid was then dried in a vacuum oven at 30 ºC overnight.

Zn_2MgAl-CO_3-SLDH – M2 (pH 9, hydrothermal ageing)

$MgNH_4PO_4.6H_2O$ (12.5 mmol) was dispersed in 33 cm^3 1 M NaOH in a three-neck round bottom flask. The mixture was stirred (1000 rpm) at 85 ºC for 1 hour under a flow of N_2. The ammonia off-gases were collected via a trap containing 1 M HCl. Na_2CO_3 (50.0 mmol) was added to the mixture and stirred for a further 5 minutes. A solution of $Al(NO_3)_3.9H_2O$ (12.5 mmol) and $Zn(NO_3)_2.6H_2O$ (25.0 mmol) in 33 cm^3 D.I. water was added to the basic struvite mixture dropwise (2 cm^3 min^{-1}), keeping the temperature at 85 ºC and maintaining pH 9 by addition of 1 M NaOH. Once addition was complete, the mixture was transferred to a Teflon-lined stainless steel autoclave and heated in an oven at 120 ºC for 2 hours. After the ageing period, the autoclave was cooled, and the slurry was filtered and washed with D.I. water until the supernatant was pH 7. The solid was then dried in a vacuum oven at 30 ºC overnight.

2.2.6 Synthesis of aqueous miscible organic SLDH (AMO-SLDH)

$MgNH_4PO_4.6H_2O$ (37.5 mmol) was dispersed in 33 cm^3 1 M NaOH in a three-neck round bottom flask. The mixture was stirred (1000 rpm) at 85 ºC for 1 hour under a flow of N_2. The ammonia off-gases were collected via a trap containing 1 M HCl. Na_2CO_3 (50.0 mmol) was added to the mixture and stirred for a further 5 minutes. A solution of $Al(NO_3)_3.9H_2O$ (12.5 mmol) in 33 cm^3 D.I. water was added to the basic struvite mixture dropwise (2 cm^3 min^{-1}), keeping the temperature at 85 ºC and maintaining pH 11.5 by addition of 1 M NaOH. Once addition was complete, the mixture was stirred at 85 ºC for 2 hours. After the ageing period, the slurry was filtered and washed with D.I. water until the supernatant was pH 7. The wet cake was rinsed with 400 cm^3 EtOH and redispersed in 400 cm^3 EtOH for 4 hours at room temperature. The product was collected by vacuum filtration and dried in a vacuum oven at 30 ºC overnight.

2.2.7 Synthesis of conventional LDH (c-LDH)

Ref-LDH (Mg_3Al-CO_3-c-LDH, M2 conditions)

Na_2CO_3 (50 mmol) was dissolved in 33 cm^3 D.I water in a three-neck round bottom flask heated in an 85 ºC oil bath. The pH was adjusted to pH 10 by addition of 10 wt.% HNO_3 solution. Separately, $Mg(NO_3)_2.6H_2O$ (37.5 mmol) and $Al(NO_3)_3.9H_2O$ (12.5 mmol) were dissolved in 33 cm^3 D.I. water and transferred to a syringe. The metal salt solution was added dropwise (2 cm^3 min^{-1}) to the Na_2CO_3 solution, stirring at 1000 rpm. The pH of the mixture was maintained at pH 11.5 by dropwise addition of 1 M NaOH. Once the addition was complete, the suspension was stirred for 2 hours. After the ageing period, the LDH suspension was filtered and the wet solid was washed with D.I. water until the supernatant was pH 7. The solid was dried in a vacuum oven at 30 ºC overnight.

Table 2.2 Properties of a reference Mg_3Al-CO_3-c-LDH prepared under M2 conditions.

Yield (%)	Colour	N_2 BET specific surface area (m^2 g^{-1})	Tap density (g cm^{-3})	XRD (º, *hkl*)	FTIR (cm^{-1})
83	White	85	0.69	11.37 (003), 60.45 (110)	3491 (broad), 1647 (medium), 1367 (strong), 857 (m), 685 (s)

2.3 Experimental details for Chapter 4

2.3.1 Materials

Tetraethyl orthosilicate (TEOS, 98%), nitric acid (HNO_3, 70%), sodium carbonate (Na_2CO_3), sodium hydroxide (NaOH), magnesium nitrate hexahydrate ($Mg(NO_3)_2.6H_2O$), aluminium nitrate nonahydrate ($Al(NO_3)_3.9H_2O$), urea ($CO(NH_2)_2$) and ethanol (EtOH, ≥99.8%) were purchased from Sigma Aldrich and used without further purification. Ammonia solution ($NH_3.H_2O$, 35 wt.%) was purchased from Fisher Scientific and used without further purification.

2.3.2 Synthesis of silica (modified Stöber method)

9.2 cm^3 TEOS was added to a mixed solution of 10 cm^3 $NH_3.H_2O$ (35 wt.%), 30 cm^3 D.I. water and 50 cm^3 EtOH. The white suspension was stirred vigorously for 17 hours. The final solid was washed with EtOH thoroughly and dried under vacuum overnight.

2.3.3 General synthesis procedure for core-shell SiO_2@Mg_2Al-CO_3-AMO-LDHs (*in situ* co-precipitation)

Silica (SiO_2, d ~500 nm, 100 mg) was dispersed in 20 cm^3 D.I. water using ultrasonication for 25 minutes. Na_2CO_3, 0.96 mmol) was then added to the solution and a further 5 minutes of sonication was carried out to form solution A. The pH of solution A was adjusted to pH 10 using a 10 wt.% HNO_3 solution. Separately, $Mg(NO_3)_2.6H_2O$ (0.96 mmol) and $Al(NO_3)_3.9H_2O$ (0.48 mmol) were dissolved in 20 cm^3 D.I. water to form solution B. Solution B was added to solution A at room temperature at various rates (15, 30, 60, or 120 cm^3 h^{-1}) and the suspension stirred at various speeds (0, 250, 500, 750, or 1000 rpm). The pH of the reaction solution was maintained at pH 10 by addition of 1 M NaOH. After the addition of B to A was complete, the suspension was aged at room temperature with stirring for 1 hour. The solid was isolated by centrifugation and washed

with D.I. water until the supernatant was pH 7. The wet solid was then washed with EtOH and re-dispersed in 40 cm^3 EtOH for 1 hour. The product was collected by centrifugation and dried under vacuum overnight.

2.3.4 Synthesis of SiO_2@Mg_2Al-CO_3-AMO-LDHs using commercial SiO_2

IMP1a

Commercial SiO_2 (0.1 g) was ground together in a pestle and mortar with $Al(NO_3)_3.9H_2O$ (0.16 mmol) and *P* cm^3 D.I. water, where *P* is the pore volume of the SiO_2 used. The wet solid was dried in an oven (120 ºC) for 1 hour. Separately, Na_2CO_3 (0.32 mmol) was dissolved using the minimum volume of D.I. water (~270 μL). Once cooled, the pre-treated SiO_2 was combined with the Na_2CO_3 solution in a three-neck round bottom flask. $Mg(NO_3)_2.6H_2O$ (0.32 mmol) was dissolved in 10 cm^3 D.I. water and added to the basic SiO_2 solution dropwise (1 cm^3 min^{-1}) with stirring (500 rpm). The suspension was kept at pH 10 using 1 M NaOH. Once addition was complete, the suspension was aged at room temperature for 1 hour. The solid was isolated by centrifugation and washed with D.I water until the supernatant was pH 7. The wet solid was washed with EtOH and re-dispersed in 40 cm^3 EtOH for 1 hour. The product was collected by centrifugation and dried in a vacuum oven overnight.

IMP1b

Commercial SiO_2 (0.1 g) was ground together in a pestle and mortar with $Al(NO_3)_3.9H_2O$ (0.16 mmol) and *P* cm^3 D.I. water, where *P* is the pore volume of the silica used. The wet solid was dried in an oven (120 ºC) for 1 hour. Separately, Na_2CO_3 (0.32 mmol) was dissolved using the minimum volume of D.I. water (~270 μL). Once cooled, the pre-treated SiO_2 was combined with the Na_2CO_3 solution in a three-neck round bottom flask. $Mg(NO_3)_2.6H_2O$ (0.32 mmol) was dissolved in 10 cm^3 D.I. water and added to the basic SiO_2 solution dropwise (1 cm^3 min^{-1}) with stirring (500 rpm). The suspension was kept

at pH 10 using 1 M NaOH. Once addition was complete, the suspension was aged at room temperature for 1 hour. The solid was isolated by centrifugation and washed with D.I water until the supernatant was pH 7. The wet solid was then washed with EtOH and re-dispersed in 40 cm^3 EtOH for 1 hour. The product was collected by centrifugation and dried in a vacuum oven overnight.

IMP2

Commercial SiO_2 (0.1 g) was combined in a mortar with $Al(NO_3)_3.9H_2O$ (25 mg) and *P* cm^3 D.I. water, where *P* is the pore volume of the SiO_2 used. The wet solid was dried in an oven (120 ºC) for 1 hour. Separately, Na_2CO_3 (0.32 mmol) was dissolved using the minimum volume of D.I. water (~270 µL). Once cooled, the pre-treated SiO_2 was combined with the Na_2CO_3 solution in a three-neck round bottom flask. The metal solution was prepared by dissolving $Mg(NO_3)_2.6H_2O$ (0.32 mmol) and the remaining $Al(NO_3)_3.9H_2O$ (0.16 mmol – 25 mg) in 10 cm^3 D.I. water. The metal solution was added to the basic SiO_2 solution dropwise (0.25, 0.5, 1, or 2 cm^3 min^{-1}) at room temperature with stirring (500 rpm). The suspension was kept at pH 10 using 1 M NaOH. Once addition was complete, the suspension was aged for 1 hour. The solid was isolated by centrifugation and washed with D.I water until the supernatant was pH 7. The wet solid was then washed with EtOH and re-dispersed in 40 cm^3 EtOH for 1 hour. The product was collected by centrifugation and dried in a vacuum oven overnight.

IMP2 scale-up (no AMOST)

Commercial SiO_2 (1.8 g) was combined in a mortar with $Al(NO_3)_3.9H_2O$ (225 mg) and *P* cm^3 D.I. water, where *P* is the pore volume of the SiO_2 used. The wet solid was dried in an oven (120 ºC) for 1 hour. Separately, Na_2CO_3 (5.76 mmol) was dissolved using the minimum volume of D.I. water (~4.5 cm^3). Once cooled, the pre-treated SiO_2 was combined with the Na_2CO_3 solution in a three-neck round bottom flask. The metal

solution was prepared by dissolving $Mg(NO_3)_2.6H_2O$ (5.76 mmol) and the remaining $Al(NO_3)_3.9H_2O$ (2.88 mmol – 225 mg) in 60 cm^3 D.I. water. The metal solution was added to the basic SiO_2 solution dropwise (3 or 6 cm^3 min^{-1}) at room temperature with stirring (500 rpm). The suspension was kept at pH 10 using 1 M NaOH. Once addition was complete, the suspension was aged for 1 hour. The solid was isolated by centrifugation and washed with D.I water until the supernatant was pH 7. The product was collected by centrifugation and dried in a vacuum oven overnight.

Urea hydrolysis

Commercial SiO_2 (0.5 g) was combined with $Mg(NO_3)_2.6H_2O$ (6.67 mmol), $Al(NO_3)_3.9H_2O$ (3.33 mmol) and $CO(NH_2)_2$ (20 mmol) in 20 cm^3 D.I. water. The mixed solution was transferred to a Teflon-lined stainless steel autoclave and heated at 100 ºC for 24 hours. After the ageing period, the autoclave was cooled in an ice bath. The suspension was filtered using vacuum filtration and the solid was washed with D.I. water until the supernatant was pH 7. The solid was dried under vacuum overnight.

Hydrothermal

Commercial SiO_2 (1.0 g) was combined with $Mg(NO_3)_2.6H_2O$ (9.6 mmol) and $Al(NO_3)_3.9H_2O$ (4.8 mmol) with *P* cm^3 D.I. water, where *P* is the pore volume of the silica used. The wet solid was dried in an oven (120 ºC) for 1 hour. Separately, Na_2CO_3 (9.6 mmol) was dissolved using the minimum volume of D.I. water (~2.7 cm^3). Once cooled, the pre-treated SiO_2 was combined with the Na_2CO_3 solution in a Teflon-lined stainless steel autoclave. The vessel was sealed and heated in an oven (120 ºC) for 18 hours. After heating, the solid was collected by suction filtration and washed with D.I. water until the supernatant was pH 7. The wet solid was then washed with 400 cm^3 EtOH. The product was collected by vacuum filtration and dried under vacuum overnight.

2.4 Experimental details for Chapter 5

2.4.1 Materials

Synthetic struvite ($MgNH_4PO_4.6H_2O$) was purchased from Alfa Aesar and used without further purification. Struvite was also procured from NuReSys (Clarebout Potatoes, Belgium) and used without further purification.

Hydrochloric acid (HCl, 37%), nitric acid (HNO_3, 70%), sodium carbonate (Na_2CO_3), sodium hydroxide (NaOH), aluminium nitrate nonahydrate ($Al(NO_3)_3.9H_2O$), magnesium nitrate hexahydrate ($Mg(NO_3)_2.6H_2O$), and ethanol (EtOH, ≥99.8%) were purchased from Sigma Aldrich and used without further purification.

A commercial LDH (PURAL MG70 HT) was obtained from Sasol Chemicals and used without further purification.

2.4.2 Thermal treatment of SLDHs and SiO_2@LDHs

SLDHs were prepared using M2 (Section 2.2.3) and core-shell SiO_2@LDHs were prepared by *in situ* co-precipitation (Section 2.3.3).

Typically, 0.5 g of the sample (*e.g.* SLDH or SiO_2@LDH) was heated in an alumina crucible in a muffle oven. The temperature ramp rate was set at 5 ºC min^{-1} and the temperature was held at the target temperature (200, 300, 400, and 500 ºC) for 5 hours.

2.4.3 Synthesis of reference LDHs

Conventional: MgAl-CO_3-c-LDH

Na_2CO_3 (50 mmol) was dissolved in 100 cm^3 D.I. water in a three-neck round bottom flask. The pH was adjusted to pH 10 by addition of 10 wt.% HNO_3 solution. Separately, $Mg(NO_3)_2.6H_2O$ (66.7 or 75 mmol) and $Al(NO_3)_3.9H_2O$ (33.3 or 25 mmol) were dissolved in 20 cm^3 D.I. water (100 mmol total metal nitrates, amounts refer to Mg/Al

ratios of 2 and 3, respectively) and transferred to a syringe. The metal salt solution was added dropwise at a rate of 1 cm^3 min^{-1} to the Na_2CO_3 solution at room temperature, stirring at 500 rpm. The pH of the mixture was maintained at pH 10 by dropwise addition of 4 M NaOH. Once addition was complete, the suspension was stirred at room temperature for 16 hours. After the ageing period, the LDH suspension was filtered and the wet solid was washed with D.I. water until the supernatant was pH 7. Finally, the product was dried in a vacuum oven overnight to yield a white powder (7–8 g).

AMOST: MgAl-CO_3-AMO-LDH

Na_2CO_3 (50 mmol) was dissolved in 100 cm^3 D.I. water in a three-neck round bottom flask. The pH was adjusted to pH 10 by addition of 10 wt.% HNO_3 solution. Separately, $Mg(NO_3)_2.6H_2O$ (66.7 or 75 mmol) and $Al(NO_3)_3.9H_2O$ (33.3 or 25 mmol) were dissolved in 20 cm^3 D.I. water (100 mmol total metal nitrates, amounts refer to Mg/Al ratios of 2 and 3, respectively) and transferred to a syringe. The metal salt solution was added dropwise at a rate of 1 cm^3 min^{-1} to the Na_2CO_3 solution at room temperature, stirring at 500 rpm. The pH of the mixture was maintained at pH 10 by dropwise addition of 4 M NaOH. Once addition was complete, the suspension was stirred at room temperature for 16 hours. After the ageing period, the LDH suspension was filtered and the wet solid was washed with D.I. water until the supernatant was pH 7. The wet cake was rinsed with 300 cm^3 of AMO solvent (*e.g.* EtOH) then re-dispersed and stirred in 500 cm^3 of this solvent at room temperature for 4 hours. The solvent was removed by filtration and the solid was further rinsed by 200 cm^3 of fresh solvent. Finally, the product was dried in a vacuum oven at room temperature overnight to yield a white powder (7–8 g).

2.4.4 Carbon dioxide adsorption

TGA measurements

Carbon dioxide (CO_2) adsorption was carried out using a PerkinElmer TGA 8000 Thermogravimetric Analyser. The LDHs were calcined *in situ* to form mixed oxides (SLDOs) and six temperatures were investigated (200, 300, 350, 400, 450, and 500 ºC). Typically, 10 mg of sample was loaded into an alumina crucible on the carousel and heated at a ramp rate of 5 ºC min^{-1} under a flow of N_2 (100 cm^3 min^{-1}), holding at the desired temperature for 2 hours. The samples were returned to 30 ºC and the gas switched to an 80:20 N_2/CO_2 mixture (100 cm^3 min^{-1}). The mass of the sample was recorded for 3 hours. At the end of the measurement the sample was purged with N_2. The mass changes were calculated and converted into amounts of CO_2 adsorbed, assuming all mass increases were due to CO_2.

3Flex measurements

CO_2 adsorption was also carried out by Mr Justin Leung (University of Oxford) on a Micromeritics 3Flex instrument fitted with a chemisorption attachment. The LDHs were first calcined *ex situ*. Typically, 100 mg of the LDO sample was placed in the machine for further calcination at 400 ºC at a ramp of 100 ºC min^{-1} for 1 hour. The sample was cooled to 40 ºC using a ramp of 30 ºC min^{-1} and left to evacuate to a vacuum at 40 ºC for 3 hours. The CO_2 measurements were then carried out twice at 40 ºC. The first value provides the total adsorption value, the second physisorption. The difference between the two values provides the chemisorption value.

Chapter 3: Development of mineral sources for LDH syntheses

3.1 Introduction

Synthetic metal salts and oxides are convenient and effective reagents for preparing LDHs, especially at industrial scales, but as previously mentioned in Sections 1.5 and 1.6, sustainable production of chemical materials necessitates the implementation of green chemistry and circular economy principles. In this chapter, a magnesium phosphate commonly found in wastewater is investigated as an alternative source of magnesium for MgAl-LDH synthesis. The aim of the work was to develop new LDH syntheses that could be cost effective, environmentally friendly, and scalable. Full utilisation of the mineral is explored in order to increase the atom economy and reduce salt residues.

3.1.1 Struvite – magnesium ammonium phosphate ($MgNH_4PO_4.6H_2O$)

Water is one of the most important resources in the world, but the growing world population generates a huge amount of wastewater every day through domestic and industrial use. If untreated, these can cause widespread pollution and deterioration of the quality of water sources. One of the most problematic consequences of water pollution is eutrophication (Figure 3.1a), which is defined as excessive plant and algal growth due to the increased availability of one or more limiting growth factors needed for photosynthesis.[1] In wastewater effluents, the "growth factors" are nutrients such as phosphorus, in the form of phosphate (PO_4^{3-}), and nitrogen, in the form of ammonium (NH_4^+), which form during the anaerobic digestion of waste. Global phosphorus demand for agriculture is also rising with the increasing world population, so phosphorus recovery from wastewater is also desirable from an economic standpoint.

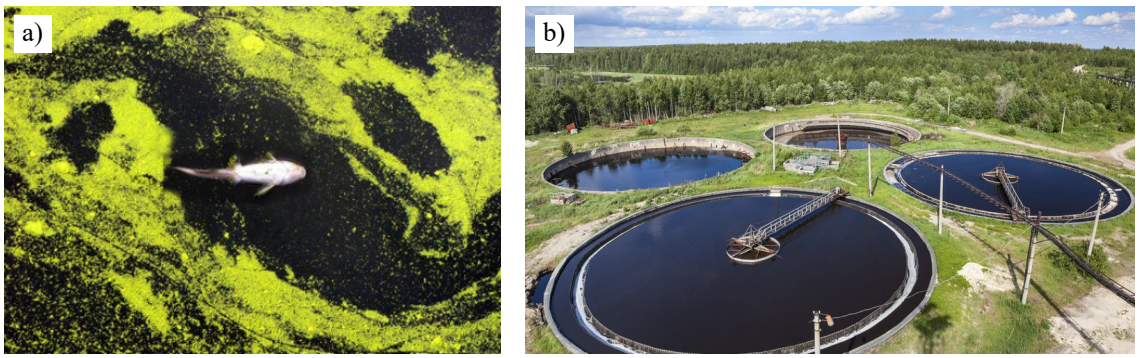


Figure 3.1 a) Toxic algal blooms are caused by eutrophication and b) an aerial view of a WWTP.

Wastewater treatment plants (WWTPs, Figure 3.1b) may employ biological or chemical processes in order to recover phosphorus and denitrify wastewater. At present, the most common technologies are those based on the precipitation of phosphoric minerals from sludge or leachate.[2] One such mineral is struvite (magnesium ammonium phosphate, $MgNH_4PO_4 \cdot 6H_2O$, Equation 3.1).[3]

$$Mg^{2+} + NH_4^+ + H_nPO_4^{(3-n)-} + 6H_2O \rightarrow MgNH_4PO_4.6H_2O + nH^+ \quad \text{Equation 3.1}$$

Struvite is a naturally occurring mineral that forms in aqueous systems of high ammonium and phosphate concentrations including in living organisms such as humans and dogs, where it is one of the main components of urinary stones.[4] It was first identified in WWTPs in the late 1930s.[5] Struvite is sparingly soluble in water (169.2 mg cm^{-3} at 25 ºC)[6] so in some areas of WWTPs where the pH, temperature, ion concentration, and turbulence are suitable, it precipitates spontaneously.[7] Hard crystalline deposits of struvite are still known to cause blockages in the pipelines (Figure 3.2a) and WWTP operators spend significant time and money on cleaning and maintenance.[5] To alleviate pipeline blockages and recover phosphorus, intentional precipitation in a dedicated vessel can be achieved by regulating the concentrations of PO_4^{3-}, NH_4^+, and Mg^{2+} (Figure 3.2b).[8] Usually, the limiting factor is the magnesium content so the effluent is dosed with

magnesium compounds such as magnesium oxide (MgO) and magnesium chloride ($MgCl_2$).[9-11]

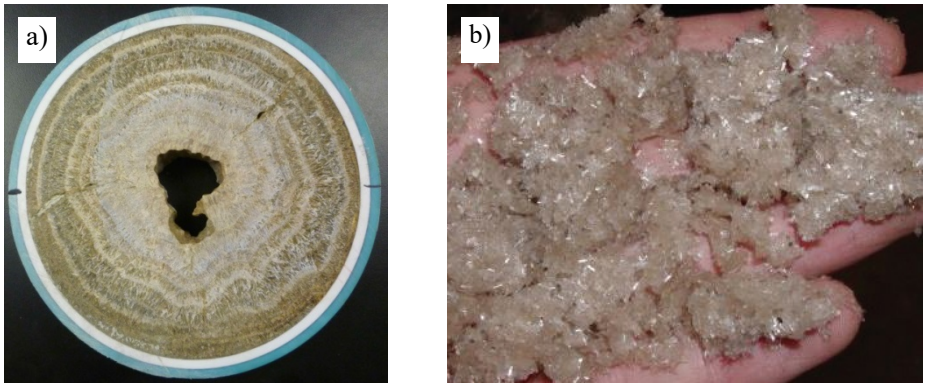


Figure 3.2 a) Undesired struvite deposits in WWTP pipes[12] and b) struvite precipitated intentionally at a WWTP using PHOSPAQ technology.[10]

Struvite's low solubility gives it potential as a slow-release fertiliser that is unlikely to contribute further to eutrophication. However, struvite recovered from wastewater is classified as waste, even after hygienisation to remove hazardous organic pollutants and potential pathogens. The legal status of this material differs between countries so it is often not utilised.[13] Japan remains the only country to implement complete phosphorus removal and recovery from anaerobically digested sludge as struvite, which is then sold to fertiliser companies.[14] An alternative application of this material is thus desirable and to this end, this work explores struvite as an alternative starting material for hierarchical MgAl-LDHs.

3.1.2 Properties of struvite

Struvite crystallises in an orthorhombic system (space group $Pmn2_1$) and has cell dimensions a_0 = 6.941 Å, b_0 = 6.137 Å and c_0 = 11.199 Å.[15] The structure contains hydrogen-bonded PO_4^{3-} tetrahedra, NH_4^+ tetrahedra and distorted $Mg(H_2O)_6^{2+}$ octahedra. The unit cell is non-centrosymmetric, *i.e.* the faces are different at opposite ends of the *c*-axis, due to the preferential alignment of the PO_4^{3-} tetrahedra apexes towards the +*c*-

axis (Figure 3.3a).[16, 17] The hemimorphic nature of the mineral has implications for its crystal morphologies as the two faces will have different properties and grow differently. For example, under conditions of low supersaturation, the crystals are elongated along the *x*-axis and terminated by inequivalent pedions (faces).[18] Usually the $00\bar{1}$ pedion is larger than the 001 and this gives rise to a coffin-lid habit.[17] Other factors that affect struvite morphology are temperature, pH, rate of change of pH, seeding conditions and stirring speed.[19] When struvite is precipitated in low pH conditions where the change in pH is slow, single coffin-lid crystals are typically formed (Figure 3.3b). On the other hand, dendritic X-shaped crystals result from rapid changes in pH.[20]

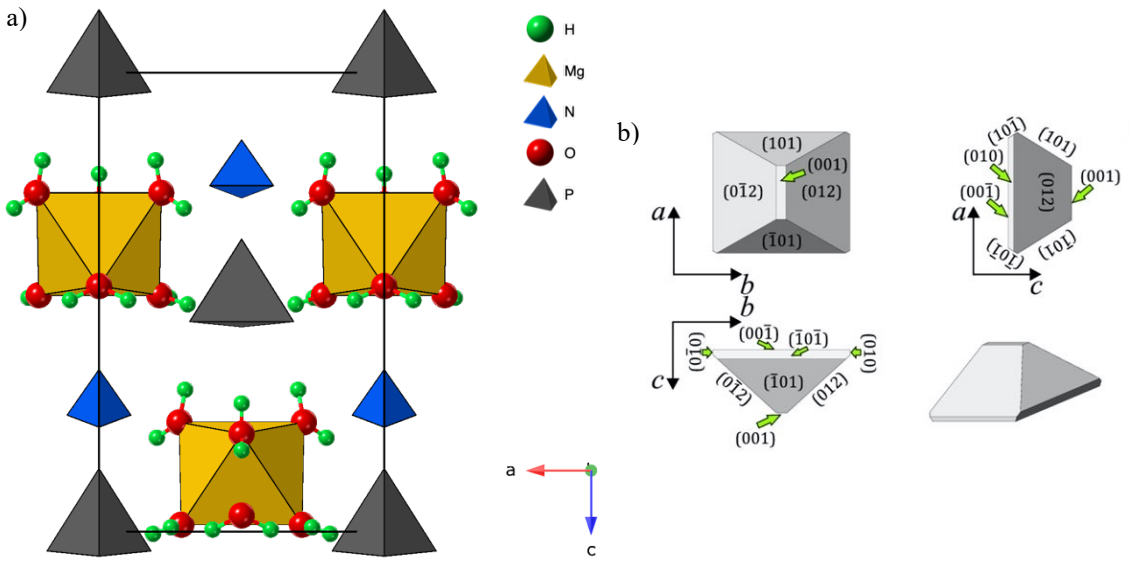


Figure 3.3 Schematic representations of the a) struvite unit cell and b) coffin-lid crystal habit observed at low pH (pH < 8.5).[20]

Struvite solubility must be increased in order to be used as a source of magnesium for LDH synthesis, and this may be achieved by increasing the solution temperature. Studies by Bhuiyan *et al.*[6] and Ariyanto *et al.*[21] found that the maximum solubility of struvite, at all pH values tested, occurs at 35 ºC (212.7 mg cm^{-3}). Therefore, this temperature was initially used for all LDH syntheses with struvite.

3.2 Atom efficient syntheses of LDHs from struvite

3.2.1 Method 1 (M1)

Using a constant pH co-precipitation method (low supersaturation, pH 10, 35 ºC), an Mg_3Al-CO_3-LDH was prepared from struvite purchased from Alfa Aesar (ammonium magnesium phosphate hexahydrate, 98%, Figure 3.4).

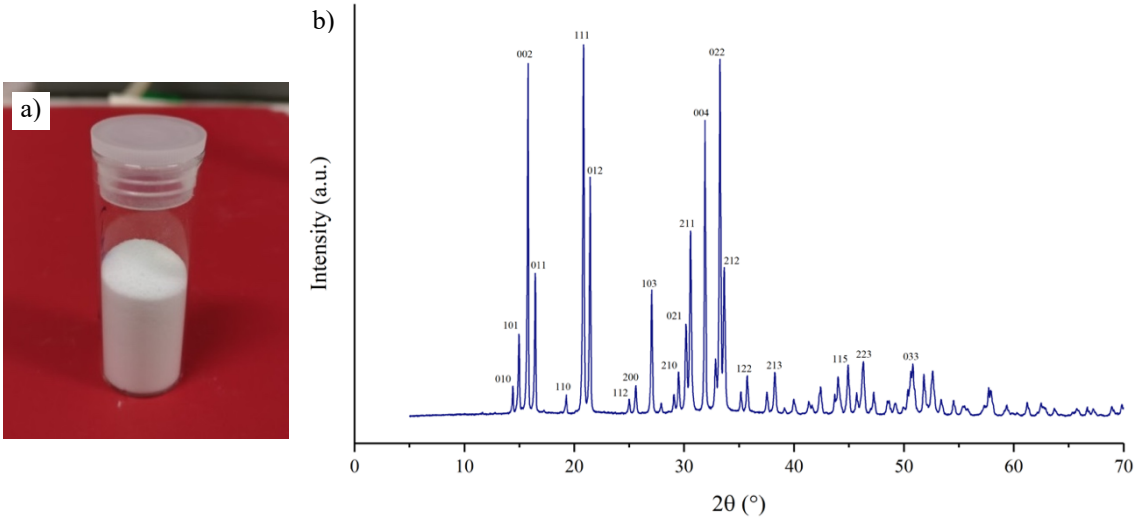


Figure 3.4 a) White crystals and b) XRD diffractogram of struvite purchased from Alfa Aesar. Bragg reflections indexed according to JCPDS Card No. 1-077-2303.

Struvite-derived LDHs will be termed SLDHs throughout this chapter. The first synthesis method involves the dispersion of struvite in deionised (D.I.) water prior to the addition of Mg^{2+}, and will be henceforth referred to as method 1, M1. In a standard co-precipitation procedure, the LDH suspension is typically aged for 18–24 h at room temperature. For the SLDH however, an ageing time of 72 h (at 35 ºC) was required in order to produce an LDH that was free of the starting mineral (Figure 3.5).

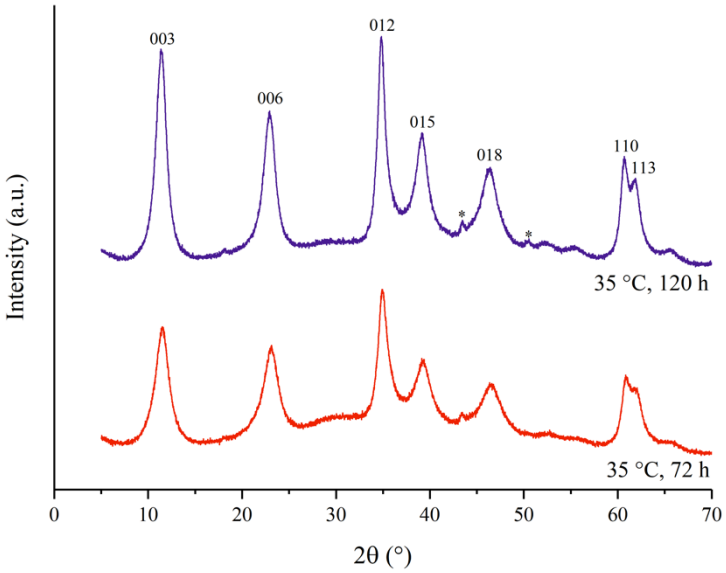


Figure 3.5 Powder XRD diffractograms of M1-SLDHs prepared at 35 ºC. Mg/Al = 3. *Reflections due to the sample holder.

In order to reduce the total synthesis time, two higher temperatures (55 and 75 ºC) were studied. These SLDHs will be termed M1-55-SLDH and M1-75-SLDH, respectively. Figure 3.6 shows the powder X-ray diffraction (XRD) diffractograms of M1-SLDHs synthesised at these two temperatures whilst ageing time was decreased incrementally.

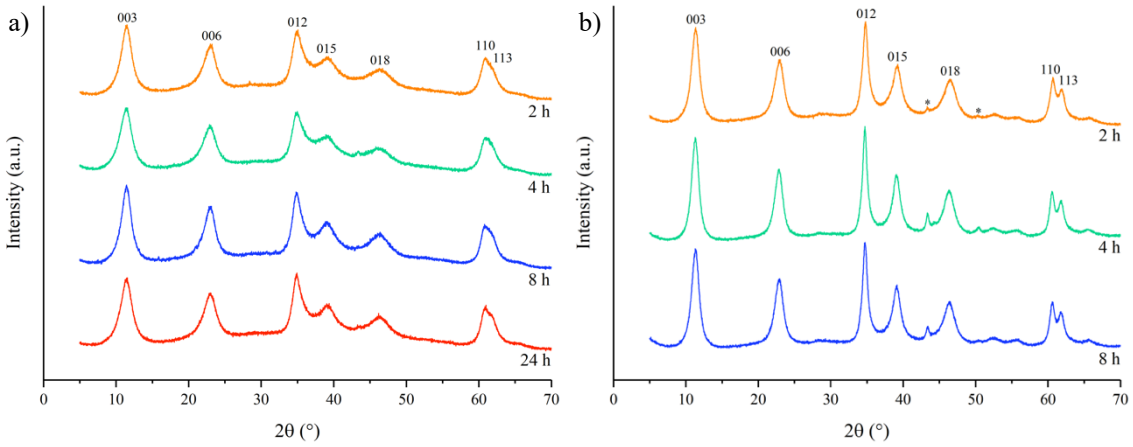


Figure 3.6 Powder XRD diffractograms of a) M1-55-SLDHs and b) M1-75-SLDHs. Mg/Al = 3. *Reflections due to the sample holder.

The XRD diffractograms show that the characteristic LDH Bragg reflections (*e.g.* 00*l*) are present in all cases, whilst reflections due to the struvite phase are not present. Thus, it can be seen that struvite is successfully transformed to LDH at elevated temperatures

after just 2 h. The position of the 003 Bragg reflection gives the *d*-spacing of the SLDHs to be approximately 7.80 Å, which suggests that the interlayer region is occupied by carbonate anions predominantly, with phosphate as a minor component (Table 3.1). The intercalated phosphorus species may be PO_4^{3-} and/or HPO_4^{2-}.

Table 3.1 *d*-spacing values of LDHs. Mg/Al = 3.

Mg/Al	Interlayer species	d_{003} (Å)	Notes
3	CO_3^{2-}	7.65	c-LDH (conventional), water-washed[22]
3	CO_3^{2-}	7.79	SLDH, Alfa Aesar struvite, water-washed
3	PO_4^{3-}	8.07	c-LDH, water-washed[23]

Fourier transform infra-red (FTIR) analyses also confirm the transformation of struvite to an LDH (Figure 3.7). Both materials exhibit a number of unique strong absorption bands, so the degree of transformation is quite apparent. The FTIR spectrum of struvite contains a broad absorption band between *ca*. 2250–3250 cm^{-1}, which is due to O–H stretching vibrations of water molecules of crystallisation and the ν_1 asymmetric N–H stretching mode in NH_4^+. The ν_4 asymmetric H–N–H bending vibration in NH_4^+ gives rise to strong absorptions around 1450 cm^{-1}.[4] These are absent in the SLDH FTIR spectra, so reflect the release of ammonium ions during the synthesis.

In the SLDH FTIR spectra there is a broad absorption between 3000–3600 cm^{-1}. There are contributions to this absorption from the stretching modes of hydroxyl groups bonded to metal ions in the hydroxide layers (M–OH) and stretching vibrations of surface and interlayer water molecules.[24] Moreover, the shoulder at *ca.* 3000 cm^{-1} can be attributed to hydrogen bonding between water and carbonate anions in the interlayer galleries.[24]

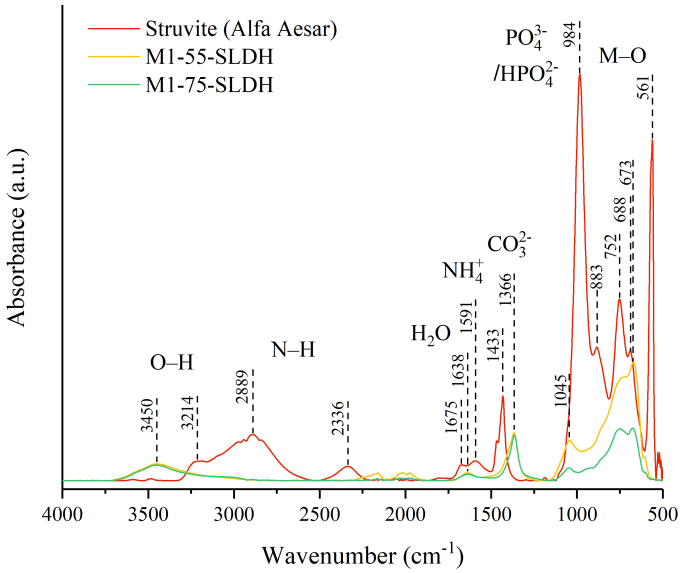


Figure 3.7 FTIR spectra of struvite and M1-SLDHs with 2 h ageing time. Mg/Al = 3.

The synthesis introduces carbonate into the system, so a strong, sharp absorption is observed in the SLDH spectra at *ca*. 1360 cm^{-1} which corresponds to the v_3 antisymmetric stretching vibration of interlayer CO_3^{2-} anions. In the FTIR spectrum of struvite, the absorption peaks around 1000 cm^{-1} can be assigned to the antisymmetric v_3 stretching vibrations of HPO_4^{2-}/PO_4^{3-} and symmetric vibrations of PO_4^{3-}.[25] A small absorption in this region of the SLDH spectra further proves that phosphate is not completely replaced by carbonate.

Differences in the region below 1000 cm^{-1} may be attributed to the bending modes of CO_3^{2-} as well as additional metal-oxygen bonds arising from the incorporation of Al^{3+} into the material. Generally, the intensity of these absorptions increases with increasing ageing time, although the differences become smaller above 4 h (Figure 3.8). This suggests that after 4 h the structure reaches an equilibrium.

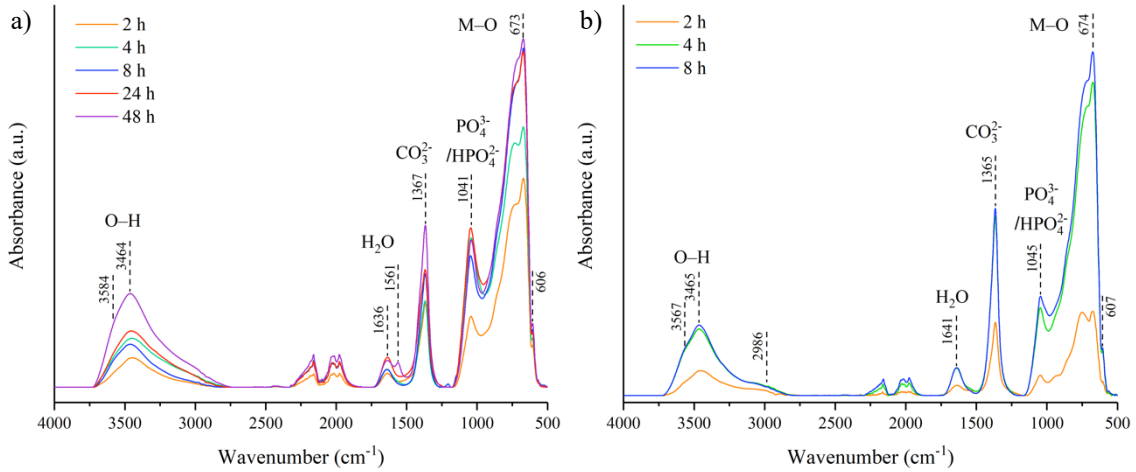


Figure 3.8 FTIR spectra of a) M1-55-SLDHs and b) M1-75-SLDHs prepared with different ageing times. Mg/Al = 3.

The morphologies of struvite and M1 SLDHs were studied using scanning electron microscopy (SEM). The starting material has the characteristic coffin, twin and star shapes expected of this mineral (Figure 3.9a and b).[4, 20] In the SLDHs that were aged for 2 h, sand rose-like clusters, which are typical of LDHs formed by co-precipitation, are present in addition to particles that have retained the morphology of the parent struvite (Figure 3.9c–f). This indicates that SLDH formation occurs alongside struvite dissolution, giving rise to hierarchical products.

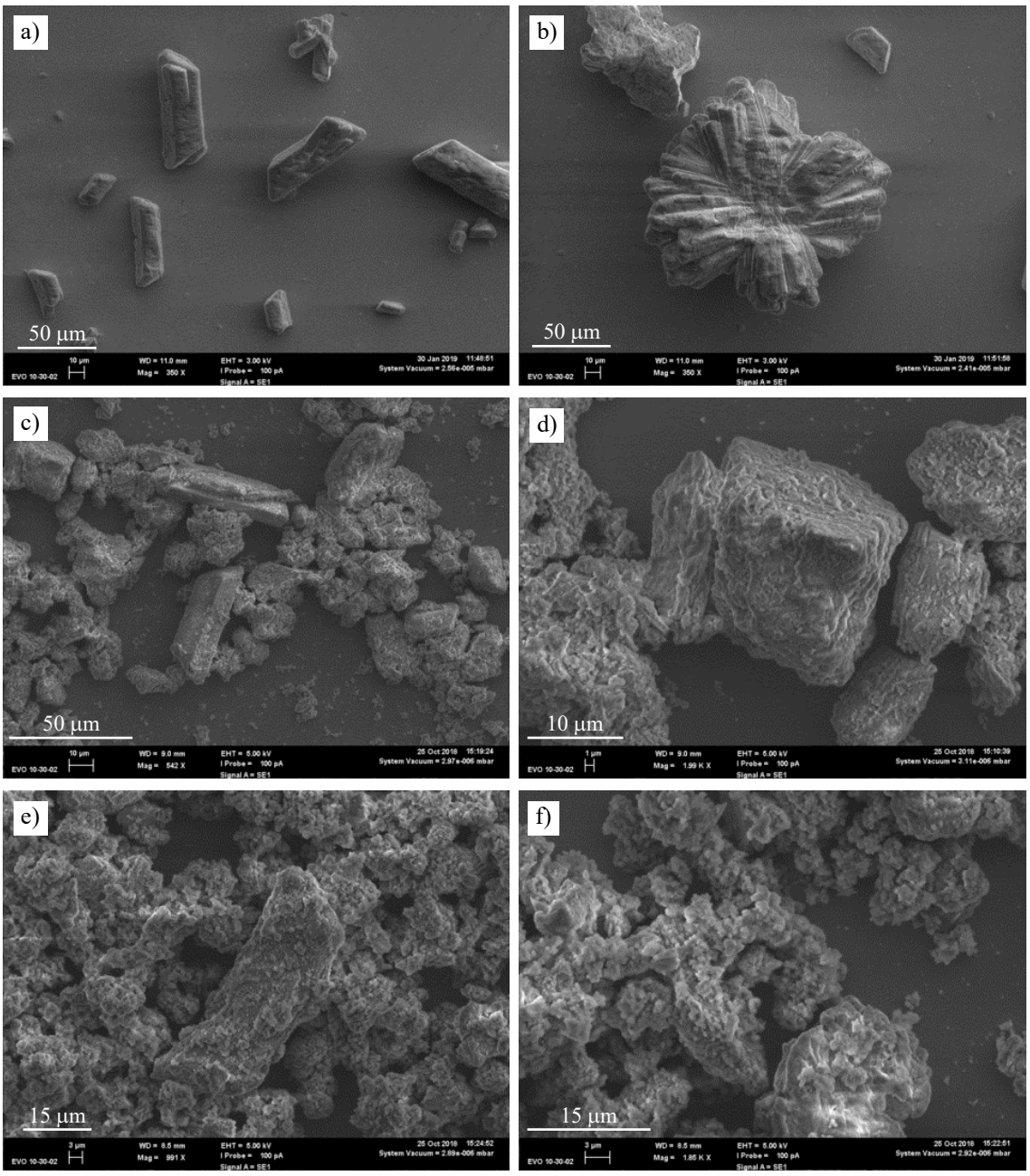


Figure 3.9 SEM images of pure struvite (a and b), M1-55-SLDH (c and d) and M1-75-SLDH (e and f) with 2 h ageing time. Mg/Al = 3. Uncoated samples.

The SLDHs prepared at higher temperature have fewer prismatic (straight-edged) particles, and this is also seen for SLDHs aged over longer periods of time (Figure 3.10). For M1-75-SLDH, the higher temperature promotes greater dissolution of the struvite and thus SLDH growth occurs on smaller, less crystalline scaffolds. Similarly, over extended ageing times, growth of the SLDH is accompanied by Ostwald ripening, which

reshapes the angular crystals into rounder clusters containing larger LDH platelets. This results in sharper Bragg reflections in the XRD.

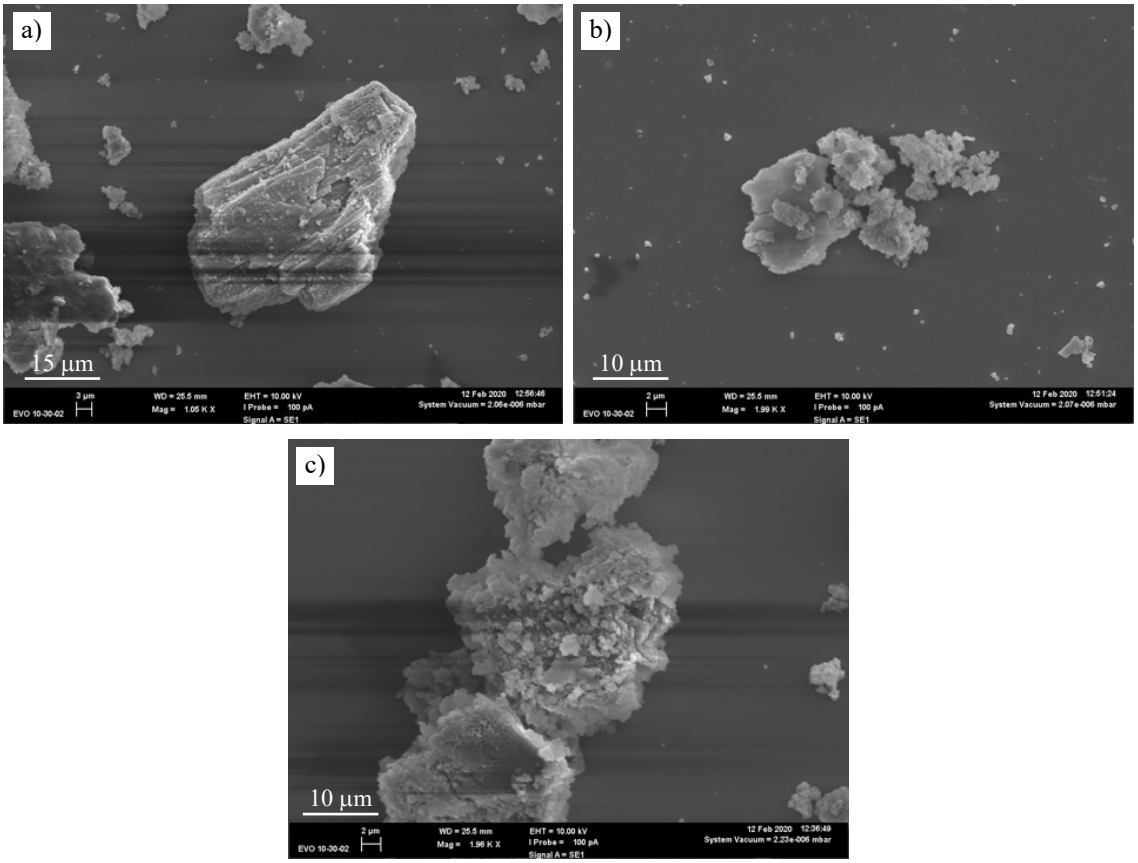


Figure 3.10 SEM images of M1-55-SLDH aged over different periods of time: a) 4, b) 8, and c) 24 h. Mg/Al = 3. Pt-coated samples.

Thermogravimetric analyses (TGA) were carried out to elucidate the thermal stability and decomposition pathways of struvite and the SLDHs (Figure 3.11). Struvite loses approximately 45% of its mass before *ca.* 120 ºC and this is attributed to the liberation of ammonia (NH_3) and water of crystallisation (Equation 3.2). Further heating causes loss of structural water and the formation of magnesium phosphates (Equations 3.3 and 3.4). At 800 ºC, the material has lost almost 55% of its original mass.

$$MgNH_4PO_4.6H_2O \rightarrow MgHPO_4.3H_2O + NH_3 + 3H_2O \qquad \text{Equation 3.2}$$

$$MgHPO_4.3H_2O \rightarrow MgHPO_4 + 3H_2O \qquad \text{Equation 3.3}$$

$$2MgHPO_4 \rightarrow Mg_2P_2O_7 + H_2O \qquad \text{Equation 3.4}$$

In comparison to struvite, the SLDHs show higher thermal stability at low temperatures and only lose *ca.* 42% of their original mass up to 800 ºC. The decomposition of SLDHs is archetypical of LDHs: loss of surface and interlayer water between *ca.* 100–200 ºC, followed by dehydroxylation and loss of interlayer carbonate as CO_2 above *ca.* 200 ºC.[26] The variation in dTGA lines below 200 ºC may indicate a structural difference between the SLDHs caused by dissolution in water at different temperatures. It is known that heating struvite in excess water produces bobierrite, $Mg_3(PO_4)_2.8H_2O$ (Figure 3.12) and this was confirmed by a control reaction (Appendix A, Figures A.1 and A.2). The transformation of struvite to bobierrite is less complete when the reaction is carried out at 55 ºC so some NH_4^+ may remain in the lattice and contribute to the larger mass loss below 100 ºC.

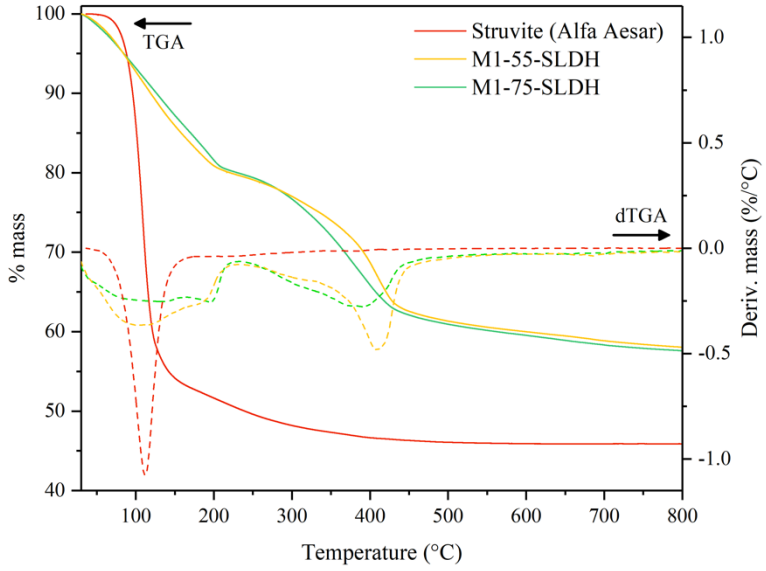


Figure 3.11 TGA and dTGA plots of struvite and M1-SLDHs. Mg/Al = 3.

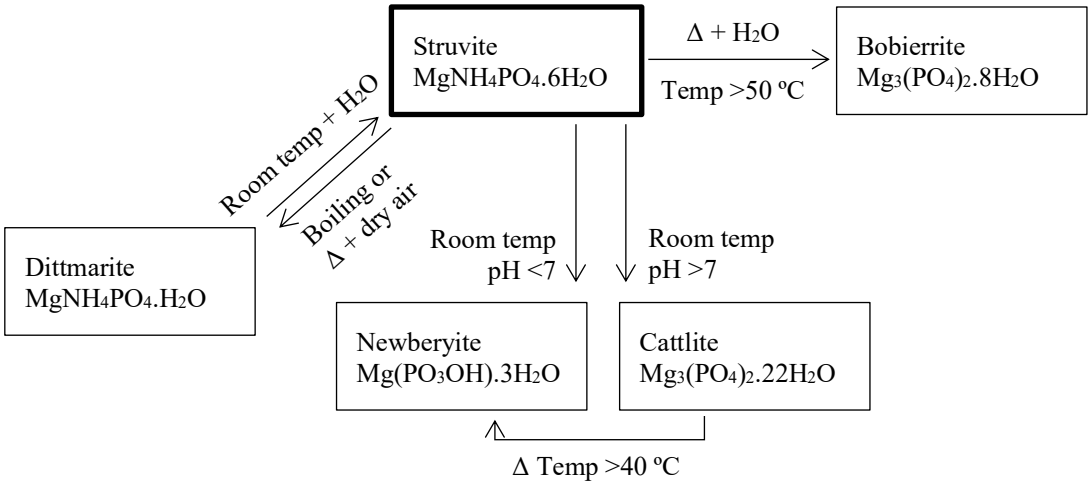


Figure 3.12 Transformation of struvite under wet heating conditions.[27]

The surface areas and pore size distributions of struvite and the M1 SLDHs were recorded using Brunauer-Emmett-Teller (BET) and Barrett-Joyner-Halenda (BJH) methods (Figures 3.13 and 3.14). The N_2 absorption and desorption isotherms (Figure 3.13a) are classified as Type IV, which correspond to mesoporous materials (20–500 Å). [28, 29] The pore size distributions (Figure 3.13b) reflect this, although the surface area of struvite is so low that its pore size distribution is barely visible compared to those of the SLDHs. Under magnification, it can be seen that struvite has a narrow pore size distribution around 20 Å. The narrow peak in the BJH distribution at *ca.* 40 Å is an artefact caused by the spontaneous evaporation of metastable pore liquid (N_2) at $p/p_0 = 0.43$ (closure of the isotherm).[30]

Both struvite and M1-55-SLDH exhibit Type H4 hysteresis curves that are characteristic of narrow slit-shaped pores.[31] The pore size distribution of M1-55-SLDH does not show any clear maxima in the mesoporous range but the enlargement of the pores, relative to the parent struvite, may be due to the liberation of pore space by ammonia during the synthesis and *in situ* growth of LDH within the existing framework.

M1-75-SLDH exhibits a H3 hysteresis loop. This is common for LDHs prepared by co-precipitation and indicates the material has slit-shaped pores that are formed by non-rigid aggregates of plate-like particles.[31] The pore size distribution for this sample has a wide range (*ca.* 40–400 Å) and is similar to the multi-pore distributions observed for AMO-LDHs.[32] The higher synthesis temperature is likely to have enhanced the dissolution of the struvite starting material, resulting in greater fragmentation and dispersion of Mg^{2+}. Thus, exposing more nucleation sites and creating a larger number of small SLDH clusters with morphologies more akin to c-LDH than struvite (Figure 3.9e and f). These effects would also explain the fourfold increase in surface area recorded for M1-75-SLDH compared to M1-55-SLDH (81 and 20 m^2 g^{-1}, respectively, Figure 3.14).

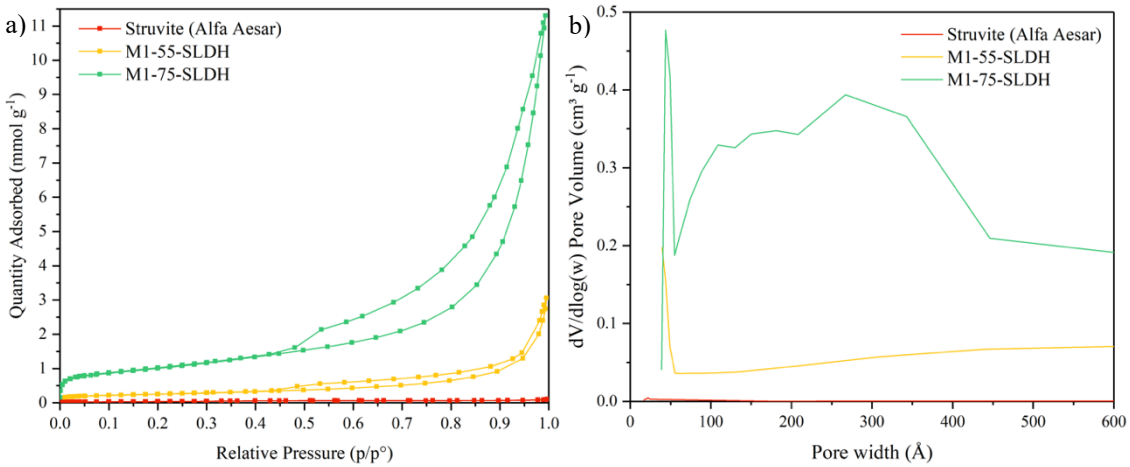


Figure 3.13 a) N_2 absorption and desorption isotherms and b) BJH desorption pore size distributions of struvite and M1-SLDHs. Mg/Al = 3.

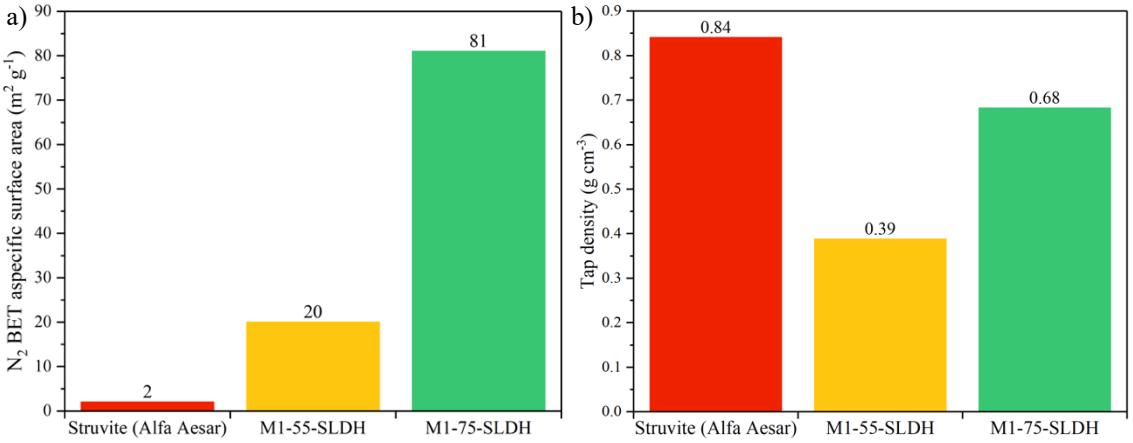


Figure 3.14 a) N_2 BET specific surface areas and b) tap densities of struvite and M1-SLDHs. Mg/Al = 3.

M1-75-SLDH has a similar tap density to an equivalent conventional LDH, c-LDH (0.68 and 0.64 g cm^{-1}, respectively) but almost twice the surface area (81 and 43 m^2 g^{-1}, respectively). Struvite may therefore provide a dense but porous template for LDH growth under these conditions.

3.2.2 Method 2 (M2)

Synthesis method M1 has demonstrated that struvite can be successfully transformed into MgAl-CO_3-LDHs with yields of over 95%. The analyses also show that struvite can be used as a precursor to high surface area LDHs without the need for core-shell or solvent treatment methods. However, the overall atom economy of the M1 method is low because both the ammonium and phosphate in the starting material are discarded.

3.2.2.1 Modification to M1 to capture ammonia

The first modification to the M1 procedure was to liberate and capture the ammonia as a by-product. To achieve this, struvite was heated in alkali, instead of deionised water, prior to the co-precipitation step. Equation 3.5 describes a possible decomposition pathway, which will be investigated in more detail in Section 3.3. The reaction vessel was sealed, and the only outlet was through a bubbler containing hydrochloric acid (1M HCl), so the

liberated ammonia gas would be acidified and collected as NH_4^+. This method has been designated M2.

$$MgNH_4PO_4.6H_2O + NaOH \rightarrow MgNaPO_4.6H_2O + NH_3 + H_2O \qquad \text{Equation 3.5}$$

As in M1, 35 ºC was investigated first because of the greater solubility of struvite at this temperature. Again, a long reaction time (72 h) was required to produce an SLDH free of the starting material so the reaction was repeated at higher temperatures in order to reduce the ageing time.

It was found that M2 SLDH synthesis was successful at 65 ºC with 2 h ageing time (Figure 3.15a). The M2-SLDH shows a similar FTIR spectrum to the M1-SLDHs (Figure 3.15b). TGA analysis of M2-SLDH (Figure 3.16, blue line) shows greater mass loss below 200 ºC than the M1-SLDHs. This may indicate a structural difference between the materials resulting from the liberation of NH_3 prior to Al^{3+} addition and consequently a difference in the amount, and the strength of adsorption, of water molecules in the SLDH.

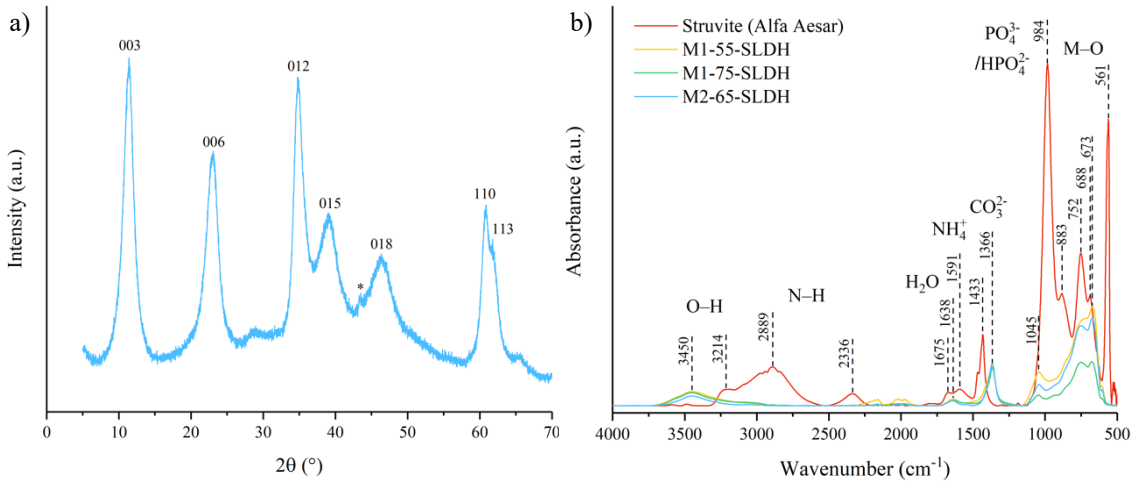


Figure 3.15 a) Powder XRD diffractogram of M2-65-SLDH and b) FTIR spectra of struvite, M1 and M2 SLDHs. Mg/Al = 3. *Reflection due to the sample holder.

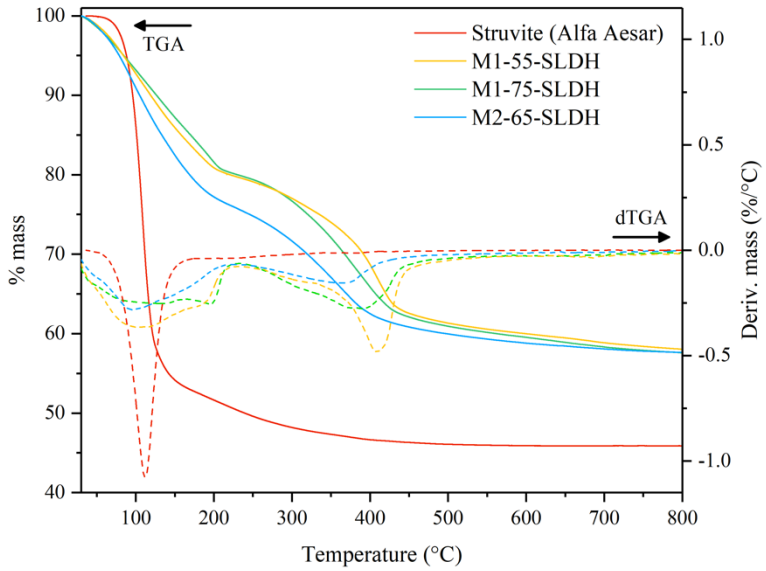


Figure 3.16 TGA and dTGA analyses of struvite, M1 and M2 SLDHs. Mg/Al = 3.

In comparison to the SLDHs prepared by M1 – and, likewise, c-LDHs – the N_2 BET specific surface area of M2-65-SLDH was found to be significantly higher (Figure 3.17). This is likely to be due to the decomposition of struvite in NaOH in step 1 of this synthesis method, with the replacement of NH_4^+ in the structure with smaller Na^+ creating additional pores in the material and thus increasing the surface area. Studies of a potassium analogue of struvite, $MgKPO_4.6H_2O$, have shown that interactions between the larger cation (K^+ or NH_4^+) and the oxygen atoms are weak in struvite-type structures, so substitution of K^+ for NH_4^+ has little effect on the structure.[33] This suggests that the lattice of $Mg(H_2O)_6^{2+}$ octahedra and PO_4^{3-} tetrahedra is approximately undisturbed when Na^+ replaces NH_4^+.

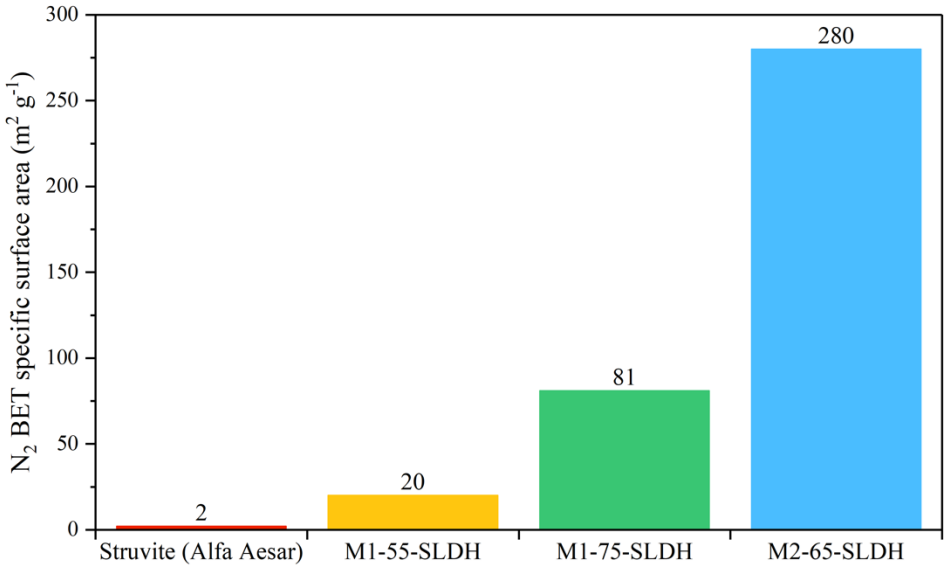


Figure 3.17 N_2 BET specific surface areas of struvite, M1 and M2 SLDHs. Mg/Al = 3.

The N_2 adsorption and desorption isotherms of M2-65-SLDH give rise to a H2 hysteresis curve (Figure 3.18a). These suggest that bottleneck constrictions are present.[29] The pore size distribution for M2-65-SLDH is dominated by the artefact at *ca.* 42 Å (Figure 3.18b). The superiority of the surface areas achievable using M2 means that further investigations have been pursued using M2.

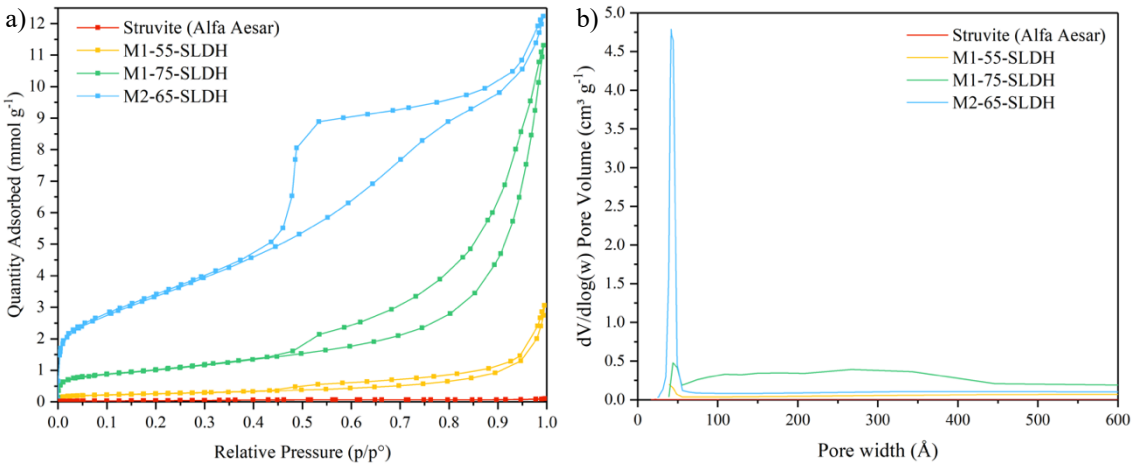


Figure 3.18 a) N_2 adsorption and desorption isotherms and b) BJH pore size distributions of struvite, M1 and M2 SLDHs. Mg/Al = 3.

3.2.2.2 Modification of M2 to utilise phosphate

Phosphate is a known interlayer species in LDHs.[34-36] It is typically more difficult to prepare because of competition from carbonate (from the atmosphere and dissolved in water), which has a stronger affinity for the interlayer gallery.[37] Nevertheless, measures can be taken to minimise the reaction mixture's exposure to carbonate (*e.g.* degassed water and a nitrogen atmosphere). Using M2 under these conditions, phosphate-intercalated SLDHs (M2-PO_4-SLDHs) were successfully prepared.

The atom economy of the M2 transformation of struvite to PO_4-SLDHs is higher than that of CO_3-SLDHs since a greater proportion of the struvite is utilised in the desired product and an additional salt is not required. Assuming 100% yield and stoichiometric amounts, *e.g.* such that the products are $Mg_3Al(OH)_8(CO_3)_{0.5}.4H_2O$ and $Mg_3Al(OH)_8(PO4)_{0.33}.4H_2O$, the atom economies of struvite transformations to SLDH using M2 are 22.77 and 23.36%, respectively. These increase to 26.22 and 26.93% if ammonia is taken to be a useful product. In comparison, the atom efficiency of an LDH synthesis using the nitrate salt, $Mg(NO_3)_2.6H_2O$, is 22.27%. Thus, using struvite can improve the atom economy of LDH syntheses.

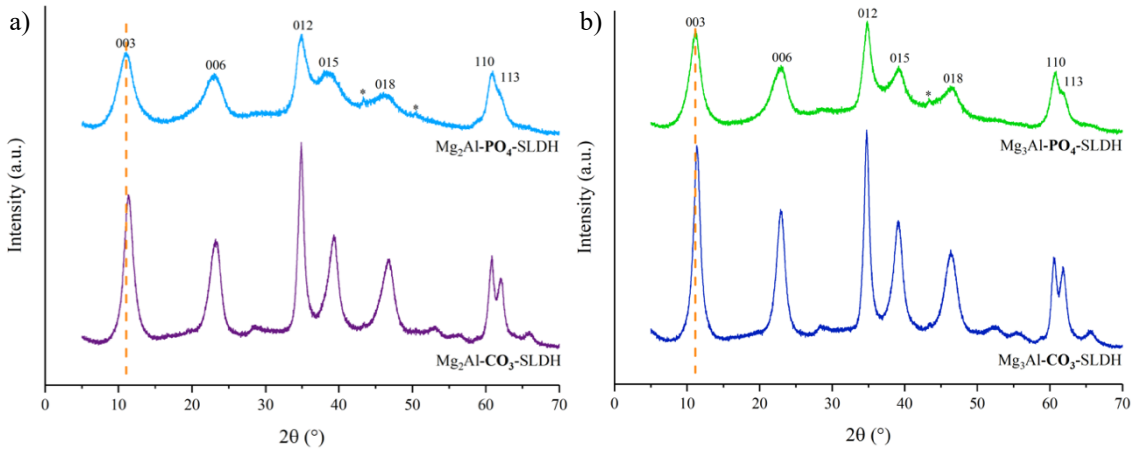


Figure 3.19 Powder XRD diffractograms of carbonate and phosphate M2-SLDHs: a) Mg/Al = 2 and b) Mg/Al = 3. *Reflections due to the sample holder.

The XRD diffractograms show that M2-PO_4-SLDHs have markedly lower crystallinity than the corresponding carbonate SLDHs (M2-CO_3-SLDHs, Figure 3.19 and Table 3.2). The higher charge and different geometry of the PO_4^{3-} anion contributes to the stacking disorder of the hydroxide sheets. Additionally, crystallinity decreases with increasing Al^{3+} content. This is due to the higher proportion of trivalent cations in the hydroxide layers causing greater distortion from the brucite structure, leading to poorer arrangement for stacking.

The dotted lines highlight the difference in basal spacing between the carbonate and phosphate SLDHs. As the PO_4^{3-} anion is larger than CO_3^{2-}, the 003 Bragg reflections for the PO_4-SLDHs appear at lower 2θ angles, which correspond to larger interlayer distances (Table 3.2). For the PO_4-SLDHs, the *d*-spacing values also suggest that carbonate impurities are present despite measures to isolate the system during the synthesis (*cf.* Table 3.1). This is corroborated by the presence of an absorption peak at *ca.* 1360 cm^{-1} in the FTIR spectra (Figure 3.20a).

Table 3.2 *d*-spacing of M2-SLDHs calculated from powder XRD diffractograms.

Mg/Al ratio[a]	Interlayer species	003[b] (º)	d_{003} (Å)	FWHM (º)
2	CO_3^{2-}	11.37	7.78	1.74
2	PO_4^{3-}	11.05	8.00	2.29
3	CO_3^{2-}	11.36	7.78	1.09
3	PO_4^{3-}	11.15	7.93	1.82

[a]Ratio of metals used in the synthesis – *cf.* Table 3.3 and Appendix A, Table A.4.
[b]Position of 003 Bragg reflection (2θ).

The TGA and dTGA data provide further evidence of this (Figure 3.20b). The second mass loss for both PO_4-SLDHs occurs at higher temperatures than that of the CO_3-SLDHs, but the peak for Mg_3Al-PO_4 is at a lower temperature than Mg_2Al-PO_4. This suggests that carbonate forms attractive interactions with phosphate, making it more

difficult to release from the interlayer region. The TGA analyses also show that the PO_4-SLDHs contain more water than CO_3-SLDHs, which is due to the higher hydrophilicity of the phosphate anion.

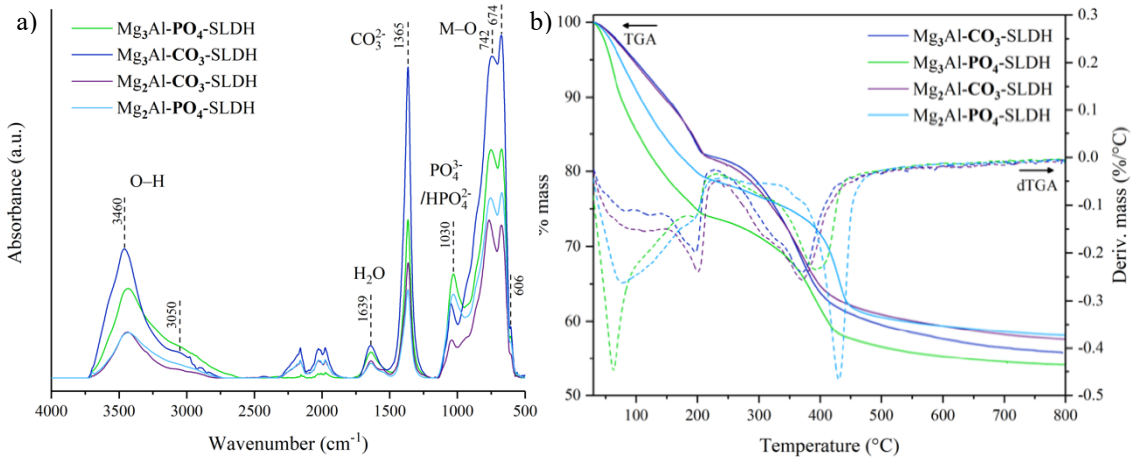


Figure 3.20 a) FTIR spectra and b) thermal analyses of carbonate and phosphate M2-SLDHs.

Solid state nuclear magnetic resonance (ssNMR) spectroscopy was used to characterise the phosphorus, aluminium and magnesium environments in the SLDHs (Figures 3.21–3.23). All four samples produced ^{31}P HPDEC (high power decoupling) ssNMR spectra with a resonance around 0 ppm, which is characteristic of PO_4^{3-}/HPO_4^{2-}. This is further evidence that not all of the phosphorus in struvite is replaced in the preparation of CO_3-SLDHs and supported by elemental analyses by inductively coupled plasma mass spectrometry (ICP-MS, Table 3.3). This resonance has a greater intensity in the spectra of the PO_4-SLDHs as expected. The ICP-MS data also reveals that the Mg/Al ratios of the SLDHs deviates from the expected values, most significantly for the PO_4-SLDH with Mg/Al = 2.

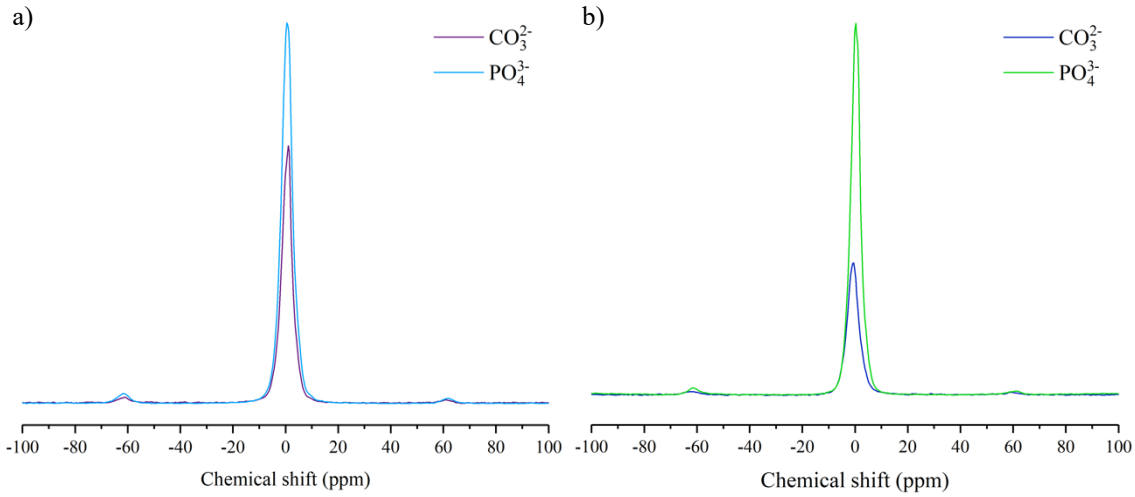


Figure 3.21 ^{31}P HPDEC ssNMR of M2-SLDHs: a) Mg/Al = 2 and b) Mg/Al = 3.

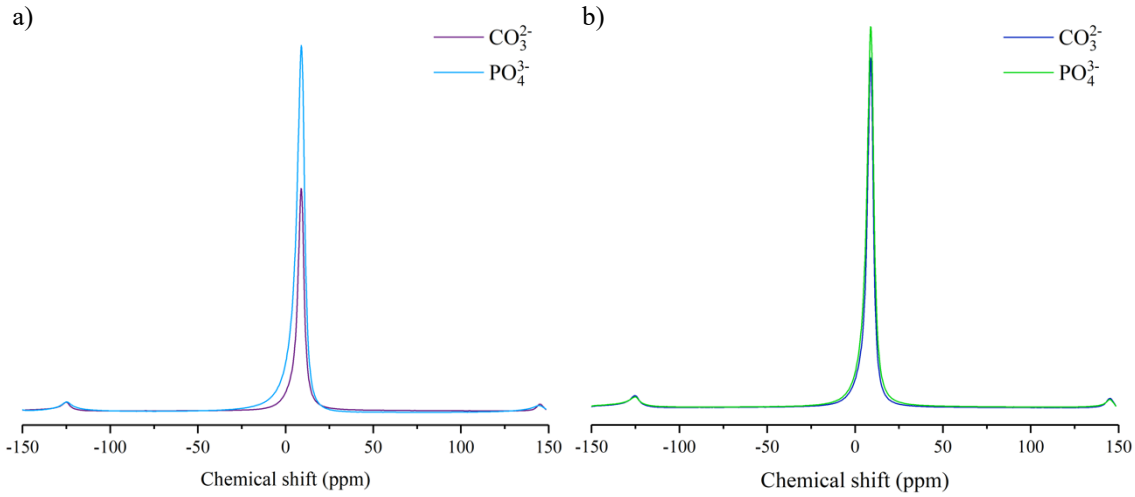


Figure 3.22 ^{27}Al DPMAS ssNMR of M2-SLDHs: a) Mg/Al = 2 and b) Mg/Al = 3.

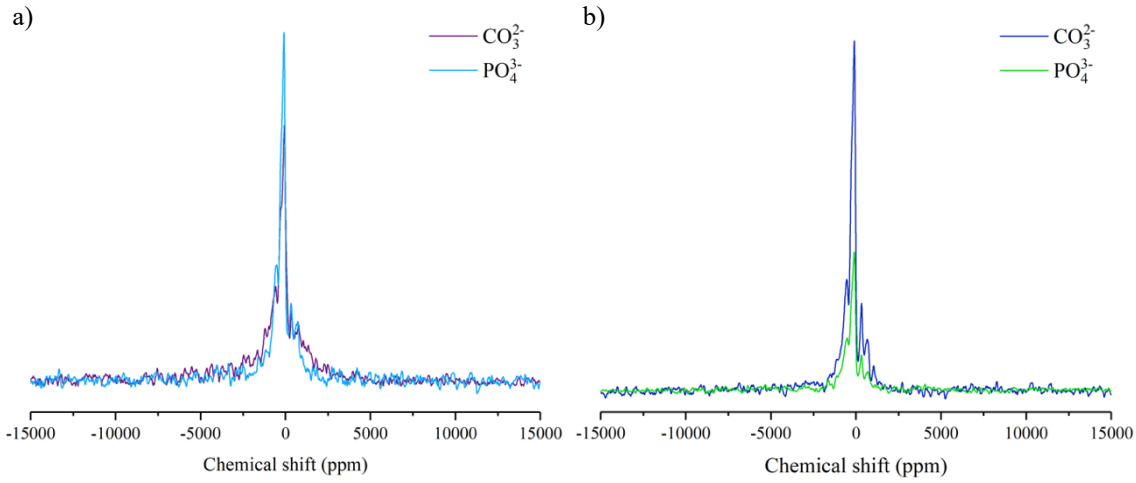


Figure 3.23 ^{25}Mg DFS-echo ssNMR spectra of M2-SLDHs: a) Mg/Al = 2 and b) Mg/Al = 3.

Table 3.3 Summary of the ICP-MS elemental analyses of M2-SLDHs.

Av. wt.%	Mg/Al = 2		Mg/Al = 3	
	CO_3^{2-}	PO_4^{3-}	CO_3^{2-}	PO_4^{3-}
Mg	20.94	20.57	21.77	19.13
Al	8.99	7.58	8.19	6.41
P	1.64	3.65	1.40	3.14
Mg/Al	2.49	2.90	2.84	3.19
Al/P	5.48	2.08	5.85	2.04

The aluminium environments were characterised by ^{27}Al DPMAS (direct polarisation magic angle spinning) ssNMR spectroscopy (Figure 3.22). Magnesium environments were probed using ^{25}Mg DFS-echo (double-frequency sweeps before Hahn-echo) ssNMR spectroscopy to enhance the signals because this isotope has a low gyromagnetic ratio (low sensitivity), low natural abundance (~10%), and large quadrupole moment, which broadens the resonances through the interaction with the local electric-field gradient at the site of the nucleus. The spectra for each Mg/Al ratio do not show significant differences as expected, since the interlayer anion does not have a strong effect on the geometry around the metal cations in the hydroxide layers.

Surface area analyses by N_2 BET show that all four SLDHs are mesoporous and the H3 hysteresis shapes indicate slit-like pores (Figure 3.24a). In Section 3.2.2.1, it was found that M2-SLDHs are high surface area, high density materials. Characterisation of M2-PO_4-SLDHs now shows that this is only true of M2-CO_3-SLDHs and not for M2-PO_4-SLDHs (Figure 3.25). Both M2-PO_4-SLDHs have high densities but low surface areas (9 and 37 $m^2\ g^{-1}$ for Mg/Al = 2 and 3, respectively). The PO_4-SLDHs have fewer pores in the size range 100–400 Å. From the SEM images (Figures 3.26 and 3.27) it can be seen that the CO_3-SLDHs are more fragmented and contain more particles having the sand-

rose morphology. This suggests that the addition of carbonate enhances the dissolution and/or decomposition of struvite, possibly through the homogeneous pH rise that occurs when Na_2CO_3 dissolves in the slurry.

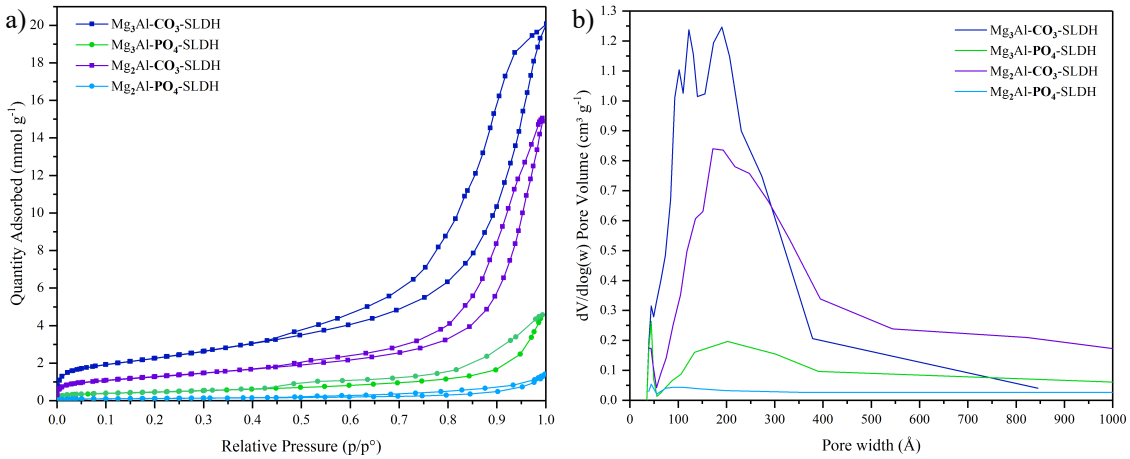


Figure 3.24 a) N_2 adsorption and desorption isotherms and b) BJH desorption pore size distributions of M2-SLDHs.

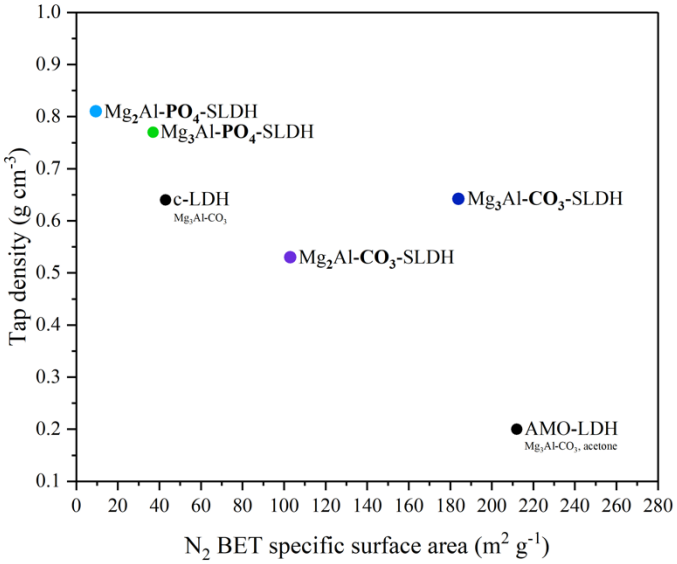


Figure 3.25 N_2 BET specific surface area and tap density comparison of various SLDHs and reference LDHs.

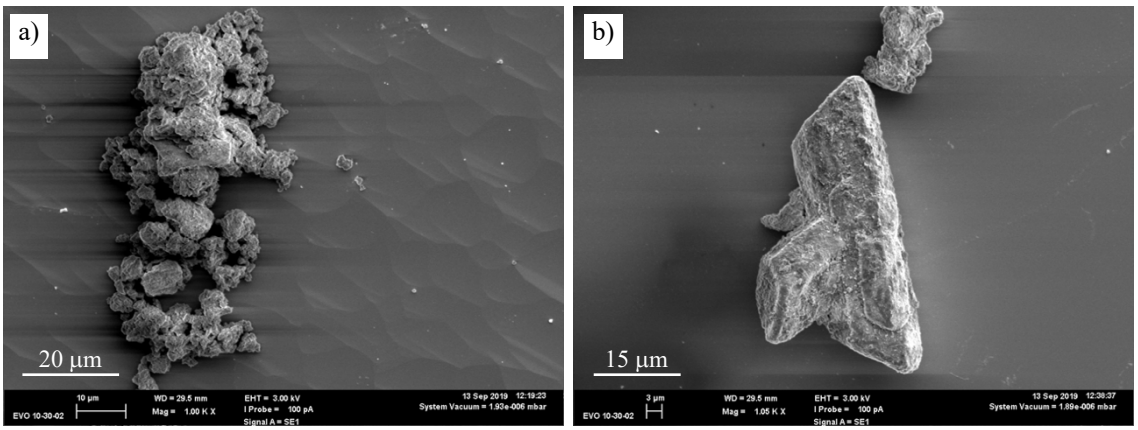


Figure 3.26 SEM images of a) carbonate and b) phosphate M2-SLDHs. Mg/Al = 2.

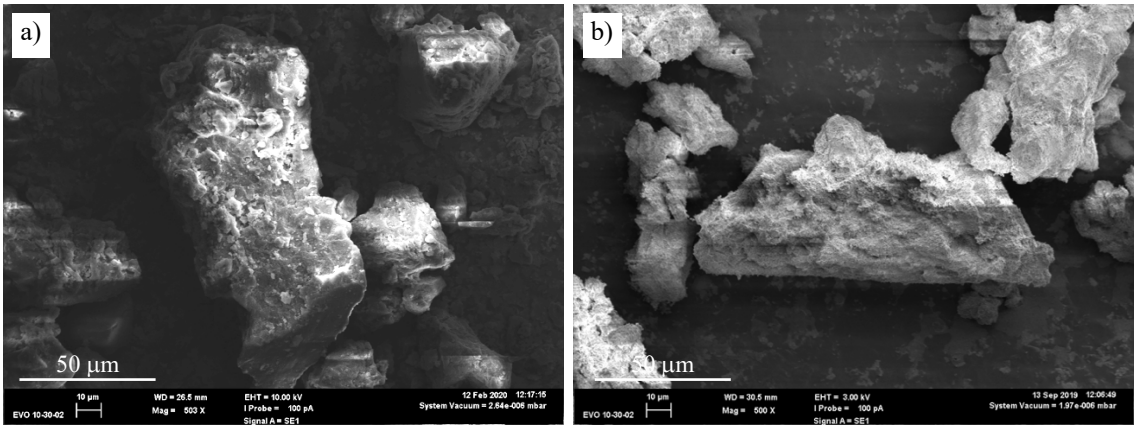


Figure 3.27 SEM images of a) carbonate and b) phosphate M2-SLDHs. Mg/Al = 3.

3.3 Study of the transformation of struvite to LDH

Section 3.2 has shown that struvite can be utilised as a source of magnesium for MgAl-LDH synthesis. Furthermore, the SLDHs are found to have unique properties. N_2 BET specific surface areas up to 184 $m^2\ g^{-1}$ were recorded for SLDHs, which is more than four times the surface area of the equivalent c-LDHs, and their tap densities were up to four times that of an equivalent AMO-LDH. The product morphologies are also unique and hint at a distinct reaction pathway that is not achieved with metal salt solutions.

To identify the active species in the reaction, struvite was heated in aqueous NaOH for 1 and 3 h. The conditions simulated the first step in the M2-SLDH synthesis, *i.e.* before the

addition of CO_3^{2-} and Al^{3+}, and also probed how prolonged heating affected the mineral. The slurries were quenched, and the materials isolated and characterised.

From the powder XRD diffractograms it can be seen that struvite decomposes gradually when heated in alkali (Figure 3.28). After 1 h, the Bragg reflections due to struvite are approximately one third of their original intensity and additional reflections have appeared. The most striking being that at *ca.* 7.8 and 9.1º as there were no reflections in the low angle region for struvite. This suggests the presence of layers and the *d*-spacings of these two low angle reflections are approximately 11.31 and 9.65 Å.

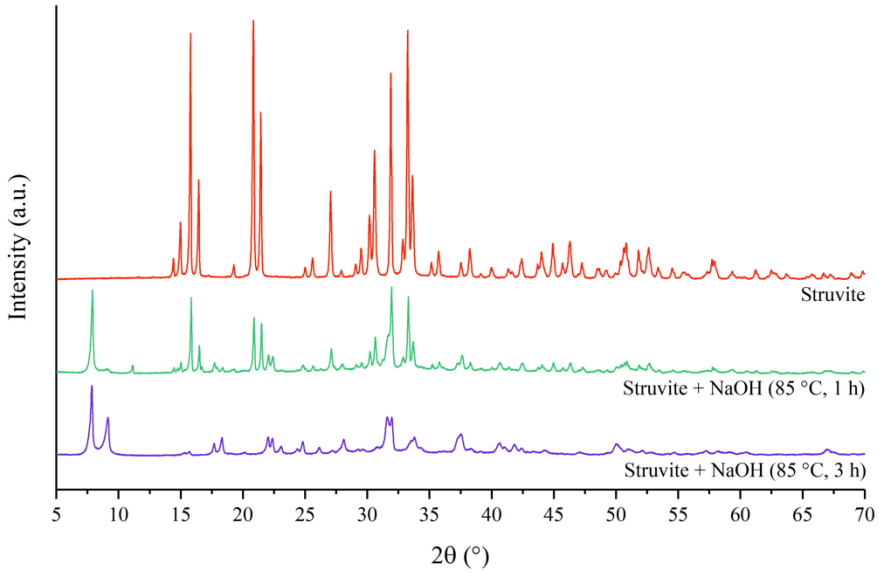


Figure 3.28 Powder XRD diffractograms of struvite and struvite heated in NaOH at 85 ºC.

In order to identify the compounds responsible for the new reflections, elemental analyses were performed by ICP-MS to elucidate the composition (Table 3.4 and Appendix A Table A.5). As mentioned in Section 3.2.2.1, the reaction between struvite and NaOH is believed to yield a magnesium sodium phosphate by exchange of NH_4^+ for Na^+ (Equation 3.5).

$$MgNH_4PO_4.6H_2O + NaOH \rightarrow MgNaPO_4.6H_2O + NH_3 + H_2O \qquad \text{Equation 3.5}$$

The ICP-MS data shows that the isolated products contain significant quantities of sodium (Na). Furthermore, unlike in struvite, the amounts of Mg and P are almost equal. This suggests that the alkaline conditions also released some phosphate, which was then washed away when the slurry was quenched. The ratio of elements (Mg:Na:P) is approximately 3.5:1.0:2.9 and 2.1:1.0:1.7 after 1 and 3 h of NaOH treatment, respectively. These results indicate partial exchange of the univalent cations.

Table 3.4 Summary of the ICP-MS elemental analyses of struvite decomposed in NaOH at 85 ºC.

Av. wt.%	$MgNH_4PO_4.6H_2O$ + NaOH (85 ºC)	
	1 h	3 h
Na	3.46	7.33
Mg	12.81	15.95
P	13.36	16.30

The three compounds behave quite differently during thermal decomposition (Figure 3.29). Whilst struvite undergoes one large mass loss event (~46 wt.%) with a dTGA minimum point at *ca.* 110 ºC, the struvites treated with NaOH undergo more complex decompositions.

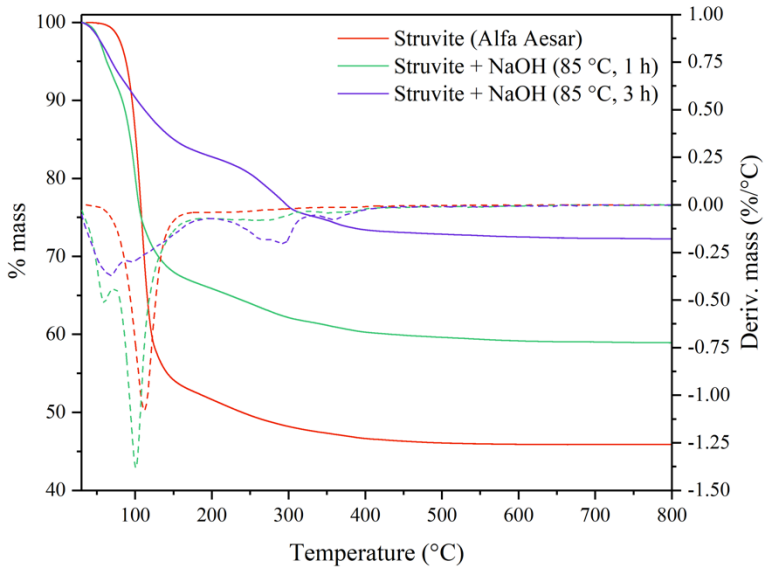


Figure 3.29 TGA and dTGA curves of struvite and struvite decomposed in NaOH (85 ºC, 1 and 3 h).

For the NaOH-treated struvites, the first dTGA minima occur at *ca.* 60 ºC and are associated with the loss of residual NH_4^+ as gaseous NH_3.[38] The struvite heated in NaOH for 1 h then shows a large mass loss at *ca.* 100 ºC, whereby its mass is reduced by ~30 wt.%. This mass loss is due to dehydration. The onset of dehydration at a lower temperature than in pristine struvite indicates the presence of water molecules that are less strongly bound than in struvite. These are likely to be water molecules in sites originally occupied by NH_4^+ (i.e. the hydration spheres of Na^+). The tail of this dTGA minimum coincides with that of struvite, which suggests that there are also water molecules of crystallisation that exist in environments similar to those in struvite, *i.e.* where NH_4^+ substitution has not occurred. A small decrease in mass (~7 wt.%) occurs between 200 – 300 ºC, due to the loss of structural water to form magnesium phosphates, and the material loses approximately 40 wt.% overall.

The struvite heated in NaOH for 3 h has a smaller percentage mass loss between 80 – 190 ºC than the other two materials. This suggests that the longer heating time allows for a greater proportion of NH_4^+ to be exchanged for Na^+. The material undergoes a greater mass loss (~9 wt.%) at higher temperatures (250–300 ºC) but loses only ~26 wt.% overall. The second mass loss caused by further dehydration and dehydroxylation of the magnesium phosphates.

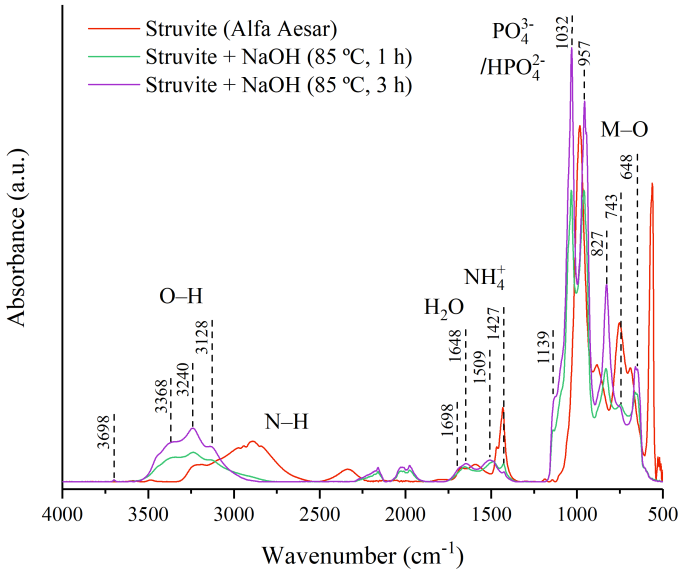


Figure 3.30 FTIR spectra of struvite and struvite decomposed in NaOH (85 ºC, 1 and 3 h). Absorption bands due to struvite are not labelled.

In the FTIR spectrum of struvite (Figure 3.30), the absorption band at 1427 cm^{-1} is due to the v_4 asymmetric H–N–H bending vibration in NH_4^+. This absorption is weaker in the spectra of the decomposed struvites, which is consistent with the theory that NH_3 is liberated during the alkaline decomposition step. The non-zero intensity of this absorption band in the spectra of the NaOH-treated struvites indicates that the expulsion of NH_3 does not go to completion. The ratio of Mg:Na:P in these samples (Table 3.4) is not unity, it would appear that a mixture of NH_4^+ and Na^+ exists in the lattice.

The absorption bands at 3368, 3240 and 3128 cm^{-1} are due to the H–O–H stretching vibrations of water molecules of crystallisation. The broadness of the bands indicate that they are strongly hydrogen bonded to the Mg cations. The H–O–H bending modes in water give rise to the bands around 1650 cm^{-1}. Mg–O bonds are responsible for the sharp absorption peaks at 827 and 648 cm^{-1}.

In the FTIR spectrum of struvite, there is a single absorption band at 984 cm^{-1} due to the v_3 P–O asymmetric stretching vibrations of phosphate. Splitting of this band in the spectra

of the NaOH-treated struvites indicates deviation of the PO_4^{3-} group from ideal tetrahedral geometry. This distortion also allows the ν_1 symmetric stretching vibration to become IR active and this gives rise to the shoulder peak at 957 cm^{-1}.[39] These suggest that the environment around the PO_4^{3-} ions was perturbed by the loss of NH_4^+ and replacement with the smaller Na^+ cation. It is possible that water molecules rearrange to stabilise the Na^+ and these will form hydrogen bonds to the PO_4^{3-} tetrahedra causing distortions of bonds. This observation is supported by ^{31}P DPMAS ssNMR spectroscopy which shows a shift and broadening of the resonance due to phosphate (Figure 3.31a).

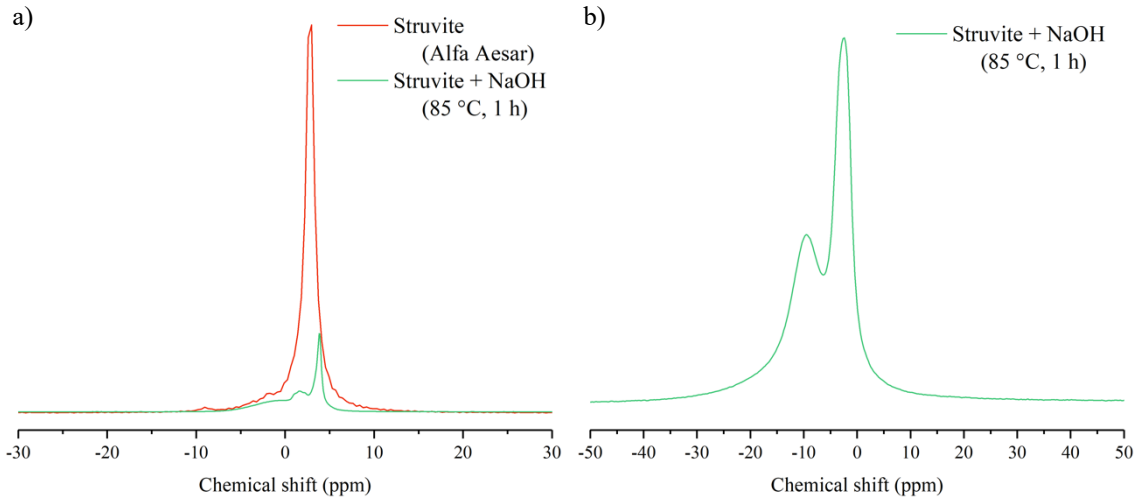


Figure 3.31 a) ^{31}P DPMAS ssNMR of struvite and struvite decomposed in NaOH (85 ºC, 1 h) and b) ^{23}Na DPMAS ssNMR of struvite decomposed in NaOH (85 ºC, 1 h).

The ^{23}Na DPMAS spectrum of NaOH-treated struvite (1 h) shows two resonances centred at –9.58 and –2.55 ppm (Figure 3.31b). ^{23}Na is quadrupolar (I = 3/2) so its magnetic relaxation is dominated by the interaction of its quadrupolar moment with the electric field gradients originating from the surrounding nuclei. The ^{23}Na relaxation rates are therefore very sensitive to the Na^+ environment. The two resonances indicate two unique crystallographic Na environments, which may be the result of partial exchange with NH_4^+. The resonance at –9.58 ppm corresponds to a more shielded environment (*e.g.* a

higher coordination number) and the broadness of this resonance also suggests asymmetry in the chemical environment.[40, 41]

Studies on other struvite analogues, $MgMPO_4.6H_2O$ ($M = K^+$, Rb^+, Cs^+, Tl^+), reported that Na^+ is too small to substitute into the struvite lattice at room temperature.[39, 42] This suggests that with the aid of heat, the reaction pathway taken during the M2 synthesis forms a unique, metastable compound with some Na^+ cations occupying cavities vacated by NH_4^+. Upon addition of the Al^{3+} solution, it is able to return to a lower energy state by forming SLDH in a topotactic fashion.

Surface area analyses and SEM imaging provide further evidence that NH_4^+ is partially replaced with Na^+ (Figures 3.32–3.37). The products are significantly more porous, and the N_2 BET specific surface area increases almost twenty-fold after 1 h of thermal alkali treatment (38 $m^2\ g^{-1}$, Figures 3.32 and 3.33). The SEM images show that the coffin-lid crystals are cracked and fragmented, presumably due to the escape of NH_3 gas and penetration by NaOH (Figures 3.34 and 3.35). There may also be some swelling of the external layers, which will contribute to the decrease in tap density. A mixture of small clusters and coffin shapes exist, and these provide a soft template for SLDH growth so are responsible for the morphologies observed in Section 3.2.

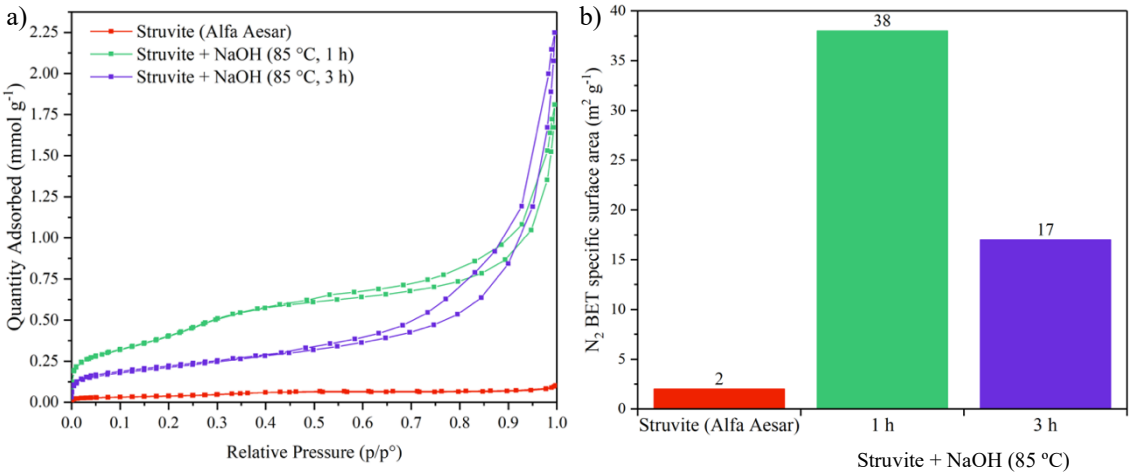


Figure 3.32 a) N_2 adsorption and desorption isotherms and b) N_2 BET specific surface areas of struvite and struvite decomposed in NaOH (85 ºC, 1 and 3 h).

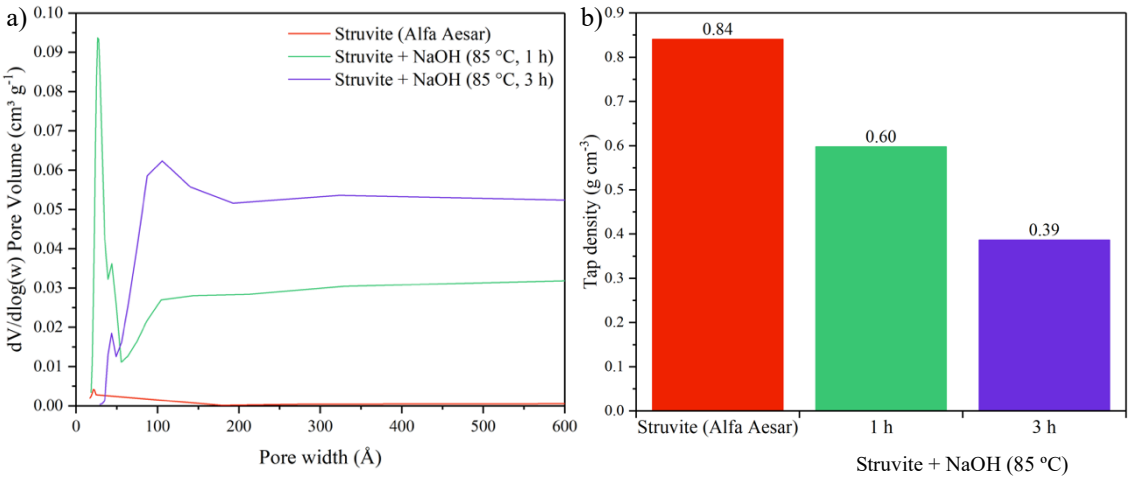


Figure 3.33 a) BJH pore size distributions and b) tap densities of struvite and struvite decomposed in NaOH (85 ºC, 1 and 3 h).

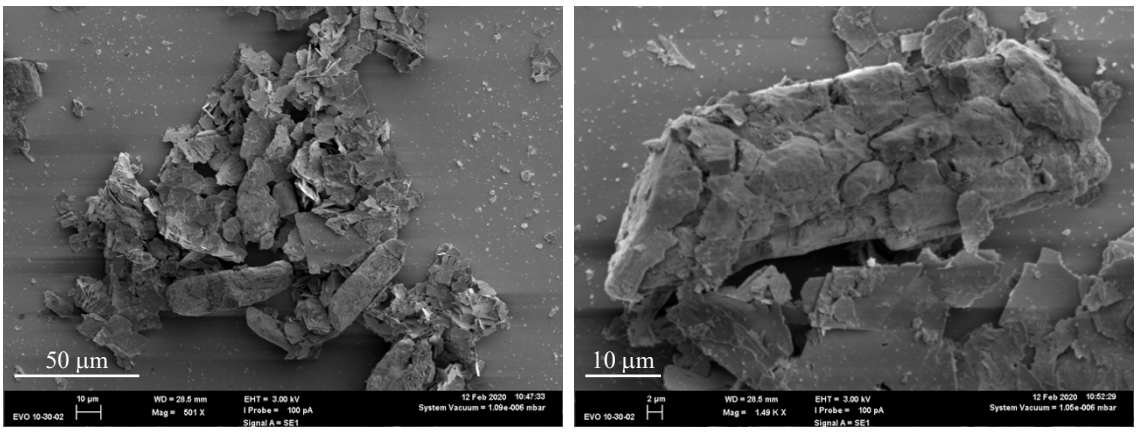


Figure 3.34 SEM images of struvite decomposed in NaOH (85 ºC, 1 h).

The surface area after 3 h is ~46 % the value after 1 h (17 m^2 g^{-1}). It can be seen in the SEM images that after 3 h the majority of coffin-lid crystals have been destroyed and the morphology is predominantly platelet-like (Figure 3.35). These platelets are larger and more crystalline than in the sample quenched after 1 h. Consequently, the number of small pores within a particle are reduced and large interplatelet voids are responsible for the macropore population (> 500 Å) recorded by the BJH method. These results suggest that the dispersion time of 1 h is appropriate for generating a reactive intermediate with an enhanced surface area.

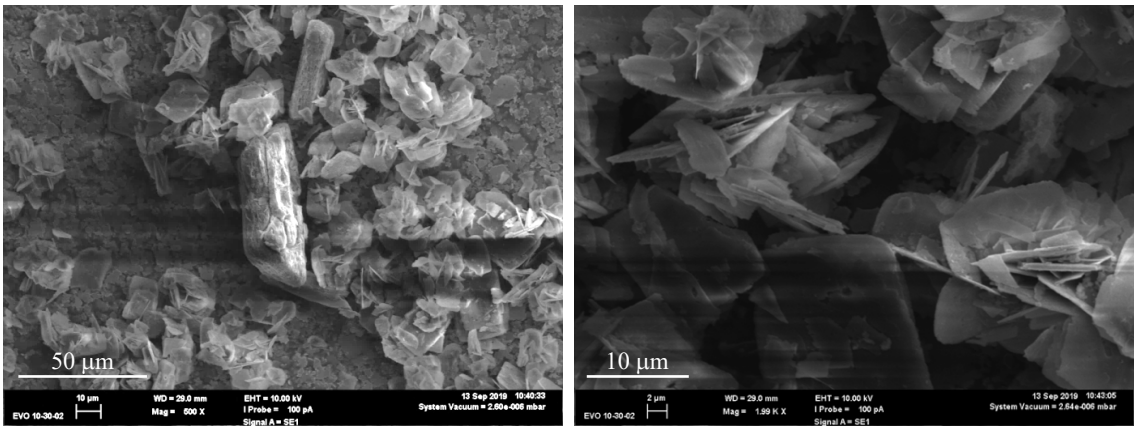


Figure 3.35 SEM images of struvite decomposed in NaOH (85 ºC, 3 h).

Elemental mapping by high-resolution SEM energy-dispersive X-ray spectroscopy (HR-SEM EDX) shows a uniform distribution of Mg, P, Na and O throughout the material (Figure 3.36). The ratio of elements (Mg:Na:P) given by EDX analysis indicates a higher amount of sodium in the material than the ICP-MS results, namely 1.4:1.0:1.2 (Figure 3.37). This may be due to inhomogeneity in the material: the SEM images show that EDX analysis took place on a platelet-like fragment, which is believed to be a particle that has undergone more decomposition than one which retains the coffin-like structure.

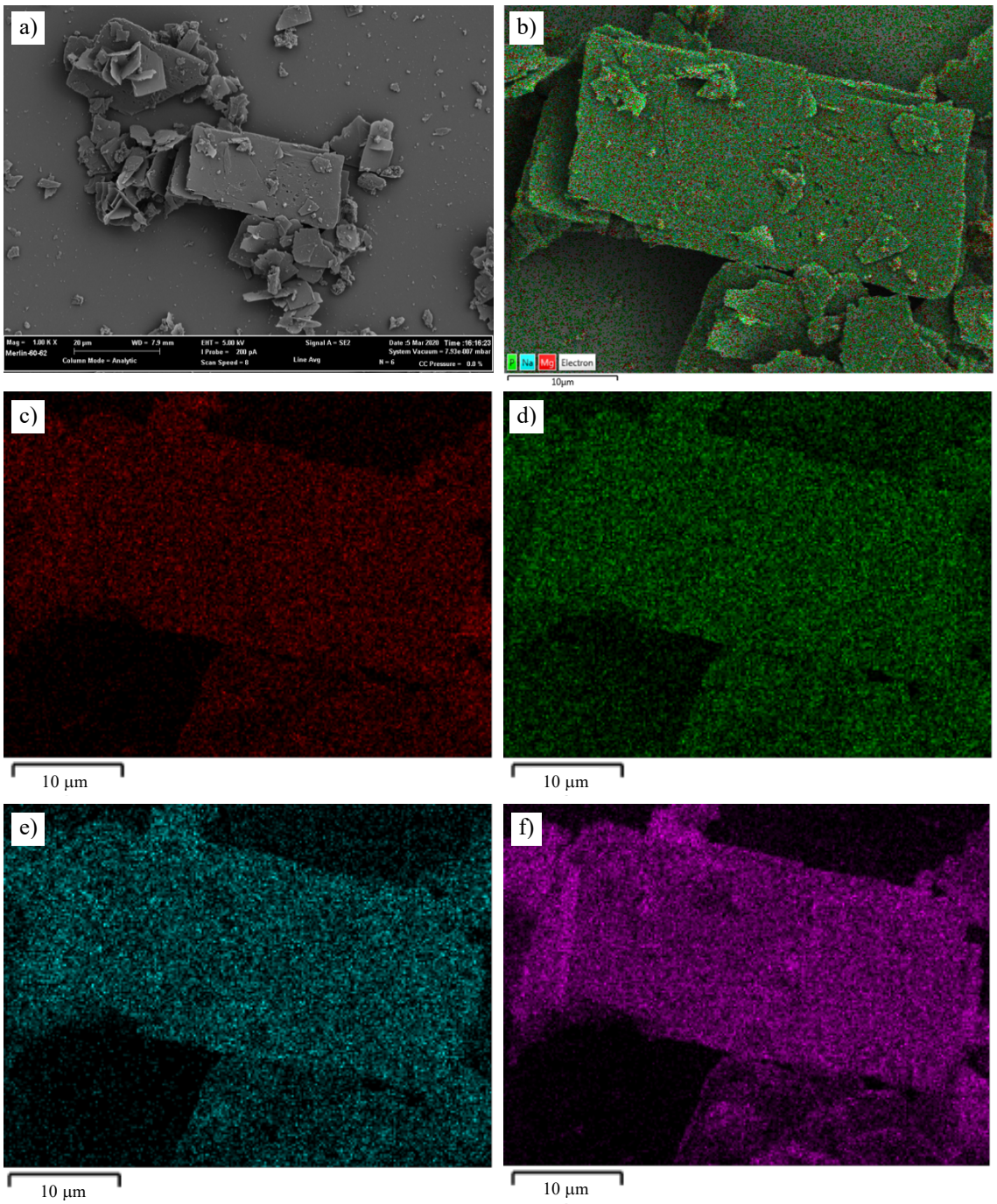


Figure 3.36 a) HR-SEM image and b) HR-SEM EDX layered image of struvite decomposed in NaOH (85 ºC, 1 h). Mapping of c) Mg, d) P, e) Na, and f) O. Pt-coated samples.

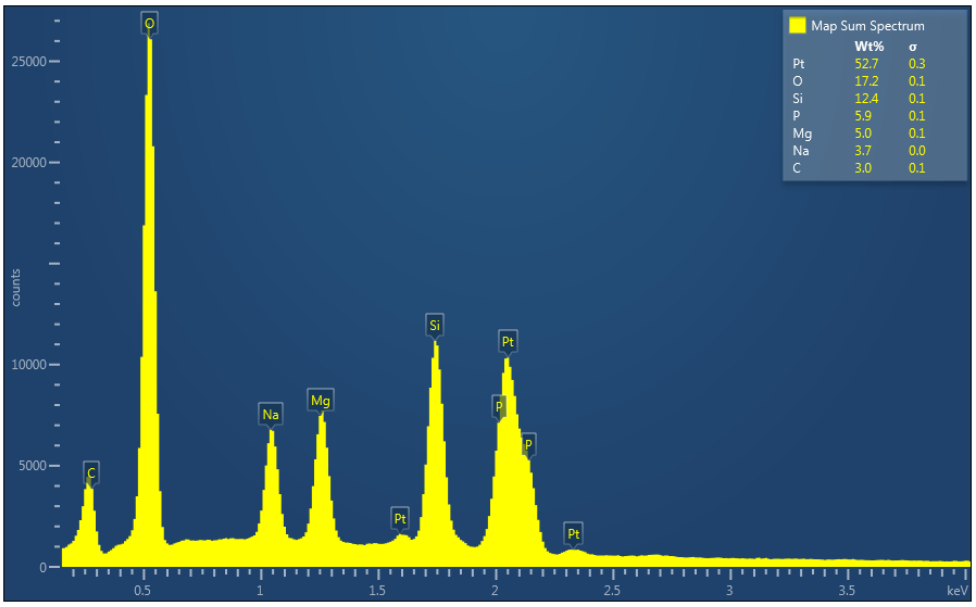


Figure 3.37 HR-SEM EDX elemental analysis of struvite decomposed in NaOH (85 ºC, 1 h). Si and Pt present as the sample holder and coating agent, respectively.

This investigation has shown that the M2 synthesis method proceeds via a reactive intermediate that is unique to the synthesis route. The struvite-like structure of the $MgMPO_4.6H_2O$ ($M = Na^+$ and NH_4^+) provides the architecture for high surface area, high density SLDHs. Nucleation and growth of the SLDH directly on the surface of the intermediate points to a dissolution-crystallisation mechanism.

3.4 Synthesis of SLDHs containing zinc

3.4.1 Introduction

Polypropylene (PP) is a widely used polymer due to its availability, processability, and relatively low cost. However, PP is highly combustible and generates smoke and harmful gases during combustion.[43, 44] In order to improve the gas permeability, flame-retardancy and thermal stability, many organic and inorganic flame-retardant additives have been developed. Among those considered to be environmentally friendly are inorganic materials such as magnesium hydroxide, aluminium trihydroxide (ATH), and LDHs.[43]

Unlike some flame retardants that release corrosive and toxic gases, LDHs lose water and intercalated anions during combustion. It is believed that LDHs have a dual mode of action to inhibit the spread of flames in polymers: 1) endothermic release of interlayer and structural water, which provides significant heat absorption and dilution of combustible gases; and 2) dehydration of the hydroxide layers to form mixed metal oxides (also called layered double oxides, LDO) that hinder the transport of oxygen to the bulk polymer under the burning surface.[45] The LDH metal cation combinations commonly employed include MgAl,[46] ZnAl,[45] CoAl,[47] and ZnMgAl.[48] Furthermore, it has been shown that ZnAl-LDH forms a more compact char when burned compared to MgAl-LDH.[44]

The incorporation of LDH into polymers is not straight forward because LDHs are typically hydrophilic and polymers hydrophobic, so modifications must be made to either component to improve compatibility.[43] To facilitate their interaction with polymers, LDHs may be intercalated with organic anions to alter their surface properties and expand their basal spacing. Alternatively, the polymer can be functionalised with polar substituents. Reductions in the peak heat release rate (PHRR) of around 50%, relative to

the pristine polymer, have been reported for polymers blended with organically modified LDHs.[49]

However, undesirable changes to the polymer properties can occur as a result of such modifications (*e.g.* loss of mechanical stability). To overcome this, it is possible to augment LDHs with other flame retardants and produce synergistic additives.[44] Zinc borate and ammonium polyphosphate (APP) are two halogen-free additives that can work synergistically with LDHs.[50] Zinc borate promotes char formation, suppresses smoke, and acts as a protective layer on the surface of polymers.[51, 52] APP functions through intumescence. When exposed to fire, APP will decompose into ammonia and polyphosphoric acid. The acid will react with a carbonising agent within the polymer to produce a polyphosphate ester, which chars to form a carbonaceous foam that acts as a barrier against the heat.[53] The polyphosphoric acid can also form a viscous molten surface layer or surface glass that can prevent heat and oxygen from entering the substrate.[54]

3.4.2 Preparation of Zn_2MgAl-SLDH

Following the success of binary MgAl-LDH formation from struvite, investigations were carried out to see if this approach could be adopted for the synthesis of ternary LDHs. A zinc magnesium aluminium combination (2:1:1) was chosen for its potential in flame retardancy applications.

Initially, Zn_2MgAl-SLDH was prepared following an unmodified M2 procedure with the addition of a zinc salt. However, SLDH synthesis was unsuccessful and the product obtained was predominantly hexagonal wurtzite-type zinc oxide, ZnO (Figure 3.38, JCPDS card no. 36-1451). The lattice parameters are $a = b = 2 \times 3^{-0.5}\ d_{100} = 3.249$ Å, $c = 2d_{002} = 5.207$ Å. The average crystallite size is 19 nm (using the 101 reflection and Scherrer equation, Appendix A, Table A.7). The sharp reflections indicate high

crystallinity. The experimental *c*/*a* ratio, 1.60, is smaller than 1.633 which corresponds to a closed-packed hexagonal structure, indicating some strain in the crystals.[55] Additionally, the baseline is not flat: broad features around 2θ = 11 and 23º could correspond to the 00*l* Bragg reflections of an LDH phase.

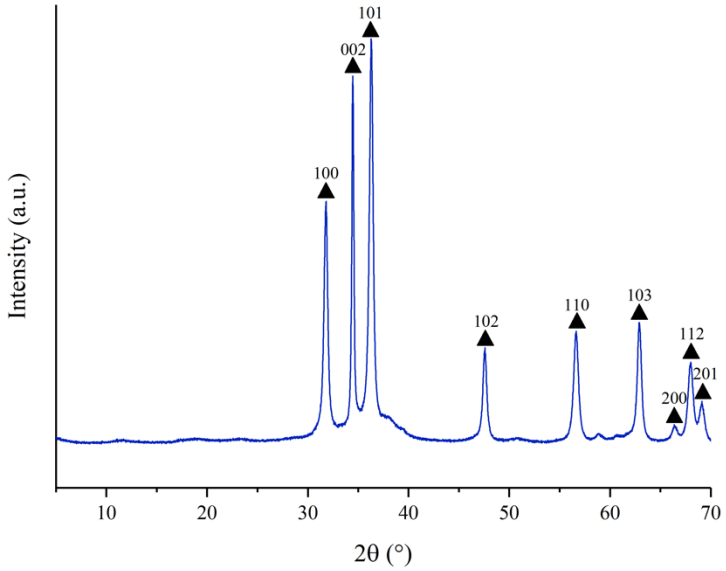


Figure 3.38 Powder XRD diffractogram of zinc product of M2 synthesis (85 °C, pH 11.5, 2 h ageing). ▲ZnO.

The preferential formation of ZnO is due to the high pH conditions employed in the M2 synthesis procedure.[56] Thus, the reaction was repeated at a lower pH (pH 9) to prevent ZnO precipitation and also promote the dissolution of any ZnO that may form.[57] The XRD diffractogram of the product contains broad features that can be indexed to an amorphous LDH (Figure 3.39). The LDH reflections are weak however, and other amorphous species are present. The most intense features at *ca.* 35º suggests that amorphous ZnO is a component.

The lattice parameters for the SLDH are approximately $a = 2d_{110} = 30.6$ Å, $c = 3d_{003} = 21.3$ Å. This SLDH has the same M^{2+}/M^{3+} ratio as the MgAl-SLDHs prepared in Section 3.2, but the substitution of some Mg^{2+} for Zn^{2+} (a larger dication)[58] is responsible for

increasing the average intralayer M–O distances. There is also a shift in the 00*l* reflections to higher 2θ, which suggests that there is a different interlayer species (*i.e.* not CO_3^{2-}), which corroborates with FTIR (Figure 3.41). The low value of the *c* lattice parameter suggests the intercalated anion may be OH^-, which would correspond to a meixnerite-type LDH.

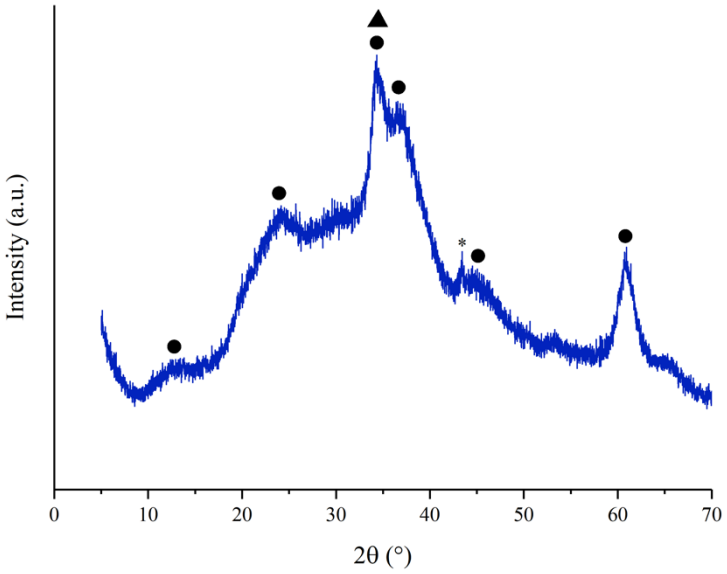


Figure 3.39 Powder XRD diffractogram of Zn_2MgAl-CO_3-SLDH synthesised at pH 9 using M2. *Reflection due to the sample holder. ●LDH. ▲ZnO.

To improve the crystallinity of the product, the pH 9 M2 synthesis was repeated with hydrothermal ageing of the slurry. The diffraction features in the XRD diffractogram were sharpened to a small extent but the product remains predominantly amorphous (Figure 3.40). The poor crystallinity of the Zn_2MgAl-SLDH may be due to the low magnesium content. Struvite was used as a precursor and it is known to act as a template for SLDH growth (Section 3.3). When the Zn^{2+}/Al^{3+} solution is added dropwise to the alkaline struvite mixture, it is possible that there is an insufficient amount of Mg^{2+} available to create a perfect 2:1:1 Zn/Mg/Al ratio, leading to an inhomogeneous product that contains LDHs of various metal ratios and side products such as ZnO. Moreover, this will result in different levels of anion incorporation because LDH phases with lower M^{2+}

content will require more interlayer anions to compensate for the higher cationic charge of the hydroxide layers.[59]

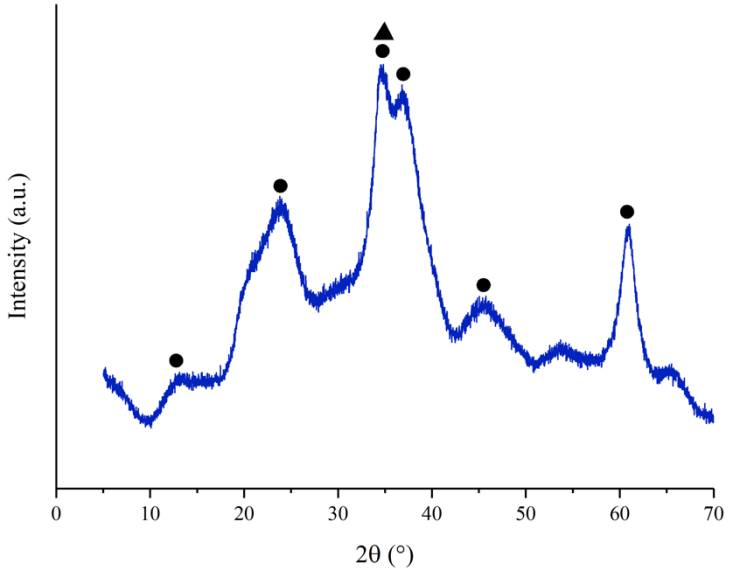


Figure 3.40 Powder XRD diffractogram of Zn_2MgAl-CO_3-SLDH synthesised at pH 9 and aged hydrothermally. ●LDH. ▲ZnO.

Table 3.5 ICP-MS elemental analysis of Zn-SLDHs (M2, pH 9). Full ICP-MS results in Appendix A, Table A.8.

Av. wt.%	Regular ageing	Hydrothermal ageing
Na	0.45	0.03
Mg	3.68	5.45
Al	4.20	5.85
P	4.61	6.36
Zn	22.24	30.71
Av. Zn/Mg	2.25	2.10
Av. Mg/Al	0.94	1.00

The FTIR spectra indicate that the predominant interlayer species in both samples is phosphate since the absorptions at *ca.* 1030 cm^{-1} are strong, whilst the *ca.* 1360 cm^{-1} absorption band which is characteristic of the v_3 antisymmetric stretching vibration of CO_3^{2-} is very weak (Figure 3.41). It is not possible to deduce whether the broad

absorption band in the OH region (3600–3000 cm^{-1}) has contributions from interlayer OH^-.

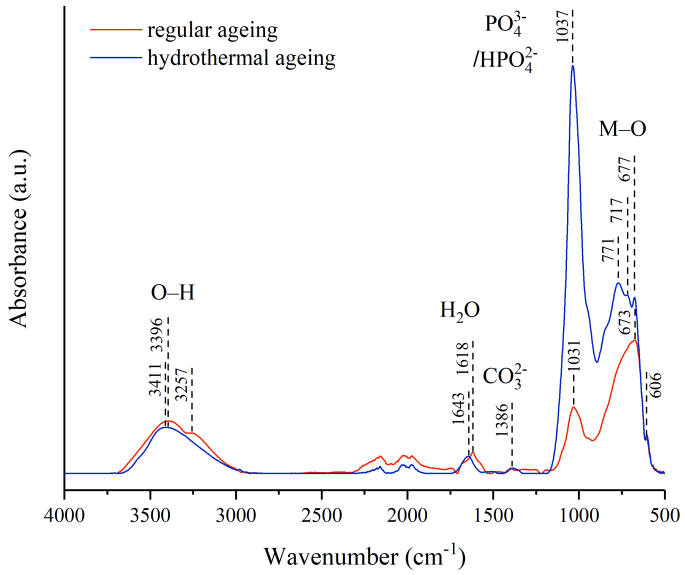


Figure 3.41 FTIR spectra of Zn_2MgAl-SLDHs prepared using M2 (pH 9).

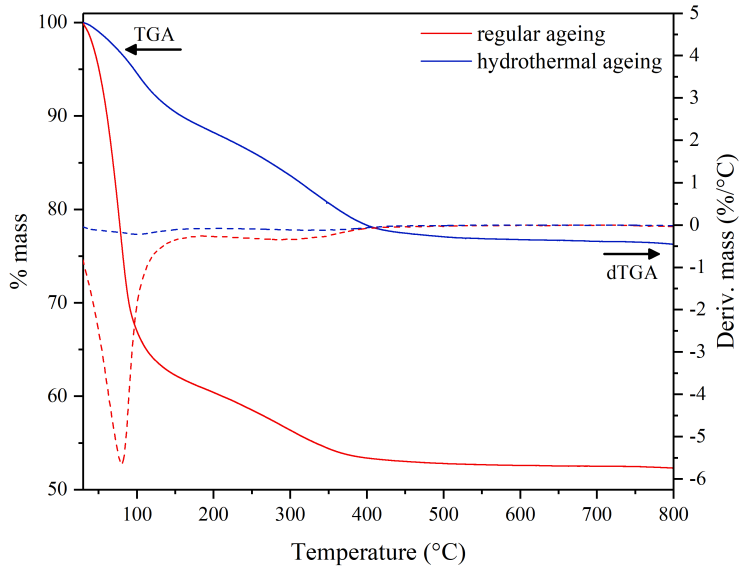


Figure 3.42 TGA and dTGA plots of Zn_2MgAl-SLDHs prepared by M2 (pH 9).

Both samples have TGA profiles characteristic of LDHs, although the sample aged hydrothermally loses considerably less mass upon thermal treatment (Figure 3.42). The mass of the sample aged regularly falls steeply when the temperature is raised above room temperature: the first dTGA minimum occurs at 80.1 ºC and the mass falls by

~35 wt.%. This mass loss may be attributed to the expulsion of residual ammonium in the structure, interparticle pore water and adsorbed surface water. The sample aged regularly also contains a significant amount of sodium (0.45 wt.%, Table 3.5) which will have water molecules of solvation associated with it.

In comparison, the sample aged hydrothermally has a dTGA minimum at 99.6 ºC and loses ~10 wt.%. Hydrothermal aging influences crystallinity and particle texture significantly, which in turn influences the loss of interlayer species and also the composition.[60]

The morphology of the Zn_2MgAl-SLDHs is different to that of Mg_3Al-SLDHs (Section 3.2). In the SEM images, there are some fragmented coffin-shaped particles and lots of smaller clusters that have rough surfaces (Figure 3.43). These structures are characteristic of LDHs. The lower prevalence of prismatic crystals is due to the low concentration of struvite used, since the ratio of Mg:Zn is 1:2.

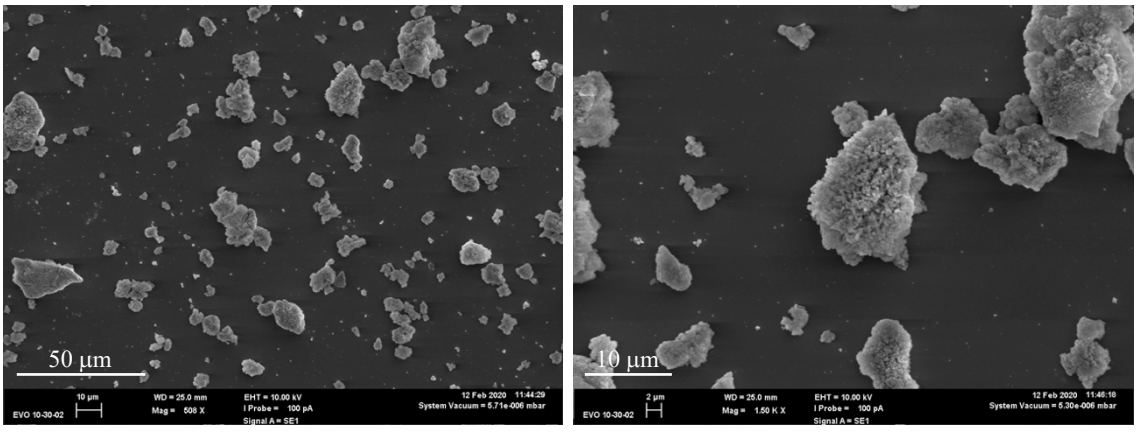


Figure 3.43 SEM images of Zn_2MgAl-SLDH prepared by M2 (pH 9) and aged hydrothermally.

This investigation has shown that ternary SLDHs may be prepared if the conditions are appropriately adjusted to suit the precipitating cations. The crystallinity of the Zn_2MgAl-SLDHs was low as the struvite content was low and struvite significantly affects the growth of the LDH because it has a unique structure and templating effect.

3.5 Aqueous miscible organic solvent treatment (AMOST) of SLDHs

The AMOST method an effective post-synthesis modification of c-LDHs for producing high surface area LDHs (Section 1.4.2).[61] In Section 3.2, struvite has been shown to be a precursor for high surface area SLDHs without the need for solvent treatment. These SLDHs also have high tap densities and unique morphologies as a result of the synthesis method. It was therefore of interest to investigate if the AMOST method could be applied to SLDHs to enhance the surface area further.

Mg_3Al-CO_3-AMO-SLDHs (AMO-SLDHs) were prepared using the M2-method (85 ºC, 2 h ageing) and dispersed in ethanol (EtOH) prior to drying using the conditions previously developed by Chen *et al.*.[61] As expected, the positions of the Bragg reflections in the XRD diffractogram of the AMO-SLDH are unchanged relative to the SLDH – since AMOST is primarily a surface modification and does not alter the chemical composition of the hydroxide layers nor the content of the interlayer galleries (Figure 3.44a and Table 3.6). However, the AMO-SLDH gives rise to broader and less intense Bragg reflections. This is most significant for the basal (00*l*) Bragg reflections and the ratio of peak intensities of the basal and non-basal reflections, I_{003}/I_{110}, decreases, which indicates a reduction in the number of hydroxide layers stacked together along the *c*-axis. The mean crystallite domain length (CDL) in the *c*-direction of the AMO-SLDH is also smaller than that of the SLDH (60.7 and 77.9 Å, respectively). These observations are consistent with the AMOST mechanism, whereby exfoliation of some of the hydroxide layers occurs under the influence of the AMO solvent.

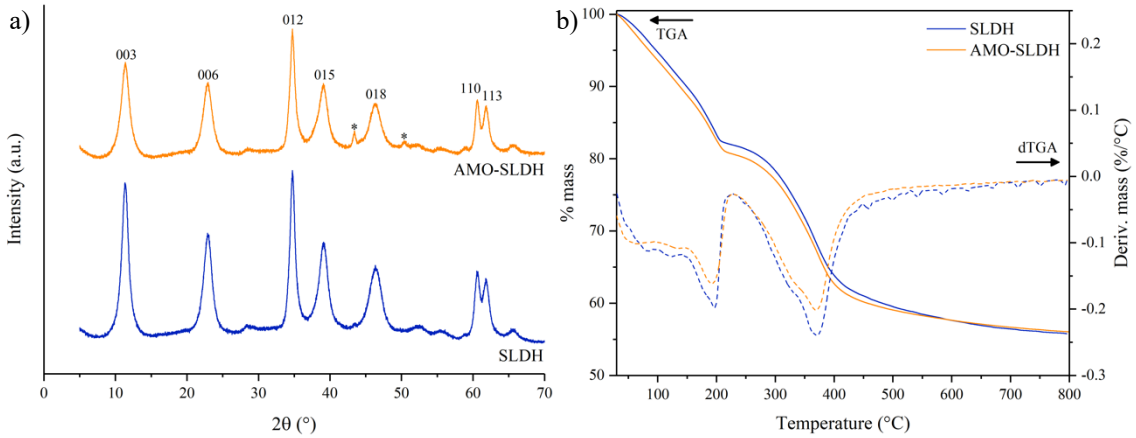


Figure 3.44 a) Powder XRD diffractograms and b) TGA and dTGA curves of M2-85-SLDHs prepared with and without AMOST. Mg/Al = 3. AMO solvent = EtOH. *Reflections due to the sample holder.

Table 3.6 Lattice parameters and mean crystallite domain lengths (CDLs) of M2-85-SLDHs prepared with and without AMOST. Mg/Al = 3. AMO solvent = EtOH.

	d-spacing (Å)		Lattice parameter (Å)		CDL (Å)	
	d_{003}	d_{110}	$c^{\dagger}$	$a^{\ddagger}$	*c*-axis	*ab*-plane
SLDH	7.78	1.53	23.37	3.06	77.9	203.3
AMO-SLDH	7.77	1.53	23.31	3.06	60.7	208.3

†Lattice parameter $c = 3d_{003}$. ‡Lattice parameter $a = 2d_{110}$.
CDL = 0.89λ/βcosθ, λ = 1.541847 Å, β = FWHM in radians.

Table 3.7 Bragg reflection intensities of M2-85-SLDHs prepared with and without AMOST. Mg/Al = 3. AMO solvent = EtOH.

	003[a] (º)	I_{003}[b] (a.u.)	110[a] (º)	I_{110}[b] (a.u.)	I_{003}/I_{110}
SLDH	11.35	8469	60.53	4290	1.97
AMO-SLDH	11.37	5526	60.57	3705	1.49

[a]Position of Bragg reflection (2θ). [b]Intensity of Bragg reflection.

The residual mass at 800 ºC of both SLDHs is the same (~57 wt.%) which suggests that both materials have a similar metal content (Figure 3.44b). This is corroborated by the ICP-MS data (Table 3.8 and Appendix A Table A.10). The mass loss undergone by AMO-SLDH below *ca.* 200 ºC is larger than for the untreated SLDH, which is due to the AMO-solvent. EtOH has a lower boiling point than water (b.p. 78 ºC) and it is only

weakly adsorbed onto the SLDH surface. Thus, the endothermic step between 40–90 ºC can be ascribed to the loss of EtOH.

Table 3.8 Summary of the ICP-MS elemental analyses of M2-85-SLDHs with and without AMOST. AMO solvent = EtOH.

Av. wt.%	SLDH	AMO-SLDH
Mg	21.77	21.67
Al	8.19	8.17
P	1.40	1.47
Av. Mg/Al	2.84	2.83

For the AMO-SLDH, hydrogen bonding between the AMO solvent and interlayer/surface water molecules disrupts, and weakens, the interactions between the water molecules and the hydroxide layers.[62] Consequently, the dTGA minimum associated with dehydration (*ca.* 200 ºC) is ~5 ºC lower for the AMO-SLDH.

However, in comparison to previously reported AMO-LDHs,[61, 63] the AMO-SLDH appears to contain less AMO-solvent and the minima in the dTGA graph are less perturbed relative to the untreated material. For example, Yang *et al.*[63] reported that the mass loss of interlayer water occurred ~20 ºC lower for an AMO-LDH (EtOH) compared with an equivalent c-LDH, and decarboxylation and dehydroxylation occurred ~45 ºC lower. The decrease in onset temperatures was attributed to the thinner nanosheets and higher surface area of the AMO-LDHs. For the SLDH and AMO-SLDH, the differences are an order of magnitude smaller (*e.g.* ~5 ºC). This suggests that AMOST is less effective at delaminating SLDHs. This is reasonable because the SLDH grows from the struvite lattice and many of the large coffin-shaped crystals remain intact, so the AMO solvent cannot solvate the layers as efficiently. The SEM images (Figure 3.45) show that

the surfaces of the AMO-SLDH are more porous and some swelling has occurred, but the primary particle size and morphology is retained.

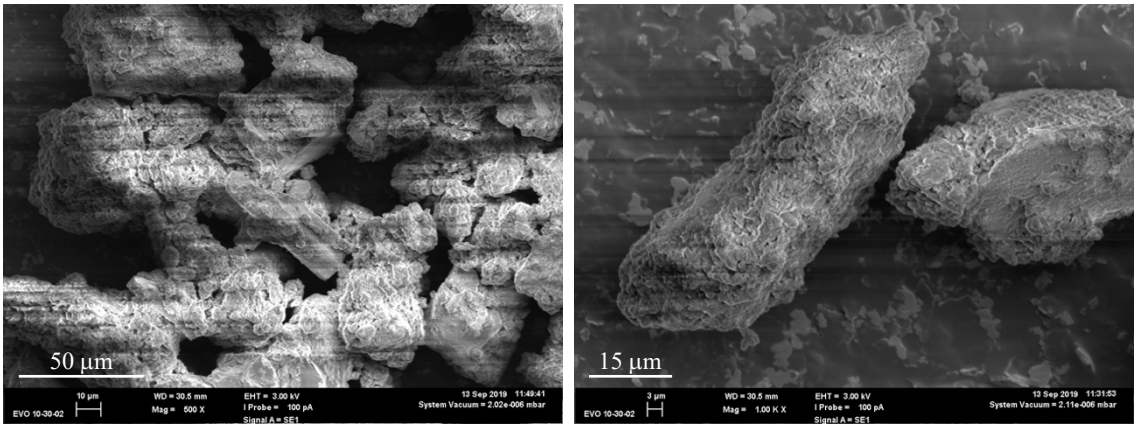


Figure 3.45 SEM images of AMO-SLDH. Mg/Al = 3. AMO solvent =EtOH.

Table 3.9 N_2 BET specific surface area and BJH pore volume of M2-85-SLDHs with and without AMOST. Mg/Al = 3. AMO solvent = EtOH.

	N_2 BET specific surface area (m^2 g^{-1})	Pore volume[a] (cm^3 g^{-1})
SLDH	184	0.67
AMO-SLDH	233	1.39

[a]BJH method.

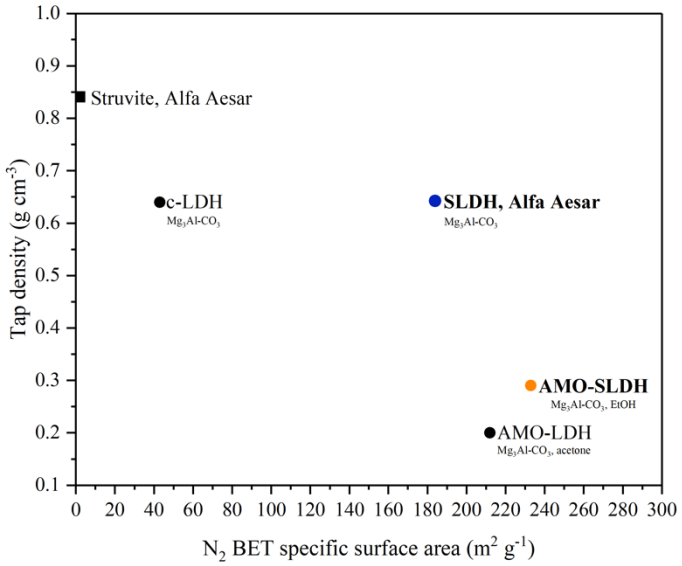


Figure 3.46 Tap density plotted as a function of N_2 BET specific surface area for struvite, SLDHs and reference LDHs. Mg/Al = 3. AMO solvent (where applicable) = EtOH.

Similarly, whilst the N_2 BET specific surface area of the AMO-SLDH is very high (233 m^2 g^{-1}, Table 3.9 and Figure 3.46), the percentage increase is smaller than between the equivalent c-LDHs and AMO-LDHs. For example, Yang *et al.*[63] recorded the N_2 BET specific surface area of an AMO-LDH (EtOH) to be 240 m^2 g^{-1}, which is more than twice that of a c-LDH prepared under the same conditions (110 m^2 g^{-1}). For the SLDHs, AMO treatment increases the surface area by *ca.* 50 m^2 g^{-1}, which is only a 27% increase from the surface area of the SLDH.

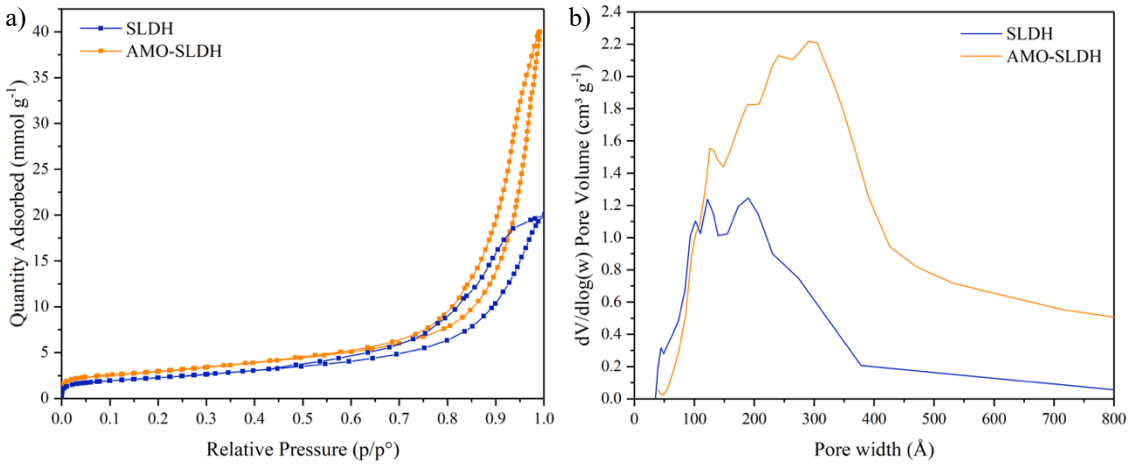


Figure 3.47 a) N_2 adsorption and desorption isotherms and b) BJH pore size distributions of M2-85-SLDHs with and without AMOST. Mg/Al = 3. AMO solvent = EtOH.

The pore volume of the AMO-SLDH is double the pore volume of the untreated SLDH (Table 3.9). The BJH pore size distributions show that the increases in surface area and pore volume are due to the increase in the number of larger pores and reduction in the population of pores below 100 Å (Figure 3.47b). The pore sizes remain in the mesoporous range.

The increase in surface area is accompanied by a significant decrease in density: the AMO-SLDH is three-times less dense than the untreated SLDH (Figure 3.46). Solvation of the layers results in swelling of the structures and the smaller AMO-SLDH particles have a loose flower-like morphology. The tap density of AMO-SLDHs is *ca.* 0.9 g cm^{-3}

higher than the tap density of the SLDH. This supports the theory that the AMO solvent is unable to penetrate the larger SLDH crystals (which are in the minority).

The investigation has shown that AMOST is less effective at increasing the surface area of SLDHs because of their unique morphology. SLDHs are high surface area materials without surface treatment and to enhance this further, without compromising its desirable high density, different techniques will be required.

3.6 Study of struvite from wastewater treatment plants (WWTPs)

The wider aim of this work is to find industrially relevant alternate sources of magnesium to create new atom-efficient, cost-effective syntheses of LDHs. As a result, over thirty struvite suppliers (*e.g.* WWTPs) were contacted and six commercial struvite samples were obtained (Table 3.10). In its pure form, struvite is a white, crystalline material containing equimolar quantities of magnesium, ammonium, and phosphate, but its composition and crystal morphology is strongly dependent on growth parameters such as ion concentration, pH, temperature, stirring speed, and residence time.[19] The technologies used to precipitate these struvites vary and as a result, the composition and morphology of the samples differ from that observed of the pure struvite purchased from Alfa Aesar.

In a few cases, purification steps were carried out to clean the materials before putting them through analyses (Figures 3.48 and 3.49). The sample was received from Aa en Maas was a wet crystalline material, so this was dried at 30 ºC in a vacuum oven overnight before analysis and use in future syntheses. All other samples were used as received.

Table 3.10 Struvite samples obtained from WWTPs.

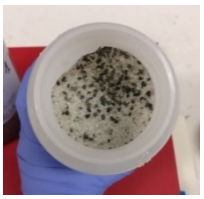
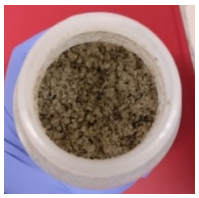
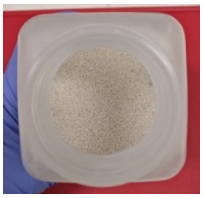
Company	Source location	Struvite-recovery technology	Image
Niersverband	MG-Neuwerk WWTP, Germany	AirPrex	
ASG	Salzgitter WWTP, Germany	AirPrex	
NuReSys	Clarebout Potatoes NV, Belgium	NuReSys	
Clean Water Services	Tigard WWTP, USA	Ostara PEARL	
Aa en Maas	Land von Cuijk WWTP, Netherlands	NuReSys	
Aarhus Vand	Aaby WWTP, Denmark	PhosphorCare	



Figure 3.48 Purification steps performed on the struvite from Niersverband: a) sieving, b) physical removal of large debris using tweezers, and c) decanting off debris in D.I. water.

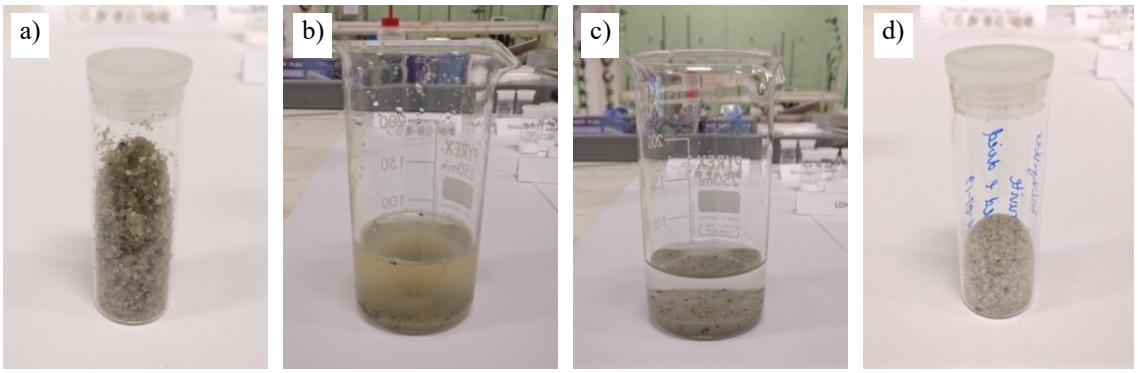


Figure 3.49 Purification steps performed on the struvite from ASG: a) vial of unprocessed wet crystals from the WWTP, b) D.I. water was added repeatedly to remove soluble impurities, and c) when the effluent ran colourless, the crystals were filtered to dryness and d) dried in a 30 ºC vacuum oven overnight to give "cleaned" crystals.

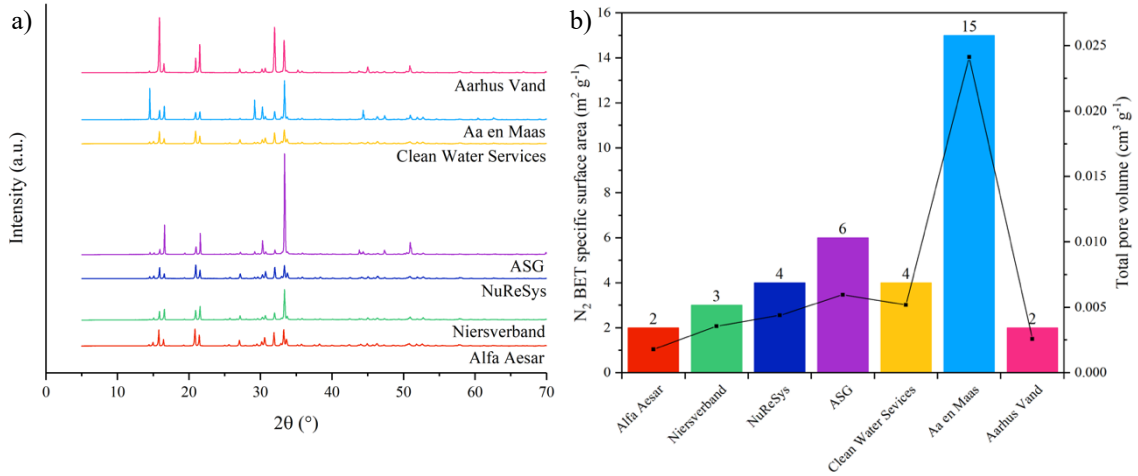


Figure 3.50 a) Powder XRD diffractograms and b) N_2 BET specific surface areas (bars) and pore volumes (lines) of WWTP struvites.

Figure 3.50a shows the powder XRD diffractograms of the WWTP struvites. If the XRD diffractogram of the pure struvite from Alfa Aesar is taken to be standard, it can be seen that the sample from NuReSys has the most similar peak profile. For the others, peaks are observed at the same positions but with variation in the peak intensities. This is due to the precipitation conditions differing between the sources and giving rise to different crystallinities. No significant additional peaks due to impurities are observed in these diffractograms.

To measure the N_2 BET specific surface areas the degassing conditions had to be altered to accommodate for the decomposition of struvite above *ca.* 55 ºC. Overnight degassing of the samples was therefore performed at 30 ºC. This is likely to mean that the surface of the materials will still be occupied by some adsorbed water molecules. Nevertheless, a comparison can be made between the samples and generally very low surface areas and pore volumes are observed (Figure 3.50b). The isotherms (Figure 3.51a) are type IV, characteristic of mesoporous materials, and the hysteresis curves are type H4, characteristic of narrow slit pores. The pore sizes are generally below 100 Å and have narrow size distribution (Figure 3.51b). The exception is the Aa en Maas struvite which shows a wide pore size distribution between *ca.* 100–400 Å.

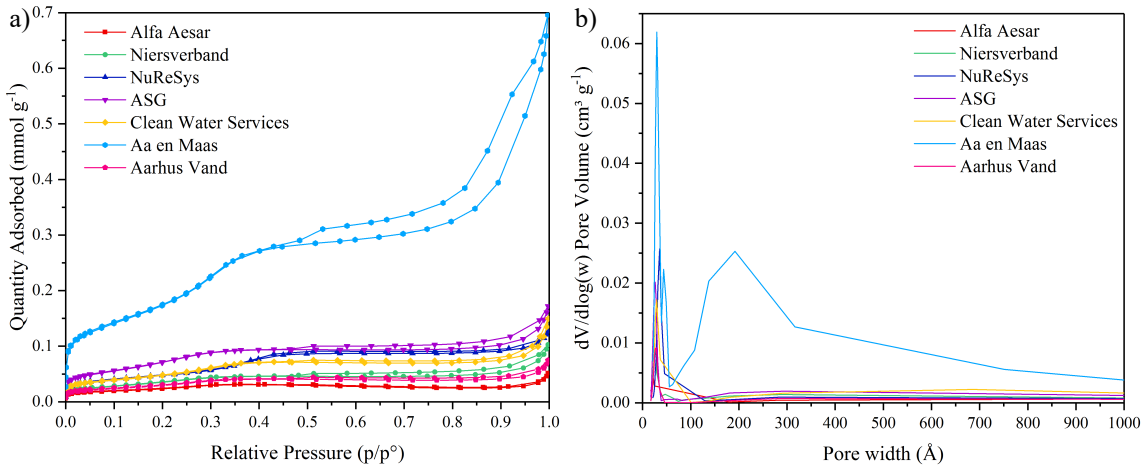


Figure 3.51 a) N_2 adsorption and desorption isotherms and b) BJH pore size distributions of WWTP struvites.

No significant differences are observed between the FTIR spectra of the WWTP struvites (Figure 3.52a). The absorption bands observed are those expected of struvite (Section 3.2). For ASG and Aa en Maas additional absorption bands are present between 1150–1250 cm^{-1} and these are due to the asymmetric stretching vibrations of PO_4 units.

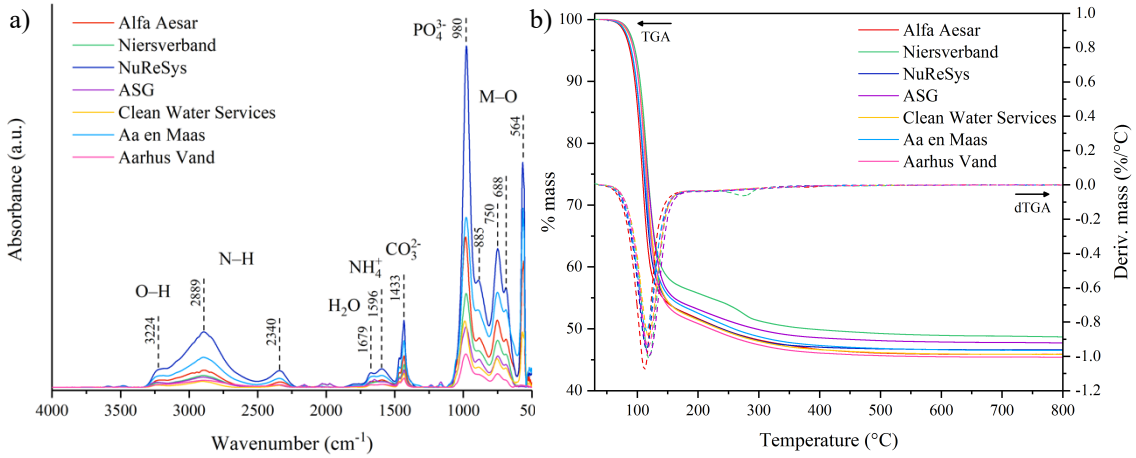


Figure 3.52 a) FTIR spectra and b) thermal analyses of WWTP struvites.

TGA data (Figure 3.52b) was also collected and the same decomposition profiles for the WWTP struvites are observed except for the Niersverband sample. This sample (green lines) shows an additional mass loss event at 270 ºC. The WWTP samples all have a higher residual mass at 800 ºC than the synthetic struvite from Alfa Aesar. This is due to impurities, including the binder used to produce the granular samples as well as debris.

The primary peak in the dTGA plots of WWTP struvites shifts to higher temperatures (by 3–7 ºC), and higher onset temperatures, relative to Alfa Aesar (112 ºC). This shift has been observed by Ma *et al.*[64] during an investigation into the influence of initial pH on struvite crystallisation. The authors reported decreasing decomposition temperatures with increasing precipitation pH. This was attributed to changes in the physical properties of the crystals, such as their size and shape, when the initial pH was raised. Struvite precipitated at pH 8 formed well-defined orthorhombic crystals; at pH 9 the crystals were elongated and bar-shaped; and pH 11 produced flat, tablet-shaped crystals. The thinner crystals formed at higher pH have a higher surface area as a result of their morphology, which in turn made them more susceptible to thermal decomposition. Thus, one of the explanations for the higher decomposition temperatures of the WWTP struvites is that they were formed at lower pH than the synthetic struvite from Alfa Aesar.

The dTGA minimum occurs at the lowest temperature for the struvite from Aa en Maas (115.0 ºC). This material is more susceptible to thermal decomposition as it has the highest surface area (Figure 3.50) and lowest tap density (Figure 3.53). The NuReSys struvite also has one of the lowest decomposition temperatures (115.1 ºC). This struvite has been processed and formulated into grains for use in agriculture, so may also contain less thermally stable additives in addition to being precipitated at a higher pH than the other WWTP struvites.

The samples precipitated using Airprex technology, Niersverband and ASG, have the highest decomposition temperatures (119.4 and 119.6 ºC, respectively). This technology uses an aerator to strip CO_2 from anaerobically digested waste, which increases the pH of the mixture to pH 7–8.[65] The decomposition temperature is also consistent with the values reported by Ma *et al.*[64] for struvite precipitated at pH 8.

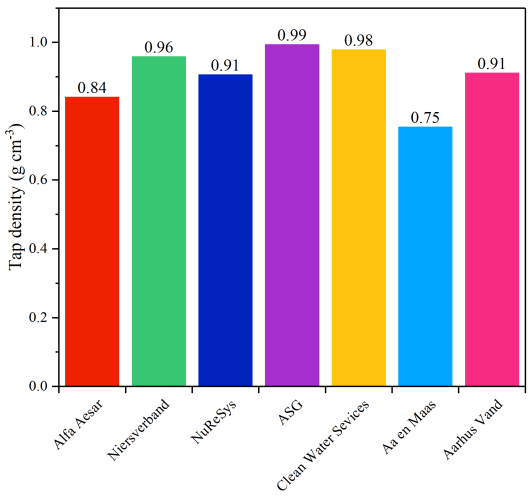


Figure 3.53 Tap densities of WWTP struvites.

Elemental analyses were carried out to confirm the Mg and P content, as well as to identify and quantify impurities (Table 3.11). From the chemical formula of struvite, $MgNH_4PO_4.6H_2O$, the composition should be 9.90 wt.% Mg and 12.60 wt.% P. The synthetic struvite purchased from Alfa Aesar was expected to be the purest and have a composition closest to the ideal chemical formula. The ICP-MS data shows that the phosphorus content is as expected but the magnesium content is approximately 0.15 wt.% lower. The table shows that other alkali/alkali earth metals, namely potassium and calcium, are present. Both these metals readily fix phosphorus and are known to be common impurities in this mineral.[66] The Alfa Aesar struvite also contains trace amounts of nickel, which is not observed in the other struvites. This is likely to be due to leaching of the reaction vessel during production.

Table 3.11 Summary of the ICP-MS elemental analyses of WWTP struvites

Av. wt.%	Struvite						
	Alfa Aesar	Niersverband	NuReSys	ASG	Clean Water Services	Aa en Maas	Aarhus Vand
Mg	9.75	9.44	8.22	8.36	9.35	9.76	9.40
Al	0.002	0.003	0.003	0.020	0.008	0.003	0.002
P	12.60	12.41	11.97	12.21	12.68	12.84	12.60
K	0.001	1.207	0.030	0.032	0.038	0.087	0.058
Ca	0.093	0.024	0.152	0.027	0.523	0.027	0.102
Cr	B.D.L.	B.D.L.	B.D.L.	B.D.L.	B.D.L.	B.D.L.	B.D.L.
Ni	0.007	B.D.L.	B.D.L.	B.D.L.	B.D.L.	B.D.L.	B.D.L.
Cu	B.D.L.	B.D.L.	B.D.L.	B.D.L.	B.D.L.	B.D.L.	B.D.L.
Zn	B.D.L.	0.0005	0.0005	0.0006	B.D.L.	0.0007	0.0004
As	B.D.L.	B.D.L.	B.D.L.	B.D.L.	B.D.L.	B.D.L.	B.D.L.
Cd	B.D.L.	B.D.L.	B.D.L.	B.D.L.	B.D.L.	B.D.L.	B.D.L.
Hg	B.D.L.	B.D.L.	B.D.L.	B.D.L.	B.D.L.	B.D.L.	B.D.L.
Pb	B.D.L.	B.D.L.	B.D.L.	B.D.L.	B.D.L.	B.D.L.	B.D.L.

B.D.L. = below detection limit

Wastewater is a heterogeneous mixture of ions and nutrients, with variable composition depending on the source of the water and the treatments it passes through. In Table 3.11, the elements in addition to Mg and P are common impurities in wastewater streams, as well as those that are strictly regulated (*e.g.* Hg and Pb). Some impurities, such as Al and Cu, are known to form competing phosphates and so can hinder the crystallisation of struvite.[66] These analyses have found the most common impurities to be Al, K, Ca, and Zn. It is important to identify any impurities in the compounds as a potential application for SLDHs is catalysis, an application that can be very sensitive to impurities.

The struvites were examined by SEM and a range of morphologies was observed (Figures 3.54–3.57). The crystal habit is variable according to the precipitation conditions, so the different morphologies are the result of the different processes used to precipitate the struvite from wastewater.

Rectangular prismatic crystals are observed in the samples from Niersverband and ASG (Figure 3.54). These WWTPs both use AirPrex technology to achieve struvite precipitation so this demonstrates consistency in this method. In both, the crystals vary considerably in size. Many are macroscopic (up to 2 mm long) but smaller fragments were also observed. These crystals are significantly larger than those in the Alfa Aesar struvite (*ca.* 50–200 μm), which may contribute to their higher thermal decomposition temperatures (Figure 3.52). It can be seen that the crystal surfaces are not perfectly smooth but mottled and cracked (Figure 3.54b and d). This suggests that larger struvite crystals are formed by the aggregation of smaller units.

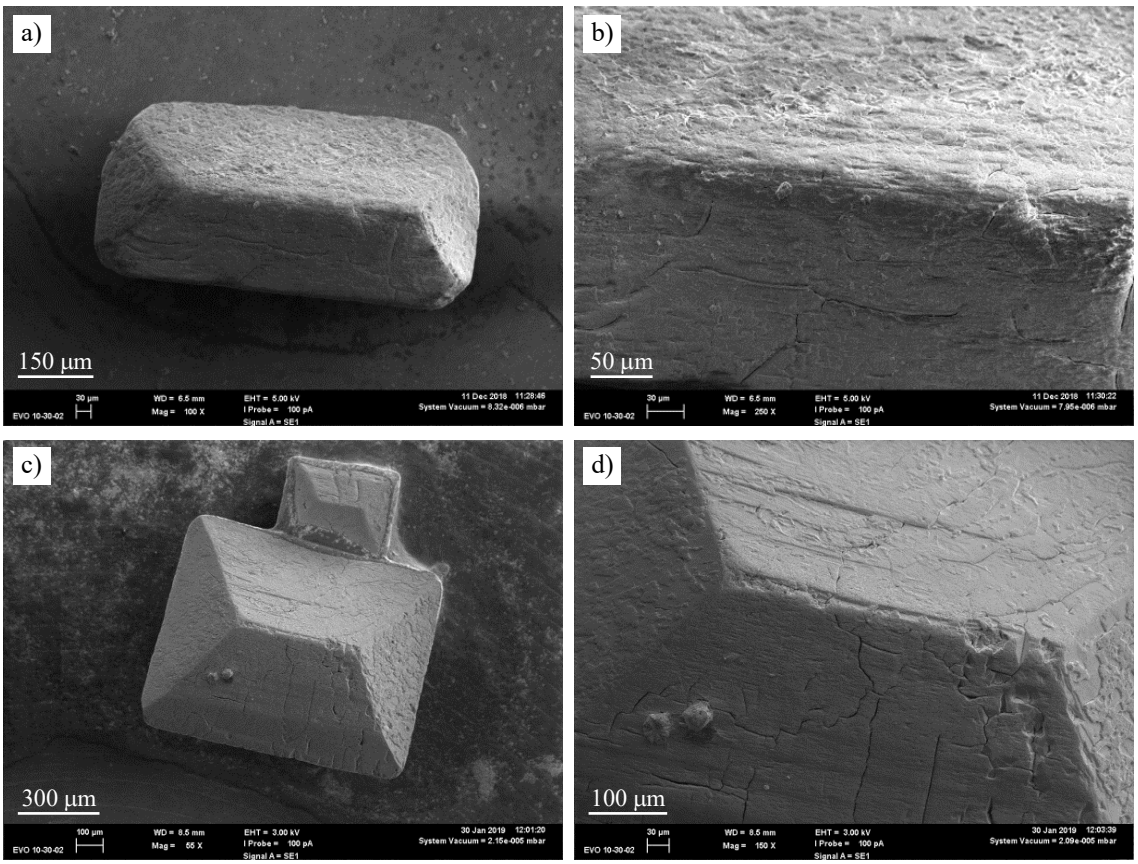


Figure 3.54 SEM images of struvite from Niersverband (a and b) and ASG (c and d). Both WWTPs use the AirPrex technology to precipitate struvite. Uncoated samples.

In comparison, the samples from NuReSys and Aa en Maas have very different morphologies despite being produced by the same technology from NuReSys (Figure 3.55). The sample of struvite from NuReSys is a commercial fertiliser called BioStru and has a granular form, with grain sizes between 0.5–2 mm. In contrast, the Aa en Maas struvite consists of small orthorhombic crystals up to *ca.* 300 µm long. It can be seen however, that the BioStru grains are composed of much smaller coffin-shaped crystals that have been compacted together, likely with the addition of a binding agent (Figure 3.55b).

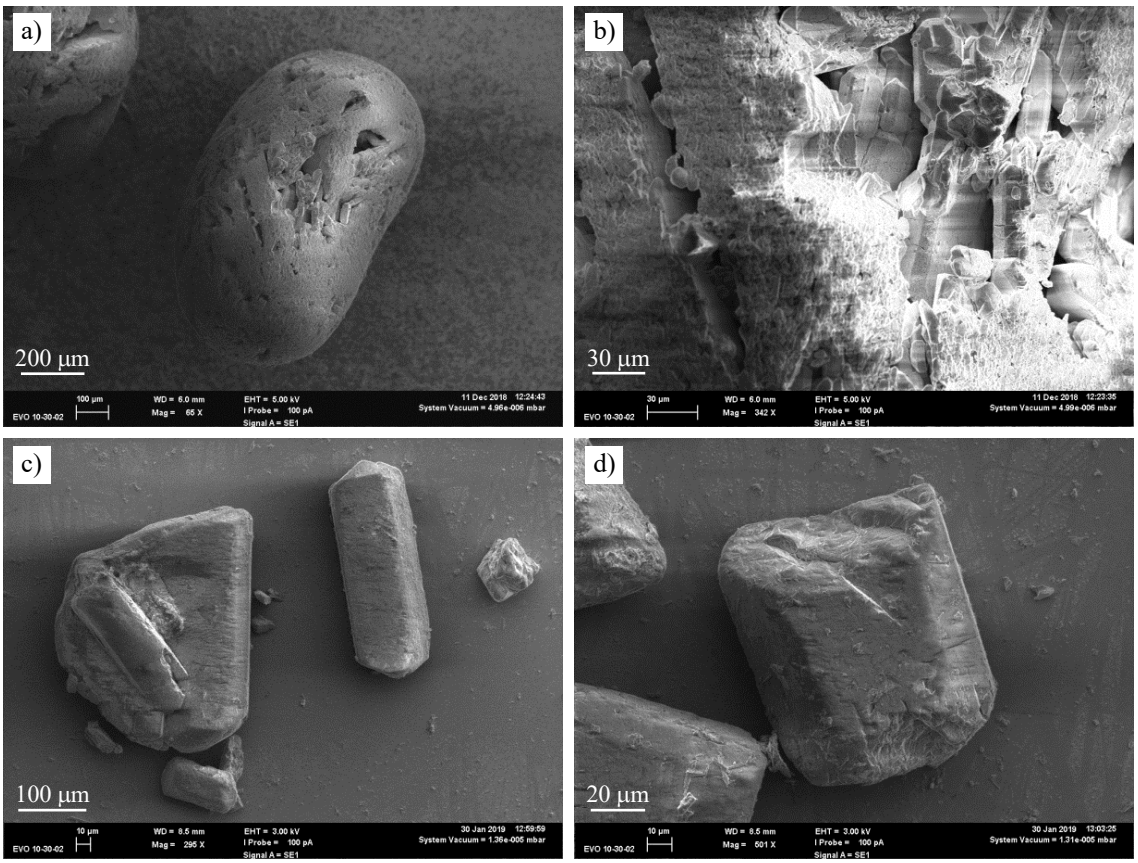


Figure 3.55 SEM images of struvite from NuReSys (a and b) and Aa en Maas (c and d). Both WWTPs use the NuReSys technology to precipitate struvite. Uncoated samples.

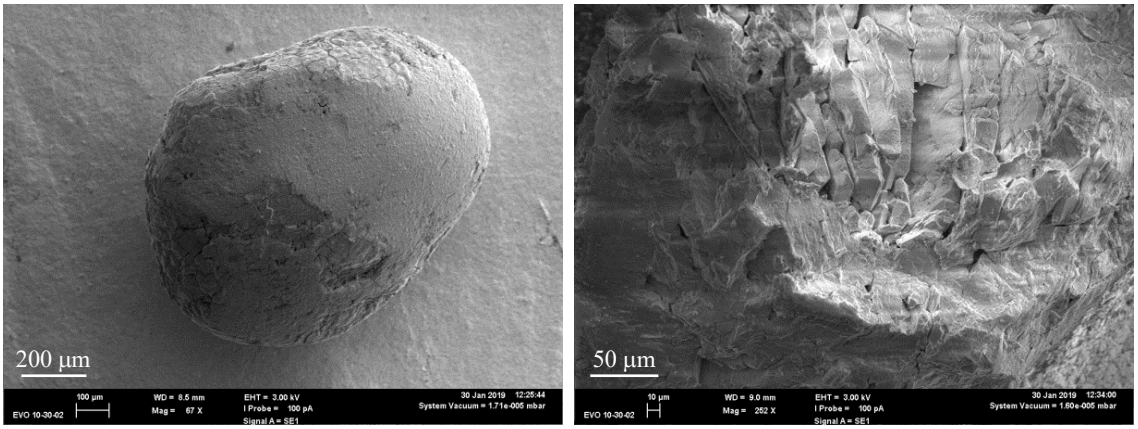


Figure 3.56 SEM images of struvite from Clean Water Services. Uncoated samples.

The struvite from Clean Water Services is also a granular fertiliser (Figure 3.56) – sold as Crystal Green. The sample received has a prill size of 0.9 mm but larger grains are also available from this supplier. Splitting the grains and viewing the fragments under SEM

revealed that, like the NuReSys struvite, these macroscopic particles are aggregates of smaller crystals.

The crystals from Aarhus Vand (Figure 3.57) are coffin-shaped and also clustered (penetrating twin crystals and X-shaped dendritic). These crystals are up to *ca.* 600 μm in length – smaller than the AirPrex struvites (Figure 3.54) but larger than Alfa Aesar (Figure 3.9a and b).

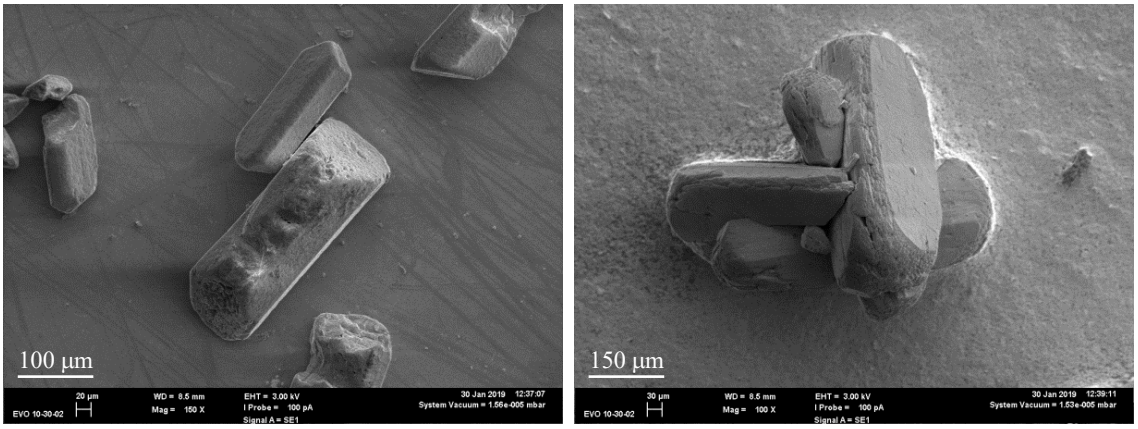


Figure 3.57 SEM images of struvite from Aarhus Vand. Uncoated samples.

3.7 Preparation of SLDH from WWTP struvite

Two WWTP struvites were chosen to be studied and compared against the synthetic struvite from Alfa Aesar. The sample from NuReSys was chosen because it has an XRD pattern most similar to that of the pure struvite. Aa en Maas was chosen because it has the highest BET surface area, which may have a positive effect on the surface area of the product.

SLDH was prepared from NuReSys struvite using the M2 procedure (Section 3.2.2). It was found upon scaling up that a higher temperature was required to ensure complete conversion of the starting material to SLDH (Figure 3.58). SLDHs can be reliably produced on a 9 g scale using M2 at 85 ºC with an ageing time of 2 h (Figure 3.59).

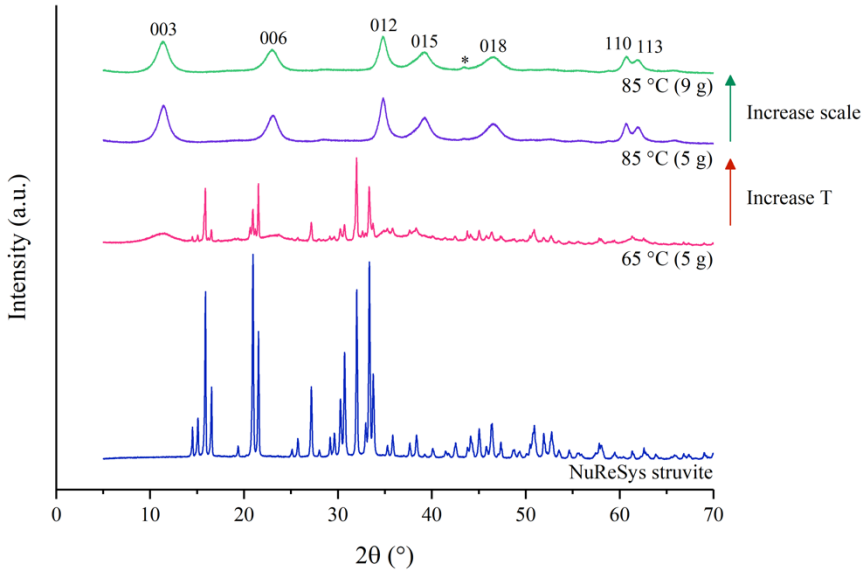


Figure 3.58 Powder XRD diffractograms of NuReSys struvite and M2-SLDHs. Mg/Al = 3.

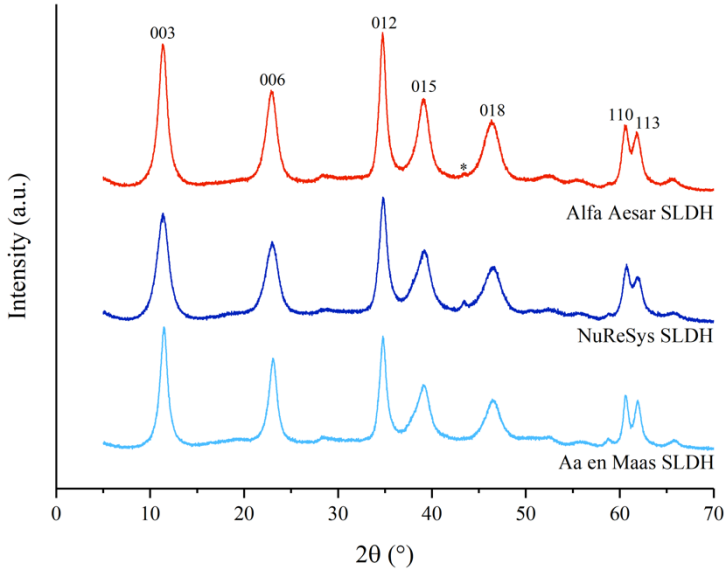


Figure 3.59 Powder XRD diffractograms of M2-85-SLDHs prepared from Alfa Aesar, NuReSys and Aa en Maas struvites. Mg/Al = 3. *Reflection due to the sample holder.

The XRD diffractograms for all three SLDHs exhibit sharp Bragg reflections, indicating a high degree of crystallinity (Figure 3.59). The FWHM of both the basal and non-basal peaks are greatest for NuReSys SLDH which suggests that it has the smallest crystallite size of the three (Table 3.12). The *d*-spacing, d_{003}, is *ca.* 0.779 nm, which suggests the interlayer galleries contain a mixture of carbonate and residual phosphate. Elemental analysis by ICP-MS confirms the presence of phosphorus in all samples (Table 3.13).

Table 3.12 Lattice parameters and mean CDLs of M2-85-SLDHs. Mg/Al =3.

M2-85-SLDH	*d*-spacing (Å)		Lattice parameter (Å)		CDL (Å)	
	d_{003}	d_{110}	$c^{\dagger}$	$a^{\ddagger}$	*c*-axis	*ab*-plane
Alfa Aesar	7.78	1.53	23.37	3.06	77.9	203.3
NuReSys	7.77	1.52	23.31	3.04	54.9	197.5
Aa en Maas	7.72	1.53	23.16	3.06	88.8	260.6

†Lattice parameter $c = 3d_{003}$. ‡Lattice parameter $a = 2d_{110}$.
CDL = $0.89\lambda/\beta\cos\theta$, $\lambda = 1.541847$ Å, β = FWHM in radians.

A c-LDH was synthesised using metal nitrates under the same conditions (85 ºC, 2 h ageing) for reference. This c-LDH, termed Ref-LDH, had sharper and more intense Bragg reflections in its XRD diffractogram (Figure 3.60). These correspond to larger crystallite sizes: the mean CDLs of the reference LDH are 220.3 and 369.2 Å, along the *c*-axis and in the *ab*-plane, respectively (Appendix A Table A.14). The relative intensities of the reflections indicate that the third peak in this spectrum is due to the 009 plane, unlike the SLDH spectra that have a stronger 012 reflection at *ca.* 35º.

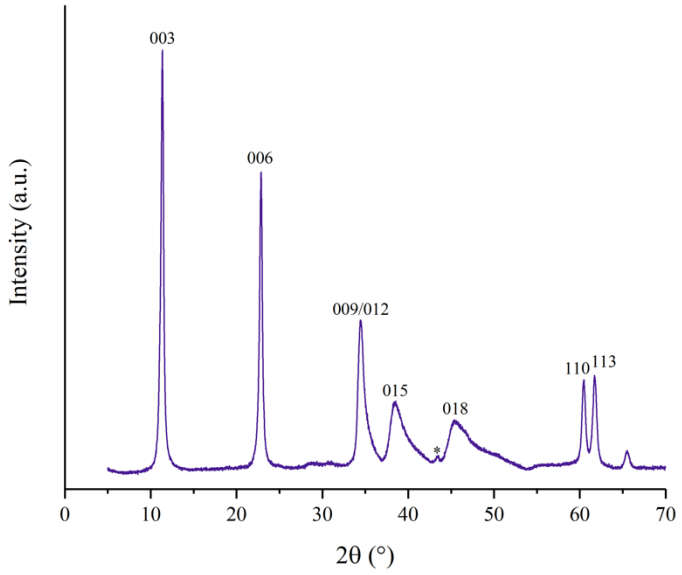


Figure 3.60 Powder XRD diffractogram of a reference c-LDH synthesised under the M2-85-SLDH reaction conditions (Ref-LDH). Mg/Al = 3.

Furthermore, the 01*l* reflections have a "shark's fin" shape, which is associated with turbostratic structures.[67] This indicates stacking faults along the *c*-direction in the layered

structure, *i.e.* adjacent layers are rotationally or translationally displaced. This was not observed in the XRD diffractogram of the SLDHs and, as such, suggests that the struvite lattice, which contains a regular array of Mg^{2+}, aids cation ordering during SLDH precipitation (*i.e.* the transformation is topotactic).

Table 3.13 Summary of the ICP-MS elemental analyses for Mg, Al, and P content of M2-85-SLDHs

Av. wt.%	M2-85-SLDH (9 g batches)		
	Alfa Aesar	NuReSys	Aa en Maas
Mg	21.77	20.28	20.83
Al	8.19	7.71	7.67
P	1.40	2.46	1.03
Av. Mg/Al	2.84	2.81	2.90

Elemental analyses also show that the Mg/Al ratio in the SLDHs is very close to the expected ratio, 3. For the NuReSys SLDH, the larger primary particle size of the struvite may have resulted in less complete dispersion in the initial stages of the synthesis, thus causing a greater amount of PO_4^{3-} being retained. This SLDH has a lower Mg content because the NuReSys struvite had a lower Mg content (Table 3.11). Furthermore, the NuReSys SLDH has a higher residual mass at 800 ºC than the SLDH prepared from synthetic struvite (Figure 3.59b). This is due to the presence of impurities, including a binding agent for the pellets, in amounts that are undetectable by XRD.

The ICP-MS data reveals that Aa en Maas SLDH contains the lowest amount of phosphorus. The low density and high surface area of this material may have resulted in more efficient decomposition in the alkali, causing more Na^+ substitution into the lattice and destabilising the phosphate. The phosphate ions would then be more readily substituted for carbonate.

Common impurities in all the SLDHs are alkali, alkali earth and transition metals (Appendix A, Table A.12), which are found in the struvites. Residual sodium may be due to incomplete washing during the syntheses.

The colours of the products also indicate the presence of impurities. The SLDH prepared from Alfa Aesar struvite has the white colour expected for MgAl-LDHs (Figure 3.61a). For both WWTP struvites, the SLDH bears to colour of the struvite, *i.e.* the impurities causing discolouration are not expelled during the procedure. The NuReSys SLDH is off-white and the Aa en Maas SLDH is light tan (Figure 3.61b and c). The colour of these compounds may be due to traces of manganese and iron, respectively (Appendix A, Table A.12).

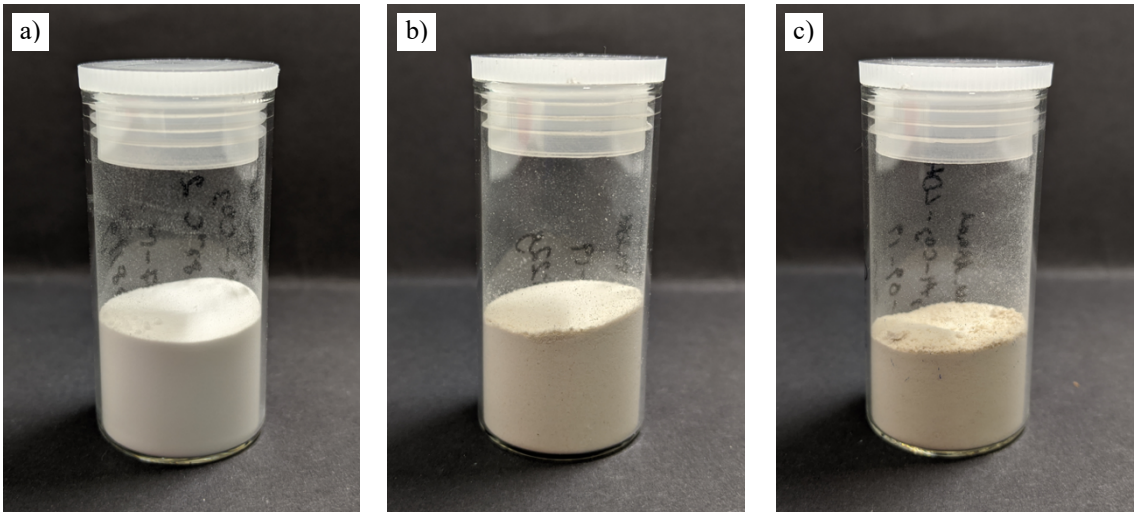


Figure 3.61 a) Alfa Aesar, b) NuReSys and c) Aa en Maas M2-85-SLDHs. Mg/Al = 3.

The dTGA peaks for the Aa en Maas SLDH occur ~20 ºC higher than for the other two SLDHs (Figure 3.62). The Aa en Maas struvite had the highest surface area (15 $m^2\ g^{-1}$ compared to 2 and 4 $m^2\ g^{-1}$, Figure 3.50b) and one of the lowest decomposition temperatures (Figure 3.52b) so it will have decomposed in the alkaline solution more efficiently. This may have allowed for more crystalline SLDH particles to form, and this

is supported by the XRD data that shows the narrowest Bragg reflections for the SLDH prepared from struvite obtained from Aa en Maas (Figure 3.59 and Table 3.12).

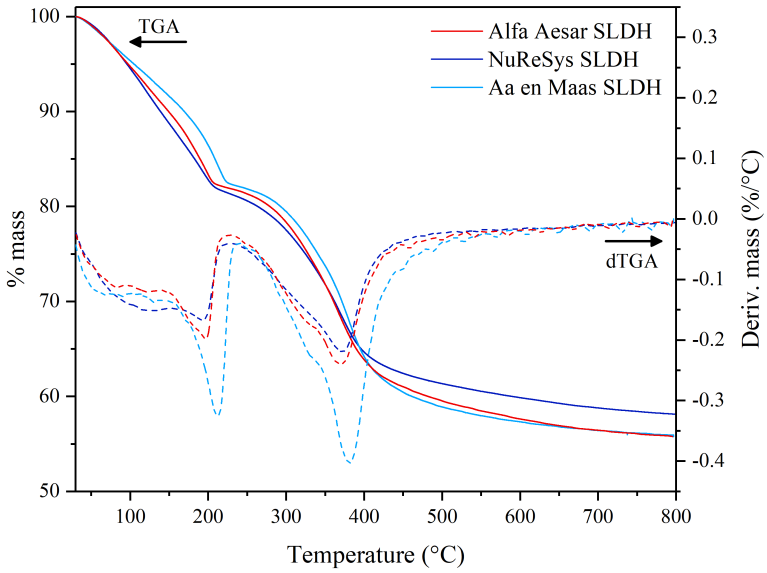


Figure 3.62 TGA and dTGA curves of M2-85-SLDHs prepared from Alfa Aesar, NuReSys and Aa en Maas struvites. Mg/Al = 3.

The peak widths of the Bragg reflections in the XRD diffractograms also indicate that the NuReSys SLDH has the lowest crystallinity and/or smallest crystallite sizes, and this can be observed in the SEM images (Figure 3.63). In all samples, sand rose-like clusters are observed. For the Alfa Aesar and Aa en Maas SLDHs, which came from coffin-shaped struvite crystals (*ca.* 50 and 300 nm, respectively), large straight-edged crystals are also present (Figure 3.63a and c). This is consistent with the observations in Section 3.2. The absence of these large structures in the NuReSys SLDH suggests that the NuReSys struvite is less resistant to high pH and high temperatures. The primary particles of NuReSys struvite were more than one order of magnitude larger than those of Alfa Aesar and Aa en Maas, but the interior of the pellets consists of small prismatic crystals compressed together (Figure 3.55). Once the binding agents are overcome by the alkalinity and heat, these small crystals would be more susceptible to decomposition. Thus, the NuReSys SLDH consists of much smaller clusters (Figure 3.63b).

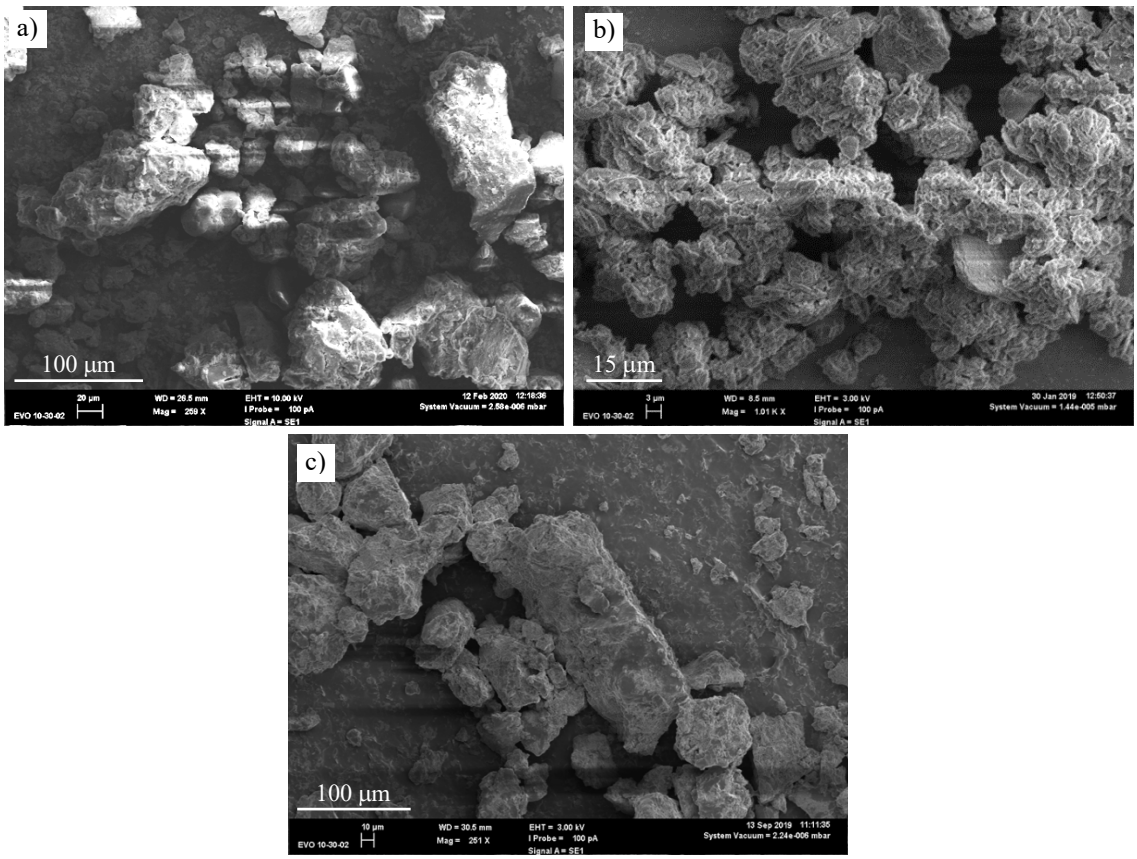


Figure 3.63 SEM images of a) Alfa Aesar, b) NuReSys and c) Aa en Maas M2-85-SLDHs. Mg/Al = 3.

As the LDH particles prepared by co-precipitation are generally less than 500 nm in diameter, transmission electron microscopy (TEM) was also used to investigate the morphology of the M2-85-SLDHs (Figure 3.64). The TEM images reveal significant differences in the morphology of the SLDHs. The Alfa Aesar SLDH is flower-like (*e.g.* clustered) whilst both the NuReSys SLDH and Aa en Maas SLDH comprise of much smaller platelets that are not interconnected. For the NuReSys SLDH, the small crystallite size was to be expected from the broad reflections in the XRD diffractogram (Figure 3.59). In the Aa en Maas SLDH, the platelets are approximately hexagonal, which is a known morphology for LDHs. The particles are less well-defined in NuReSys SLDH. This difference in morphology is reflected in their tap densities (Figure 3.66).

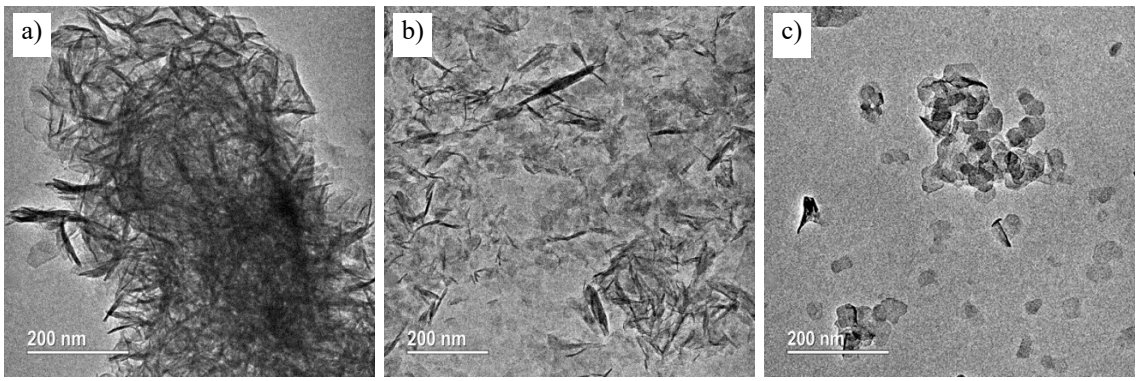


Figure 3.64 TEM images of a) Alfa Aesar, b) NuReSys and c) Aa en Maas M2-85-SLDHs. Mg/Al = 3.

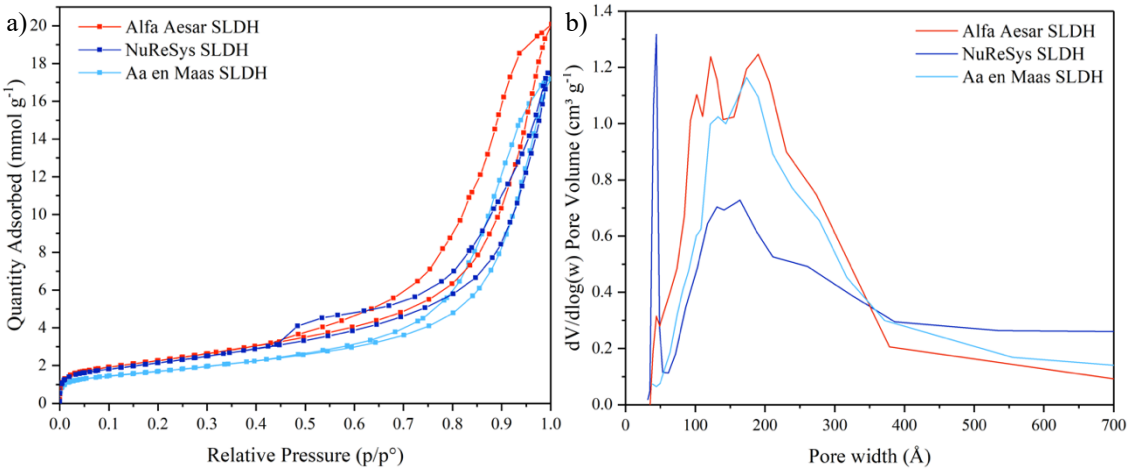


Figure 3.65 a) N_2 adsorption and desorption isotherms and b) BJH pore size distributions of M2-85-SLDHs. Mg/Al = 3.

All three SLDHs are mesoporous and have multi pore distributions (Figure 3.65). The NuReSys SLDH has a much smaller population of pores between *ca.* 50–350 Å than the Alfa Aesar and Aa en maas SLDHs. Furthermore, the pore volume of the NuReSys SLDH appears to have contributions from macropores (>500 Å) and these may be attributed to interparticle voids.

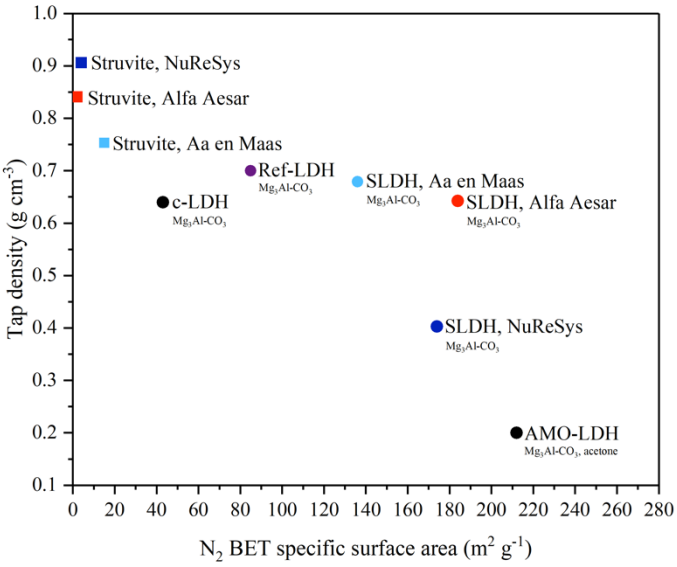


Figure 3.66 Tap density plotted as a function of BET area for struvite, SLDHs and reference LDHs.

Compared to the equivalent conventional LDHs (Ref-LDH and c-LDH), the Alfa Aesar and NuReSys M2-85-SLDHs have very high surface areas (184 and 174 $m^2\ g^{-1}$, respectively) that are even in the range of AMO-LDHs (Figure 3.66). The LDH synthesised under the same conditions (Ref-LDH) has less than half the surface area of the Alfa Aesar SLDH (85 $m^2\ g^{-1}$).

Struvite from Aa en Maas produces an SLDH with the lowest surface area (136 $m^2\ g^{-1}$) and highest tap density (0.68 $g\ cm^{-3}$). This supports the theory that the Aa en Maas struvite disperses most efficiently, as it has the highest surface area and lowest tap density, which enhances interactions between the ions in the slurry and thereby allowing a more crystalline SLDH to form.

The three SLDHs are two to four times denser than the equivalent AMO-LDH and three to six times the surface area of the equivalent c-LDH. Struvite is a therefore a promising precursor to high density, high surface area LDHs without the need for surface modification.

3.8 Conclusion

The synthesis of MgAl-LDHs has been successfully achieved using the mineral struvite, $MgNH_4PO_4.6H_2O$, as a source of magnesium. Scalable methods have been developed and optimised to give crystalline MgAl-SLDHs in yields up to 95%. Calculations also suggest that preparation of MgAl-LDHs from struvite can be up to 5% more atom efficient than from magnesium nitrate. Carbonate and phosphate interlayer species were studied in this investigation, as were ternary metal combinations, and it is expected that SLDHs have the compositional flexibility of LDHs synthesised by conventional methods.

The procedures developed were suitable for struvites originating from WWTPs. The composition of these struvites varied widely as a result of the different precipitating conditions used in different plants, but SLDH preparation remained facile and yielded crystalline products. Trace amounts of impurities (*e.g.* Ca, K, Mn and Fe) were present in the final SLDHs though, as these ions were also soluble under the reaction conditions. If struvite from wastewater sources is to be utilised, steps to purify the mineral will be required.

Importantly, the investigation has shown that SLDHs possess unique properties: namely, high surface area (*ca.* 184 $m^2\ g^{-1}$) and high tap density (*ca.* 0.68 $g\ cm^{-3}$). These properties are the result of the topotactic transformation of struvite to SLDH, involving dissolution and recrystallisation steps.

SLDHs are therefore a very promising green alternative to c-LDHs that have high tap densities but low surface areas, and AMO-LDHs in which high surface areas are accompanied with low tap densities.

3.9 References

1. M. F. Chislock, E. Doster, R. A. Zitomer and A. Wilson, *Nature Education Knowledge*, 2013, **4**, 10.
2. B. Cieślik and P. Konieczka, *J. Clean. Prod.*, 2017, **142**, 1728-1740.
3. M. Darwish, A. Aris, M. H. Puteh, M. Z. Abideen and M. N. Othman, *Sep. Purif. Rev.*, 2016, **45**, 261-274.
4. C. K. Chauhan and M. J. Joshi, *J. Cryst. Growth*, 2013, **362**, 330-337.
5. Y. Jaffer, T. A. Clark, P. Pearce and S. A. Parsons, *Water Res.*, 2002, **36**, 1834-1842.
6. M. I. H. Bhuiyan, D. S. Mavinic and R. D. Beckie, *Environ. Technol.*, 2007, **28**, 1015-1026.
7. K. S. Le Corre, E. Valsami-Jones, P. Hobbs and S. A. Parsons, *Crit. Rev. Environ. Sci. Technol.*, 2009, **39**, 433-477.
8. S. Kataki, H. West, M. Clarke and D. C. Baruah, *Resour. Conserv. Recy.*, 2016, **107**, 142-156.
9. W. R. Abma, W. Driessen, R. Haarhuis and M. C. M. van Loosdrecht, *Water Sci. Technol.*, 2010, **61**, 1715-1722.
10. W. Driessen, T. Hendrickx, R. Maxime and R. Haarhuis, in *Phosphorus: Polluter and Resource of the Future – Removal and Recovery from Wastewater*, ed. C. Schaum, IWA Publishing, 2018.
11. I. Stratful, M. D. Scrimshaw and J. N. Lester, *Water Res.*, 2001, **35**, 4191-4199.
12. Struvite Removal Solution https://www.struvite.info/struvite-wastewater-treatment/struvite-removal/how-to-remove-struvite.
13. Struvite Product Factsheet, https://systemicproject.eu/downloads/factsheet-product-struvite-06032019/.
14. K. S. Le Corre, E. Valsami-Jones, P. Hobbs, B. Jefferson and S. A. Parsons, *Water Res.*, 2007, **41**, 2449-2456.
15. A. Whitaker and J. Jeffery, *Acta Crystallogr. Sect. B: Struct. Sci. Cryst. Chem.*, 1970, **26**, 1429-1440.
16. Z. Romanowski, P. Kempisty, J. Prywer, S. Krukowski and A. Torzewska, *J. Phys. Chem. A*, 2010, **114**, 7800-7808.
17. J. Prywer, L. Sieroń and A. Czylkowska, *Crystals*, 2019, **9**, 89.
18. F. Abbona and R. Boistelle, *J. Cryst. Growth*, 1979, **46**, 339-354.
19. E. Ariyanto, T. K. Sen and H. M. Ang, *Adv. Powder Technol.*, 2014, **25**, 682-694.
20. R. R. Sadowski, J. Prywer and A. Torzewska, *Cryst. Res. Technol.*, 2014, **49**, 478-489.
21. E. Ariyanto, H. M. Ang and T. Sen, presented in part at the *Chemeca 2011: Engineering a Better World*, 2011.
22. F. Cavani, F. Trifirò and A. Vaccari, *Catal. Today*, 1991, **11**, 173-301.
23. R. L. Frost, A. W. Musumeci, M. O. Adebajo and W. Martens, *J. Therm. Anal. Calorim.*, 2007, **89**, 95-99.
24. J. T. Kloprogge, L. Hickey and R. L. Frost, *J. Raman Spectrosc.*, 2004, **35**, 967-974.
25. R. L. Frost, Y. Xi, R. Scholz, A. López and F. M. Belotti, *Vib. Spectrosc.*, 2013, **66**, 69-75.
26. W. Yang, Y. Kim, P. K. T. Liu, M. Sahimi and T. T. Tsotsis, *Chem. Eng. Sci.*, 2002, **57**, 2945-2953.
27. B. Tansel, G. Lunn and O. Monje, *Chemosphere*, 2018, **194**, 504-514.
28. A. D. McNaught and A. Wilkinson, *Compendium of chemical terminology, 2nd Edition*, Blackwell Scientific Publications, Oxford, 1997.

29. M. Thommes, K. Kaneko, A. V. Neimark, J. P. Olivier, F. Rodriguez-Reinoso, J. Rouquerol and K. S. Sing, *Pure Appl. Chem.*, 2015, **87**, 1051-1069.
30. M. Thommes, *Chem. Ing. Tech.*, 2010, **82**, 1059-1073.
31. K. S. Sing, *Pure Appl. Chem.*, 1985, **57**, 603-619.
32. C. P. Chen, A. Wangriya, J.-C. Buffet and D. O'Hare, *Dalton Trans.*, 2015, **44**, 16392-16398.
33. M. Mathew and L. W. Schroeder, *Acta Crystallogr. Sect. B*, 1979, **35**, 11-13.
34. A. Legrouri, M. Badreddine, A. Barroug, A. De Roy and J. P. Besse, *J. Mater. Sci. Lett.*, 1999, **18**, 1077-1079.
35. T. Satoko, C. Ramesh, S. Kohji, S. Akinari, O. Kenta and T. Tahei, *Bull. Chem. Soc. Jpn.*, 2004, **77**, 2101-2107.
36. J. Das, B. S. Patra, N. Baliarsingh and K. M. Parida, *Appl. Clay Sci.*, 2006, **32**, 252-260.
37. S. Miyata, *Clays Clay Miner.*, 1983, **31**, 305-311.
38. R. L. Frost, M. L. Weier and K. L. Erickson, *J. Therm. Anal. Calorim.*, 2004, **76**, 1025-1033.
39. E. Banks, R. Chianelli and R. Korenstein, *Inorg. Chem.*, 1975, **14**, 1634-1639.
40. P. J. Dirken, J. B. H. Jansen and R. D. Schuiling, *Am. Mineral.*, 1992, **77**, 718-724.
41. A. Wong and G. Wu, *J. Phys. Chem. A*, 2000, **104**, 11844-11852.
42. M. Weil, *Cryst. Res. Technol.*, 2008, **43**, 1286-1291.
43. Q. Wang, J. P. Undrell, Y. Gao, G. Cai, J.-C. Buffet, C. A. Wilkie and D. O'Hare, *Macromolecules*, 2013, **46**, 6145-6150.
44. K. Shanmuganathan and C. J. Ellison, in *Polymer Green Flame Retardants*, eds. C. D. Papaspyrides and P. Kiliaris, Elsevier, Amsterdam, 2014, pp. 675-707.
45. Y. Gao, Q. Wang, J. Wang, L. Huang, X. Yan, X. Zhang, Q. He, Z. Xing and Z. Guo, *ACS Appl. Mater. Interfaces*, 2014, **6**, 5094-5104.
46. Y. Gao, Y. Zhang, G. R. Williams, D. O'Hare and Q. Wang, *Sci. Rep.*, 2016, **6**, 35502.
47. D.-Y. Wang, A. Das, F. R. Costa, A. Leuteritz, Y.-Z. Wang, U. Wagenknecht and G. Heinrich, *Langmuir*, 2010, **26**, 14162-14169.
48. C. Manzi-Nshuti, P. Songtipya, E. Manias, M. d. M. Jimenez-Gasco, J. M. Hossenlopp and C. A. Wilkie, *Polym. Degrad. Stab.*, 2009, **94**, 2042-2054.
49. L. Wang, X. He, H. Lu, J. Feng, X. Xie, S. Su and C. A. Wilkie, *Polym. Adv. Technol.*, 2011, **22**, 1131-1138.
50. Y. Gao, Q. Wang and W. Lin, *Polymers*, 2018, **10**, 1114.
51. S. Bourbigot, M. L. Bras, R. Leeuwendal, K. K. Shen and D. Schubert, *Polym. Degrad. Stab.*, 1999, **64**, 419-425.
52. K. K. Shen and R. W. Sprague, *J. Vinyl Technol.*, 1982, **4**, 120-123.
53. K.-S. Lim, S.-T. Bee, L. T. Sin, T.-T. Tee, C. T. Ratnam, D. Hui and A. R. Rahmat, *Compos. B. Eng.*, 2016, **84**, 155-174.
54. J. Green, *J. Fire Sci.*, 1992, **10**, 470-487.
55. Ü. Özgür, Y. I. Alivov, C. Liu, A. Teke, M. Reshchikov, S. Doğan, V. Avrutin, S.-J. Cho and a. H. Morkoç, *J. Appl. Phys.*, 2005, **98**, 11.
56. F. L. Theiss, G. A. Ayoko and R. L. Frost, *Appl. Surf. Sci.*, 2016, **383**, 200-213.
57. A. Shaporev, V. Ivanov, A. Baranchikov, O. Ivanova Polezhaeva and Y. Tretyakov, *Russ. J. Inorg. Chem.*, 2007, **52**, 1811-1816.
58. R. D. Shannon, *Acta Crystallogr. Sect. A*, 1976, **32**, 751-767.
59. E. M. Seftel, E. Popovici, M. Mertens, K. D. Witte, G. V. Tendeloo, P. Cool and E. F. Vansant, *Micropor. Mesopor. Mat.*, 2008, **113**, 296-304.
60. S. K. Yun and T. J. Pinnavaia, *Chem. Mater.*, 1995, **7**, 348-354.

61. C. Chen, M. Yang, Q. Wang, J.-C. Buffet and D. O'Hare, *J. Mater. Chem. A*, 2014, **2**, 15102-15110.
62. V. Erastova, M. T. Degiacomi, D. O'Hare and H. C. Greenwell, *RSC Adv.*, 2017, **7**, 5076-5083.
63. M. S. Yang, O. McDermott, J.-C. Buffet and D. O'Hare, *RSC Adv.*, 2014, **4**, 51676-51682.
64. N. Ma, A. A. Rouff and B. L. Phillips, *ACS Sus. Chem. Eng.*, 2014, **2**, 816-822.
65. T. J. Rulseh, *Treatment Plant Operator*, October 2015, 58-60
66. S. Kataki, H. West, M. Clarke and D. C. Baruah, *Waste Manage.*, 2016, **49**, 437-454.
67. X. Duan and D. G. Evans, *Layered Double Hydroxides*, Struct. Bond., Springer-Verlag Berlin Heidelberg, 2005.

Chapter 4: Core-shell silica@layered double hydroxide hybrid materials

4.1 Introduction

Hierarchical, core-shell materials have gained increasing attention in recent years due to the hybridisation of properties from the individual components and potential synergistic interactions between them.[1] Layered double hydroxides (LDHs) may be immobilised onto other functional supports and this is a useful strategy for the design of new LDH-based catalysts. Core materials that have been studied include acidic silica (SiO_2),[2, 3] magnetic iron oxide (Fe_3O_4),[4, 5] photocatalytic titanium dioxide (TiO_2),[6, 7] and high surface area zeolites.[8, 9]

Three commonly employed methods for core@LDH synthesis are direct deposition, sol-gel, and *in situ* co-precipitation.[10] Direct deposition involves the physical combination of LDH nanoparticles and the core material after their separate syntheses via electrostatic attraction. Li *et al.*[11] have used this self-assembly method to create magnetic supraparticles@LDH nanocomposites for biomedical applications. LDH nanosheets have also been successfully coated onto core materials through layer-by-layer deposition.[4] However, physical deposition techniques have three notable disadvantages: 1) the adhesion between LDH crystallites is generally weaker than that created by *in situ* growth methods, 2) the shape of the scaffold cannot be very complicated if deposition is to be successful, and 3) the layer-by-layer approach is very time-consuming.

Originally used to describe hydrolysis and condensation processes, the term "sol-gel" now broadly describes the synthesis of solid-state materials from solution-state precursors.[12, 13] The sol-gel process consists of two steps: 1) condensation of the

precursors – most commonly metal alkoxides – to form a colloidal suspension termed the "sol", and 2) cross-linking reactions in the sol to form the "gel".[14] For hybrid materials containing LDHs, the core material is firstly immersed in a solution containing aluminium alkoxides (*e.g.* $Al(OPr)_3$) and several cycles of sol-gel deposition generates an AlOOH coating on the surface of the core.[15-17] This coating acts as a source of aluminium which allows for crystallisation of an LDH shell to take place on the surface. This technique was applied by Shao *et al.*[17] to produce Fe_3O_4@SiO_2@NiAl-LDH microspheres that were used to selectivity adsorb a histidine-tagged protein from an E.coli lysate (Figure 4.1).

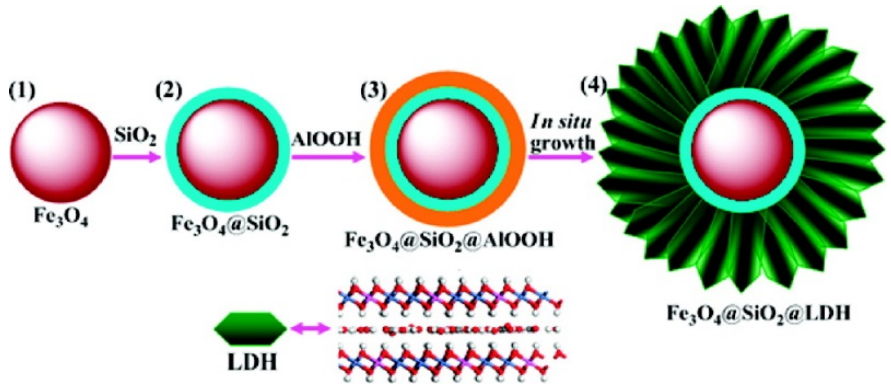


Figure 4.1 Schematic illustration of the fabrication of Fe_3O_4@SiO_2@LDH microspheres.[17]

Co-precipitation is a facile method of core@LDH preparation. Typically, metal cations are adsorbed onto the surface of a core material and subsequent addition of a precipitating agent, such as a base, affects the precipitation of LDH directly onto the core.[18] Growth of the LDH shell is facilitated by ageing and/or hydrothermal treatment.[19] Ultrasound can also be applied to assist the dispersion of the cations on the surface and thus promote homogeneous LDH growth over the core.[20] Chen *et al.*[2] have also reported the effect of pH and temperature on the growth of LDH on silica. Both high pH and high temperatures cause dissolution of the silica core, leading to yolk- and hollow-shell nanocomposites (Figure 4.2).

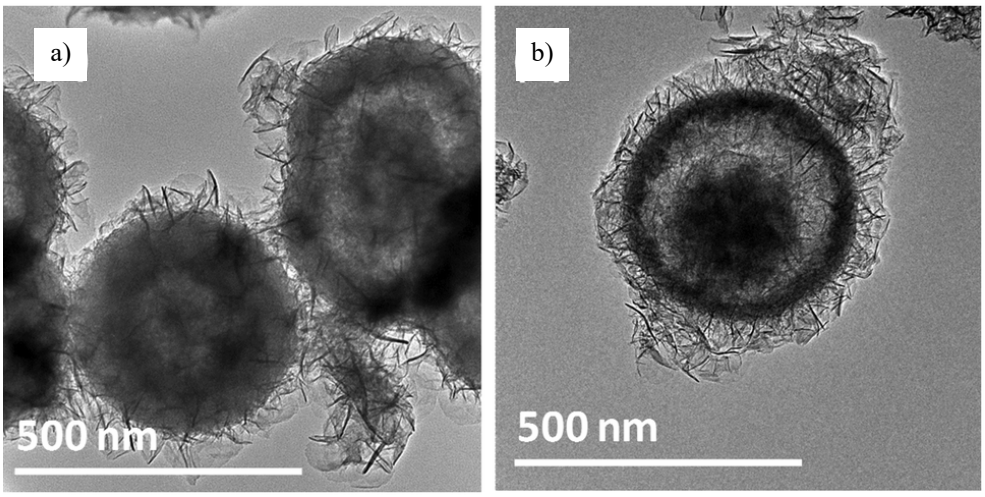


Figure 4.2 Transmission electron microscopy (TEM) images of a) hollow- and b) yolk-shell SiO_2@Mg_2Al-CO_3-LDHs.[2]

The aim of this chapter is to study the effect of experimental parameters (*e.g.* stirring speed and metal addition rate) on the composition, morphological and physical properties of core-shell SiO_2@Mg_2Al-CO_3-AMO-LDHs. A series of SiO_2@Mg_2Al-CO_3-AMO-LDHs have been synthesised by *in situ* co-precipitation of Mg_2Al-CO_3-LDH at room temperature in the presence of amorphous spherical silica particles (*d*. ~500 nm, Figure 4.3). Aqueous miscible organic solvent treatment (AMOST) was performed on the wet solid using ethanol (EtOH) before isolation of the final products. This work will focus on optimising the synthetic procedure to produce homogeneous samples with desirable properties such as high surface area and porosity.

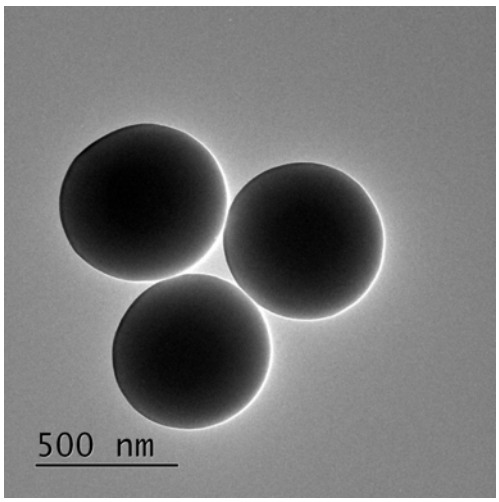


Figure 4.3 TEM image of SiO_2 used in SiO_2@Mg_2Al-CO_3-AMO-LDH preparation. Synthesised by a modified Stöber method.[2] Additional characterisations are available in Appendix B (Figures B.1 and B.2).

4.2 Variation of stirring speed

Chemical reactions are typically agitated (*i.e.* mechanically stirred) to facilitate homogeneous mixing of reagents. For reactions in which precipitation or crystallisation occur, it is often important to control the speed of mixing as this can affect the deposition of crystallites. Fragmentation may also result if the forces on the particles are too high.

In the synthesis of core-shell SiO_2@Mg_2Al-CO_3-AMO-LDHs, metal cations are precipitated in the presence of silica spheres at pH 10. The stirring speed will therefore have a twofold effect on the synthesis. Firstly, to form hybrid materials there must be sufficient contact between the silica and the ions. This also applies to successfully formed nucleation sites, which need to be accessible to incoming ions. Secondly, to avoid fragmentation and allow large LDH platelets to grow, the shearing forces caused by stirring must be kept low. To investigate which stirring conditions are appropriate for core-shell SiO_2@Mg_2Al-CO_3-AMO-LDHs, small batches (*ca.* 1.5 g) were prepared using different stirring speeds between 0–1000 rpm.

Elemental analysis by inductively coupled plasma mass spectrometry (ICP-MS, Appendix B Table B.1) and data from thermogravimetric analysis (TGA, Appendix B Figure B.3) suggest the chemical composition of the samples to be SiO_2@[[$Mg_{0.67}Al_{0.33}(OH)_2(CO_3)_{0.17}$]·$a(H_2O)$·$b$(EtOH)]$_c$ where $0.21 \leq a \leq 0.30$, $0.12 \leq b \leq 0.18$, and $0.59 \leq c \leq 0.66$. The Mg/Al ratios are consistent and show little variation from the amounts of metal salts used in the syntheses.

Powder X-ray diffraction (XRD) was used to identify the compounds (Figures 4.4 and 4.5). SiO_2 gives rise to a broad Bragg reflection around 2θ = 23°. It is an amorphous material with short range order. In contrast, Mg_2Al-CO_3-LDHs are crystalline compounds that have a distinct powder XRD diffraction pattern. For core-shell SiO_2@Mg_2Al-CO_3-AMO-LDHs, reflections from both components are overlaid (Figure 4.4).

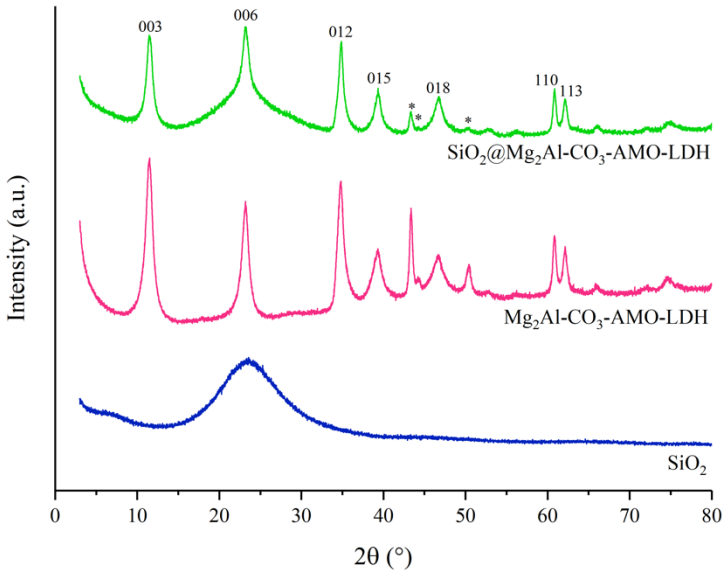


Figure 4.4 Powder XRD diffractograms of SiO_2, Mg_2Al-CO_3-AMO-LDH, and SiO_2@Mg_2Al-CO_3-AMO-LDH. Metal addition rate = 1.1 mmol h^{-1}. Stirring speed = 500 rpm. AMO solvent = EtOH. *Reflections due to the sample holder.

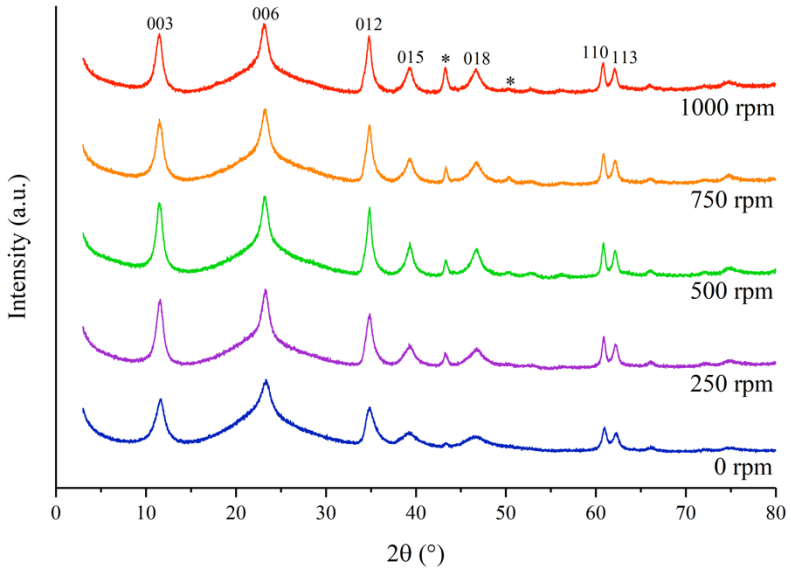


Figure 4.5 Powder XRD diffractograms of SiO_2@Mg_2Al-CO_3-AMO-LDHs prepared using different stirring speeds. Metal addition rate = 1.1 mmol h^{-1}. AMO solvent = EtOH. *Reflections due to the sample holder.

Figure 4.5 compares the powder XRD diffractograms of SiO_2@Mg_2Al-CO_3-AMO-LDHs prepared using different stirring speeds. The same comparison is made for a higher metal addition rate in Appendix B (Figure B.23). All samples show the characteristic Bragg reflections of LDH that may be indexed to the unit cell corresponding to Mg_2Al-CO_3-LDH ($a = b = 3.04$ Å, $c = 22.9$ Å, Table 4.1). These Bragg reflections are superimposed upon a broad feature between $2\theta = 15–30^{o}$ that is due to the amorphous silica.

The Bragg reflections corresponding to the LDH component are broadest for the samples prepared with stirring speeds 0 (*i.e.* no stirring) and 1000 rpm, and sharpest for 250 and 500 rpm. Factors contributing to broadening include crystallite size, instrument profile, microstrain, and inhomogeneity.[21] If it is assumed that all factors except crystallite size are consistent across samples, then the Scherrer equation (Equation 4.1) indicates that peak broadness, β, is inversely proportional to crystallite size, Λ, which is also referred to as the mean crystallite domain length, CDL.[22, 23]

$$\beta\,(2\theta) = \frac{K\lambda}{\Lambda\,\cos\theta} \qquad \text{Equation 4.1}$$

where θ is the Bragg angle, λ is the wavelength of radiation, and K is the Scherrer constant. The Scherrer constant is commonly taken to be 0.89 but its value is known to depend on factors such as crystallite shape and crystallite size distribution.[23]

Table 4.1 Lattice parameters and mean CDLs of SiO_2@Mg_2Al-CO_3-AMO-LDHs prepared using different stirring speeds. Metal addition rate = 1.1 mmol h^{-1}.

Stirring speed (rpm)	*d*-spacing (Å)		Lattice parameter (Å)		CDL (Å)	
	d_{003}	d_{110}	$c^{\dagger}$	$a^{\ddagger}$	*c*-axis	*ab*-plane
0	7.66	1.52	22.98	3.04	119.9	403.4
250	7.61	1.52	22.83	3.04	400.0	439.0
500	7.60	1.52	22.80	3.04	479.8	1209.1
750	7.69	1.52	23.07	3.04	299.8	876.9
1000	7.70	1.52	23.10	3.04	199.8	481.8

†Lattice parameter $c = 3d_{003}$. ‡Lattice parameter $a = 2d_{110}$.
CDL = 0.89λ/βcosθ, λ = 1.541847 Å, β = FWHM in radians.

Thus, broad 00*l* and 0*kl* reflections correspond to small crystallite size in the *c*-direction, and broad *hk*0 reflections correspond to small crystallite size in the *ab*-plane. The XRD patterns therefore indicate that the unstirred sample has the smallest crystallite size in both the *c*-direction and *ab*-plane (*ca.* 120 and 400 Å, respectively), whilst the sample prepared using a stirring speed of 500 rpm has the largest crystallite size in both dimensions (*ca.* 480 and 1200 Å, respectively). When the solution is not stirred, the metal solution is not homogeneously dispersed into the silica suspension. Contact between metal ions, and between metal ions and silica, is therefore inconsistent and mostly poor, so crystallites struggle to grow in size.

Stirring the reaction mixture at 1000 rpm also appears to have an unfavourable effect on LDH crystallisation. The small crystallite sizes (*ca.* 200 and 480 Å) may be due to fragmentation of larger LDH platelets during ageing as a result of shearing forces exerted

on the particles at such high stirring speed. In addition, collisions between ions may be too brief for successful precipitation under these conditions, thereby reducing nucleation and growth rates.

Like the XRD diffractograms, the Fourier transform infra-red (FTIR) spectra of SiO_2@Mg_2Al-CO_3-AMO-LDHs are combinations of the spectra of both pristine compounds (SiO_2 and Mg_2Al-CO_3-AMO-LDH, Figure 4.6 and Appendix B Figure B.29). The absorption band at *ca.* 1100 cm^{-1} is due to the Si–O stretching mode of the silica core and the remaining features are characteristic of the LDH component. The broad band between 3000–3500 cm^{-1} is due to the stretching vibration of metal-bound hydroxyl groups (MO–H, M = Mg^{2+}, Al^{3+}). For some samples a small shoulder peak is present *ca.* 3000 cm^{-1}, which is attributed to C–H stretching of EtOH (the AMO solvent). The v_3 anti-symmetric stretching mode of interlayer carbonate gives rise to the band at *ca.* 1360 cm^{-1} and the bending mode of water occurs at *ca.* 1650 cm^{-1}.

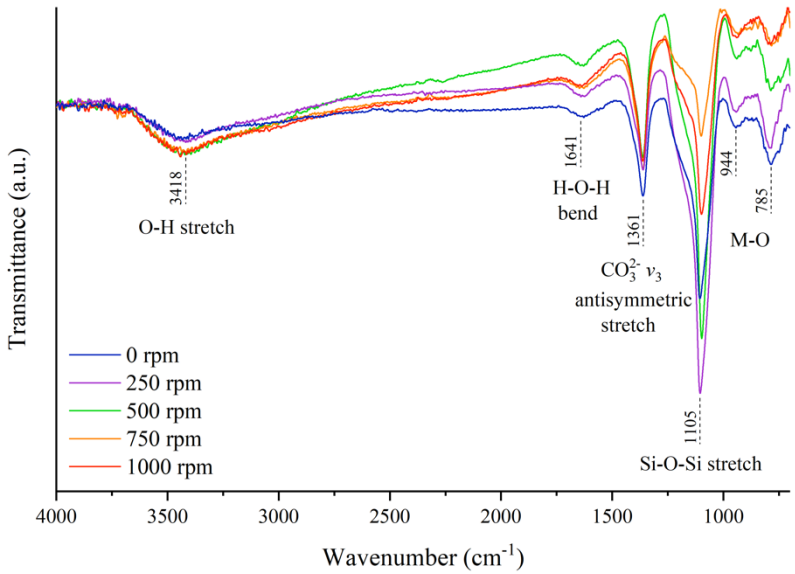


Figure 4.6 FTIR spectra of SiO_2@Mg_2Al-CO_3-AMO-LDHs prepared using different stirring speeds. Metal addition rate = 1.1 mmol h^{-1}. AMO solvent = EtOH.

The zeta potentials of the core-shell SiO_2@Mg_2Al-CO_3-AMO-LDHs have also been analysed (Figure 4.7). Zeta potential is a parameter that evaluates the surface charge and

dispersity of a material. SiO_2 has a high negative charge (–41 mV) whilst pristine Mg_2Al-CO_3-AMO-LDH has a high positive charge (34 mV). For a SiO_2@Mg_2Al-CO_3-AMO-LDH hybrid, the negative surface charge of the silica will be camouflaged if there is sufficient coverage of the silica surface by LDH. The positive zeta potentials of the core-shell samples therefore strongly indicate that the external surfaces of the hybrid are occupied by LDH.

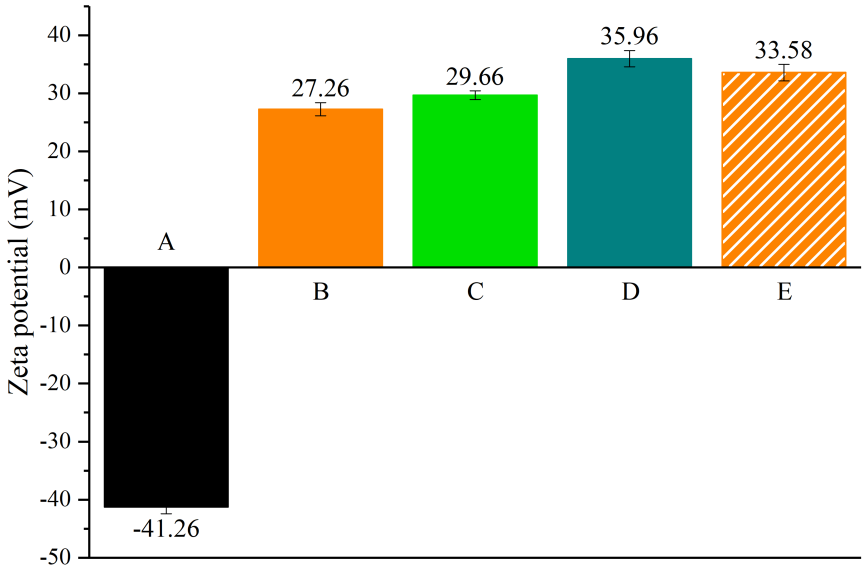


Figure 4.7 Zeta potentials of A) SiO_2; core-shell SiO_2@Mg_2Al-CO_3-AMO-LDHs prepared using stirring speeds B) 500, C) 750 and D) 1000 rpm; and E) a reference Mg_2Al-CO_3-AMO-LDH (stirring speed = 500 rpm). Metal addition rate = 4.3 mmol h^{-1}. AMO solvent = EtOH.

Nevertheless, it is also possible that excess LDH will result in a higher positive zeta potential. At a fixed metal addition rate, the zeta potential of the core-shell materials increases with increasing stirring speed from 27 to 36 mV. A high positive zeta potential may indicate small aggregates of LDH in addition to core-shell particles.

The morphology of the SiO_2@Mg_2Al-CO_3-AMO-LDHs was studied using electron microscopy (Figure 4.8 and Appendix B Figures B.4–B.18, B.20–B.22, B.24–B.28, B.33–B.36). Transmission electron microscopy (TEM) revealed non-uniform LDH coverage on the silica cores and the presence of unbound ("free") LDH in the sample

synthesised without stirring (Figure 4.8a). LDH coverage is poor because the lack of stirring means that the metal cations are not intimately mixed with the silica cores and so LDH precipitates independently in the basic solution.

The presence of free LDH is also high in in the samples synthesised at the highest stirring speeds, 750 and 1000 rpm (Figure 4.8d and e). The core-shell hybrids also have thinner LDH shells, which is consistent with the CDL values in the *ab*-plane. These are due to strong shearing forces exerted on the particles suspended in solution.

In comparison, intimate mixing of the metal cations and silica particles is facilitated at lower stirring speeds (250 and 500 rpm). These samples have large LDH platelets because the shear forces at these speeds are weaker and therefore less likely to pull existing particles apart, thus allowing the LDH platelets to grow larger under Ostwald ripening. Furthermore, there is a tendency for vertically oriented platelets at lower stirring speeds and horizontal platelets at higher stirring speeds. This can be explained in terms of the abundance of LDH nuclei on the surface of the silica cores (Figure 4.9). When the stirring speed is moderate (*e.g.* 500 rpm), LDH nuclei are densely packed on the silica surface, so competition for space means that the dominant direction of platelet growth is perpendicular to the surface (*i.e.* vertical).

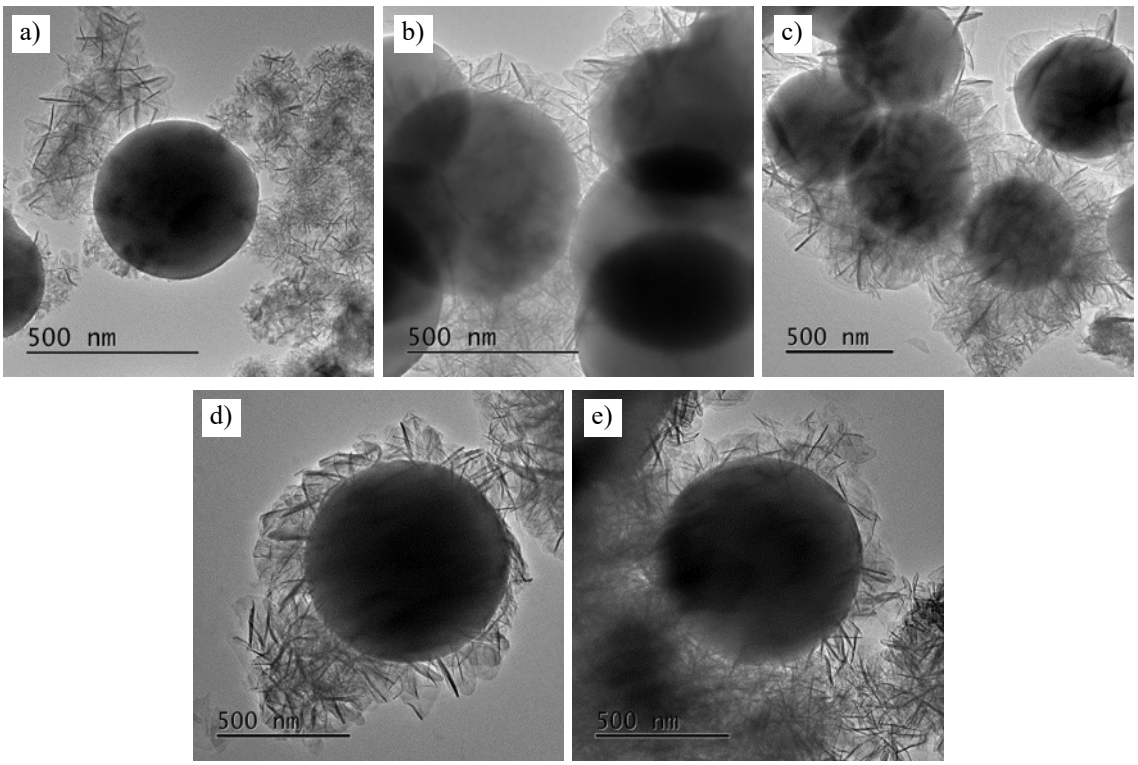


Figure 4.8 TEM images of SiO_2@Mg_2Al-CO_3-AMO-LDHs prepared using different stirring speeds: a) 0, b) 250, c) 500, d) 750, and e) 1000 rpm. Metal addition rate = 1.1 mmol h^{-1}. AMO solvent = EtOH.

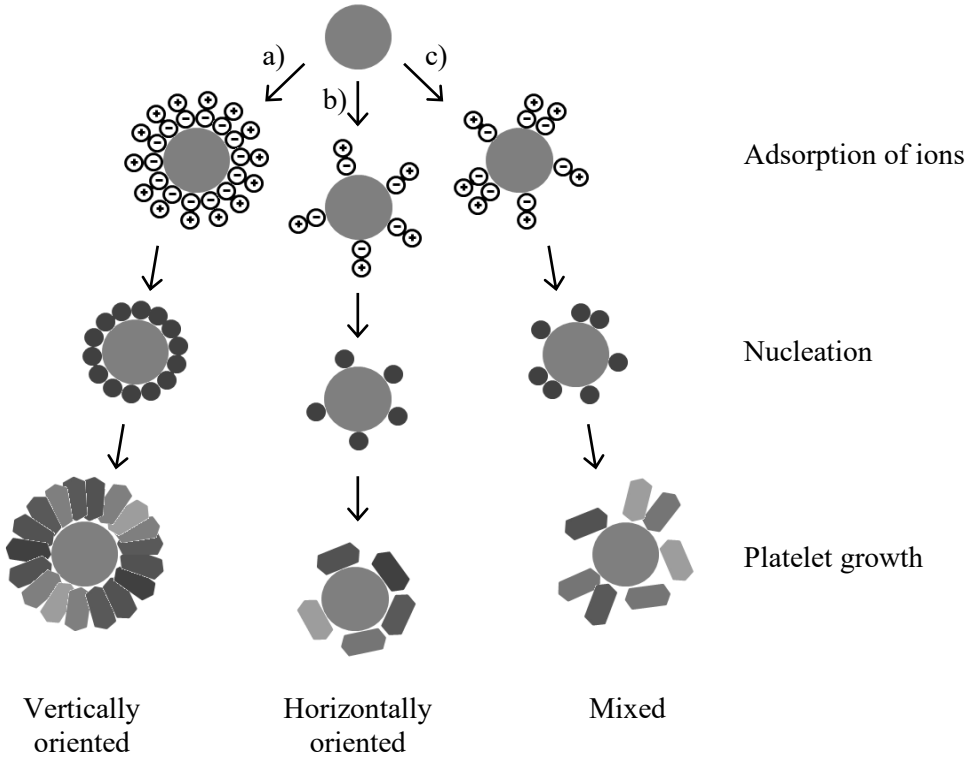


Figure 4.9 Schematic representation of LDH crystallite growth on silica under different conditions: a) high, b) low, and c) intermediate metal cation concentrations.

The specific surface areas and pore volumes recorded by the Brunauer-Emmett-Teller (BET) method show a peak at 500 rpm (Figure 4.10). This supports the TEM images in showing that this stirring speed is the optimum for achieving large, vertically oriented platelets that create an open honeycomb-like LDH shell. As stirring speed increases, fewer large interplatelet voids are created because the abundance of LDH nuclei on the silica surface is low and vertical growth is less favourable.

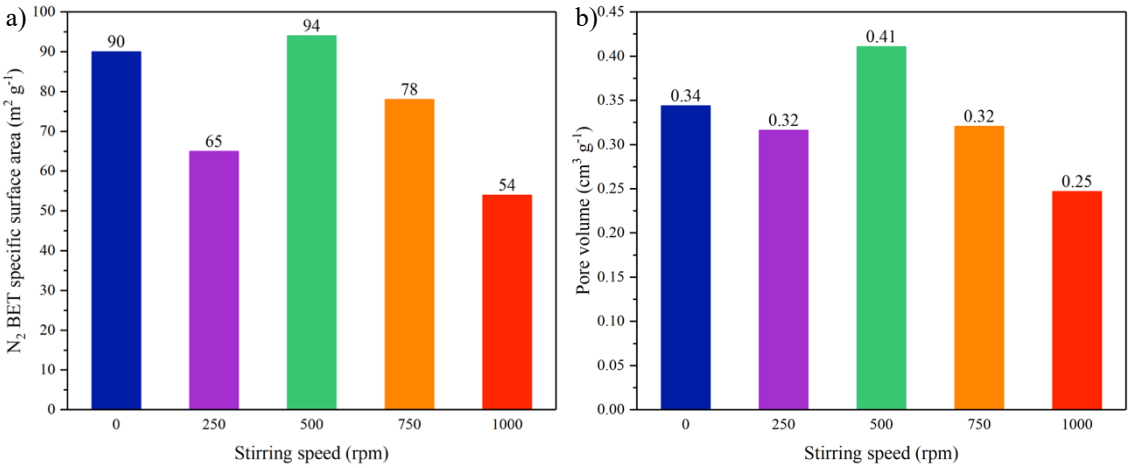


Figure 4.10 a) N_2 BET specific surface areas and b) pore volumes of SiO_2@Mg_2Al-CO_3-AMO-LDHs prepared using different stirring speeds. Metal addition rate = 1.1 mmol h^{-1}. AMO solvent = EtOH.

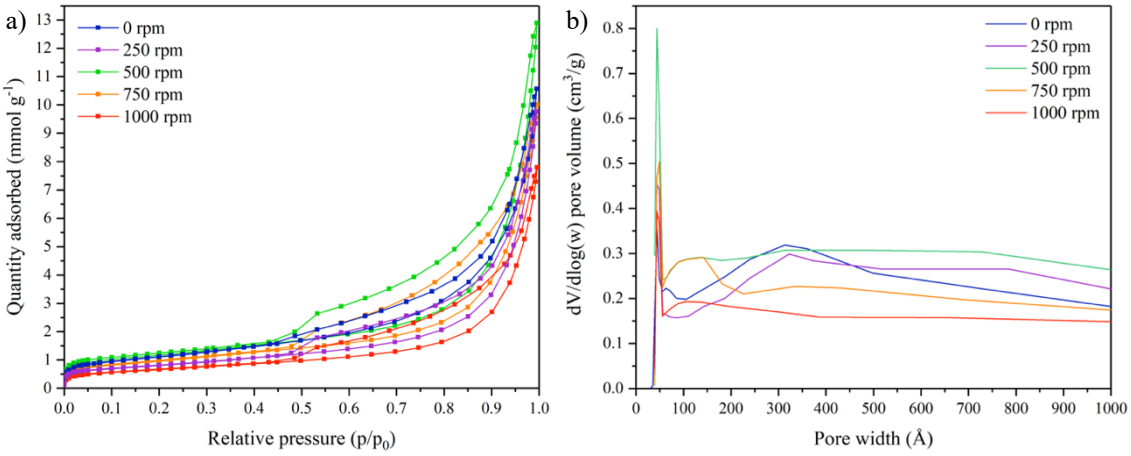


Figure 4.11 a) N_2 adsorption and desorption isotherms and b) BJH pore size distributions of SiO_2@Mg_2Al-CO_3-AMO-LDHs prepared using different stirring speeds. Metal addition rate = 1.1 mmol h^{-1}. AMO solvent = EtOH.

The SiO_2@Mg_2Al-CO_3-AMO-LDHs exhibit type IV isotherms, according to the IUPAC classification, which are characteristic of mesoporous materials (Figure 4.11a).[24] The N_2 isotherms do not exhibit any limiting adsorption at high relative pressure so are classified as having type H3 hysteresis loops. This indicates that the pores are slit-shaped and formed by non-rigid aggregated of plate-like particles. The BJH pore size distributions also show that the pores are in the mesoporous size range (20–500 Å,[25] Figure 4.11b). As previously mentioned in Section 3.2.2, the narrow peak in the BJH distribution at *ca.* 40 Å is an artefact caused by the spontaneous evaporation of metastable pore liquid (N_2) at $p/p_0 = 0.43$.[26]

All SiO_2@Mg_2Al-CO_3-AMO-LDHs have multi-pore distributions and there are two distinct distribution shapes in the BJH graph. The lowest stirring speeds (0 and 250 rpm) have maxima centred at *ca.* 300 Å, whilst the highest stirring speeds (750 and 1000 rpm) have maxima at *ca.* 120 Å. The sample prepared with a stirring speed of 500 rpm has no clear maximum. These pore diameters are similar to the CDLs calculated from the XRD diffractograms (Table 4.1) so the pores can be described as interplatelet and interparticle voids. The larger pore diameters of the 0 and 250 rpm samples suggest that the nanosheets are interconnected (*e.g.* forming honeycomb-like structures) rather than stacked.

For quantitative analyses of LDH coverage on silica, solid state nuclear magnetic resonance spectroscopy (ssNMR) was used. ^{27}Al direct polarisation magic angle spinning (DPMAS) ssNMR spectra were recorded to probe the Al^{3+} environments. In pure MgAl-LDH phases, aluminium occupies only octahedral (O_h) sites within the hydroxide layers and this gives rise to a single resonance at *ca.* 10 ppm.[2] This resonance is also observed in the spectra of SiO_2@Mg_2Al-CO_3-AMO-LDHs but a second resonance is also present (Figure 4.12). The chemical shift for the additional resonance occurs at *ca.* 60 ppm and

is characteristic of tetrahedrally coordinated (T_d) Al^{3+}. These have been assigned to Al^{3+} sites bridging to the silica surface forming Si–O–Al bonds.[2]

The ratio of Al^{3+} in T_d and O_h environments may be obtained from the integration of the ^{27}Al DPMAS ssNMR spectra and provides a more quantitative analysis of the degree of LDH coverage on the silica surface. The integrated intensity of the T_d:O_h ^{27}Al resonances changes from 1:8 to 1:11 between the sample prepared at 500 rpm compared to 750 rpm (Table 4.2). A greater proportion of T_d environments in the sample prepared at a stirring speed of 500 rpm suggests a higher level of LDH coverage on the silica surface.

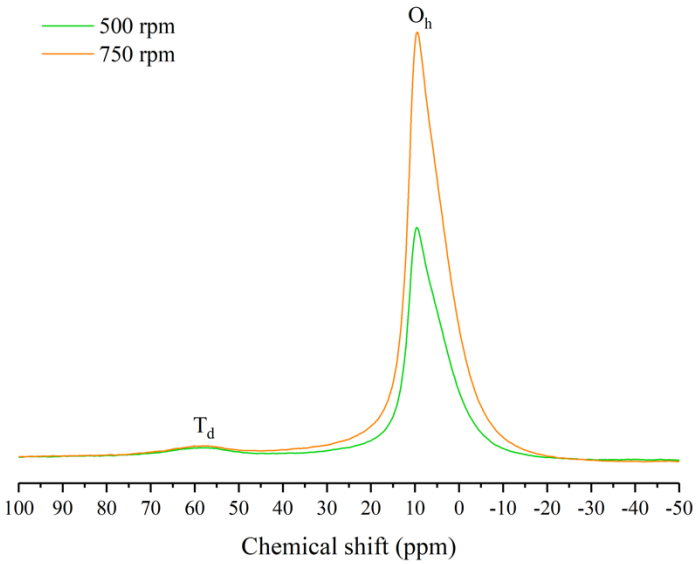


Figure 4.12 ^{27}Al DPMAS ssNMR spectra of SiO_2@Mg_2Al-CO_3-AMO-LDHs prepared using different stirring speeds. Metal addition rate = 4.3 mmol h^{-1}. AMO solvent = EtOH.

Table 4.2 Ratio of T_d and O_h aluminium species in SiO_2@Mg_2Al-CO_3-AMO-LDHs calculated from ^{27}Al DPMAS ssNMR. Metal addition rate = 4.3 mmol h^{-1}.

Stirring speed (rpm)	T_d:O_h Al
500	1:8
750	1:11

The interface between the silica and LDH was probed using ^{29}Si DPMAS ssNMR (Figure 4.13). All three samples exhibit similar resonances between –80 to –130 ppm and these

were fitted to three peaks corresponding to Si–O–Si, Si–O–H, and Si–O–Al bonds.[2] The assignments are given in Table 4.3.

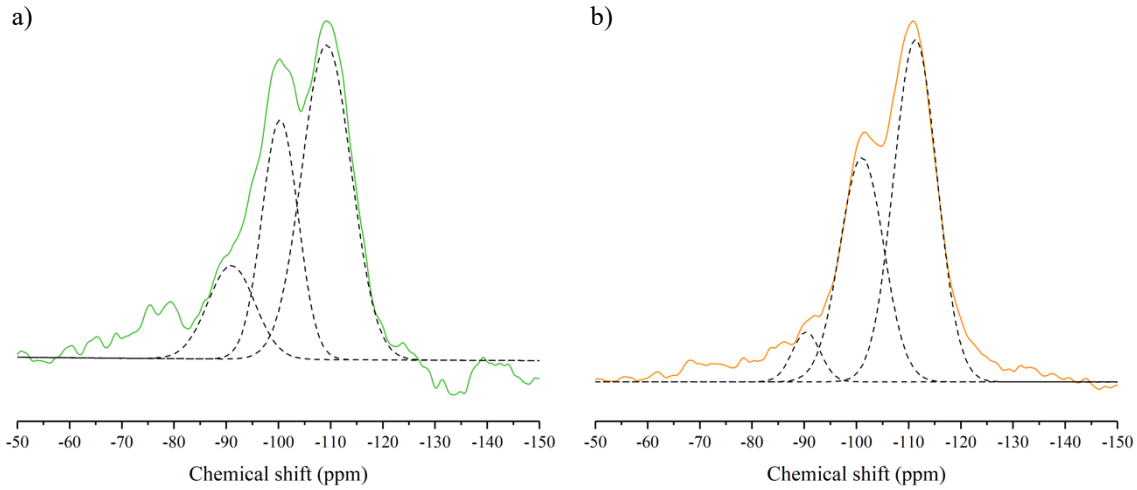


Figure 4.13 ^{29}Si DPMAS ssNMR spectra of SiO_2@Mg_2Al-CO_3-AMO-LDHs prepared using different stirring speeds: a) 500 and b) 750 rpm. Metal addition rate = 4.3 mmol h^{-1}. AMO solvent = EtOH.

The sample prepared with a stirring speed of 500 rpm has a higher percentage of Si-O-Al environments (δ = –91 ppm) than the sample prepared at 750 rpm. This indicates a higher level of LDH growth on the silica surfaces when the sample is prepared with a slower stirring speed.

Table 4.3 Silicon environments in core-shell SiO_2@Mg_2Al-CO_3-AMO-LDHs determined by ^{29}Si DPMAS ssNMR. Metal addition rate = 4.3 mmol h^{-1}.

δ (ppm)	Assignment[a]	Percentage (%)	
		500 rpm	750 rpm
–91	Q^4 Si(2Al) Q^3 $(SiO)_2(AlO)SiOH$ Q^2 $(SiO)_2Si(OH)_2$	15.3	5.4
–101	Q^4 Si(1Al) Q^3 $(SiO)_3SiOH$	30.2	37.8
–110	Q^4 Si(0Al)	54.5	56.8

[a]Q^n Si(*m*Al); *n* refers to the number of bridging atoms around the central Si, and *m* refers to number of Al atoms substituting Si atoms in the first coordination sphere.

4.3 Variation of metal addition rate

The rate at which reagents are added in a reaction can also be an important factor in synthesis as this affects the concentration of active species in the mixture. Crystallisation occurs through nucleation and growth of crystals. Nucleation can be 1) primary, *e.g.* spontaneously from solution in the absence of any other crystal, or 2) secondary, *e.g.* in the presence of existing crystals. Crystal growth occurs through the deposition of solute. Both of these processes are controlled by supersaturation, S, which is the difference between the solution concentration and the equilibrium saturation concentration, and their relationship is summarised in two simplified equations (Equations 4.2 and 4.3).[27, 28]

$$\text{Nucleation rate, } N = k_N S^n \qquad \text{Equation 4.2}$$

$$\text{Growth rate, } G = k_G S^g \qquad \text{Equation 4.3}$$

where k_N and k_G are the nucleation and growth constants, respectively, n is the nucleation order, and g is the growth order.

For the preparation of core-shell silica@Mg_2Al-CO_3-AMO-LDHs, the metal salt solution is added to a basic suspension (pH 10) of silica particles and carbonate, CO_3^{2-}. At one extreme, the entire metal salt solution can be added at once, which leads to high supersaturation (Appendix B, Figures B.37 and B.38). This kinetically favours nucleation and crystal growth is suppressed because no further metal ions are added. In this investigation, conditions of low supersaturation are employed and effect of varying the rate at which the metal salt solution is added is studied.

Different batches of SiO_2@Mg_2Al-CO_3-AMO-LDHs have been prepared at different metal salt addition rates and fixed stirring speed. Figure 4.14 and Appendix B Figure B.39 compare the powder XRD diffractograms of SiO_2@Mg_2Al-CO_3-AMO-LDHs

samples prepared using a stirring speed of 500 and 1000 rpm, respectively. All samples show the characteristic Bragg reflections of Mg_2Al-CO_3-AMO-LDH superimposed upon the broad silica scattering feature, which were described in Section 4.2. A change in the FWHM of the reflections associated with the LDH is observed, indicating that the crystallite size of the silica-grafted LDH plates is influenced by the metal salt addition rate (Table 4.4). For each fixed stirring speed, the samples prepared using the fastest metal addition rate (8.6 mmol h^{-1}) have the smallest crystallite domain lengths (CDLs, *ca.* 55 and 370 Å, in the *c*-direction and *ab*-plane, respectively). In comparison, the samples prepared using the slowest metal addition rate (1.1 mmol h^{-1}) have the largest CDLs (*ca.* 480 and 1200 Å, in the *c*-direction and *ab*-plane, respectively). The validity of the Scherrer equation, which is used to calculate the CDL, is limited to small crystallites (<100–200 nm) because diffraction peak broadening decreases with increasing crystallite size, so it becomes difficult to accurately estimate the contribution of the sample from the measured peak width.[29] The calculated CDL values should therefore be used with caution on their own, else in support of other measurements.

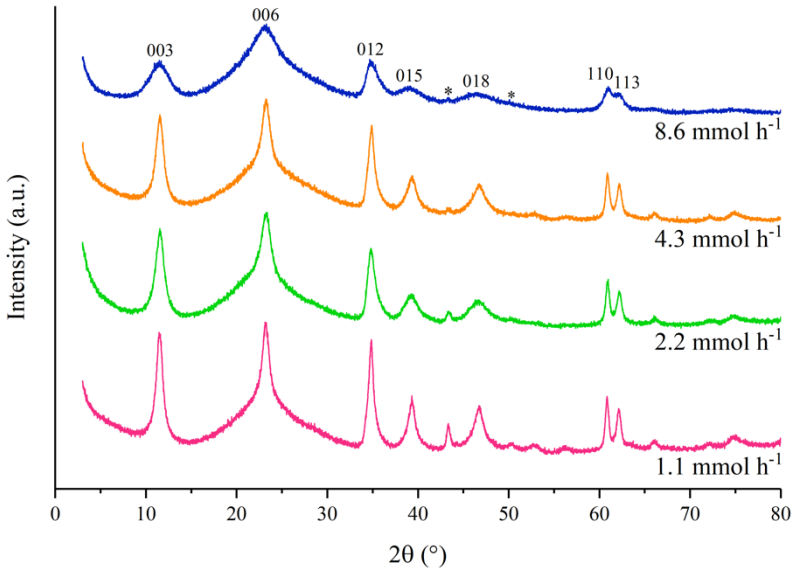


Figure 4.14 Powder XRD diffractograms of SiO_2@Mg_2Al-CO_3-AMO-LDHs prepared using different metal addition rates. Stirring speed = 500 rpm. AMO solvent = EtOH. *Reflections due to the sample holder.

Table 4.4 Lattice parameters and mean CDLs of SiO_2@Mg_2Al-CO_3-AMO-LDHs prepared using different metal addition rates. Stirring speed = 500 rpm.

Metal addition rate (mmol h^{-1})	*d*-spacing (Å)		Lattice parameter (Å)		CDL (Å)	
	d_{003}	d_{110}	$c^{\dagger}$	$a^{\ddagger}$	*c*-axis	*ab*-plane
1.1	7.76	1.52	23.28	3.04	479.8	1209.1
2.2	7.72	1.52	23.16	3.04	479.5	439.4
4.3	7.67	1.52	23.01	3.04	239.8	439.1
8.6	7.71	1.52	23.13	3.04	54.5	369.6

†Lattice parameter $c = 3d_{003}$. ‡Lattice parameter $a = 2d_{110}$.
CDL = $0.89\lambda/\beta\cos\theta$, $\lambda = 1.541847$ Å, β = FWHM in radians.

The TEM images support the XRD results (Figure 4.15). Smaller crystallites and thinner LDH shells are observed for the SiO_2@Mg_2Al-CO_3-AMO-LDHs synthesised at the highest metal addition rate (8.6 mmol h^{-1}, Figure 4.15c).

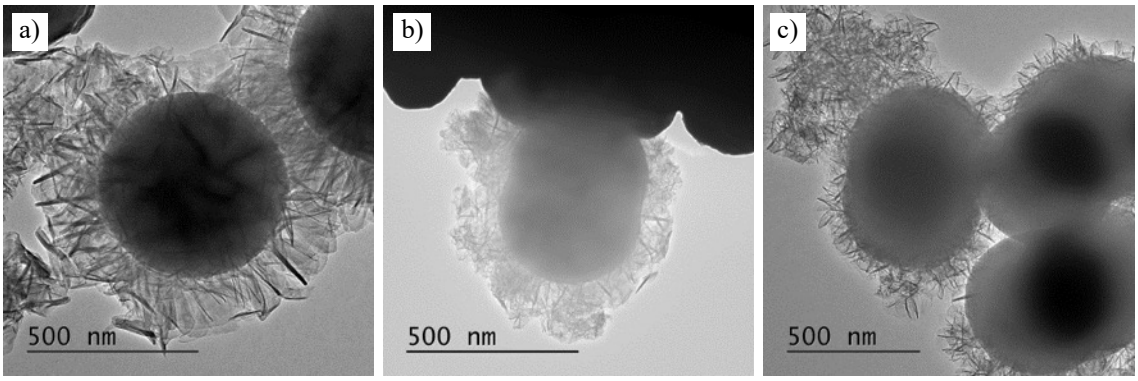


Figure 4.15 TEM images of SiO_2@Mg_2Al-CO_3-AMO-LDHs synthesised with metal addition rates of a) 2.2, b) 4.3, and c) 8.6 mmol h^{-1}. Stirring speed = 750 rpm. AMO solvent = EtOH.

The SiO_2@Mg_2Al-CO_3-AMO-LDHs prepared using the fastest metal addition rates also have a lower zeta potential than that prepared using the slowest addition rate (27 and 29 mV, respectively, Figure 4.16). This suggests that they have thinner LDH coverage on the silica cores. In comparison to the pure LDHs, the core-shell materials have lower zeta potentials and this suggests that the electronic properties of the LDH are perturbed by hybridisation (Figure 4.17).

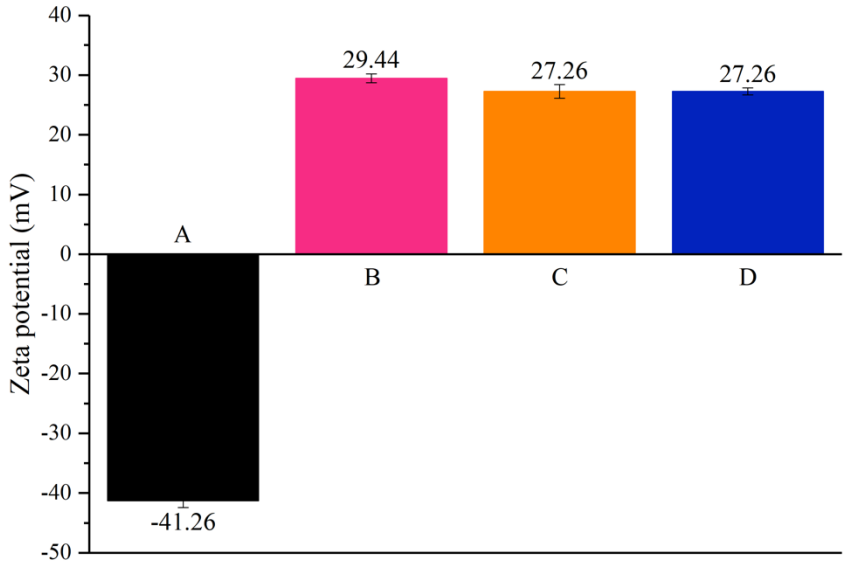


Figure 4.16 Zeta potentials of A) SiO_2 and B) – D) core-shell SiO_2@Mg_2Al-CO_3-AMO-LDHs prepared with different metal addition rates (1.1, 4.3, and 8.6 mmol h^{-1}, respectively). Stirring speed = 500 rpm. AMO solvent = EtOH.

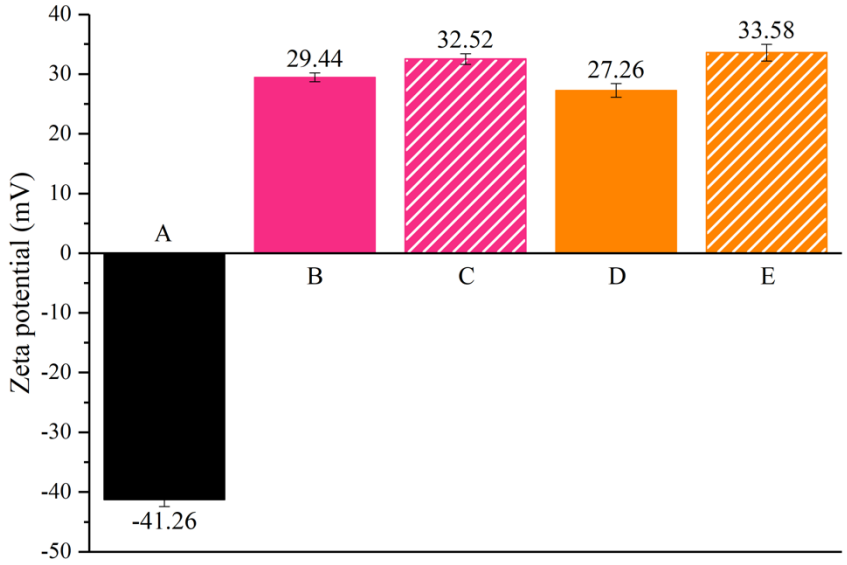


Figure 4.17 Zeta potentials of A) SiO_2; B) and D) core-shell SiO_2@Mg_2Al-CO_3-AMO-LDHs prepared with different metal addition rates (1.1 and 4.3 mmol h^{-1}, respectively); C) and E) reference Mg_2Al-CO_3-AMO-LDHs prepared under the same conditions as the core-shells (1.1 and 4.3 mmol h^{-1}, respectively). Stirring speed = 500 rpm. AMO solvent = EtOH.

These results can be rationalised by taking into account the ageing process. With slower metal addition rates (1.1 and 2.2 mmol h^{-1}), the addition time is longer for the same volume of solution, so the LDH crystallites undergo a longer period of Ostwald ripening. Thus, the LDH platelets have larger CDLs and the LDH shell thickness is greater.

In comparison, with fast metal addition rates (4.3 and 8.6 mmol h^{-1}), supersaturation is high, so the rate of nucleation exceeds that of crystal growth. The LDH platelets also appear to be predominantly vertical with respect to the silica surface. This is due to the conditions of higher saturation generating a large number of nuclei that become compactly packed on the surface, so the *ab*-plane is more accessible to incoming cations than the 003.

Table 4.5 summarises the N_2 BET specific surface areas of SiO_2@Mg_2Al-CO_3-AMO-LDHs synthesised with different metal addition rates. It can be seen that for a given stirring speed the N_2 BET specific surface area is approximately constant. Stirring speed has a greater impact on the surface area.

Table 4.5 N_2 BET specific surface areas and pore volumes of SiO_2@Mg_2Al-CO_3-AMO-LDHs.

Stirring speed (rpm)	Metal addition rate (mmol h^{-1})	N_2 BET specific surface area (m^2 g^{-1})	BET pore volume (cm^3 g^{-1})
250	1.1	65	0.32
250	4.3	74	0.33
500	1.1	94	0.41
500	8.6	100	0.30
1000	1.1	54	0.25
1000	4.3	58	0.27

4.4 Synthesis of SiO_2@AMO-LDHs using commercial silica

4.4.1 Commercial SiO_2

The wider aim of this project is to develop scalable synthesis procedures for the preparation of core-shell SiO_2@LDHs. The modified Stöber synthesis used to prepare SiO_2 for Sections 4.2 and 4.3 is difficult to scale up in the research laboratory, as it involves significant volumes of solvent and washing steps. Therefore, nine commercial SiO_2 were obtained for syntheses of core-shell SiO_2@Mg_2Al-CO_3-AMO-LDHs on a larger scale. The physical properties of the SiO_2 samples are listed in Table 4.6.

In comparison to the SiO_2 prepared by a modified Stöber method, which have a particle size of ~500 nm and an N_2 BET specific surface area of ~6 m^2 g^{-1}, the commercial SiO_2 have much larger size and surface area. The commercial samples are also not all spherical nor uniform in size. As observed in the SEM, the surfaces of the particles are irregular (Figure 4.18). Smooth and uneven surfaces are present in all samples, with some having textured surfaces due to the agglomeration of smaller particles on their surface.

Table 4.6 Physical properties of SiO_2 samples.

Silica	Particle morphology	Particle size (μm)	N_2 BET specific surface area ($m^2\ g^{-1}$)	Av. pore diameter (Å)	Pore volume ($cm^3\ g^{-1}$)
Stöber silica	Spherical	0.5	5.94	39.54	0.006
Grace Davison Davisil® LC60A 20-45	Granular	20 – 45[a] 20 – 80[b]	550[a] 607[b]	60[a] 67[b]	0.9[a] 1.02[b]
Grace Davison Davisil® LC60A 35-70	Granular	35 – 70[a] 30 – 100[b]	550[a] 450[b]	60[a] 68[b]	0.9[a] 0.77[b]
Grace Davison Davisil® LC60A 70-200	Granular	70 – 200[a]	550[a]	60[a]	0.9[a]
Grace Davison Davisil® LC150A 35-70	Granular	35 – 70[a] 40 – 100[b]	330[a] 338[b]	150[a] 138[b]	1.2[a] 1.17[b]
Fuji 1	Spherical	2 – 15[b]	39[b]	123[b]	0.12[b]
Fuji 2	Spherical	2 – 20[b]	45[b]	121[b]	0.14[b]
PQ Corporation ES757 CS6241	Spherical	Median 25[a] 5 – 50[b]	295[a] 270[b]	215[a]	1.6[a]
PQ Corporation ES70X CS6243	Spherical	Median 50[a] 10 – 80[b]	295[a]	215[a]	1.6[a]
PQ Corporation ES70Y CS5764	Spherical	Median 100[a] 30 – 140[b]	295[a]	215[a]	1.6[a]

[a]Manufacturer's data.
[b]Recorded data.

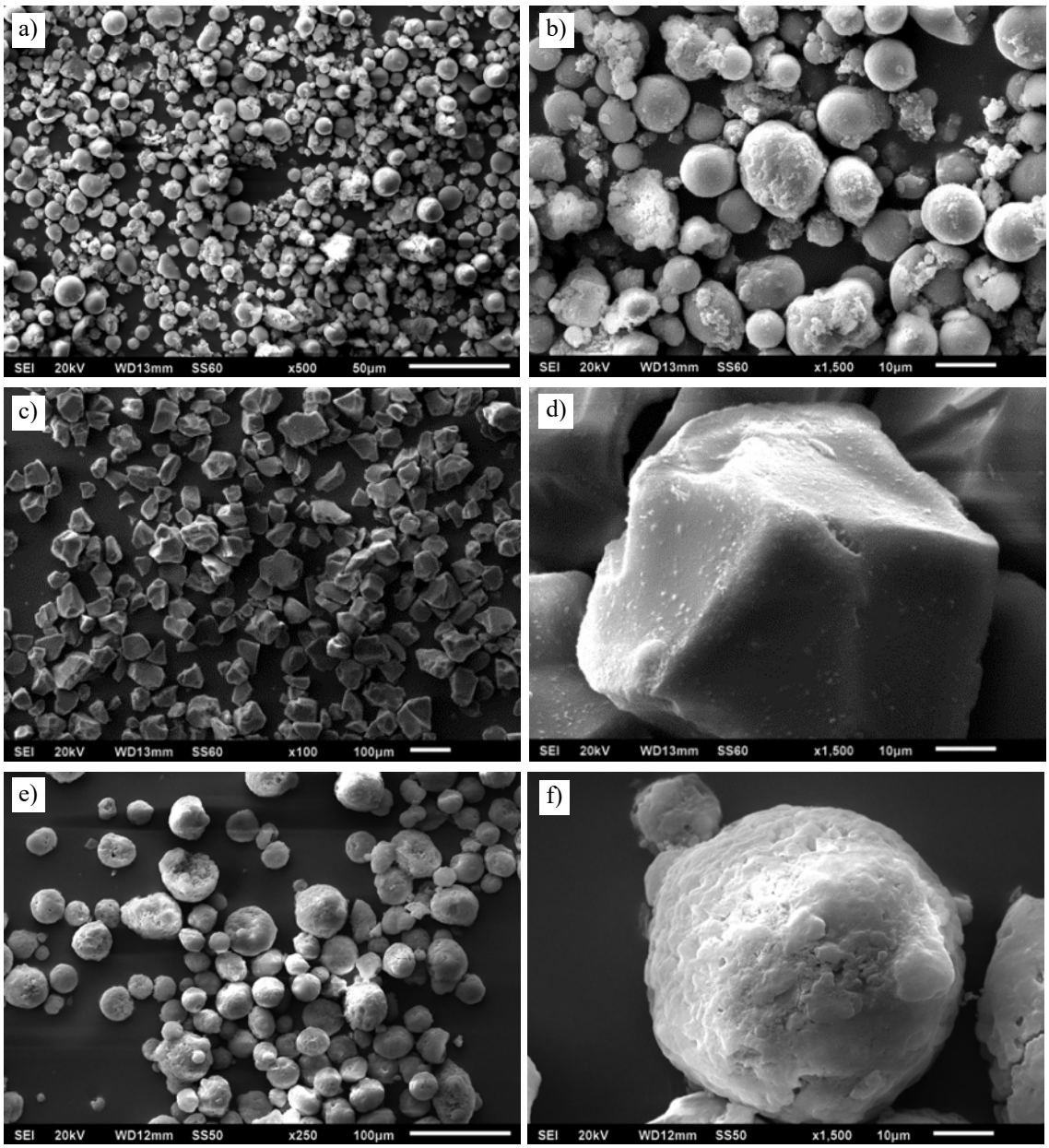


Figure 4.18 SEM images of commercial SiO_2 representing the different morphologies: Fuji 2 (a, b), Grace Davison Davisil® LC60A 35-70 (c, d), and PQ Corp. ES70X (e, f). SEM images for the other commercial SiO_2 may be found in Appendix B, Section B.6.

4.4.2 Commercial SiO_2@LDH preparation

4.4.2.1 *In situ* co-precipitation method

For the initial experiments, spherical silica from Fuji was used as well as a granular silica from Grace Davison. The optimal reaction conditions from Section 4.3 were employed and the *in situ* co-precipitation method was unmodified. A urea hydrothermal method was briefly explored but not pursued further because the results were less promising, and the method was more difficult to scale up (Appendix B Section B.8).

The powder XRD diffractograms of the products contain the Bragg reflections expected of amorphous SiO_2 and crystalline Mg_2Al-CO_3-AMO-LDH (Figure 4.19). The Mg2Al-CO3-AMO-LDH component has lattice parameters a = 3.04 and 3.06 Å, c = 23.10 and 23.31 Å (for Fuji 2 and Grace Davison LC60A 35-70 core-shells, respectively). The characteristic absorption bands are also present in the FTIR spectra (Figure 4.20). However, the limitations of these techniques in differentiating between physically mixed SiO_2 and Mg_2Al-CO_3-AMO-LDH, and chemically bonded SiO_2@Mg_2Al-CO_3-AMO-LDH is apparent when the SEM micrographs are examined (Figures 4.21 and 4.22).

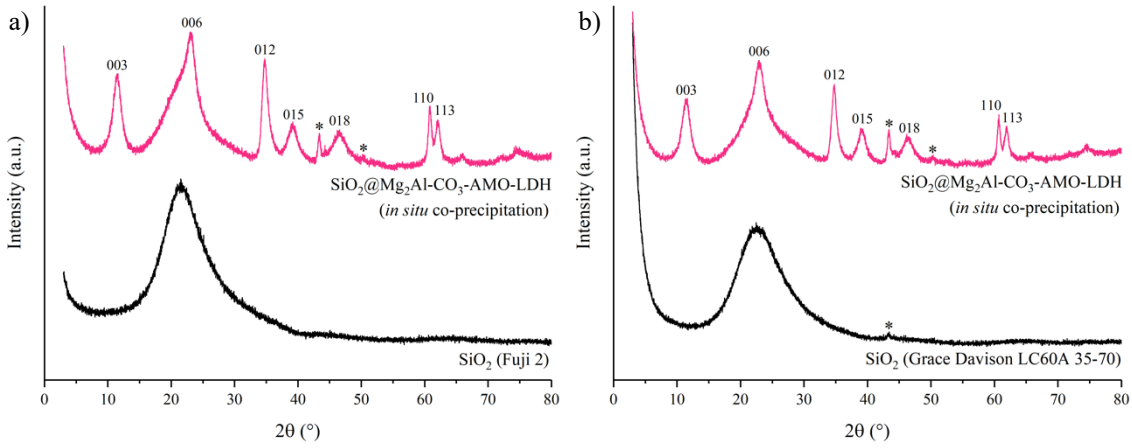


Figure 4.19 Powder XRD diffractograms of SiO_2 and core-shell SiO_2@Mg_2Al-CO_3-AMO-LDH prepared by *in situ* co-precipitation using a) Fuji 2 and b) Grace Davison LC60A 35-70 silicas. Metal addition rate = 1.0 cm^3 min^{-1}. Stirring speed = 500 rpm. AMO solvent = EtOH. *Reflections due to the sample holder.

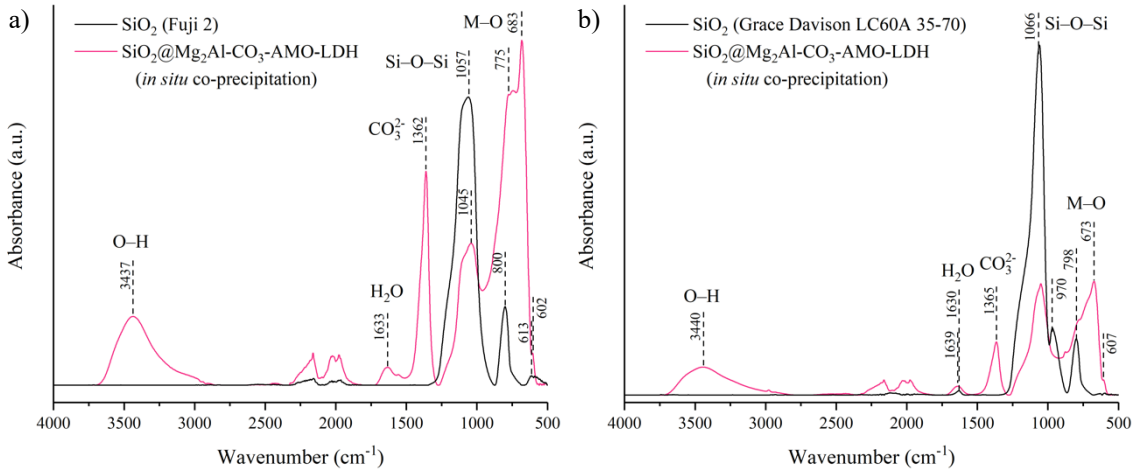


Figure 4.20 FTIR spectra of commercial SiO_2 and core-shell SiO_2@Mg_2Al-CO_3-AMO-LDH prepared by *in situ* co-precipitation using a) Fuji 2 and b) Grace Davison LC60A 35-70 silicas. Metal addition rate = 1.0 cm^3 min^{-1}. Stirring speed = 500 rpm. AMO solvent = EtOH.

In the SEM images there are significant amounts of free LDH. For the Fuji sample, the presence of spherical particles with rough surfaces indicate that core-shell synthesis was successful. Textured angular particles in the Grace Davison sample also indicate the formation of core-shell SiO_2@Mg_2Al-CO_3-AMO-LDH. However, a large proportion of the granular silica particles are uncoated.

The difference in LDH adherence to the granular silicas may be due to a difference in surface properties. On the surface of SiO_2 there exists OH groups (silanols) and bridging Si–O–Si groups (siloxanes). Silanols may be subdivided into (i) isolated, ≡Si–OH; (ii) geminal, =Si–$(OH)_2$; and (iii) vicinal/bridged, ≡Si–OH···HO–Si≡. The relative concentrations of surface silanols and siloxanes depends on the temperature at which the silica is prepared and /or treated. Silanols are hydrophilic and able to form strong hydrogen bonds, whilst siloxanes are hydrophobic,[30] thus resulting in different reactivities towards ions in aqueous solution.

For the spherical silica particles, the surface may contain more silanol groups and defects, resulting in higher reactivity and thus more facile crystallisation of LDH on the surface. In comparison, the granular silica has different crystallographic faces exposed, and these

will have different surface energy, silanol/siloxane concentration and reactivity towards ions.[31] It is possible that these materials exhibit difference surface potentials, but this was not measurable by the zeta potential set-up used in Sections 4.2 and 4.3 because the larger silica particles did not stay suspended in EtOH during measurement.

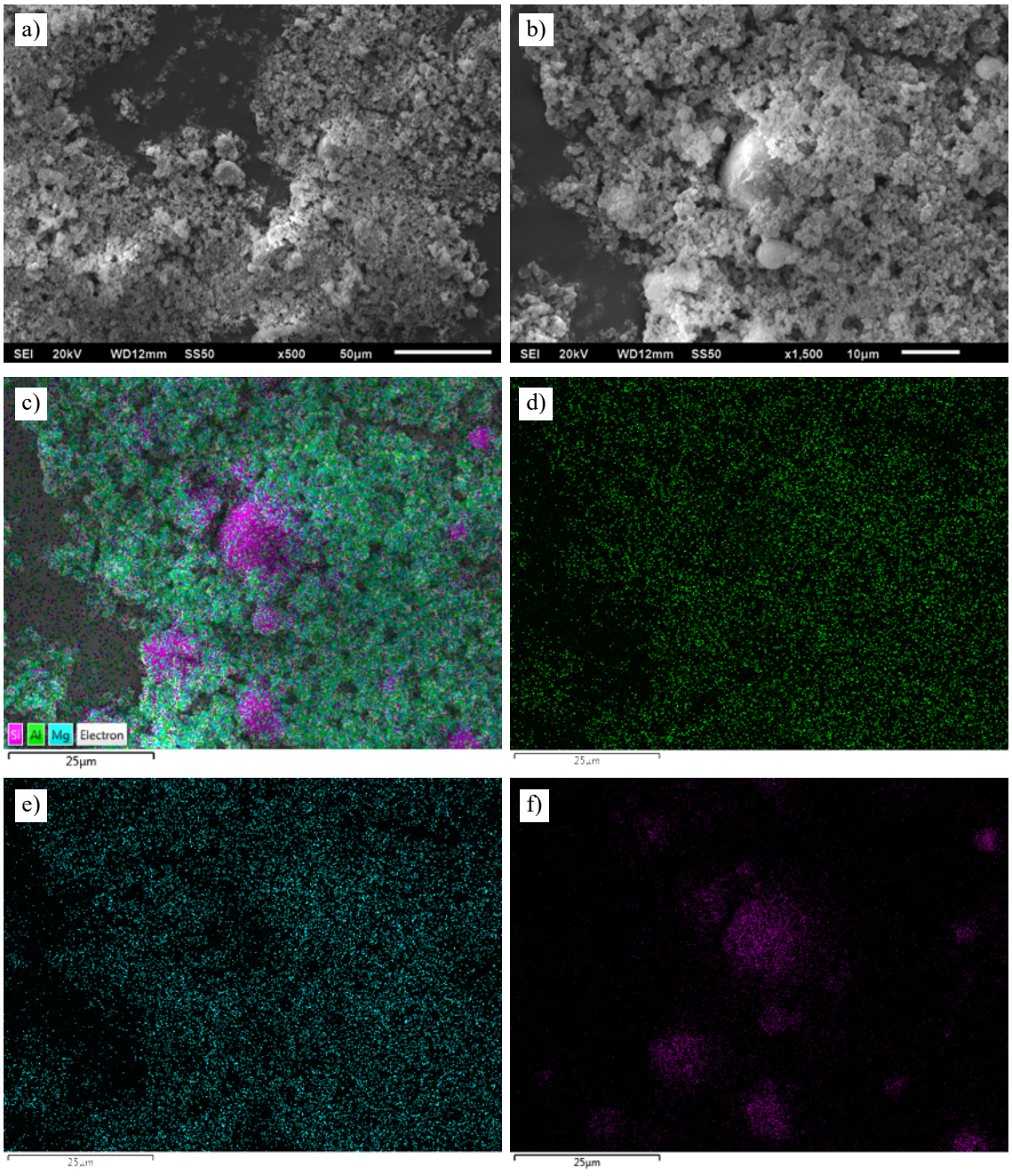


Figure 4.21 a) and b) SEM images of SiO_2@Mg_2Al-CO_3-AMO-LDH prepared by *in situ* co-precipitation using Fuji 2 silica. SEM-EDX c) layered image and analyses of d) Al, e) Mg, and f) Si. Metal addition rate = 1.0 cm^3 min^{-1}. Stirring speed = 500 rpm. AMO solvent = EtOH.

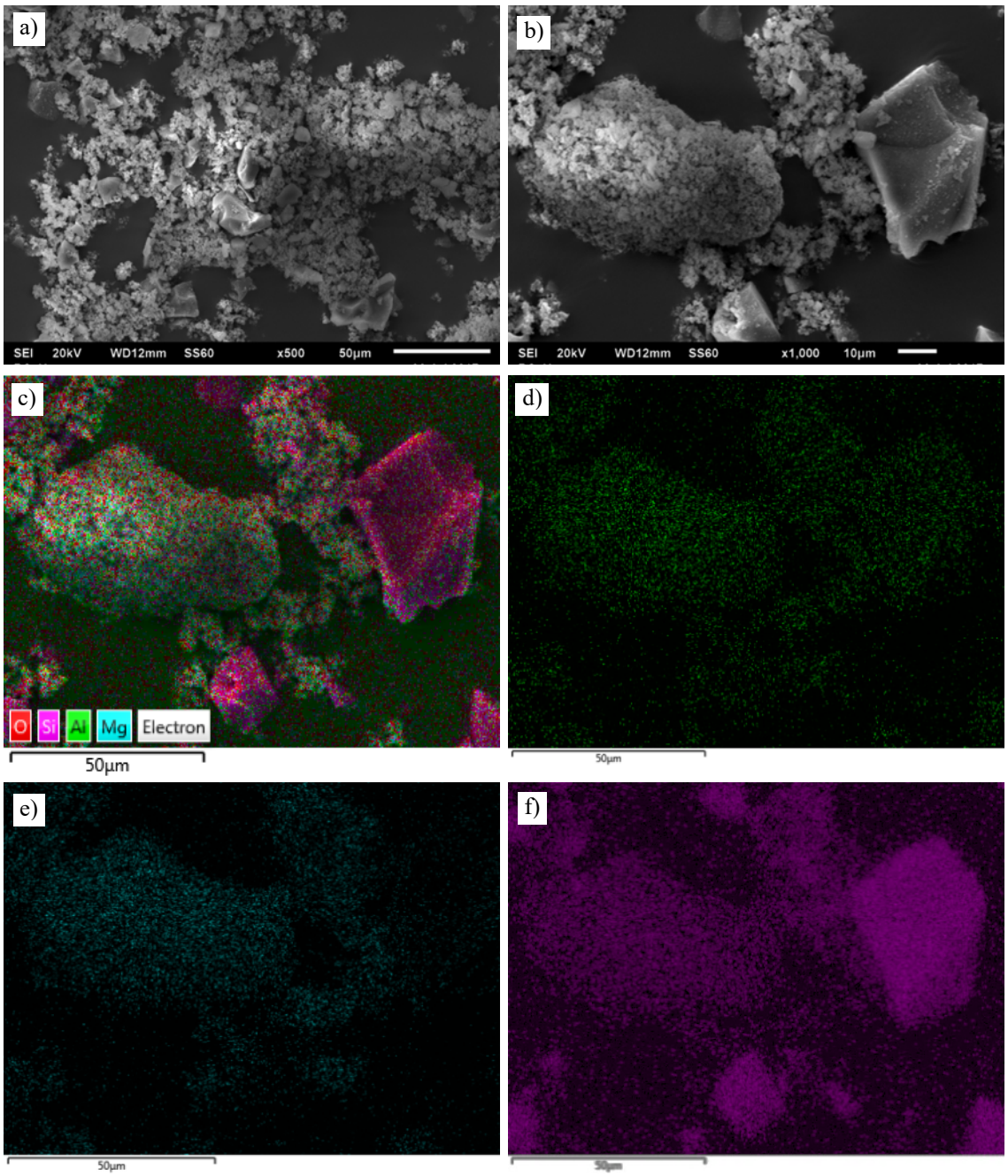


Figure 4.22 a) and b) SEM images of SiO_2@Mg_2Al-CO_3-AMO-LDH prepared by *in situ* co-precipitation using Grace Davison LC60A 35-70 silica. SEM-EDX c) layered image and analyses of d) Al, e) Mg, and f) Si. Metal addition rate = 1.0 cm^3 min^{-1}. Stirring speed = 500 rpm. AMO solvent = EtOH.

In an attempt to isolate the Fuji 2 SiO_2@Mg_2Al-CO_3-AMO-LDH hybrids, the sample was re-dispersed in EtOH and centrifuged at a lower speed to facilitate the separation of the free LDH from the core-shell species. The powder XRD diffractograms and FTIR spectra both show a reduction in intensity of the LDH reflections and bands, respectively

(Figure 4.23). Core-shell species can be observed in the SEM images of the centrifugate and less free LDH is present as well (Figure 4.24 and Appendix B Figure B.95). Furthermore, the cloudy supernatant was examined under SEM and was found to contain the Mg_2Al-CO_3-AMO-LDH almost exclusively (Figure 4.25). This has shown that low speed centrifugation can be a useful post-synthesis step for removing excess free LDH from SiO_2@Mg_2Al-CO_3-AMO-LDH samples. It was a time-consuming procedure however, so it was more effective to target an alternative synthesis technique.

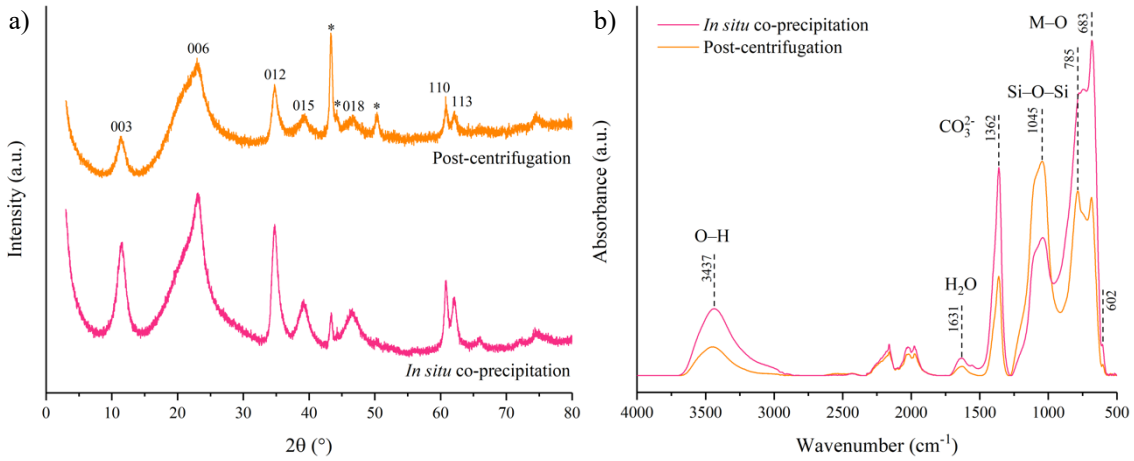


Figure 4.23 a) Powder XRD diffractograms and b) FTIR spectra of SiO_2@Mg_2Al-CO_3-AMO-LDH prepared by *in situ* co-precipitation using Fuji 2 silica, before and after low speed centrifugation (1000 rpm, 5 minutes; four times). Metal addition rate = 1.0 cm^3 min^{-1}. Stirring speed = 500 rpm. AMO solvent = EtOH. *Reflections due to the sample holder.

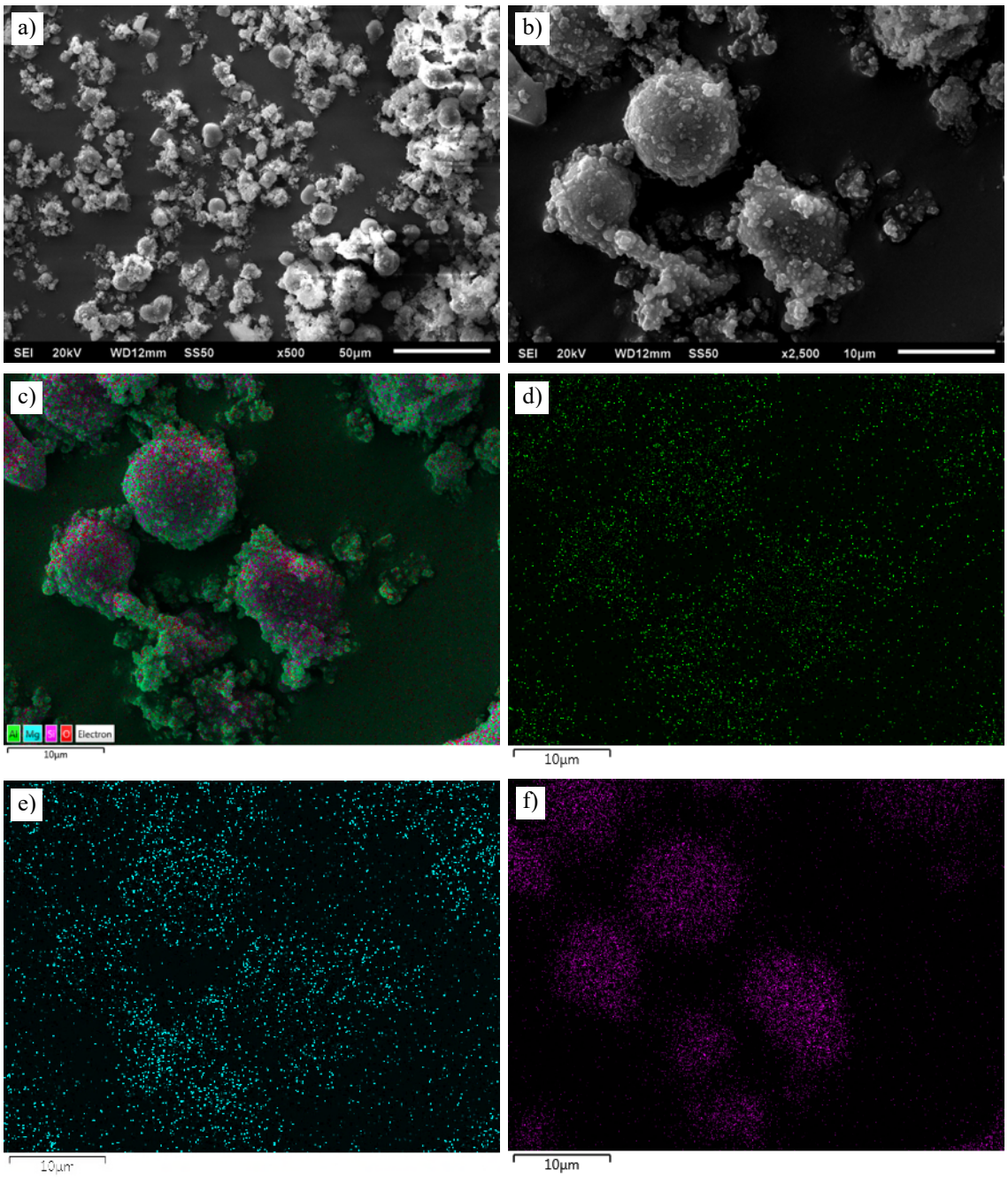


Figure 4.24 a) and b) SEM images of SiO_2@Mg_2Al-CO_3-AMO-LDH obtained after low speed centrifugation of SiO_2@Mg_2Al-CO_3-AMO-LDH prepared by *in situ* co-precipitation using Fuji 2 silica. SEM-EDX c) layered image and analyses of d) Al, e) Mg and f) Si. The dried product was re-dispersed in EtOH and centrifugated (1000 rpm, 5 minutes) four times.

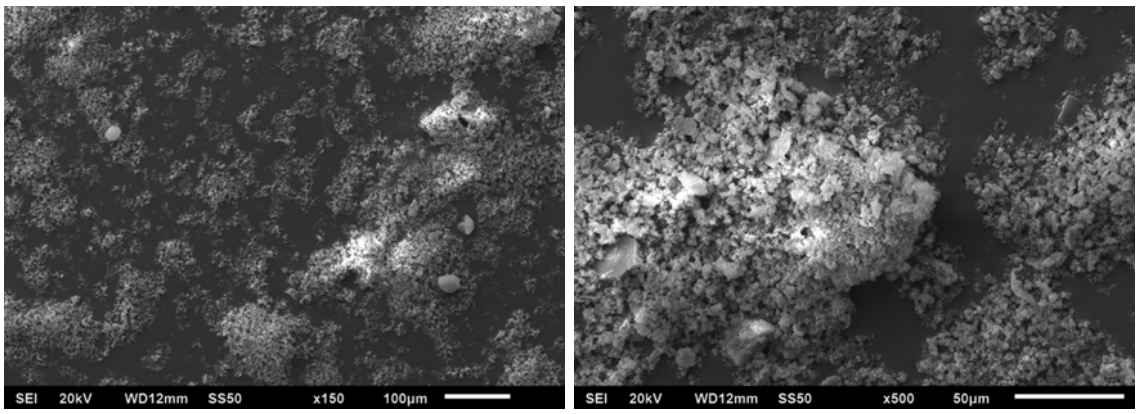


Figure 4.25 SEM images of free LDH obtained by low speed centrifugation (1000 rpm, 5 minutes; four times) of SiO_2@Mg_2Al-CO_3-AMO-LDH prepared by *in situ* co-precipitation using Fuji 2 silica.

4.4.2.2 Modified synthesis method 1 – IMP1

The poor LDH coverage of the granular silica in comparison to the spherical particles suggested that the *in situ* co-precipitation method was not optimal for these particles. In order to promote LDH adhesion and growth to the silica surface, the LDH:SiO_2 ratio was decreased and a wet impregnation step was introduced before the coprecipitation. By first filling the pores of the silica with an aqueous solution containing aluminium cations (Al^{3+}), aluminium-oxygen-silicon bonds (Al–O–Si) could be formed (possibly via rehydration of surface siloxane groups) and these could facilitate LDH nucleation on the surface. In one experiment, all the Al^{3+} was added in the impregnation step and in a separate experiment, only *ca.* 40% of the aluminium salt was used in the impregnation step. Details of these methods, IMP1a and IMP1b, are summarised below.

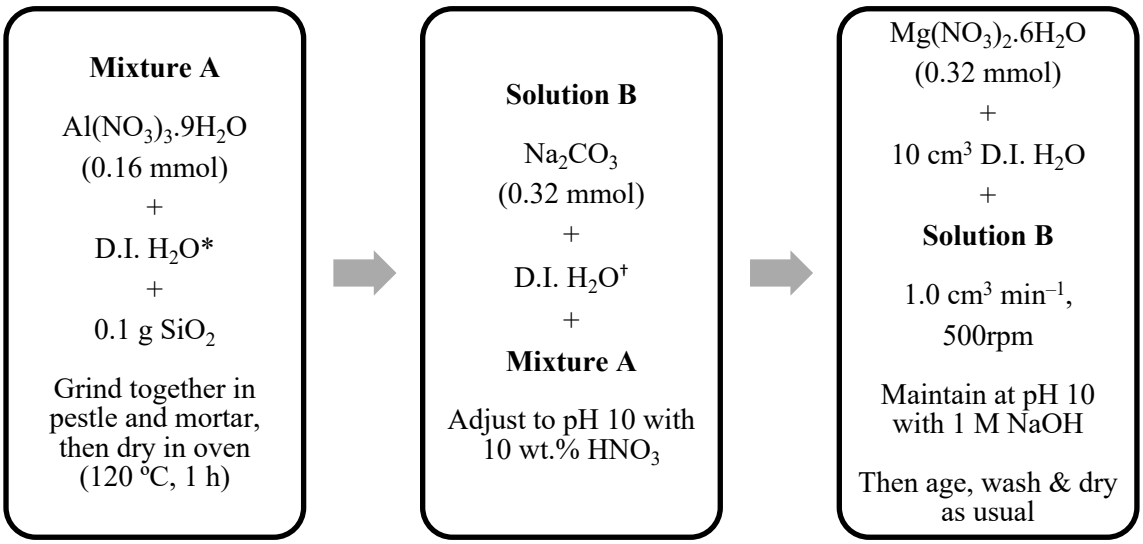


Figure 4.26 Experimental procedure for IMP1a (impregnation with all Al^{3+}). Mg/Al = 2. *equal to pore volume of SiO_2 used. †minimum volume required to dissolve Na_2CO_3.

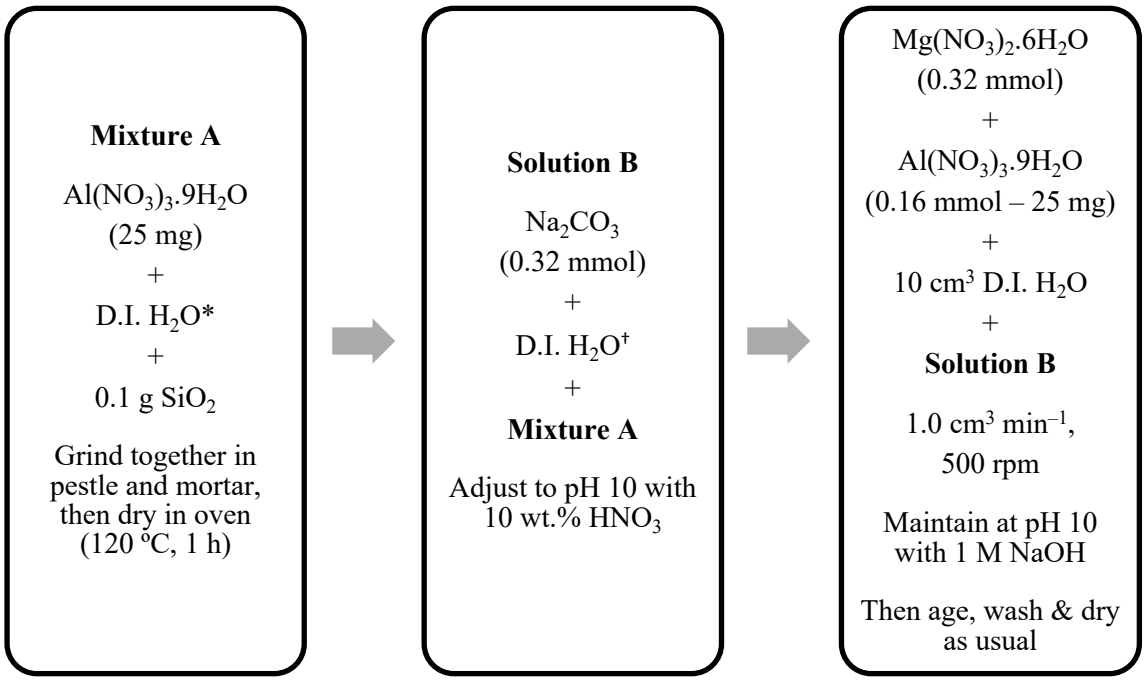


Figure 4.27 Experimental procedure for IMP1b (impregnation with a portion of the Al^{3+}). Mg/Al = 2. *equal to pore volume of SiO_2 used. †minimum volume required to dissolve Na_2CO_3.

The powder XRD diffractograms of the products show the characteristic Bragg reflections of Mg_2Al-CO_3-AMO-LDH and SiO_2 (Figure 4.28a). The intensities of the Bragg reflections due to the Mg_2Al-CO_3-AMO-LDH phase are lower than those in the spectrum of the SiO_2@Mg_2Al-CO_3-AMO-LDH prepared by *in situ* co-precipitation (Section 4.4.2.1) because the total amount of Mg_2Al-CO_3-AMO-LDH has been reduced

by approximately two thirds. The lower LDH:SiO_2 ratio is also responsible for the low intensity of the absorption bands due to the LDH component in the FTIR spectra (Figure 4.28b).

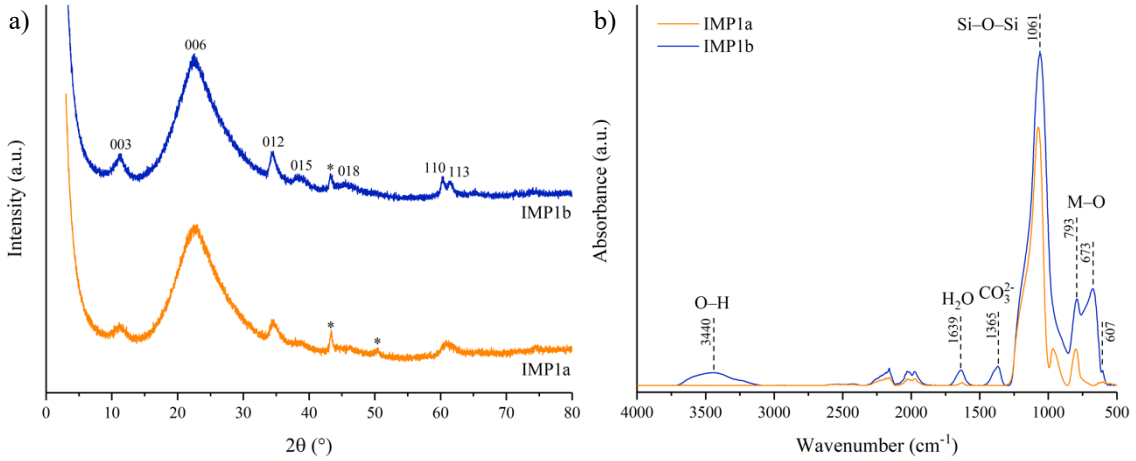


Figure 4.28 a) Powder XRD diffractograms and b) FTIR spectra of SiO_2@Mg_2Al-CO_3-AMO-LDHs prepared by the IMP1a and IMP1b methods using Grace Davison LC60A 35-70 silica. Metal addition rate = 1.0 cm^3 min^{-1}. Stirring speed = 500 rpm. AMO solvent = EtOH. *Reflections due to the sample holder.

Table 4.7 Lattice parameters and mean CLDs of SiO_2@Mg_2Al-CO_3-AMO-LDHs prepared by the IMP1a and IMP1b methods using Grace Davison LC60A 35-70 silica. Metal addition rate = 1.0 cm^3 min^{-1}. Stirring speed = 500 rpm. AMO solvent = EtOH.

Synthesis method	*d*-spacing (Å)		Lattice parameter (Å)		CDL (Å)	
	d_{003}	d_{110}	$c^{\dagger}$	$a^{\ddagger}$	*c*-axis	*ab*-plane
IMP1a	7.90	1.52	23.70	3.04	149.7	301.6
IMP1b	7.88	1.54	23.64	3.08	99.8	677.4

†Lattice parameter $c = 3d_{003}$. ‡Lattice parameter $a = 2d_{110}$.
CDL = $0.89\lambda/\beta\cos\theta$, λ = 1.541847 Å, β = FWHM in radians.

The Bragg reflections due to the Mg_2Al-CO_3-AMO-LDH are broad, indicating a low degree of crystallinity. The 110 Bragg reflection is sharper in the IMP1b sample and corresponds to a larger crystallite size in the *ab*-direction (Table 4.7).

The reflections are less well-defined for the material prepared by IMP1a where the Al^{3+} is all added in the impregnation step. When all the Al^{3+} is added during impregnation,

there are no Al^{3+} cations added alongside Mg^{2+} during coprecipitation. In order for an MgAl-LDH to form, Al^{3+} that is adsorbed onto the silica surface must diffuse into the solution. This rearrangement of ions may take place slower than the rate of Mg^{2+} addition so the growth of the LDH crystallites is slow, thus leading to lower crystallinity. The smaller *a* lattice parameter for the IMP1a sample (3.04 Å) also suggests a higher amount of Al^{3+} in the brucite-like layers.

Analyses with SEM reveal that the amount of free LDH has been reduced, but the particles have a very non-uniform particle size as a result of the grinding technique used to impregnate the silica (Figures 4.29 and 4.30). Elemental analyses by SEM-EDX show regions in the IMP1a sample that contain high concentrations of Si and Al, but low amounts of Mg (highlighted in Figure 4.29c). The distribution of Mg and Al over silica is more uniform in the sample prepared by IMP1b.

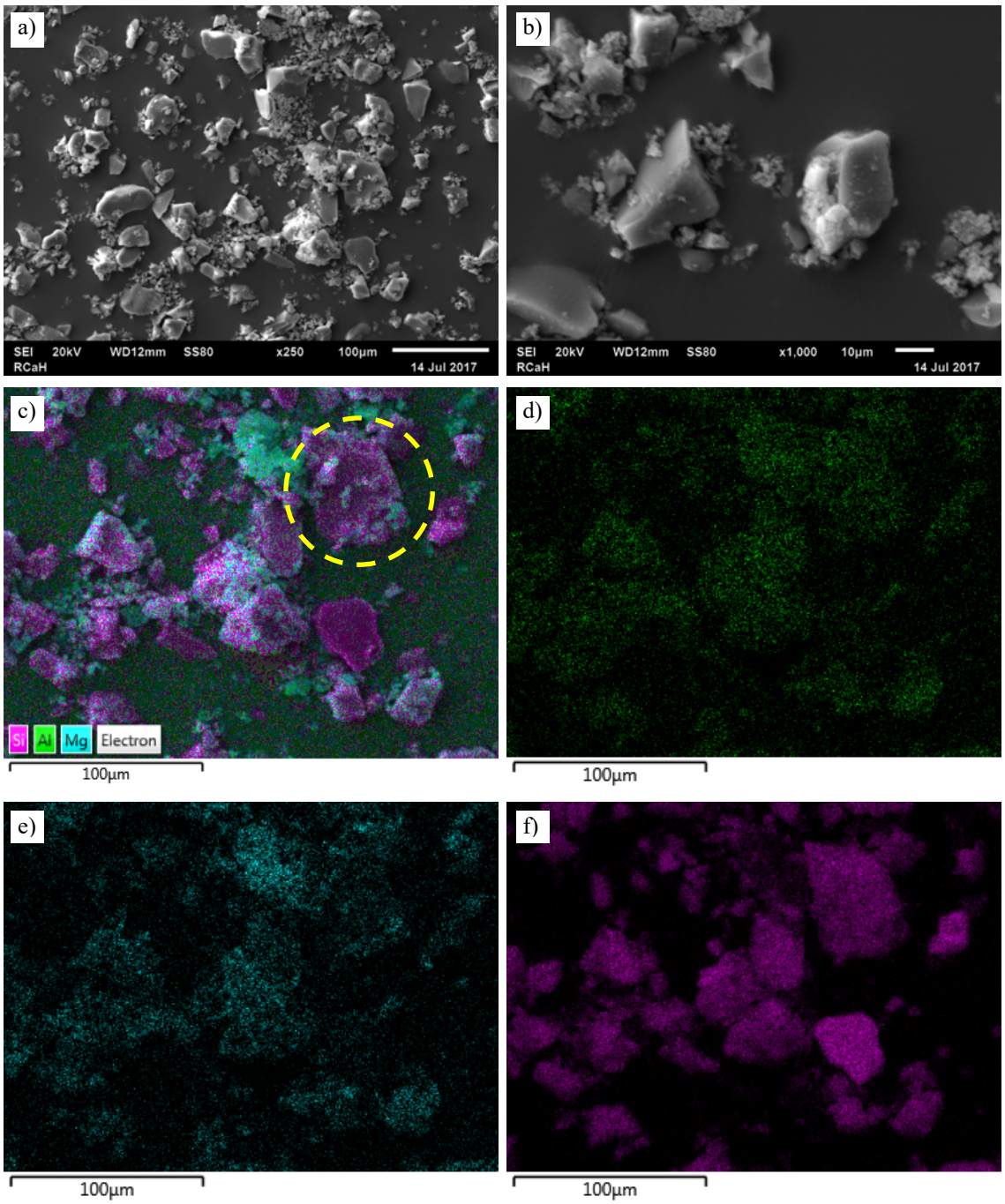


Figure 4.29 a) and b) SEM images of SiO_2@Mg_2Al-CO_3-AMO-LDH prepared by the IMP1a method using Grace Davison LC60A 35-70 silica. SEM-EDX c) layered image and analyses of d) Al, e) Mg, and f) Si. Metal addition rate = 1.0 cm^3 min^{-1}. Stirring speed = 500 rpm. AMO solvent = EtOH.

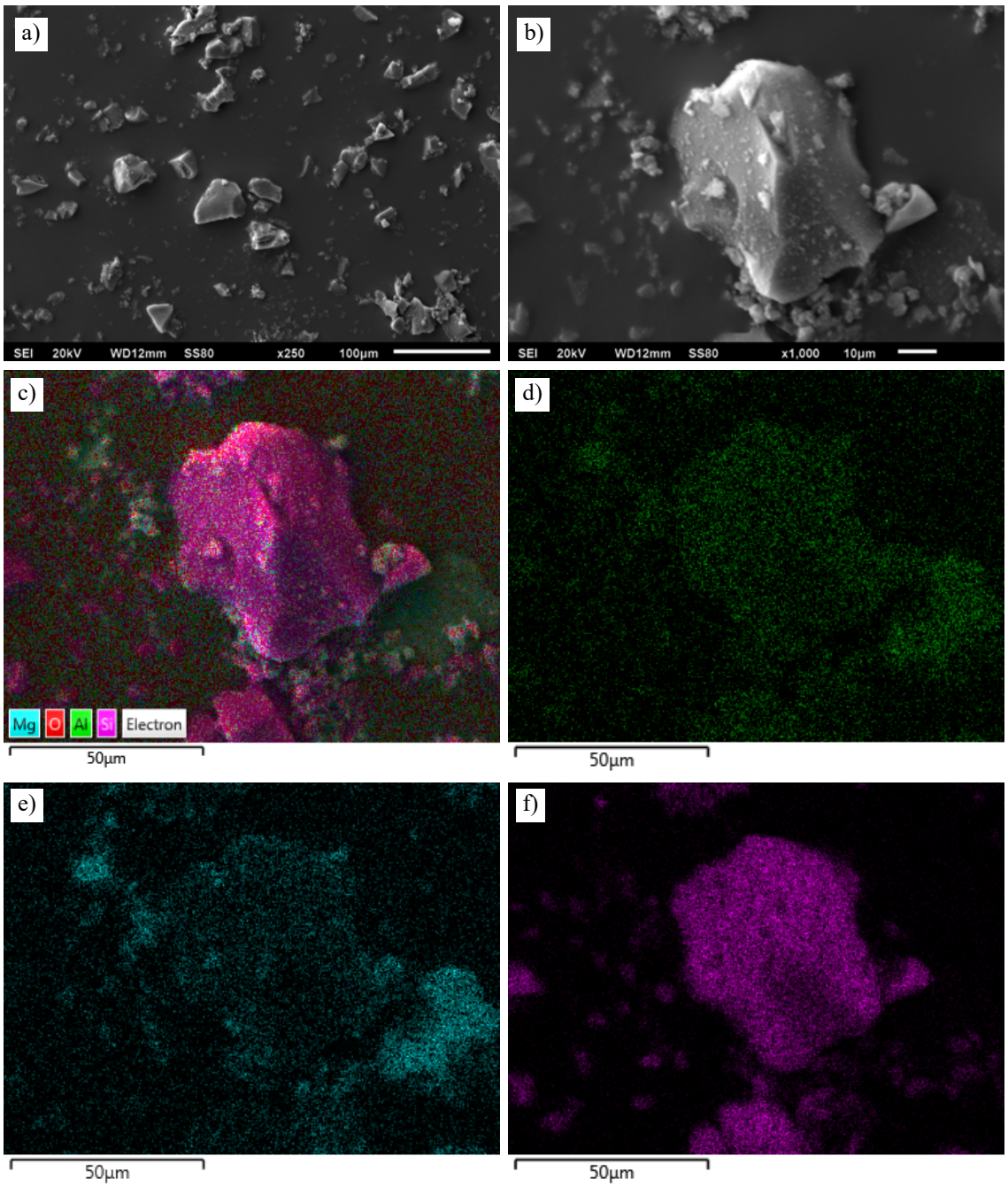


Figure 4.30 a) and b) SEM images of SiO_2@Mg_2Al-CO_3-AMO-LDH prepared by the IMP1b method using Grace Davison LC60A 35-70 silica. SEM-EDX c) layered image and analyses of d) Al, e) Mg, and f) Si. Metal addition rate = 1.0 cm^3 min^{-1}. Stirring speed = 500 rpm. AMO solvent = EtOH.

4.4.2.3 Modified synthesis method 2 – IMP2

In order to preserve the primary particle size and homogeneity, the method was modified to have the silica and Al^{3+} solution mixed in a mortar using a thin spatula instead of the pestle. This method, IMP2, is summarised in Figure 4.31.

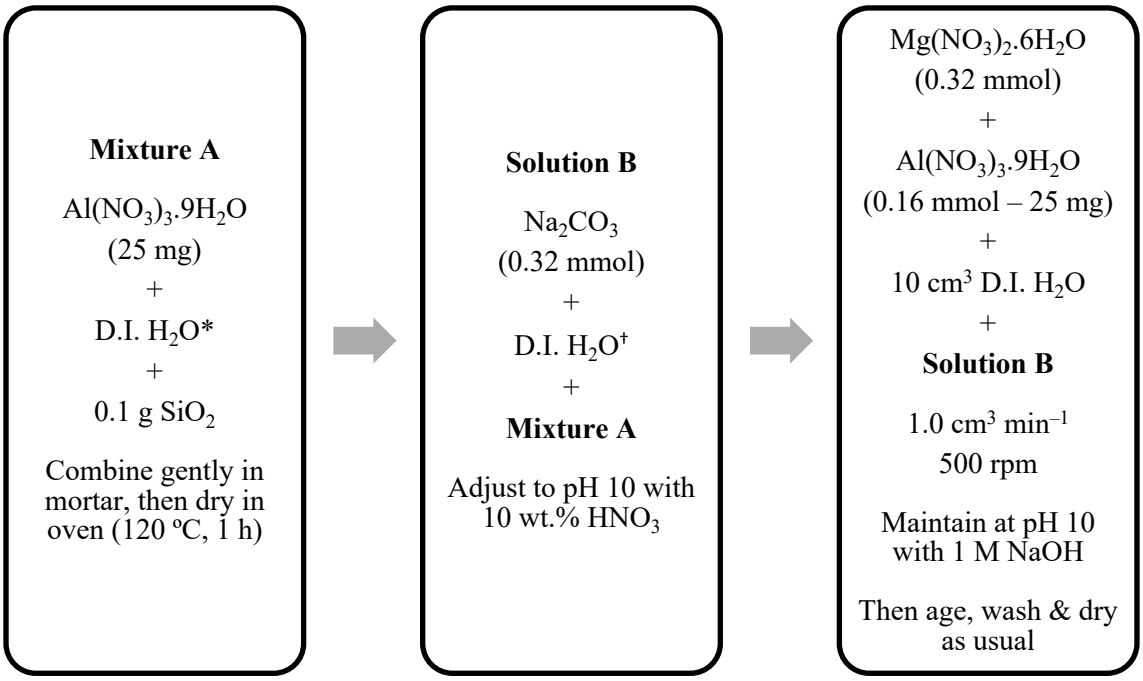


Figure 4.31 Experimental procedure for IMP2 (gentle impregnation with a portion of the Al^{3+}). Mg/Al = 2. *equal to pore volume of SiO_2 used. †minimum volume required to dissolve Na_2CO_3.

The powder XRD diffractogram and FTIR spectrum of the IMP2 SiO_2@Mg_2Al-CO_3-AMO-LDH are very similar to the IMP1b spectra (Figure 4.32). The main difference between the XRD diffraction patterns is the broader Bragg reflections for the IMP2 SiO_2@Mg_2Al-CO_3-AMO-LDH. This may be due to there being fewer small SiO_2 cores available for LDH to grow on in the IMP2 case, as the silica particles are not milled into smaller pieces during the impregnation step, thus promoting LDH growth over larger surface areas, so the LDH shells are thinner with less aggregation of LDH in small clusters.

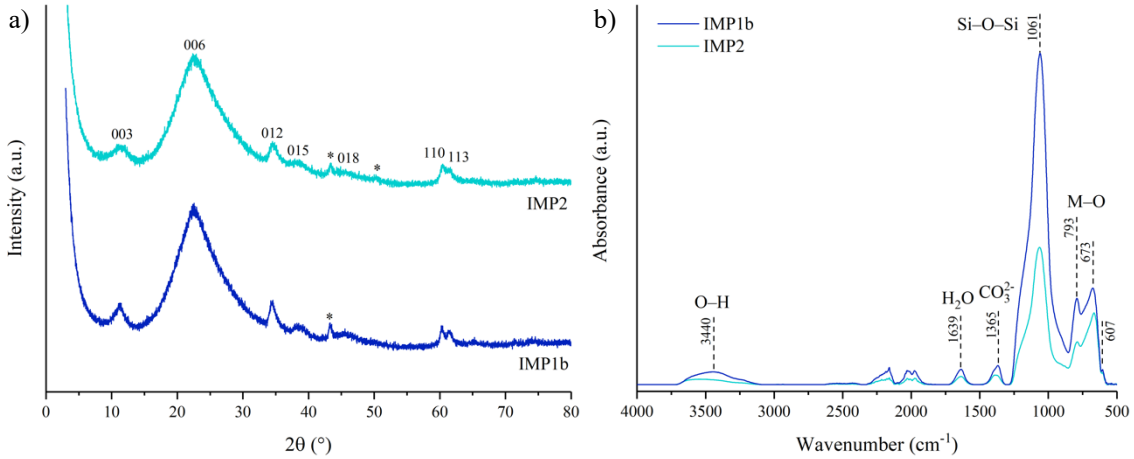


Figure 4.32 a) Powder XRD diffractograms and b) FTIR spectra of SiO_2@Mg_2Al-CO_3-AMO-LDH prepared by the IMP1b and IMP2 methods using Grace Davison LC60A 35-70 silica. Metal addition rate = 1.0 cm^3 min^{-1}. Stirring speed = 500 rpm. AMO solvent = EtOH. *Reflections due to the sample holder.

The crystallinity of the LDH component can be increased by extending the ageing time at room temperature (Figure 4.33). This is due to Ostwald ripening.

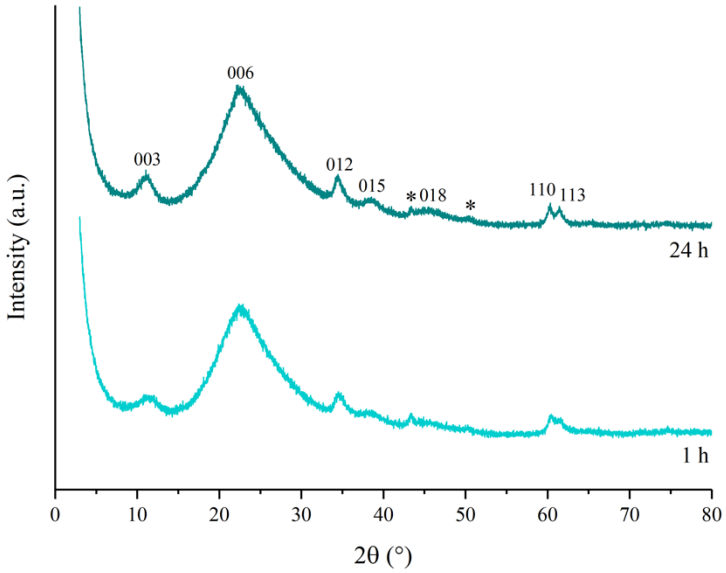


Figure 4.33 Powder XRD diffractograms of SiO_2@Mg_2Al-CO_3-AMO-LDH prepared by the IMP2 method with different ageing times using Grace Davison LC60A 35-70 silica. Metal addition rate = 1.0 cm^3 min^{-1}. Stirring speed = 500 rpm. AMO solvent = EtOH. *Reflections due to the sample holder.

The SEM images show that the gentler mixing method allows the silica particles to remain intact whilst also promoting LDH growth on the silica surfaces (Figure 4.34).

Some free LDH remains present but element mapping by SEM-EDX shows uniform distributions of the metals over the silica particles.

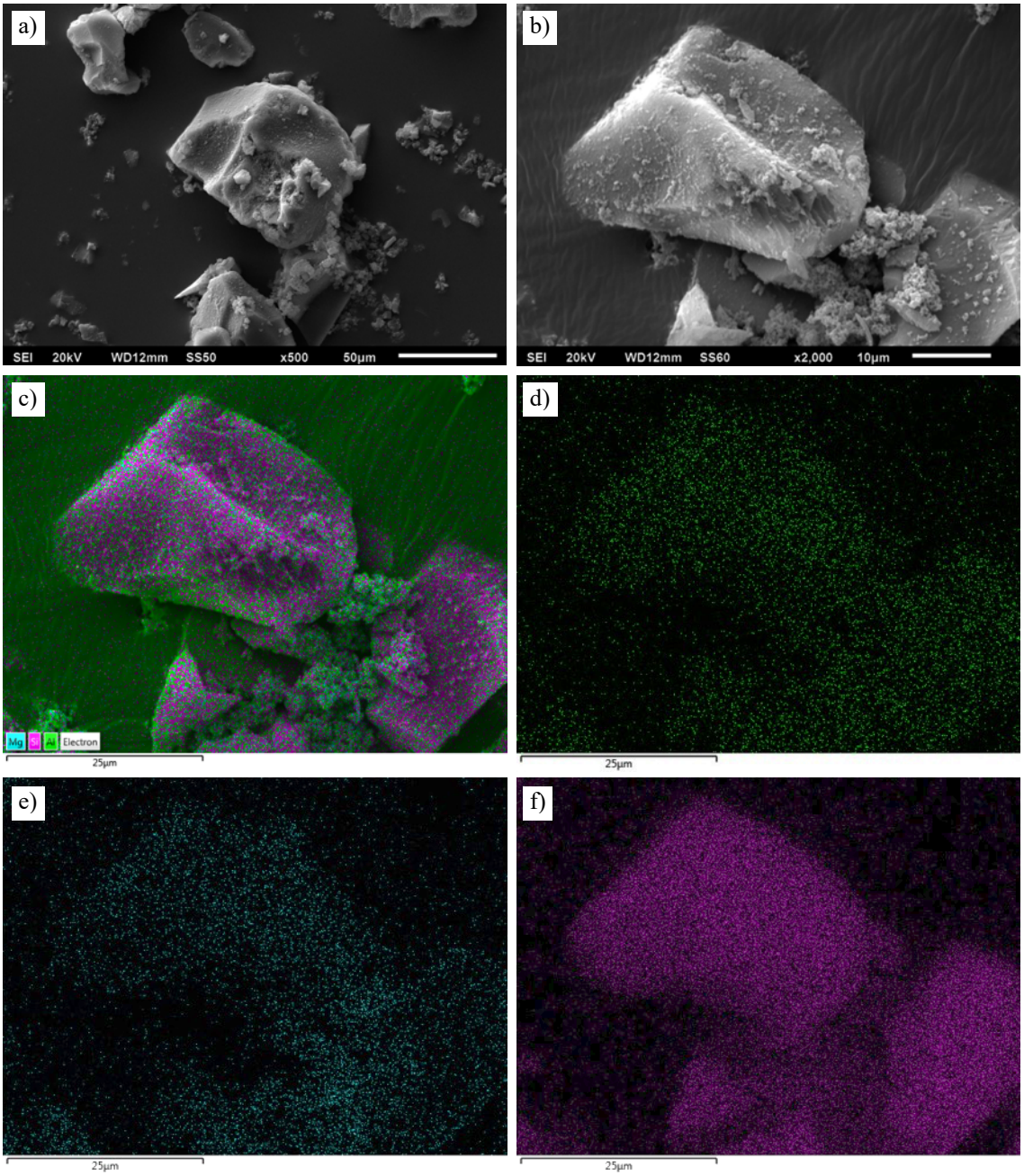


Figure 4.34 a) and b) SEM images of SiO_2@Mg_2Al-CO_3-AMO-LDH prepared by the IMP2 method using Grace Davison LC60A 35-70 silica. SEM-EDX c) layered image and analyses of d) Al, e) Mg, and f) Si. Metal addition rate = 1.0 cm^3 min^{-1}. Stirring speed = 500 rpm. AMO solvent = EtOH.

With this improvement in LDH coverage, the IMP2 was applied to Fuji 2 silica and scaled up. The powder XRD diffractograms and FTIR spectra confirm the presence of LDH in

the samples (Figure 4.35). The SEM images show almost no free LDH and very good LDH coverage of the SiO_2 particles (Figures 4.36 and 4.37).

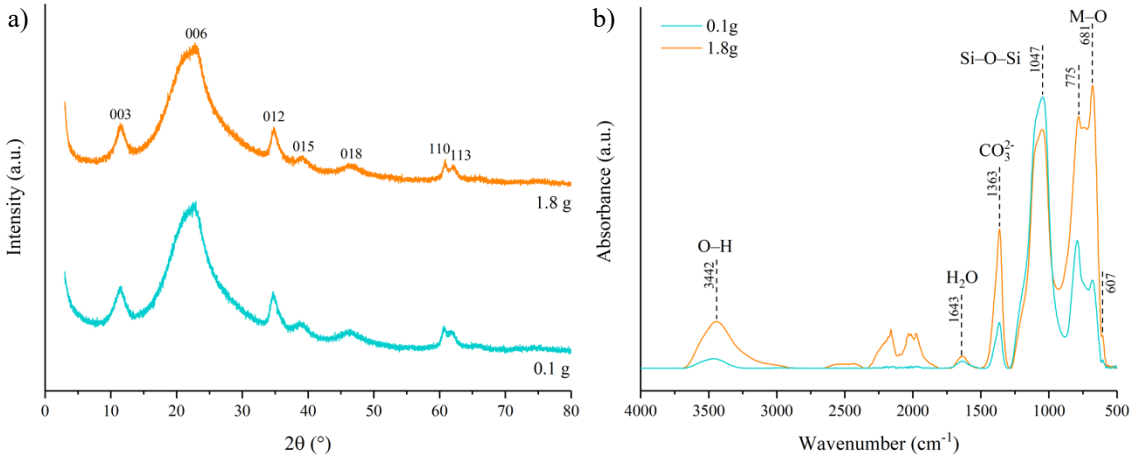


Figure 4.35 a) Powder XRD diffractograms and b) FTIR spectra of SiO_2@Mg_2Al-CO_3-AMO-LDHs prepared by the IMP2 method using Fuji 2 silica. Batch sizes: 0.1 and 1.8 g. Metal addition rate = 1.0 cm^3 min^{-1}. Stirring speed = 500 rpm. AMO solvent = EtOH.

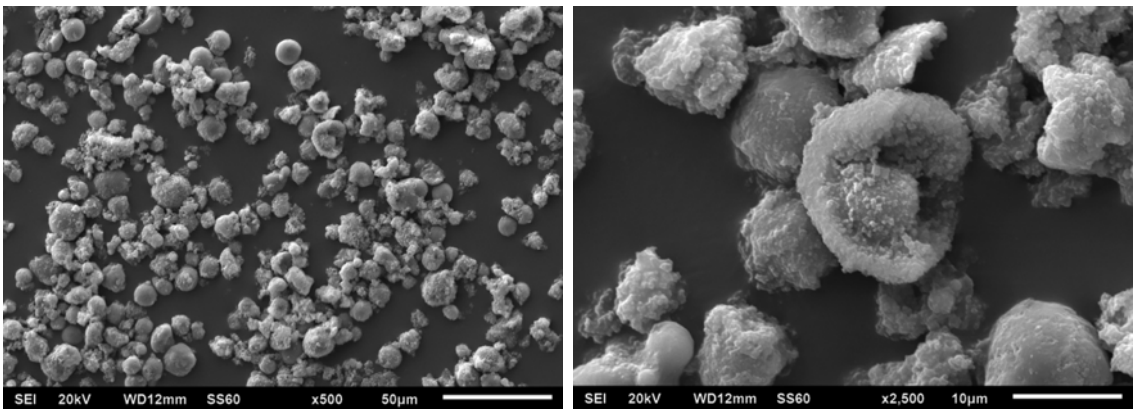


Figure 4.36 SEM images of SiO_2@Mg_2Al-CO_3-AMO-LDH prepared by the IMP2 method using Fuji 2 silica. Batch size: 0.1 g. Metal addition rate = 1.0 cm^3 min^{-1}. Stirring speed = 500 rpm. AMO solvent = EtOH.

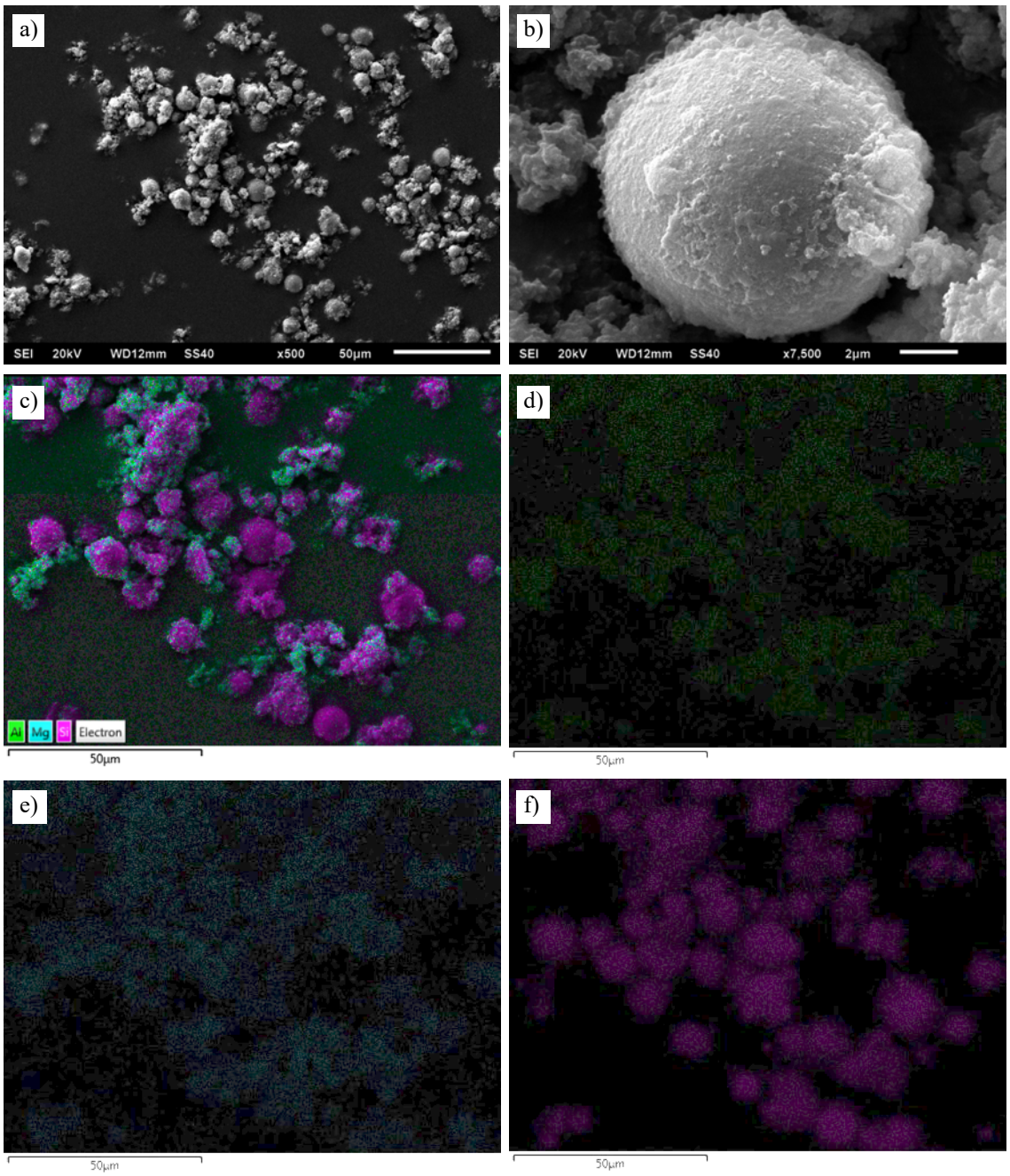


Figure 4.37 a) and b) SEM images of SiO_2@Mg_2Al-CO_3-AMO-LDH prepared by the IMP2 method using Fuji 2 silica. Batch size = 1.8 g. SEM-EDX c) layered image and analyses of d) Al, e) Mg, and f) Si. Metal addition rate = 1.0 cm^3 min^{-1}. Stirring speed = 500 rpm. AMO solvent = EtOH.

The core-shell SiO_2@Mg_2Al-CO_3-AMO-LDH prepared with Fuji 2 silica using the IMP2 method has an N_2 BET specific surface area of 64 cm^3 g^{-1}, which is a 42% increase on the surface area of the silica (Figure 4.38a). The total pore volume of the SiO_2@Mg_2Al-CO_3-AMO-LDHs are approximately double the pore volume of the pure silica (Figure

4.38b). Both of the N_2 isotherms are classified as Type IV, corresponding to mesoporous materials, and the hysteresis curves are Type H3, characteristic of non-rigid aggregated of plate-like particles (Figure 4.39a). The BJH pore size distribution shows that the increase in surface area and pore volume is due to an increase in the number of pores having widths between 50–350 Å (Figure 4.39b).

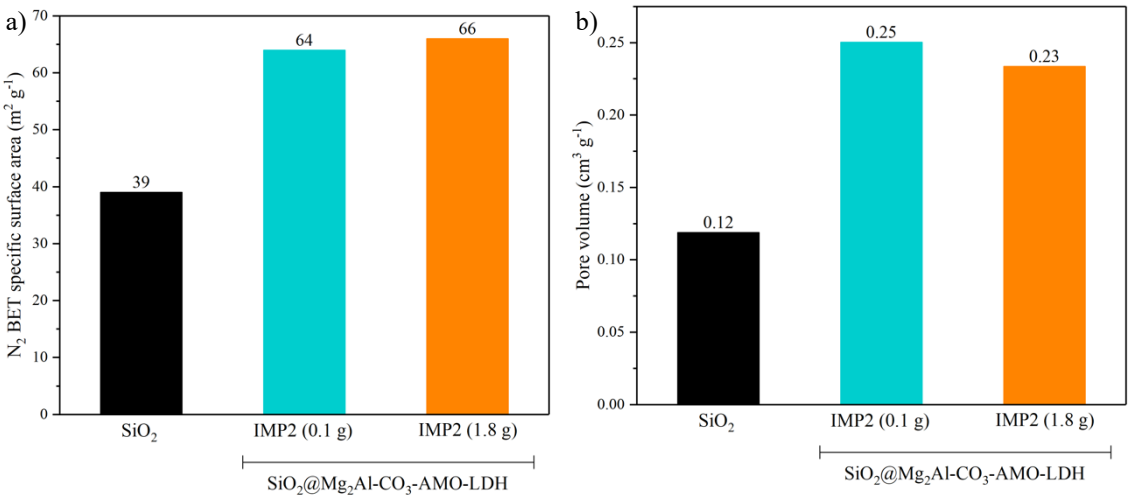


Figure 4.38 a) N_2 BET specific surface areas and b) pore volumes of SiO_2 and SiO_2@Mg_2Al-CO_3-AMO-LDH prepared by the IMP2 method using Fuji 2 silica. Batch sizes: 0.1 and 1.8 g. Metal addition rate = 1.0 cm^3 min^{-1}. Stirring speed = 500 rpm. AMO solvent = EtOH.

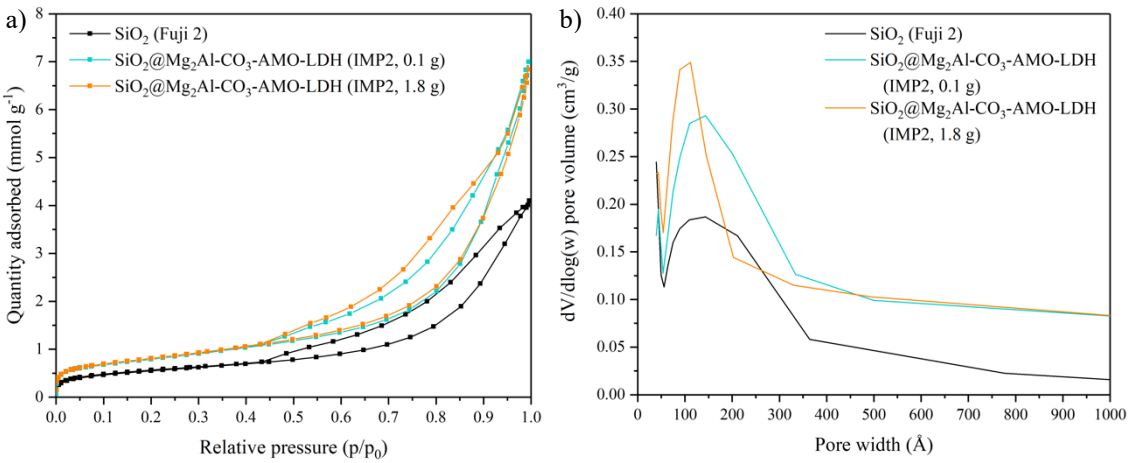


Figure 4.39 a) N_2 adsorption and desorption isotherms and b) BJH pore size distributions of SiO_2 and SiO_2@Mg_2Al-CO_3-AMO-LDH prepared by the IMP2 method using Fuji 2 silica. Batch sizes: 0.1 and 1.8 g. Metal addition rate = 1.0 cm^3 min^{-1}. Stirring speed = 500 rpm. AMO solvent = EtOH.

4.4.2.4 Effect of metal addition rate

The effect of metal addition rate was studied using the IMP2 method. As shown in Figure 4.40a and Table 4.8, the crystallinities of the LDH component vary between the different addition speeds. The sharpest basal (*e.g.* 00*l*) Bragg reflections are observed for the slowest addition rates (0.25 and 0.50 cm^3 min^{-1}) and this is due to the longer overall reaction time that these samples experience, which allows them to undergo Ostwald ripening and growth in the *c*-direction. In contrast, the *hk*0 Bragg reflections at 2θ = 60–63° do not show as much variation in peak width nor intensity as the basal reflections. This suggest that the metal addition speed does not have significant influence on the growth of the LDH platelets in the *ab*-direction.

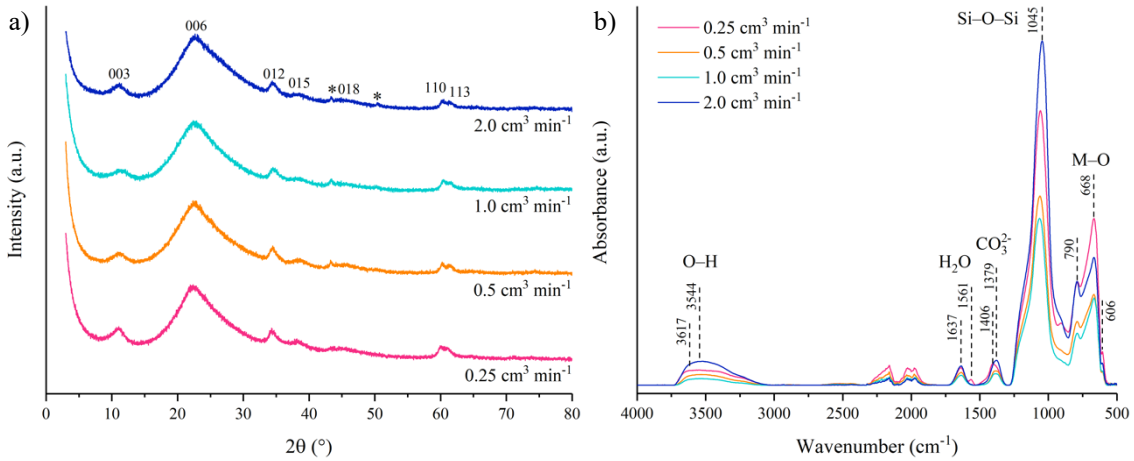


Figure 4.40 a) Powder XRD diffractograms and b) FTIR spectra of SiO_2@Mg_2Al-CO_3-AMO-LDH prepared by the IMP2 method with different metal addition rates using Grace Davison LC60A 35-70 silica. Stirring speed = 500 rpm. AMO solvent = EtOH. *Reflections due to the sample holder.

Table 4.8 Lattice parameters and mean CDLs of SiO_2@Mg_2Al-CO_3-AMO-LDH prepared by the IMP2 method with different metal addition rates using Grace Davison LC60A 35-70 silica. Stirring speed = 500 rpm. AMO solvent = EtOH.

Metal addition rate (cm^3 min^{-1})	*d*-spacing (Å)		Lattice parameter (Å)		CDL (Å)	
	d_{003}	d_{110}	$c^{\dagger}$	$a^{\ddagger}$	*c*-axis	*ab*-plane
0.25	8.02	1.52	24.06	3.04	66.5	241.9
0.5	7.96	1.54	23.88	3.08	119.8	788.1
1.0	7.91	1.53	23.73	3.06	66.5	297.8
2.0	7.98	1.53	23.94	3.06	85.5	395.3

†Lattice parameter $c = 3d_{003}$. ‡Lattice parameter $a = 2d_{110}$.
CDL = $0.89\lambda/\beta\cos\theta$, λ = 1.541847 Å, β = FWHM in radians.

The core-shell synthesised with the fastest metal addition rate has the strongest Si–O–Si absorption band, relative to the intensity of the carbonate absorption at *ca*. 1360 cm^{-1} (Figure 4.40b). This suggests that it has the lowest LDH:SiO_2 ratio, which may arise from the short overall reaction time. The SEM images also show that the sample prepared with fast metal addition rates contain more free LDH and also LDH clusters on the surface of the silica particles (Figure 4.41 and Appendix B Figures B.76–B.80). In contrast, a uniform LDH shell if observed in the sample prepared with the slowest addition speed (0.25 cm^3 min^{-1}, Figure 4.42). When the Mg^{2+}/Al^{3+} solution is added slowly, the concentration of metal ions in the suspension is low so the rate of nucleation in solution is slow. The metal ions and/or LDH nuclei preferentially adsorb onto the silica surfaces where there are Si–O–Al (from the impregnation step) that can facilitate LDH growth.

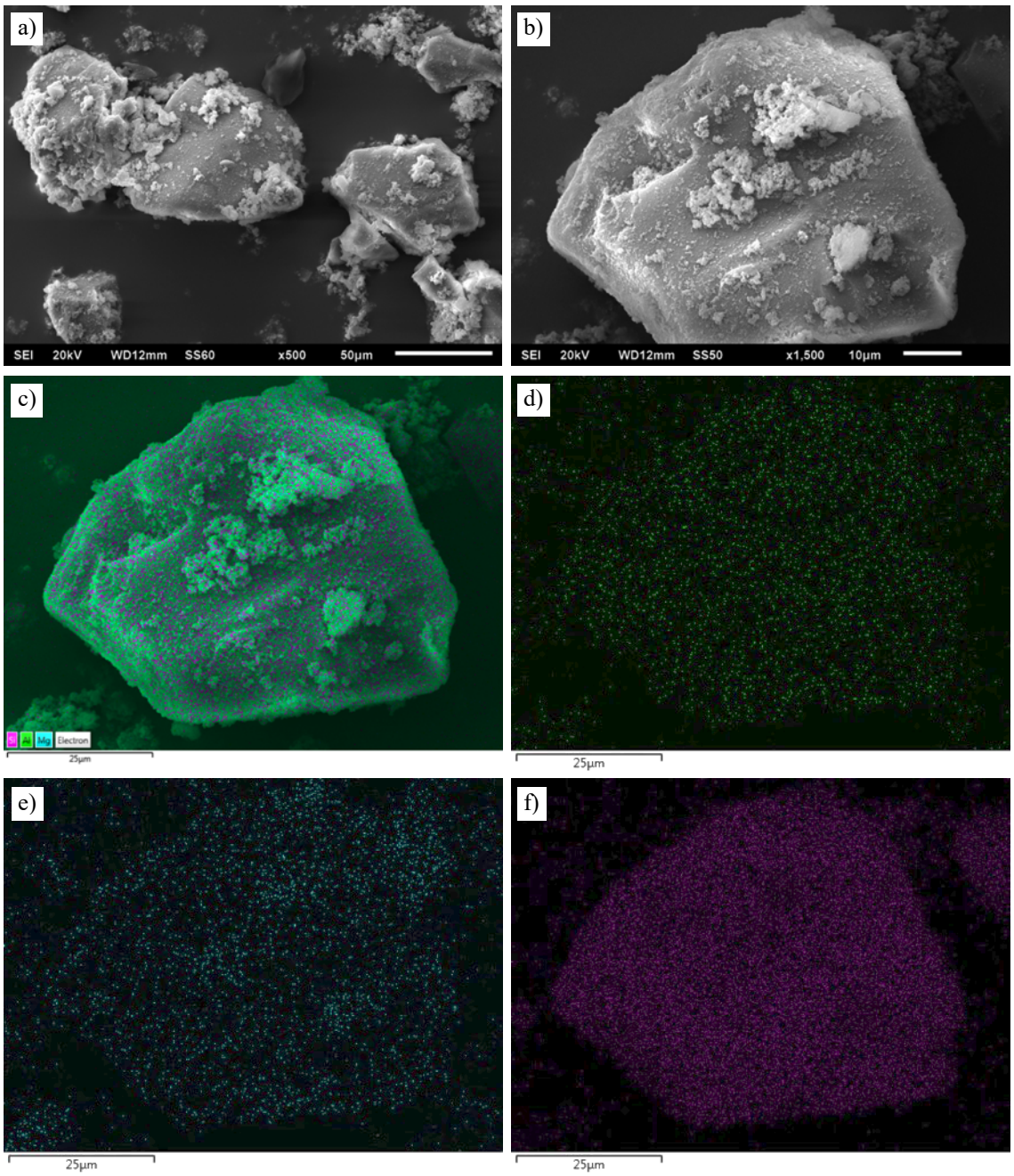


Figure 4.41 a) and b) SEM images of SiO_2@Mg_2Al-CO_3-AMO-LDH prepared by the IMP2 method using Grace Davison LC60A 35-70 silica. SEM-EDX c) layered image and analyses of d) Al, e) Mg, and f) Si. Metal addition rate = 2.0 cm^3 min^{-1}. Stirring speed = 500 rpm. AMO solvent = EtOH.

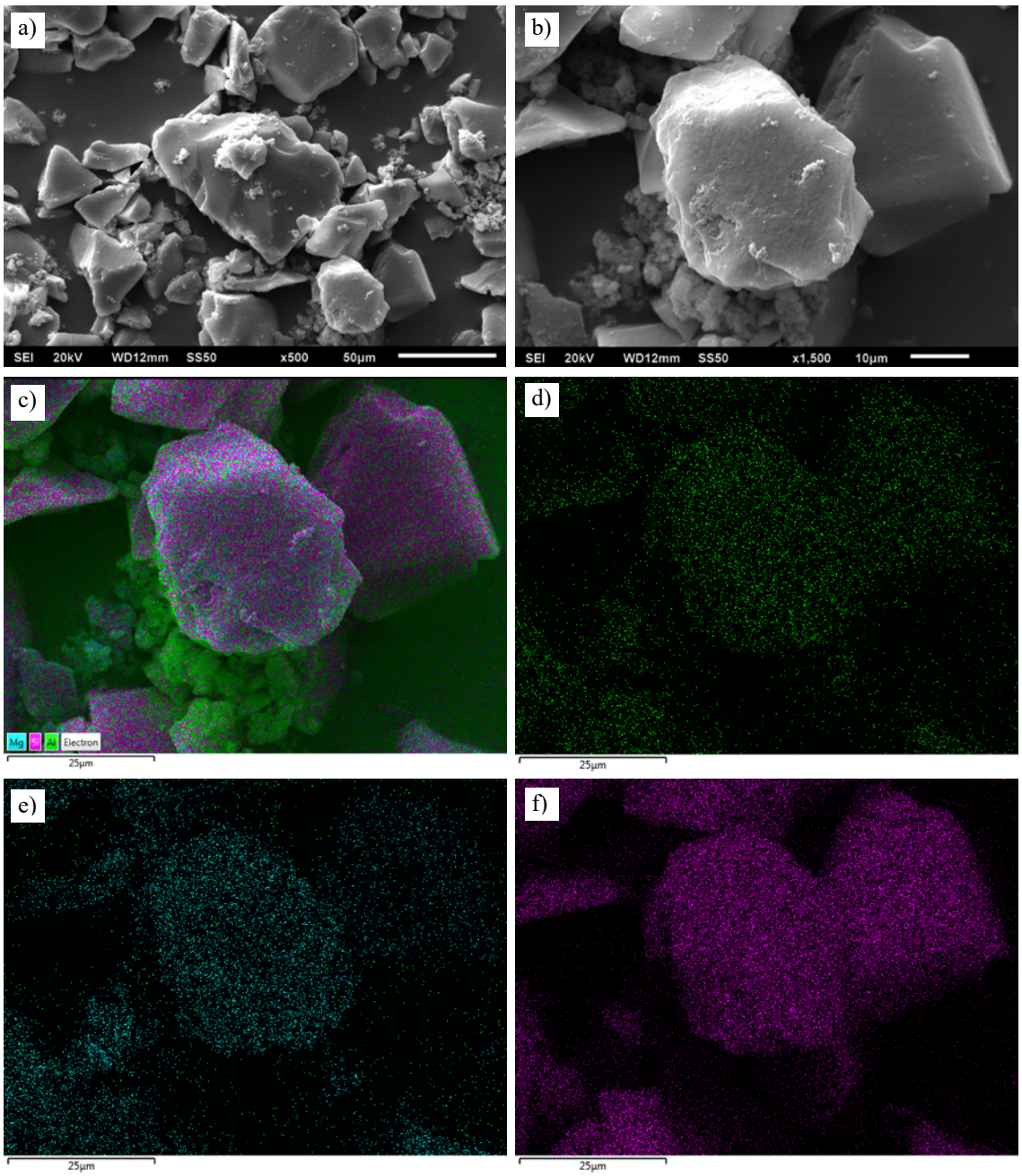


Figure 4.42 a) and b) SEM images of SiO_2@Mg_2Al-CO_3-AMO-LDH prepared by the IMP2 method using Grace Davison LC60A 35-70 silica. SEM-EDX c) layered image and analyses of d) Al, e) Mg, and f) Si. Metal addition rate = 0.25 cm^3 min^{-1}. Stirring speed = 500 rpm. AMO solvent = EtOH.

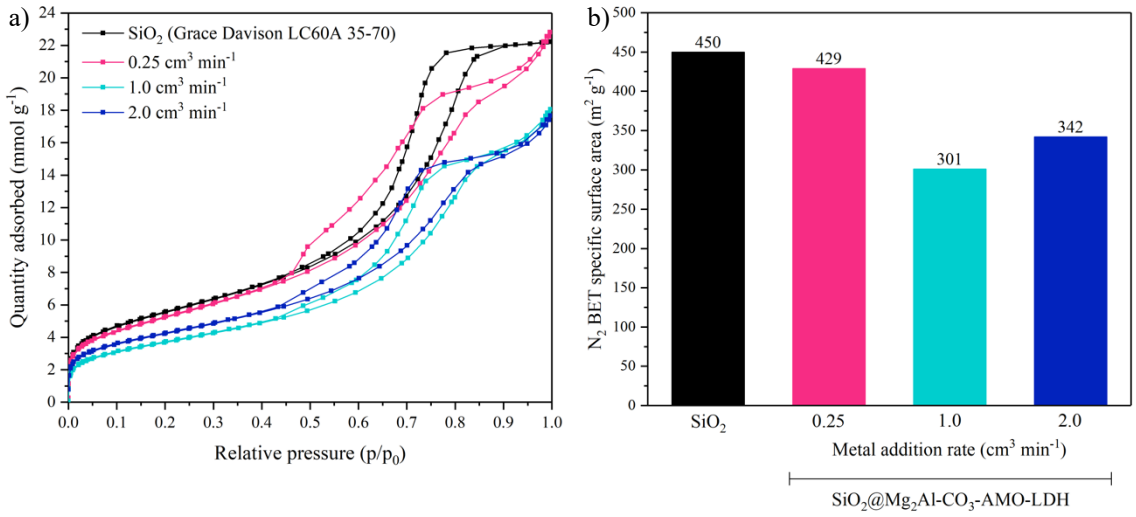


Figure 4.43 a) N_2 adsorption and desorption isotherms and b) N_2 BET specific surface areas of SiO_2@Mg_2Al-CO_3-AMO-LDH prepared by the IMP2 method with different metal addition rates using Grace Davison LC60A 35-70 silica. Stirring speed = 500 rpm. AMO solvent = EtOH.

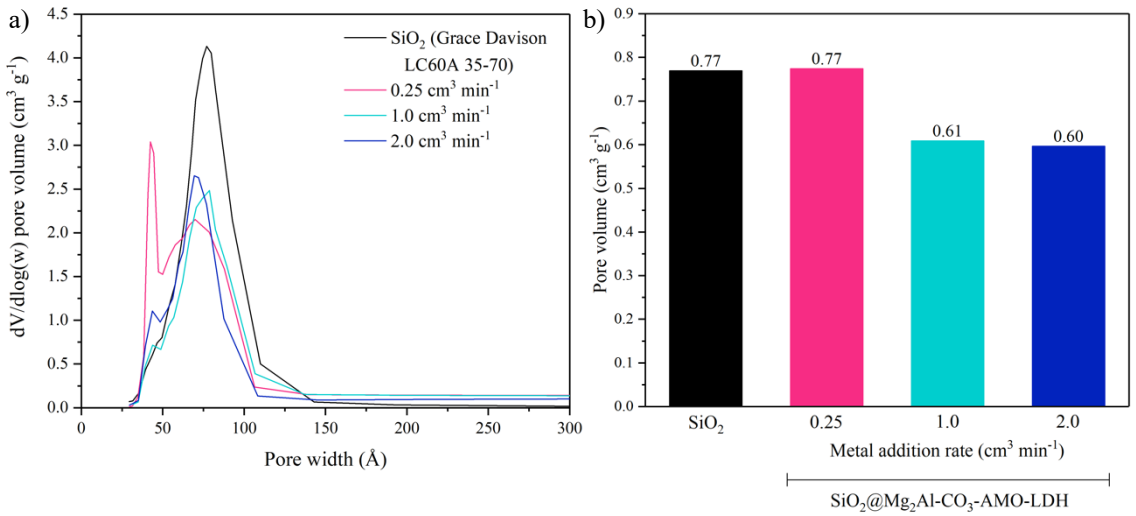


Figure 4.44 a) BJH pore size distributions and b) pore volumes of SiO_2@Mg_2Al-CO_3-AMO-LDH prepared by the IMP2 method with different metal addition rates using Grace Davison LC60A 35-70 silica. Stirring speed = 500 rpm. AMO solvent = EtOH.

Unlike the core-shell materials synthesised from Stöber and Fuji silicas, the N_2 BET specific surface areas of SiO_2@Mg_2Al-CO_3-AMO-LDHs prepared from Grace Davison LC60A 35-70 silica are lower than that of the parent silica (Figure 4.43). The commercial silica from Grace Davison has a high surface area (450 m^2 g^{-1}) and well-defined pore structure, whilst MgAl-AMO-LDHs typically have a lower surface area (*ca.* 200–

350 m^2 g^{-1}) and multi-pore distributions.[32] Thus, hybridisation of the higher surface area silica with the lower surface area LDH will not result in an increase in surface area. The decreases in surface area and pore volume can be attributed to pore blocking by the growth of LDH in existing pores (Figure 4.44).

The core-shell prepared using the fastest addition rate (*e.g.* 2.0 cm^3 min^{-1}) has a higher surface area than that prepared at an intermediate rate (*e.g.* 1.0 cm^3 min^{-1}). This may be due to the greater prevalence of free LDH at higher addition rates, leading to less LDH coverage on the silica particles and therefore, less pore blocking. The free LDH will also have an enhanced surface area because it is more susceptible to AMO treatment than LDH that is grafted to a core.

4.5 Preliminary synthesis of core-shell SiO_2@SLDH from struvite

It was shown in Chapter 2 that MgAl-LDHs could be prepared from the waste mineral struvite, $MgNH_4PO_4.6H_2O$. Since environmentally friendly routes are also desirable for core-shell SiO_2@LDH preparation, herein follows an investigation into the synthesis of core-shell SiO_2@SLDHs using struvite.

The large particle size of struvite (Alfa Aesar) occasioned the use of a commercial silica with a large particle size (PQ ES757, Figure 4.45). The first attempt to synthesise core-shell SiO_2@SLDHs used a procedure adapted from Section 4.4.2 involving the impregnation of silica with Al^{3+}. Struvite was heated in NaOH and added dropwise to the SiO_2/Al^{3+} slurry. This method will be termed CSS1.

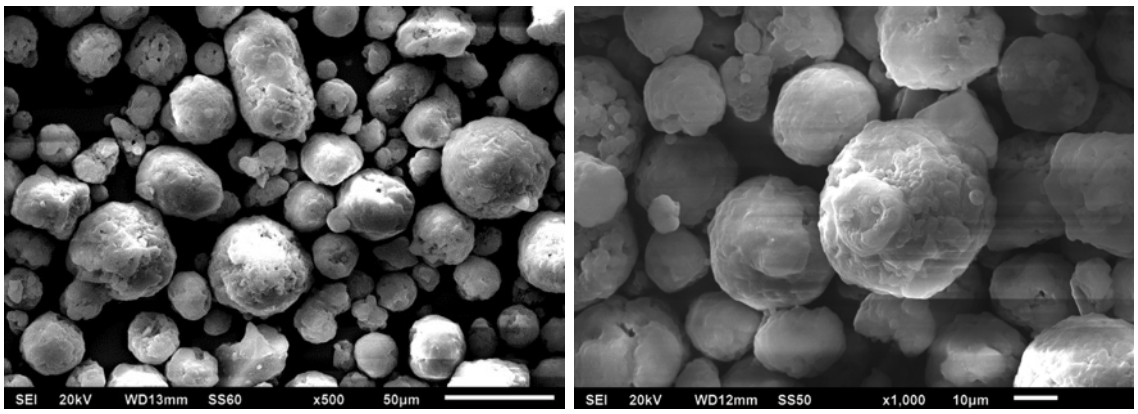


Figure 4.45 SEM images of PQ ES757 silica.

Characterisation of the product by powder XRD showed that core-shell SiO_2@SLDH synthesis was unsuccessful by this method (Figure 4.46). The broad feature between 2θ = 15–30º is due to scattering by amorphous silica. Superimposed on this are reflections that can be indexed to magnesium hydroxide, $Mg(OH)_2$ (JCPDS card no. 00-007-0239), and aluminium hydroxide, $Al(OH)_3$ (JCPDS no. 74-1775). The precipitation of separate hydroxides may have resulted from the cooling of the struvite-alkali mixture whilst it was added dropwise to the silica, as struvite has low solubility below 35 ºC. Consequently,

the concentration of Mg^{2+} would have been low, leading to the preferential precipitation of $Al(OH)_3$.

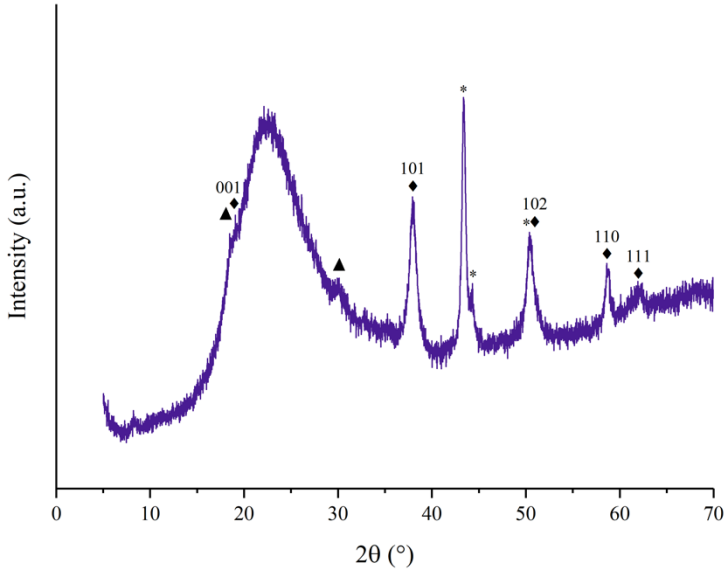


Figure 4.46 Powder XRD diffractogram of the product of method CSS1. *Reflections due to the sample holder. ♦$Mg(OH)_2$ (indexed). ▲$Al(OH)_3$

To promote SLDH growth on the silica cores, the reaction was repeated under hydrothermal conditions. This method is designated CSS2. The XRD diffractogram shows a product of low crystallinity but the reflections may be indexed to an Mg_3Al-CO_3-LDH phase in the presence of SiO_2 (Figure 4.47). The intensity of the 003 Bragg reflection is unusually low relative to the 110/113 reflections, which suggests that the product either contains very thin LDH nanoplatelets or is a mixture of phases.

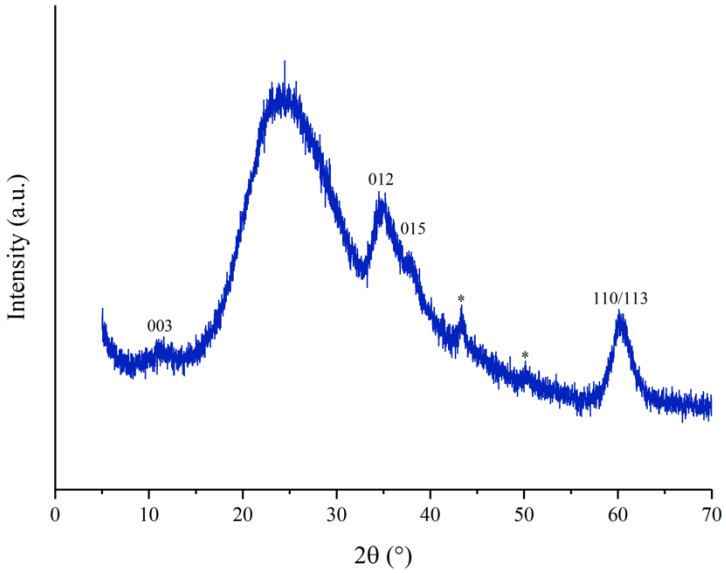


Figure 4.47 Powder XRD diffractogram of the product of method CSS2. Bragg reflections due to Mg_3Al-CO_3-SLDH indexed. *Reflections due to the sample holder.

Absorption peaks in the FTIR spectrum (Figure 4.48a) and the thermal decomposition profile (Figure 4.48b) of the product are also characteristic of SiO_2 and SLDH.

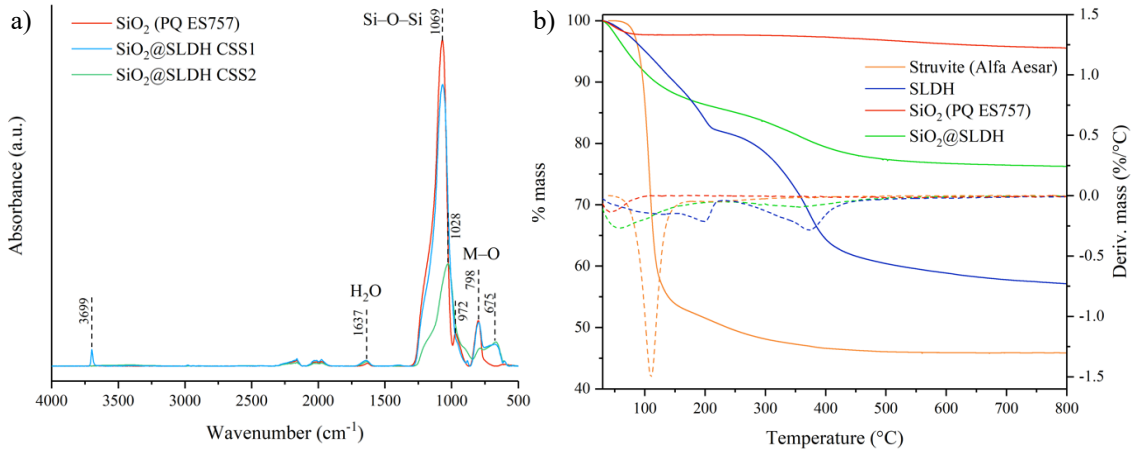


Figure 4.48 a) FTIR spectra of SiO_2 (PQ ES757) and SiO_2@SLDH prepared by both methods, and b) TGA and dTGA graphs of struvite, SLDH, SiO_2 (PQ ES757) and SiO_2@SLDH prepared by CSS2. Mg/Al = 3.

ICP-MS data gives the Mg/Al ratio to be 3.03, which is very good agreement with the amounts used in the synthesis (Table 4.9).

Table 4.9 Summary of the ICP-MS elemental analyses of SiO_2@SLDH prepared using the CSS2 method

Av. wt.%	SiO_2@SLDH (CSS2)
Na	0.85
Mg	8.95
Al	3.16
Si*	0.60
P	0.60
Ca	0.14
Av. Mg/Al	3.03

*acid-soluble fraction

The N_2 BET specific surface area of the product is *ca.* 6 m^2 g^{-1} lower than that of the untreated SiO_2 (Figure 4.49). This was observed in Section 4.4.2 and is attributed to the blocking of pores in the SiO_2 cores due to SLDH growth. Here, the blockage of existing pores in SiO_2 is compensated for by the formation of new pores in the SLDH shell so the surface area does not decrease significantly overall. These new pores have a broad size distribution between 100–500 Å (Figure 4.50).

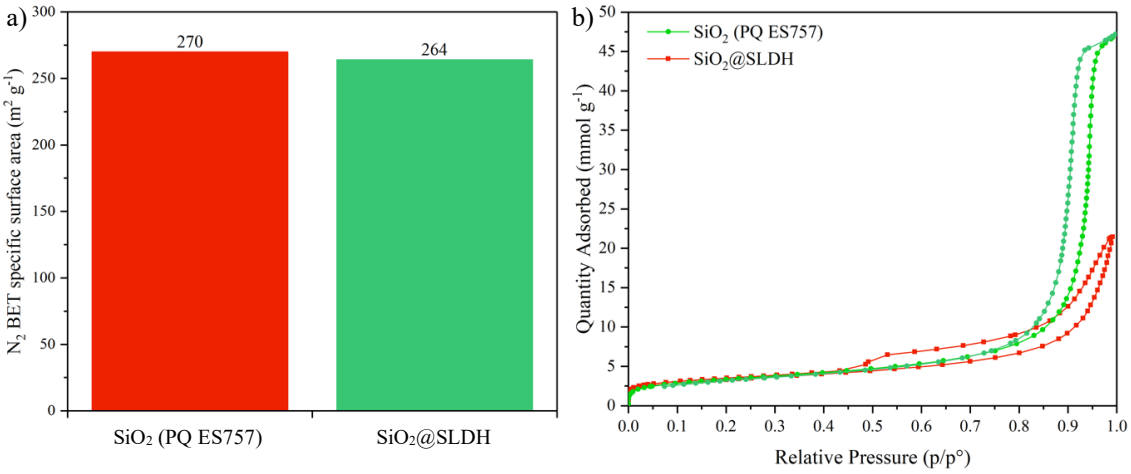


Figure 4.49 a) N_2 BET specific surface areas and b) N_2 adsorption and desorption isotherms of SiO_2 (PQ ES757) and SiO_2@SLDH prepared by CSS2. Mg/Al = 3.

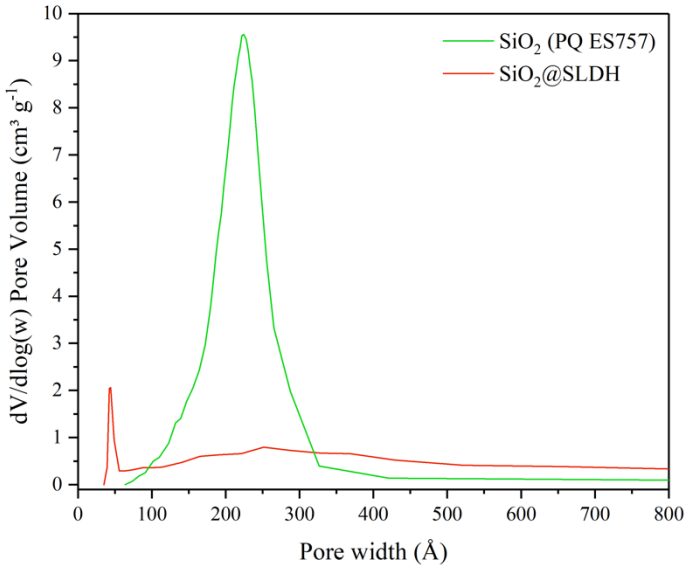


Figure 4.50 BJH pore size distributions of SiO_2 (PQ ES757) and SiO_2@SLDH prepared by CSS2. Mg/Al = 3.

Core-shell structures were confirmed by high resoltuion SEM (HR-SEM) imaging, but struvite-like particles were also present (Figure 4.51). As seen in Section 3.2, some struvite crystals retain their coffin-lid morphology when transformed into SLDH – this occurs most often for the largest particles, as they are most difficult to decompose. These SLDH particles are too large to adhere to the SiO_2 so grow independently. For the smaller struvite fragments that decompose more efficiently, SLDH growth occurs on the surface of the SiO_2 particles. These are visible as interpenetrating platelets and clusters. Elemental mapping by HR-SEM EDX shows uniform Mg and Al coverage on the spherical units (Figure 4.52).

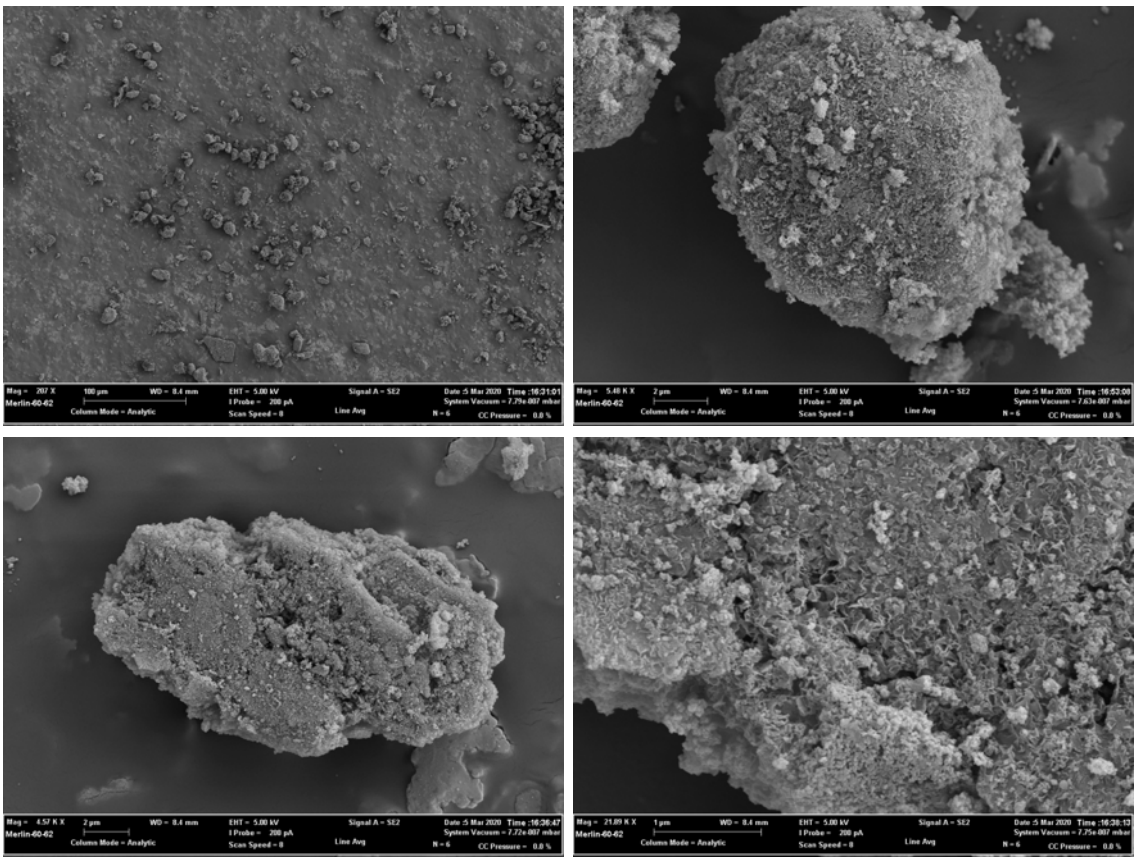


Figure 4.51 HR-SEM images of SiO_2@SLDH prepared using CSS2. Mg/Al = 3.

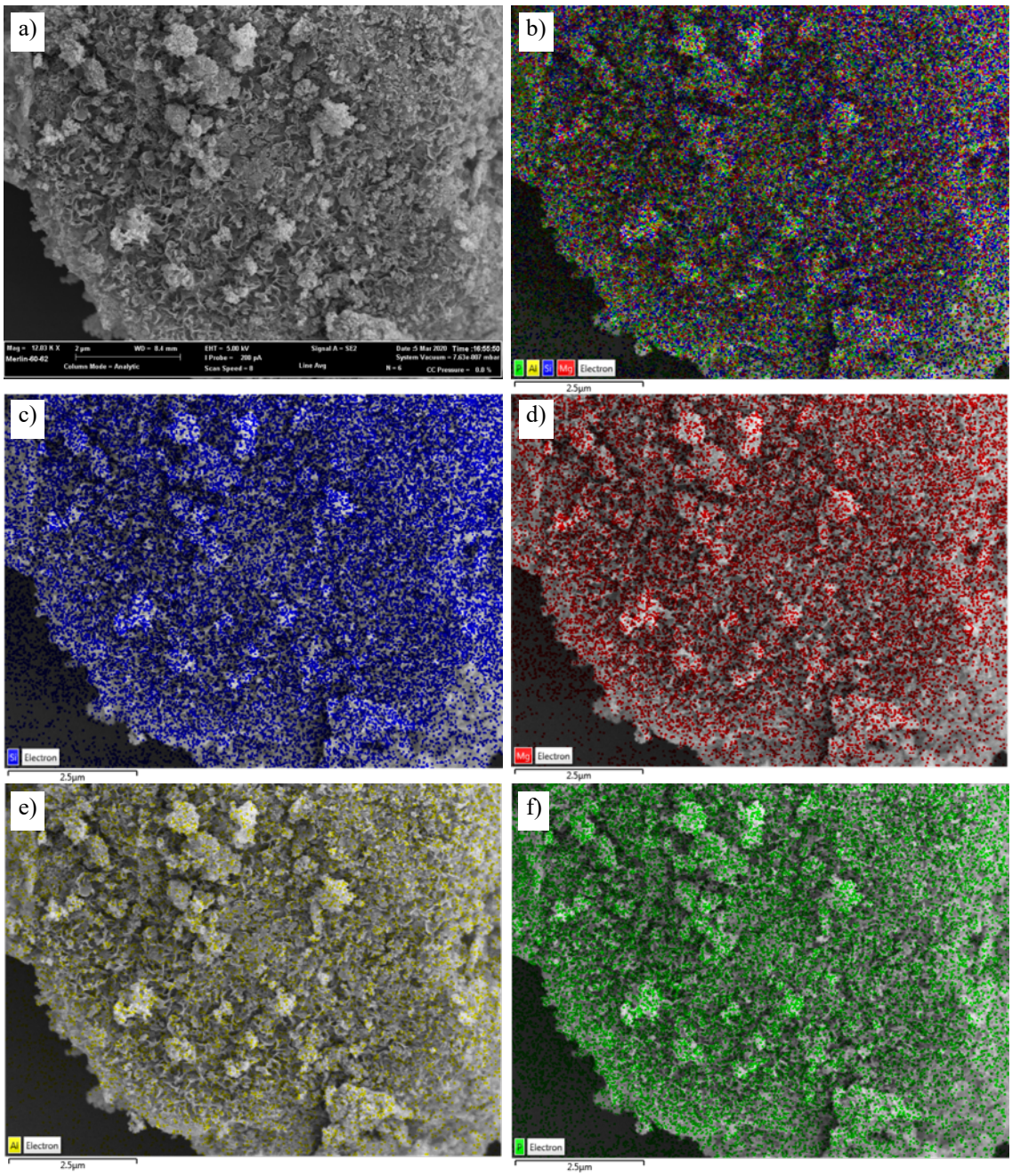


Figure 4.52 a) HR-SEM image and b) HR-SEM EDX layered image of SiO_2@SLDH prepared by CSS2. Elemental mapping of c) Si, d) Mg, e) Al, and f) P.

These results show that core-shell SiO_2@SLDH can be prepared using struvite as a precursor for Mg. SLDH may not adhere to SiO_2 because of its large size, so it may be recommended that struvites with smaller particle sizes are used. The decomposition time should also be reduced to prevent the formation of a less reactive intermediate.

4.6 Conclusion

Over fifty SiO_2@Mg_2Al-CO_3-AMO-LDHs were synthesised and characterised in order to evaluate the effect of changing various synthetic parameters on morphological and physical properties. Moderate stirring speeds (*e.g.* 500 rpm) are found to promote the formation of large, vertically aligned LDH platelets with respect to the silica surface and also reduce the occurrence of free LDH. Slow metal addition rates are similarly found to create thicker shells of vertically aligned LDH platelets but the effect of stirring speed is more significant with respect to surface area. The highest surface area (*ca.* 100 m^2 g^{-1}) was achieved with a stirring speed of 500 rpm.

Preliminary studies show that struvite may be used for the preparation of core-shell SiO_2@SLDHs. The formation of hybrid materials from this precursor is complicated by the morphology of the mineral which confers unique physicochemical properties to the SLDH (*i.e.* size and shape incompatibility). Thus, further investigations will be required to optimise this synthesis.

Through the preparation of SiO_2@Mg_2Al-CO_3-AMO-LDHs using commercial silica it was found that pre-soaking the support in a solution of Al^{3+} and decreasing the volume of the solutions affected better LDH growth on the silica surface. When these changes were combined with a slow metal addition rate and moderate stirring speed, the LDH coverage improved significantly.

Upon the findings of this study, it is suggested that future syntheses of such core-shell materials use moderate stirring speeds and slow metal addition rates in order to achieve an optimal honeycomb-like morphology with the highest surface area.

4.7 References

1. M. Zubair, M. Daud, G. McKay, F. Shehzad and M. A. Al-Harthi, *Appl. Clay Sci.*, 2017, **143**, 279-292.
2. C. Chen, R. Felton, J.-C. Buffet and D. O'Hare, *Chem. Commun.*, 2015, **51**, 3462-3465.
3. H. Suo, C. Chen, J.-C. Buffet and D. O'Hare, *Dalton Trans.*, 2018, **47**, 16413-16417.
4. L. Li, Y. Feng, Y. Li, W. Zhao and J. Shi, *Angew. Chem. Int. Ed.*, 2009, **48**, 5888-5892.
5. H. Zhang, D. Pan, K. Zou, J. He and X. Duan, *J. Mater. Chem.*, 2009, **19**, 3069-3077.
6. Y. Dou, S. Zhang, T. Pan, S. Xu, A. Zhou, M. Pu, H. Yan, J. Han, M. Wei, D. G. Evans*, et al.*, *Adv. Funct. Mater.*, 2015, **25**, 2243-2249.
7. X.-T. Wang, X.-B. Ning, Q. Shao, S.-S. Ge, Z.-Y. Fei, J. Lei and B.-R. Hou, *Sci. Rep.*, 2018, **8**, 4116-4116.
8. C. Chen, C. F. H. Byles, J.-C. Buffet, N. H. Rees, Y. Wu and D. O'Hare, *Chem. Sci.*, 2016, **7**, 1457-1461.
9. J.-C. Buffet, C. F. H. Byles, R. Felton, C. Chen and D. O'Hare, *Chem. Commun.*, 2016, **52**, 4076-4079.
10. Z. Gu, J. J. Atherton and Z. P. Xu, *Chem. Commun.*, 2015, **51**, 3024-3036.
11. D. Li, Y.-T. Zhang, M. Yu, J. Guo, D. Chaudhary and C.-C. Wang, *Biomaterials*, 2013, **34**, 7913-7922.
12. J. Livage, *Bull. Mater. Sci.*, 1999, **22**, 201-205.
13. A. E. Danks, S. R. Hall and Z. Schnepp, *Mater. Horiz.*, 2016, **3**, 91-112.
14. S. Pandey and S. B. Mishra, *J. Sol-Gel Sci. Technol.*, 2011, **59**, 73-94.
15. Y. Zhao, S. He, M. Wei, D. G. Evans and X. Duan, *Chem. Commun.*, 2010, **46**, 3031-3033.
16. J. Wang, R. Zhu, B. Gao, B. Wu, K. Li, X. Sun, H. Liu and S. Wang, *Biomaterials*, 2014, **35**, 466-478.
17. M. Shao, F. Ning, J. Zhao, M. Wei, D. G. Evans and X. Duan, *J. Am. Chem. Soc.*, 2012, **134**, 1071-1077.
18. H. Zhang, D. Pan and X. Duan, *J. Phys. Chem. C*, 2009, **113**, 12140-12148.
19. C. Chen, P. Gunawan and R. Xu, *J. Mater. Chem.*, 2011, **21**, 1218-1225.
20. C. Chen, P. Wang, T.-T. Lim, L. Liu, S. Liu and R. Xu, *J. Mater. Chem. A*, 2013, **1**, 3877-3880.
21. T. Ungár, *Scripta Mater.*, 2004, **51**, 777-781.
22. P. Scherrer, in *Kolloidchemie Ein Lehrbuch*, Springer Berlin Heidelberg, Berlin, Heidelberg, 1912, pp. 387-409.
23. J. I. Langford and A. J. C. Wilson, *J. Appl. Crystallogr.*, 1978, **11**, 102-113.
24. K. S. Sing, *Pure Appl. Chem.*, 1985, **57**, 603-619.
25. A. D. McNaught and A. Wilkinson, *Compendium of chemical terminology, 2nd Edition*, Blackwell Scientific Publications, Oxford, 1997.
26. M. Thommes, *Chem. Ing. Tech.*, 2010, **82**, 1059-1073.
27. J. Nývlt, *J. Cryst. Growth*, 1968, **3-4**, 377-383.
28. M. Celikbilek Ersundu and A. E. Ersundu, in *Advances in Crystallization Processes*, 2012, pp. 127-162.
29. U. Holzwarth and N. Gibson, *Nature Nanotechnology*, 2011, **6**, 534-534.
30. L. T. Zhuravlev, *Colloids Surf. Physicochem. Eng. Aspects*, 2000, **173**, 1-38.
31. Y. K. Shchipalov, *Glass Ceram.*, 2000, **57**, 374-377.
32. C. P. Chen, A. Wangriya, J.-C. Buffet and D. O'Hare, *Dalton Trans.*, 2015, **44**, 16392-16398.

Chapter 5: Calcined materials and applications

5.1 Introduction

5.1.1 Climate change

Anthropogenic climate change is one of the greatest issues facing our planet today. The concept of carbon dioxide (CO_2) as a greenhouse gas (GHG) has been known since the 19th Century[1] and the role of fossil fuel combustion in raising atmospheric CO_2 levels has been understood since the 1930s.[2] Methane (CH_4), nitrous oxide (N_2O), water, ozone (O_3), and chlorofluorocarbons (CFCs) are also known to contribute to the greenhouse effect.

The latest report from the Intergovernmental Panel on Climate Change (IPCC) estimates human activity to have caused approximately 1.0 ºC of global warming above pre-industrial levels and predicts the rise to reach 1.5 ºC between 2030 and 2052 if it continues to increase at the current rate.[3] Changes in precipitation and extreme weather patterns are already being observed.[4-6] Global warming has a deeper impact than many appreciate, with consequences to health, livelihoods, food security, human security, and economic growth. Limiting global warming requires both a decrease in GHG emissions and increase in GHG removal from the atmosphere.

5.1.2 Carbon capture

Carbon capture and storage (CCS) was introduced in 1977[7] and is considered critical in any climate change mitigation programs. Two key approaches to CCS are pre-combustion capture and post-combustion capture. In the former, a fuel (usually coal or natural gas) is pre-treated to form a syngas consisting of mainly CO and H_2, and the water-gas shift reaction (WSGR) is used to convert the CO into CO_2. The value of this process is in the conversion of carbon fuel to a carbonless fuel, hydrogen.[8]

Post-combustion capture involves separating CO_2 from the flue gases produced by fuel combustion. Large volumes of gas must be handled because of the low concentration and partial pressure of CO_2 in flue gases and this means large equipment sizes and high capital costs. In comparison, in pre-treatment capture, the high concentration of CO_2 in the gaseous products facilitates its separation (*e.g.* smaller equipment and lower energy penalties).[8]

The main technologies for CO_2 separation are absorption, adsorption, membrane separation, cryogenic distillation, and chemical looping combustion.[8] Chemical absorption using amines, such as monoethanolamine (MEA) and methyl diethanolamine (MDEA), is one of the most mature technologies used commercially.[9] Acidic CO_2 is captured by neutralisation in the basic solvent and then stripped from solution using steam. This gives a highly concentrated CO_2 stream that can be compressed for utilisation or storage.[10] Unfortunately, this process suffers from high equipment corrosion rate, high energy consumption and amine degradation by impurities in flue gases (*e.g.* SO_2).

Attention has been turned towards adsorbents because they are lower in cost and require less energy than the other technologies.[11] Adsorption is a dry process that leads to the transfer of a molecule from bulk fluid to the surface of a solid material. Physical adsorption (physisorption) is caused by van der Waals intermolecular forces and occurs when the attractive forces between solute and sorbent are greater than those between the solute molecules themselves. Chemical adsorption (chemisorption) involves the formation of a chemical bond (*e.g.* transfer, exchange or sharing of electrons) between the adsorbate and sorbent. Bonds formed by physisorption are weaker than those in chemisorption as they are due to electron density fluctuations rather than charge transfer.

CO_2 adsorption and desorption may be achieved by changing the pressure and/or temperature.[11] In pressure swing adsorption (PSA), the adsorption step takes place at high pressure and regeneration of the sorbent occurs at a lower pressure. If adsorption is performed at atmospheric pressure and desorption is induced at reduced pressures, the process is called vacuum swing adsorption (VSA). Temperature swing adsorption (TSA) is an alternative approach where selective adsorption at a certain temperature is subsequently reversed by providing additional heat. PSA and TSA are often combined in industry to lower the energy demand and increase the adsorption efficiency.[12]

5.1.3 Capturing CO_2 with inorganic materials

In order for a material to be a good sorbent, it should be selective for the desired substrate and adsorb the substrate in large quantities under the appropriate conditions. The sorbent should also have a high regeneration ability.

A variety of solvent and solid-based sorbents have been investigated in recent years. Common sorbents such as activated carbons, zeolites and metal-organic frameworks (MOFs) have been applied in CO_2 capture as they have high surface areas, tuneable porosities and good chemical resistance.[13-15] No single sorbent is ideal, however. Activated carbons have a low enthalpy of adsorption for CO_2 as a result of the electric potential on their surface, so they have a low adsorption capacity at low pressures (*e.g.* 2.5 mmol g^{-1} at 298 K and 1 bar, compared to 4.5 mmol g^{-1} by zeolite 13X).[15, 16] The higher enthalpy of adsorption of zeolites means that they require higher regeneration temperatures. Furthermore, both zeolites and MOFs are sensitive to water so suffer from decomposition and decreased capacities over time. MOFs are also challenging to prepare in high yields and crystallinity.[14]

Metal oxide-based sorbents such as calcium oxide (CaO) and magnesium oxide (MgO) are promising materials for CO_2 capture because of their low cost, wide availability and relatively high adsorption capacity.[15, 17] One mole of an alkaline earth metal oxide can chemically adsorb one mole of CO_2 to form a metal carbonate (Equation 5.1). This process is exothermic so the reverse reaction (*i.e.* decomposition and release of CO_2) can be affected by thermal treatment. This pair of reactions can be utilised for *in situ* removal of CO_2 in high temperature applications.[18] Comparatively, activated carbons and zeolites are not attractive for high-temperature applications because their CO_2 adsorption capacities decrease drastically with temperature.[19]

$$MO_{(s)} + CO_{2\,(g)} \rightleftharpoons MCO_{3\,(s)} \qquad \text{Equation 5.1}$$

Given the stoichiometric reaction in Equation 5.1, the maximum theoretical amount of CO_2 adsorbed by CaO is 17.8 mmol g^{-1}.[15] Whilst the typical capacities recorded are usually lower than this, they are still greater than those for other inorganic sorbents. However, the challenge with CaO is that its CO_2 adsorption capacity suffers rapid degeneration as the carbonation/calcination cycles repeat. The reduction is attributed to pore blocking and adsorbent sintering.[20, 21]

MgO has been explored as an alternative to CaO because it has a lower energy requirement for regeneration (*ca.* 500 ºC compared to >700 ºC).[17] CO_2 reacts with basic O^{2-} sites depending on their coordination. Oxygen atoms located at edges and corners of the surfaces have lower coordination, so are more basic than those in the basal planes.[22] Monodentate adsorption is typically observed on edge sites, and bidentate adsorption on corner sites.[23] The CO_2 adsorption capacity of pure MgO is fairly low so investigations have been conducted to prepare high surface area MgO-based sorbents.[24] These include

mesoporous MgO and binary oxides such as CaO-MgO and MgO-Al_2O_3, which can be derived from thermally treated LDHs.[17]

5.2 Calcination of LDH-based materials

Fresh LDH does not possess significant CO_2 capture capacity but LDOs generated by the calcination of LDHs possess high surface area and high surface basicity, which makes them suitable for CO_2 adsorption.[25] In Chapter 3, novel high surface area and high density LDHs were prepared from struvite (SLDHs) and in Chapter 4, LDH crystallisation on silica cores was optimised to give high surface area core-shell SiO_2@LDH hybrid materials. In this chapter, the properties of calcined SLDHs and core-shell SiO_2@LDHs are evaluated and their potential as CO_2 adsorbents is investigated.

5.2.1 Calcination of core-shell SiO_2@Mg_2Al-CO_3-AMO-LDHs

The TGA profiles of SiO_2, Mg_2Al-CO_3-AMO-LDH and SiO_2@Mg_2Al-CO_3-AMO-LDH are compared in Figure 5.1. When heated to 800 ºC, SiO_2 undergoes significantly less mass loss (*ca.* 15 wt.%) than the Mg_2Al-CO_3-AMO-LDH (*ca.* 45 wt.%). For SiO_2, the mass loss is due to the removal of adsorbed water and dehydroxylation of the surface.[26] The thermal behaviour of Mg_2Al-CO_3-AMO-LDH and SiO_2@Mg_2Al-CO_3-AMO-LDH is more complex, with three distinct endothermic events.[27, 28] In order of increasing temperature, the mass losses correspond to (i) loss of ethanol (the AMO-solvent), (ii) loss of surface and interlayer water, and (iii) dehydroxylation and decarboxylation of the LDH layers to form mixed metal oxides. The TGA curves obtained for SiO_2@Mg_2Al-CO_3-AMO-LDHs are dominated by mass losses associated with the LDH component.

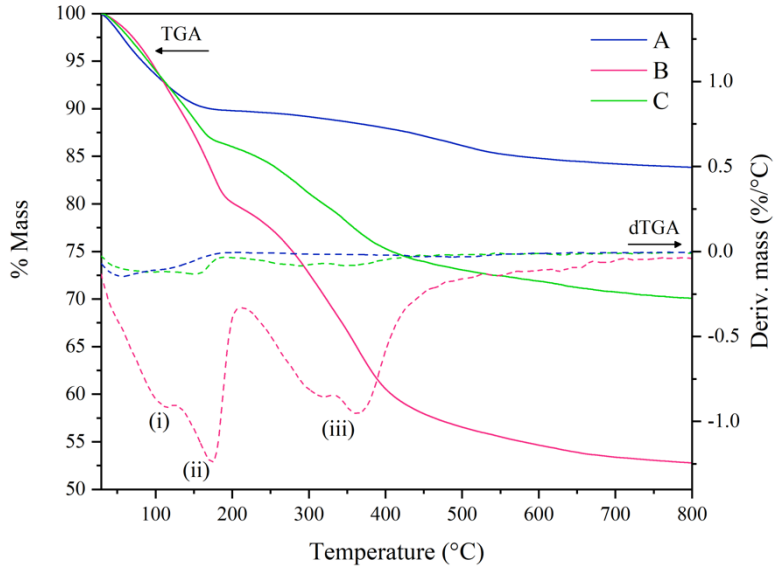


Figure 5.1 TGA and dTGA curves for A) SiO_2, B) Mg_2Al-CO_3-AMO-LDH, and C) SiO_2@Mg_2Al-CO_3-AMO-LDH. Stirring speed = 500 rpm. Metal addition rate = 1.1 mmol h^{-1}. AMO solvent = EtOH.

The TGA and dTGA profiles of SiO_2@Mg_2Al-CO_3-AMO-LDHs prepared using different stirring speeds and metal addition rates show subtle differences (Figure 5.2 and Appendix B, Figures B.3 and B.43). For example, the sample prepared without stirring (*i.e.* stirring speed = 0 rpm) has the highest residual mass at 800 ºC, which suggests that it has the lowest LDH:SiO_2 ratio.

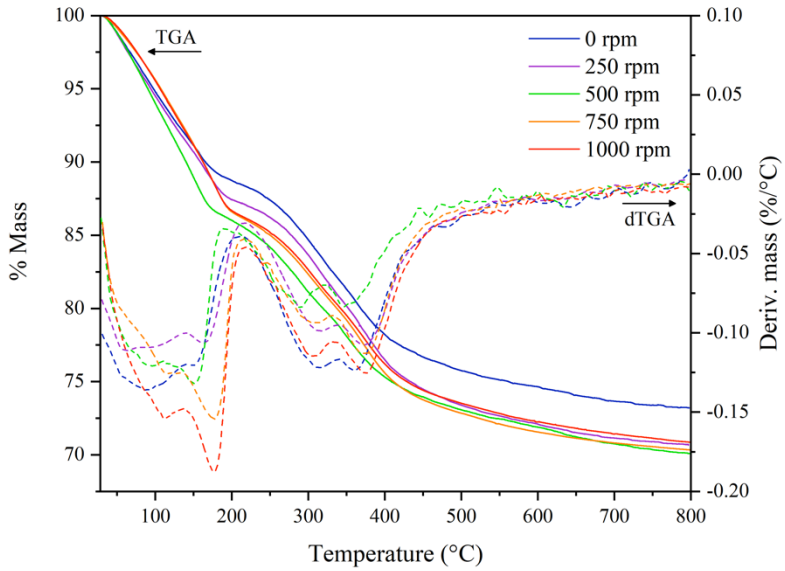


Figure 5.2 TGA and dTGA curves for SiO_2@Mg_2Al-CO_3-AMO-LDH prepared using different stirring speeds. Metal addition rate = 1.1 mmol h^{-1}. AMO solvent = EtOH.

The sample prepared using a stirring speed of 500 rpm undergoes the highest rate of mass loss between 30–160 ºC and this can be attributed to the high surface area, honeycomb-like structure that allows solvent molecules to desorb more efficiently. In the other core-shells, the LDH nanosheets are stacked sub-optimally so solvent molecules may be trapped in closed channels and thus require higher temperatures to effect desorption.

Core-shell SiO_2@Mg_2Al-CO_3-AMO-LDHs were calcined at two temperatures (350 and 700 ºC) for further investigation. The TGA curves indicate that at 350 ºC the LDH component undergoes dehydroxylation and decarboxylation, whilst 700 ºC is a temperature at which this decomposition is mostly complete. In the XRD diffractograms, the calcined core-shells exhibit fewer, and less intense, diffraction peaks compared to the parent material (Figure 5.3).

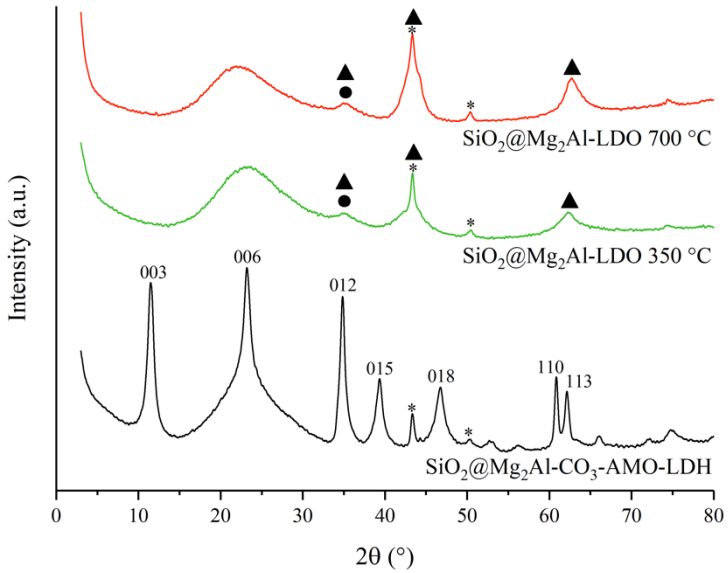


Figure 5.3 Powder XRD diffractograms of SiO_2@Mg_2Al-CO_3-AMO-LDH and its calcined products. Synthesis conditions for core-shell: stirring speed = 500 rpm, metal addition rate = 1.1 mmol h^{-1}. Calcination conditions: temperature ramp rate = 5 ºC min^{-1}, hold at temperature for 5 h. *Reflections due to the sample holder. ▲MgO. ●$Mg_3Al_2(SiO_4)_3$.

Table 5.1 Lattice parameters and mean crystallite domain lengths (CDLs) of SiO_2@Mg_2Al-LDOs prepared at different temperatures.

Calcination temperature (ºC)	*d*-spacing (Å)		Lattice parameter (Å)	CDL (Å)
	d_{200}	d_{220}	$a^{\dagger}$	*a*-axis
350	2.09	1.49	4.18	461.6
700	2.09	1.48	4.18	538.4

†Lattice parameter $a = b = c = 2d_{200}$.
CDL = $0.89\lambda/\beta\cos\theta$, $\lambda = 1.541847$ Å, β = FWHM in radians.

The absence of sharp reflections between 2θ = 11–35º indicates the collapse of the layered structure and the Bragg reflections at 2θ = 35.1, 42.9 and 62.3º may be indexed to the 111, 200 and 220 reflections of a periclase magnesium oxide (MgO) phase (JCPDS card no. 43-1022). The broadness of the reflections in the spectra suggest the oxides are amorphous and have small crystallite size (Table 5.1).[29] Furthermore, the lattice parameter of the MgO phase ($a = b = c$ = 4.18 Å) is smaller than that of pure MgO (4.21 Å),[30] indicating some incorporation of Al^{3+} in the structure.

The broad reflection at 2θ = 35.1º may also have contributions from aluminium oxide (α-Al_2O_3, 104 plane, JCPDS 46-1212) and a magnesium aluminium silicate called pyrope ($Mg_3Al_2(SiO_4)_3$, JCPDS 15-0742). This silicate is formed by the reaction of SiO_2 with MgO and AlO_x at the core-LDH interface. The intensity of sharpness of the Bragg reflections increases when the calcination temperature is raised to 700 ºC, indicating an increase in crystallinity.

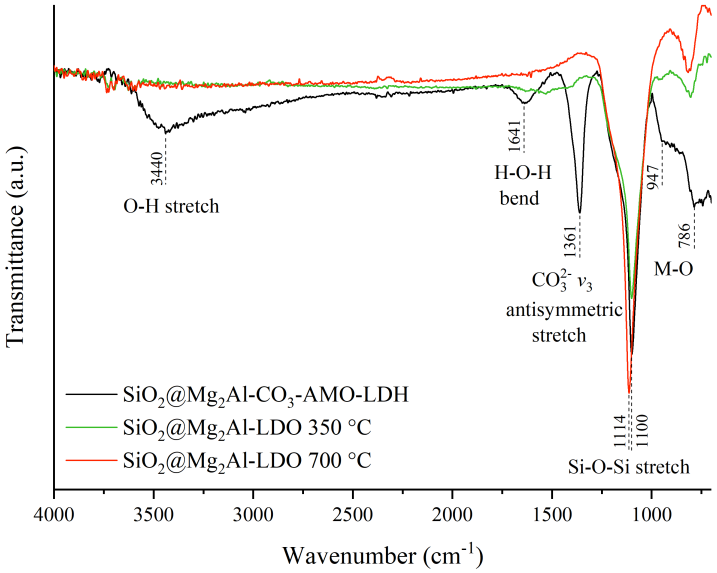


Figure 5.4 FTIR spectra of SiO_2@Mg_2Al-CO_3-AMO-LDH and its calcined products. Synthesis conditions for core-shell: stirring speed = 500 rpm, metal addition rate = 1.1 mmol h^{-1}. Calcination conditions: temperature ramp rate = 5 ºC min^{-1}, hold at temperature for 5 h.

The Fourier transform infrared (FTIR) spectra of SiO_2@Mg_2Al-LDOs also show significant differences to that of the parent SiO_2@Mg_2Al-CO_3-AMO-LDH (Figure 5.4). The disappearance of the broad absorption band between 3000–3600 cm^{-1} indicates that dehydration and dehydroxylation has occurred.[31] The loss of water also results in the absence of the absorption peak at *ca.* 1640 cm^{-1}.

The collapse of the layered structure is accompanied by the loss of interlayer carbonate as carbon dioxide (CO_2) gas.[31] The absorption band at *ca.* 1360 cm^{-1} is therefore absent in both spectra. The structural change also promotes the formation of metal-oxygen (M–O–M, M = Mg^{2+}, Al^{3+}) bonds, which may bridge formerly adjacent layers.[32] These bonds give rise to sharp absorptions below 1000 cm^{-1}.[33]

Transmission electron microscopy (TEM) analyses reveal no apparent changes in the overall morphology of the core-shell upon thermal treatment (Figure 5.5 and Appendix C Figures C.1–C.4). However, the LDH platelets become increasingly “spotty” which suggests that the structure of the LDO is more porous than the parent LDH (an example

is highlighted in Figure 4.5d). This is the result of the transformation of the hydroxide to an amorphous oxide, which involves cation migration and the release of CO_2.[29, 32, 34]

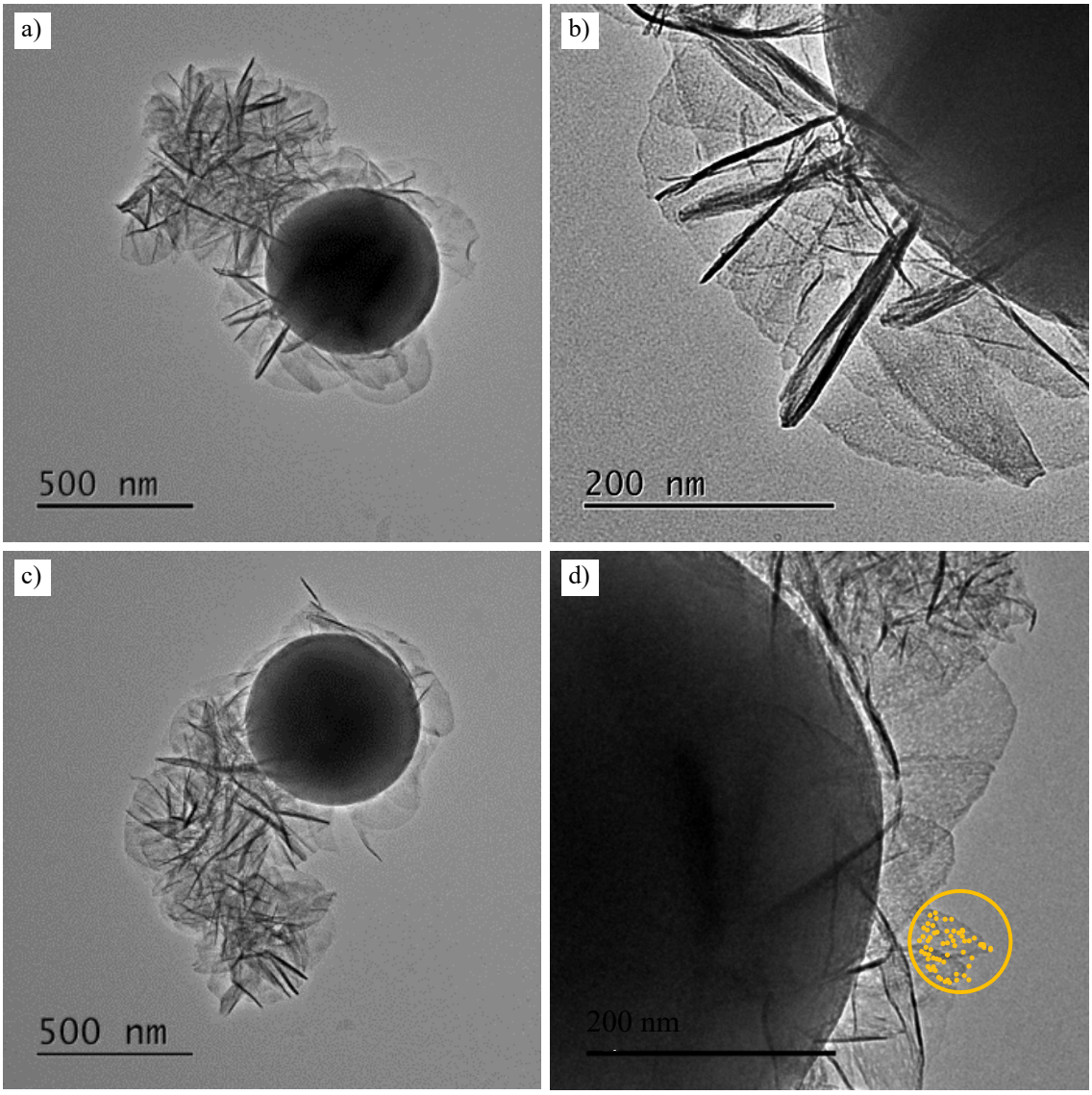


Figure 5.5 TEM images of SiO_2@Mg_2Al-LDH prepared at 350 (a and b) and 700 ºC (c and d). Synthesis conditions for core-shell: stirring speed = 500 rpm, metal addition rate = 1.1 mmol h^{-1}. Calcination conditions: temperature ramp rate = 5 ºC min^{-1}, hold at temperature for 5 h.

5.2.2 Calcination of SLDHs

To investigate the progressive thermal decomposition of the SLDHs, Alfa Aesar and NuReSys M2-85-SLDHs were calcined in a muffle oven at four different temperatures. The XRD diffraction patterns of the SLDOs show that the SLDHs undergo stepwise transformation (Figure 5.6). As discussed in Section 3.7, the NuReSys SLDH has a lower degree of crystallinity than the Alfa Aesar SLDH. As a result, it decomposes more readily, which is illustrated by the broadness of the reflections between *ca.* 33–45º in the samples prepared at 200 ºC.

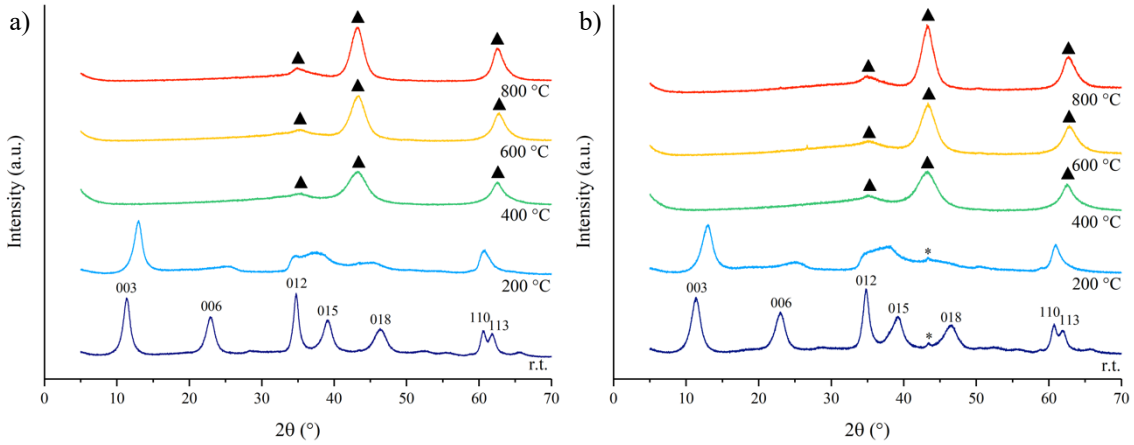


Figure 5.6 Powder XRD diffractograms of M2-85-SLDHs and SLDOs prepared from a) Alfa Aesar and b) NuReSys struvite. Mg/Al = 3. *Reflections due to the sample holder. ▲MgO.

At 200 ºC, dehydration occurs both on the surface and in the interlayer gallery. An upwards shift of the 003 peak, relative to its position in the spectrum of the fresh SLDH, indicates a decrease in the basal spacing of ~ 0.9 Å (Table 5.2). This is consistent with the observations recorded in the literature.[31, 35, 36] The diminished intensities of the 006, 009 and 01*l* peaks indicate partial collapse of the layered structure.

Table 5.2 Lattice parameters and mean crystallite domain lengths (CDLs) of M2-85-SLDHs and SLDOs prepared at 200 ºC. Mg/Al = 3.

	d-spacing (Å)		Lattice parameter (Å)		CDL (Å)	
	d_{003}	d_{110}	$c^{\dagger}$	$a^{\ddagger}$	*c*-axis	*ab*-plane
Alfa Aesar SLDH	7.78	1.53	23.37	3.06	77.9	203.3
Alfa Aesar SLDO 200 ºC	6.84	1.52	20.52	3.04	58.3	125.6
NuReSys SLDH	7.77	1.52	23.31	3.04	54.9	197.5
NureSys SLDO 200 ºC	6.83	1.52	20.49	3.04	49.4	136.9

†Lattice parameter $c = 3d_{003}$. ‡Lattice parameter $a = 2d_{110}$.
CDL = 0.89λ/βcosθ, λ = 1.541847 Å, β = FWHM in radians.

Dehydration and dehydroxylation of the SLDH can also be observed by FTIR (Figure 5.7). The broad peak in the OH region of the spectrum (3000–3600 cm^{-1}) diminishes because hydrogen bonding to adsorbed and interlayer water molecules is no longer possible.[31, 32] The loss of water is also indicated by the absence of the absorption band at *ca.* 1640 cm^{-1} that is due to the bending mode of water. Broadening of the band due to the antisymmetric stretching vibration of carbonate at *ca.* 1360 cm^{-1} can also be attributed to dehydration: the interlayer environment is perturbed upon the loss of H_2O, which changes the symmetry/point group of the carbonate anions.[37]

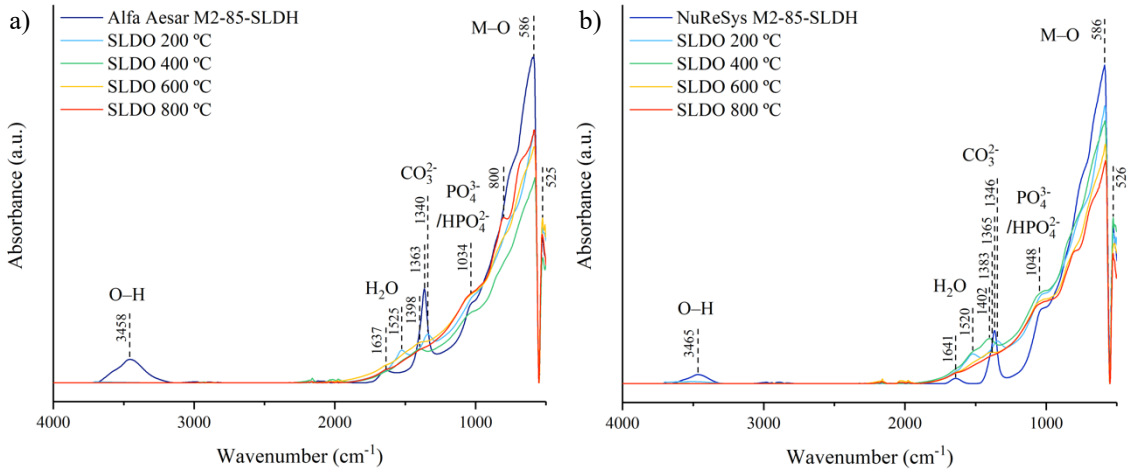


Figure 5.7 FTIR spectra of M2-85-SLDHs and SLDOs prepared from a) Alfa Aesar and b) NuReSys struvite. Mg/Al = 3.

The disappearance of the peak at *ca.* 1360 cm^{-1} indicates that decarbonation occurs above 400 ºC, which is consistent with the values reported in the literature.[31] The loss of the interlayer species is associated with the collapse of the layered structure and this promotes the formation of metal-oxygen bonds. These account for the absorptions below 800 cm^{-1}.

As with the core-shell materials in Section 5.2.1, the XRD diffractograms of the SLDOs prepared at and above 400 ºC exhibit broad Bragg reflections at 2θ = 35.1, 42.9 and 62.3º which can be indexed to MgO (Table 5.3). The broadness of these reflections suggests that the oxides are amorphous and/or consist of small particles. The reflections sharpen with increasing temperature which indicates increased ordering. There may also be contributions to the reflection at 2θ = 35.1º from α-Al_2O_3 (104 plane), but the low aluminium content (Mg/Al = 3) of the SLDH means that this phase is likely to contain defects.

Gao *et al.*[25] have studied the thermal decomposition of conventional Mg_3Al-CO_3-LDHs using ^{27}Al solid state nuclear magnetic resonance spectroscopy (ssNMR). In an uncalcined LDH, Al^{3+} occupies octahedrally coordinated sites (O_h) exclusively. Thermal treatment causes Al^{3+} cations to migrate from the MgO lattice to tetrahedral sites (T_d), creating O_h vacancies. Gao *et al.* reported that the *d*-spacing of the MgO phase increased when the temperature was raised from 400 to 800 ºC and attributed this to the migration of Al^{3+} out of the MgO lattice. For the SLDOs, there is a small decrease in the lattice parameter.

Table 5.3 Lattice parameter and mean CDL of SLDOs prepared from M2-85-SLDHs. Mg/Al = 3.

Calcination temperature (ºC)	200[†] (º)	d_{200} (Å)	Lattice parameter $a^{‡}$ (Å)	CDL (Å)
Alfa Aesar SLDO				
400	43.10	2.10	4.19	32.2
600	43.26	2.09	4.18	41.8
800	43.19	2.09	4.19	49.7
NuReSys SLDO				
400	43.11	2.10	4.19	31.7
600	43.32	2.09	4.17	40.8
800	43.27	2.09	4.18	50.4

[†]Position of the 200 Bragg reflection (2θ) of the MgO phase.
[‡]Lattice parameter $a = 2d_{200}$.
CDL = $0.89\lambda/\beta\cos\theta$, λ = 1.541847 Å, β = FWHM in radians.

The thermal decomposition of the SLDHs is accompanied by changes in surface area and porosity (Figures 5.8–5.11). By IUPAC classification, all the SLDHs and SLDOs exhibit Type IV isotherms, which correspond to mesoporous materials (Figure 5.8).[38] The hystereses are Type H3 and these are characteristic of solids consisting of aggregates, or agglomerates of particles forming slit shaped pores that are non-uniform in size and/or shape. The hysteresis loops for Alfa Aesar SLDOs are wider than those of NuReSys SLDOs, indicating a larger surface area and greater amount of mesopores. Type H3 hystereses can also indicate the presence of macropores and the BJH pore size distribution confirms this is the case for the NuReSys SLDH and SLDOs (Figure 5.9b).

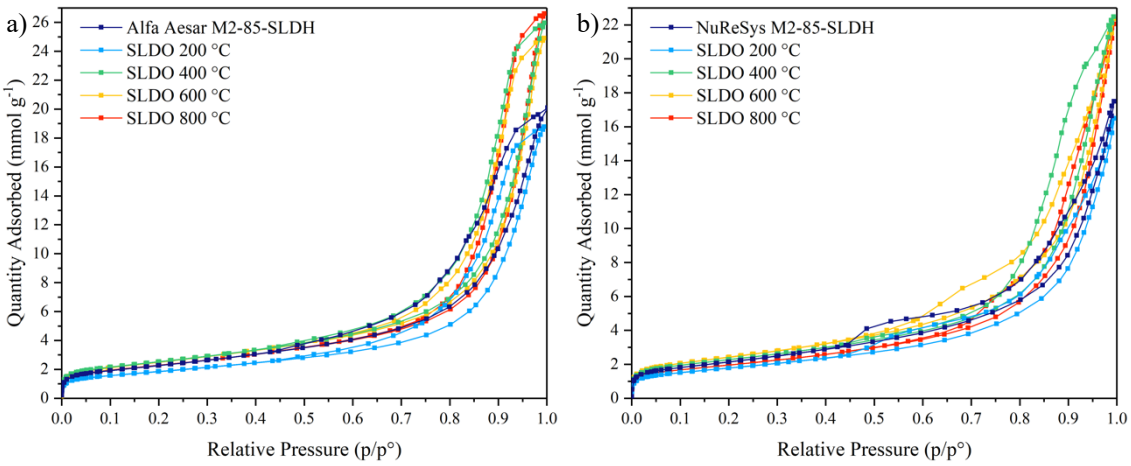


Figure 5.8 N_2 adsorption and desorption isotherms of M2-85-SLDHs and SLDOs prepared from a) Alfa Aesar and b) NuReSys struvite. Mg/Al = 3.

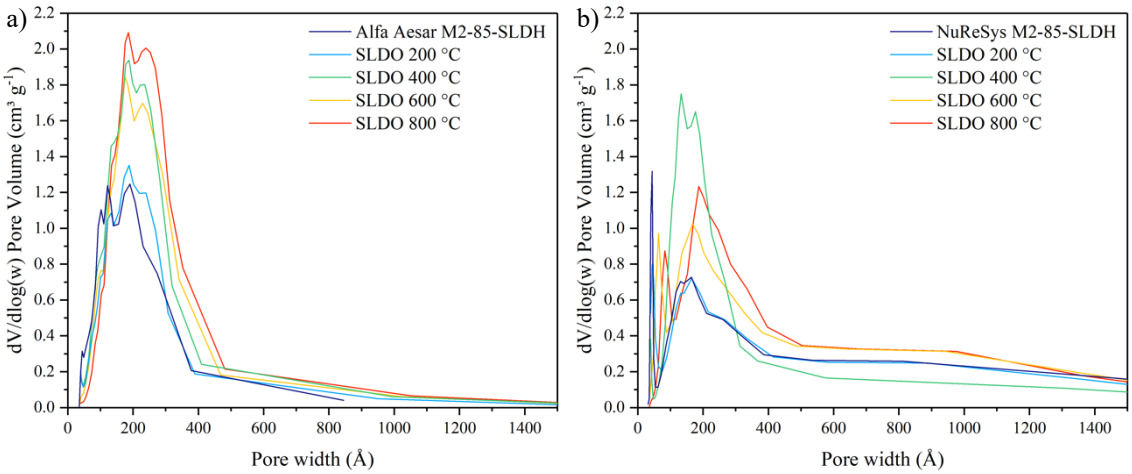


Figure 5.9 BJH pore size distributions of M2-85-SLDHs and SLDOs prepared from a) Alfa Aesar and b) NuReSys struvite. Mg/Al = 3.

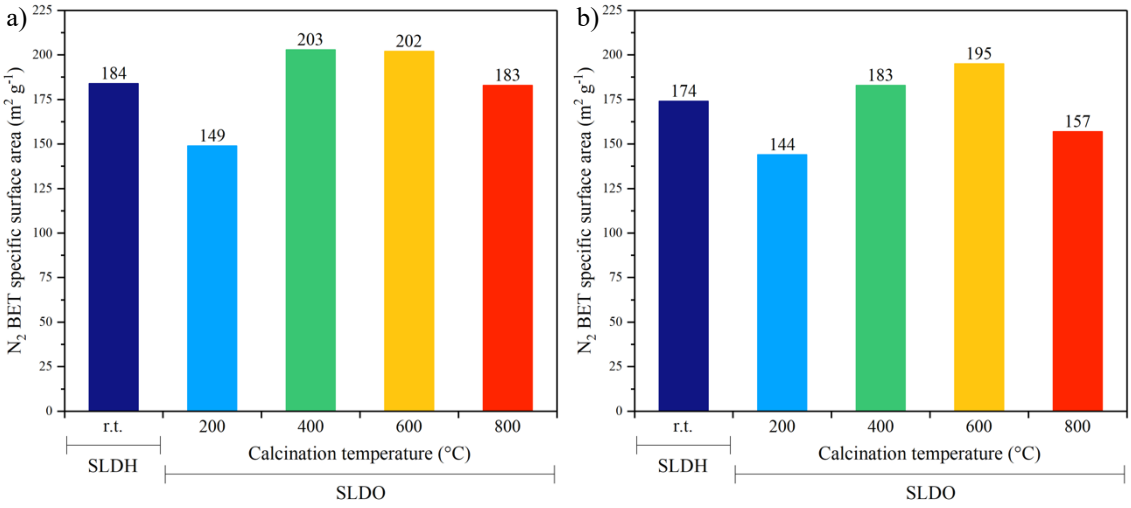


Figure 5.10 N_2 BET specific surface areas of M2-85-SLDHs and SLDOs prepared from a) Alfa Aesar and b) NuReSys struvite. Mg/Al = 3.

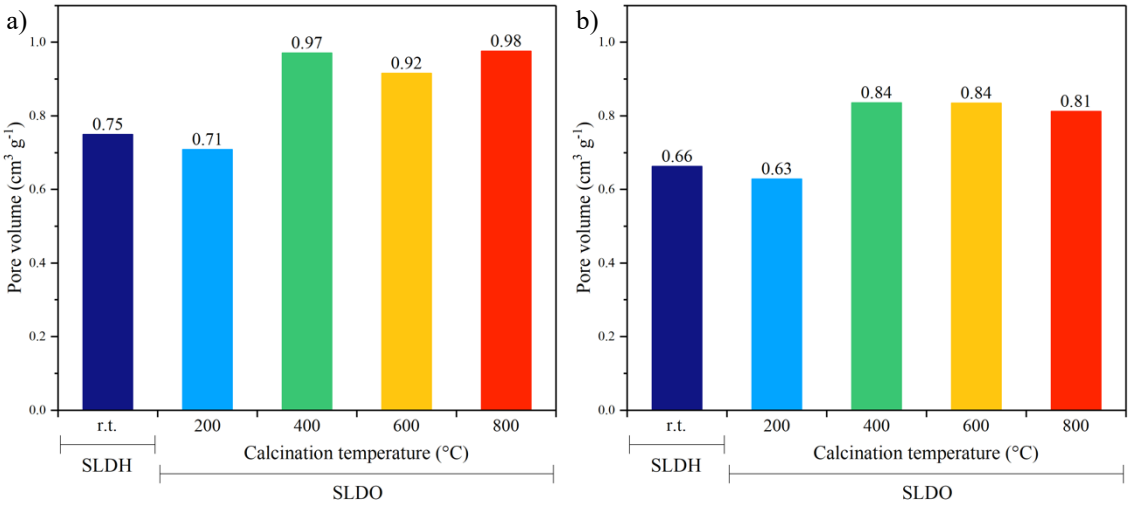


Figure 5.11 Pore volumes of M2-85-SLDHs and SLDOs prepared from a) Alfa Aesar and b) NuReSys struvite. Mg/Al = 3.

The surface area of the material calcined at 200 ºC is approximately 20% lower than that of the as-prepared SLDH because of dehydration and contraction of the interlayer distance (Figure 5.10). This decrease is also seen in the pore volumes of the materials (Figure 5.11).

There is a rapid increase in surface area between 200 and 400 ºC as the layered structure collapses and an amorphous mixed oxide is formed. For the Alfa Aesar SLDO, the N_2 BET specific surface area maximum (203 m^2 g^{-1}) occurs at 400 ºC, whilst for NuReSys SLDO the maximum (195 m^2 g^{-1}) was recorded at 600 ºC. It is possible that the surface area measured for the NuReSys SLDO calcined at 400 ºC is anomalously low – *e.g.* some rehydration may have occurred, or it was not sufficiently evacuated before measurement. Nevertheless, there is a large decrease in surface area for both SLDOs upon heating to 800 ºC. This is consistent with the XRD diffraction patterns which indicate increased crystallinity after calcination at the highest temperatures, as Mg and Al react to form a more compact $MgAl_2O_4$ spinel oxide.[25, 39]

In comparison to conventional LDHs (c-LDHs), the percentage increase in surface area that occurs upon calcination is smaller for SLDHs. For example, the N_2 BET surface area

of a conventional Mg_3Al-CO_3-LDH, that was synthesised for comparison, increased by over 200% from 43 to 147 $m^2\ g^{-1}$ after calcination at 400 ºC. Similar increases have been reported in the literature.[32] The increase was approximately 20% for the analogous SLDH and SLDO. The highly aggregated nature of c-LDHs means that a greater amount of concealed internal surface area exists. Therefore, upon thermal decomposition there is a greater proportional increase in surface area. For the already porous SLDHs, there is less surface area to uncover through calcination.

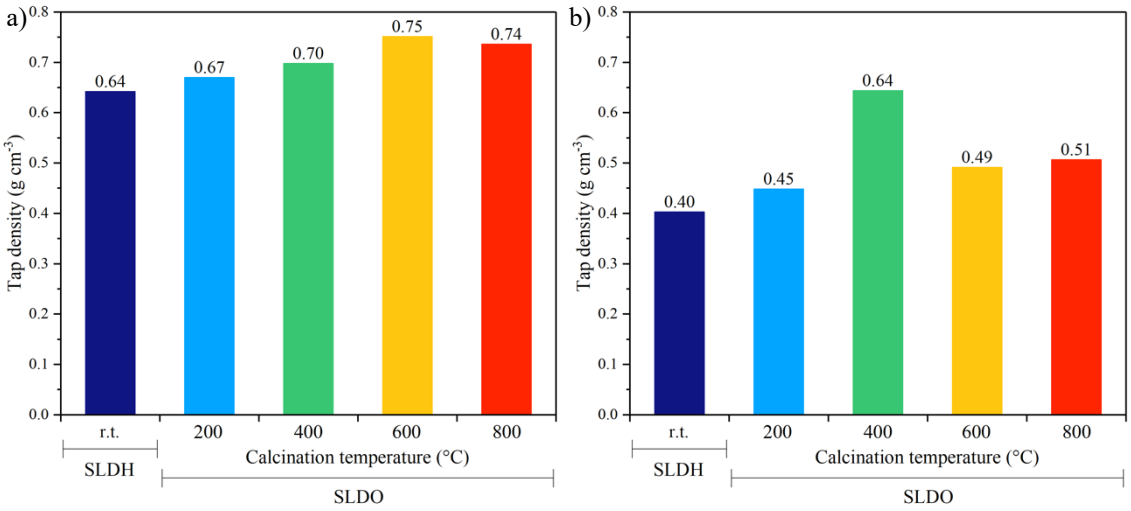


Figure 5.12 Tap densities of M2-85-SLDHs and SLDOs prepared from a) Alfa Aesar and b) NuReSys struvite. Mg/Al = 3.

The tap densities of the SLDOs has also been measured (Figure 5.12). Generally, the tap density increases with increasing calcination temperature. This is expected since the SLDH is firstly dehydrated, which causes the interlayer distance to decrease, and then the amorphous mixed metal oxide becomes more crystalline as the temperature is raised. The anomalous tap density recorded for the NuReSys SLDO prepared at 400 ºC may be due to static charge during the measurement.

5.3 CO_2 adsorption – TGA measurement

The CO_2 adsorption capacity of struvite and SLDOs was firstly evaluated using thermogravimetric analysis (TGA). This method measured the CO_2 adsorption of the

materials over a period of time (Figure 5.13). Struvite was found not to possess any sorption ability (*i.e.* 0 mmol g^{-1}). The trend in total CO_2 adsorption capacity of the SLDOs approximately follows that of N_2 BET specific surface area (Figure 5.14, *cf.* Figure 5.10).

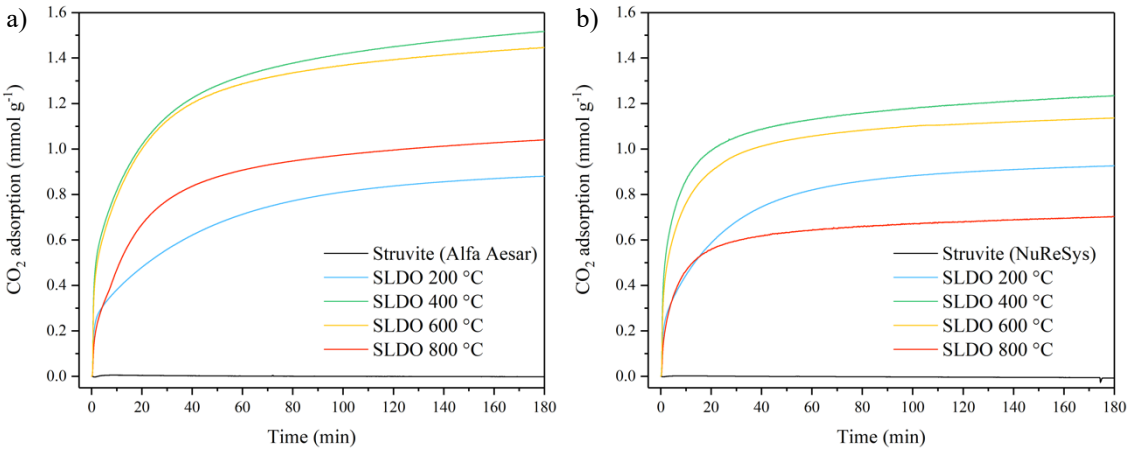


Figure 5.13 CO_2 adsorption as a function of time by struvite and SLDOs prepared from a) Alfa Aesar and b) NuReSys M2-85-SLDHs. The SLDHs were calcined *in situ* (ramp rate = 5 ºC min^{-1}, hold 2 h, 100 cm^3 min^{-1} N_2) and adsorption was measured at 30 ºC (100 cm^3 min^{-1} 20:80 CO_2:N_2).

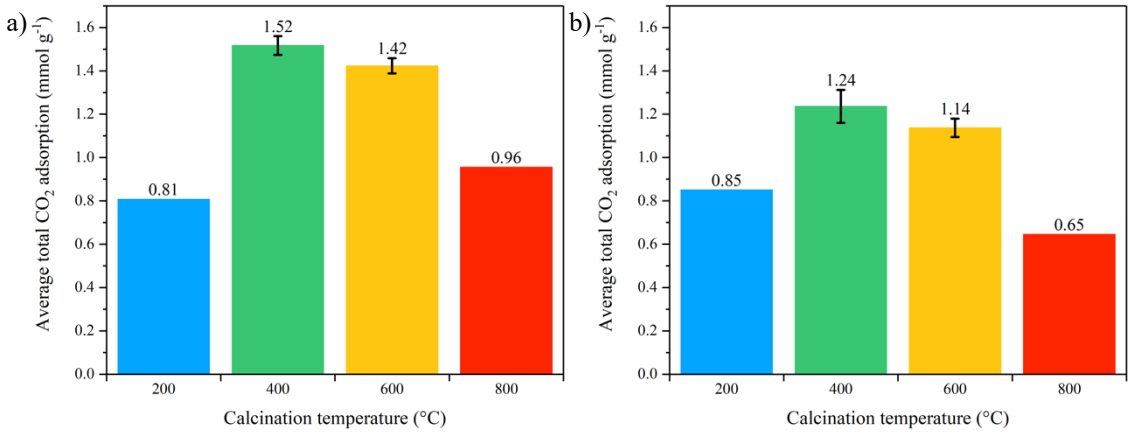


Figure 5.14 Average CO_2 adsorption by SLDOs prepared from a) Alfa Aesar and b) NuReSys M2-85-SLDHs. The SLDHs were calcined *in situ* (ramp rate = 5 ºC min^{-1}, hold 2 h, 100 cm^3 min^{-1} N_2) and adsorption was measured at 30 ºC (100 cm^3 min^{-1} 20:80 CO_2:N_2).

CO_2 may adsorb as a monodentate, bidentate, or bicarbonate species depending on the basicity of the surface sites (Figure 5.15).[40, 41] Monodentate coordination requires strong basic sites, which are low-coordination oxygen anions (O^{2-}) in LDOs formed by either

Mg^{2+} substitution with Al^{3+}, or Al^{3+} migration from the lattice during calcination. Bidentate carbonate forms on metal-oxygen pairs ($M–O^{2-}$, where M = Mg^{2+} or Al^{3+}). Bicarbonate requires surface hydroxyl groups, which are weak basic sites, so this mode is not prevalent above 200 ºC.

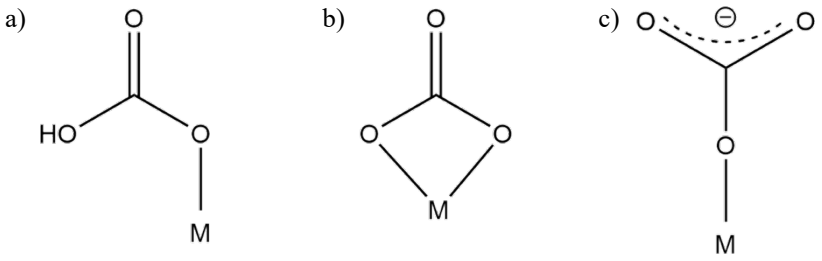


Figure 5.15 Binding modes of CO_2 on metal oxides: a) bicarbonate, b) bidentate and c) monodentate.

The samples prepared at 200 and 800 ºC show the lowest adsorption capacity. Yong *et al.*[42] have also reported low CO_2 adsorption with commercial MgAl-LDHs calcined at 200 ºC. As explained in Section 5.2.2, the samples prepared at 200 ºC are dehydrated SLDHs with low surface areas. Therefore, the low adsorption capacity is attributed to dehydration of the interlayer gallery, which causes a decrease in the interlayer spacing and reduces the amount of gas that can be accommodated.[19] Furthermore, the layered structure is intact and carbonate anions still occupy the interlayer region, thus blocking basic sites on the hydroxide layers. Additionally, the CO_2 adsorption sites available in SLDOs prepared at 200 ºC are predominantly weak (OH^- groups). Consequently, these materials have low CO_2 adsorption capacities.

Above 300 ºC, dehydroxylation of the layers and liberation of interlayer carbonate causes structural changes (*e.g.* collapse of the layered structure and formation of pores) that increase the amount of adsorption sites and increase surface basicity.[29, 32, 43] However, above ~600 ºC, the amorphous mixed metal oxide transforms to a more ordered spinel structure. This results in a decrease in surface area, which leads to a lower CO_2 adsorption capacity.[19, 25]

The results suggest that the samples calcined at 400 ºC have the optimum balance between surface area and active basic sites. At 400 ºC, the SLDOs are amorphous mixed oxides containing MgO- and Al_2O_3-like phases, and the liberation of interlayer anions means that surface basic sites are available to adsorb CO_2. Two additional CO_2 adsorption experiments were carried out either side of 400 ºC, and these also indicate that 400 ºC is the optimum calcination temperature for adsorbent preparation (Figure 5.16). These results are in good agreement with the studies performed by Gao *et al.*[25] on conventional MgAl-CO_3-LDHs.

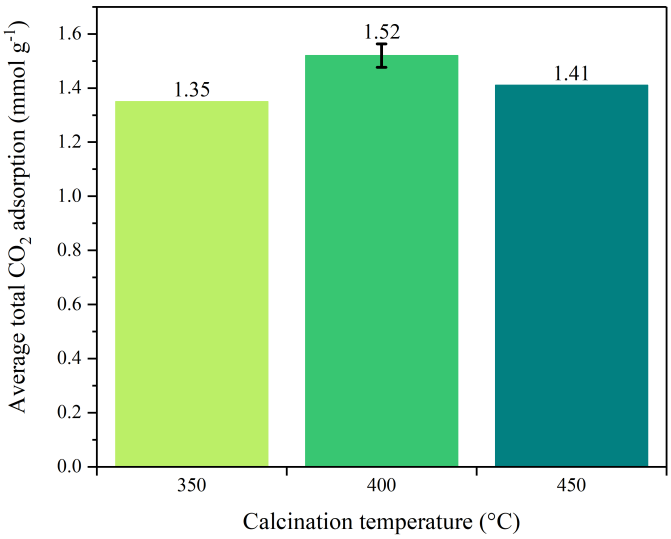


Figure 5.16 Average CO_2 adsorption by SLDOs prepared from Alfa Aesar M2-85-SLDH. The SLDHs were calcined *in situ* (ramp rate = 5 ºC min^{-1}, hold 2 h, 100 cm^3 min^{-1} N_2) and adsorption was measured at 30 °C (100 cm^3 min^{-1} 20:80 CO_2:N_2).

At all temperatures, the SLDOs prepared from NuReSys M2-85-SLDH have lower CO_2 adsorption capacities compared to the equivalent Alfa Aesar samples. The poorer CO_2 absorption ability of NuReSys SLDOs may be related to their elemental composition (Table 5.4). It is widely acknowledged that the active species for CO_2 adsorption is coordinatively unsaturated surface O^{2-} species.[25] In the mixed oxides prepared from MgAl-LDHs, coordinatively unsaturated O^{2-} arise when Al^{3+} is incorporated into the MgO lattice to compensate for the higher positive charge of the cation. ICP-MS data

shows that the NuReSys SLDH contains ~2 wt.% less Mg than the Alfa Aesar SLDH, so its SLDOs will also contain a lower amount of MgO and active species for CO_2 adsorption. Furthermore, the NuReSys SLDH contains a higher amount of Na, P (*e.g.* residual phosphate), Mn, and Fe. These impurities may have prohibited the formation of uncoordinatively saturated Mg–O sites.

Table 5.4 Summary of ICP-MS analyses on M2-85-SLDHs.

Av. wt.%	M2-85-SLDH	
	Alfa Aesar	NuReSys
Mg	21.77	20.28
Al	8.19	7.71
P	1.40	2.45
Na	0.0155	0.0366
K	0.0034	0.0006
Ca	0.2290	0.0901
Mn	0.0071	0.0299
Fe	0.0099	0.0133
Ni	0.0142	0.0003
Cu	0.0008	0.0003
Av. Mg/Al	2.84	2.81

The Alfa Aesar SLDH also contains a higher amount of Ca and K. Since CaO is a known CO_2 adsorbent (Section 5.1.3), this component may contribute to the total CO_2 adsorption capacity of the Alfa Aesar SLDOs. It has been reported in the literature that doping LDHs with potassium carbonate (K_2CO_3) can enhance CO_2 adsorption. Meis *et al.*[44] propose that K^+ substitute Mg^{2+} on the surface of the oxide, creating more oxygen vacancies. The increased adsorption capacity of the K-doped material is attributed to the higher concentration of low-coordinate oxygen sites (Figure 5.17).

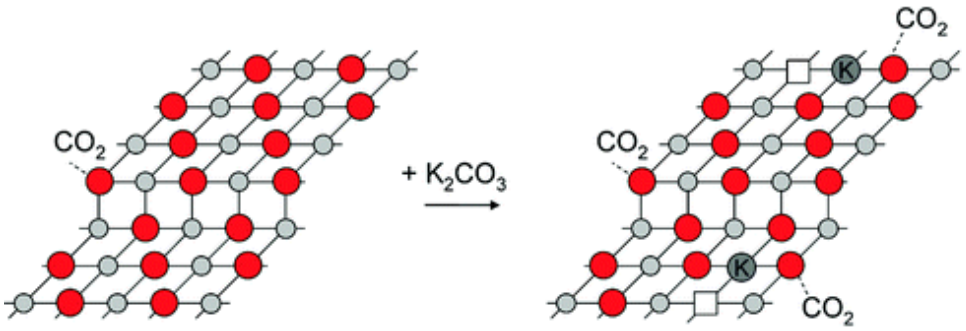


Figure 5.17 Schematic representation of K_2CO_3 addition to an Mg-based LDH and CO_2 adsorption on the surfaces. Red circles are O, light grey circles are Mg and dark grey circles are K.[44]

The CO_2 adsorption capacities of the SLDOs has been compared to the performance of a commercial LDH (Sasol PURAL MG70 HT) and a conventional LDH (c-LDH) with the same Mg/Al ratio, 3. The optimal calcination temperature determined for the SLDHs was used (400 ºC). The recorded CO_2 adsorption capacities indicate that the oxides derived from SLDHs are superior sorbents compared to both the commercial and c-LDOs (Figure 5.18). The Alfa Aesar SLDO has the highest CO_2 adsorption of *ca.* 1.5 mmol g^{-1}.

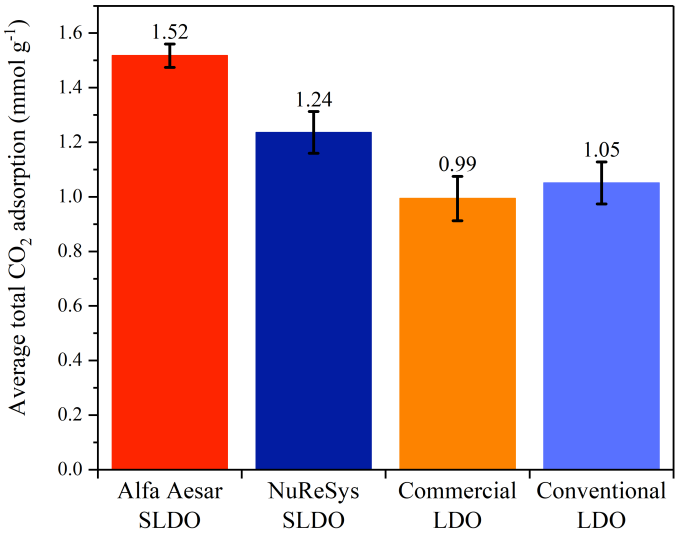


Figure 5.18 Comparison of CO_2 adsorption capacities of various LDOs. LDOs were calcined *in situ* at 400 ºC (ramp rate = 5 ºC min^{-1}, hold 2 h, 100 cm^3 min^{-1} N_2) and adsorption was measured at 30 ºC (100 cm^3 min^{-1} 20:80 CO_2:N_2).

One of the factors influencing the CO_2 adsorption capacities is surface area. The LDOs prepared from the commercial LDH and c-LDH have lower N_2 BET specific surface areas (<147 m^2 g^{-1}) than the SLDOs (>183 m^2 g^{-1}). For the c-LDO, strong attractive

forces between the hydroxide layers and counter anions results in significant *ab*-face staking and a highly aggregated LDH. The topotactic transformation of the LDH to LDO during calcination means that the morphology of the LDH is carried through to the LDO.[45] The density of adsorption sites is therefore low.

The commercial LDH was prepared using a different synthesis method: PURAL MG70 HT is a Mg_3Al-CO_3-LDH synthesised from the oxides MgO and Al_2O_3 (Appendix C Figures C.5 and C.6). This method may not allow the atoms/ions to be intimately mixed, so the elements may not be as well dispersed as in the LDHs and SLDHs.

5.4 CO_2 adsorption – static measurement

Experiments were also performed on a Micromeritics 3Flex instrument to analyse the sorption of CO_2 on the SLDOs in more depth. The SLDOs were prepared at 400 ºC as this was the optimal temperature determined in Section 5.3, and two heating (ramp) rates were used. Again, the Alfa Aesar SLDOs recorded higher CO_2 adsorption capacities than the NuReSys SLDOs (Figure 5.19).

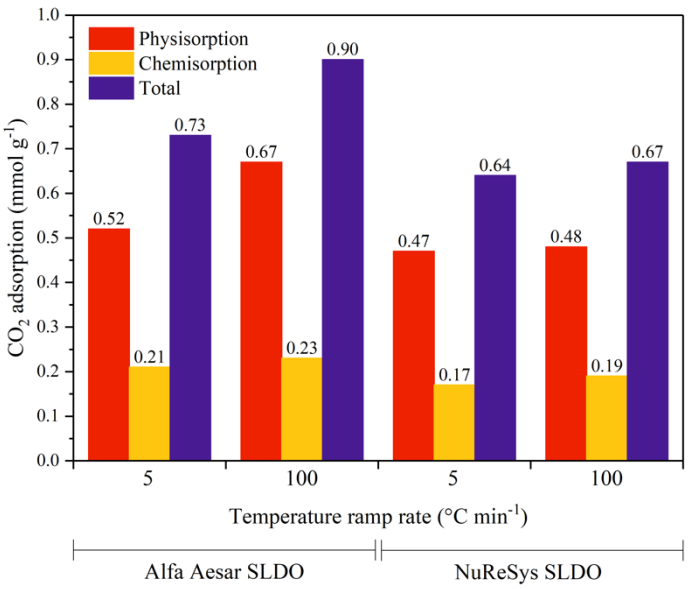


Figure 5.19 CO_2 adsorption of SLDOs prepared from Alfa Aesar and NuReSys M2-85-SLDHs using different ramp rates. Mg/Al = 3. Calcination temperature = 400 ºC.

The 3Flex is able to quantify the contributions from physisorption and chemisorption. Physisorption is defined as adsorption due to Van der Waals interactions. As these are weak dipole interactions, the enthalpy associated with physisorption is low (10–40 kJ mol^{-1}).[46] Mono- and multilayer physisorption is possible. In contrast, chemisorption is adsorption by the formation of a chemical bond between the adsorbent and adsorptive. Chemisorption is highly specific and limited to monolayer adsorption since the adsorbed molecules are linked to the surface via chemical bonds. The enthalpy of chemisorption is of the same order of magnitude as the energy change in a chemical reaction, so it may be exo- or endothermic, and may be very small or very large (20–400 kJ mol^{-1}).[46]

In all cases, physisorption was the dominant CO_2 adsorption mechanism. Additionally, the chemisorption values were approximately constant for each SLDO. The faster ramp rate (100 ºC min^{-1}) appears to enhance the CO_2 adsorption capacity of the Alfa Aesar SLDO. Rapid heating may result in the formation of more defects (*e.g.* cation and oxygen vacancies) that enhance the CO_2 adsorption capacity of the SLDO. Defects are known to affect the electronic properties of oxides, leading to changes in the physicochemical properties of the material and thus aiding the adsorption of substrates.[47, 48]

It is also reasonable to propose that the SLDHs undergo different thermal decomposition mechanisms when they are heated at different rates, thereby forming SLDOs with different compositions. As the rate of heating increases, the material will experience thermal lag – that is, a time delay for heat to be conducted through a material.[49] Studies on a number of other materials show that decomposition temperature increases with increasing heating rate.[49-52] Zhang *et al.*[53] have used thermodynamic data to explain this trend. The conversion rate can be defined in terms of the activation energy and heating rate as follows:

$$\text{Conversion fraction, } x = \frac{m_0 - m_t}{m_0 - m_\infty} \qquad \text{Equation 5.2}$$

where m_0 is the initial sample mass (g), m_t is the sample mass at a particular time (t), and m_∞ is the theoretical mass loss.

$$k(\mathrm{T}) = Ae^{-\frac{E_a}{RT}} \qquad \text{Equation 5.3}$$

where k(T) is the temperature dependence of the rate constant, T is the temperature (Kelvin, K), A is the pre-exponential factor, E_a is the activation energy, and R is the universal gas constant (8.3145 J mol^{-1} K^{-1}).

$$\text{Heating rate, } \beta = \frac{d\mathrm{T}}{dt} \qquad \text{Equation 5.4}$$

$$\text{Conversion rate} = \frac{dx}{dt} = \beta\frac{dx}{d\mathrm{T}} = k(\mathrm{T})\,f(x) = Ae^{-\frac{E_a}{RT}} \cdot f(x) \qquad \text{Equation 5.5}$$

where f(x) is the differential conversion function.

The results suggest that both the activation energy, E_a, and pre-exponential factor, A, of thermal decomposition increases with increasing heating rate. Therefore, in the case of the SLDO prepared using the fast ramp rate, the oxide may be less crystalline and have a higher density of suitable CO_2 adsorption sites.

The performance of the SLDOs has also been compared to an analogous c-LDO and an ethanol-washed AMO-LDO (Figure 5.20). The AMO-LDO has the highest CO_2 adsorption capacity (*ca.* 1.4 mmol g^{-1}), followed by the Alfa Aesar SLDO. The high CO_2 adsorption capacity of the AMO-LDH is attributed to its high surface area (243 m^2 g^{-1}). Furthermore, recent investigations from the O'Hare group indicate that AMO treatment can modify the density of acid and basic sites on LDHs. For some solvents, the interaction of the solvent molecules with the LDH/LDO surfaces can result in blocking of the active sites.

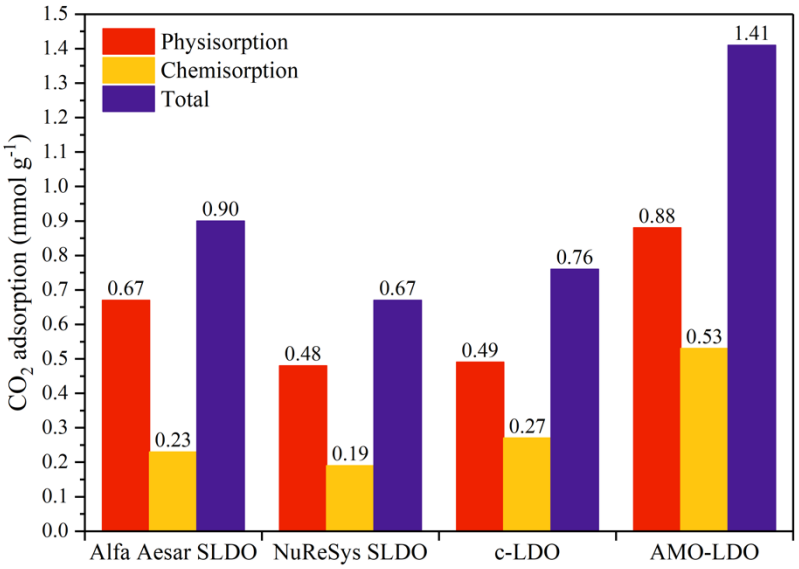


Figure 5.20 CO_2 adsorption of SLDOs, c-LDO and AMO-LDO. Mg/Al = 3. Calcination temperature = 400 ºC. Temperature ramp rate = 100 ºC min^{-1}.

The physisorption capacity of the c-LDO is similar to that of the NuReSys SLDO, but the c-LDO has a higher chemisorption capacity. This suggests that the c-LDO has higher availability of Mg^{2+} than the NuReSys SLDO.[43] The low adsorption capacity of the c-LDO is due to its low surface area (147 m^2 g^{-1}).

Unfortunately, comparison with a core-shell SiO_2@MgAl-LDO was not possible because of instrument repairs and the untimely shutdown of the laboratory due to the global pandemic.

5.5 Conclusion

The thermal decomposition of core-shell SiO_2@Mg_2Al-CO_3-LDHs and Mg_3Al-CO_3-SLDHs has been studied by a number of techniques including powder XRD, FTIR, TEM, BET and TGA. The core-shell material retains its morphology upon heating to 700 ºC and the mass loss it undergoes is dominated by contributions from the LDH component, which transforms into a porous mixed oxide.

The high surface area SLDHs were similarly thermally decomposed into porous oxides. The SLDOs also possessed high surface areas (up to 203 $m^2\ g^{-1}$) and high tap densities (up to 0.75 g cm^{-3}), the latter of which increased with increasing calcination temperature, reflecting the increasing crystallinity of the oxide. The SLDOs have been tested in CO_2 adsorption experiments and recorded higher adsorption capacities (*ca.* 1.5 mmol g^{-1}) than the equivalent commercial and c-LDOs. The higher adsorption capacity of the SLDOs may be attributed to the higher surface area of these oxides, but detailed analysis of the nature of the acid and basic sites was not possible.

Nevertheless, these investigations have shown that struvite-derived LDOs are promising carbon capture materials and that, like c-LDOs, the temperature at which the oxide is generated has a strong influence on the surface area and its CO_2 adsorption capacity. The studies here have found the optimal calcination temperature to be 400 ºC. The heating rate has also been found to affect the CO_2 adsorption capacity of the SLDOs. A fast heating rate (100 ºC min^{-1}) increased the physisorption capacity of the Alfa Aesar SLDO by ~23% and it is hypothesised that "flash heating" results in a different decomposition mechanism and forms more defects in the oxide. There is scope for further optimisation and understanding of this process.

5.6 References

1. S. Arrhenius, *Lond. Edinb. Dubl. Phil. Mag.*, 1896, **41**, 237-276.
2. G. S. Callendar, *Q. J. R. Meteorol. Soc.*, 1938, **64**, 223-240.
3. V. Masson-Delmotte, P. Zhai, H.-O. Pörtner, D. Roberts, J. Skea, P.R. Shukla, A. Pirani, Moufouma-Okia, C. Péan, R. Pidcock, S. Connors, J.B.R. Matthews, Y. Chen, X. Zhou, M.I. Gomis, E. Lonnoy, Maycock, M. Tignor, and T. Waterfield, *IPCC, 2018: Summary for Policymakers*, World Meteorological Organization, Geneva, Switzerland, 2018.
4. C. Rosenzweig, A. Iglesius, X.-B. Yang, P. R. Epstein and E. Chivian, *Global Change Hum. Health*, 2001, **2**, 90-104.
5. R. C. Babcock, R. H. Bustamante, E. A. Fulton, D. J. Fulton, M. D. E. Haywood, A. J. Hobday, R. Kenyon, R. J. Matear, E. E. Plagányi, A. J. Richardson*, et al.*, *Front. Mar. Sci.*, 2019, **6**.
6. S. C. Herring, N. Christidis, A. Hoell, M. P. Hoerling and P. A. Stott, *Bull. Am. Meteorol. Soc.*, 2020, **101**, S1-S128.
7. C. Marchetti, *Clim. Change*, 1977, **1**, 59-68.
8. D. Y. C. Leung, G. Caramanna and M. M. Maroto-Valer, *Renew. Sustain. Energy Rev*, 2014, **39**, 426-443.
9. B. Thitakamol, A. Veawab and A. Aroonwilas, *Int. J. Greenh. Gas Con.*, 2007, **1**, 318-342.
10. A. A. Olajire, *Energy*, 2010, **35**, 2610-2628.
11. F. Hussin and M. K. Aroua, *J. Clean. Prod.*, 2020, **253**, 119707.
12. M. K. Mondal, H. K. Balsora and P. Varshney, *Energy*, 2012, **46**, 431-441.
13. M. Hasib-ur-Rahman, M. Siaj and F. Larachi, *Chem. Eng. Process.*, 2010, **49**, 313-322.
14. K. Sumida, D. L. Rogow, J. A. Mason, T. M. McDonald, E. D. Bloch, Z. R. Herm, T.-H. Bae and J. R. Long, *Chem. Rev.*, 2012, **112**, 724-781.
15. S. Choi, J. H. Drese and C. W. Jones, *ChemSusChem*, 2009, **2**, 796-854.
16. R. V. Siriwardane, M.-S. Shen, E. P. Fisher and J. A. Poston, *Energy Fuels*, 2001, **15**, 279-284.
17. S. Wang, S. Yan, X. Ma and J. Gong, *Energy Environ. Sci.*, 2011, **4**, 3805-3819.
18. J. C. Abanades, E. J. Anthony, J. Wang and J. E. Oakey, *Environ. Sci. Technol.*, 2005, **39**, 2861-2866.
19. M. K. Ram Reddy, Z. P. Xu, G. Q. Lu and J. C. Diniz da Costa, *Ind. Eng. Chem. Res.*, 2006, **45**, 7504-7509.
20. R. Barker, *J. Appl. Chem. Biotechnol.*, 1973, **23**, 733-742.
21. D. Mess, A. F. Sarofim and J. P. Longwell, *Energy Fuels*, 1999, **13**, 999-1005.
22. N. N. A. H. Meis, J. H. Bitter and K. P. de Jong, *Ind. Eng. Chem. Res.*, 2010, **49**, 1229-1235.
23. M. B. Jensen, L. G. M. Pettersson, O. Swang and U. Olsbye, *J. Phys. Chem. B*, 2005, **109**, 16774-16781.
24. Q. Wang, J. Luo, Z. Zhong and A. Borgna, *Energy Environ. Sci.*, 2011, **4**, 42-55.
25. Y. Gao, Z. Zhang, J. Wu, X. Yi, A. Zheng, A. Umar, D. O'Hare and Q. Wang, *J. Mater. Chem. A*, 2013, **1**, 12782-12790.
26. L. T. Zhuravlev, *Colloids Surf. Physicochem. Eng. Aspects*, 2000, **173**, 1-38.
27. C. Chen, M. Yang, Q. Wang, J.-C. Buffet and D. O'Hare, *J. Mater. Chem. A*, 2014, **2**, 15102-15110.
28. M. S. Yang, O. McDermott, J.-C. Buffet and D. O'Hare, *RSC Adv.*, 2014, **4**, 51676-51682.

29. K. J. D. MacKenzie, R. H. Meinhold, B. L. Sherriff and Z. Xu, *J. Mater. Chem.*, 1993, **3**, 1263-1269.
30. O. Madelung, U. Rössler and M. Schulz, in *II-VI and I-VII Compounds; Semimagnetic Compounds*, Springer Berlin Heidelberg, Berlin, Heidelberg, 1999, pp. 1-6.
31. W. Yang, Y. Kim, P. K. T. Liu, M. Sahimi and T. T. Tsotsis, *Chem. Eng. Sci.*, 2002, **57**, 2945-2953.
32. F. Rey, V. Fornes and J. M. Rojo, *J. Chem. Soc., Faraday Trans.*, 1992, **88**, 2233-2238.
33. F. Millange, R. I. Walton and D. O'Hare, *J. Mater. Chem.*, 2000, **10**, 1713-1720.
34. W. T. Reichle, S. Y. Kang and D. S. Everhardt, *J. Catal.*, 1986, **101**, 352-359.
35. M. Bellotto, B. Rebours, O. Clause, J. Lynch, D. Bazin and E. Elkaïm, *J. Phys. Chem.*, 1996, **100**, 8535-8542.
36. D. Tichit, M. N. Bennani, F. Figueras and J. R. Ruiz, *Langmuir*, 1998, **14**, 2086-2091.
37. M. del Arco, C. Martin, I. Martin, V. Rives and R. Trujillano, *Spectrochim. Acta, Pt. A: Mol. Spectrosc.*, 1993, **49**, 1575-1582.
38. K. S. Sing, *Pure Appl. Chem.*, 1985, **57**, 603-619.
39. W. L. J. Kwok, MChem Part II, University of Oxford, 2016.
40. J. I. Di Cosimo, V. K. Díez, M. Xu, E. Iglesia and C. R. Apesteguía, *J. Catal.*, 1998, **178**, 499-510.
41. V. K. Díez, C. R. Apesteguía and J. I. Di Cosimo, *J. Catal.*, 2003, **215**, 220-233.
42. Z. Yong, Mata and A. E. Rodrigues, *Ind. Eng. Chem. Res.*, 2001, **40**, 204-209.
43. N. D. Hutson, S. A. Speakman and E. A. Payzant, *Chem. Mater.*, 2004, **16**, 4135-4143.
44. N. N. A. H. Meis, J. H. Bitter and K. P. de Jong, *Ind. Eng. Chem. Res.*, 2010, **49**, 8086-8093.
45. Q. Meng and H. Yan, *Mol. Simul.*, 2017, **43**, 1338-1347.
46. M. Králik, *Chem. Pap.*, 2014, **68**, 1625-1638.
47. G. Wang, H. Wang, Y. Ling, Y. Tang, X. Yang, R. C. Fitzmorris, C. Wang, J. Z. Zhang and Y. Li, *Nano Lett.*, 2011, **11**, 3026-3033.
48. D. Zu, H. Wang, S. Lin, G. Ou, H. Wei, S. Sun and H. Wu, *Nano Res.*, 2019, **12**, 2150-2163.
49. L. P. Domingues, R. L. Wilfong and L. R. R. Furlong, *Pyrolysis of Five Salts of Yttrium, Lanthanum and Cerium*, U.S. Department of the Interior, Bureau of Mines, 1962.
50. G. F. M. Pinheiro, V. L. Lourenço and K. Iha, *J. Therm. Anal. Calorim.*, 2002, **67**, 445-452.
51. P. Gimenez and S. Fereres, *Energy Procedia*, 2015, **69**, 654-662.
52. A. Ammasi, *Trans. Indian Inst. Met.*, 2020, **73**, 93-98.
53. X. Zhang, Y. Han, Y. Li and Y. Sun, *Minerals*, 2017, **7**, 211.

Chapter 6: Conclusion and outlook

The work in this thesis has focused on developing and optimising syntheses of layered double hydroxides (LDHs) and hybrid LDH materials. The importance of seemingly trivial parameters, such as stirring speed and solution addition rate, were realised and quantified in terms of their effect on the surface area of core-shell silica@LDH materials (SiO_2@Mg_2Al-CO_3-AMO-LDH). It was found that stirring speed has a greater influence on morphology and surface area than the metal addition rate, with moderate stirring speeds (*e.g.* 500 rpm) giving rise to products with honeycomb-like LDH shells and the highest N_2 BET specific surface areas (*ca.* 95 m^2 g^{-1}).[1]

To prepare core-shell SiO_2@Mg_2Al-CO_3-AMO-LDH using commercial silicas, a wet impregnation step was introduced to aid LDH crystallisation on the silica surface. By introducing Al^{3+} to the silica before the co-precipitation step, Si–O–Al bonds are formed and facilitate LDH growth on the silica. This method is now routinely used for the synthesis of SiO_2@LDH catalyst supports for ethylene polymerisation. Further investigations on the SiO_2@LDH interface have taken place since this work was first published: an optimum amount of Al^{3+} for impregnation has been determined experimentally and characterised by solid state nuclear magnetic resonance spectroscopy (ssNMR).[2]

In line with the drive for industries to become "greener", this thesis presents struvite, $MgNH_4PO_4.6H_2O$, as a promising alternative starting material for magnesium based LDHs. The transformation of this wastewater mineral has been studied using a synthetic struvite and optimised to produce atom efficient and scalable methods with yields of Mg_3Al-CO_3-SLDH up to 95%. The optimised method involves pre-treatment of struvite in alkali prior to the co-precipitation step, which allows ammonium (NH_4^+) to be

collected and potentially recycled. The reaction conditions can also be adjusted to allow the struvite phosphate (PO_4^{3-}) to be incorporated into the final SLDH as the interlayer anion. With these adjustments, the synthesis is approximately 5% more atom economical than a co-precipitation performed using magnesium nitrate hexahydrate. This method was also successfully applied to struvites obtained directly from wastewater treatment plants (WWTPs) without modification, further demonstrating its potential as an alternative starting material for circular economy approaches.

The investigations indicate that the transformation proceeds through a metastable intermediate in which partial substitution of NH_4^+ by Na^+ has occurred. A dissolution-crystallisation mechanism is proposed as the morphology of the SLDHs has been observed by scanning electron microscopy (SEM) to resemble that of the parent struvite. Furthermore, the SLDHs have been found to possess high surface areas (*ca.* 184 $m^2\ g^{-1}$) and high tap densities (*ca.* 0.68 $g\ cm^{-3}$). This combination of properties is lacking in both conventional and aqueous miscible solvent treated LDHs (c-LDHs and AMO-LDHs, respectively), which may allow SLDHs to be used in applications hitherto unsuitable for these LDHs.

Finally, the thermal decomposition of SLDHs and SiO_2@Mg_2Al-CO_3-AMO-LDHs was studied in order to prepare the most suitable layered double oxides (LDOs) for testing in carbon dioxide (CO_2) adsorption. The SLDHs undergo stepwise thermal decomposition (dehydration, dehydroxylation and decarboxylation) similar to c-LDHs. The highest surface area (*ca.* 203 $m^2\ g^{-1}$) and porosity (*ca.* 0.97 $g\ cm^{-3}$) were recorded for the SLDOs prepared at 400 ºC, which is consistent with the literature.[3] These SLDOs are porous mixed oxides: the calcination temperature is sufficient to destroy the layered structure but not so high as to affect the ordering of cations into spinel-like domains.

The CO_2 adsorption capacities of the SLDOs were higher than those of LDOs prepared from a commercial LDH and a c-LDH. The highest adsorption was recorded for the SLDO prepared from a synthetic struvite (Alfa Aesar, *ca.* 1.5 mmol g^{-1}) and is attributed to the high surface area of this material (203 m^2 g^{-1}). Sorption tests were also carried out to determine the physisorption and chemisorption contributions to the adsorption capacities. In all cases, physisorption was the dominant mechanism and was found to be affected by the rate of calcination. For example, a fast heating rate (100 ºC min^{-1} compared to 5 ºC min^{-1}) increased the physisorption capacity of the Alfa Aesar SLDO by ~23%. It is hypothesised that rapid heating alters the decomposition pathway, resulting in an LDO containing more defects. There is scope for further optimisation and understanding of the surface properties of SLDOs and the CO_2 adsorption mechanism.

The application of SLDHs should be complemented by further investigations into the transformation mechanism (*e.g. in situ* X-ray diffraction and *in situ* AFM) to enable a deeper understanding of the reaction, which could lead to enhancement of the synthesis. The work here also yielded promising results in preliminary studies into the preparation of ternary SLDHs and core-shell SiO_2@SLDHs, so it will be of interest to optimise these procedures to extend the library of SLDHs and investigate whether these possess equally interesting properties as the MgAl-SLDHs created in this thesis.

References

1. W. L. J. Kwok, D.-G. Crivoi, C. Chen, J.-C. Buffet and D. O'Hare, *Dalton Trans.*, 2018, **47**, 143-149.
2. R. Strachan, MChem Part II, University of Oxford, 2019.
3. Y. Gao, Z. Zhang, J. Wu, X. Yi, A. Zheng*, et al.*, *J. Mater. Chem. A*, 2013, **1**, 12782-12790.

Appendix A: Appendix for Chapter 3

A.1 M1-SLDHs

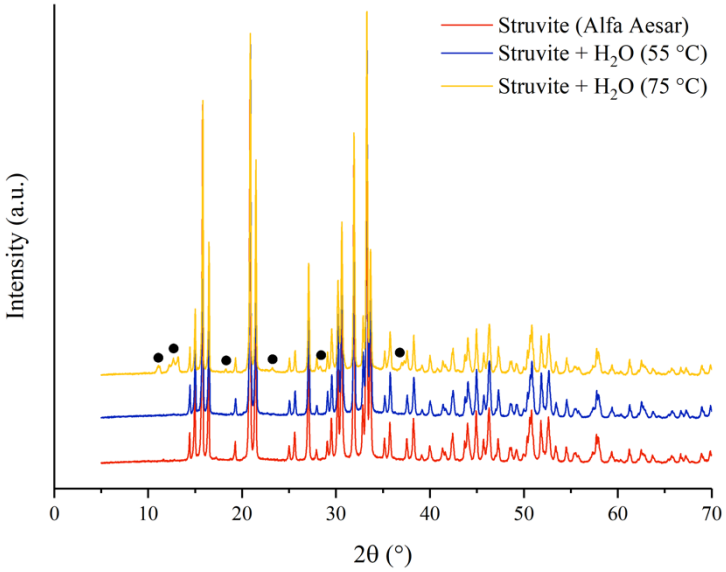


Figure A.1 Powder XRD diffractograms of struvite and struvite heated in D.I. water at different temperatures for 1 h. ● $Mg_3(PO_4)_2.8H_2O$ (bobierrite).

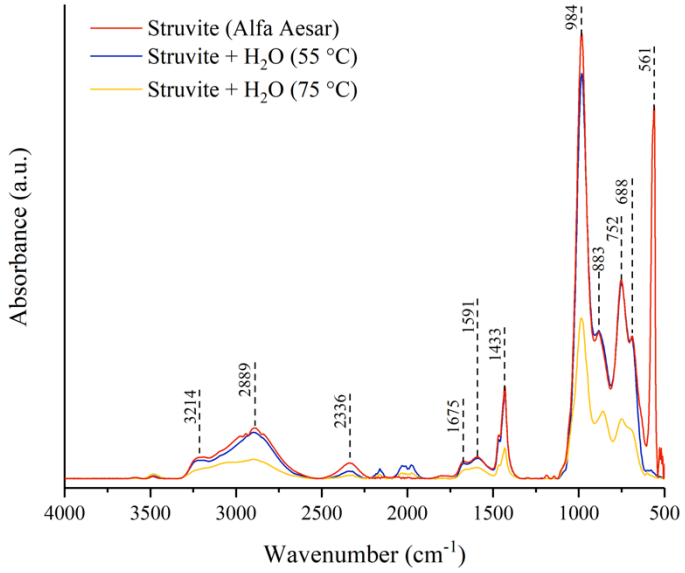


Figure A.2 FTIR spectra of struvite and struvite heated in D.I. water at different temperatures for 1 h.

Table A.1 ICP-MS elemental analysis of M1-SLDHs prepared from Alfa Aesar and WWTP struvites.

Struvite	Alfa Aesar		NuReSys	Niersverband
Av. wt.%	M1-55-SLDH	M1-75-SLDH	M1-75-SLDH	M1-75-SLDH
Na	0.5993	0.0058	0.4178	B.D.L.
Mg	16.2875	20.8521	19.7401	16.9294
Al	6.4262	7.8703	7.7932	7.5642
P	6.5548	1.7249	2.3682	1.8434
K	B.D.L.	B.D.L.	0.0039	0.0005
Ca	0.1942	0.1906	0.0942	0.2251
V	B.D.L.	B.D.L.	B.D.L.	B.D.L.
Cr	0.0003	0.0003	0.0003	0.0007
Mn	0.0006	0.0007	0.0282	0.1001
Fe	0.0077	0.0083	0.0195	4.9045
Co	B.D.L.	B.D.L.	B.D.L.	0.0002
Ni	0.0115	0.0136	0.0002	0.0004
Cu	0.0006	0.0007	0.0002	0.0012
Zn	0.0030	0.0028	0.0038	0.0048
As	B.D.L.	B.D.L.	B.D.L.	B.D.L.
Mo	B.D.L.	B.D.L.	B.D.L.	B.D.L.
Ag	B.D.L.	B.D.L.	B.D.L.	B.D.L.
Cd	B.D.L.	B.D.L.	B.D.L.	B.D.L.
Sb	B.D.L.	B.D.L.	B.D.L.	B.D.L.
Ba	0.0005	0.0006	0.0005	0.0013
Tl	B.D.L.	B.D.L.	B.D.L.	B.D.L.
Pb (208)	B.D.L.	B.D.L.	B.D.L.	0.0001
U	B.D.L.	B.D.L.	B.D.L.	B.D.L.

B.D.L. = below detection limit.

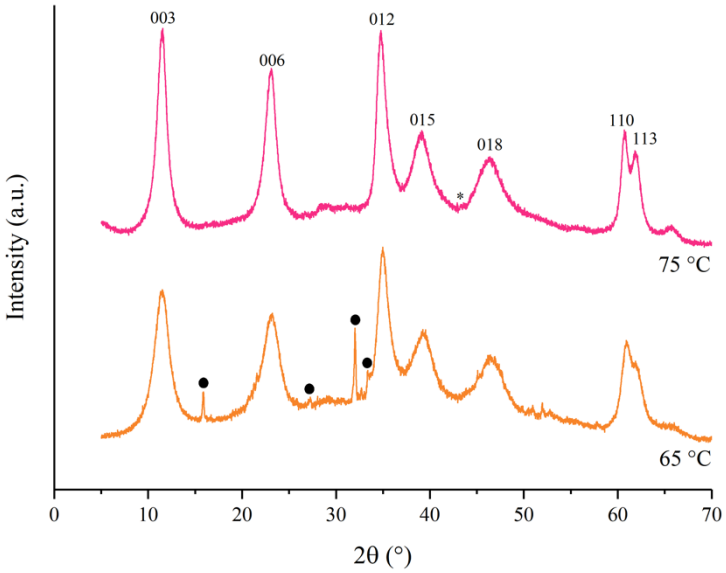


Figure A.3 Powder XRD diffractograms of M1-SLDHs prepared from NuReSys struvite at 65 and 75 ºC. *Reflections due to the sample holder. ● Unreacted struvite.

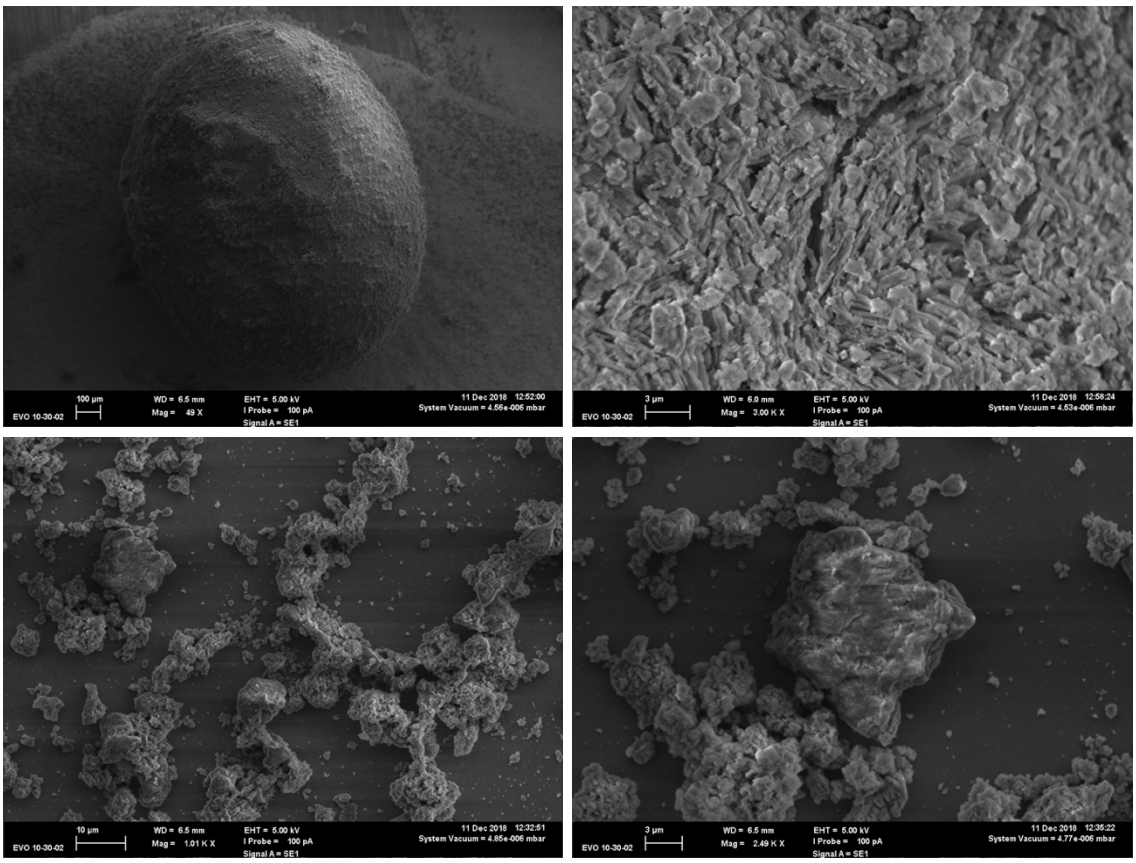


Figure A.4 SEM images of M1-65-SLDH prepared from NuReSys struvite. Top row: large struvite granules did not fully decompose but transformation to SLDH was able to take place on the surface and through the crevices that developed. Bottom row: sand rose-like clusters of SLDH.

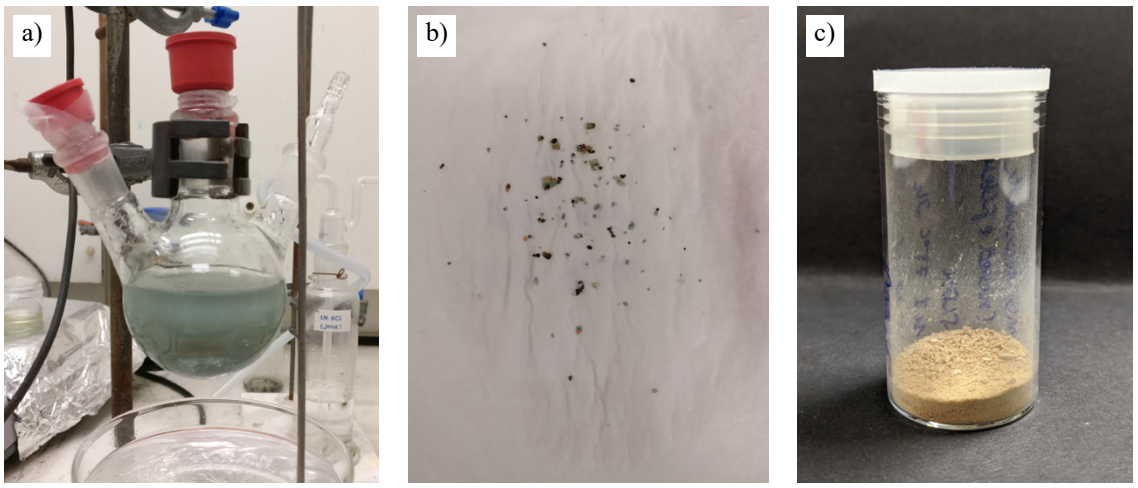


Figure A.5 a) Niersverband struvite transformation to SLDH: the reaction mixture initially turned grey-blue but became brown after ageing; b) undissolved debris filtered out of the slurry before washing with D.I. water; c) dried Niersverband M1-75-SLDH: the tan colour is attributed to the presence of iron.

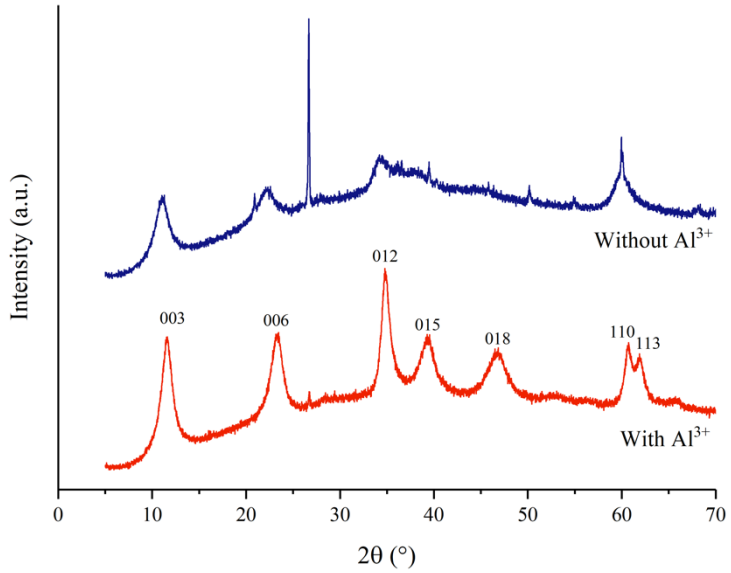


Figure A.6 Niersverband struvite was used to make an M1-75-SLDH (red line). Separately, a control reaction was performed because unusual colour changes occurred during the reaction (Figure A.5). In the control reaction, Niersverband struvite was heated in water, Na_2CO_3 and NaOH without Al^{3+}. The product of the control reaction (blue line) has Bragg reflections that indicate the presence of an LDH-phase. This is likely to be due to the reaction of other metals in the impure struvite, as ICP-MS data indicates the presence of iron and manganese (Table A.1). The curved baseline in the spectra is due to fluorescence caused by iron.

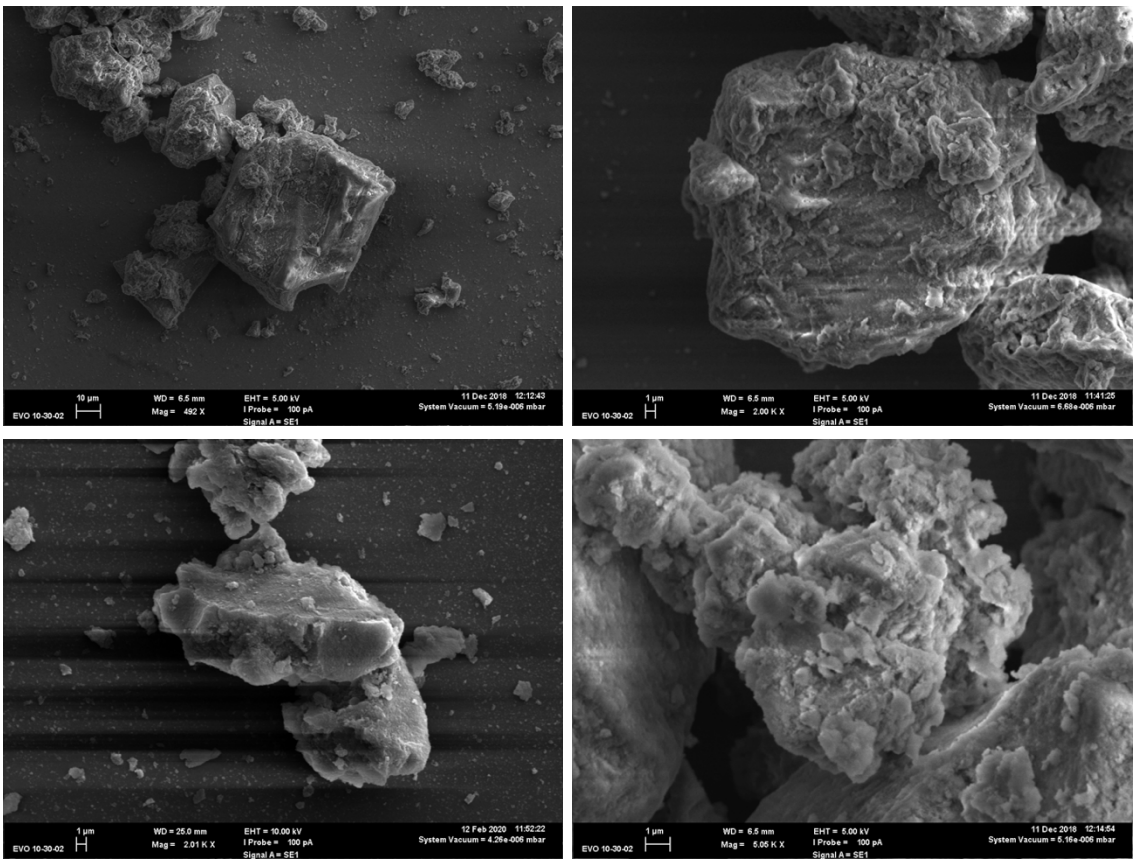


Figure A.7 SEM images of Niersverband M1-75-SLDH. Mg/Al = 3.

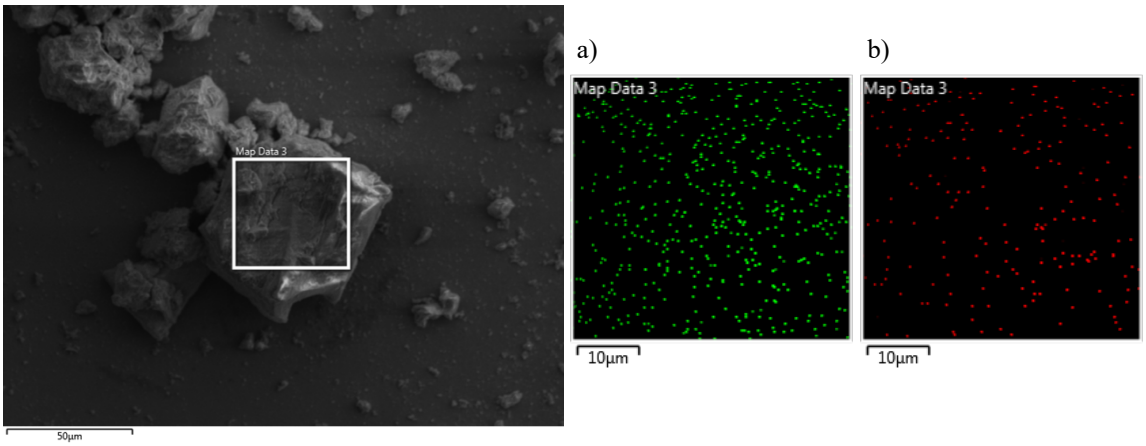


Figure A.8 SEM-EDX elemental analysis of a) Mg and b) Al of Niersverband M1-75-SLDH. Mg: 64.26 wt.%. Al: 35.74 wt.%.

Table A.2 Lattice parameters and mean crystallite domain lengths (CDLs) of M1-75-SLDHs prepared from WWTP struvites. Mg/Al = 3.

M1-75-SLDH	*d*-spacing (Å)		Lattice parameter (Å)		CDL (Å)	
	d_{003}	d_{110}	$c^{\dagger}$	$a^{\ddagger}$	*c*-axis	*ab*-plane
Niersverband	7.66	1.53	22.98	3.06	50.4	167.0
NuReSys	7.70	1.52	23.10	3.04	62.8	163.4
NuReSys (65 ºC)	7.72	1.52	23.16	3.04	42.9	135.1

†Lattice parameter $c = 3d_{003}$. ‡Lattice parameter $a = 2d_{110}$.
CDL = 0.89λ/βcosθ, λ = 1.541847 Å, β = FWHM in radians.

Table A.3 Powder XRD Bragg reflection data for M1-75-SLDHs. Mg/Al = 3.

M1-75-SLDH	003[a] (º)	FWHM[b] (º)	110[c] (º)	FWHM[d] (º)
Niersverband	11.55	1.59	60.67	0.96
NuReSys	11.48	1.28	60.67	0.98
NuReSys (65 ºC)	11.46	1.87	60.91	1.20

[a]Position of the 003 Bragg reflection (2θ), [b]FWHM of the 003 reflection.
[c]Position of the 110 Bragg reflection (2θ), [d]FWHM of 110 reflection.

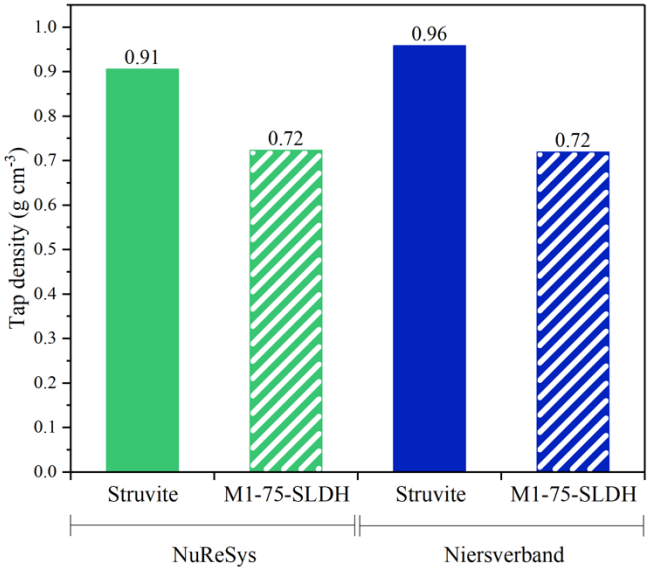


Figure A.9 Tap density of struvites and M1-SLDHs prepared from two WWTP struvites. Mg/Al = 3.

A.2 M2-SLDHs

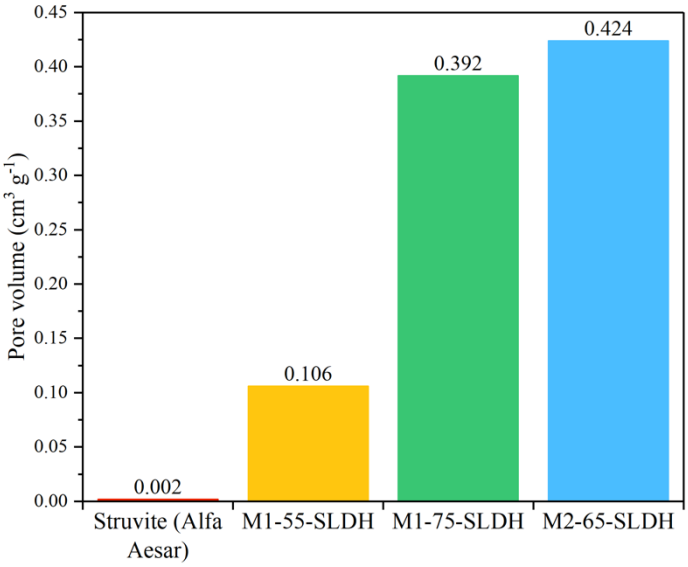


Figure A.10 Pore volumes of struvite, M1- and M2-SLDHs.

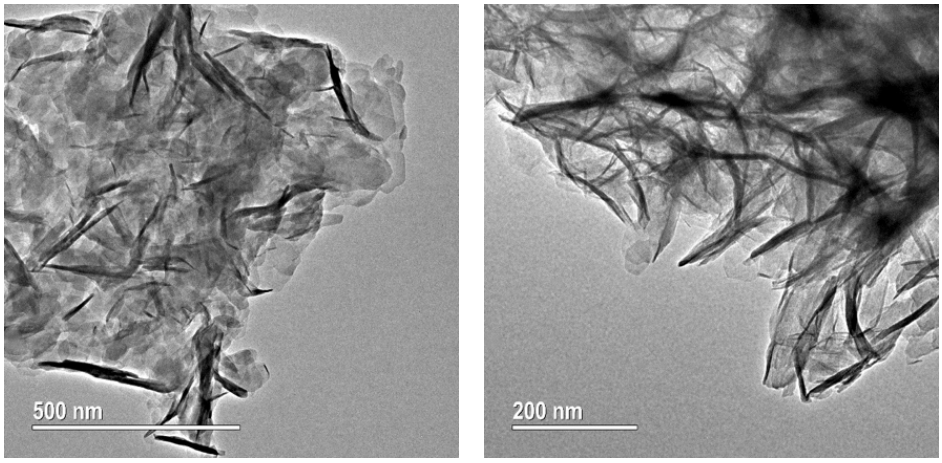


Figure A.11 SEM images of Mg_3Al-PO_4-SLDH prepared by M2.

Table A.4 ICP-MS elemental analyses of M2-SLDHs with different metal ratios and interlayer anions.

Av. wt.%	Mg/Al =3		Mg/Al=2	
	CO_3^{2-}	PO_4^{3-}	CO_3^{2-}	PO_4^{3-}
Na	0.0155	0.0129	0.0080	0.0077
Mg	21.7708	19.1317	20.9425	20.5748
Al	8.1888	6.4138	8.9936	7.5840
Si	B.D.L.	B.D.L.	B.D.L.	B.D.L.
P	1.3947	3.1381	1.6384	3.6488
K	0.0034	0.0003	0.0051	0.0051
Ca	0.2290	0.1726	0.1329	0.1711
V	B.D.L.	B.D.L.	B.D.L.	B.D.L.
Cr	0.0004	0.0004	0.0003	0.0003
Mn	0.0007	0.0005	0.0006	0.0006
Fe	0.0099	0.0078	0.0062	0.0068
Co	B.D.L.	B.D.L.	B.D.L.	B.D.L.
Ni	0.0142	0.0119	0.0120	0.0124
Cu	0.0008	0.0002	0.0003	0.0004
Zn	0.0027	0.0074	0.0051	0.0044
As	B.D.L.	B.D.L.	B.D.L.	B.D.L.
Se	0.001	0.0001	0.0002	0.0001
Mo	B.D.L.	B.D.L.	B.D.L.	B.D.L.
Ag	B.D.L.	B.D.L.	B.D.L.	B.D.L.
Cd	B.D.L.	B.D.L.	B.D.L.	B.D.L.
Sb	B.D.L.	B.D.L.	B.D.L.	B.D.L.
Ba	0.0006	0.0003	0.0007	0.0006
Hg	B.D.L.	B.D.L.	B.D.L.	B.D.L.
Tl	B.D.L.	B.D.L.	B.D.L.	B.D.L.
Pb (208)	0.0001	B.D.L.	B.D.L.	B.D.L.
Th	B.D.L.	B.D.L.	B.D.L.	B.D.L.
U	B.D.L.	B.D.L.	B.D.L.	B.D.L.

B.D.L. = below detection limit.

A.3 Study of the transformation of struvite to LDH

Table A.5 ICP-MS elemental analysis of struvite heated in NaOH (85 ºC).

Av. wt.%	1 h	3 h
Na	3.4588	7.3276
Mg	12.8137	15.9466
Al	0.0007	0.0474
Si	B.D.L.	B.D.L.
P	13.3627	16.3016
K	0.0009	0.0078
Ca	0.1027	0.1355
V	B.D.L.	B.D.L.
Cr	0.0001	0.0002
Mn	0.0003	0.0008
Fe	0.0028	0.0050
Co	B.D.L.	B.D.L.
Ni	0.0079	0.0099
Cu	0.0001	0.0014
Zn	0.0006	0.0019
As	B.D.L.	B.D.L.
Se	B.D.L.	0.0003
Mo	B.D.L.	B.D.L.
Ag	B.D.L.	B.D.L.
Cd	B.D.L.	B.D.L.
Sb	B.D.L.	B.D.L.
Ba	0.0001	0.0002
Hg	B.D.L.	B.D.L.
Tl	B.D.L.	B.D.L.
Pb (208)	B.D.L.	0.0002
Th	B.D.L.	B.D.L.
U	B.D.L.	B.D.L.

B.D.L. = below detection limit.

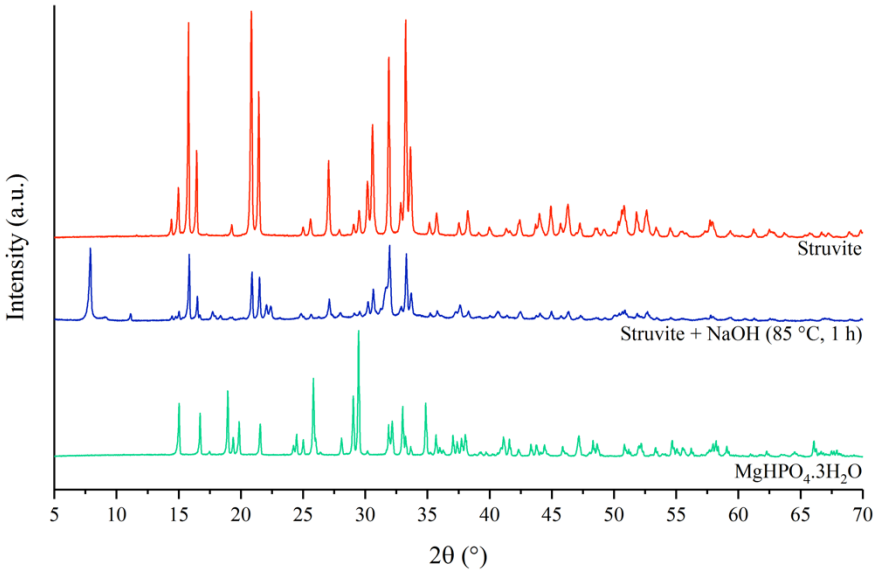


Figure A.12 Powder XRD diffractograms of struvite, struvite decomposed in NaOH (85 ºC, 1 h) and magnesium hydrogen phosphate, $MgHPO_4.3H_2O$. XRD patterns were recorded for different Mg, Na, PO_4 compounds for comparison to the spectrum of the decomposition product.

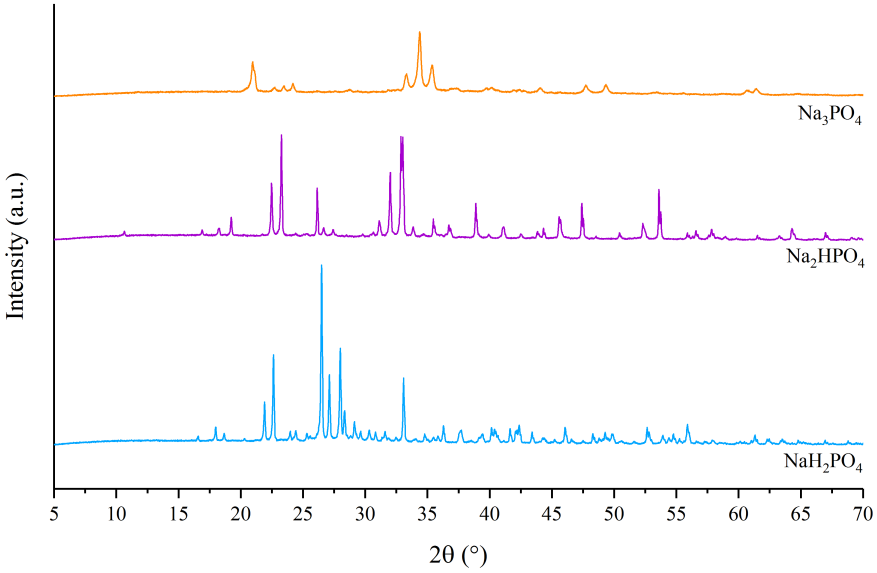


Figure A.13 Powder XRD diffractograms of sodium phosphates. These were recorded for comparison to the spectrum of the decomposition product.

Table A.6 Chemical shift data for ^{23}Na DPMAS ssNMR spectrum of struvite decomposed in NaOH (85 ºC, 1 h).

Chemical shift (ppm)	%
–2.55	55.2
–9.58	44.8

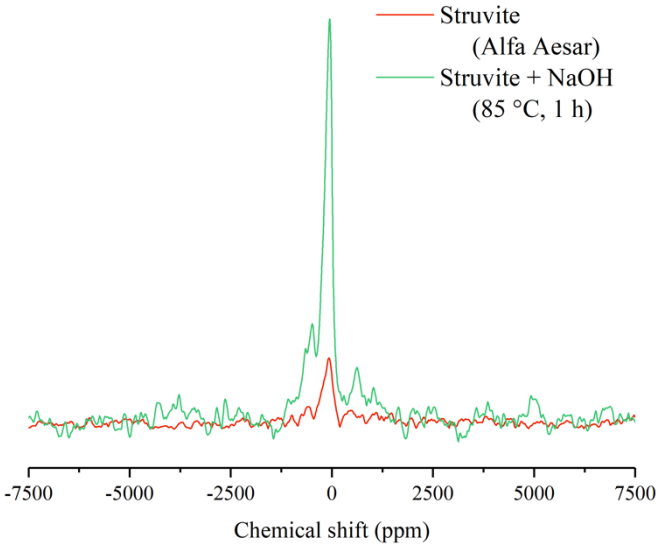


Figure A.14 ^{25}Mg DFS-echo ssNMR spectra of struvite and struvite heated in NaOH (85 ºC, 1 h).

A.4 Synthesis of SLDHs containing zinc

Table A.7 Bragg reflections and Miller indices of ZnO (Figure 3.38). In the hexagonal ZnO the lattice parameters are related to the Miller indices by $1/d^2 = 4/3\ (h^2+hk+k^2)/a + l^2/c^2$.

hkl	2θ (º)
100	31.81
002	34.45
101	36.27
102	47.58
110	56.66
103	62.91
112	68.00
201	69.12

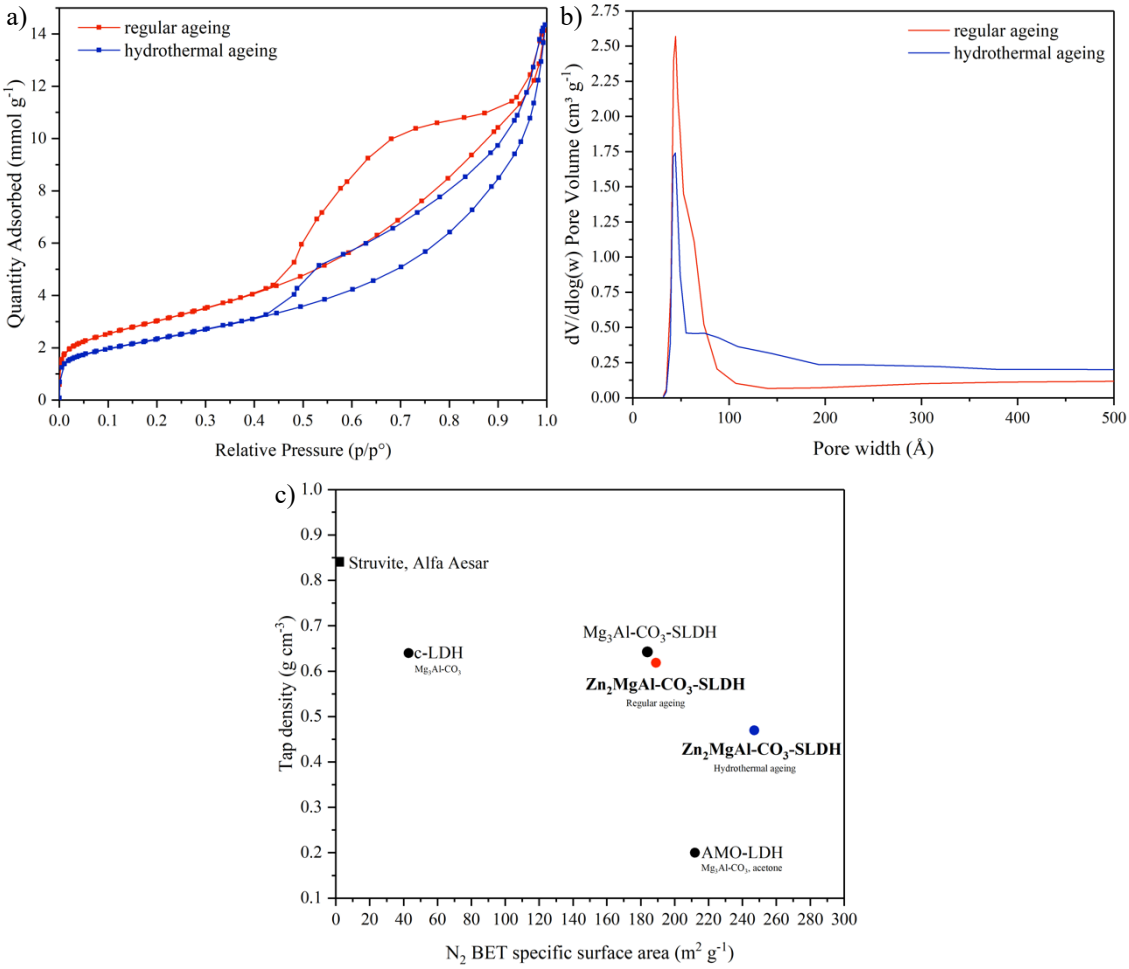


Figure A.15 a) N_2 adsorption and desorption isotherms, b) BJH pore size distributions, and c) N_2 BET specific surface area and tap densities of Zn-SLDHs prepared using M2 (pH 9).

Table A.8 ICP-MS analyses of Zn-SLDHs (M2, pH 9).

Av. wt.%	Regular ageing	Hydrothermal ageing
Na	0.4536	0.0271
Mg	3.6779	5.4458
Al	4.1928	5.8470
P	4.6095	6.3587
K	0.0007	0.0006
Ca	0.0298	0.0643
V	B.D.L.	B.D.L.
Cr	B.D.L.	B.D.L.
Mn	B.D.L.	0.0002
Fe	0.0016	0.0073
Co	B.D.L.	B.D.L.
Ni	0.0023	0.0035
Cu	B.D.L.	0.0003
Zn	22.2438	30.7092
As	B.D.L.	B.D.L.
Mo	B.D.L.	B.D.L.
Ag	B.D.L.	B.D.L.
Cd	B.D.L.	B.D.L.
Sb	B.D.L.	B.D.L.
Ba	0.0001	0.0001
Tl	B.D.L.	B.D.L.
Pb (208)	B.D.L.	B.D.L.
U	B.D.L.	B.D.L.

B.D.L. = below detection limit.

A.5 Aqueous miscible organic solvent treatment (AMOST) of SLDHs

Table A.9 Powder XRD Bragg reflection data for SLDH prepared with and without AMOST (XRD diffractogram = Figure 3.44a). Mg/Al = 3. AMO solvent = EtOH.

	003[a] (º)	FWHM[b] (º)	110[c] (º)	FWHM[d] (º)
SLDH	11.35	1.03	60.61	0.79
AMO-SLDH	11.39	1.32	60.60	0.77

[a]Position of the 003 Bragg reflection (2θ), [b]FWHM of the 003 reflection.
[c]Position of the 110 Bragg reflection (2θ), [d]FWHM of 110 reflection.

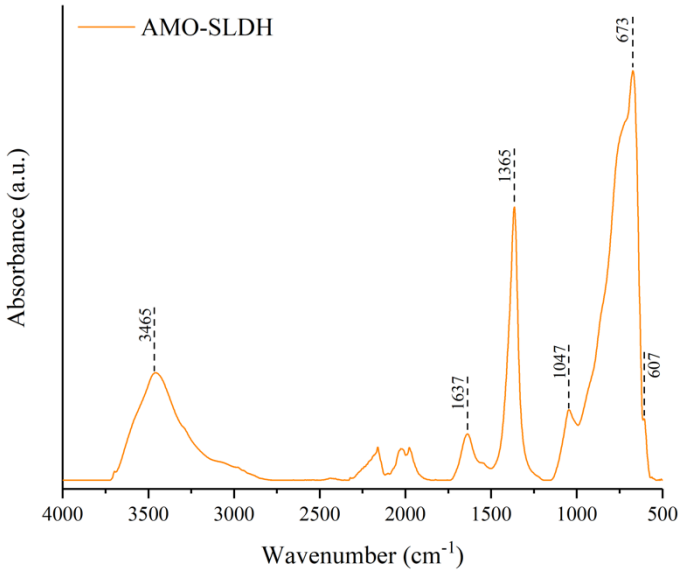


Figure A.16 FTIR spectrum of Mg_3Al-CO_3-AMO-SLDH. AMO solvent = EtOH.

The broad absorption band at *ca.* 3400 cm^{-1} is due to the vibrational and stretching modes of O–H groups (water and EtOH). The absorption band at 1637 cm^{-1} is due to the H–O–H bending mode of water, which indicates that there is still some water present in the SLDH even after AMOST. Intercalated carbonate gives rise to the sharp absorption at 1363 cm^{-1} and the absorption band at 1047 cm^{-1} indicates the presence of residual phosphate from the struvite starting material. The absorptions below 1000 cm^{-1} are due to M–O vibrational modes.

Table A.10 ICP-MS elemental analysis of AMO-SLDH. AMO solvent = EtOH.

Av. wt.%	AMO-SLDH
Na	0.0162
Mg	21.6726
Al	8.1732
Si*	0.0967
P	1.4693
K	0.0058
Ca	0.1527
V	B.D.L.
Cr	0.0003
Mn	0.0006
Fe	0.0060
Co	0.0001
Ni	0.0129
Cu	0.0003
Zn	0.0024
As	B.D.L.
Se	0.0003
Mo	B.D.L.
Ag	B.D.L.
Cd	B.D.L.
Sb	B.D.L.
Ba	0.0003
Hg	B.D.L.
Tl	B.D.L.
Pb (208)	B.D.L.
Th	B.D.L.
U	B.D.L.
Av. Mg/Al	2.65

B.D.L. = below detection limit.
*soluble fraction.

A.6 Preparation of SLDH from WWTP struvite

Table A.11 Powder XRD Bragg reflection data for M2-85-SLDHs (Figure 3.59). Mg/Al = 3.

M2-85-SLDH	003[a] (º)	FWHM[b] (º)	110[c] (º)	FWHM[d] (º)
Alfa Aesar	11.35	1.03	60.61	0.79
NuReSys	11.37	1.46	60.72	0.81
Aa en Maas	11.46	0.90	60.63	0.62

[a]Position of the 003 Bragg reflection (2θ), [b]FWHM of the 003 reflection.
[c]Position of the 110 Bragg reflection (2θ), [d]FWHM of 110 reflection.

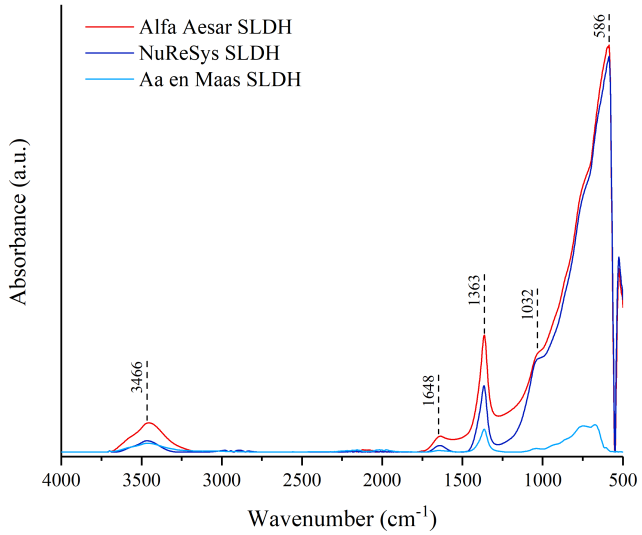


Figure A.17 FTIR spectra of M2-85-SLDHs. Mg/Al = 3.

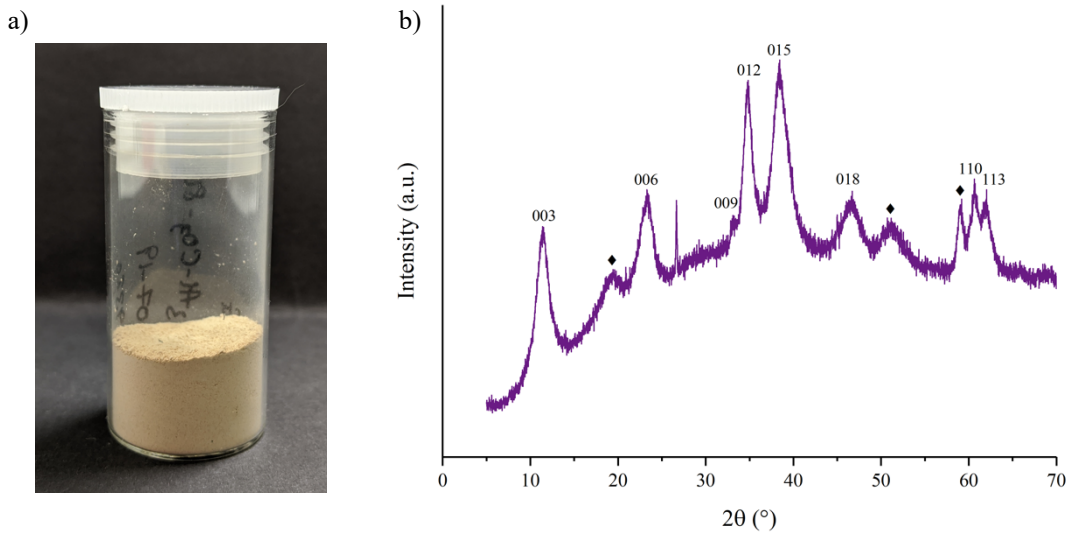


Figure A.18 a) Photo and b) powder XRD diffractogram of M2-85-SLDH prepared using ASG struvite. The tan colour of the product is due to Fe (Table A.13). Bragg reflections corresponding to $Mg(OH)_2$ (♦) are present in addition to reflections due to MgAl-SLDH. Fluorescence due to Fe is also observed. N_2 BET specific surface area = 247 m^2 g^{-1}. Tap density = 0.77 g cm^{-3}.

Table A.12 ICP-MS elemental analysis of M2-85-SLDH (9 g batches).

Av. wt.%	M2-85-SLDH					
	Alfa Aesar I	Alfa Aesar II	Alfa Aesar III	NuReSys	Aa en Maas I	Aa en Maas II
Na	0.0155	0.0054	0.0121	0.0366	0.0064	0.2059
Mg	21.7708	21.0664	21.6123	20.2784	20.83	19.32
Al	8.1888	7.8990	8.1848	7.7085	7.67	6.70
P	1.3947	1.3590	1.4126	2.4496	1.03	3.72
K	0.0034	B.D.L.	0.0008	0.0006	0.0002	B.D.L.
Ca	0.2290	0.1716	0.2014	0.0901	0.0491	0.0634
V	B.D.L.	B.D.L.	0.0001	B.D.L.	B.D.L.	B.D.L.
Cr	0.0004	0.0003	0.0003	0.0004	0.0001	0.0001
Mn	0.0007	0.0006	0.0006	0.0299	0.0072	0.0066
Fe	0.0099	0.0061	0.0071	0.0133	0.2859	0.2659
Co	B.D.L.	B.D.L.	B.D.L.	B.D.L.	B.D.L.	B.D.L.
Ni	0.0142	0.0126	0.0188	0.0003	0.0003	0.0002
Cu	0.0008	0.0002	0.0003	0.0003	0.0002	0.0002
Zn	0.0027	0.0019	0.0023	0.0037	0.0017	0.0017
As	B.D.L.	B.D.L.	B.D.L.	B.D.L.	B.D.L.	B.D.L.
Se	0.0001	0.0001	0.0002	0.0001	B.D.L.	B.D.L.
Mo	B.D.L.	B.D.L.	B.D.L.	B.D.L.	B.D.L.	B.D.L.
Ag	B.D.L.	B.D.L.	B.D.L.	B.D.L.	B.D.L.	B.D.L.
Cd	B.D.L.	B.D.L.	B.D.L.	B.D.L.	B.D.L.	B.D.L.
Sb	B.D.L.	B.D.L.	B.D.L.	B.D.L.	B.D.L.	B.D.L.
Ba	0.0006	0.0005	0.0006	0.0006	0.0004	0.0004
Hg	B.D.L.	B.D.L.	B.D.L.	B.D.L.	B.D.L.	B.D.L.
Tl	B.D.L.	B.D.L.	B.D.L.	B.D.L.	B.D.L.	B.D.L.
Pb (208)	0.0001	B.D.L.	B.D.L.	B.D.L.	B.D.L.	B.D.L.
Th	B.D.L.	B.D.L.	B.D.L.	B.D.L.	B.D.L.	B.D.L.
U	B.D.L.	B.D.L.	B.D.L.	B.D.L.	B.D.L.	B.D.L.
Mg/Al	2.84	2.85	2.82	2.81	2.90	2.95

B.D.L. = below detection limit.

Table A.13 ICP-MS elemental analysis of ASG M2-85-SLDH (mixture of $Mg(OH)_2$ and SLDH).

Struvite	ASG
Av. wt.%	M2-85-SLDH
Na	0.0121
Mg	20.7949
Al	5.0800
P	1.6590
K	0.0004
Ca	0.2083
V	B.D.L.
Cr	0.0002
Mn	0.3588
Fe	5.0185
Co	B.D.L.
Ni	0.0005
Cu	0.0008
Zn	0.0056
As	B.D.L.
Mo	B.D.L.
Ag	B.D.L.
Cd	B.D.L.
Sb	B.D.L.
Ba	0.0018
Tl	B.D.L.
Pb (208)	0.0002
U	B.D.L.

B.D.L. = below detection limit.

A.7 Reference c-LDH (Ref-LDH)

Table A.14 Lattice parameters and mean CDLs of a reference c-LDH synthesised under the same conditions as M2-85-SLDH (XRD diffractogram = Figure 3.60). Mg/Al = 3.

	d-spacing (Å)		Lattice parameter (Å)		CDL (Å)	
	d_{003}	d_{110}	$c^{\dagger}$	$a^{\ddagger}$	*c*-axis	*ab*-plane
Ref. c-LDH	7.78	1.53	23.34	3.06	220.3	369.2

†Lattice parameter $c = 3d_{003}$. ‡Lattice parameter $a = 2d_{110}$.
CDL = 0.89λ/βcosθ, λ = 1.541847 Å, β = FWHM in radians.

Table A.15 Powder XRD Bragg reflection data of a reference c-LDH synthesised under the same conditions as M2-85-SLDH (Figure 3.60). Mg/Al = 3.

	003[a] (º)	FWHM[b] (º)	110[c] (º)	FWHM[d] (º)
Ref. c-LDH	11.37	0.36	60.47	0.43

[a]Position of the 003 Bragg reflection (2θ), [b]FWHM of the 003 reflection.
[c]Position of the 110 Bragg reflection (2θ), [d]FWHM of 110 reflection.

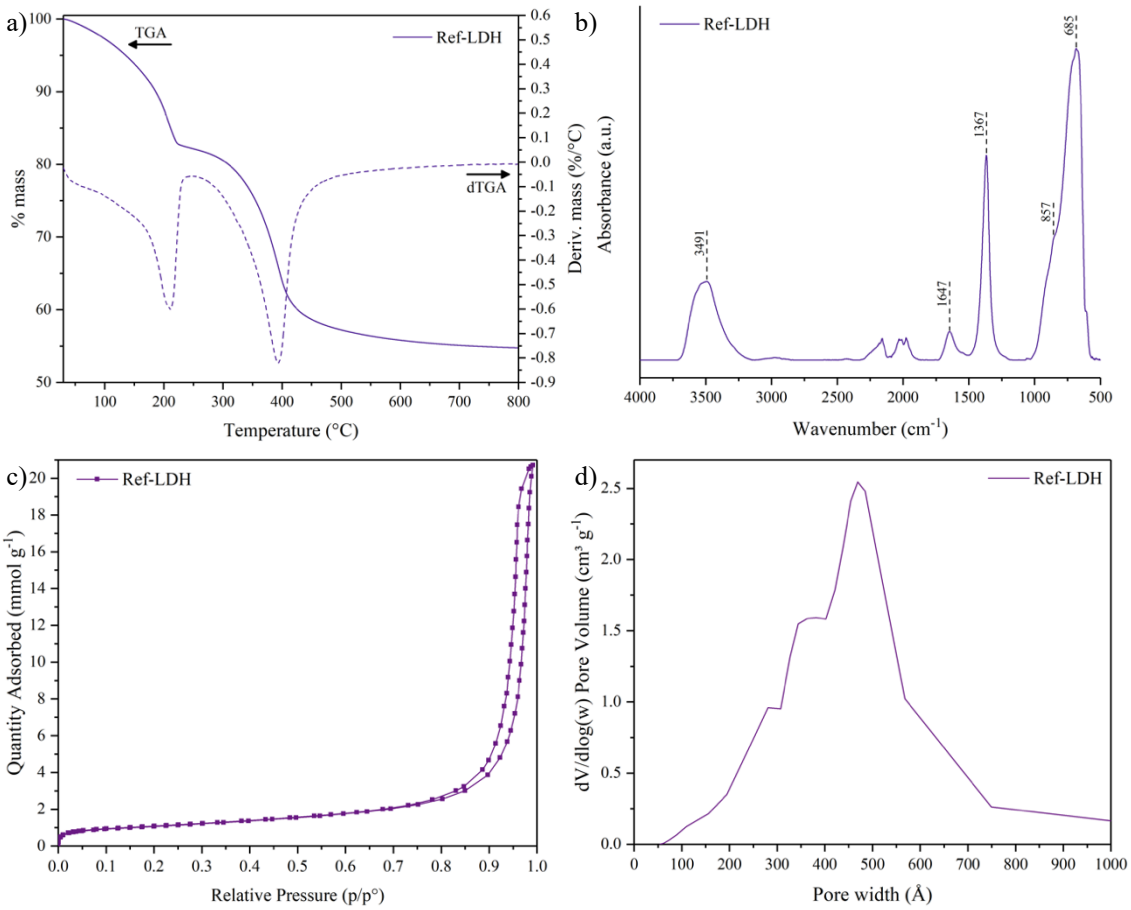


Figure A.19 a) TGA and dTGA curves, b) FTIR spectrum, c) N_2 adsorption and desorption isotherms and d) BJH pore size distribution of a reference c-LDH synthesised under the same conditions as M2-85-SLDH. Mg/Al = 3. N_2 BET specific surface area = 85 m^2 g^{-1}.

Table A.16 ICP-MS elemental analysis of a reference c-LDH synthesised under the same conditions as M2-85-SLDH.

Av. wt.%	Reference c-LDH
Na	B.D.L.
Mg	22.1430
Al	8.4816
P	B.D.L.
K	B.D.L.
Ca	0.0040
V	B.D.L.
Cr	0.0003
Mn	0.0001
Fe	0.0025
Co	B.D.L.
Ni	0.0004
Cu	B.D.L.
Zn	0.0011
As	B.D.L.
Mo	B.D.L.
Ag	B.D.L.
Cd	B.D.L.
Sb	B.D.L.
Ba	0.0001
Tl	B.D.L.
Pb (208)	B.D.L.
U	B.D.L.
Av. Mg/Al	2.61

B.D.L. = below detection limit.

A.8 Attempted synthesis of SLDH in acidic conditions

Although struvite is sparingly soluble in water, it is readily soluble in acid. The dissociated struvite was combined with $Al(NO_3)_3.9H_2O$ and precipitated in a basic solution containing Na_2CO_3. In all cases, struvite reformed when the pH was raised, despite the presence of Al^{3+} (Figure A.20).

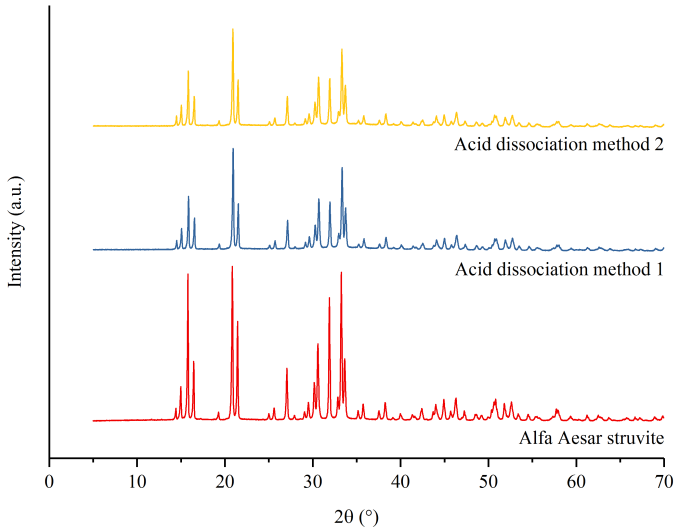


Figure A.20 Powder XRD diffractograms of struvite and products of acid dissociation SLDH syntheses.

The XRD diffractograms (Figure A.20) show that the products were less crystalline than the starting material. The high stirring speed (1000 rpm) during the synthesis may be a factor in this because high shearing forces prevent the aggregation of nuclei and platelets, resulting in porous networks. Fragmentation of crystallites can also occur under high turbulence.

Appendix B: Appendix for Chapter 4

B.1 Chemical composition of core-shell SiO_2@Mg_2Al-CO_3-AMO-LDHs

Table B.1 ICP-MS elemental analyses of core-shell SiO_2@Mg_2Al-CO_3-AMO-LDHs

Metal addition rate†		Stirring speed (rpm)	Av. wt.%				Av. Mg/Al
mL h^{-1}	mmol h^{-1}		Mg	Al	Si*	Na	
15	1.1	0	9.2017	5.2618	1.0770	0.2015	1.94
15	1.1	250	10.1764	5.7958	1.0651	0.1326	1.95
15	1.1	500	10.3974	5.7664	0.8392	0.0198	2.00
15	1.1	750	10.4262	5.7367	0.9422	0.0484	2.02
15	1.1	1000	10.3292	5.7167	1.0074	0.1122	2.01
30	2.2	500	10.0856	5.5168	1.0310	0.1811	2.03
30	2.2	1000	10.4871	5.6788	3.0180	0.0198	2.05
60	4.3	500	10.3170	5.6541	0.6765	0.0157	2.03
60	4.3	750	9.2460	5.3107	0.8891	0.0928	1.93
60	4.3	1000	10.5977	5.8945	0.8661	0.0353	2.00
120	8.6	500	10.2082	5.6554	0.7332	0.0101	2.00
120	8.6	1000	10.5588	5.8374	0.6333	0.1039	2.01

†conversion based on 20 cm^3 metal salt solution.
*acid-soluble fraction.

B.2 Characterisation of Stöber silica

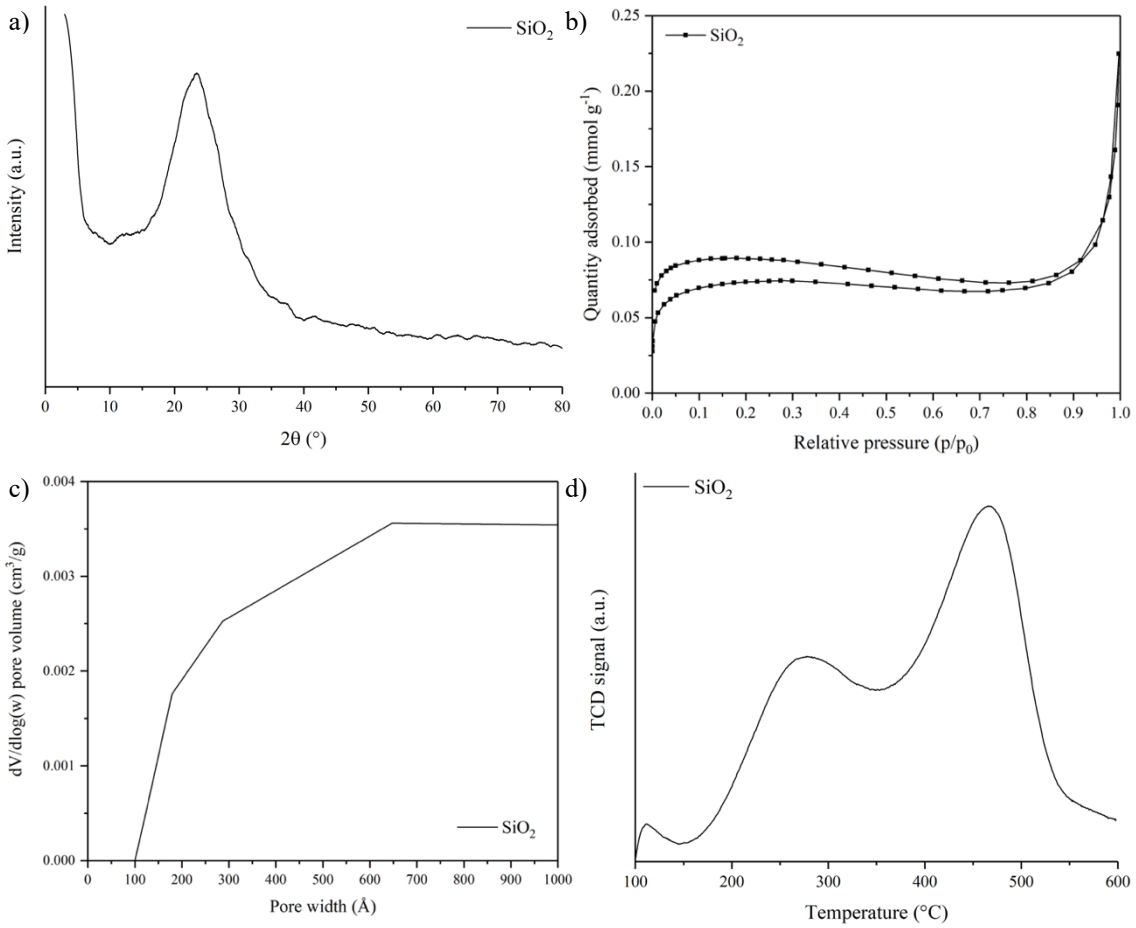


Figure B.1 a) Powder XRD diffractogram, b) N_2 adsorption and desorption isotherms, c) BJH pore size distribution, and d) TPD-CO_2 analysis of of SiO_2 prepared by a modified Stöber method.

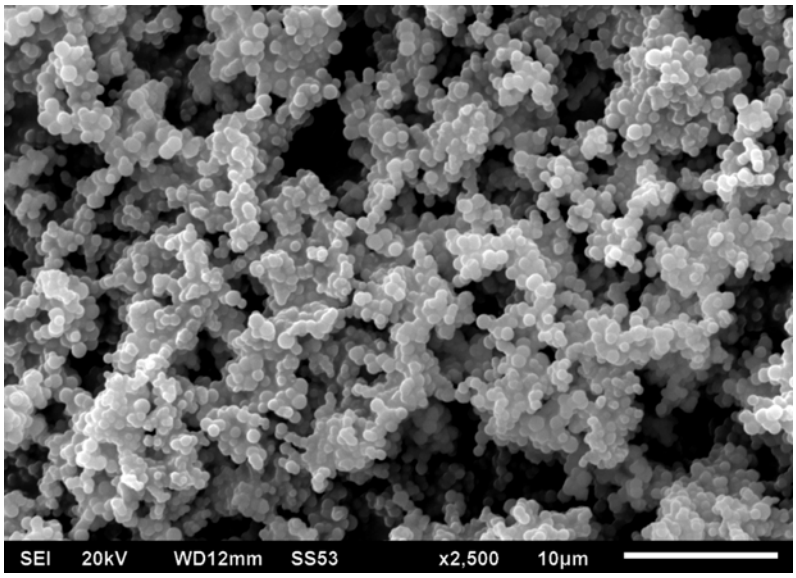


Figure B.2 SEM image of SiO_2 prepared by a modified Stöber method.

B.3 Variation of stirring speed

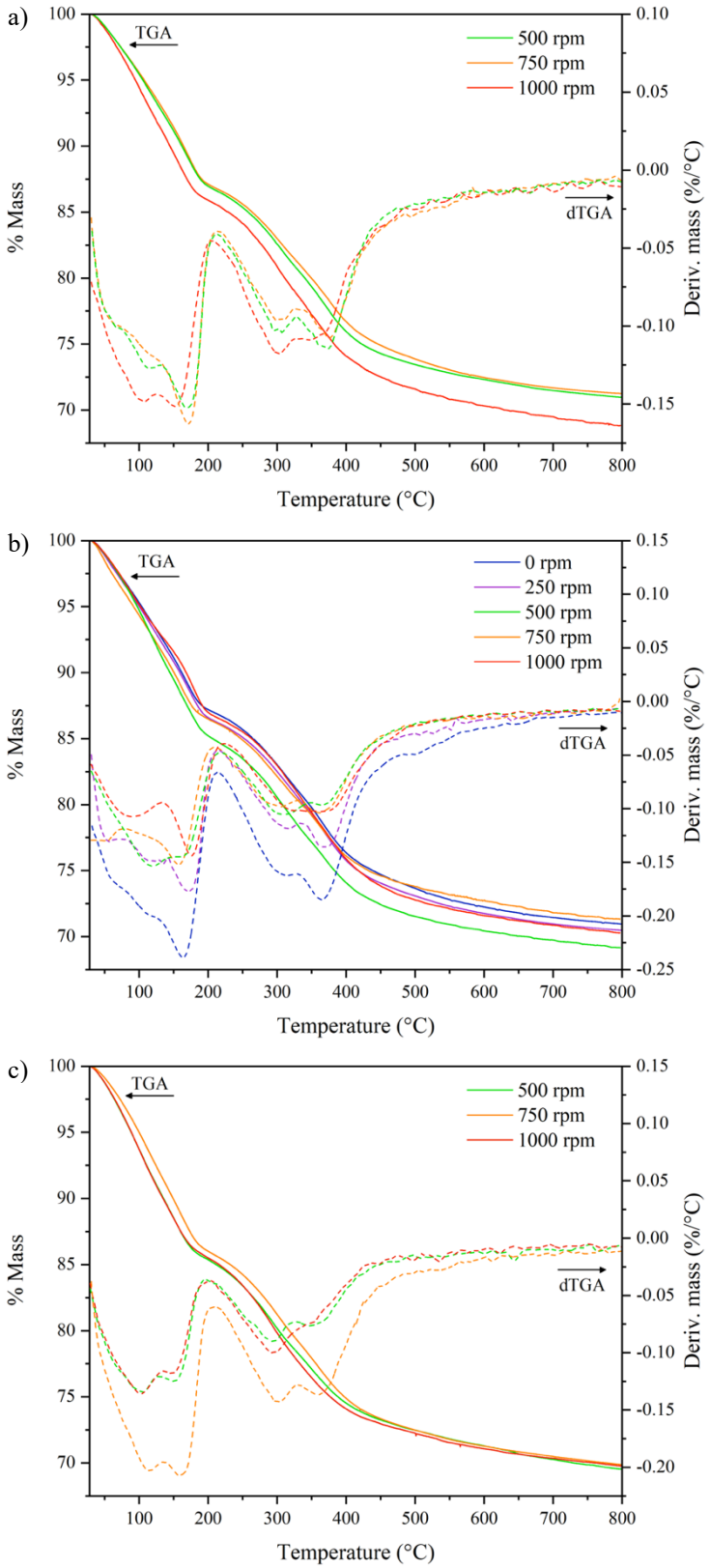


Figure B.3 TGA and dTGA curves SiO_2@Mg_2Al-CO_3-AMO-LDHs prepared using different stirring speeds. Metal addition rate = a) 2.2, b) 4.3 and c) 8.6 mmol h^{-1}. AMO solvent = EtOH.

Table B.2 Powder XRD Bragg reflection data of SiO_2@Mg_2Al-CO_3-AMO-LDHs prepared using different stirring speeds (XRD diffractogram = Figure 4.5). Metal addition rate = 1.1 mmol h^{-1}. AMO solvent = EtOH.

Stirring speed (rpm)	003[a] (º)	FWHM[b] (º)	110[c] (º)	FWHM[d] (º)
0	11.55	0.67	60.96	0.40
250	11.63	0.20	60.88	0.37
500	11.64	0.17	60.85	0.13
750	11.51	0.27	60.84	0.18
1000	11.49	0.40	60.81	0.33

[a]Position of the 003 Bragg reflection (2θ), [b]FWHM of the 003 reflection.
[c]Position of the 110 Bragg reflection (2θ), [d]FWHM of 110 reflection.

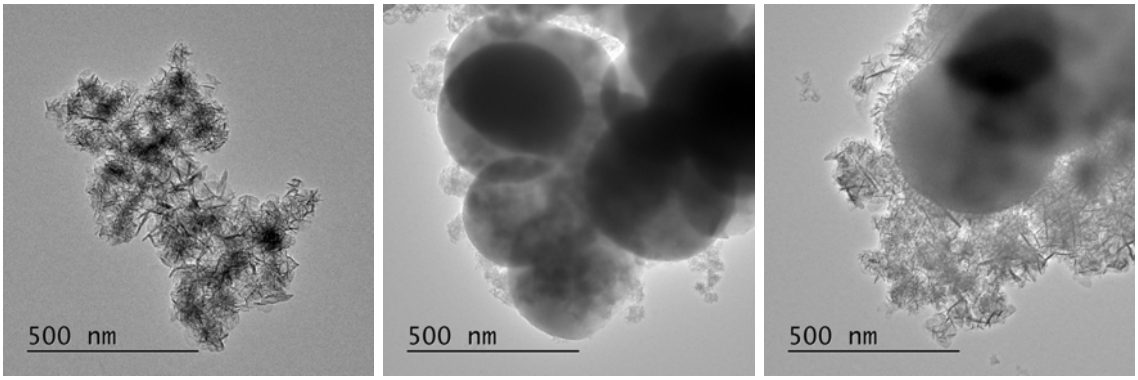


Figure B.4 TEM images of SiO_2@Mg_2Al-CO_3-AMO-LDHs showing free LDH and non-uniform LDH growth on the silica cores. Metal addition rate = 1.1 mmol h^{-1}. Stirring speed = 0 rpm. AMO solvent = EtOH.

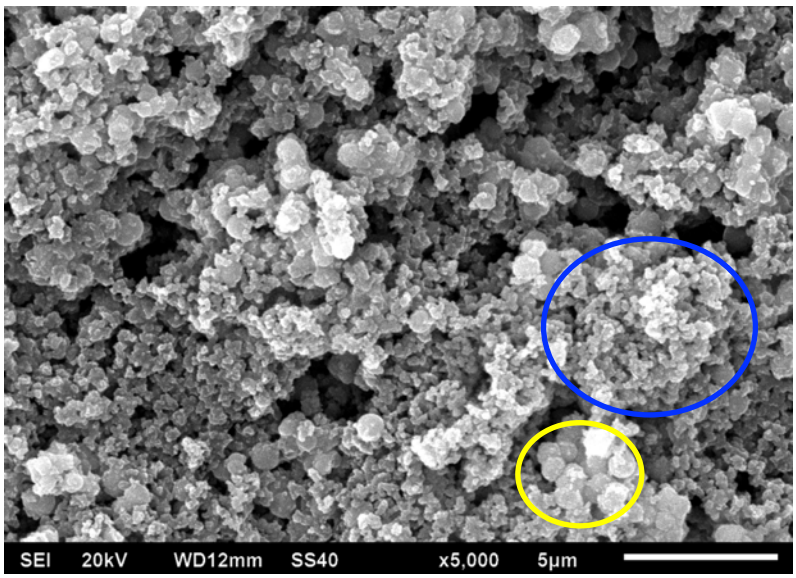


Figure B.5 SEM image of SiO_2@Mg_2Al-CO_3-AMO-LDHs. An area of free LDH is highlighted in blue. An area containing spherical SiO_2 and SiO_2@Mg_2Al-CO_3-AMO-LDHs is highlighted in yellow. Metal addition rate = 1.1 mmol h^{-1}. Stirring speed = 0 rpm. AMO solvent = EtOH.

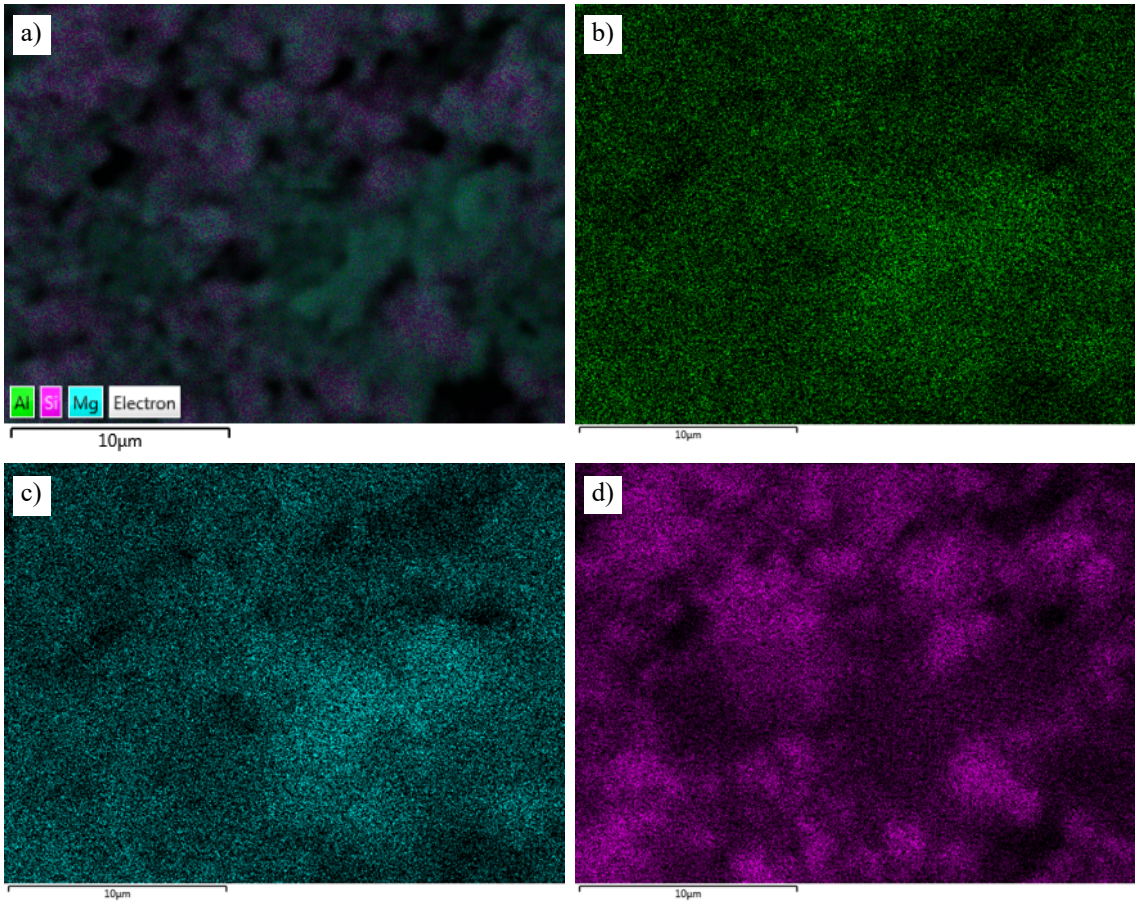


Figure B.6 SEM-EDX analysis of Figure B.5. a) layered image and elemental analyses of b) Al, c) Mg, and d) Si. Metal addition rate = 1.1 mmol h^{-1}. Stirring speed = 0 rpm. AMO solvent = EtOH.

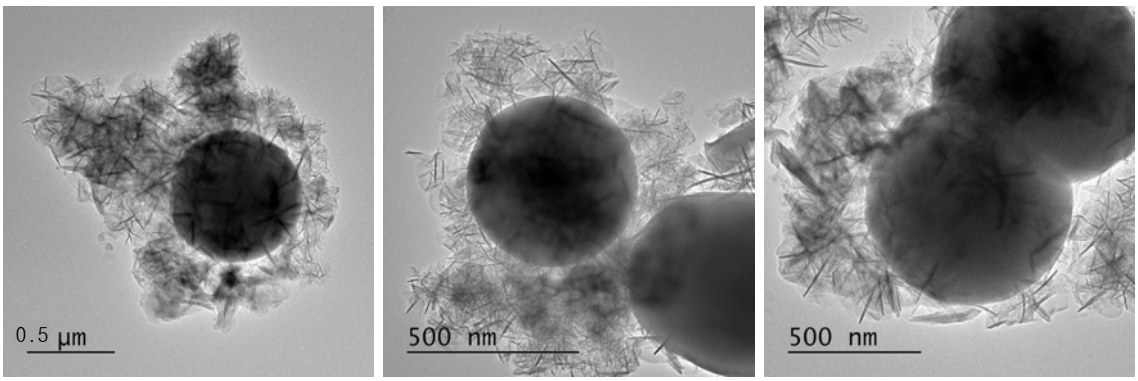


Figure B.7 TEM images of SiO_2@Mg_2Al-CO_3-AMO-LDHs. Metal addition rate = 1.1 mmol h^{-1}. Stirring speed = 250 rpm. AMO solvent = EtOH.

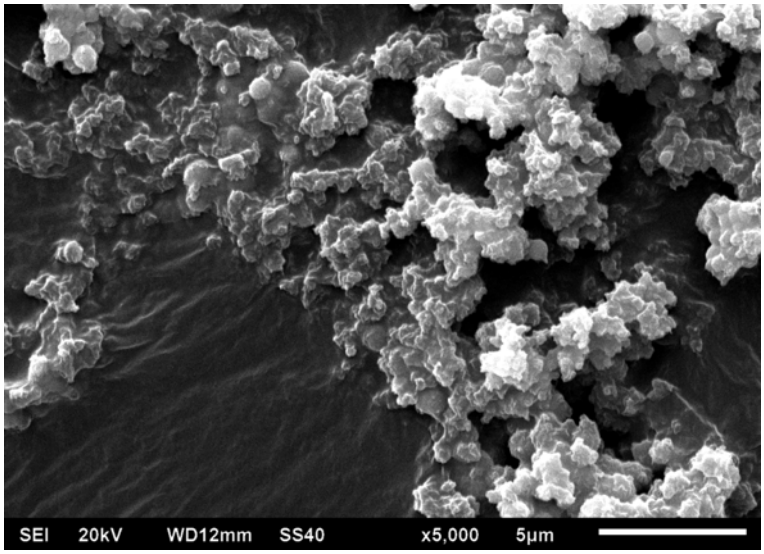


Figure B.8 SEM image of SiO_2@Mg_2Al-CO_3-AMO-LDHs. Metal addition rate = 1.1 mmol h^{-1}. Stirring speed = 250 rpm. AMO solvent = EtOH.

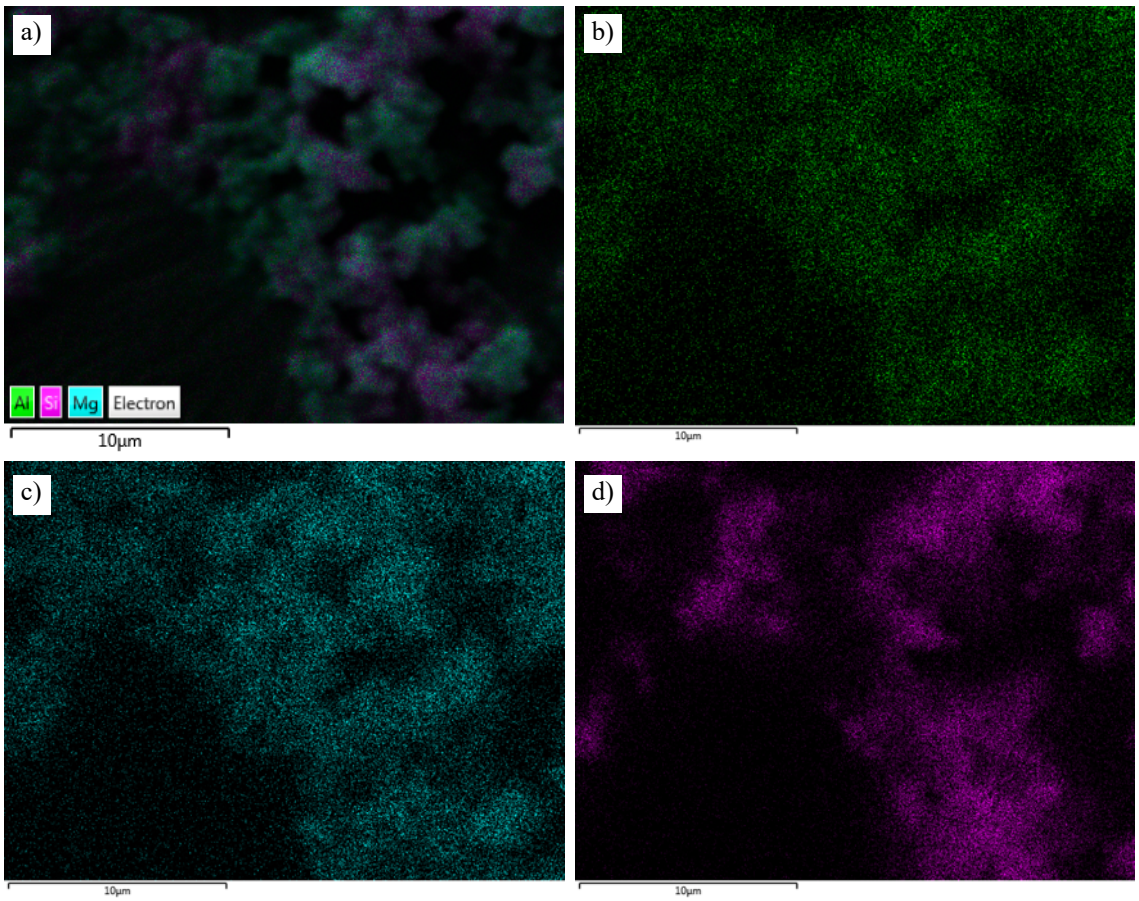


Figure B.9 SEM-EDX analysis of Figure B.8. a) layered image and elemental analyses of b) Al, c) Mg, and d) Si. Metal addition rate = 1.1 mmol h^{-1}. Stirring speed = 250 rpm. AMO solvent = EtOH.

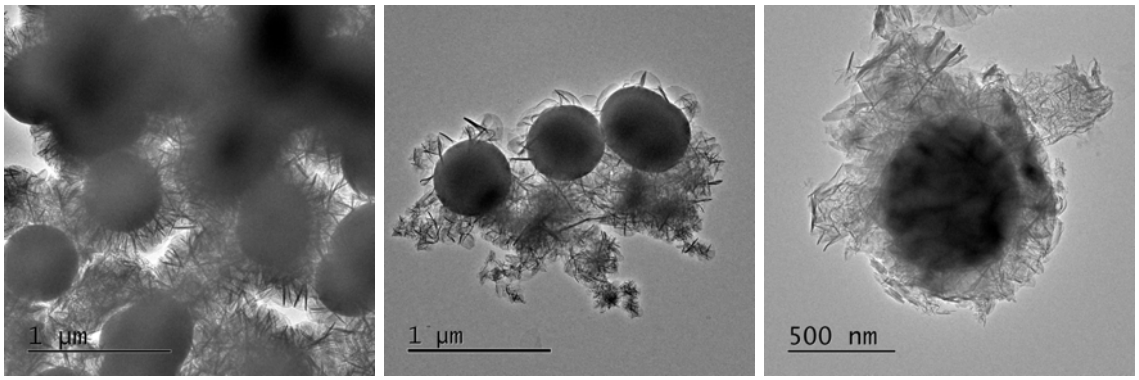


Figure B.10 TEM images of SiO_2@Mg_2Al-CO_3-AMO-LDHs. Metal addition rate = 1.1 mmol h^{-1}. Stirring speed = 500 rpm. AMO solvent = EtOH.

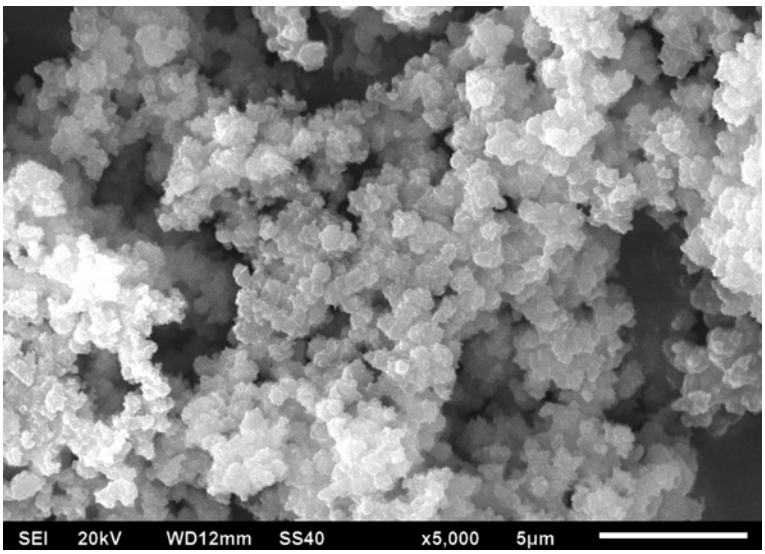


Figure B.11 SEM image SiO_2@Mg_2Al-CO_3-AMO-LDHs. Metal addition rate = 1.1 mmol h^{-1}. Stirring speed = 500 rpm. AMO solvent = EtOH.

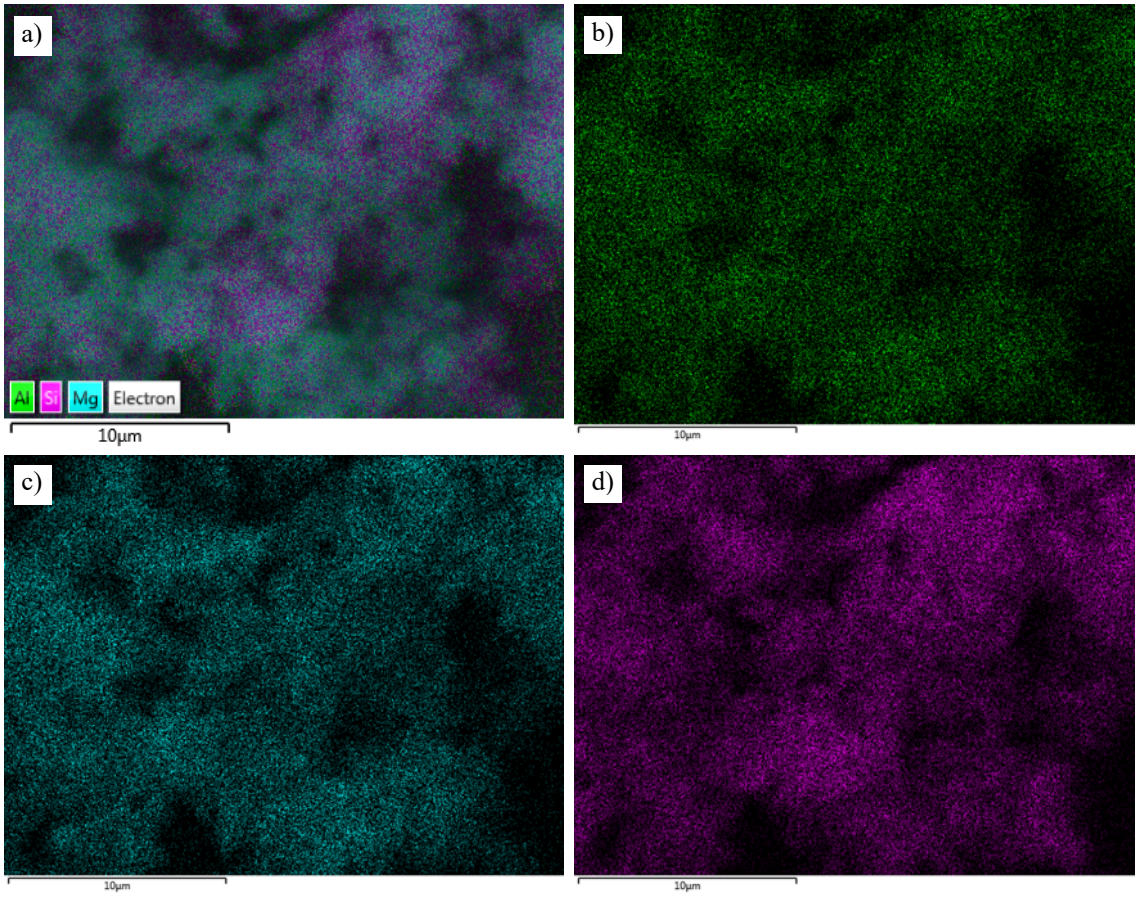


Figure B.12 SEM-EDX analysis of Figure B.11. a) layered image and elemental analyses of b) Al, c) Mg, and d) Si. Metal addition rate = 1.1 mmol h^{-1}. Stirring speed = 500 rpm. AMO solvent = EtOH.

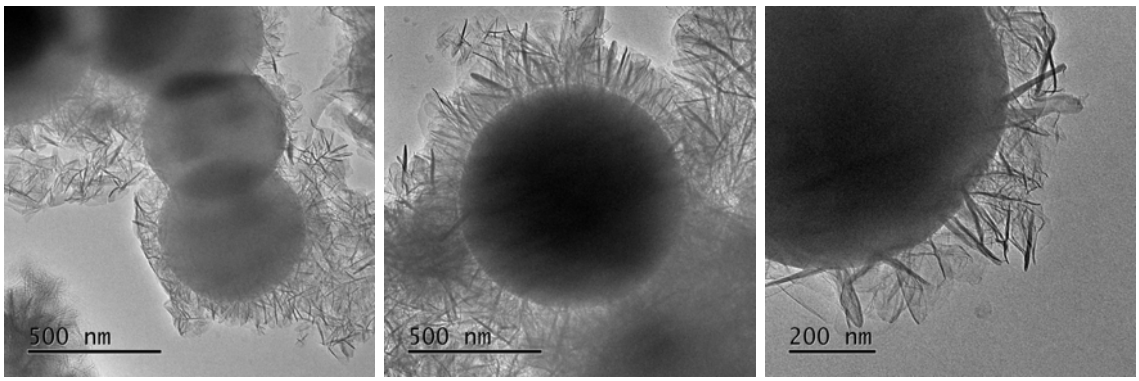


Figure B.13 TEM images of SiO_2@Mg_2Al-CO_3-AMO-LDHs. Metal addition rate = 1.1 mmol h^{-1}. Stirring speed = 750 rpm. AMO solvent = EtOH.

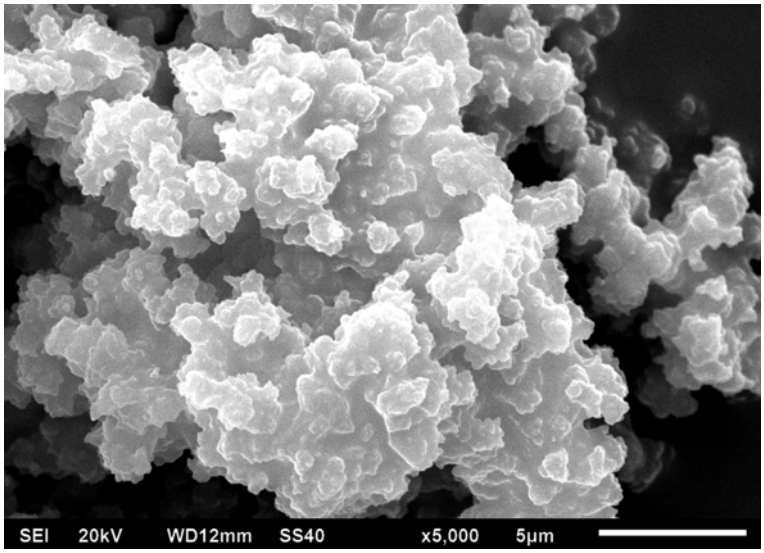


Figure B.14 SEM image SiO_2@Mg_2Al-CO_3-AMO-LDHs. Metal addition rate = 1.1 mmol h^{-1}. Stirring speed = 750 rpm. AMO solvent = EtOH.

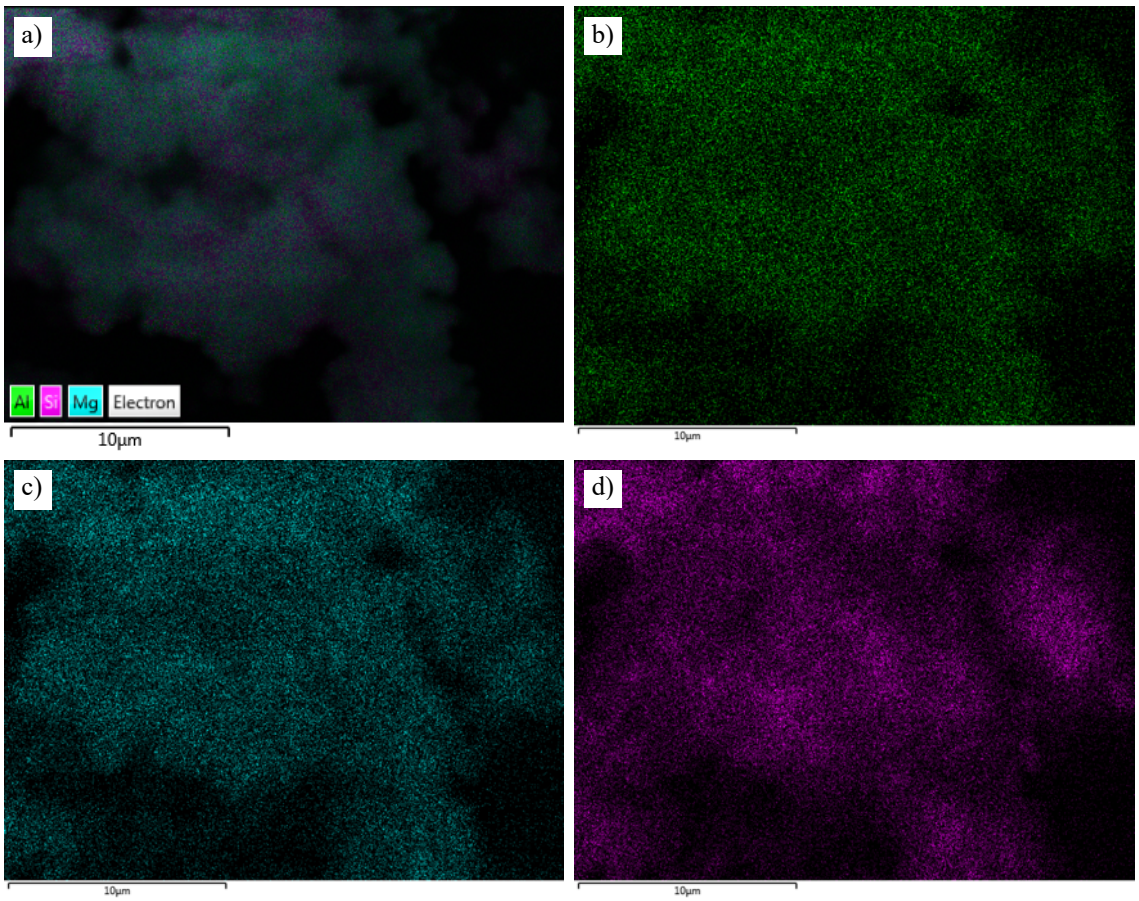


Figure B.15 SEM-EDX analysis of Figure B.14. a) layered image and elemental analyses of b) Al, c) Mg, and d) Si. Metal addition rate = 1.1 mmol h^{-1}. Stirring speed = 750 rpm. AMO solvent = EtOH.

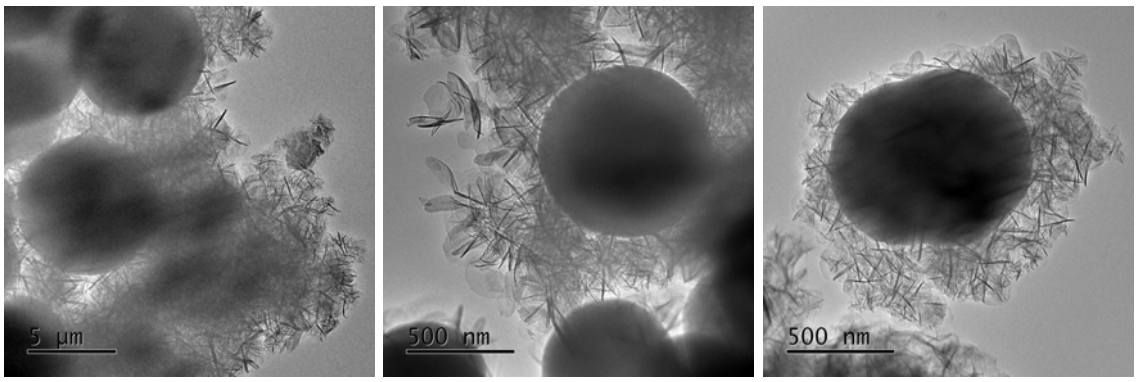


Figure B.16 TEM images of SiO_2@Mg_2Al-CO_3-AMO-LDHs. Metal addition rate = 1.1 mmol h^{-1}. Stirring speed = 1000 rpm. AMO solvent = EtOH.

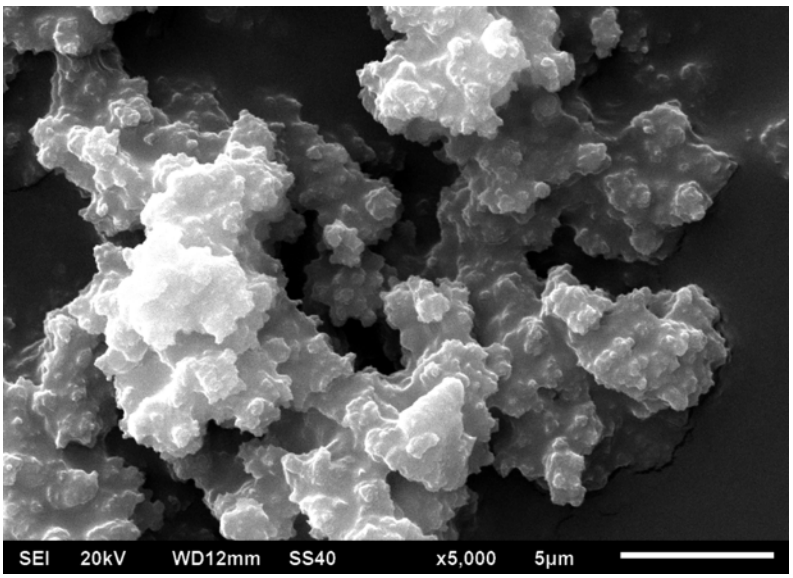


Figure B.17 SEM image SiO_2@Mg_2Al-CO_3-AMO-LDHs. Metal addition rate = 1.1 mmol h^{-1}. Stirring speed = 1000 rpm. AMO solvent = EtOH

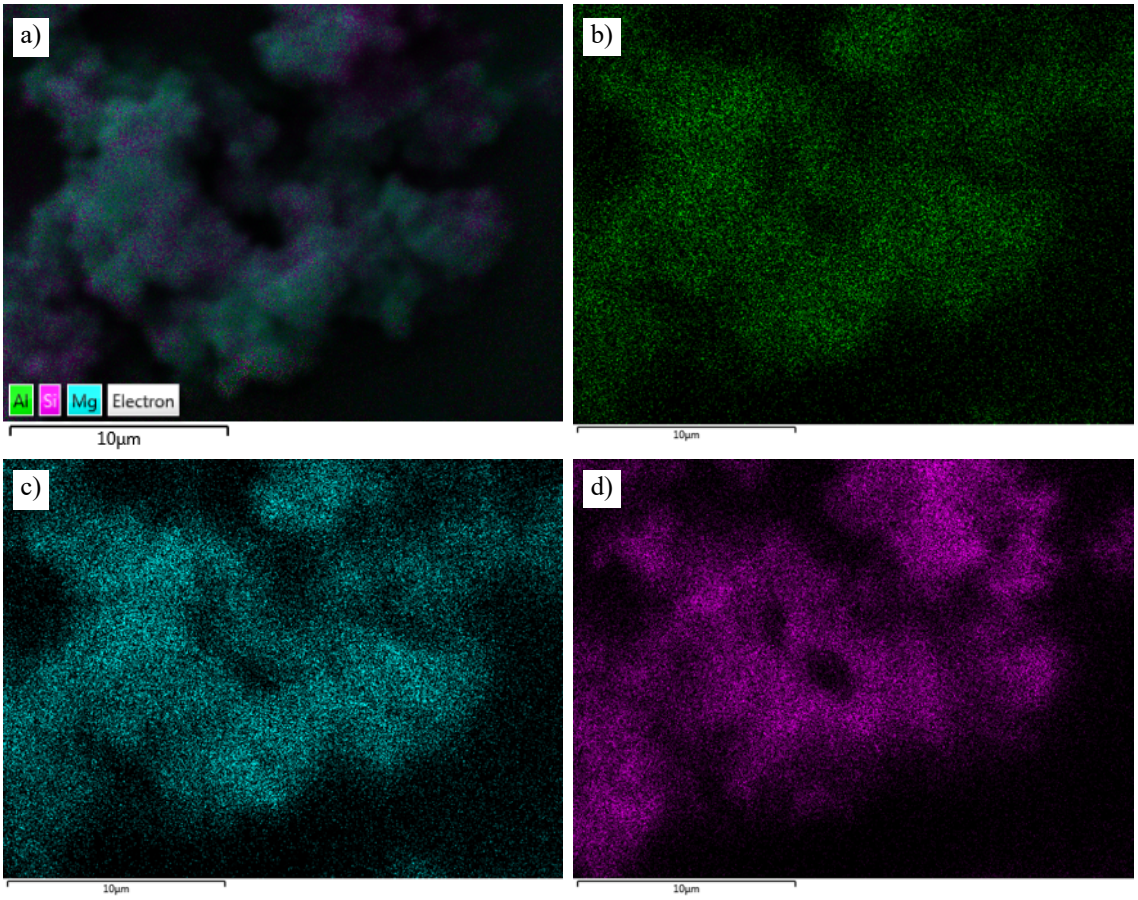


Figure B.18 SEM-EDX analysis of Figure B.17. a) layered image and elemental analyses of b) Al, c) Mg, and d) Si. Metal addition rate = 1.1 mmol h^{-1}. Stirring speed = 750 rpm. AMO solvent = EtOH.

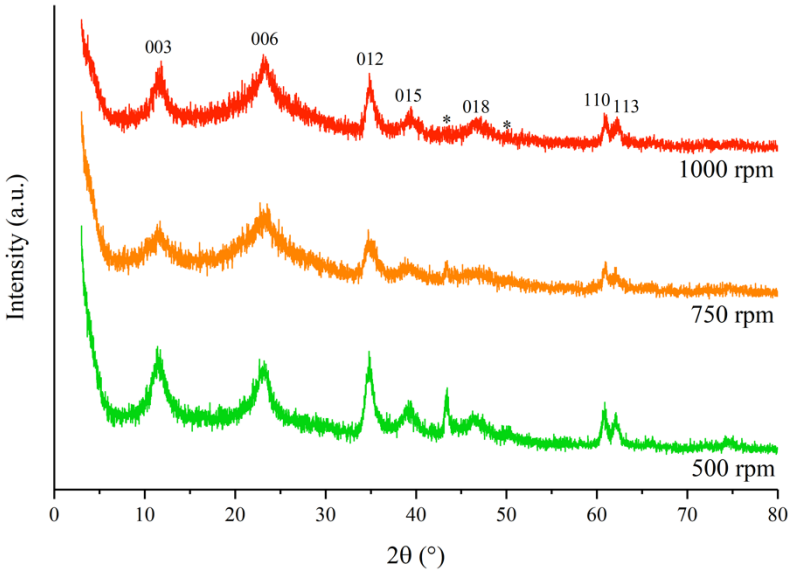


Figure B.19 Powder XRD diffractograms of SiO_2@Mg_2Al-CO_3-AMO-LDHs prepared using different stirring speeds. Metal addition rate = 2.2 mmol h^{-1}. AMO solvent = EtOH. *Reflections due to the sample holder.

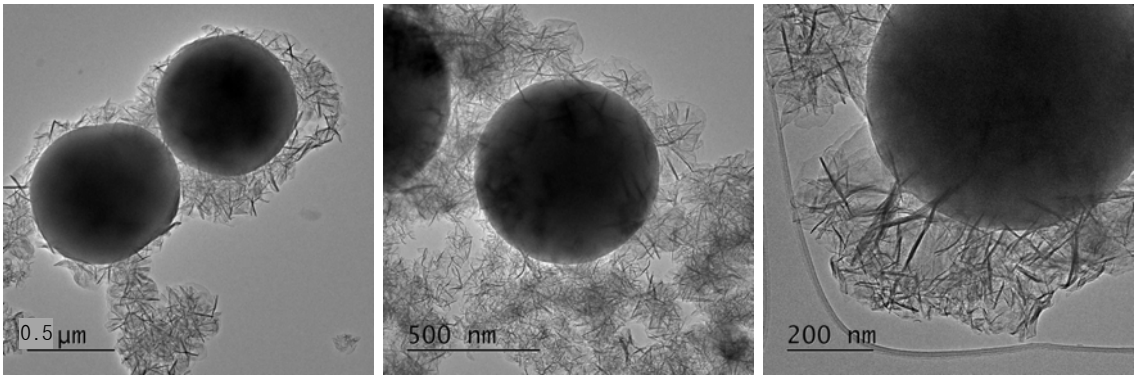


Figure B.20 TEM images of SiO_2@Mg_2Al-CO_3-AMO-LDHs. Metal addition rate = 2.2 mmol h^{-1}. Stirring speed = 500 rpm. AMO solvent = EtOH.

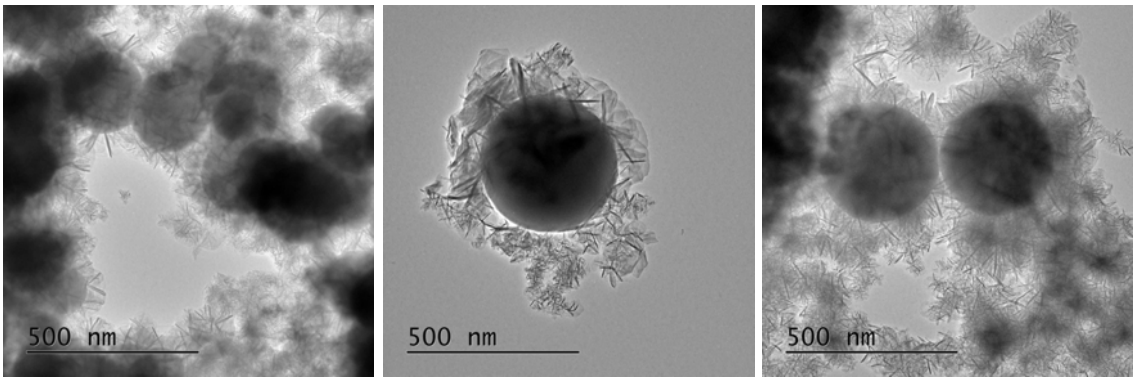


Figure B.21 TEM images of SiO_2@Mg_2Al-CO_3-AMO-LDHs. Metal addition rate = 2.2 mmol h^{-1}. Stirring speed = 750 rpm. AMO solvent = EtOH.

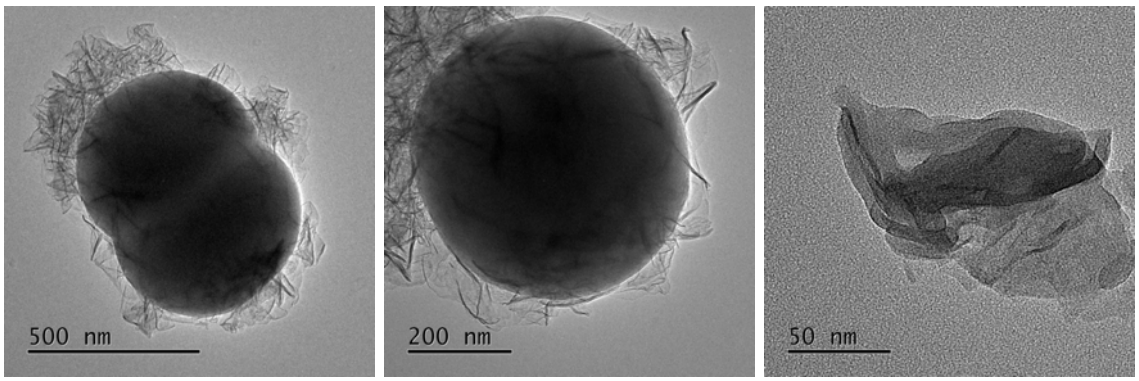


Figure B.22 TEM images of SiO_2@Mg_2Al-CO_3-AMO-LDHs. Lattice fringes are visible in the free LDH. Metal addition rate = 2.2 mmol h^{-1}. Stirring speed = 1000 rpm. AMO solvent = EtOH.

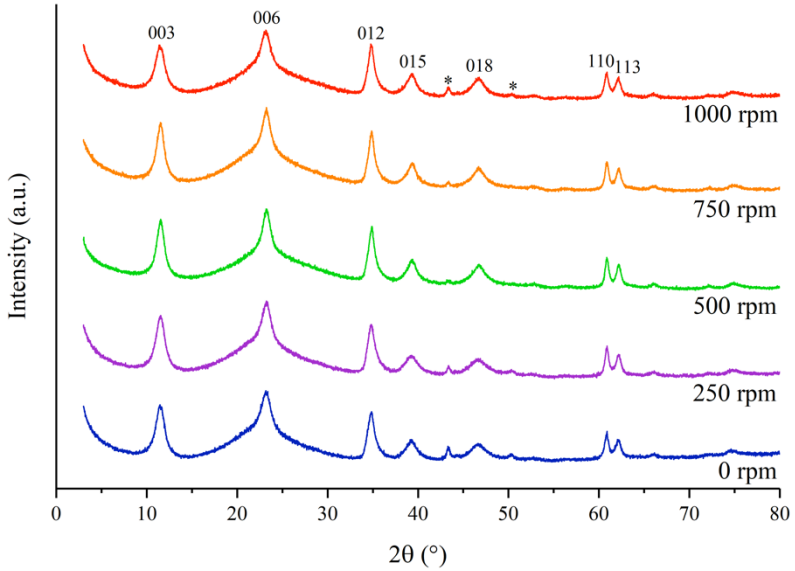


Figure B.23 Powder XRD diffractograms of SiO_2@Mg_2Al-CO_3-AMO-LDHs prepared using different stirring speeds. Metal addition rate = 4.3 mmol h^{-1}. AMO solvent = EtOH. *Reflections due to the sample holder.

Table B.3 Lattice parameters and mean crystallite domain lengths (CDLs) of SiO_2@Mg_2Al-CO_3-AMO-LDHs prepared using different stirring speeds. Metal addition rate = 4.3 mmol h^{-1}. AMO solvent = EtOH.

Stirring speed (rpm)	*d*-spacing (Å)		Lattice parameter (Å)		CDL (Å)	
	d_{003}	d_{110}	$c^{\dagger}$	$a^{\ddagger}$	*c*-axis	*ab*-plane
0	7.73	1.52	23.19	3.04	299.8	965.7
250	7.68	1.52	23.04	3.04	184.5	536.7
500	7.67	1.52	23.01	3.04	239.8	439.1
750	7.57	1.52	22.71	3.04	300.0	483.1
1000	7.57	1.52	22.71	3.04	200.0	689.3

†Lattice parameter $c = 3d_{003}$. ‡Lattice parameter $a = 2d_{110}$.
CDL = $0.89\lambda/\beta\cos\theta$, λ = 1.541847 Å, β = FWHM in radians.

Table B.4 Powder XRD Bragg reflection data of SiO_2@Mg_2Al-CO_3-AMO-LDHs prepared using different stirring speeds. Metal addition rate = 4.3 mmol h^{-1}. AMO solvent = EtOH.

Stirring speed (rpm)	003[a] (º)	FWHM[b] (º)	110[c] (º)	FWHM[d] (º)
0	11.44	0.27	60.88	0.17
250	11.52	0.43	60.89	0.30
500	11.54	0.33	60.89	0.37
750	11.69	0.27	60.89	0.33
1000	11.69	0.40	60.85	0.23

[a]Position of the 003 Bragg reflection (2θ), [b]FWHM of the 003 reflection.
[c]Position of the 110 Bragg reflection (2θ), [d]FWHM of 110 reflection.

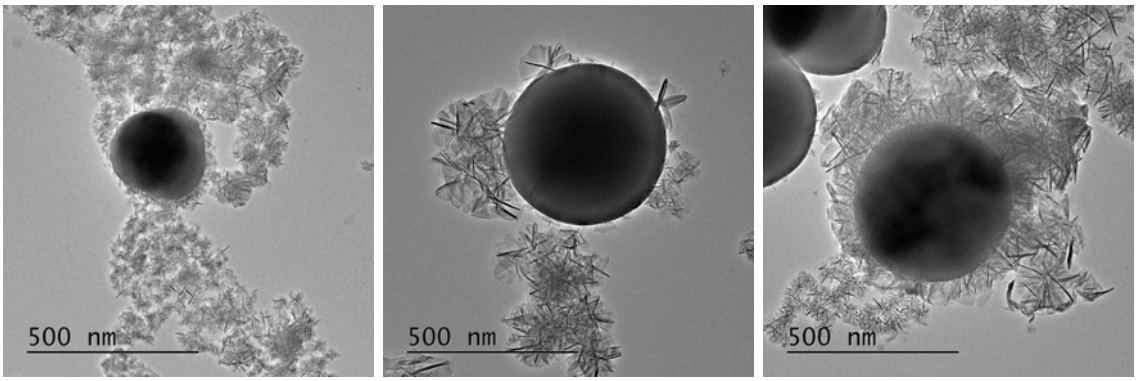


Figure B.24 TEM images of SiO_2@Mg_2Al-CO_3-AMO-LDHs. Metal addition rate = 4.3 mmol h^{-1}. Stirring speed = 0 rpm. AMO solvent = EtOH.

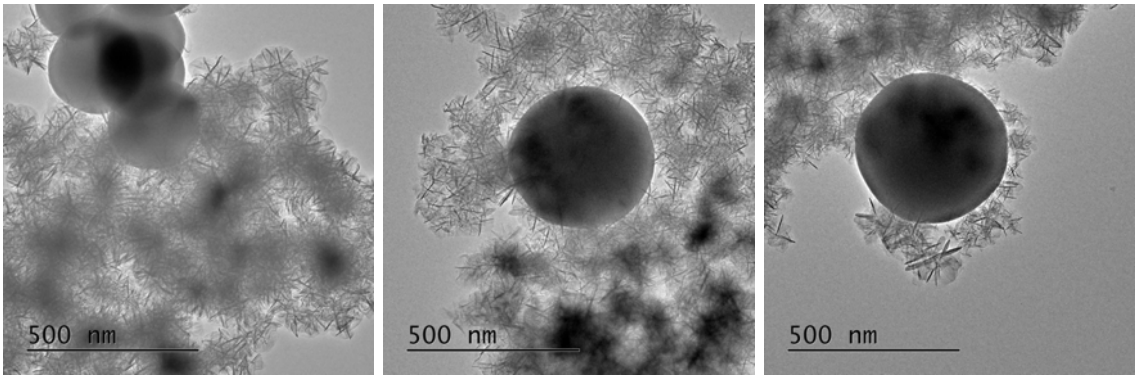


Figure B.25 TEM images of SiO_2@Mg_2Al-CO_3-AMO-LDHs. Metal addition rate = 4.3 mmol h^{-1}. Stirring speed = 250 rpm. AMO solvent = EtOH.

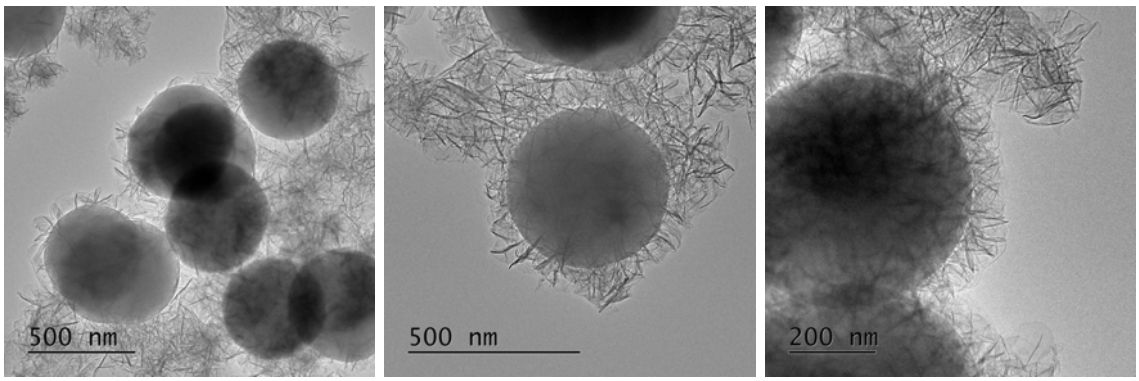


Figure B.26 TEM images of SiO_2@Mg_2Al-CO_3-AMO-LDHs. Metal addition rate = 4.3 mmol h^{-1}. Stirring speed = 500 rpm. AMO solvent = EtOH.

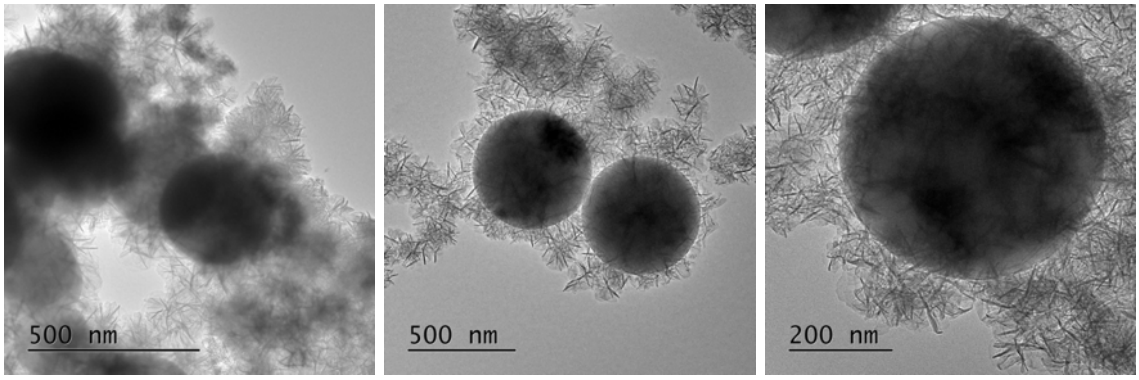


Figure B.27 TEM images of SiO_2@Mg_2Al-CO_3-AMO-LDHs. Metal addition rate = 4.3 mmol h^{-1}. Stirring speed = 750 rpm. AMO solvent = EtOH.

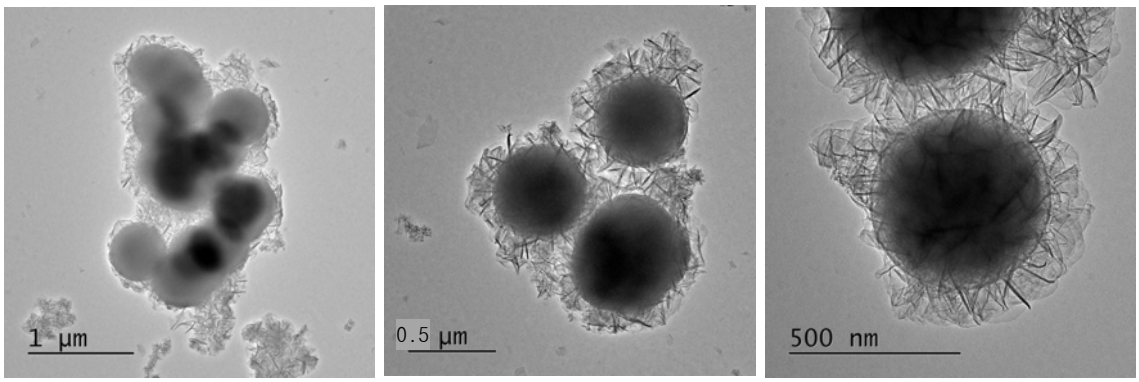


Figure B.28 TEM images of SiO_2@Mg_2Al-CO_3-AMO-LDHs. Metal addition rate = 4.3 mmol h^{-1}. Stirring speed = 1000 rpm. AMO solvent = EtOH.

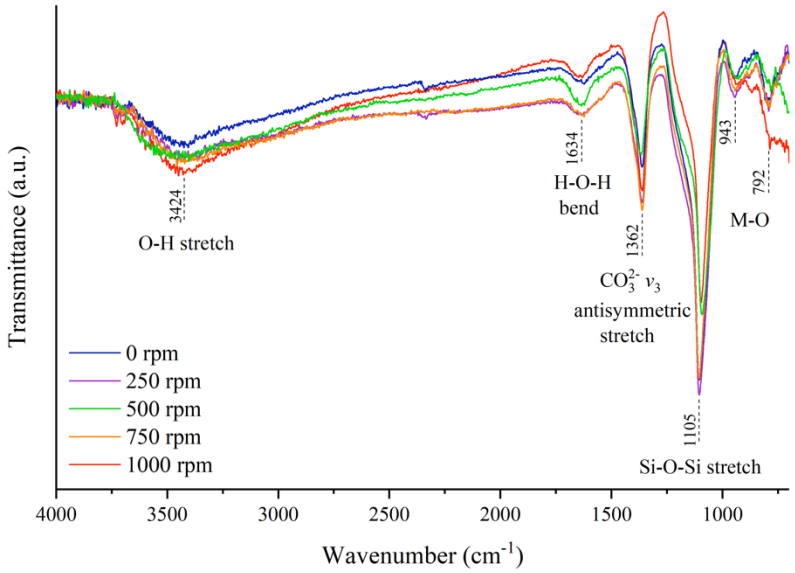


Figure B.29 FTIR spectra of SiO_2@Mg_2Al-CO_3-AMO-LDHs prepared using different stirring speeds. Metal addition rate = 4.3 mmol h^{-1}. AMO solvent = EtOH.

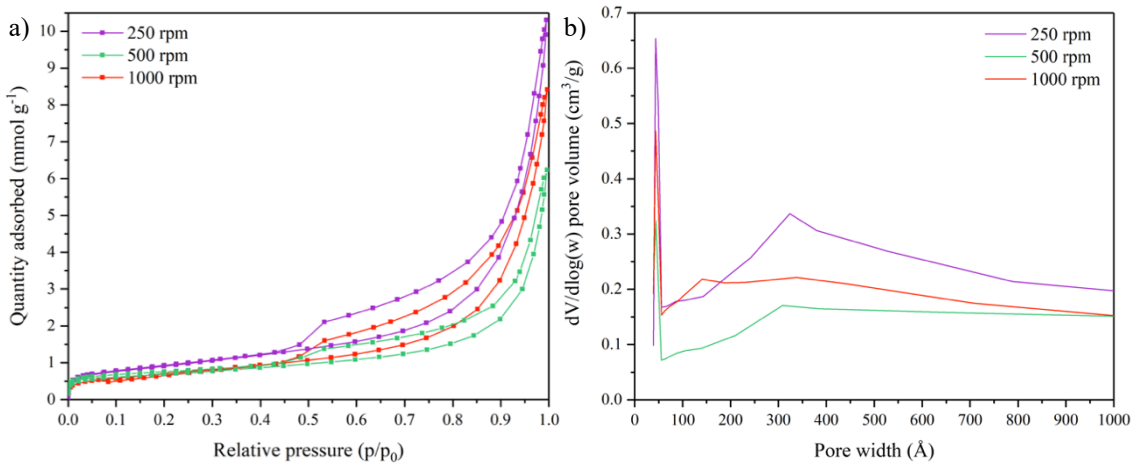


Figure B.30 a) N_2 adsorption and desorption isotherms and b) BJH pore size distributions of SiO_2@Mg_2Al-CO_3-AMO-LDHs prepared using different stirring speeds. Metal addition rate = 4.3 mmol h^{-1}. AMO solvent = EtOH.

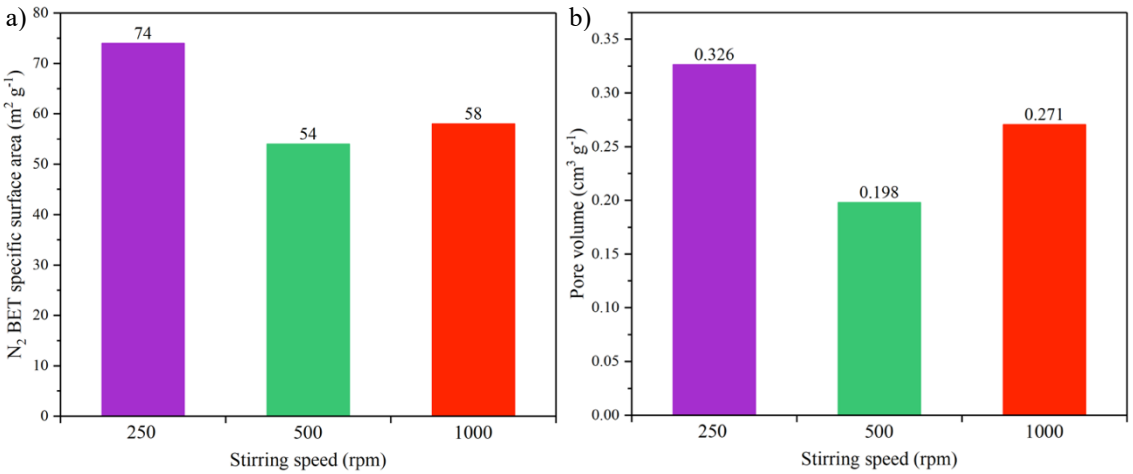


Figure B.31 a) N_2 BET specific surface areas and b) pore volumes of SiO_2@Mg_2Al-CO_3-AMO-LDHs prepared using different stirring speeds. Metal addition rate = 4.3 mmol h^{-1}. AMO solvent = EtOH.

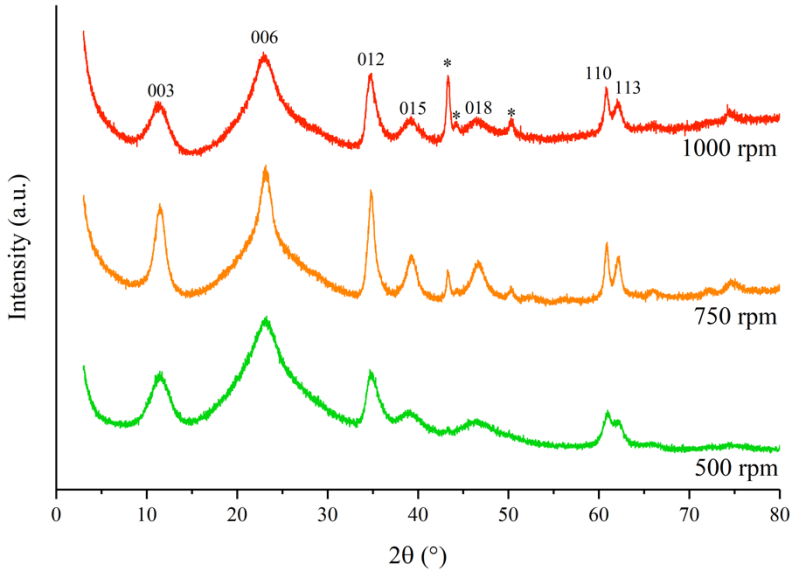


Figure B.32 Powder XRD diffractograms of SiO_2@Mg_2Al-CO_3-AMO-LDHs prepared using different stirring speeds. Metal addition rate = 8.6 mmol h^{-1}. AMO solvent = EtOH. *Reflections due to the sample holder.

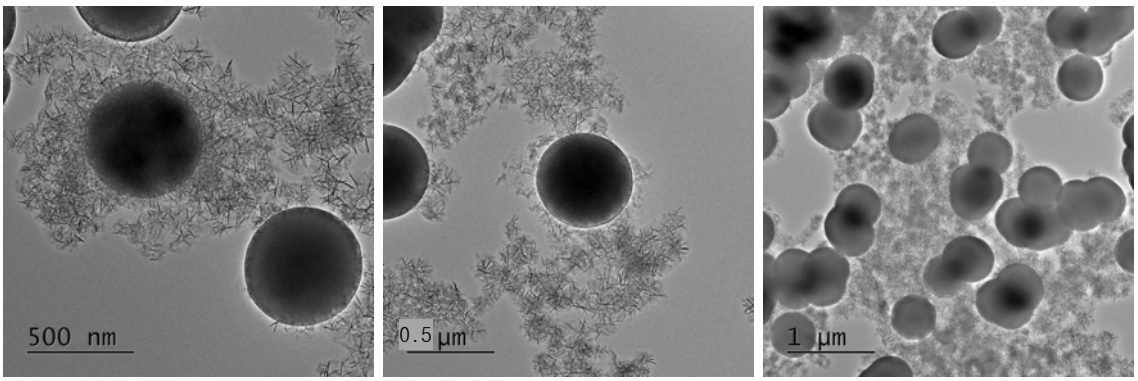


Figure B.33 TEM images of SiO_2@Mg_2Al-CO_3-AMO-LDHs. Metal addition rate = 8.6 mmol h^{-1}. Stirring speed = 500 rpm. AMO solvent = EtOH.

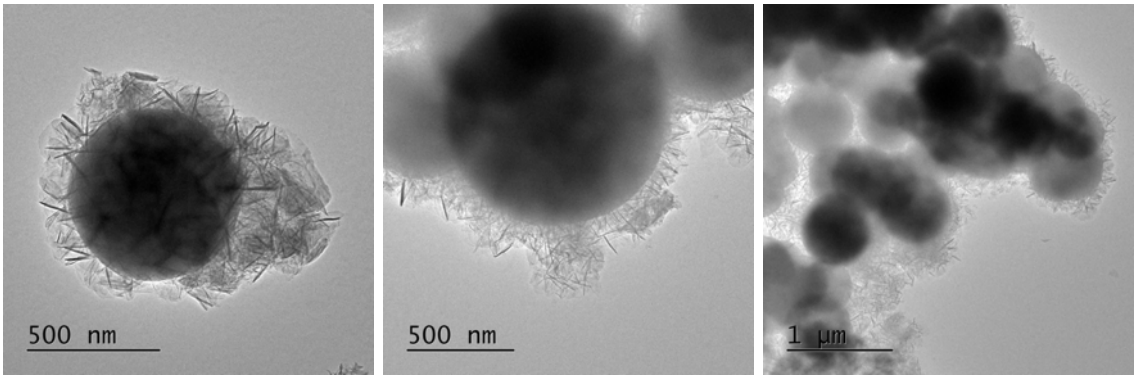


Figure B.34 TEM images of SiO_2@Mg_2Al-CO_3-AMO-LDHs prepared with an Al^{3+} impregnation step before *in situ* co-precipitation (IMP2 method used in Section 4.4.2.3). LDH growth on the silica surface is improved with the impregnation step. Metal addition rate = 8.6 mmol h^{-1}. Stirring speed = 500 rpm. AMO solvent = EtOH.

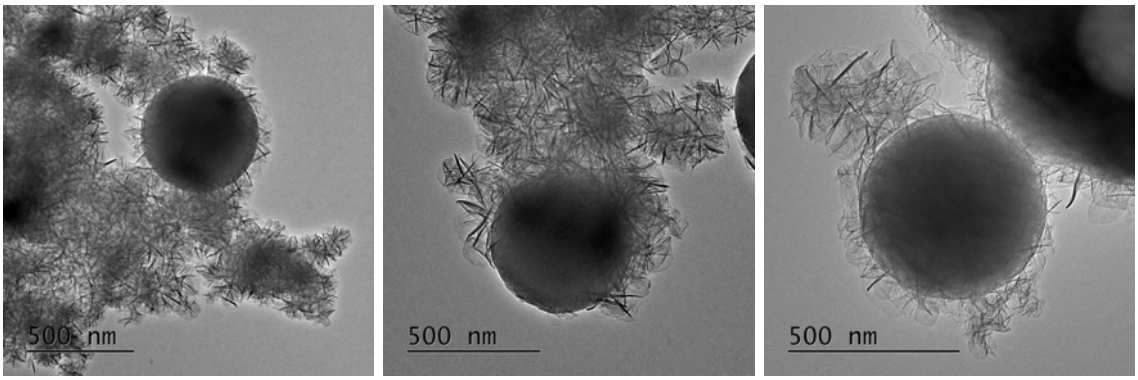


Figure B.35 TEM images of SiO_2@Mg_2Al-CO_3-AMO-LDHs. Metal addition rate = 8.6 mmol h^{-1}. Stirring speed = 750 rpm. AMO solvent = EtOH.

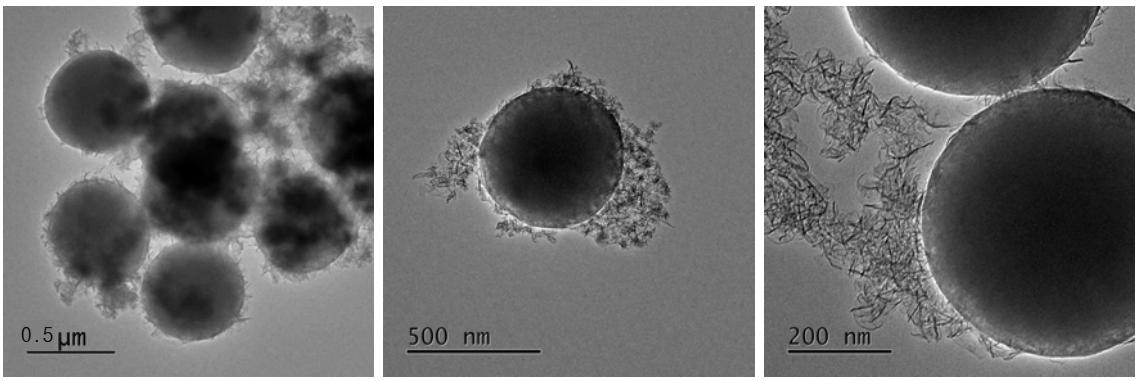


Figure B.36 TEM images of SiO_2@Mg_2Al-CO_3-AMO-LDHs. Metal addition rate = 8.6 mmol h^{-1}. Stirring speed = 1000 rpm. AMO solvent = EtOH.

B.4 Variation of metal addition rate

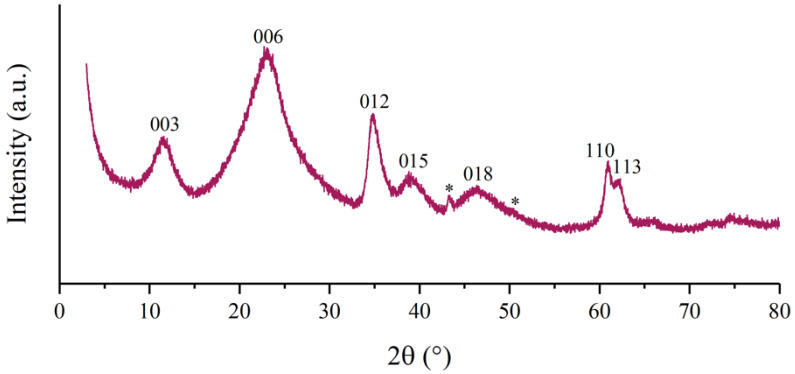


Figure B.37 Powder XRD diffractogram of SiO_2@Mg_2Al-CO_3-AMO-LDH prepared by addition of the entire metal solution at once. Stirring speed = 500 rpm. AMO solvent = EtOH. *Reflections due to the sample holder.

Table B.5 Lattice parameters and mean CDLs of SiO_2@Mg_2Al-CO_3-AMO-LDH prepared by addition of the entire metal solution at once. Stirring speed = 500 rpm. AMO solvent = EtOH.

hkl	$2\theta^a$ (º)	d_{hkl} (Å)	FWHM (º)	Lattice parameters[b] (Å)	CDL (Å)
003	11.48	7.71	0.80	c = 23.13	99.9
110	60.95	1.52	0.54	a = 3.04	302.5

[a]Position of *hkl* Bragg reflection.
[b]Lattice parameter $c = 3d_{003}$, $a = 2d_{110}$.

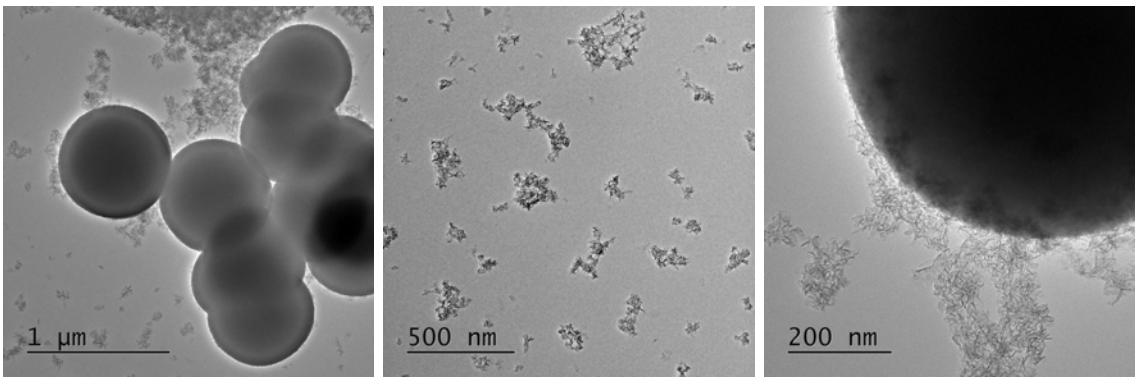


Figure B.38 SEM images of SiO_2@Mg_2Al-CO_3-AMO-LDH prepared by addition of the entire metal solution at once. Stirring speed = 500 rpm. AMO solvent = EtOH.

Under these conditions of high supersaturation, the rate of nucleation exceeds that of crystal growth so the LDH crystallites are small. The amount of LDH that is covalently bonded to the silica is low because nucleation of the LDH in solution was rapid.

Table B.6 Powder XRD Bragg reflection data of SiO_2@Mg_2Al-CO_3-AMO-LDHs prepared using different metal addition rates (XRD diffractogram = Figure 4.14). Stirring speed = 500 rpm. AMO solvent = EtOH.

Metal addition rate (mmol h^{-1})	003[a] (º)	FWHM[b] (º)	110[c] (º)	FWHM[d] (º)
1.1	11.64	0.17	60.85	0.13
2.2	11.46	0.17	60.91	0.37
4.3	11.54	0.33	60.89	0.37
8.6	11.48	1.47	60.85	0.43

[a]Position of the 003 Bragg reflection (2θ), [b]FWHM of the 003 reflection.
[c]Position of the 110 Bragg reflection (2θ), [d]FWHM of 110 reflection.

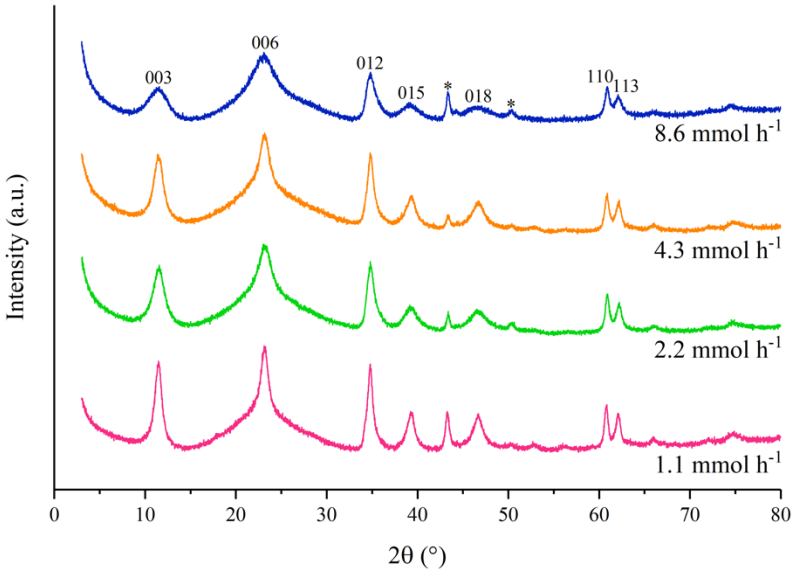


Figure B.39 Powder XRD diffractograms of SiO_2@Mg_2Al-CO_3-AMO-LDHs prepared using different metal addition rates. Stirring speed = 1000 rpm. AMO solvent = EtOH. *Reflections due to the sample holder.

Table B.7 Lattice parameters and mean CDLs of SiO_2@Mg_2Al-CO_3-AMO-LDHs prepared using different metal addition rates. Stirring speed = 1000 rpm.

Metal addition rate (mmol h^{-1})	*d*-spacing (Å)		Lattice parameter (Å)		CDL (Å)	
	d_{003}	d_{110}	$c^{\dagger}$	$a^{\ddagger}$	*c*-axis	*ab*-plane
1.1	7.70	1.52	23.10	3.04	199.8	481.8
2.2	7.68	1.52	23.04	3.04	92.2	402.5
4.3	7.75	1.52	23.25	3.04	200.0	689.3
8.6	7.76	1.52	23.28	3.04	49.9	482.4

†Lattice parameter $c = 3d_{003}$. ‡Lattice parameter $a = 2d_{110}$.
CDL = $0.89\lambda/\beta\cos\theta$, λ = 1.541847 Å, β = FWHM in radians.

Table B.8 Powder XRD Bragg reflection data of SiO_2@Mg_2Al-CO_3-AMO-LDHs prepared using different metal addition rates. Stirring speed = 1000 rpm.

Metal addition rate (mmol h^{-1})	003[a] (º)	FWHM[b] (º)	110[c] (º)	FWHM[d] (º)
1.1	11.49	0.40	60.81	0.33
2.2	11.52	0.87	60.89	0.40
4.3	11.69	0.40	60.85	0.23
8.6	11.40	1.61	60.85	0.33

[a]Position of the 003 Bragg reflection (2θ), [b]FWHM of the 003 reflection.
[c]Position of the 110 Bragg reflection (2θ), [d]FWHM of 110 reflection.

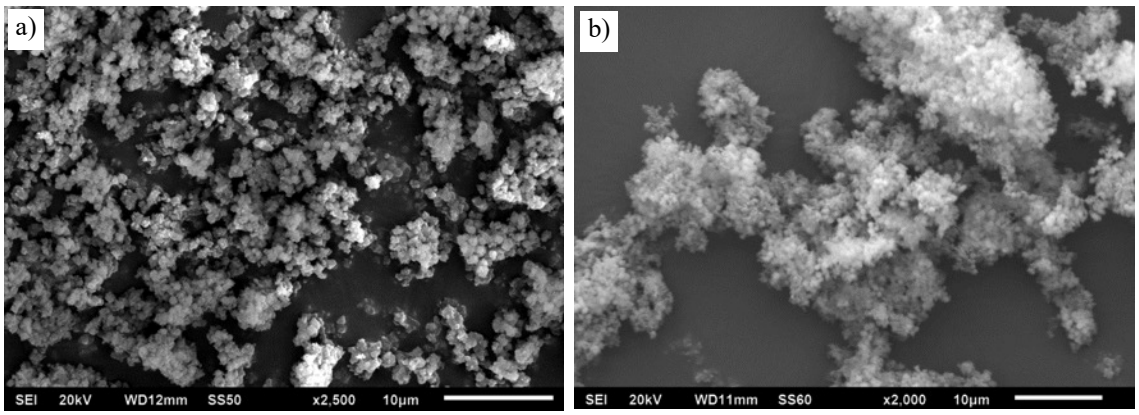


Figure B.40 SEM images of SiO_2@Mg_2Al-CO_3-AMO-LDHs prepared using metal addition rates of a) 2.2 and b) 8.6 mmol h^{-1}. Stirring speed = 750 rpm. AMO solvent = EtOH.

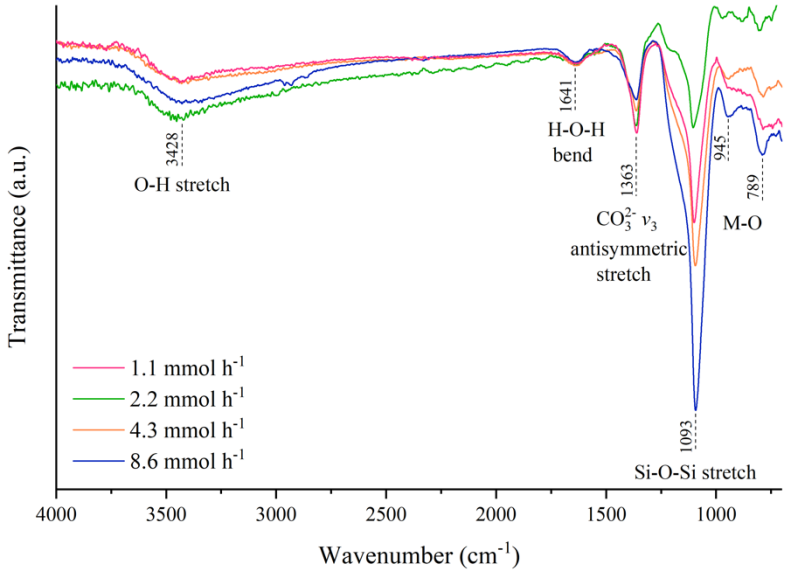


Figure B.41 FTIR spectra of SiO_2@Mg_2Al-CO_3-AMO-LDHs prepared using different metal addition rates. Stirring speed = 500 rpm. AMO solvent = EtOH.

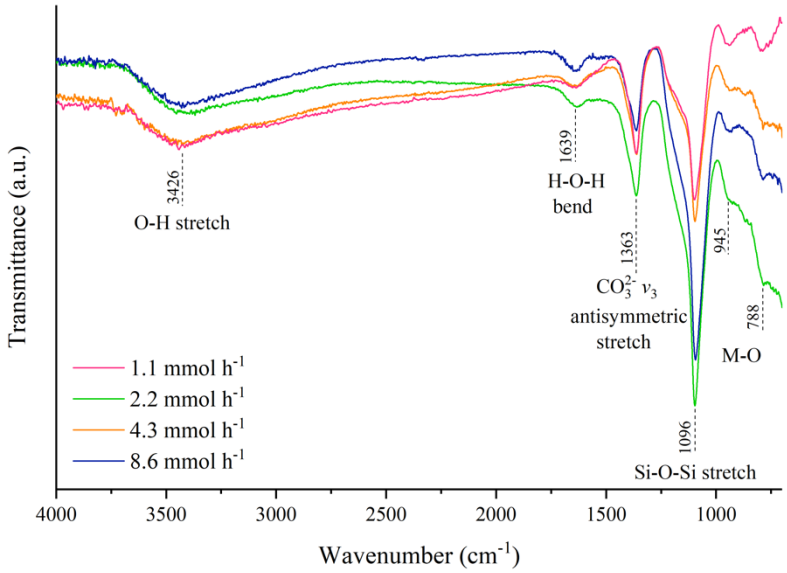


Figure B.42 FTIR spectra of SiO_2@Mg_2Al-CO_3-AMO-LDHs prepared using different metal addition rates. Stirring speed = 1000 rpm. AMO solvent = EtOH.

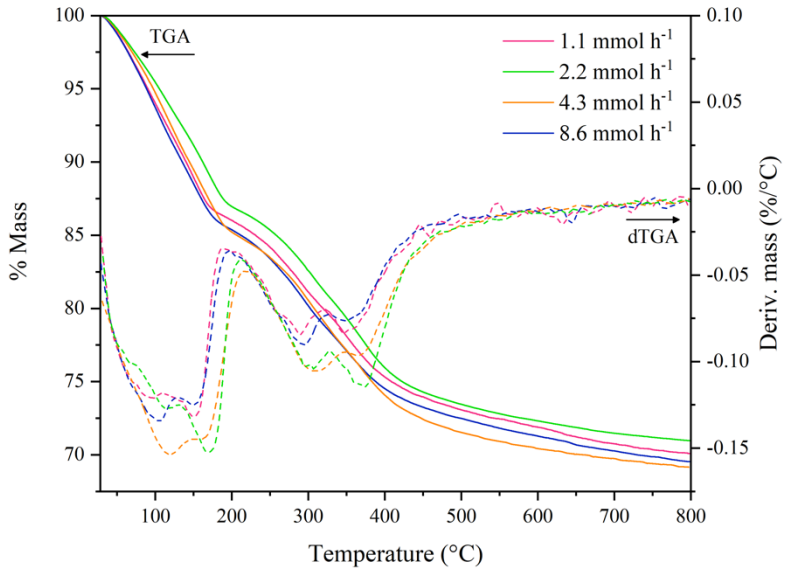


Figure B.43 TGA and dTGA curves of SiO_2@Mg_2Al-CO_3-AMO-LDHs prepared using different metal addition rates. Stirring speed = 500 rpm. AMO solvent = EtOH.

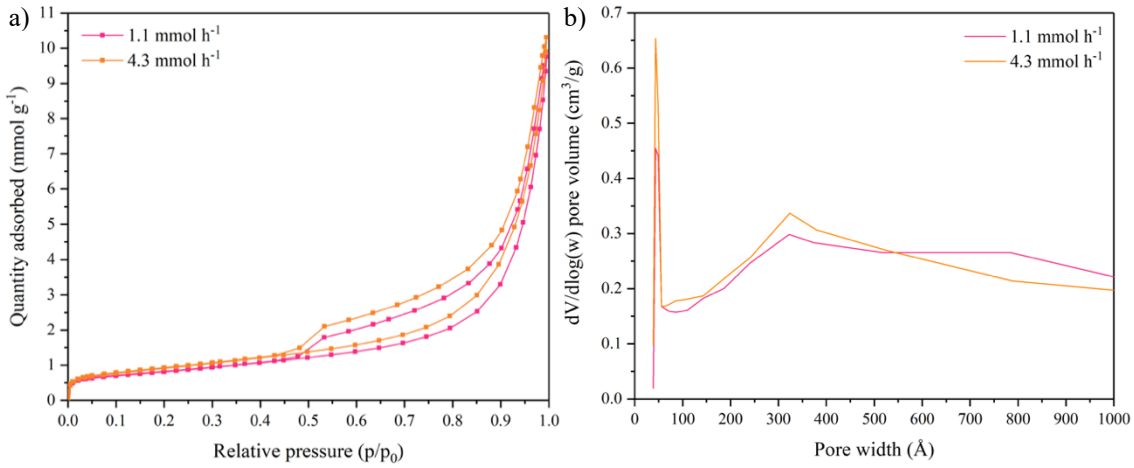


Figure B.44 a) N_2 adsorption and desorption isotherms and b) BJH pore size distributions of SiO_2@Mg_2Al-CO_3-AMO-LDHs prepared using different metal addition rates. Stirring speed = 250 rpm. AMO solvent = EtOH.

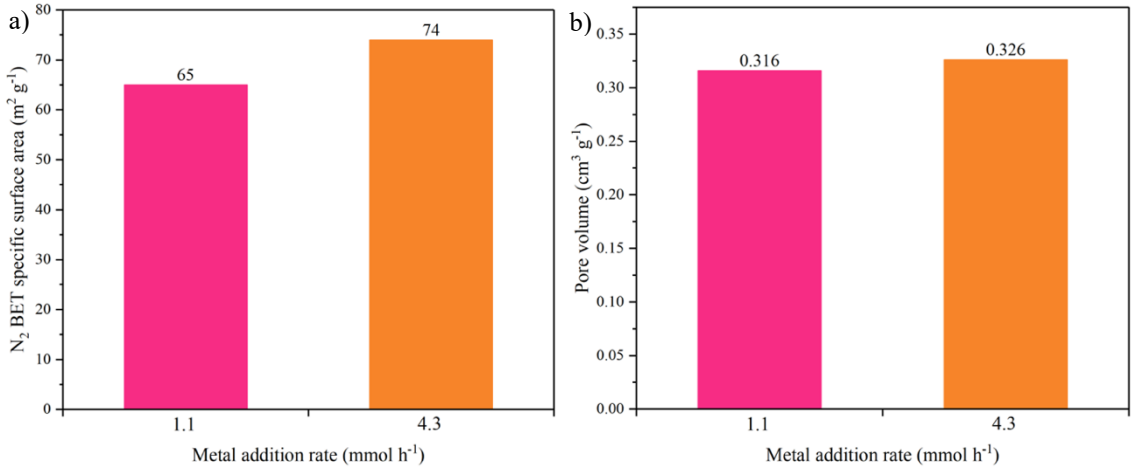


Figure B.45 a) N_2 BET specific surface areas and b) pore volumes of SiO_2@Mg_2Al-CO_3-AMO-LDHs prepared using different metal addition rates. Stirring speed = 250 rpm. AMO solvent = EtOH.

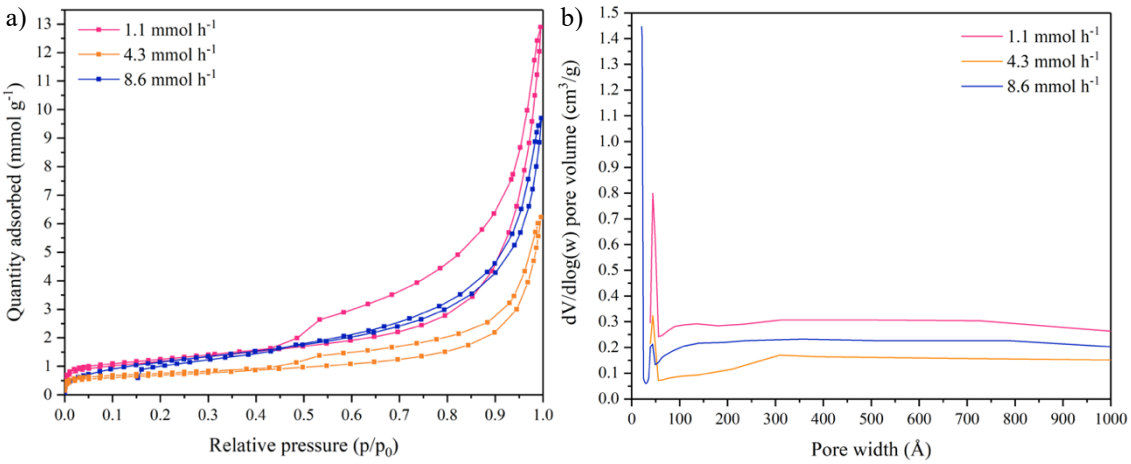


Figure B.46 a) N_2 adsorption and desorption isotherms and b) BJH pore size distributions of SiO_2@Mg_2Al-CO_3-AMO-LDHs prepared using different metal addition rates. Stirring speed = 500 rpm. AMO solvent = EtOH.

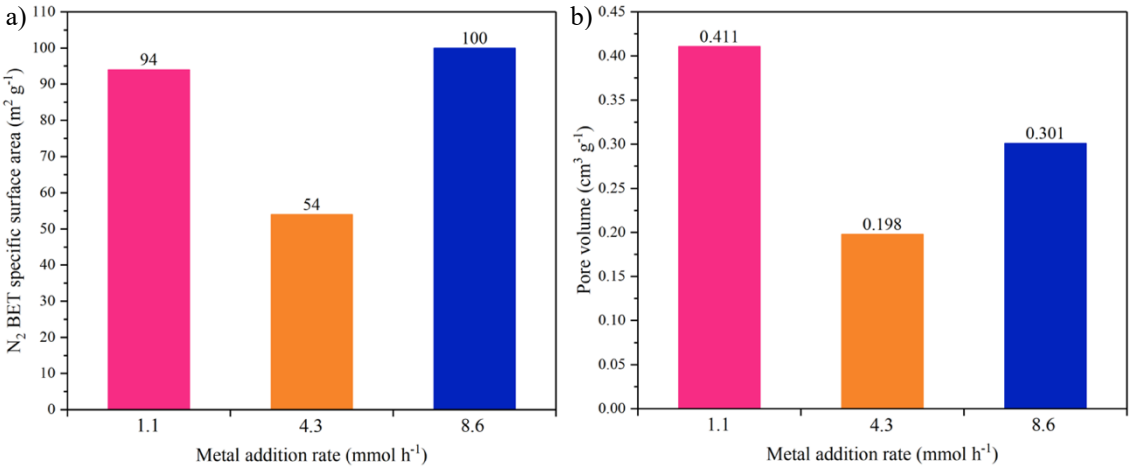


Figure B.47 a) N_2 BET specific surface areas and b) pore volumes of SiO_2@Mg_2Al-CO_3-AMO-LDHs prepared using different metal addition rates. Stirring speed = 500 rpm. AMO solvent = EtOH.

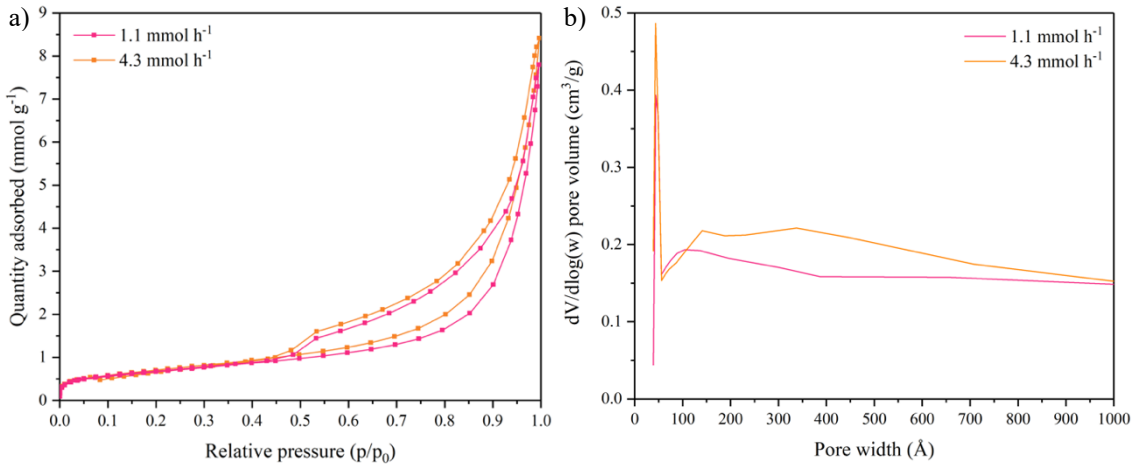


Figure B.48 N_2 adsorption and desorption isotherms of SiO_2@Mg_2Al-CO_3-AMO-LDHs prepared using different metal addition rates. Stirring speed = 1000 rpm. AMO solvent = EtOH.

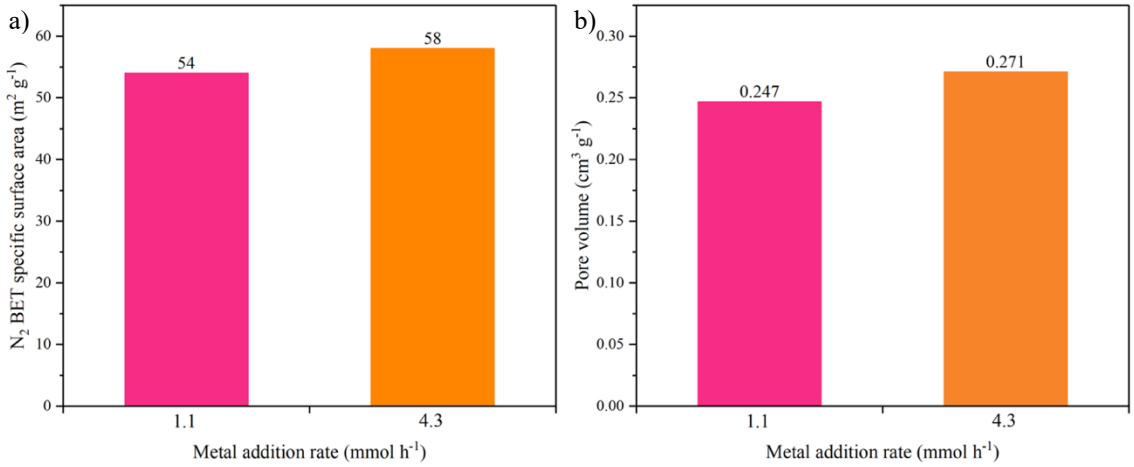


Figure B.49 a) N_2 BET specific surface areas and b) pore volumes of SiO_2@Mg_2Al-CO_3-AMO-LDHs prepared using different metal addition rates. Stirring speed = 1000 rpm. AMO solvent = EtOH.

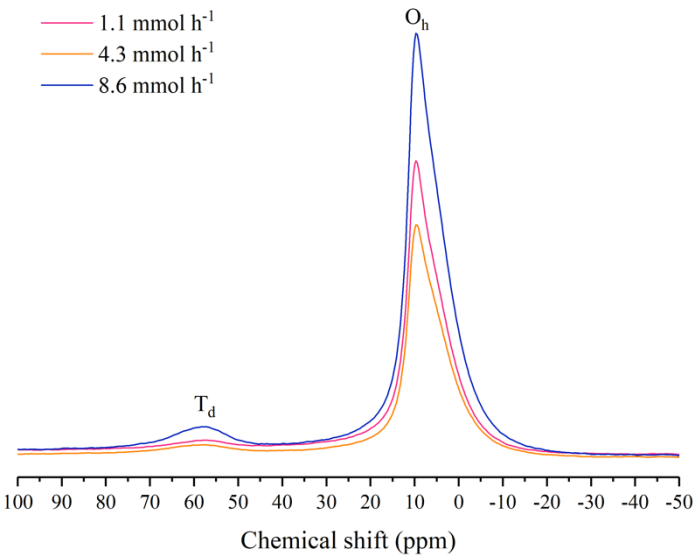


Figure B.50 ^{27}Al DPMAS (9.4 T, 104.2 MHz, MAS rate = 15 kHz) ssNMR spectra of SiO_2@Mg_2Al-CO_3-AMO-LDHs prepared using different metal addition rates. Stirring speed = 500 rpm. AMO solvent = EtOH.

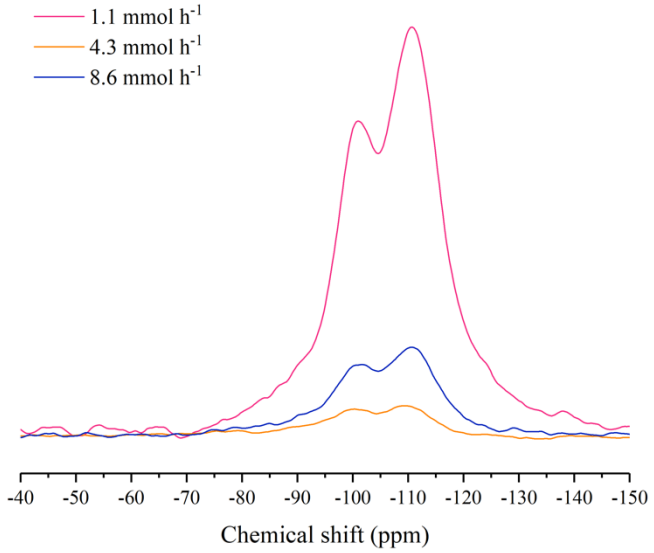


Figure B.51 ^{29}Si DPMAS (9.4 T, 79.4 MHz, MAS rate = 10 kHz) ssNMR spectra of SiO_2@Mg_2Al-CO_3-AMO-LDHs prepared using different metal addition rates. Stirring speed = 500 rpm. AMO solvent = EtOH.

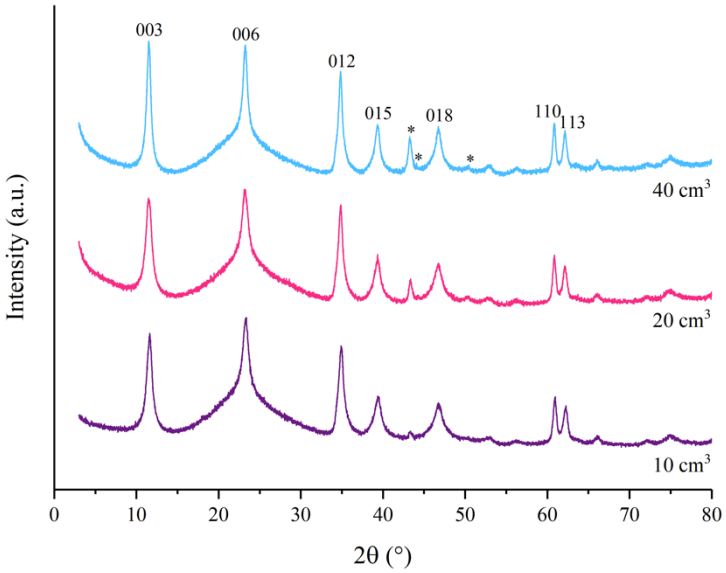


Figure B.52 Powder XRD diffractograms of SiO_2@Mg_2Al-CO_3-AMO-LDHs prepared using different metal salt solution volumes. Metal addition rate = 0.25 cm^3 min^{-1}. Stirring speed = 500 rpm. AMO solvent = EtOH. *Reflections due to the sample holder.

Table B.9 Lattice parameters and mean CDLs of SiO_2@Mg_2Al-CO_3-AMO-LDHs prepared using different metal salt solution volumes. Metal addition rate = 0.25 cm^3 min^{-1}. Stirring speed = 500 rpm. AMO solvent = EtOH.

Metal solution volume (cm^3)	*d*-spacing (Å)		Lattice parameter (Å)		CDL (Å)	
	d_{003}	d_{110}	$c^{\dagger}$	$a^{\ddagger}$	*c*-axis	*ab*-plane
10	7.62	1.52	22.86	3.04	399.9	537.1
20	7.60	1.52	22.80	3.04	479.8	1209.1
40	7.69	1.52	23.07	3.04	799.1	1376.9

†Lattice parameter $c = 3d_{003}$. ‡Lattice parameter $a = 2d_{110}$.
CDL = $0.89\lambda/\beta\cos\theta$, λ = 1.541847 Å, β = FWHM in radians.

Table B.10 Powder XRD Bragg reflection data of SiO_2@Mg_2Al-CO_3-AMO-LDHs prepared using different metal salt solution volumes. Metal addition rate = 0.25 cm^3 min^{-1}. Stirring speed = 500 rpm. AMO solvent = EtOH.

Metal solution volume (cm^3)	003[a] (º)	FWHM[b] (º)	110[c] (º)	FWHM[d] (º)
10	11.61	0.20	60.91	0.30
20	11.64	0.17	60.85	0.13
40	11.51	0.10	60.81	0.12

[a]Position of the 003 Bragg reflection (2θ), [b]FWHM of the 003 reflection.
[c]Position of the 110 Bragg reflection (2θ), [d]FWHM of 110 reflection.

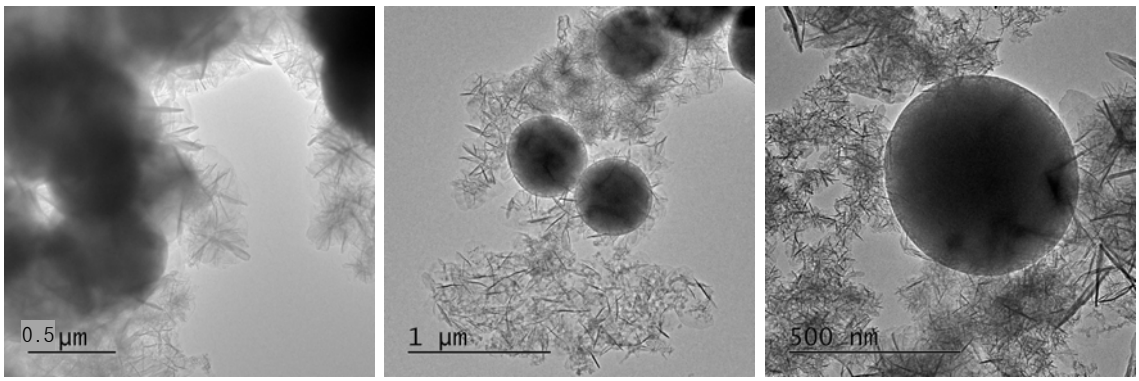


Figure B.53 TEM images of SiO_2@Mg_2Al-CO_3-AMO-LDHs. Metal solution volume = 10 cm^3. Metal addition rate = 0.25 cm^3 min^{-1}. Stirring speed = 500 rpm. AMO solvent = EtOH.

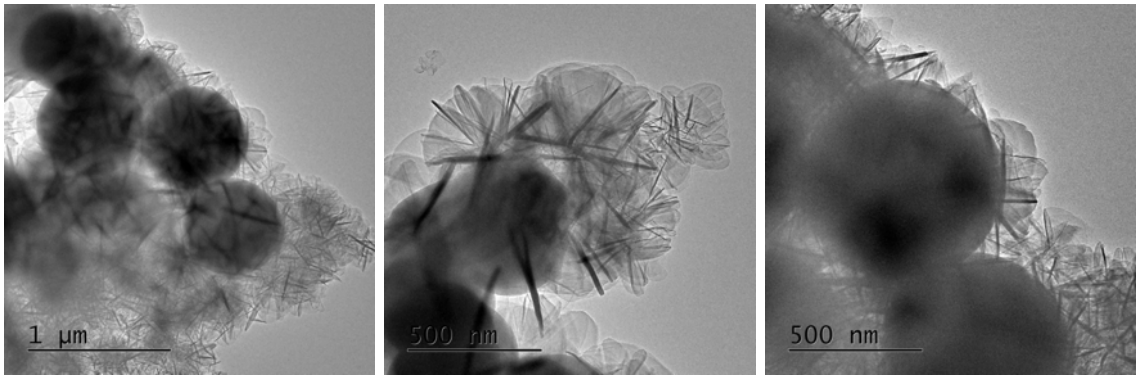


Figure B.54 TEM images of SiO_2@Mg_2Al-CO_3-AMO-LDHs. Metal solution volume = 40 cm^3. Metal addition rate = 0.25 cm^3 min^{-1}. Stirring speed = 500 rpm. AMO solvent = EtOH.

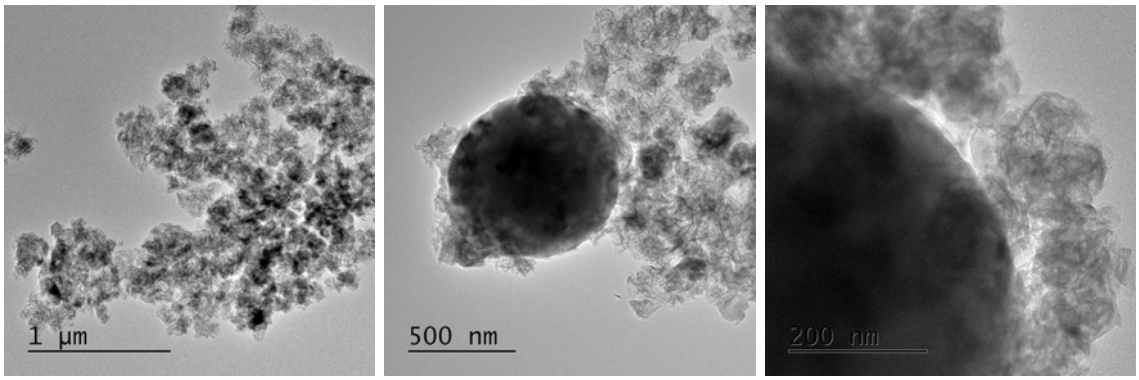


Figure B.55 TEM images of SiO_2@Mg_2Al-CO_3-AMO-LDHs. Metal solution volume = 10 cm^3. Metal addition rate = 2.0 cm^3 min^{-1}. Stirring speed = 500 rpm. AMO solvent = EtOH.

B.5 Variation of ageing time

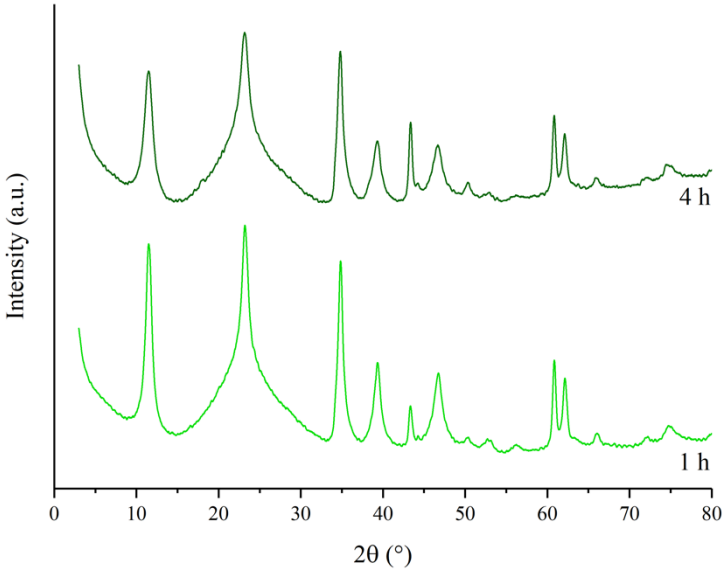


Figure B.56 Powder XRD diffractograms of SiO_2@Mg_2Al-CO_3-AMO-LDHs prepared with different ageing times. Metal addition rate = 0.11 mmol h^{-1}. Stirring speed = 500 rpm. AMO solvent = EtOH.

Table B.11 Lattice parameters and mean CDLs of SiO_2@Mg_2Al-CO_3-AMO-LDHs prepared with different ageing times. Metal addition rate = 0.11 mmol h^{-1}. Stirring speed = 500 rpm. AMO solvent = EtOH.

Ageing time (h)	*d*-spacing (Å)		Lattice parameter (Å)		CDL (Å)	
	d_{003}	d_{110}	$c^{\dagger}$	$a^{\ddagger}$	*c*-axis	*ab*-plane
1	7.60	1.52	22.80	3.04	479.8	1209.1
4	7.67	1.52	23.01	3.04	266.5	602.7

†Lattice parameter $c = 3d_{003}$. ‡Lattice parameter $a = 2d_{110}$.
CDL = 0.89λ/βcosθ, λ = 1.541847 Å, β = FWHM in radians.

Table B.12 Powder XRD Bragg reflection data of SiO_2@Mg_2Al-CO_3-AMO-LDHs prepared with different ageing times. Metal addition rate = 0.11 mmol h^{-1}. Stirring speed = 500 rpm. AMO solvent = EtOH.

Ageing time (h)	003[a] (º)	FWHM[b] (º)	110[c] (º)	FWHM[d] (º)
1	11.64	0.17	60.85	0.13
4	11.54	0.30	60.83	0.27

[a]Position of the 003 Bragg reflection (2θ), [b]FWHM of the 003 reflection.
[c]Position of the 110 Bragg reflection (2θ), [d]FWHM of 110 reflection.

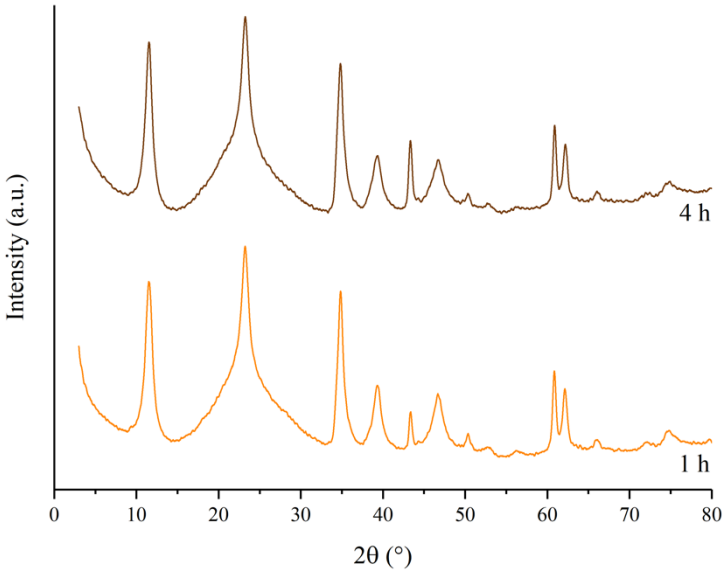


Figure B.57 Powder XRD diffractograms of SiO_2@Mg_2Al-CO_3-AMO-LDHs prepared with different ageing times. Metal addition rate = 0.11 mmol h^{-1}. Stirring speed = 750 rpm. AMO solvent = EtOH.

Table B.13 Lattice parameters and mean CDLs of SiO_2@Mg_2Al-CO_3-AMO-LDHs prepared with different ageing times. Metal addition rate = 0.11 mmol h^{-1}. Stirring speed = 750 rpm. AMO solvent = EtOH.

Ageing time (h)	*d*-spacing (Å)		Lattice parameter (Å)		CDL (Å)	
	d_{003}	d_{110}	$c^{\dagger}$	$a^{\ddagger}$	*c*-axis	*ab*-plane
1	7.69	1.52	23.07	3.04	299.8	876.9
4	7.67	1.52	23.01	3.04	299.9	495.1

†Lattice parameter $c = 3d_{003}$. ‡Lattice parameter $a = 2d_{110}$.
CDL = 0.89λ/βcosθ, λ = 1.541847 Å, β = FWHM in radians.

Table B.14 Powder XRD Bragg reflection data of SiO_2@Mg_2Al-CO_3-AMO-LDHs prepared with different ageing times. Metal addition rate = 0.11 mmol h^{-1}. Stirring speed = 750 rpm. AMO solvent = EtOH.

Ageing time (h)	003[a] (º)	FWHM[b] (º)	110[c] (º)	FWHM[d] (º)
1	11.51	0.27	60.84	0.18
4	11.54	0.27	60.89	0.33

[a]Position of the 003 Bragg reflection (2θ), [b]FWHM of the 003 reflection.
[c]Position of the 110 Bragg reflection (2θ), [d]FWHM of 110 reflection.

B.6 Characterisation of commercial SiO_2

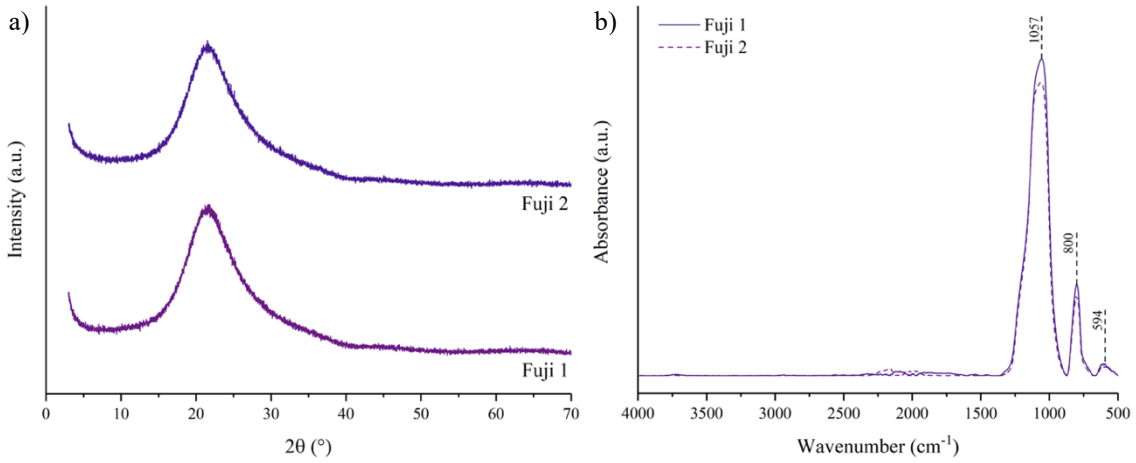


Figure B.58 a) Powder XRD diffractograms and b) FTIR spectra of Fuji silicas.
The absorption band at 1057 cm^{-1} is due to the Si–O–Si asymmetric stretching vibration. The absorption band at 800 cm^{-1} is due to the Si–O–Si symmetric stretching vibration.

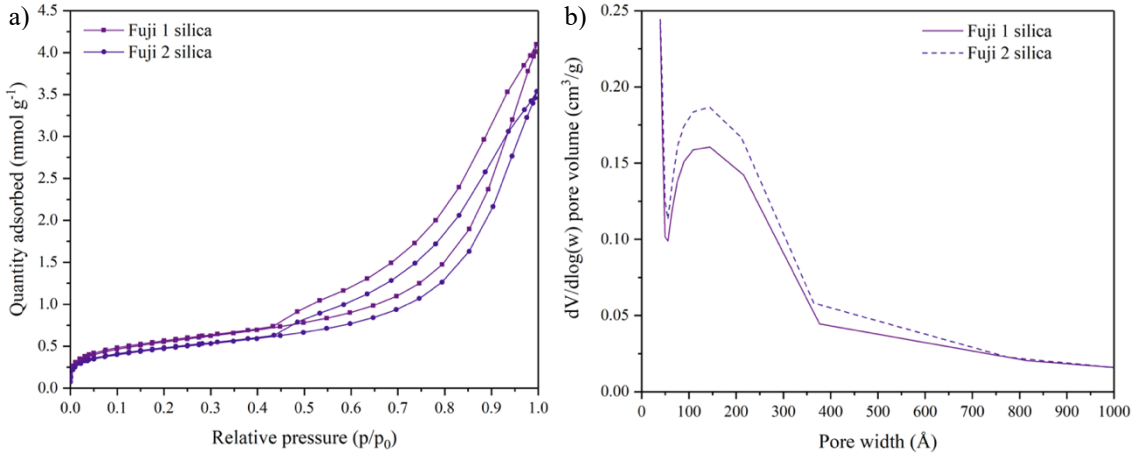


Figure B.59 a) N_2 absorption and desorption isotherms and b) BJH pore size distributions of Fuji silicas.

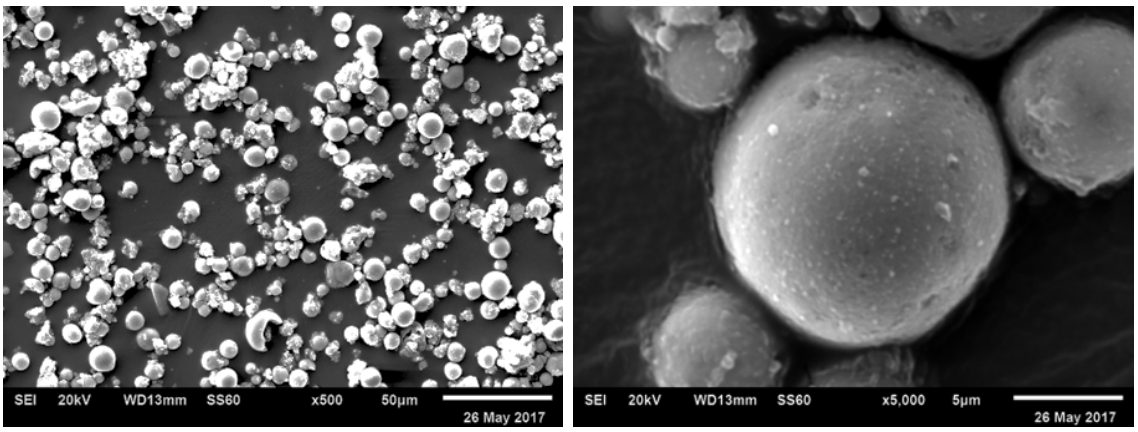


Figure B.60 SEM images of Fuji 1 silica.

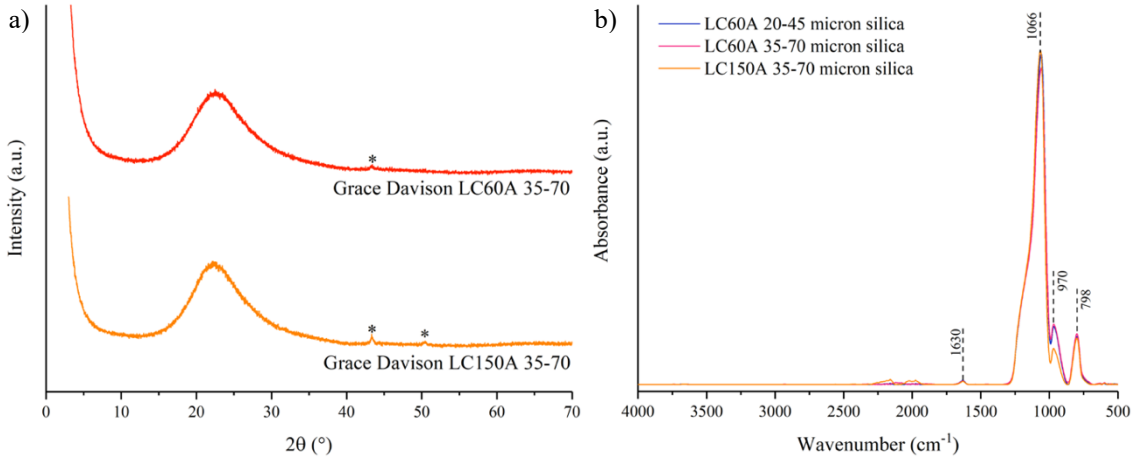


Figure B.61 a) Powder XRD diffractograms and b) FTIR spectra of Grace Davison silicas. *Reflections due to the sample holder.

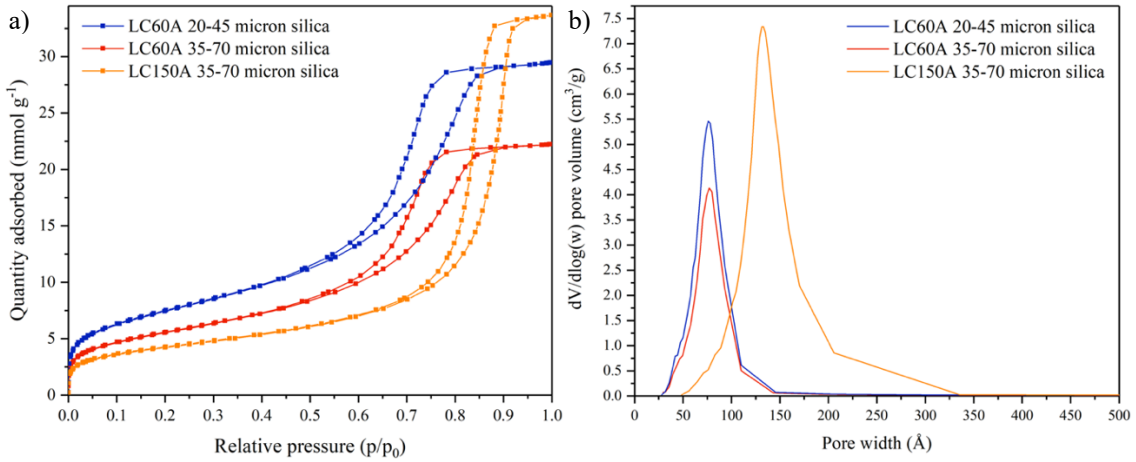


Figure B.62 a) N_2 absorption and desorption isotherms and b) BJH pore size distributions of Grace Davison silicas.

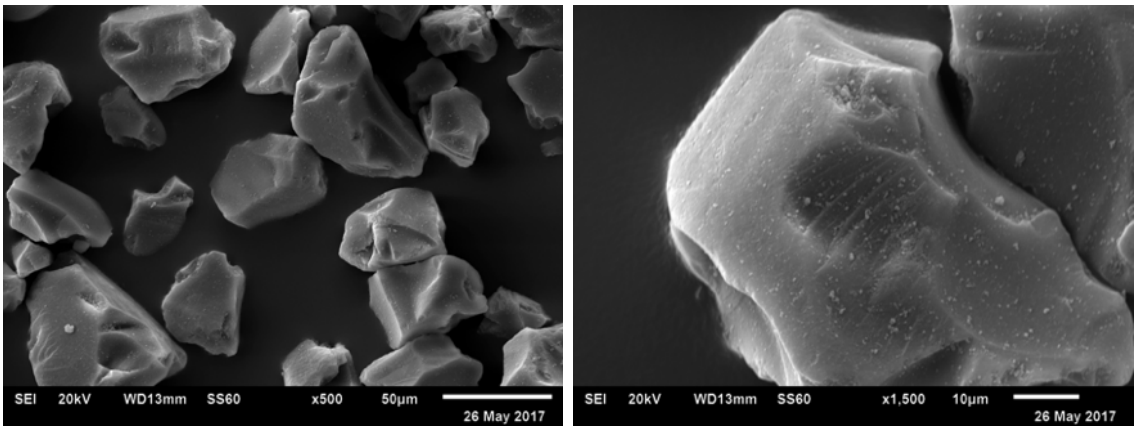


Figure B.63 SEM images of Grace Davison LC60A 20-45 silica.

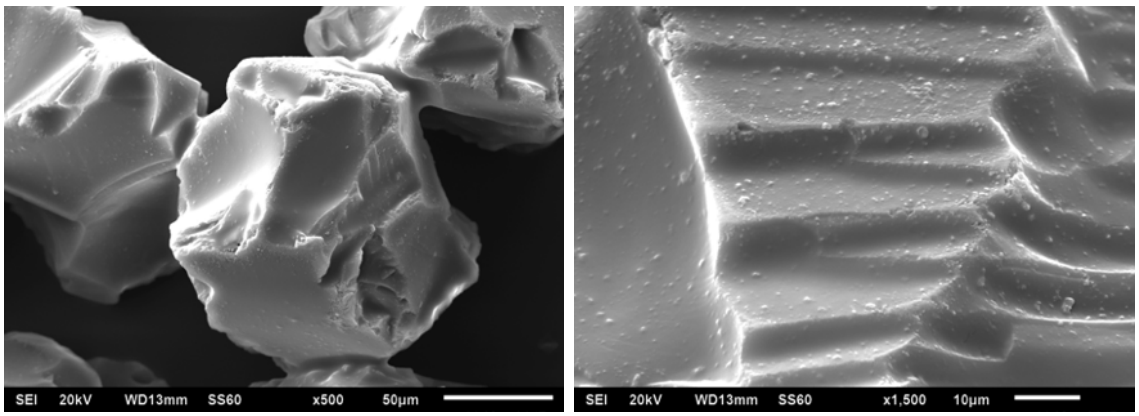


Figure B.64 SEM images of Grace Davison LC60A 70-200 silica.

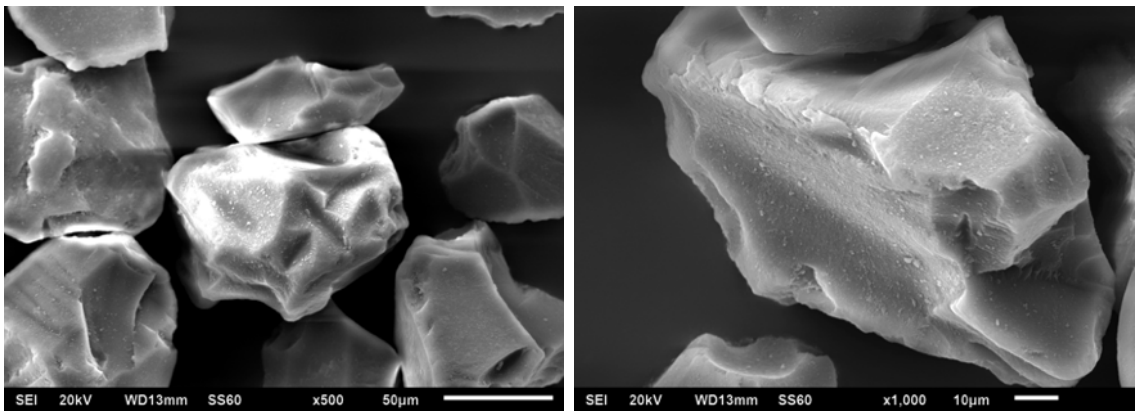


Figure B.65 SEM images of Grace Davison LC150A 35-70 silica.

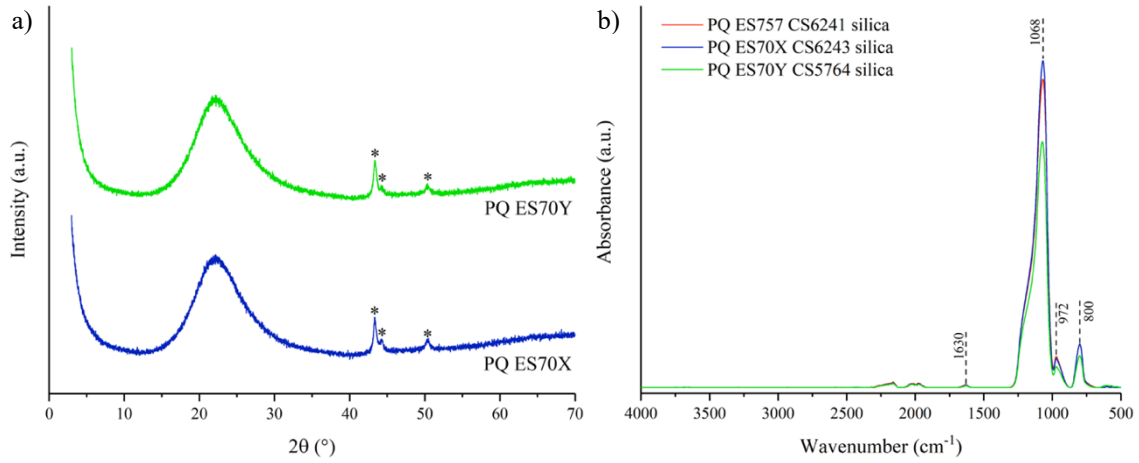


Figure B.66 a) Powder XRD diffractograms and b) FTIR spectra of PQ silicas. *Reflections due to the sample holder.

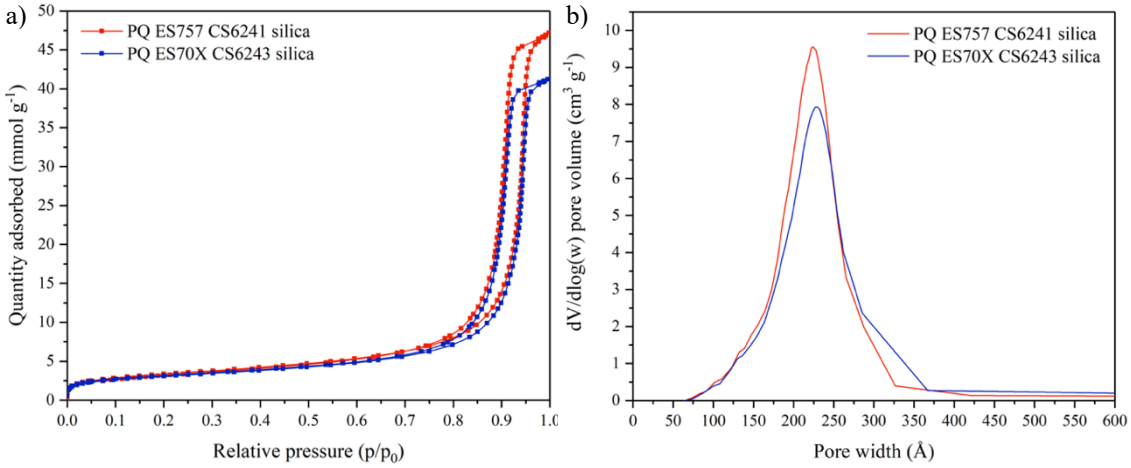


Figure B.67 a) N_2 absorption and desorption isotherms and b) BJH pore size distributions of PQ silicas.

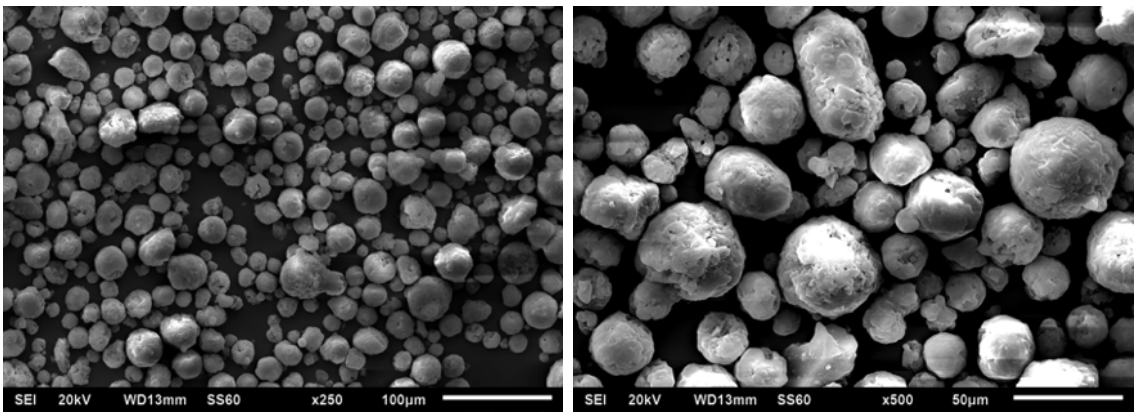


Figure B.68 SEM images of PQ ES757 silica.

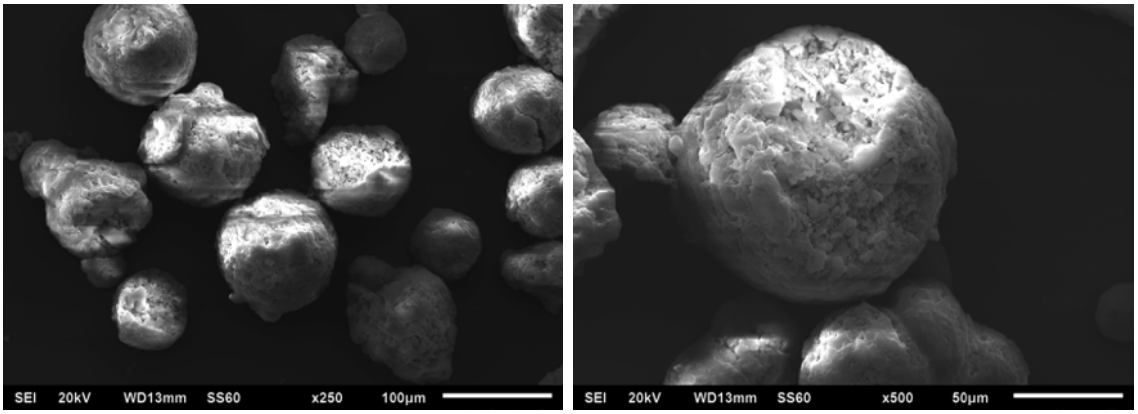


Figure B.69 SEM images of PQ ES70Y silica.

B.7 Commercial SiO_2@Mg_2Al-CO_3-AMO-LDHs

B.7.1 Grace Davison LC60A 35-70 silica

Table B.15 Lattice parameters and mean CDLs of SiO_2@Mg_2Al-CO_3-AMO-LDHs prepared using Grace Davison LC60A 35-70 silica and various synthesis methods. Stirring speed (where applicable) = 500 rpm. Metal addition rate (where applicable) = 1.0 cm^3 min^{-1}. AMO solvent = EtOH. Ageing time (unless otherwise specified) = 1 h.

Synthesis method	*d*-spacing (Å)		Lattice parameter (Å)		CDL (Å)	
	d_{003}	d_{110}	$c^{\dagger}$	$a^{\ddagger}$	*c*-axis	*ab*-plane
In situ co-precip.	7.77	1.53	23.31	3.06	133.2	599.4
IMP1a	7.90	1.52	23.70	3.04	149.7	301.6
IMP1b	7.88	1.54	23.64	3.08	99.8	677.4
IMP2	7.91	1.53	23.73	3.06	66.5	297.8
IMP2 (24 h ageing)	7.96	1.54	23.88	3.08	66.5	474.1
Hydrothermal	8.90	1.51	26.7	3.02	170.4	271.8

†Lattice parameter $c = 3d_{003}$. ‡Lattice parameter $a = 2d_{110}$.
CDL = $0.89\lambda/\beta\cos\theta$, λ = 1.541847 Å, β = FWHM in radians.

Table B.16 Powder XRD Bragg reflection data of SiO_2@Mg_2Al-CO_3-AMO-LDHs prepared using Grace Davison LC60A 35-70 silica and various synthesis methods. Stirring speed (where applicable) = 500 rpm. Metal addition rate (where applicable) = 1.0 cm^3 min^{-1}. AMO solvent = EtOH. Ageing time (unless otherwise specified) = 1 h.

Synthesis method	003[a] (º)	FWHM[b] (º)	110[c] (º)	FWHM[d] (º)
In situ co-precip.	11.39	0.60	60.65	0.27
IMP1a	11.120	0.54	60.86	0.54
IMP1b	11.23	0.80	60.29	0.23
IMP2	11.19	1.20	60.45	0.54
IMP2 (24 h ageing)	11.12	1.20	60.29	0.33
Hydrothermal	9.94	0.47	61.29	0.60

[a]Position of the 003 Bragg reflection (2θ), [b]FWHM of the 003 reflection.
[c]Position of the 110 Bragg reflection (2θ), [d]FWHM of 110 reflection.

Table B.17 Powder XRD Bragg reflection data of SiO_2@Mg_2Al-CO_3-AMO-LDHs prepared by the IMP2 method using Grace Davison LC60A 35-70 silica with different metal addition rates. Stirring speed = 500 rpm. AMO solvent = EtOH.

Metal addition rate (cm^3 min^{-1})	003[a] (º)	FWHM[b] (º)	110[c] (º)	FWHM[d] (º)
0.25	11.03	1.20	60.93	0.67
0.5	11.12	0.67	60.19	0.20
1.0	11.19	1.20	60.45	0.54
2.0	11.09	0.94	60.30	0.40

[a]Position of the 003 Bragg reflection (2θ), [b]FWHM of the 003 reflection.
[c]Position of the 110 Bragg reflection (2θ), [d]FWHM of 110 reflection.

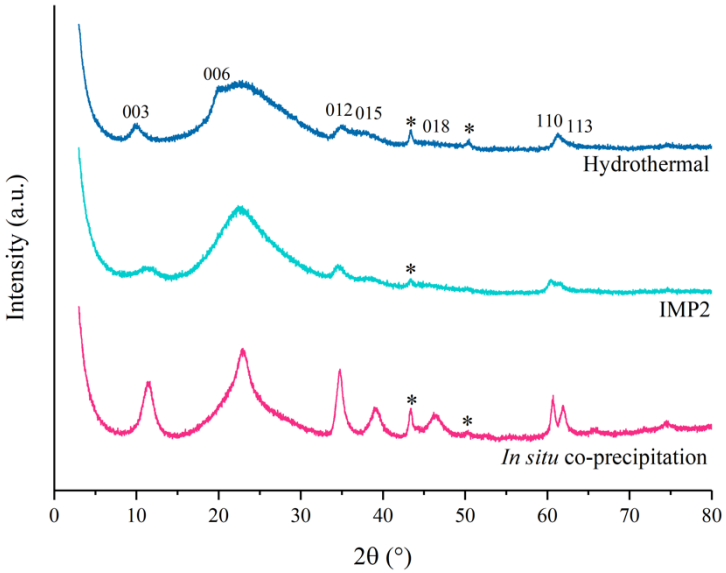


Figure B.70 Powder XRD diffractograms of SiO_2@Mg_2Al-CO_3-AMO-LDHs prepared by *in situ* co-precipitation, the IMP2 method, and hydrothermal method using Grace Davison LC60A 35-70 silica. Metal addition rate (*in-situ* co-precipitation and IMP2) = 1.0 cm^3 min^{-1}. Stirring speed (*in-situ* co-precipitation and IMP2) = 500 rpm. AMO solvent = EtOH.

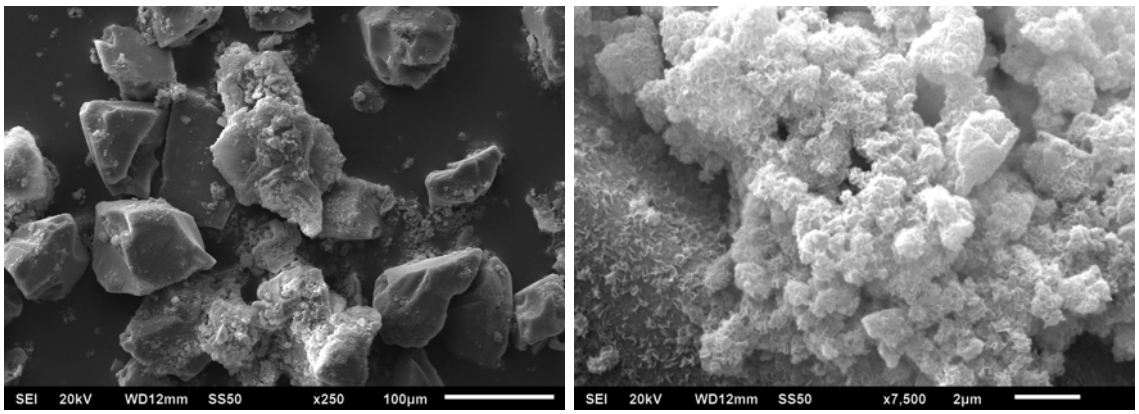


Figure B.71 SEM images of SiO_2@Mg_2Al-CO_3-AMO-LDHs prepared by a hydrothermal method using Grace Davison LC60A 35-70 silica.

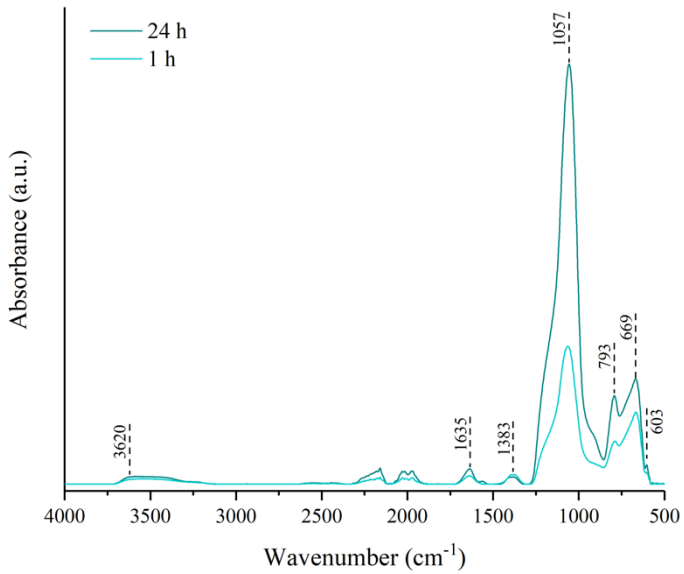


Figure B.72 FTIR spectra of SiO_2@Mg_2Al-CO_3-AMO-LDHs prepared by the IMP2 method with different ageing times using Grace Davison LC60A 35-70 silica. Metal addition rate = 1.0 cm^3 min^{-1}. Stirring speed = 500 rpm. AMO solvent = EtOH.

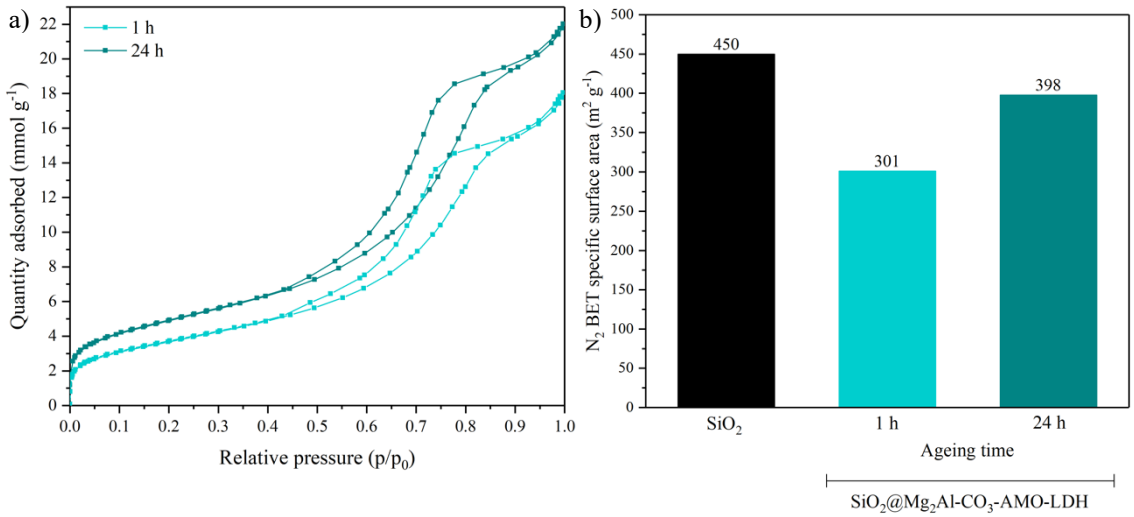


Figure B.73 a) N_2 adsorption and desorption isotherms and b) N_2 BET specific surface areas of SiO_2 and SiO_2@Mg_2Al-CO_3-AMO-LDHs prepared by the IMP2 method with different ageing times using Grace Davison LC60A 35-70 silica. Metal addition rate = 1.0 cm^3 min^{-1}. Stirring speed = 500 rpm. AMO solvent = EtOH.

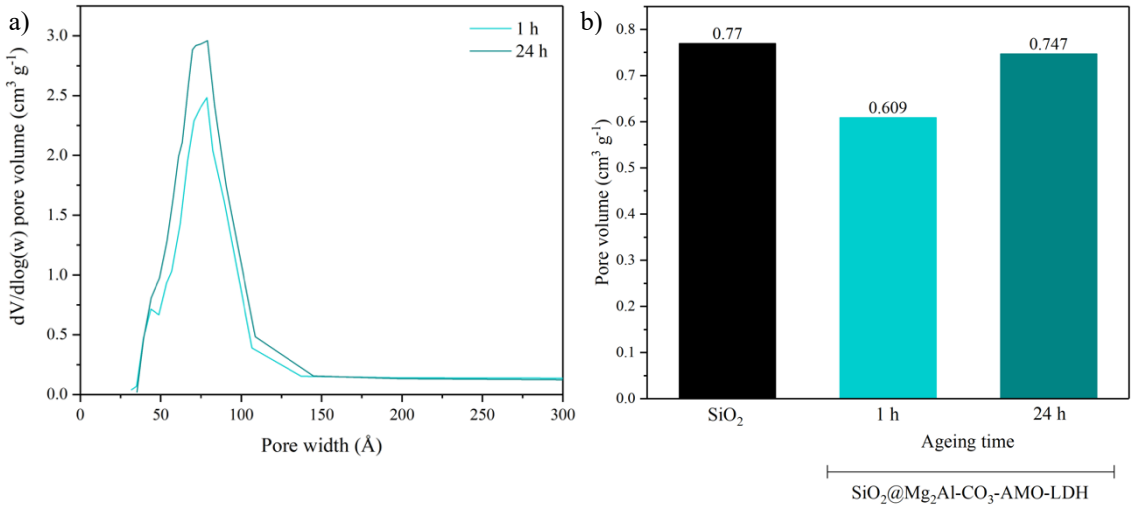


Figure B.74 a) BJH pore size distributions and b) pore volumes of SiO_2 and SiO_2@Mg_2Al-CO_3-AMO-LDHs prepared by the IMP2 method with different ageing times using Grace Davison LC60A 35-70 silica. Metal addition rate = 1.0 cm^3 min^{-1}. Stirring speed = 500 rpm. AMO solvent = EtOH.

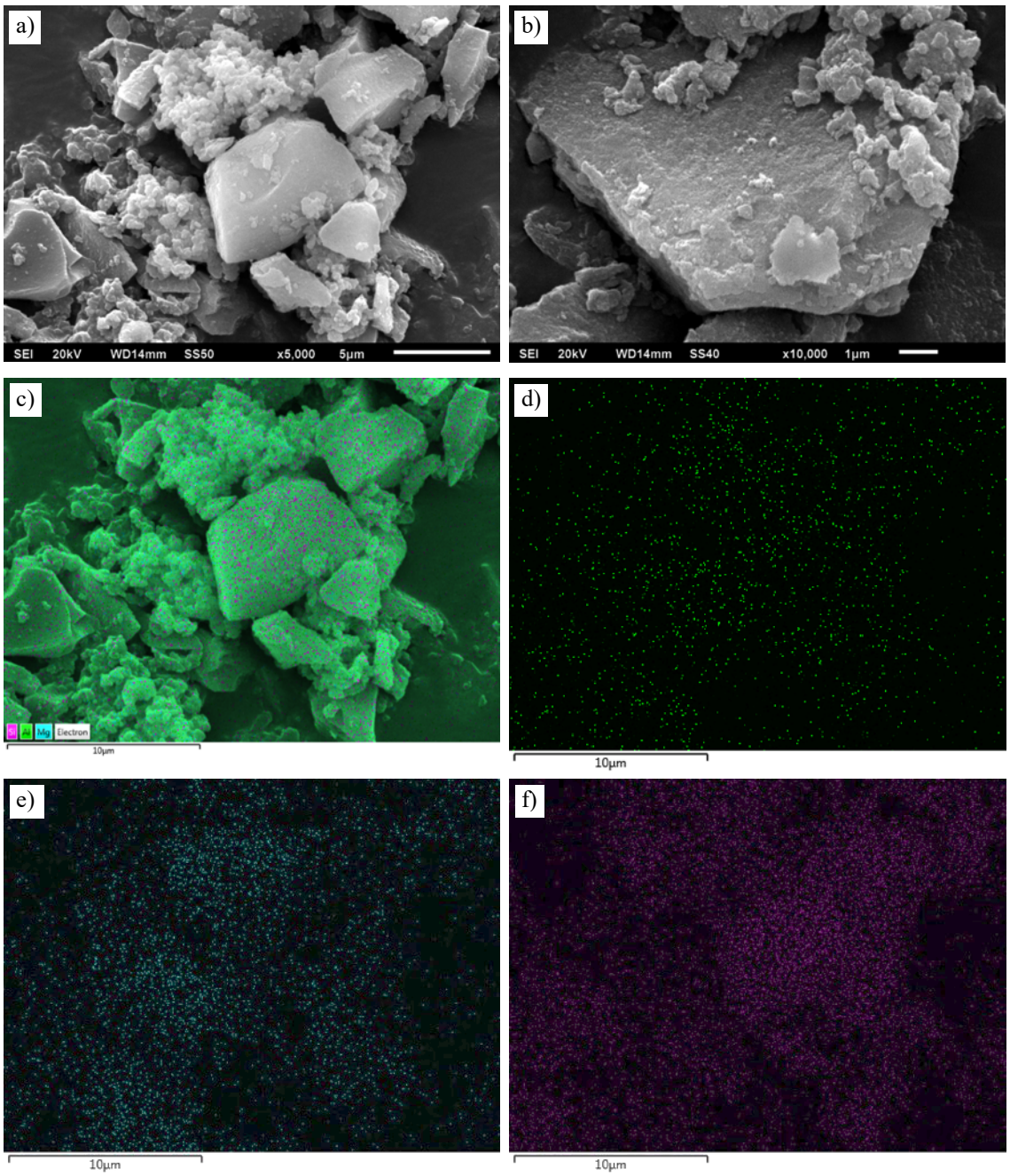


Figure B.75 a) and b) SEM images of SiO_2@Mg_2Al-CO_3-AMO-LDH prepared by the IMP2 method using Grace Davison LC60A 35-70 silica. SEM-EDX c) layered image and analyses of d) Al, e) Mg, and f) Si. Ageing time = 24 h. Metal addition rate = 1.0 cm^3 min^{-1}. Stirring speed = 500 rpm. AMO solvent = EtOH.

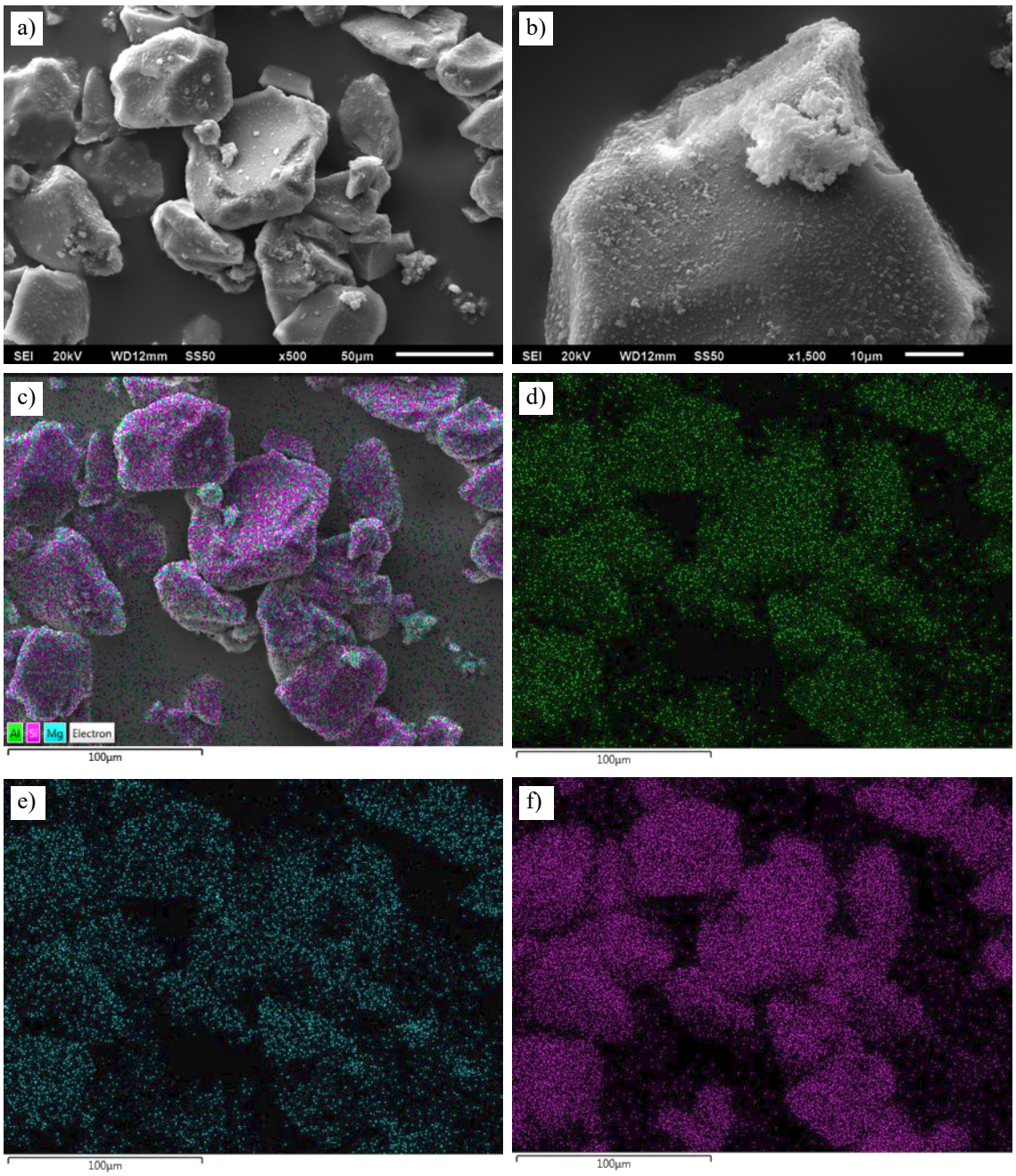


Figure B.76 a) and b) SEM images of SiO_2@Mg_2Al-CO_3-LDH prepared by the IMP2 method using Grace Davison LC60A 35-70 silica. SEM-EDX c) layered image and analyses of d) Al, e) Mg, and f) Si. Metal addition rate = 0.5 cm^3 min^{-1}. Stirring speed = 500 rpm.

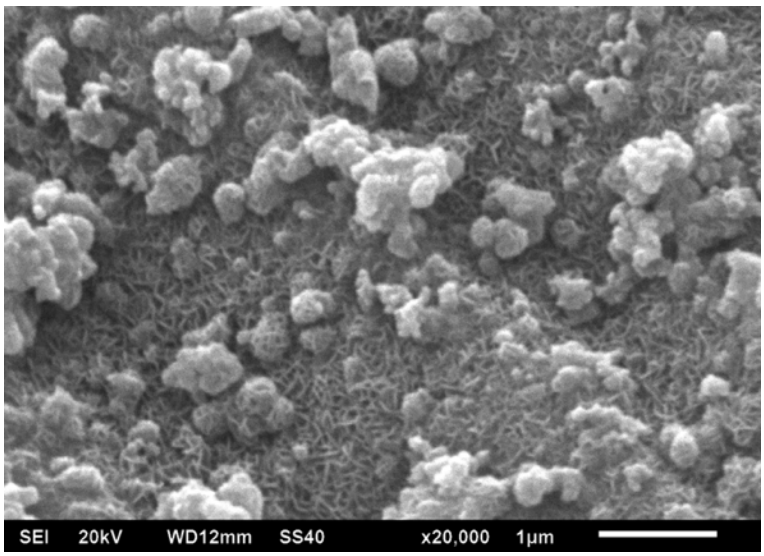


Figure B.77 High magnification SEM image of SiO_2@Mg_2Al-CO_3-LDH prepared by the IMP2 method using Grace Davison LC60A 35-70 silica. Metal addition rate = 0.5 cm^3 min^{-1}. Stirring speed = 500 rpm.

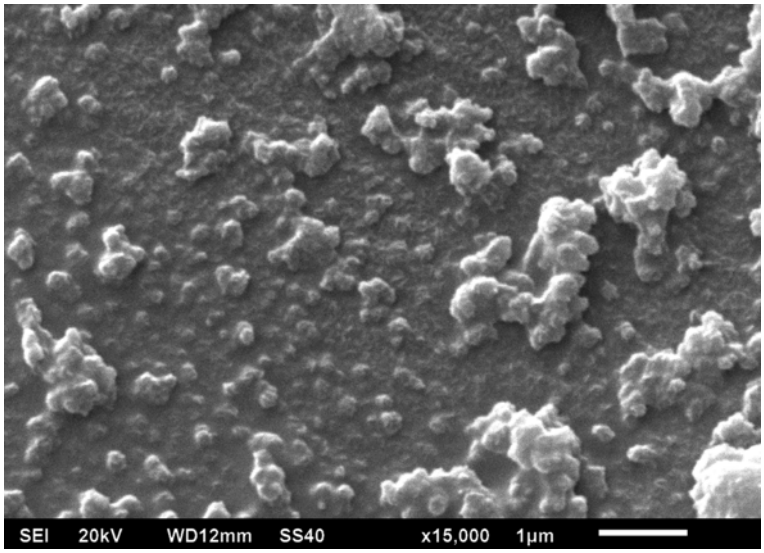


Figure B.78 High magnification SEM image of SiO_2@Mg_2Al-CO_3-LDH prepared by the IMP2 method using Grace Davison LC60A 35-70 silica. Metal addition rate = 1.0 cm^3 min^{-1}. Stirring speed = 500 rpm.

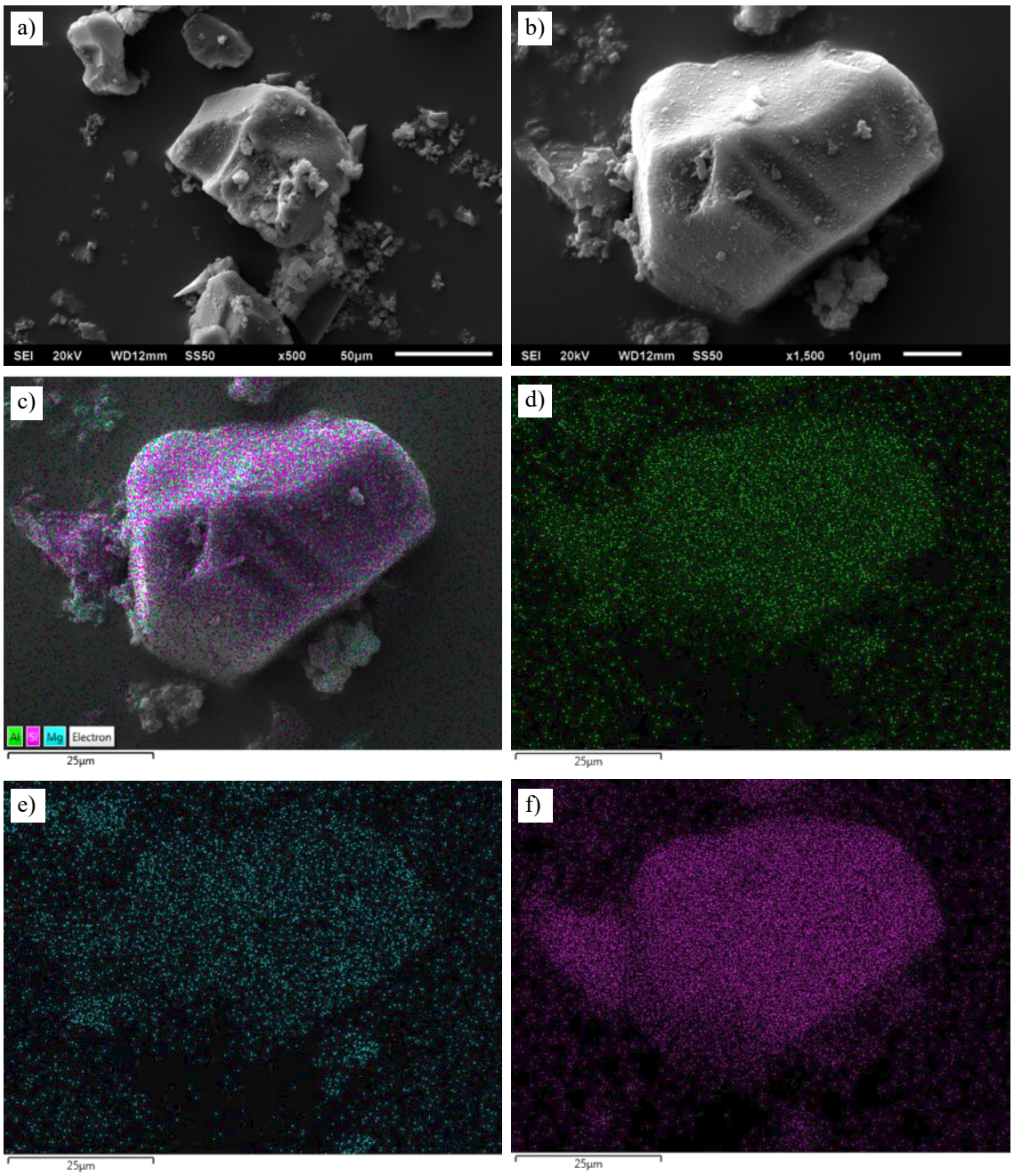


Figure B.79 a) and b) SEM images of SiO_2@Mg_2Al-CO_3-LDH prepared by the IMP2 method using Grace Davison LC60A 35-70 silica. SEM-EDX c) layered image and analyses of d) Al, e) Mg, and f) Si. Metal addition rate = 1.0 cm^3 min^{-1}. Stirring speed = 500 rpm.

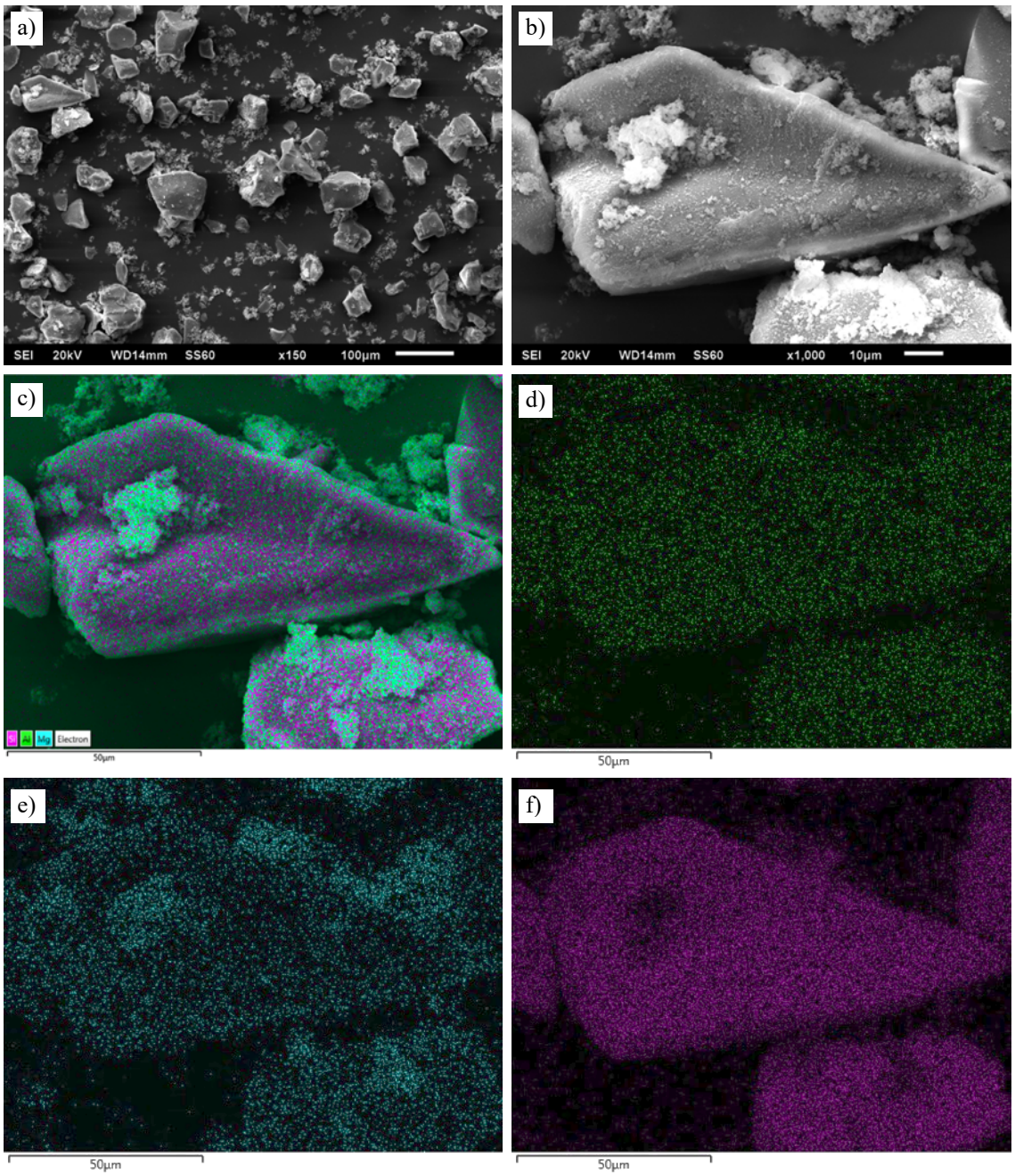


Figure B.80 a) and b) SEM images of SiO_2@Mg_2Al-CO_3-AMO-LDH prepared by the IMP2 method using Grace Davison LC60A 35-70 silica. SEM-EDX c) layered image and analyses of d) Al, e) Mg, and f) Si. Metal addition rate = 2.0 cm^3 min^{-1}. Stirring speed = 500 rpm. AMO solvent = EtOH.

B.7.2 Grace Davison LC150A 35-70 silica

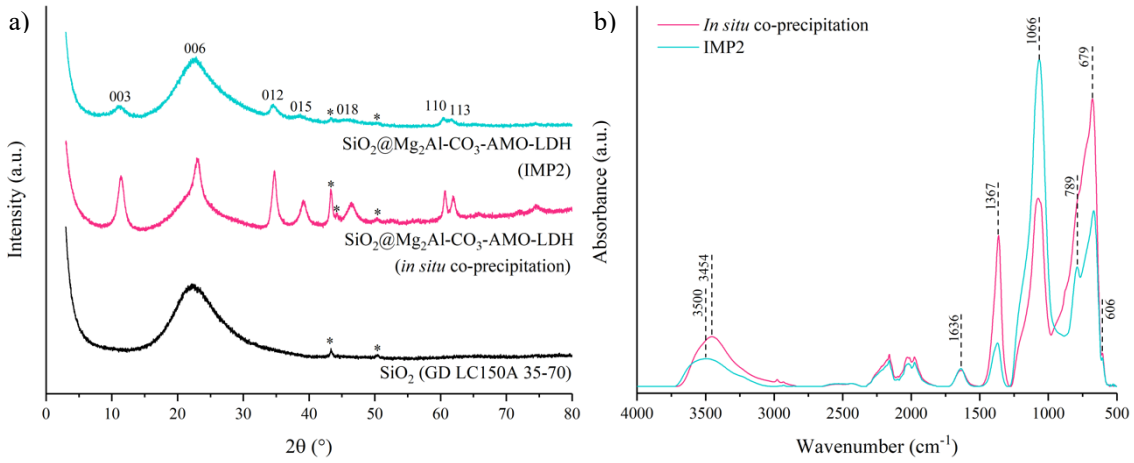


Figure B.81 a) Powder XRD diffractograms and b) FTIR spectra of SiO_2 and SiO_2@Mg_2Al-CO_3-AMO-LDHs prepared by *in situ* co-precipitation and the IMP2 method using Grace Davison LC150A 35-70 silica. Metal addition rate = 1.0 cm^3 min^{-1}. Stirring speed = 500 rpm. AMO solvent = EtOH. *Reflections due to the sample holder.

Table B.18 Lattice parameters and mean CDLs of SiO_2@Mg_2Al-CO_3-AMO-LDHs prepared by *in situ* co-precipitation and the IMP2 method using Grace Davison LC150A 35-70 silica. Stirring speed = 500 rpm. Metal addition rate = 1.0 cm^3 min^{-1}.AMO solvent = EtOH.

Synthesis method	*d*-spacing (Å)		Lattice parameter (Å)		CDL (Å)	
	d_{003}	d_{110}	$c^{\dagger}$	$a^{\ddagger}$	*c*-axis	*ab*-plane
In-situ co-precip.	7.80	1.53	23.40	3.06	266.3	479.8
IMP2	7.89	1.53	23.67	3.06	74.9	397.0

†Lattice parameter $c = 3d_{003}$. ‡Lattice parameter $a = 2d_{110}$.
CDL = $0.89\lambda/\beta\cos\theta$, λ = 1.541847 Å, β = FWHM in radians.

Table B.19 Powder XRD Bragg reflection data of SiO_2@Mg_2Al-CO_3-AMO-LDHs prepared by *in situ* co-precipitation and the IMP2 method using Grace Davison LC150A 35-70 silica. Stirring speed = 500 rpm. Metal addition rate = 1.0 cm^3 min^{-1}.AMO solvent = EtOH.

Synthesis method	003[a] (°)	FWHM[b] (°)	110[c] (°)	FWHM[d] (°)
In-situ co-precipitation	11.34	0.30	60.67	0.33
IMP2	11.23	1.07	60.45	0.40

[a]Position of the 003 Bragg reflection (2θ), [b]FWHM of the 003 reflection.
[c]Position of the 110 Bragg reflection (2θ), [d]FWHM of 110 reflection.

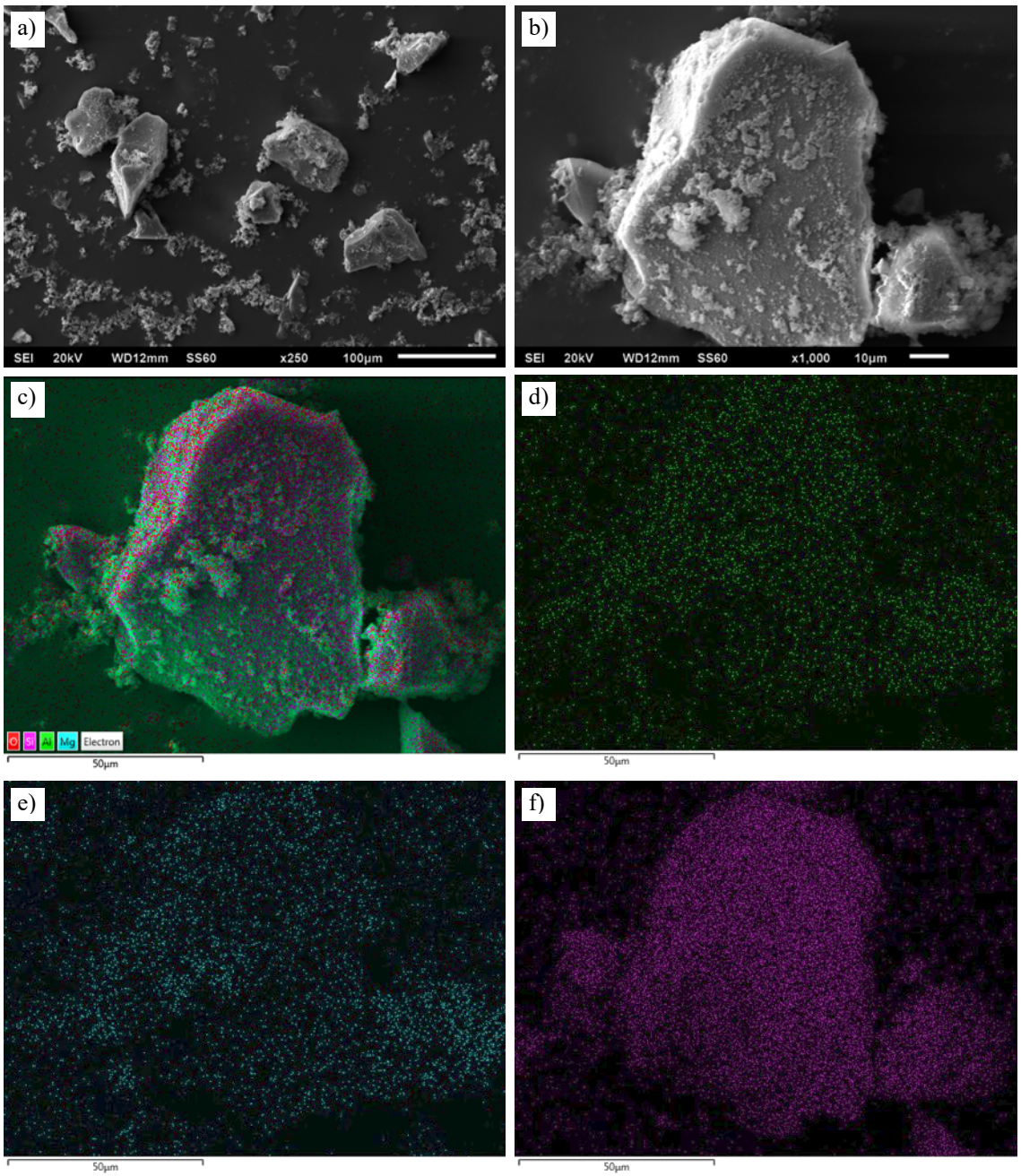


Figure B.82 a) and b) SEM images of SiO_2@Mg_2Al-CO_3-AMO-LDH prepared by *in situ* co-precipitation using Grace Davison LC150A 35-70 silica. SEM-EDX c) layered image and analyses of d) Al, e) Mg, and f) Si. Metal addition rate = 1.0 cm^3 min^{-1}. Stirring speed = 500 rpm. AMO solvent = EtOH.

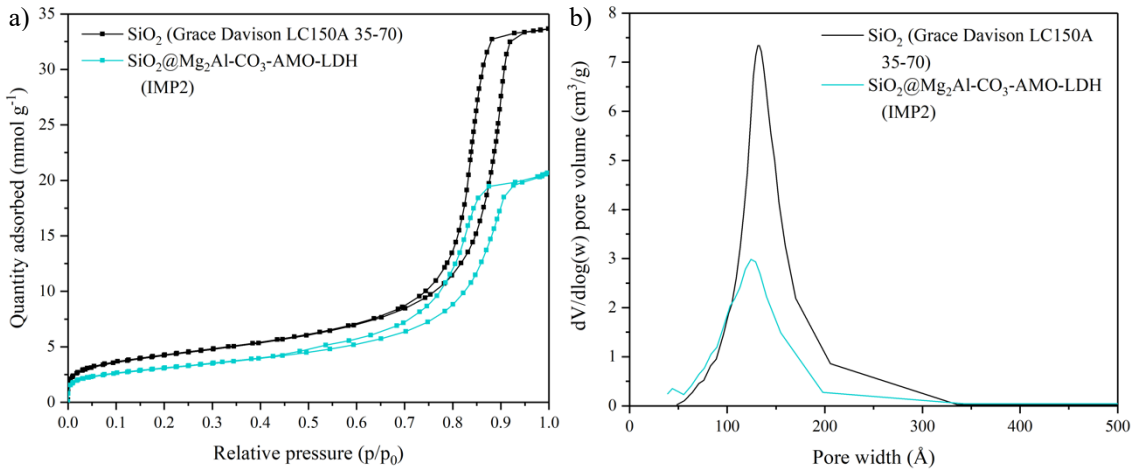


Figure B.83 a) N_2 adsorption and desorption isotherms and b) BJH pore size distributions of SiO_2 and SiO_2@Mg_2Al-CO_3-AMO-LDH prepared by the IMP2 method using Grace Davison LC150A 35-70 silica. Metal addition rate = 1.0 cm^3 min^{-1}. Stirring speed = 500 rpm. AMO solvent = EtOH.

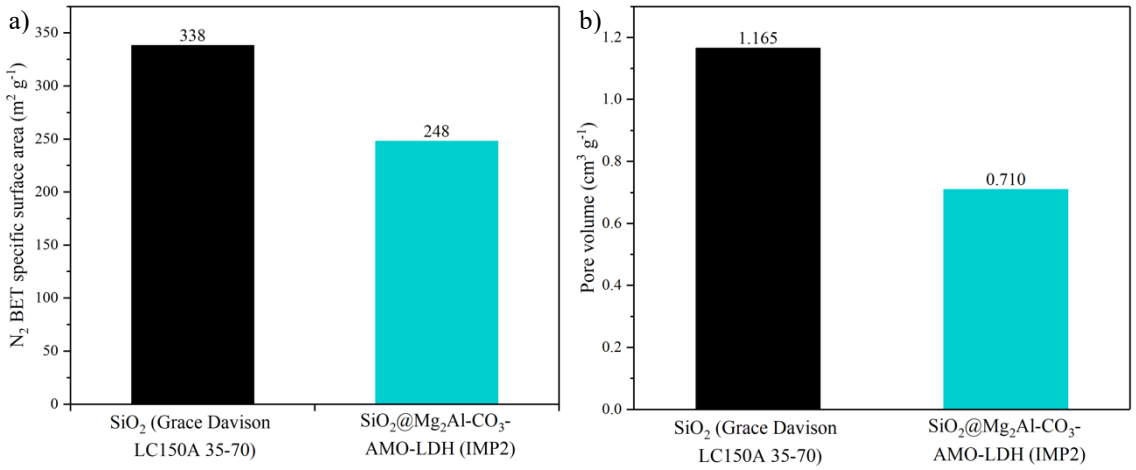


Figure B.84 a) N_2 BET specific surface areas and b) pore volumes of SiO_2 and SiO_2@Mg_2Al-CO_3-AMO-LDH prepared by the IMP2 method using Grace Davison LC150A 35-70 silica. Metal addition rate = 1.0 cm^3 min^{-1}. Stirring speed = 500 rpm. AMO solvent = EtOH.

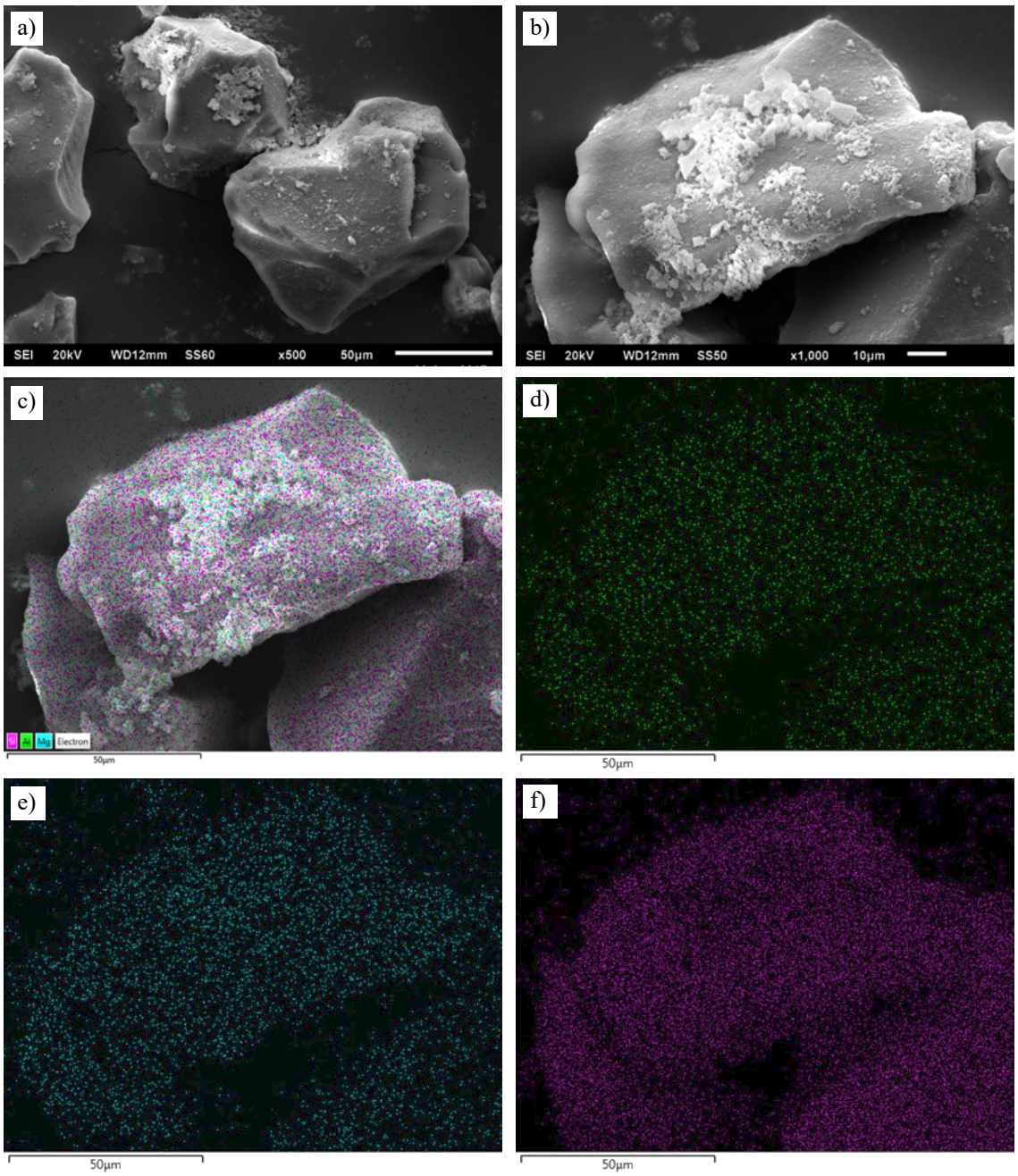


Figure B.85 a) and b) SEM images of SiO_2@Mg_2Al-CO_3-AMO-LDH prepared by the IMP2 method using Grace Davison LC150A 35-70 silica. SEM-EDX c) layered image and analyses of d) Al, e) Mg, and f) Si. Metal addition rate = 1.0 cm^3 min^{-1}. Stirring speed = 500 rpm. AMO solvent = EtOH.

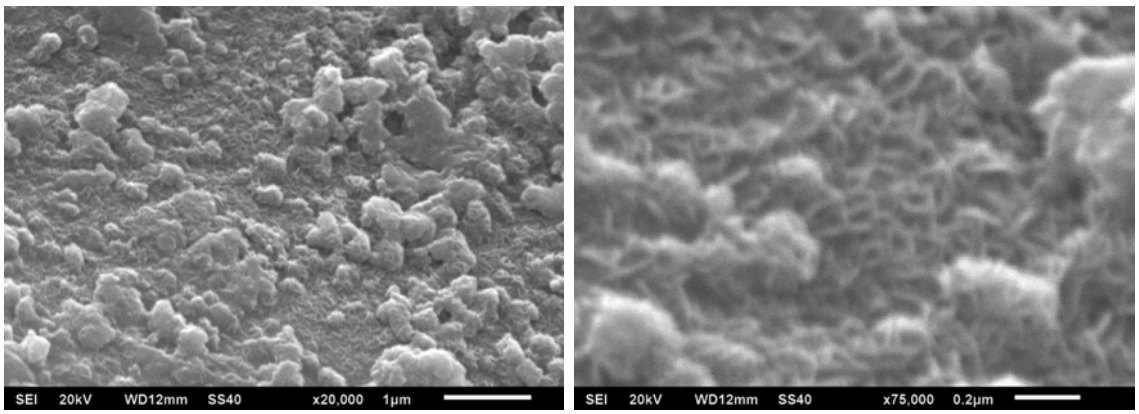


Figure B.86 High magnification SEM images of the surface of SiO_2@Mg_2Al-CO_3-AMO-LDH prepared by the IMP2 synthesis procedure using Grace Davison LC150A 35-70 silica. Metal addition rate = 1.0 cm^3 min^{-1}. Stirring speed = 500 rpm. AMO solvent = EtOH.

B.7.3 Fuji 1 silica

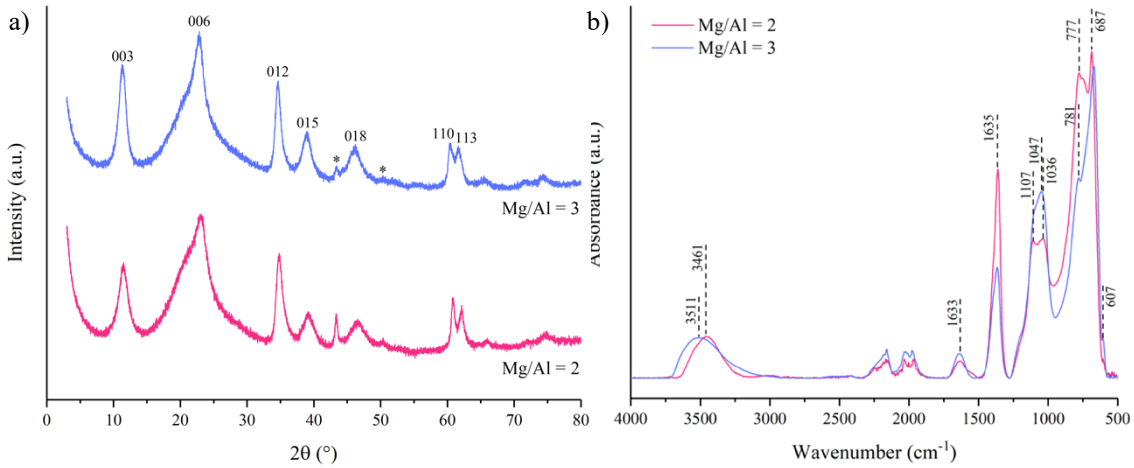


Figure B.87 a) Powder XRD diffractograms and b) FTIR spectra of SiO_2 and SiO_2@MgAl-CO_3-AMO-LDHs prepared by *in situ* co-precipitation using Fuji 1 silica with different Mg/Al ratios. Metal addition rate = 1.0 cm^3 min^{-1}. Stirring speed = 500 rpm. AMO solvent = EtOH. *Reflections due to the sample holder.

A shift of the (00*l*) peaks to lower 2θ, corresponding to larger interlayer spacing (d_{003}), is observed with increasing Mg/Al ratio. This can be attributed to the decrease in charge of the hydroxide layer as the Mg/Al ratio increases, which results in a weaker electrostatic interaction between the positively charged layers and the interlayer anions.

Table B.20 Lattice parameters and mean CDLs of SiO_2@MgAl-CO_3-AMO-LDHs prepared by *in situ* co-precipitation using Fuji 1 silica with different Mg/Al ratios. Metal addition rate = 1.0 cm^3 min^{-1}. Stirring speed = 500 rpm. AMO solvent = EtOH.

Mg/Al	*d*-spacing (Å)		Lattice parameter (Å)		CDL (Å)	
	d_{003}	d_{110}	$c^{\dagger}$	$a^{\ddagger}$	*c*-axis	*ab*-plane
2	7.68	1.52	23.04	3.04	99.9	401.7
3	7.91	1.53	23.73	3.06	266.2	339.0

†Lattice parameter $c = 3d_{003}$. ‡Lattice parameter $a = 2d_{110}$.
CDL = 0.89λ/βcosθ, λ = 1.541847 Å, β = FWHM in radians.

Table B.21 Powder XRD Bragg reflection data of SiO_2@MgAl-CO_3-AMO-LDHs prepared by *in situ* co-precipitation using Fuji 1 silica with different Mg/Al ratios. Metal addition rate = 1.0 cm^3 min^{-1}. Stirring speed = 500 rpm. AMO solvent = EtOH.

Mg/Al	003[a] (º)	FWHM[b] (º)	110[c] (º)	FWHM[d] (º)
2	11.53	0.80	60.83	0.40
3	11.18	0.30	60.32	0.47

[a]Position of the 003 Bragg reflection (2θ), [b]FWHM of the 003 reflection.
[c]Position of the 110 Bragg reflection (2θ), [d]FWHM of 110 reflection.

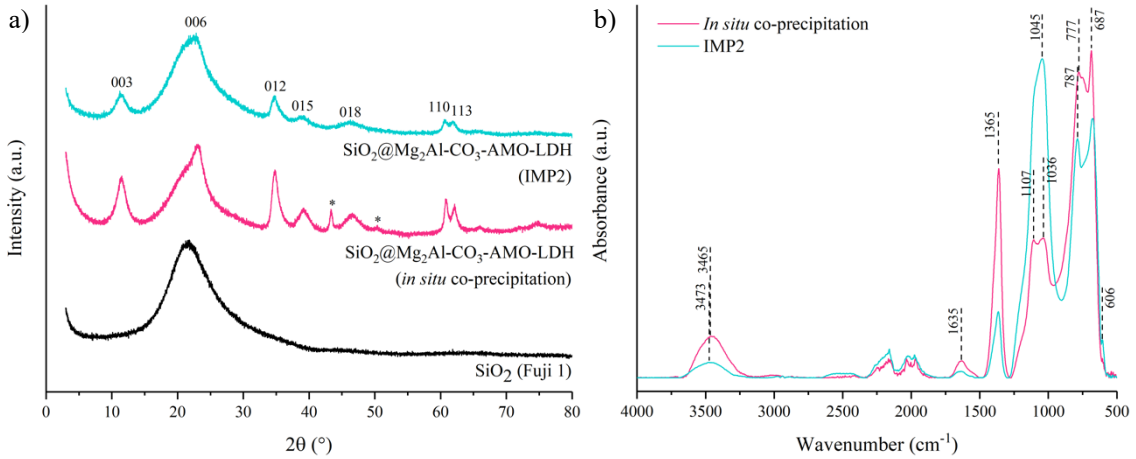


Figure B.88 a) Powder XRD diffractograms and b) FTIR spectra of SiO_2 and SiO_2@Mg_2Al-CO_3-AMO-LDHs prepared by *in situ* co-precipitation and the IMP2 method using Fuji 1 silica. Metal addition rate = 1.0 cm^3 min^{-1}. Stirring speed = 500 rpm. AMO solvent = EtOH. *Reflections due to the sample holder.

Table B.22 Lattice parameters and mean CDLs of SiO_2@Mg_2Al-CO_3-AMO-LDH prepared using the IMP2 method and Fuji 1 silica.

hkl	2θ[a] (°)	d_{hkl} (Å)	FWHM (°)	Lattice parameters (Å)	CDL (Å)
003	11.39	7.77	1.34	c = 23.31	59.9
110	60.66	1.53	0.47	a = 3.06	342.6

[a]Position of *hkl* Bragg reflection.
[b]Lattice parameter $c = 3d_{003}$, $a = 2d_{110}$.
CDL = 0.89λ/βcosθ, λ = 1.541847 Å, β = FWHM in radians.

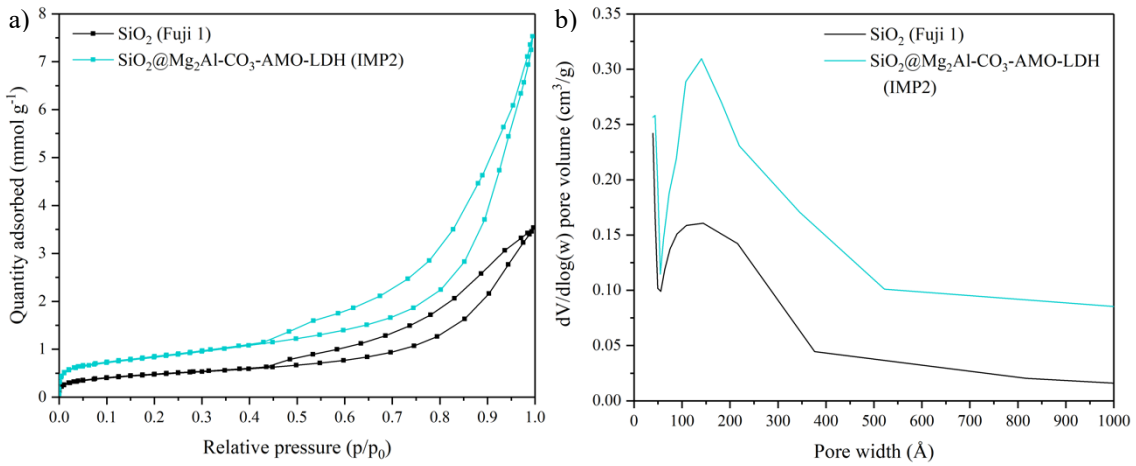


Figure B.89 a) N_2 adsorption and desorption isotherms and b) BJH pore size distributions of SiO_2 and SiO_2@Mg_2Al-CO_3-AMO-LDH prepared by the IMP2 method using Fuji 1 silica. Metal addition rate = 1.0 cm^3 min^{-1}. Stirring speed = 500 rpm. AMO solvent = EtOH.

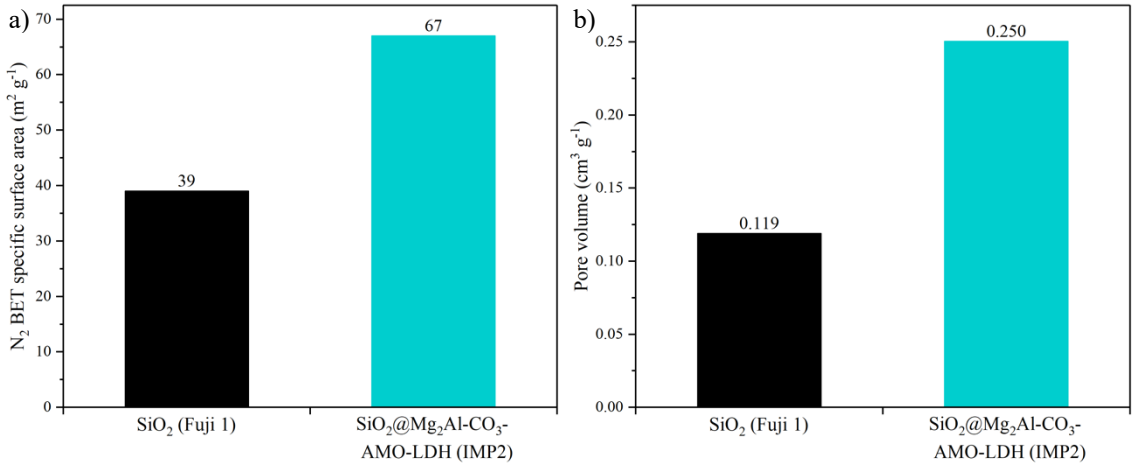


Figure B.90 a) N_2 BET specific surface areas and b) pore volumes of SiO_2 and SiO_2@Mg_2Al-CO_3-AMO-LDH prepared by the IMP2 method using Fuji 1 silica. Metal addition rate = 1.0 cm^3 min^{-1}. Stirring speed = 500 rpm. AMO solvent = EtOH.

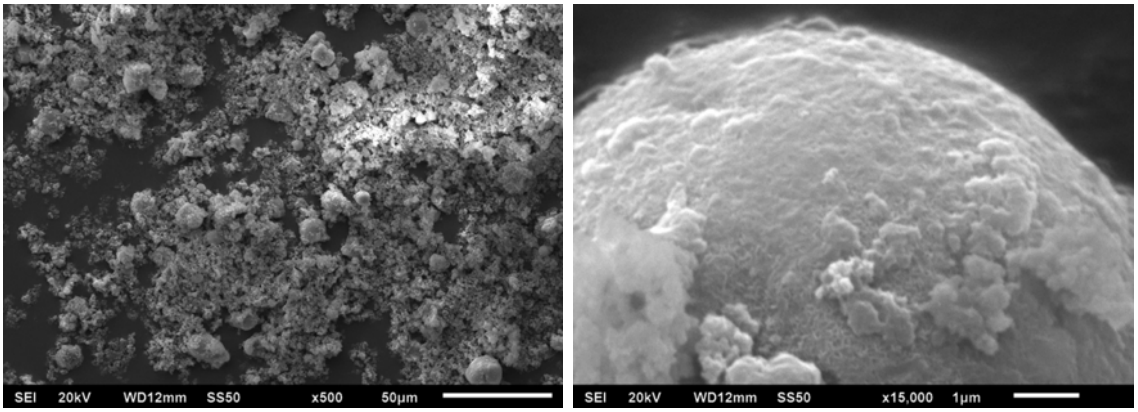


Figure B.91 SEM images of SiO_2@Mg_2Al-CO_3-AMO-LDH prepared by *in situ* co-precipitation using Fuji 1 silica. Metal addition rate = 1.0 cm^3 min^{-1}. Stirring speed = 500 rpm. AMO solvent = EtOH.

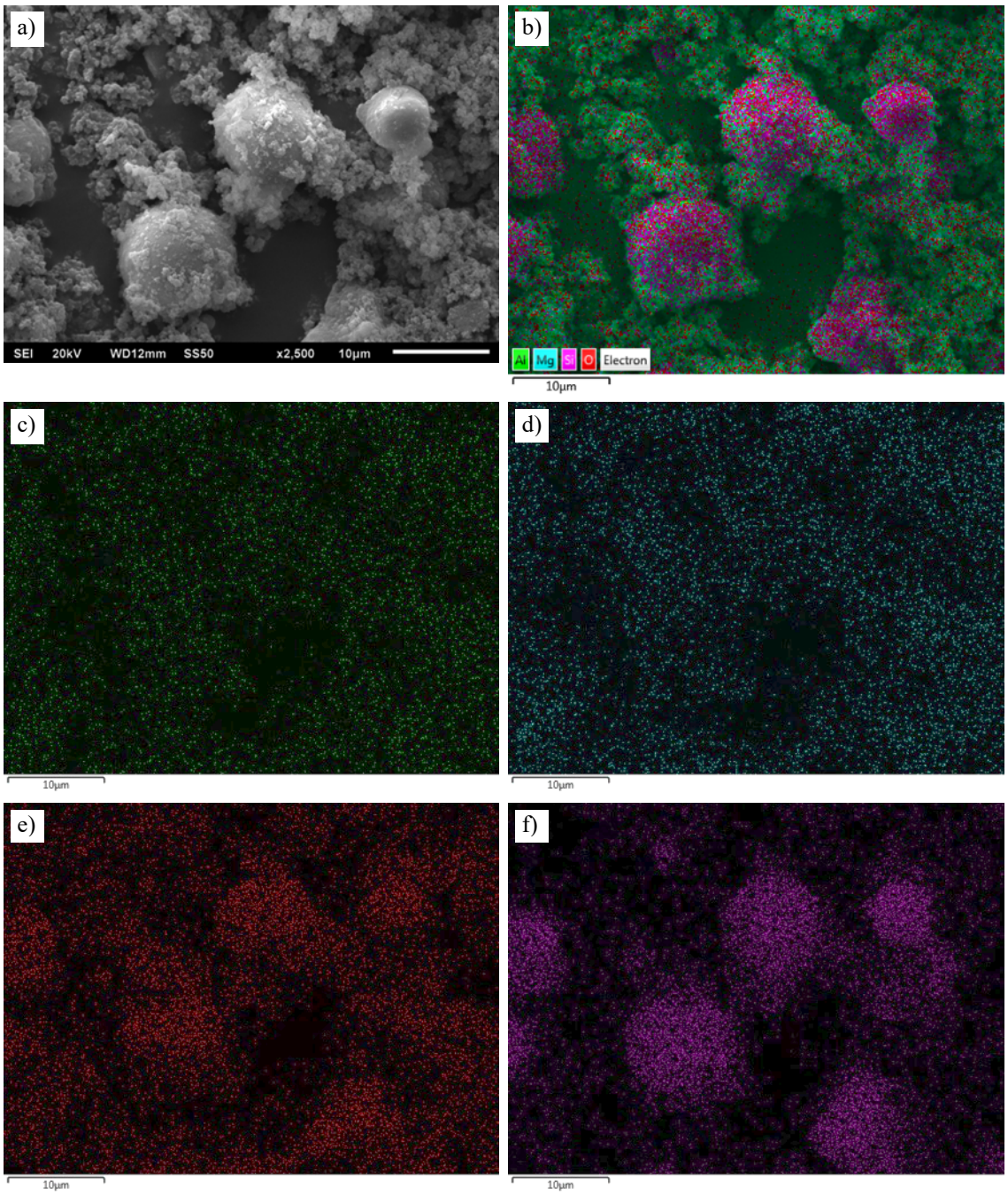


Figure B.92 a) SEM image of SiO_2@Mg_2Al-CO_3-AMO-LDH prepared by *in situ* co-precipitation using Fuji 1 silica. SEM-EDX b) layered image and analyses of c) Al, d) Mg, e) O, and f) Si. Metal addition rate = 1.0 cm^3 min^{-1}. Stirring speed = 500 rpm. AMO solvent = EtOH.

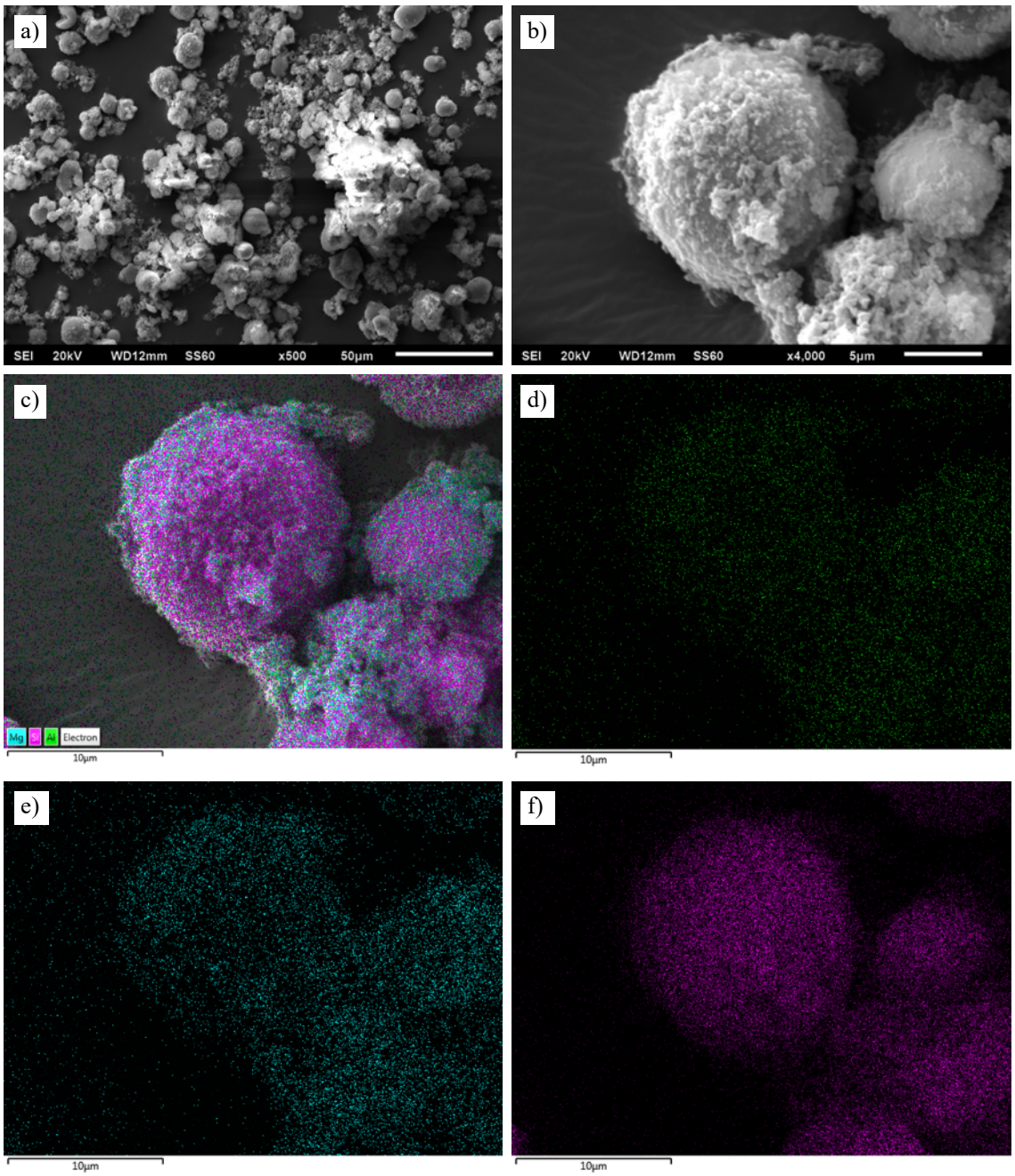


Figure B.93 a) and b) SEM images of SiO_2@Mg_2Al-CO_3-AMO-LDH prepared by the IMP2 method using Fuji 1 silica. SEM-EDX c) layered image and elemental analyses of d) Al, e) Mg, and f) Si. Metal addition rate = 1.0 cm^3 min^{-1}. Stirring speed = 500 rpm. AMO solvent = EtOH.

B.7.4 Fuji 2 silica

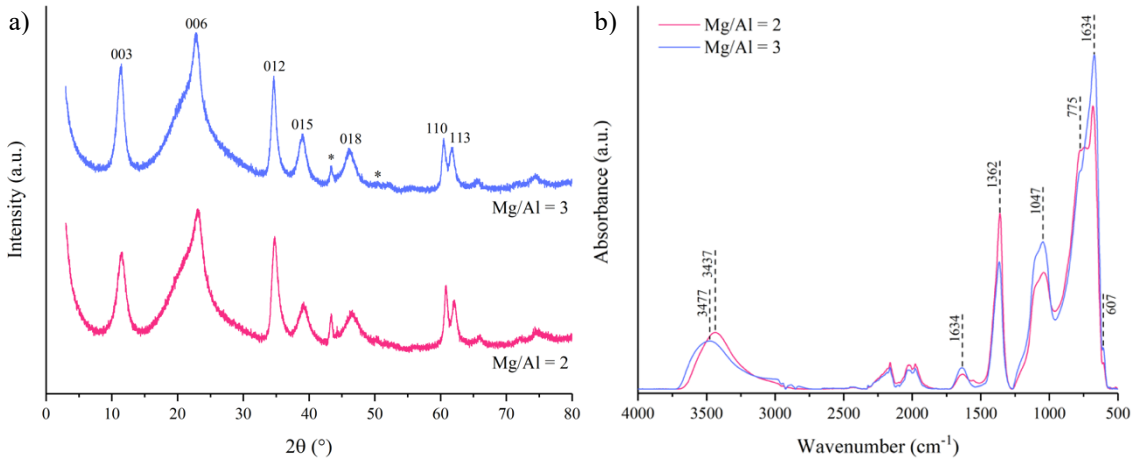


Figure B.94 a) Powder XRD diffractograms and b) FTIR spectra of SiO_2 and SiO_2@MgAl-CO_3-AMO-LDHs prepared by *in situ* co-precipitation using Fuji 2 silica with different Mg/Al ratios. Metal addition rate = 1.0 cm^3 min^{-1}. Stirring speed = 500 rpm. AMO solvent = EtOH. *Reflections due to the sample holder.

Table B.23 Lattice parameters and mean CDLs of SiO_2@MgAl-CO_3-AMO-LDHs prepared by *in situ* co-precipitation using Fuji 2 silica with different Mg/Al ratios. Metal addition rate = 1.0 cm^3 min^{-1}. Stirring speed = 500 rpm. AMO solvent = EtOH.

Mg/Al	*d*-spacing (Å)		Lattice parameter (Å)		CDL (Å)	
	d_{003}	d_{110}	$c^{\dagger}$	$a^{\ddagger}$	*c*-axis	*ab*-plane
2	7.70	1.52	23.10	3.04	123.7	401.3
3	7.74	1.53	23.22	3.06	85.6	530.1

†Lattice parameter $c = 3d_{003}$. ‡Lattice parameter $a = 2d_{110}$.
CDL = $0.89\lambda/\beta\cos\theta$, λ = 1.541847 Å, β = FWHM in radians.

Table B.24 Powder XRD Bragg reflection data of SiO_2@MgAl-CO_3-AMO-LDHs prepared by *in situ* co-precipitation using Fuji 2 silica with different Mg/Al ratios. Metal addition rate = 1.0 cm^3 min^{-1}. Stirring speed = 500 rpm. AMO solvent = EtOH.

Mg/Al	003[a] (°)	FWHM[b] (°)	110[c] (°)	FWHM[d] (°)
2	11.49	0.65	60.79	0.40
3	11.43	0.94	60.49	0.30

[a]Position of the 003 Bragg reflection (2θ), [b]FWHM of the 003 reflection.
[c]Position of the 110 Bragg reflection (2θ), [d]FWHM of 110 reflection.

Table B.25 Lattice parameters and mean CDLs of SiO_2@Mg_2Al-CO_3-AMO-LDH prepared by the IMP2 method using Fuji 2 silica.

hkl	2θ[a] (º)	d_{hkl} (Å)	FWHM (º)	Lattice parameters (Å)	CDL (Å)
003	11.52	7.68	0.27	c = 23.04	299.9
110	60.72	1.53	0.47	a = 3.06	343.2

[a]Position of *hkl* Bragg reflection.
[b]Lattice parameter $c = 3d_{003}$, $a = 2d_{110}$.
CDL = 0.89λ/βcosθ, λ = 1.541847 Å, β = FWHM in radians.

Table B.26 Lattice parameters and mean CDLs of SiO_2@Mg_2Al-CO_3-AMO-LDH prepared by the IMP2 method using Fuji 2 silica. Batch size: 1.8 g.

hkl	2θ[a] (º)	d_{hkl} (Å)	FWHM (º)	Lattice parameters (Å)	CDL (Å)
003	11.48	7.70	0.33	c = 23.10	239.8
110	60.81	1.52	0.33	a = 3.04	481.9

[a]Position of *hkl* Bragg reflection.
[b]Lattice parameter $c = 3d_{003}$, $a = 2d_{110}$.
CDL = 0.89λ/βcosθ, λ = 1.541847 Å, β = FWHM in radians.

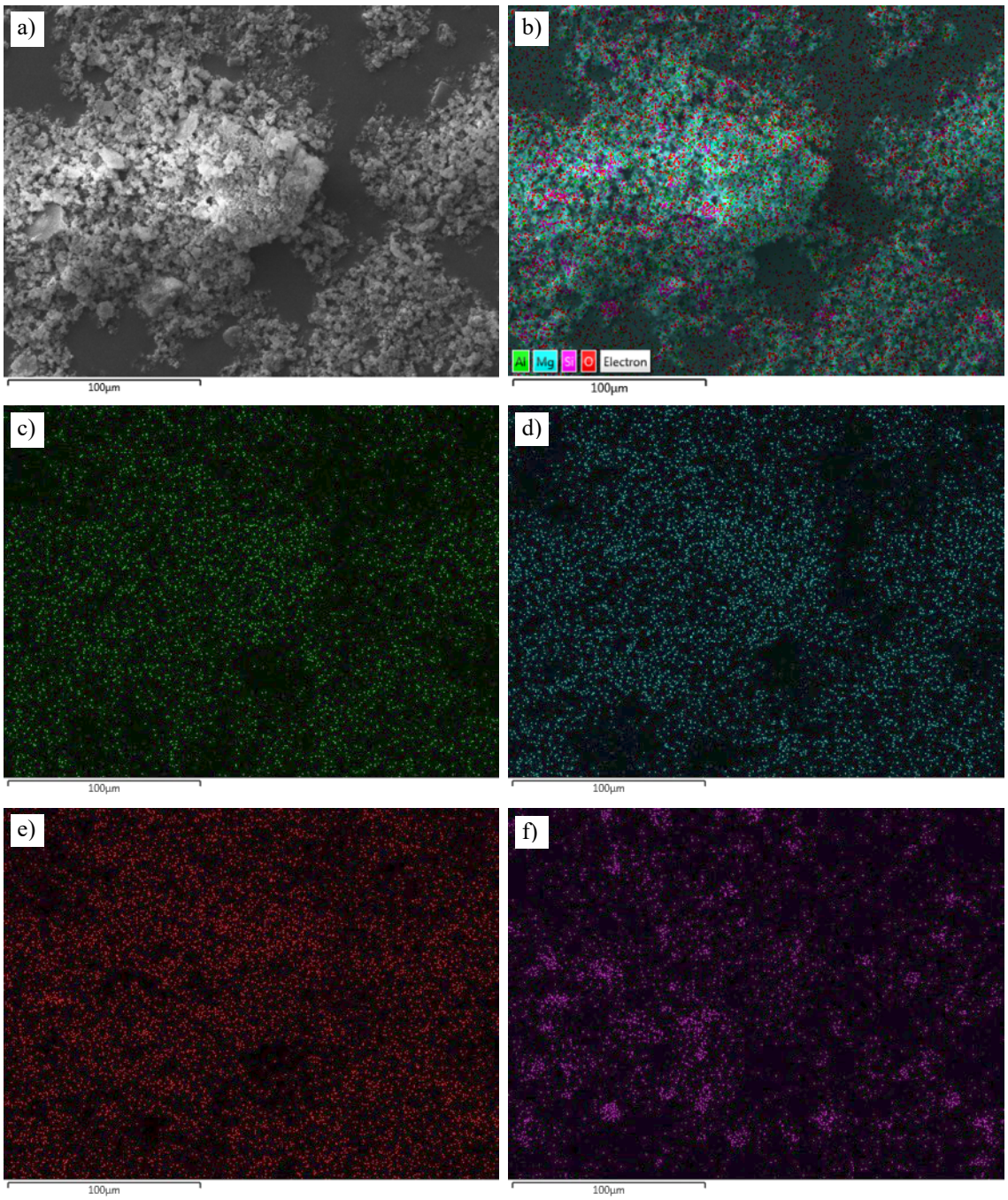


Figure B.95 a) SEM image of free LDH obtained by low speed centrifugation (1000 rpm, 5 minutes; four times) of SiO_2@Mg_2Al-CO_3-AMO-LDH prepared by *in situ* co-precipitation using Fuji 2 silica. SEM-EDX b) layered image and analyses of c) Al, d) Mg, e) O, and f) Si. Metal addition rate = 1.0 cm^3 min^{-1}. Stirring speed = 500 rpm. AMO solvent = EtOH.

B.7.5 PQ ES70X silica

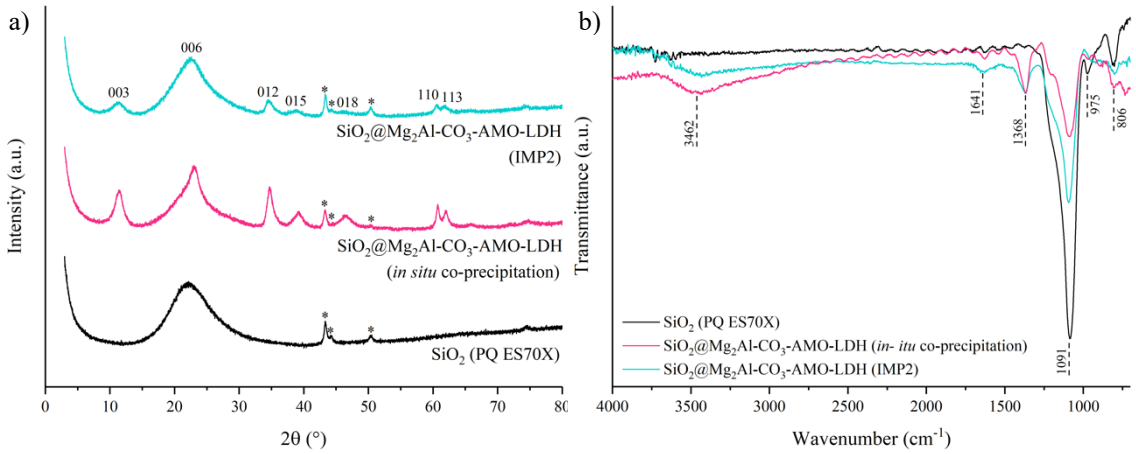


Figure B.96 a) Powder XRD diffractograms and b) FTIR spectra of SiO_2 and SiO_2@Mg_2Al-CO_3-AMO-LDHs prepared by *in situ* co-precipitation and the IMP2 method using PQ ES70X silica. Metal addition rate = 1.0 cm^3 min^{-1}. Stirring speed = 500 rpm. AMO solvent = EtOH. *Reflections due to the sample holder.

Table B.27 Lattice parameters and mean CDLs of SiO_2@Mg_2Al-CO_3-AMO-LDHs prepared by *in situ* co-precipitation and the IMP2 method using PQ ES70X silica. Metal addition rate = 1.0 cm^3 min^{-1}. Stirring speed = 500 rpm. AMO solvent = EtOH.

Synthesis method	*d*-spacing (Å)		Lattice parameter (Å)		CDL (Å)	
	d_{003}	d_{110}	$c^{\dagger}$	$a^{\ddagger}$	*c*-axis	*ab*-plane
In situ co-precip.	7.73	1.52	23.19	3.04	149.9	534.3
IMP2	7.83	1.53	23.49	3.06	85.6	398.3

†Lattice parameter $c = 3d_{003}$. ‡Lattice parameter $a = 2d_{110}$.
CDL = $0.89\lambda/\beta\cos\theta$, λ = 1.541847 Å, β = FWHM in radians.

Table B.28 Powder XRD Bragg reflection data of SiO_2@Mg_2Al-CO_3-AMO-LDHs prepared by *in situ* co-precipitation and the IMP2 method using PQ ES70X silica. Metal addition rate = 1.0 cm^3 min^{-1}. Stirring speed = 500 rpm. AMO solvent = EtOH.

Synthesis method	003[a] (º)	FWHM[b] (º)	110[c] (º)	FWHM[d] (º)
In situ co-precipitation	11.44	0.54	60.74	0.30
IMP2	11.30	0.94	60.55	0.40

[a]Position of the 003 Bragg reflection (2θ), [b]FWHM of the 003 reflection.
[c]Position of the 110 Bragg reflection (2θ), [d]FWHM of 110 reflection.

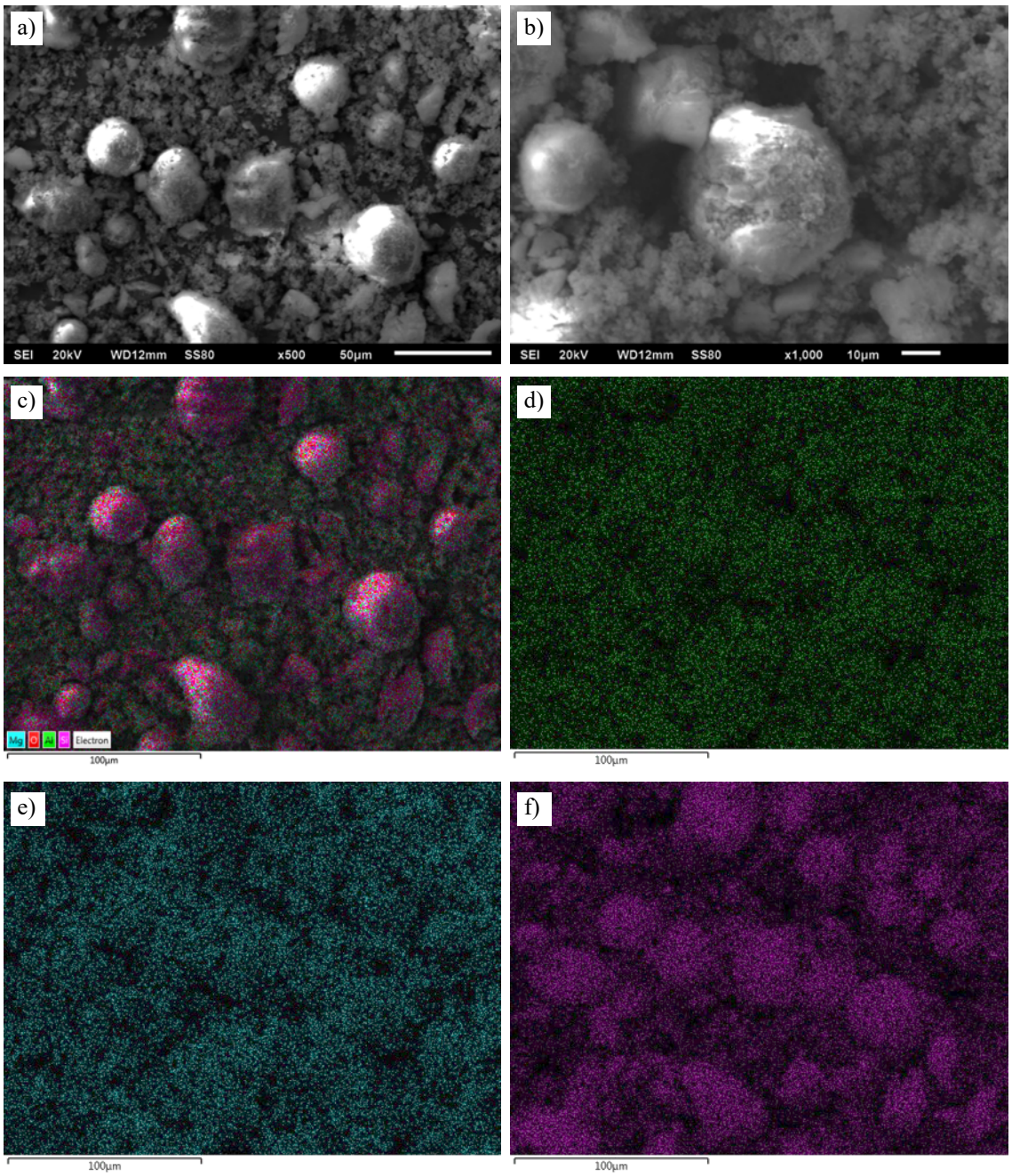


Figure B.97 a) and b) SEM images of SiO_2@Mg_2Al-CO_3-AMO-LDH prepared by *in situ* co-precipitation using PQ ES70X silica. SEM-EDX c) layered image and analyses of d) Al, e) Mg, and f) Si. Metal addition rate = 1.0 cm^3 min^{-1}. Stirring speed = 500 rpm. AMO solvent = EtOH.

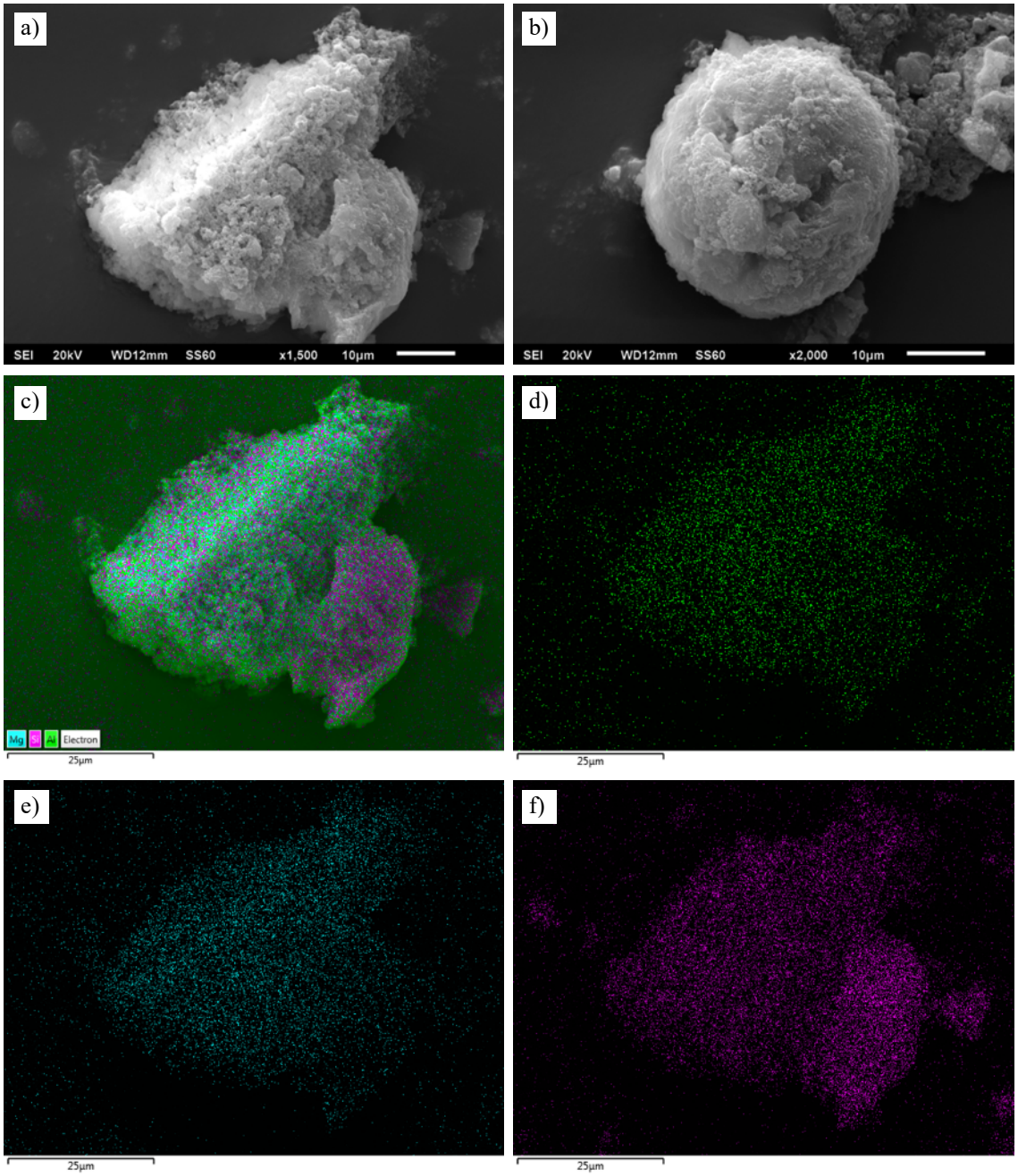


Figure B.98 a) and b) SEM images of SiO_2@Mg_2Al-CO_3-AMO-LDH prepared by the IMP2 method using PQ ES70X silica. SEM-EDX c) layered image and analyses of d) Al, e) Mg, and f) Si. Metal addition rate = 1.0 cm^3 min^{-1}. Stirring speed = 500 rpm. AMO solvent = EtOH.

B.7.6 PQ ES70Y silica

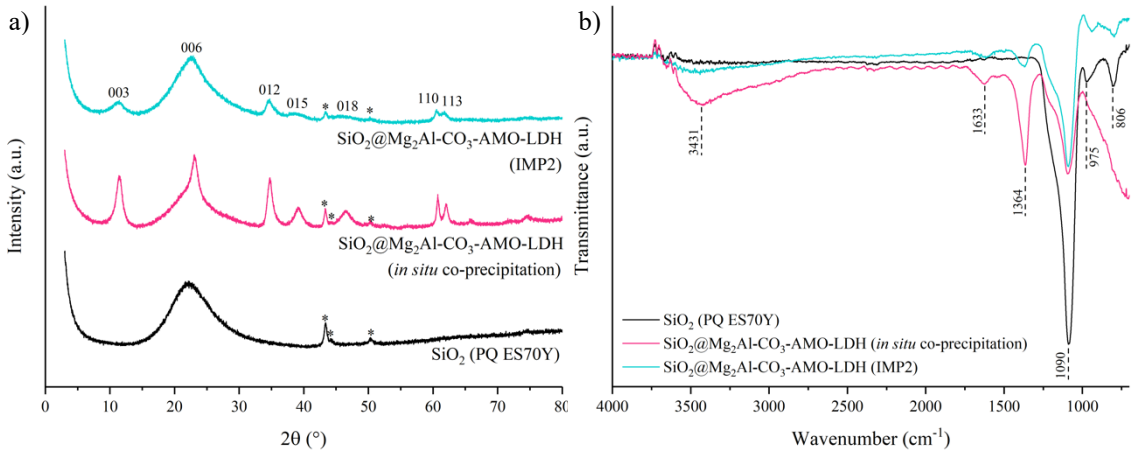


Figure B.99 a) Powder XRD diffractograms and b) FTIR spectra of SiO_2 and SiO_2@Mg_2Al-CO_3-AMO-LDHs prepared by *in situ* co-precipitation and the IMP2 method using PQ ES70Y silica. Metal addition rate = 1.0 cm^3 min^{-1}. Stirring speed = 500 rpm. AMO solvent = EtOH. *Reflections due to the sample holder.

Table B.29 Lattice parameters and mean CDLs of SiO_2@Mg_2Al-CO_3-AMO-LDHs prepared by *in situ* co-precipitation and the IMP2 method using PQ ES70Y silica. Metal addition rate = 1.0 cm^3 min^{-1}. Stirring speed = 500 rpm. AMO solvent = EtOH.

Synthesis method	*d*-spacing (Å)		Lattice parameter (Å)		CDL (Å)	
	d_{003}	d_{110}	$c^{\dagger}$	$a^{\ddagger}$	*c*-axis	*ab*-plane
In situ co-precip.	7.73	1.52	23.19	3.04	239.7	801.6
IMP2	7.80	1.53	23.40	3.06	59.9	341.2

†Lattice parameter $c = 3d_{003}$. ‡Lattice parameter $a = 2d_{110}$.
CDL = $0.89\lambda/\beta\cos\theta$, λ = 1.541847 Å, β = FWHM in radians.

Table B.30 Powder XRD Bragg reflection data of SiO_2@Mg_2Al-CO_3-AMO-LDHs prepared by *in situ* co-precipitation and the IMP2 method using PQ ES70Y silica. Metal addition rate = 1.0 cm^3 min^{-1}. Stirring speed = 500 rpm. AMO solvent = EtOH.

Synthesis method	003[a] (°)	FWHM[b] (°)	110[c] (°)	FWHM[d] (°)
In situ co-precipitation	11.45	0.33	60.74	0.20
IMP2	11.34	1.34	60.53	0.47

[a]Position of the 003 Bragg reflection (2θ), [b]FWHM of the 003 reflection.
[c]Position of the 110 Bragg reflection (2θ), [d]FWHM of 110 reflection.

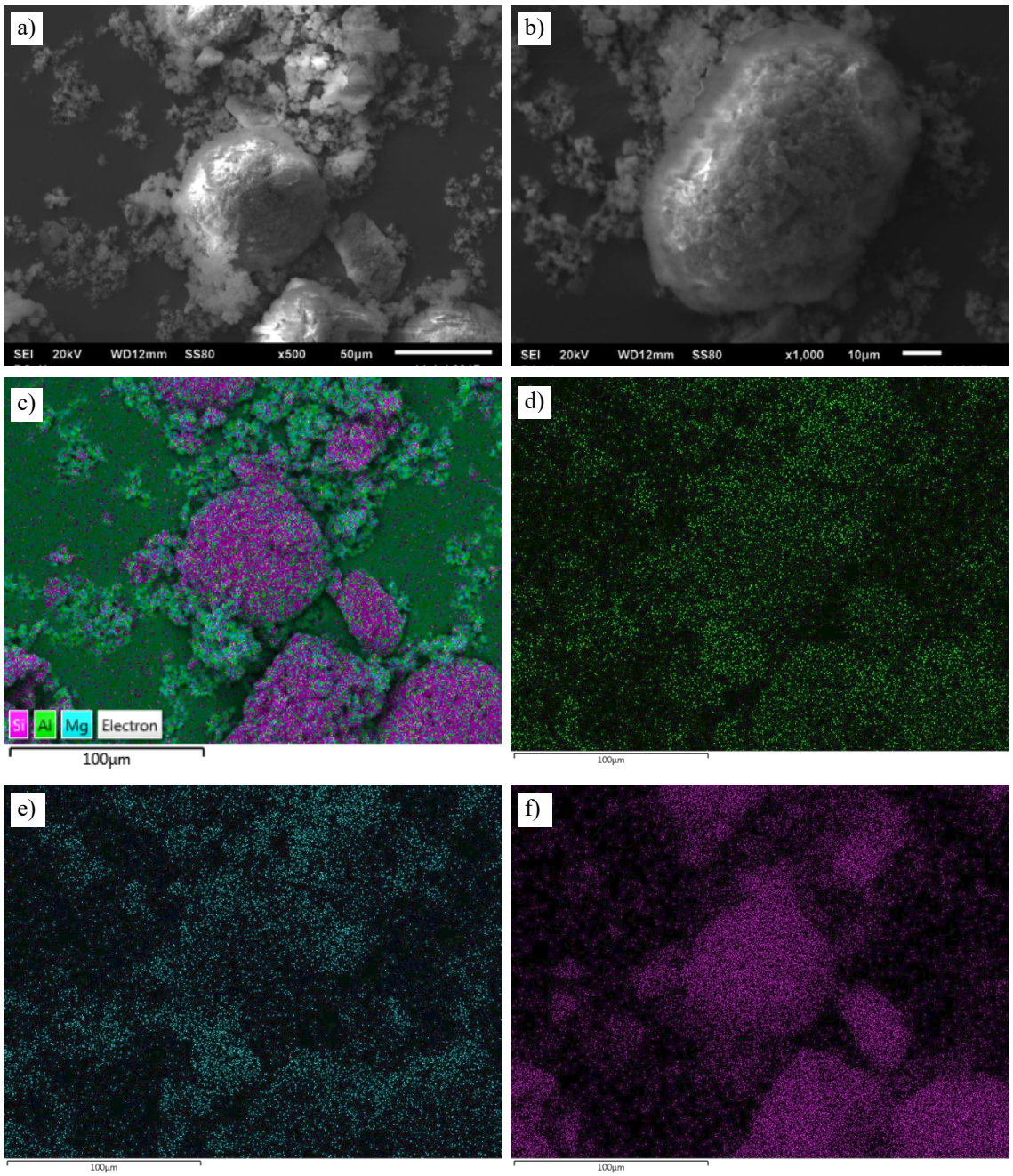


Figure B.100 a) and b) SEM images of SiO_2@Mg_2Al-CO_3-AMO-LDH prepared by *in situ* co-precipitation using PQ ES70Y silica. SEM-EDX c) layered image and analyses of d) Al, e) Mg, and f) Si. Metal addition rate = 1.0 cm^3 min^{-1}. Stirring speed = 500 rpm. AMO solvent = EtOH.

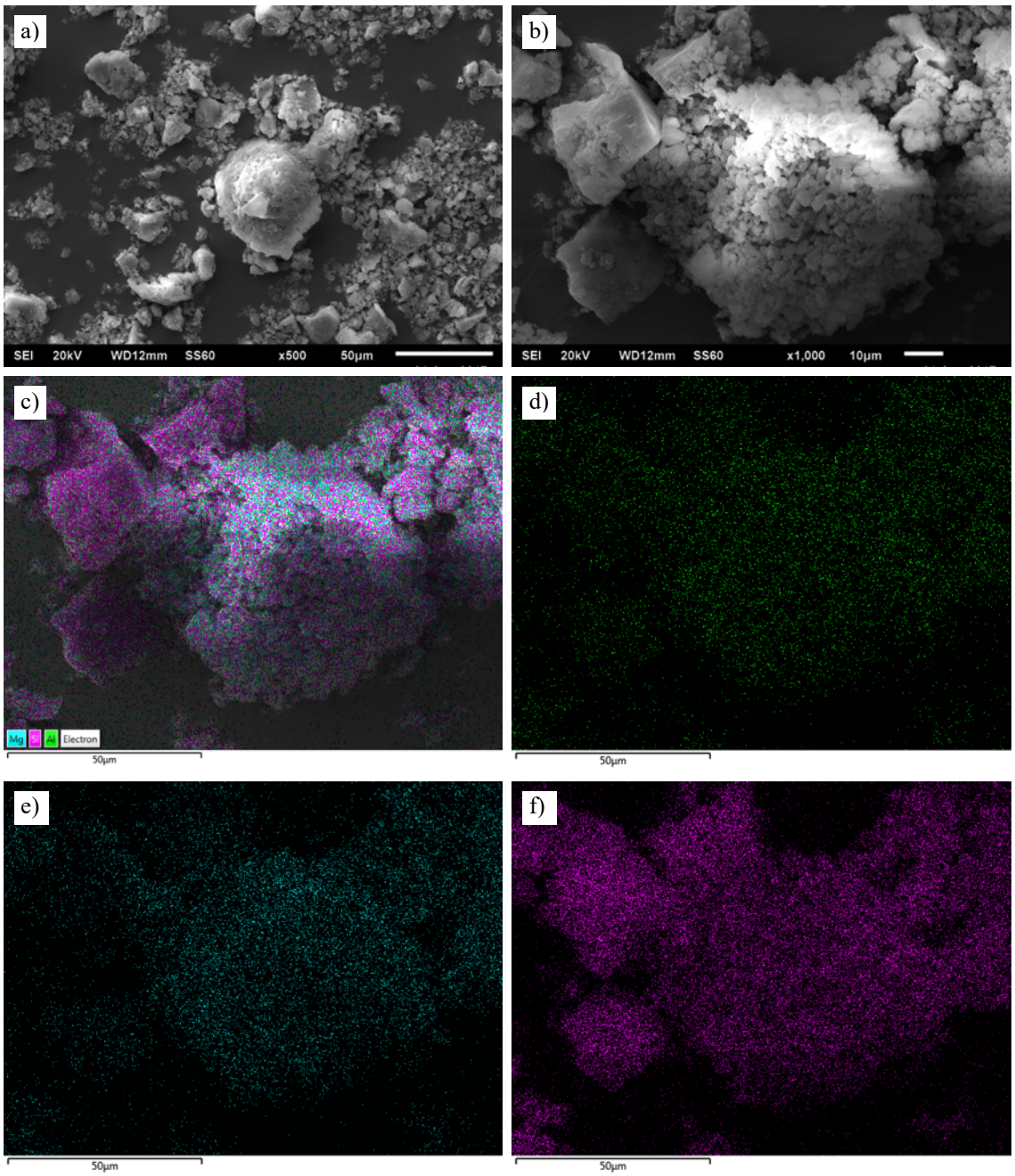


Figure B.101 a) and b) SEM images of SiO_2@Mg_2Al-CO_3-AMO-LDH prepared by the IMP2 method using PQ ES70Y silica. SEM-EDX c) layered image and analyses of d) Al, e) Mg, and f) Si. Metal addition rate = 1.0 cm^3 min^{-1}. Stirring speed = 500 rpm. AMO solvent = EtOH.

B.8 Alternative procedure – urea hydrothermal

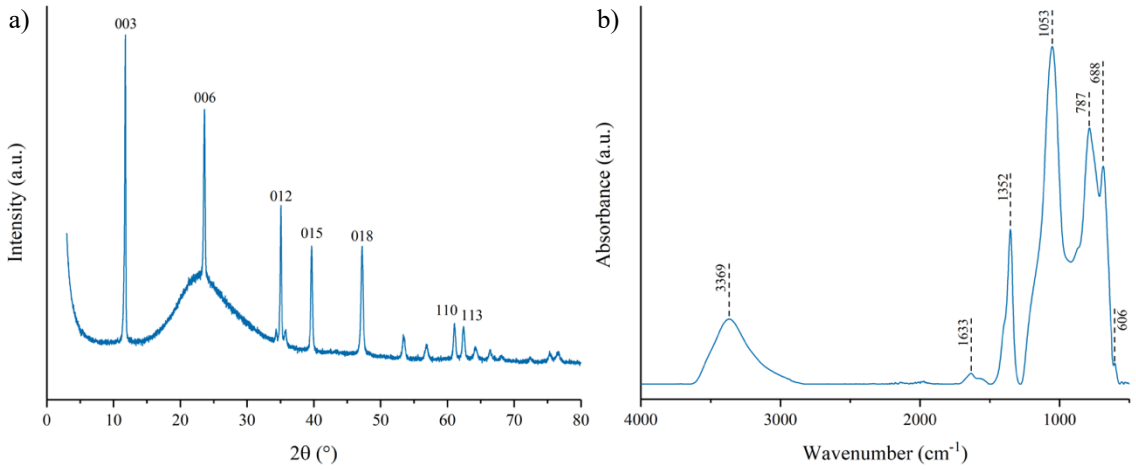


Figure B.102 a) Powder XRD diffractogram and b) FTIR spectrum of SiO_2@Mg_2Al-CO_3-LDH prepared using urea hydrolysis and Grace Davison LC60A 20-45 silica.

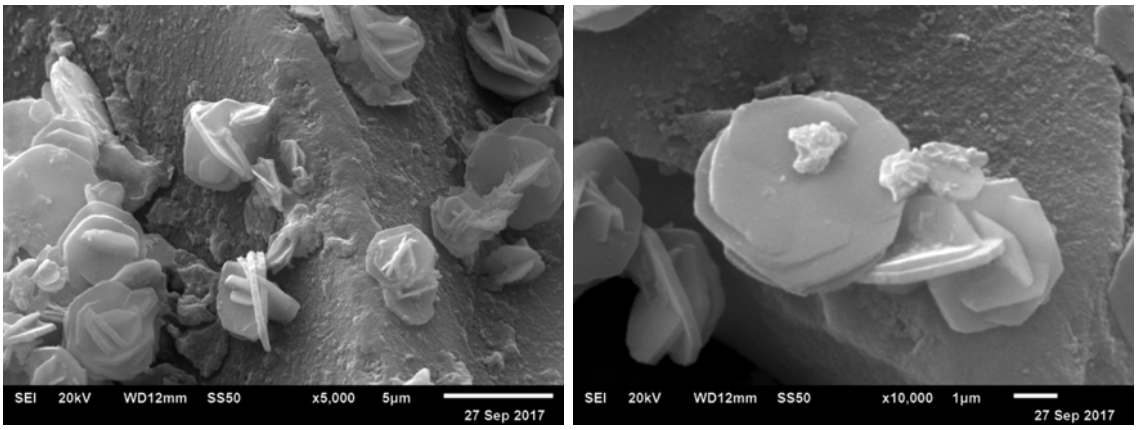


Figure B.103 High magnification SEM images of the surfaces of SiO_2@Mg_2Al-CO_3-LDH prepared by urea hydrolysis using Grace Davison LC60A 20-45 silica.

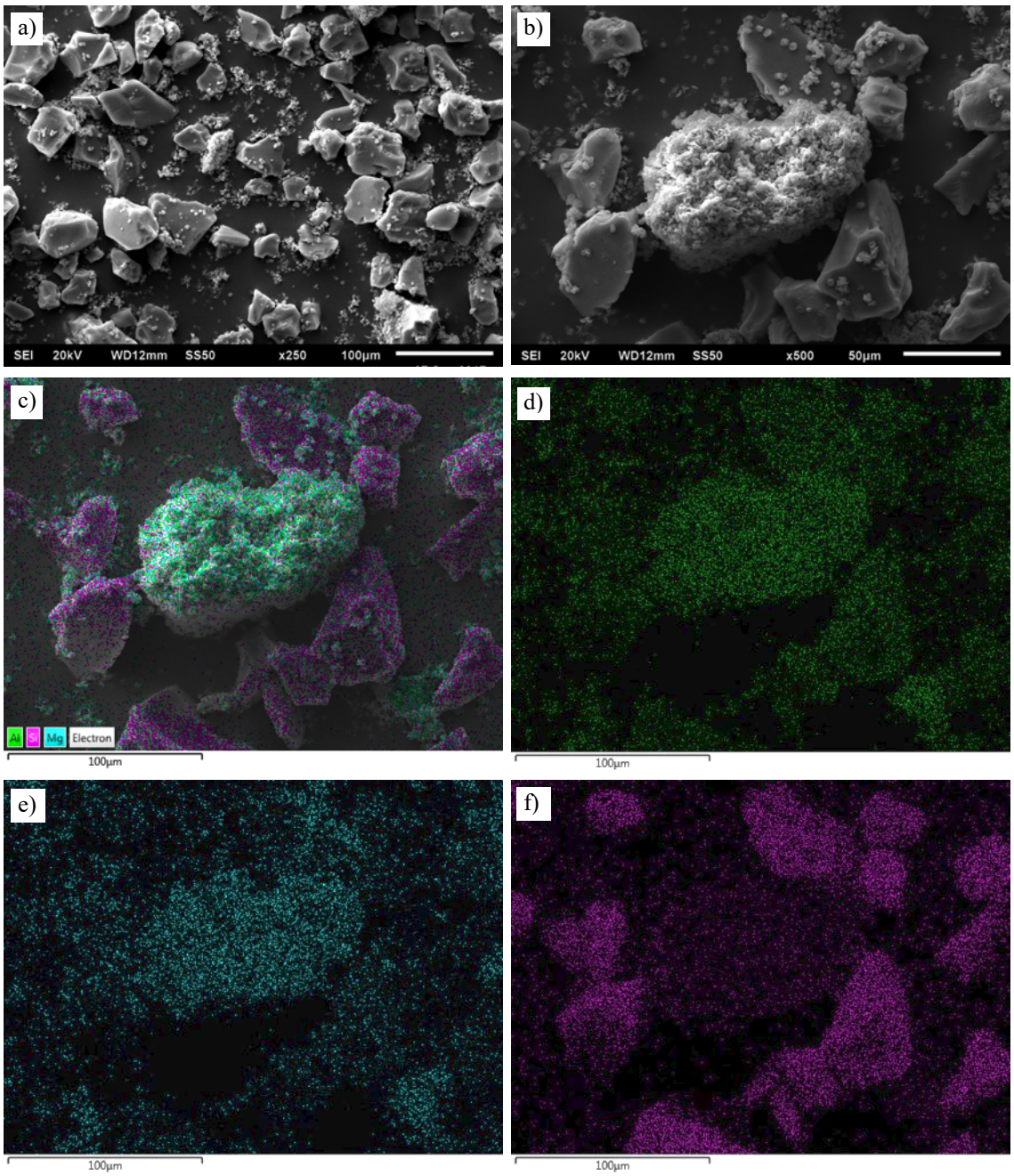


Figure B.104 a) and b) SEM images of SiO_2@Mg_2Al-CO_3-LDH prepared by urea hydrolysis using Grace Davison LC60A 20-45 silica. SEM-EDX c) layered image and analyses of d) Al, e) Mg, and e) Si.

B.9 Reference AMO-LDHs

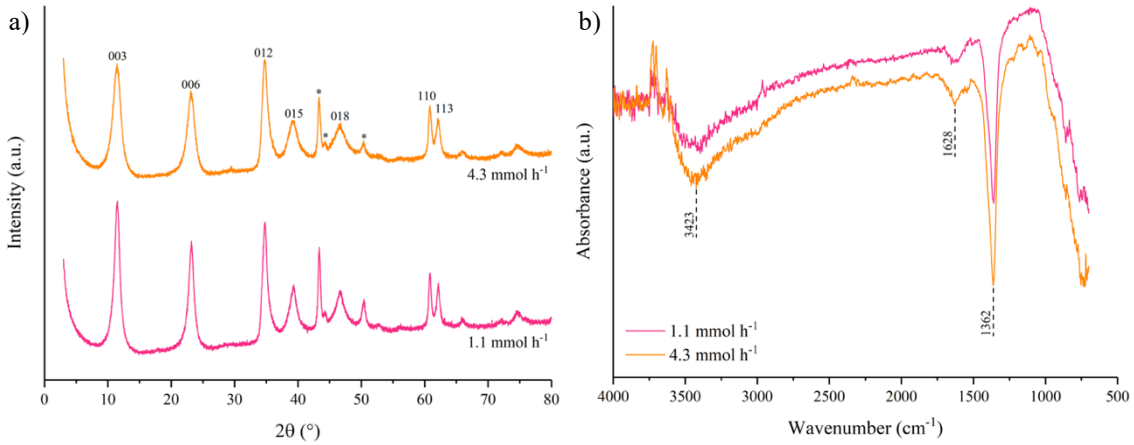


Figure B.105 a) Powder XRD diffractograms and b) FTIR spectra of reference Mg_2Al-CO_3-AMO-LDHs prepared under the same *in situ* co-precipitation conditions as the core-shell materials. Stirring speed = 500 rpm. AMO solvent = EtOH.

Table B.31 Lattice parameters and mean CDLs of reference Mg_2Al-CO_3-AMO-LDHs prepared under the same *in situ* co-precipitation conditions as the core-shell materials. Stirring speed = 500 rpm. AMO solvent = EtOH.

Metal addition rate (mmol h^{-1})	*d*-spacing (Å)		Lattice parameter (Å)		CDL (Å)	
	d_{003}	d_{110}	$c^{\dagger}$	$a^{\ddagger}$	*c*-axis	*ab*-plane
1.1	7.70	1.52	23.10	3.04	799.1	482.3
4.3	7.71	1.52	23.13	3.04	299.8	1606.3

†Lattice parameter $c = 3d_{003}$. ‡Lattice parameter $a = 2d_{110}$.
CDL = $0.89\lambda/\beta\cos\theta$, $\lambda = 1.541847$ Å, β = FWHM in radians.

Table B.32 Powder XRD Bragg reflection data of reference Mg_2Al-CO_3-AMO-LDHs prepared under the same *in situ* co-precipitation conditions as the core-shell materials. Stirring speed = 500 rpm. AMO solvent = EtOH.

Metal addition rate (mmol h^{-1})	003[a] (º)	FWHM[b] (º)	110[c] (º)	FWHM[d] (º)
1.1	11.49	0.10	60.84	0.33
4.3	11.48	0.27	60.82	0.10

[a]Position of the 003 Bragg reflection (2θ), [b]FWHM of the 003 reflection.
[c]Position of the 110 Bragg reflection (2θ), [d]FWHM of 110 reflection.

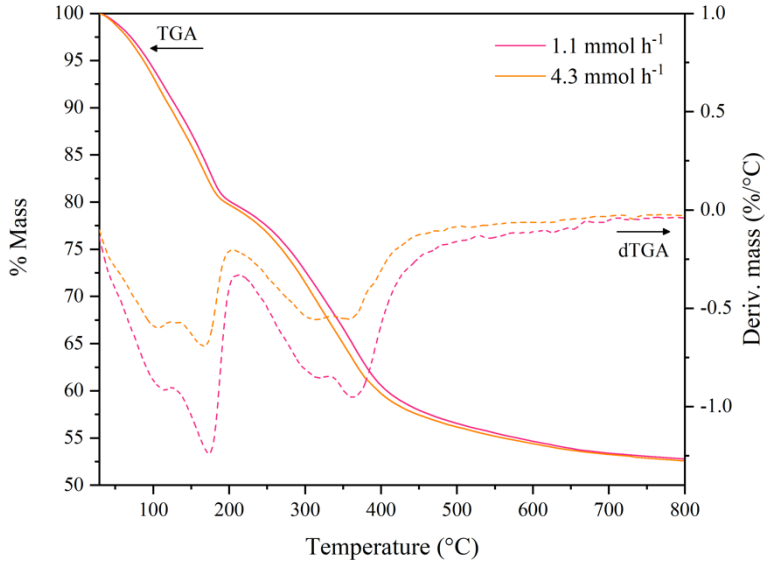


Figure B.106 TGA and dTGA curves of reference Mg_2Al-CO_3-AMO-LDHs prepared under the same *in situ* co-precipitation conditions as the core-shell materials. Stirring speed = 500 rpm. AMO solvent = EtOH.

B.10 Preliminary syntheses of SiO_2@SLDH

Table B.33 ICP-MS elemental analysis of SiO_2@SLDH prepared using the CSS2 method.

Av. wt.%	SiO_2@SLDH
Na	0.8488
Mg	8.9545
Al	3.1594
Si*	0.6026
P	0.5918
K	0.0073
Ca	0.1366
V	0.0001
Cr	0.0005
Mn	0.0003
Fe	0.0129
Co	B.D.L.
Ni	0.0057
Cu	0.0096
Zn	0.0068
As	B.D.L.
Se	0.0003
Mo	B.D.L.
Ag	B.D.L.
Cd	B.D.L.
Sb	B.D.L.
Ba	0.0014
Hg	B.D.L.
Tl	B.D.L.
Pb 208	0.0002
Th	B.D.L.
U	B.D.L.
Av. Mg/Al	2.83

B.D.L. = below detection limit
*acid-soluble fraction

Appendix C:Appendix for Chapter 5

C.1 Calcination of SiO_2@Mg_2Al-CO_3-AMO-LDHs

Table C.1 Powder XRD Bragg reflection data of SiO_2@Mg_2Al-CO_3-AMO-LDHs calcined at different temperatures (Figure 5.3). Synthesis conditions for core-shell: stirring speed = 500 rpm, metal addition rate = 1.1 mmol h^{-1}. Calcination conditions: temperature ramp rate = 5 ºC min^{-1}, hold at temperature for 5 h.

Calcination temperature (ºC)	200[a] (º)	FWHM[b] (º)	220[c] (º)	FWHM[d] (º)
350	43.34	0.23	62.36	0.94
700	43.32	0.20	62.68	1.07

[a]Position of the 200 Bragg reflection (2θ), [b]FWHM of the 200 reflection.
[c]Position of the 220 Bragg reflection (2θ), [d]FWHM of 220 reflection.

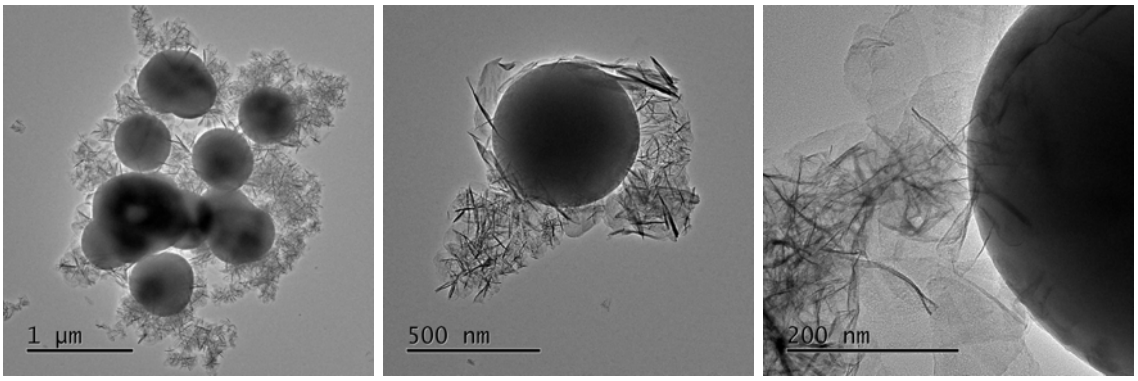


Figure C.1 TEM images of SiO_2@Mg_2Al-CO_3-AMO-LDHs calcined at 350 ºC.

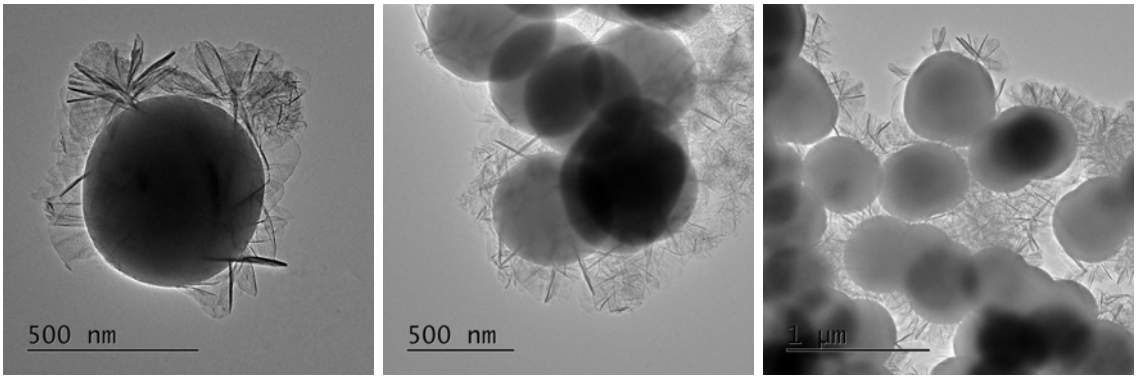


Figure C.2 TEM images of SiO_2@Mg_2Al-CO_3-AMO-LDHs calcined at 700 ºC.

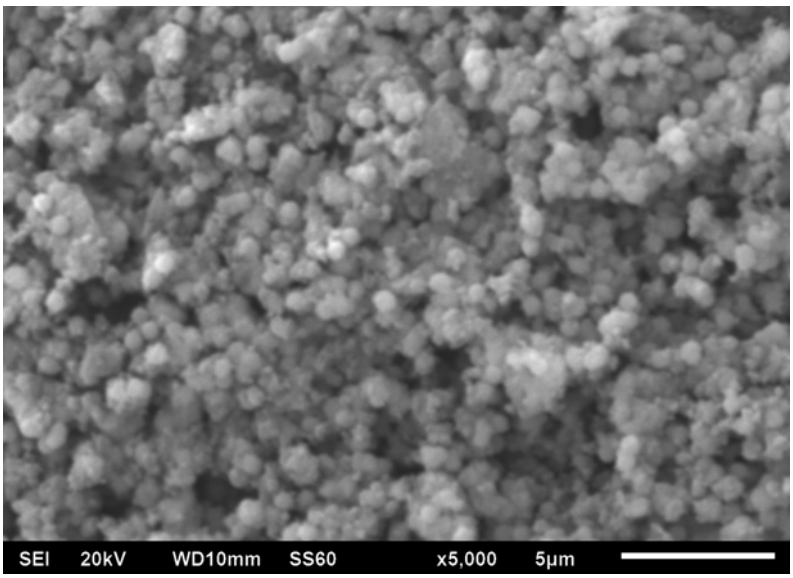


Figure C.3 SEM image of SiO_2@Mg_2Al-CO_3-AMO-LDHs calcined at 350 ºC.

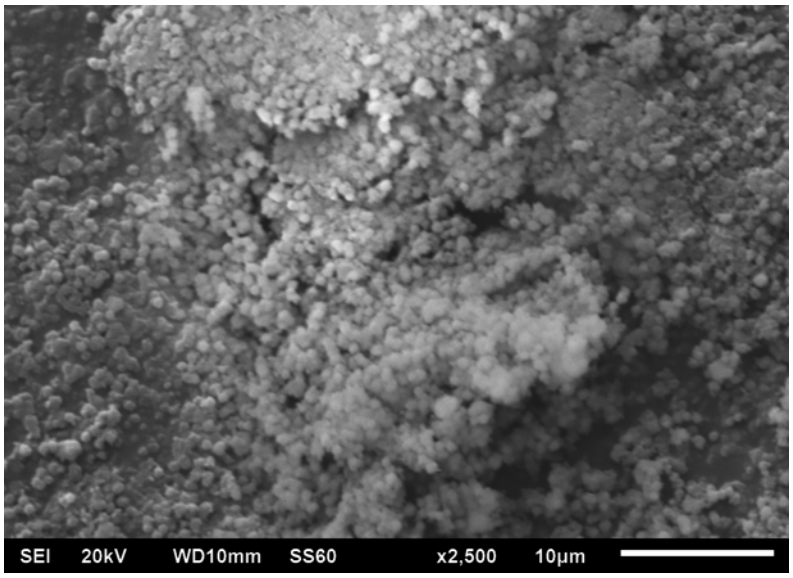


Figure C.4 SEM image of SiO_2@Mg_2Al-CO_3-AMO-LDHs calcined at 700 ºC.

C.2 Calcination of SLDHs

Table C.2 Powder XRD Bragg reflection data for SLDOs prepared from Alfa Aesar M2-85-SLDH (Figure 5.6a). Mg/Al =3.

Calcination temp. (ºC)	003[a] (º)	FWHM[b] (º)	200[c] (º)	FWHM[d] (º)
200	12.94	1.38	-	-
400	-	-	43.10	3.34
600	-	-	43.26	2.58
800	-	-	43.19	2.17

[a]Position of the 003 Bragg reflection (2θ) of the dehydrated SLDH, [b]FWHM of the 003 reflection.
[c]Position of the 200 Bragg reflection (2θ) of the MgO phase, [d]FWHM of 200 reflection.

Table C.3 Powder XRD Bragg reflection data for SLDOs prepared from NuReSys M2-85-SLDH (Figure 5.6b). Mg/Al =3.

Calcination temp. (ºC)	003[a] (º)	FWHM[b] (º)	200[c] (º)	FWHM[d] (º)
200	12.95	1.63	-	-
400	-	-	43.11	3.40
600	-	-	43.32	2.65
800	-	-	43.27	2.14

[a]Position of the 003 Bragg reflection (2θ) of the dehydrated SLDH, [b]FWHM of the 003 reflection.
[c]Position of the 200 Bragg reflection (2θ) of the MgO phase, [d]FWHM of 200 reflection.

C.3 Reference LDH

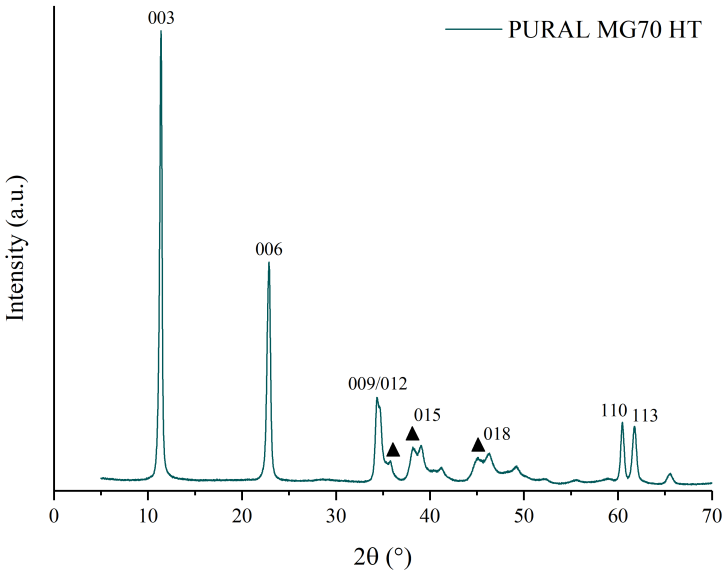


Figure C.5 Powder XRD diffractogram of the commercial LDH (Sasol PURAL MG70 HT). ▲Al_2O_3. This LDH is prepared from a physical mixture of MgO and Al_2O_3.

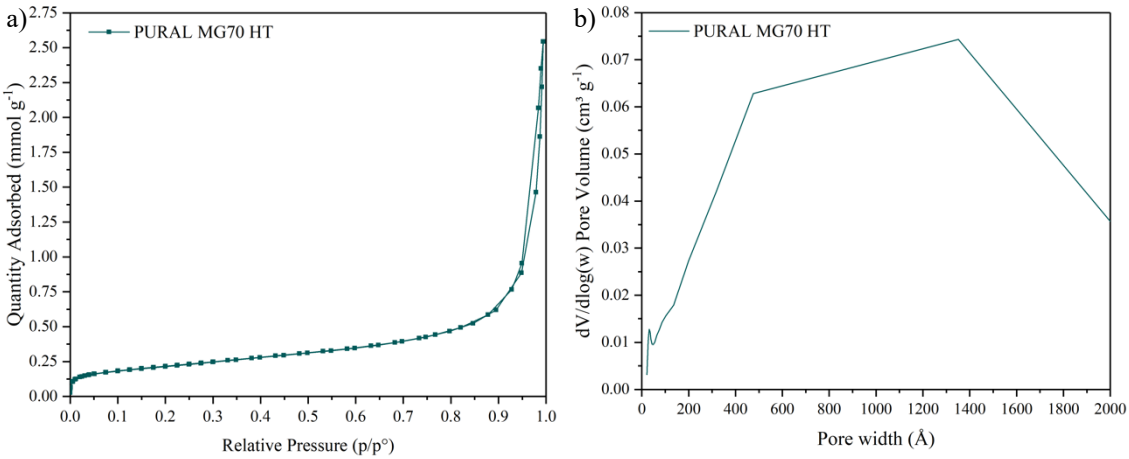


Figure C.6 a) N_2 adsorption and desorption isotherms and b) BJH pore size distribution of PURAL MG70 HT.

C.4 CO_2 adsorption – TGA measurement

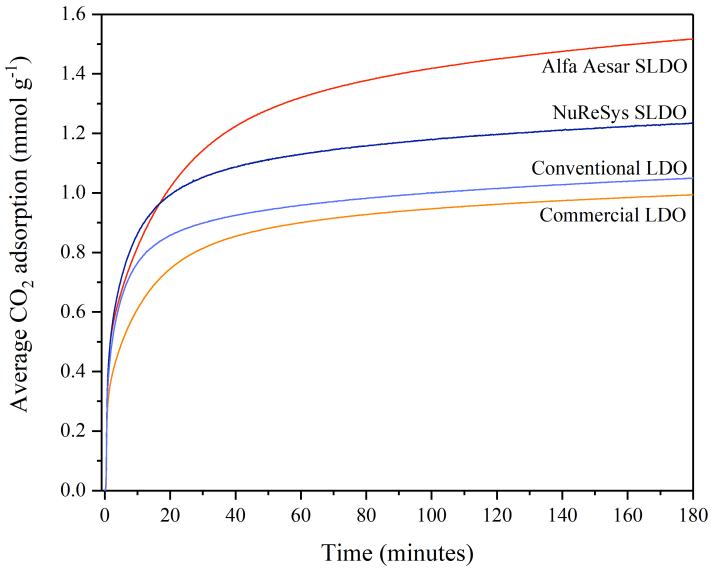


Figure C.7 CO_2 adsorption as a function of time by various LDOs. LDOs were calcined *in situ* at 400 ºC (ramp rate = 5 ºC min^{-1}, hold 2 h, 100 cm^3 min^{-1} N_2) and adsorption was measured at 30 ºC (100 cm^3 min^{-1} 20:80 CO_2:N_2).